

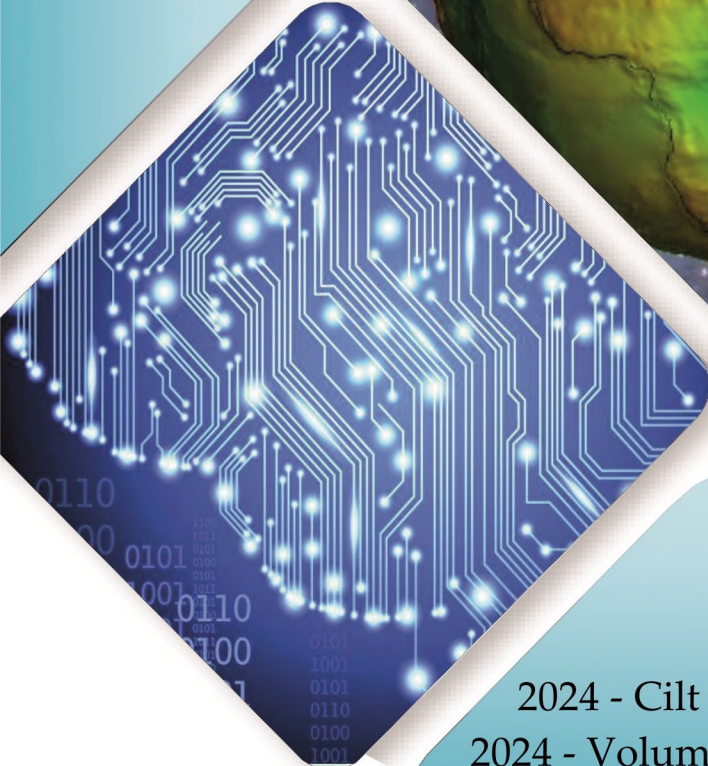


Konya Mühendislik Bilimleri Dergisi

Konya Journal of Engineering Sciences



(KONJES)
E-ISSN: 2667-8055



2024 - Cilt : 12 - Sayı : 3
2024 - Volume : 12 - Issue : 3

KONYA JOURNAL OF ENGINEERING SCIENCES (KONJES)
KONYA MÜHENDİSLİK BİLİMLERİ DERGİSİ

HAKEMLİ DERGİDİR

OWNER/SAHİBİ

Owner on Behalf of Engineering and Natural Sciences Faculty of Konya Technical University **Prof. Dr. Ali KÖKEN** Konya Teknik Üniversitesi Mühendislik ve Doğa Bilimleri Fakültesi Adına Dekan **Prof. Dr. Ali KÖKEN**

Editor-in-Chief/Şef Editör

Prof. Dr. Mustafa TABAKCI

Editors/Editörler

Prof. Dr. Halife KODAZ

Assoc. Prof. Dr. Ömer Kaan BAYKAN

Section Editors/Alan Editörleri

Prof. Dr. Niyazi B L M

Prof. Dr. Volkan KALEM

Assoc. Prof. Dr. Farabi TEMEL

Assoc. Prof. Dr. smail NCE

Assoc. Prof. Dr. Ömer Kaan BAYKAN

Assoc. Prof. Dr. Selim DO AN

Assoc. Prof. Dr. Sercan BÜLBÜL

Assist. Prof. Dr. Alper DÖYEN

Assist. Prof. Dr. Cihangir KÖYCE Z

Assist. Prof. Dr. Kemal ERDO AN

Assist. Prof. Dr. Muhammed Arif EN

Assist. Prof. Dr. Muharrem Hilmi AKSOY

Advisory Board/Danışma Kurulu

Prof.Dr. Ferruh YILDIZ, Konya Technical University

Prof.Dr. Reşat ULUSAY, Hacettepe University

Prof.Dr. Ibaraki SOICHI, Kyoto University

Prof.Dr. Matchavariani LIA, Tbilisi State University

Prof.Dr. Seref SAGIROGLU, Gazi University

Prof.Dr. Vijay P. SINGH, Texas A and M University

Prof.Dr.-Ing. Rudolf STAIGER, Bochum University of Applied Sciences

Prof.Dr. Chryssy POTSIU, National Technical University of Athens

Prof.Dr. Lena HALOUNOVA, Czech Technical University

Prof.Dr. Petros PATIAS, The Aristotle University

Prof.Dr. Sitki KULUR, Istanbul Technical University

Language Editing/Yabancı Dil Editörü

Prof. Dr. Ali BERKTAY

Secretary/Sekreter

Assist. Prof. Dr. Emel Zeray ÖZTÜRK

Composition and Printing/Baskı ve Dizgi

Assist. Prof. Dr. smail KOÇ

Res. Assist. Emir Ali D NSEL

Res. Assist. Aybüke BABADA

Correspondance Address/ Yazışma Adresi

Konya Teknik Üniversitesi Mühendislik ve Doğa Bilimleri Fakültesi Dekanlığı
42075-Kampüs, Selçuklu, Konya-TURKEY

Tel : 0 332 223 88 18

Fax : 0 332 241 06 35

E-mail : konjes@ktun.edu.tr

Web : <http://dergipark.org.tr/konjes>

Editorial Board/Yayın Kurulu

Ahmet Afsin Kulaksiz, Konya Technical University, TURKEY

Alla Anohina-Naumeca, Riga Technical University, LATVIA

Ashok K. Mishra, Clemson University, USA

Baris Binici, Middle East Technical University, TURKEY

Coskun Bayrak, University of Arkansas, USA

Demetrio Fuentes Ferrera, University of Castilla-La Mancha, SPAIN

Fahrettin Ozturk, The Petroleum Institute, UAE

Haci Murat Yilmaz, Aksaray University, TURKEY

Heinz Ruther University of Cape Town, SOUTH AFRICA

Homayoun Moghimi, Payame Noor University, IRAN

Ihsan Ozkan, Konya Technical University, TURKEY

John Trinder, The University of New South Wales, AUSTRALIA

Kerim Kocak, Konya Technical University, TURKEY

Loredana Judele, Technical University of Iasi, ROMANIA

Mohamed Bouabaz, Université 20 août 1955-Skikda, ALGERIA

Mohd Arif Wani, California State University, USA

Mortaza Yari, University of Tabriz, IRAN

Ömer Aydan, University of the Ryukyus, JAPAN

Sanchoy K. Das, New Jersey Institute of Technology, USA

Selim Dogan, Konya Technical University, TURKEY

Spase Shumka, Agricultural University of Tirana, ALBANIA

Tahira Geroeva, Baku State University, AZERBAIJAN

Vladimir Androkhonov, Novosibirsk Soil Research Institute, RUSSIA

Ali Kocak, Yildiz Technical University, TURKEY

Alpaslan Yazar, Konya Technical University, TURKEY

Ataur Rahman, University of Western Sydney, AUSTRALIA

Cihan Varol Sam Houston State University, USA

Dan Stumbea, Alexandru Ioan Cuza University of Iasi, ROMANIA

Eva Burgetova, Czech Technical University, CZECH REPUBLIC

Georgieva Lilia, Heriot-Watt University, UNITED KINGDOM

Halil Kursad Ersoy, Konya Technical University, TURKEY

Hi-Ryong Byun, Pukyong National University, SOUTH KOREA

Huseyin Devenci, Konya Technical University, TURKEY

Iraida Samofalova, Perm University, RUSSIA

Juan Maria Menendez Aguado, University of de Oviedo, SPAIN

Laramie Vance Potts, New Jersey Institute of Technology, USA

Mila Koeva, University of Twente, NETHERLANDS

Mohamed Metwaly Abu Anbar, Tanta University, EGYPT

Moonis Ali Khan, King Saud University, KSA

Murat Karakus, University of Adelaide, AUSTRALIA

Saadettin Erhan Kesen, Konya Technical University, TURKEY

Selcuk Kursat Isleyen, Gazi University, TURKEY

Shukri Maxhuni, Prizen University, KOSOVA REPUBLIC

Syed Tufail Hussain Sherazi, University of Sindh, PAKISTAN

Thomas Niedoba, AGH University of Science and Technology, POLAND

Zoran Sapuric, University American College Skopje, MACEDONIA

KONYA MÜHENDİSLİK BİLİMLERİ DERGİSİ
Konya Journal of Engineering Sciences
(KONJES)

ISSN 2667 – 8055 (Elektronik/Electronic)

Cilt	12	Eylül	2024	Sayı	3
Volume	12	September	2024	Issue	3

İÇİNDEKİLER (CONTENTS)

Araştırma Makalesi (Research Article)

INITIATED CHEMICAL VAPOR DEPOSITION (iCVD) OF POLY(ACRYLIC ACID): A COMPARISON BETWEEN CONTINUOUS AND CLOSED-BATCH iCVD APPROACHES

Kurtuluş YILMAZ, Emine SEVGİLİ MERCAN, Mehmet GÜRSOY, Mustafa KARAMAN 586-595

UNCERTAINTY EVALUATION USING LAW OF PROPAGATION AND MONTE CARLO SIMULATION METHODS WITH THE AUTOREPOWER MEASUREMENT SOFTWARE

Erkan DANACI, Aliye KARTAL DOĞAN, Engin Can CICEK, Anil CETINKAYA, Muhammed Cagri KAYA, M.S. Halit OGUZTUZUN, Gulsun TUNAY 596-607

EFFECT OF CHEMICAL MODIFICATION OF MULTIWALL CARBON NANOTUBES ON THE PROPERTIES OF POLY(LACTIC ACID) COMPOSITE FILMS: SYNTHESIS AND CHARACTERIZATION

Figen ARSLAN, Şükran Melda ESKİTOROS TOĞAY 608-629

A COMPARATIVE ANALYSIS OF LAND FRAGMENTATION, CONSOLIDATION PRACTICES AND POLICY RESPONSES IN TÜRKİYE AND KYRGYZSTAN

Ainura BATYKOVA, Orhan ERCAN, Tamchybek TULEEV, Ahmet Hilmi ERCİYES 630-651

TRAJECTORY TRACKING CONTROL OF A TWO WHEELED SELF-BALANCING ROBOT BY USING SLIDING MODE CONTROL

Mustafa DOĞAN, Ümit ÖNEN 652-670

A 3D U-NET BASED ON EARLY FUSION MODEL: IMPROVEMENT, COMPARATIVE ANALYSIS WITH STATE-OF-THE-ART MODELS AND FINE-TUNING

Beyza KAYHAN, Sait Ali UYMAZ 671-686

SYNTHESIS OF P(N-ISOPROPYL ACRYLAMIDE - HYDROXYPROPYL METHACRYLATE) THERMO RESPONSIVE COPOLYMER FILMS BY INITIATED CHEMICAL VAPOR DEPOSITION METHOD

Emine SEVGİLİ MERCAN, Kurtuluş YILMAZ, Mustafa KARAMAN 687-699

A DEEP LEARNING ENSEMBLE APPROACH FOR X-RAY IMAGE CLASSIFICATION

Engin ESME, Mustafa Servet KIRAN 700-713

REFRACTIVE INDEX BASED DETECTION WITH A HIGH SENSITIVITY BIOSENSOR ENHANCED BY GRAPHENE Ahmet Murat ERTURAN, Seyfettin Sinan GÜLTEKİN	714-724
INVESTIGATION OF THE EFFECT OF ANNUAL AVERAGE TEMPERATURE AND PRECIPITATION CHANGES ON CORS-TR STATIONS: THE CASE OF KSTM STATION Alparslan ACAR, Sercan BÜLBÜL, Fuat BAŞÇİFTÇİ, Ömer YILDIRIM	725-736
THEORETICAL INVESTIGATION FOR YTTERBIUM EFFECT ON RADIATION SHIELDING CHARACTERISTICS OF 50Bi₂O₃-15Li₂O-15PbO-(20-X)B₂O₃-Yb₂O₃ BORATE GLASSES Murat AYGÜN, Zeynep AYGÜN, İbrahim HAN, Emine NARMANLI HAN	737-755
ESTIMATING THE SOLAR EXERGY POTENTIAL OF SURFACES WITH DIFFERENT TILT ANGLES Ahmet KABUL, Fatih YİĞİT, Aslı DURAN	756-772
ADVANCING MEMORY DENSITY: A NOVEL DESIGN FOR MULTIPLE-BIT-PER-CELL PHASE CHANGE MEMORY İbrahim CINAR	773-782
DETERMINATION OF THE CARBON FOOTPRINT OF ANIMAL WASTE AND CLIMATE CHANGE; KARAMAN EXAMPLE Yusuf Alparslan ARGUN, Özgür ÇAKMAKCI	783-800

Derleme Makalesi (Review Article)

THE EFFECT OF CUTTING FORCES ON BONE RELATED OPERATIONAL PROCESSES: A LITERATURE REVIEW Yusuf Çağlar KAĞITCI, Süleyman NEŞELİ	801-821
---	---------



INITIATED CHEMICAL VAPOR DEPOSITION (iCVD) OF POLY(ACRYLIC ACID): A COMPARISON BETWEEN CONTINUOUS AND CLOSED-BATCH iCVD APPROACHES

^{1,*} Kurtuluş YILMAZ , ² Emine SEVGİLİ MERCAN , ³ Mehmet GÜRSOY , ⁴ Mustafa KARAMAN 

*Konya Technical University, Engineering and Natural Science Faculty, Chemical Engineering Department,
Konya, TÜRKİYE*

¹ kurtulusyilmaz3@gmail.com, ² esmercan@ktun.edu.tr, ³ mgursoy@ktun.edu.tr, ⁴ mkaraman@ktun.edu.tr

Highlights

- In this study, PAA films were successfully deposited by iCVD method.
- Closed-batch iCVD approach allows the fabrication of more smooth film surface.
- The amount of monomer consumed in the closed batch iCVD method was 18 times less than that of continuous iCVD method.



INITIATED CHEMICAL VAPOR DEPOSITION (iCVD) OF POLY(ACRYLIC ACID): A COMPARISON BETWEEN CONTINUOUS AND CLOSED-BATCH iCVD APPROACHES

^{1,*} Kurtuluş YILMAZ , ² Emine SEVGİLİ MERCAN , ³ Mehmet GÜRSOY , ⁴ Mustafa KARAMAN 

*Konya Technical University, Engineering and Natural Science Faculty, Chemical Engineering Department,
Konya, TÜRKİYE*

¹ kurtulusyilmaz3@gmail.com, ² esmercan@ktun.edu.tr, ³ mgursoy@ktun.edu.tr, ⁴ mkaraman@ktun.edu.tr

(Received: 08.01.2024; Accepted in Revised Form: 10.05.2024)

ABSTRACT: In this study, poly(acrylic acid) (PAA) thin films were deposited on silicon wafer and glass surfaces by initiated chemical vapor deposition (iCVD) method using di-tert-butyl peroxide (TBPO) as the initiator and acrylic acid (AA) as the monomer. During iCVD, two different precursor feeding approaches, namely continuous and closed-batch, were employed. The effects of substrate temperature and the precursor feeding approaches on the deposition rates and surface morphology of the films were investigated. The highest deposition rates for the continuous and closed-batch iCVD approaches were found as 26.1 nm/min and 18.6 nm/min, respectively, at a substrate temperature of 15 °C. FTIR analysis of the films deposited by both approaches indicated high structural retention of the monomer during the polymerization. AFM results indicated that, PAA thin films possessed low RMS roughness values of 2.76 nm and 1.84 nm using continuous and closed-batch iCVD, respectively. Due to the slightly higher surface roughness of the film deposited under continuous iCVD, that film exhibited a lower water contact angle of 16.1° than the film deposited in closed-batch iCVD. In terms of monomer utilization ratio, closed-batch system was found to be more effective, which may help to minimize the carbon footprint of iCVD process.

Keywords: Poly(acrylic acid), Thin film, Hydrophilic, Chemical vapor deposition, iCVD

1. INTRODUCTION

Poly(acrylic acid) (PAA), which is obtained by polymerization of acrylic acid monomer and is commercially available in powder form, has a wide range of industrial applications. PAA has a hydrophilic structure that has a high capacity for the retention of water molecules thanks to the carboxyl (-COOH) groups in its structure. Its easy solubility in water, non-toxicity, biodegradability, biocompatibility and excellent optical properties make PAA an important material for various applications such as superabsorbents, adhesives, pharmaceuticals, drug delivery, water treatment, personal care products, coatings and packaging [1-5]. Cross-linked PAAs with a more stable structure and superior mechanical properties can be used in applications where linear PAAs cannot be used. For example, linear PAA thin films do not offer a permanent solution for anti-fog applications because they are not resistant to water vapor. However, cross-linked PAA thin films show excellent anti-fog properties [6].

In general, PAA is synthesized commercially in nano/micro particulate, gel, and thin film forms. Thin films of PAA on various surfaces can be formed using two different approaches, namely solvent-based (wet) and vapor-based (dry) processes. Solvent-based methods do not require specialized and expensive equipment, that is why they are widely used. Solvent-based methods for producing PAA homopolymers and copolymers include reversible addition fragmentation chain transfer (RAFT) polymerization [7], atom transfer radical polymerization (ATRP) [8], electrochemically induced free radical polymerization [9], living radical polymerization [10], sol-gel [11], photopolymerization [12] and electrospinning [13]. Nevertheless, there are a number of serious drawbacks to solvent-based techniques, including the need for several time-consuming steps and the possibility of solvent surface damage. In addition, the use of solutions in solvent-based methods can cause environmental and health problems. Environmentally friendly chemical vapor deposition (CVD) technique, as a vapor-based method, eliminate solvent related

*Corresponding Author: Kurtuluş YILMAZ, kurtulusyilmaz3@gmail.com

problems. CVD offers many advantages such as being a single-step process with short synthesis time, low temperature, substrate independence, adjustable film thickness and scalability [14, 15].

It is possible to produce PAA thin films by two different CVD methods: Plasma enhanced chemical vapor deposition (PECVD) and initiated chemical vapor deposition (iCVD). In PECVD polymerization, the activation energy required to initiate polymerization is provided by plasma discharge. However, high power plasma may lead to the fragmentation of the monomers, which may cause the loss of the functional groups. Furthermore, ion bombardment during PECVD may cause a decrease in the deposition rate [16]. In iCVD process, plasma-induced problems are minimized by the use of heated filaments to initiate the polymerization process. In addition to the monomer, initiator, which has chemical bonds that can be easily radicalized at low temperatures, is fed into the chamber. The presence of initiator ensures the production of polymer thin films with highly functional groups at low temperatures [17].

In this study, iCVD technique was used for the synthesis of PAA thin films. The high-vapor pressure (4 mmHg at 20°C) of acrylic acid (AA) makes it a suitable monomer for iCVD processes. Acrylic acid monomer can be fed into the reactor by evaporation at 23°C ambient temperature, without the need for heating and without the need for a carrier gas. The effect of substrate temperature in PAA synthesis and the effect of continuous or batch chemical feed to the reactor on the deposition rate were investigated. For the first time in literature, a comparison between two monomer feeding approach, namely continuous and closed-batch, were made; and it was shown that closed-batch approach is effective in terms of monomer utilization ratio.

2. MATERIAL AND METHODS

2.1 Materials

Monomer AA (98% purity) and initiator di-tert-butyl peroxide (TBPO) (98% purity) were purchased from Aldrich. The precursors were used without any further purification process. Silicon wafer (University Wafer, 725 μm thickness, (100), p-type and 10–20 $\Omega\cdot\text{cm}$) and glass slide (ISOLAB) were used as substrates. The chemical structures of precursors are displayed in Figure 1(a).

2.2 Methods

A schematic diagram of the custom-built iCVD reactor that was used in this study is given in Figure 1(b). A more detailed description of iCVD process is given elsewhere [18]. Substrates were placed on the bottom of the reactor, which was cooled by water from a recirculating chiller (Lab Comp., RW-0525G), with the substrate temperature adjustable between 15 and 30°C. The reactor has a 2.5 cm thick quartz top plate which allows in-situ monitoring of the film thickness using a laser interferometry system. In the interferometry, the intensity of a diode laser (Huanic, DI650-1-5) with a wavelength of 650 nm light from the silicon wafer was measured using a laser power meter (Thorlabs). A vacuum was created in the reactor using a rotary vane vacuum pump (Edwards RV12). The chamber pressure was measured using a capacitive pressure sensor (MKS Baratron) and for all depositions the initial pressure set values were adjusted to be at 600 mTorr. The pressure during deposition was controlled and maintained at the desired level by a PID-controlled butterfly valve (MKS) placed between the reactor and the vacuum pump. The heat energy required to initiate polymerization during iCVD was provided by heating a 12-turn tungsten (Alfa Aesar, 99.9%) filament array that was suspended 2.5 cm above the sample surface to be deposited using a variac (Varsan). The K-type thermocouple (Omega) was used to measure the temperature of a randomly selected wire. The temperature of the filament and reactor wall were both kept constant at 230°C and 36°C, respectively. The AA monomer and TBPO initiator were evaporated at 23°C ambient temperature in two separate stainless-steel vessels and their vapors were introduced into the reactor at ambient temperature via needle valves. Two different precursor feeding approaches were employed during iCVD polymerization. In the first one, the precursors were fed to the reactor and the by-product vapors were pumped-out of the reactor in continuous manner. In the second one, the precursors were fed

to the reactor sequentially until desired pressure was reached and then the reactor in and out valves were all closed [19]. The former way of deposition is named as continuous, and the latter one is named as closed-batch. In continuous system, iCVD films were deposited at an AA flow rate of 0.95 sccm, and a TBPO flow rate of 0.95 sccm with a filament temperature of 230 C. The same filament temperature was used in closed-batch iCVD, also. The experimental details of the iCVD deposition of PAA are summarized in Table 1.

Table 1. iCVD parameters used in the experiments of this study.

Sample name	Precursor flow approach	Substrate temperature (°C)	AA / TBPO ratio	Reactor pressure (mtorr)
PAA1	Continuous	15	1/1	600
PAA2	Continuous	20	1/1	600
PAA3	Continuous	25	1/1	600
PAA4	Continuous	30	1/1	600
PAA5	Closed-batch	15	1/1	600
PAA6	Closed-batch	20	1/1	600
PAA7	Closed-batch	25	1/1	600
PAA8	Closed-batch	30	1/1	600

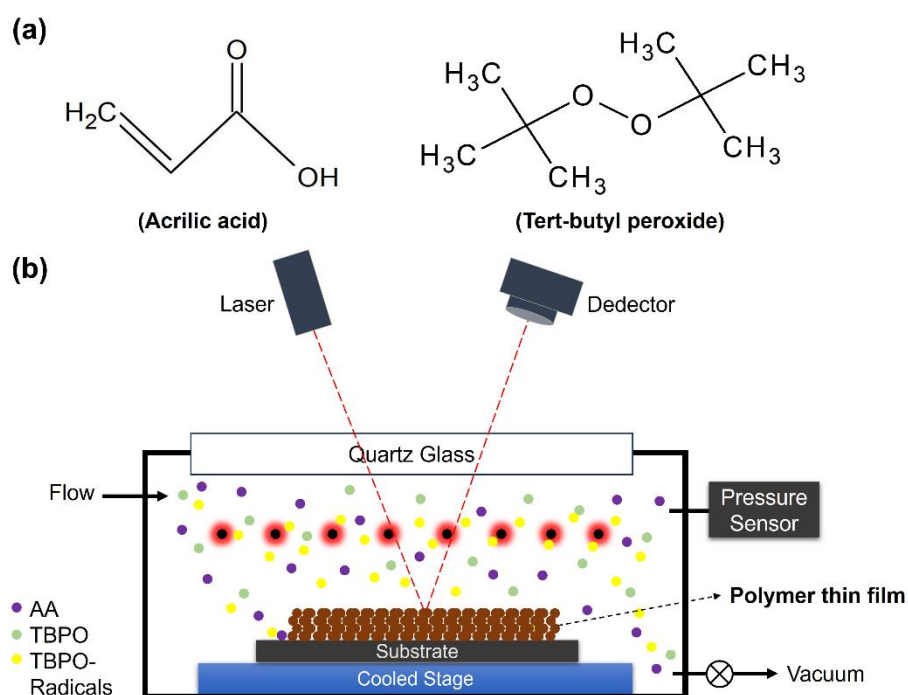


Figure 1. a) Chemical structures of the precursors used in this study, b) schematic diagram of the iCVD reactor

2.3 Characterizations

The chemical structures of the as-deposited PAA thin films were characterized by FTIR spectrophotometer (Thermo Scientific, Nicolet iS 10), which performed a total of 32 scans at 4 cm⁻¹ resolution between 400–4000 cm⁻¹ wavenumbers. The surface topographies and roughness values of the as-deposited PAA thin films on silicon wafers were analyzed by AFM (NT-MDT) in semi-contact mode with a scanning area of 10 × 10 μm². To confirm the interferometric thickness measurements of PAA thin films, an ex-situ film thickness measurement was carried out with a thin film reflectometer (Avantes Avaspec-ULS2048L). Water contact angle analysis was performed of the as-deposited PAA thin films

coated silicon wafer using 4.0 μL of DI water and a video capture system (Kruss Easy Drop). PAA thin film optical transmission spectra were obtained in the 400–800 nm wavelength range using a UV/vis spectrophotometer (Shimadzu UV-1800) with a spectral resolution of 1 nm.

3. RESULTS AND DISCUSSION

The effect of substrate temperature and feeding approaches of precursors into the reactor on the deposition rates at constant pressure and monomer/initiator ratio was investigated and the results are summarized in Figure 2. The reported deposition rates in Figure 2 were obtained by dividing the thickness of as-deposited film on the silicon wafer by the total deposition time. The deposition rates of PAA thin films deposited by the continuous iCVD method were calculated to be 26.1, 20, 15.8 and 12.4 nm/min at substrate temperatures 15, 20, 25 and 30 $^{\circ}\text{C}$, respectively. The films deposited under closed-batch conditions were deposited at rates of 18.6, 15.3, 10.4 and 8.5 nm/min at substrate temperatures 15, 20, 25 and 30 $^{\circ}\text{C}$, respectively. The lower deposition rates in closed-batch approach as compared to the continuous approach can be attributed to the decrease in the concentration of the precursor as reactants are consumed with time [19, 20]. In continuous approach, since the precursors are continuously fed to the reactor, constant reactant concentrations are achieved, which in turn keeps the deposition rates constant and high. In that perspective, it can be said that continuous approach is advantageous in terms of the deposition rates. However, in terms of the monomer consumption amount, which we define as the amount of monomer consumed per 100 nm as-deposited film, the closed batch configuration appeared to be more advantageous. In closed-batch approach, only 37.8 mg of AA monomer consumed per 100 nm as-deposited film, whereas in continuous approach the monomer consumption was found as 680 mg for the same amount of film production, which indicated a nearly 18-fold higher monomer consumption in continuous iCVD.

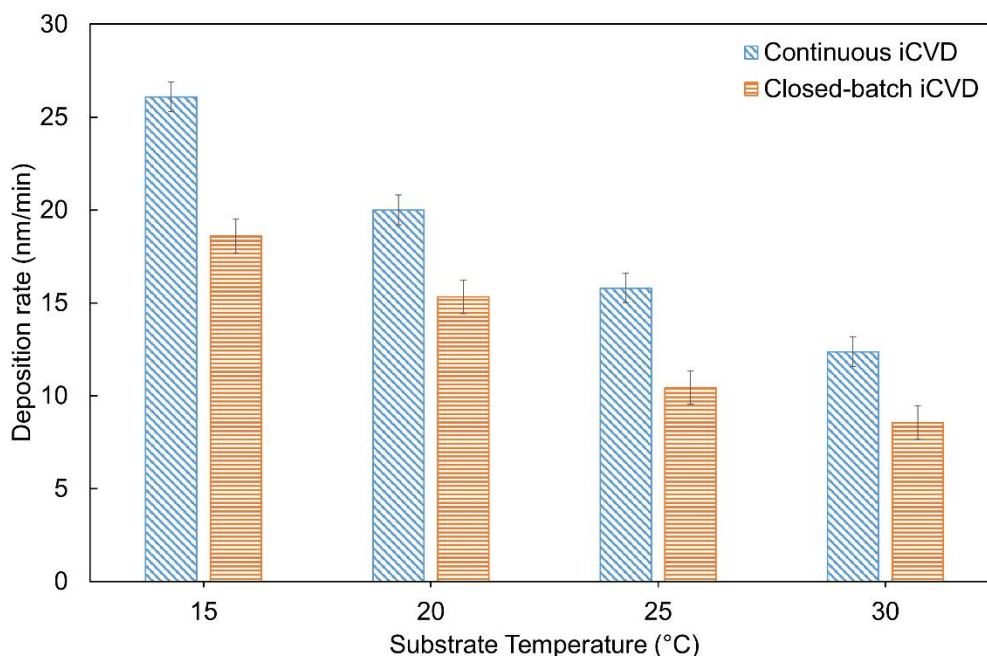


Figure 2. Effect of substrate temperature on deposition rate using continuous and closed-batch iCVD

Activation energies were calculated using Arrhenius equation to investigate the effect of substrate temperature on the deposition rates. Semilogarithmic graphic of the deposition rates on silicon wafer versus different substrate temperatures is given in Figure 3 (a,b). A negative activation energy was observed during PAA thin film depositions in both cases, indicating that PAA deposition is adsorption limited [21-23]. The activation energies of PAA thin films as-deposited by continuous and closed-batch

iCVD approaches were calculated as -35.94 kJ/mol and -39.44 kJ/mol, respectively. The observed small difference in the activation energies can be attributed to the changes in the deposition rates in both cases. In the continuous iCVD approach, the reactant concentration and reaction pressure are constant, whereas in the closed-batch iCVD approach, the reactant concentration and reaction pressure change throughout the polymerization. The reactant concentration decreases during polymerization in the closed-batch iCVD method, which in turn reduces the partial pressure (P_m)/monomer saturation pressure (P_{sat}) value [20, 24]. P_m/P_{sat} is an important parameter in iCVD kinetics that can affect the deposition rate [22, 25]. A decrease in the P_m/P_{sat} ratio can change the activation energy required to initiate polymerization, which in turn can affect the deposition rate [26, 27].

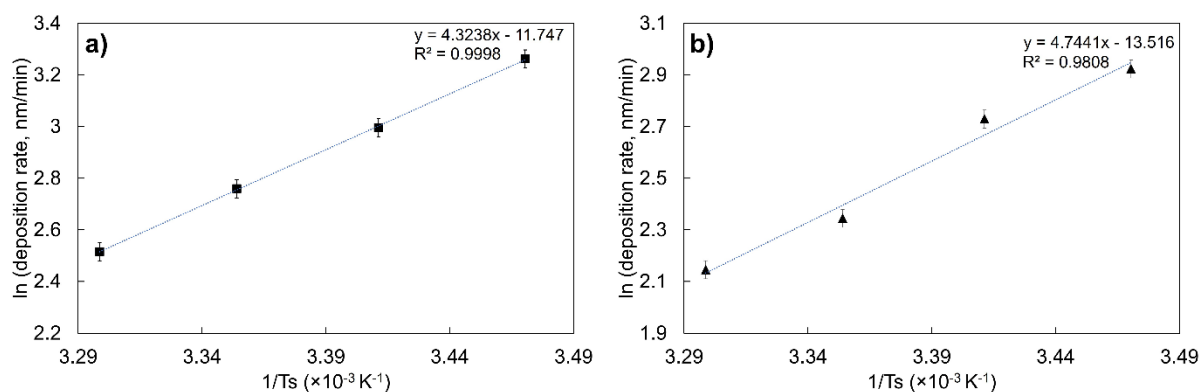


Figure 3. The deposition rate as a function of substrate temperature for PAA activation energy calculation in (a) continuous and (b) closed-batch iCVD process.

The chemical structures of PAA thin films deposited on glass substrate by both iCVD methods was revealed by FTIR analysis. The FTIR spectrum of monomer AA is compared with the spectra of PAA thin films deposited at a substrate temperature of 15°C by both iCVD approaches in Figure 4. The presence of AA is evidenced by broad O-H stretching in the $3671\text{--}2169$ cm^{-1} range. The strong absorption peak at 1701 cm^{-1} assigned the carboxyl group ($-\text{COOH}$), which is a clear fingerprint of PAA [6, 28, 29]. The other major vibrational spectra of PAA revealed the C-H stretching, C-H bending, C-O-H bending, C-O stretching and O-H bending vibrations at 2933 , 1538 , 1440 , 1237 and 805 cm^{-1} , respectively [30-33]. The peak at approximately 2351 cm^{-1} corresponds to the CO_2 bond [34]. The increase in the intensity of this peak is thought to indicate that the CO_2 in the atmosphere was not very well stabilized during the measurement. The FTIR analysis revealed a C=C stretching peak at 1634 cm^{-1} in the spectrum of the monomer, but it was not observed in the spectrum of the PAA deposited by the continuous and closed-batch iCVD method. This suggests that the polymerization occurs via an unsaturated C=C bond [35, 36]. According to the FTIR results, it is seen that the carbonyl and hydroxyl groups in the structure of the monomer are well preserved in both PAA thin films [37, 38].

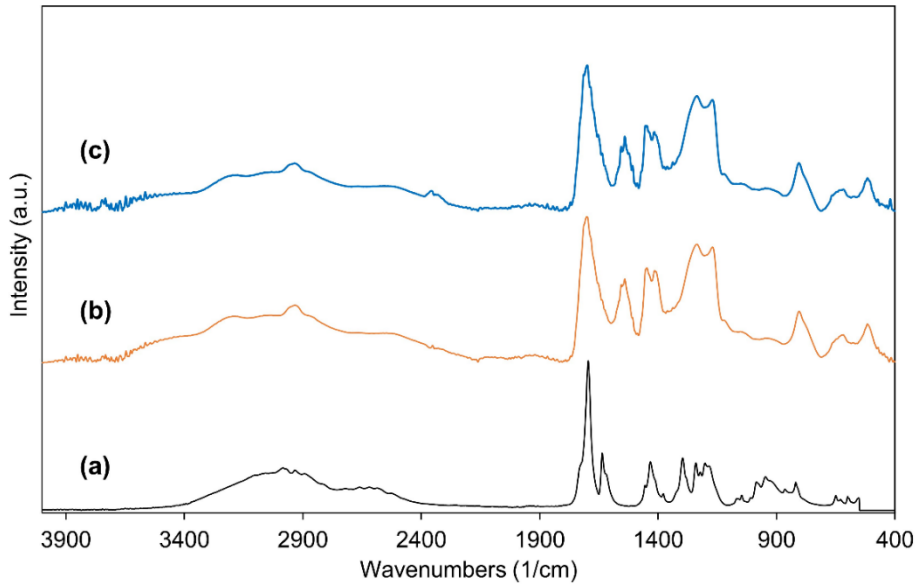


Figure 4. FTIR spectra of (a) AA monomer, PAA thin films deposited by (b) continuous and (c) closed-batch iCVD method.

UV-vis transmittance results of uncoated and PAA coated glasses at 15°C substrate temperature are presented in Figure 5. It can be clearly seen that PAA deposition on the glass slightly reduces the optical transmittance. The 100 nm-thick PAA thin film has a refractive index of 1.527 at wavelength of 633 nm [39, 40]. The refractive index of PAA thin films deposited by iCVD method is higher than the refractive index of glass ($n_{\text{glass}}=1.5$), which slightly reduced the transmittance of glass. The possible reason for the reduced transmittance can also be attributed to the changed surface structure of the PAA thin films [41-43]. The UV-vis spectra of deposited PAA thin films using both iCVD techniques gave similar results in the visible region. All samples showed a very high optical transmittance in the visible region.

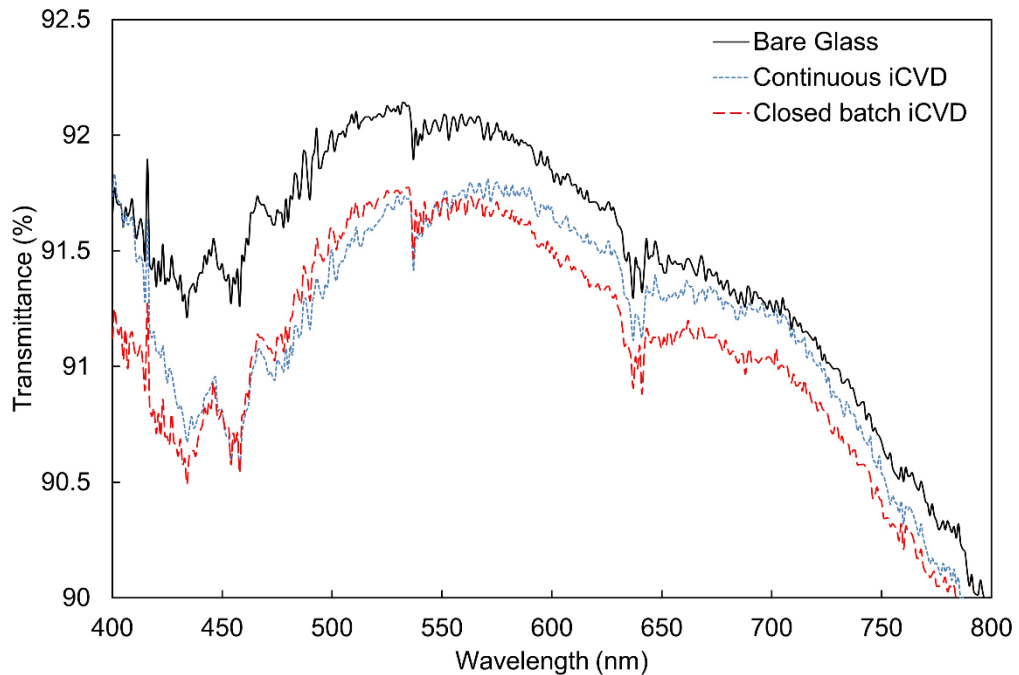


Figure 5. UV-vis spectra of bare and PAA coated glasses at 15°C substrate temperature.

The average roughness (Ra), root mean square (Rq) values and 3D AFM images of PAA films deposited by both iCVD approaches are shown in Figure 6 (a,c). Ra and Rq values of bare silicon wafer were given in our previous study as 0.482 nm and 0.596 nm, respectively [44]. PAA films deposited by the continuous iCVD approach have a rougher surface compared to those deposited by the closed-batch iCVD approach. The lower roughness of films produced by the closed-batch iCVD approach may be a consequence of the slower deposition rate [45]. The water contact angle images are given in Figure 6 (b,d). The water contact angle value of bare silicon wafer was given as $57.6 \pm 0.2^\circ$ in our previous study [44]. The water contact angle values of PAA films deposited by continuous and closed-batch iCVD methods were measured as $16.1 \pm 0.06^\circ$ and $24.4 \pm 0.73^\circ$, respectively. Wettability of materials depends on surface energy and surface roughness. The increase in surface roughness of materials with high surface energy increases wettability. [46]. This may be the reason why the PAA thin film deposited by continuous iCVD has a lower water contact angle value.

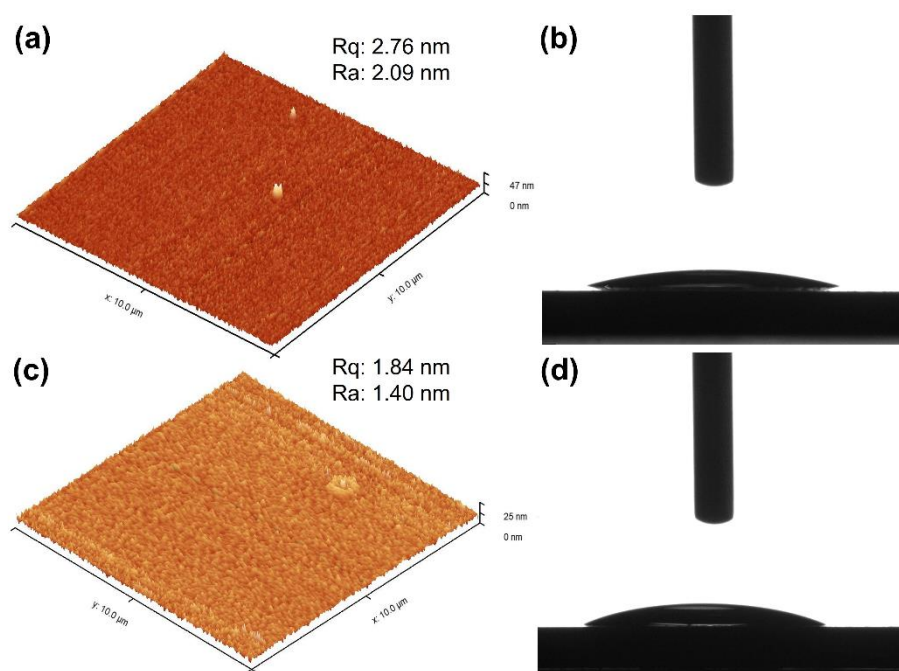


Figure 6. The AFM and water contact angle images of the PAA thin films deposited on silicon wafers by (a,b) continuous and (c,d) closed-batch iCVD at 15°C substrate temperature.

4. CONCLUSIONS

PAA films were successfully deposited by iCVD method on glass and silicon wafer surfaces. In continuous and closed-batch approaches, the highest deposition rates were obtained at a substrate temperature of 15°C . The apparent activation energies of PAA thin films deposited by continuous and closed-batch iCVD methods were calculated to be -35.94 kJ/mol and -39.44 kJ/mol, respectively. The negative activation energies implied an adsorption-limited iCVD regime. AFM results showed that the closed-batch approach allows the fabrication of more smooth film surface. The amount of monomer consumed to produce a 100-nm-thick film in the closed-batch iCVD approach was 18 times less than that of continuous iCVD approach. Therefore, in terms of monomer utilization ratio, closed-batch system appeared to be more effective, which may help to minimize the carbon footprint of iCVD process.

Declaration of Ethical Standards

The authors declare that the study complies with all applicable laws and regulations and meets ethical standards.

Declaration of Competing Interest

The authors declare that they have no known competing financial interests or personal relationships that could have appeared to influence the work reported in this paper.

Funding / Acknowledgements

The authors thank to Konya Technical University Research Foundation (Project No: 232216033) and the Scientific and Technological Research Council of Turkey (TÜBİTAK, Project No: 118M041) for the financial support of this study.

5. REFERENCES

- [1] L. Cui, R. Wang, X. Ji, M. Hu, B. Wang, and J. Liu, "Template-assisted synthesis of biodegradable and pH-responsive polymer capsules via RAFT polymerization for controlled drug release," *Materials Chemistry and Physics*, vol. 148, no. 1, pp. 87-95, 2014/11/14/ 2014, doi: <https://doi.org/10.1016/j.matchemphys.2014.07.016>.
- [2] H. Arkaban et al., "Polyacrylic acid nanoplatforms: Antimicrobial, tissue engineering, and cancer theranostic applications," *Polymers*, vol. 14, no. 6, p. 1259, 2022.
- [3] A. B. Rashid and M. E. Hoque, "Polymer nanocomposites for defense applications," in *Advanced Polymer Nanocomposites*: Elsevier, 2022, pp. 373-414.
- [4] A. Kausar, "Poly (acrylic acid) nanocomposites: Design of advanced materials," *Journal of Plastic Film & Sheeting*, vol. 37, no. 4, pp. 409-428, 2021.
- [5] Y. Zhao, J. Kang, and T. Tan, "Salt-, pH-and temperature-responsive semi-interpenetrating polymer network hydrogel based on poly (aspartic acid) and poly (acrylic acid)," *Polymer*, vol. 47, no. 22, pp. 7702-7710, 2006.
- [6] K. Yilmaz, M. Gürsoy, and M. Karaman, "Vapor Deposition of Transparent Antifogging Polymeric Nanocoatings," *Langmuir*, vol. 37, no. 5, pp. 1941-1947, 2021/02/09 2021, doi: [10.1021/acs.langmuir.0c03437](https://doi.org/10.1021/acs.langmuir.0c03437).
- [7] I. Chaduc, A. Crépet, O. Boyron, B. Charleux, F. D'Agosto, and M. Lansalot, "Effect of the pH on the RAFT polymerization of acrylic acid in water. Application to the synthesis of poly (acrylic acid)-stabilized polystyrene particles by RAFT emulsion polymerization," *Macromolecules*, vol. 46, no. 15, pp. 6013-6023, 2013.
- [8] A. Pal, D. Das, A. K. Sarkar, S. Ghorai, R. Das, and S. Pal, "Synthesis of glycogen and poly (acrylic acid)-based graft copolymers via ATRP and its application for selective removal of Pb²⁺ ions from aqueous solution," *European Polymer Journal*, vol. 66, pp. 33-46, 2015.
- [9] K. Shi, Y. Lei, S. Wang, and K. K. Shiu, "Electrochemically Induced Free-Radical Polymerization for the Fabrication of Amperometric Glucose Biosensors," *Electroanalysis*, vol. 22, no. 20, pp. 2366-2375, 2010.
- [10] C. Burguière et al., "Block copolymers of poly (styrene) and poly (acrylic acid) of various molar masses, topologies, and compositions prepared via controlled/living radical polymerization. Application as stabilizers in emulsion polymerization," *Macromolecules*, vol. 34, no. 13, pp. 4439-4450, 2001.
- [11] F. Zhang, W. Zhang, Y. Yu, B. Deng, J. Li, and J. Jin, "Sol-gel preparation of PAA-g-PVDF/TiO₂ nanocomposite hollow fiber membranes with extremely high water flux and improved antifouling property," *Journal of Membrane Science*, vol. 432, pp. 25-32, 2013.
- [12] B. Yang, Y. Zhou, W. Yu, S. Zhang, H. Chen, and J. Ye, "Photopolymerization synthesis of polyacrylic acid dispersant with methoxysilicon end groups and its application in a nano-SiO₂ aqueous system," *Polymer International*, vol. 68, no. 4, pp. 675-683, 2019.
- [13] J. Xie et al., "Phosphate functionalized poly (vinyl alcohol)/poly (acrylic acid)(PVA/PAA): an electrospinning nanofiber for uranium separation," *Journal of Radioanalytical and Nuclear*

- Chemistry, vol. 326, no. 1, pp. 475-486, 2020.
- [14] M. Gürsoy and M. Karaman, "Surface Treatments for Biological, Chemical, and Physical Applications," Wiley Online Library, 2016.
- [15] K. K. Gleason, "CVD Polymers: Fabrication of Organic Surfaces and Devices," Wiley, p. 8, 2015.
- [16] J. Xu and K. K. Gleason, "Conformal, amine-functionalized thin films by initiated chemical vapor deposition (iCVD) for hydrolytically stable microfluidic devices," *Chemistry of Materials*, vol. 22, no. 5, pp. 1732-1738, 2010.
- [17] K. K. Gleason, "Organic surface functionalization by initiated CVD (iCVD)," *Surface modification of polymers: methods and applications*, pp. 107-134, 2019.
- [18] M. Gürsoy et al., "Bioinspired fog capture and channel mechanism based on the arid climate plant *Salsola crassa*," *Colloids and surfaces a: physicochemical and engineering aspects*, vol. 529, pp. 195-202, 2017.
- [19] K. Yılmaz, H. Şakalak, M. Gürsoy, and M. Karaman, "Vapor deposition of stable copolymer thin films in a batch iCVD reactor," *Journal of Applied Polymer Science*, 2020, doi: 10.1002/app.50119.
- [20] C. D. Petruczuk, N. Chen, and K. K. Gleason, "Closed batch initiated chemical vapor deposition of ultrathin, functional, and conformal polymer films," *Langmuir*, vol. 30, no. 16, pp. 4830-7, Apr 29 2014, doi: 10.1021/la500543d.
- [21] M. Gürsoy and M. Karaman, "Effect of substrate temperature on initiated plasma enhanced chemical vapor deposition of PHEMA thin films," *physica status solidi (c)*, vol. 12, no. 7, pp. 1006-1010, 2015.
- [22] K. K. Lau and K. K. Gleason, "Initiated chemical vapor deposition (iCVD) of poly (alkyl acrylates): A kinetic model," *Macromolecules*, vol. 39, no. 10, pp. 3695-3703, 2006.
- [23] M. Gürsoy, "Vapor deposition polymerization of synthetic rubber thin film in a plasma enhanced chemical vapor deposition reactor," *Journal of Applied Polymer Science*, vol. 138, no. 4, p. 49722, 2021.
- [24] K. Yılmaz, H. Şakalak, M. Gürsoy, and M. Karaman, "Initiated Chemical Vapor Deposition of Poly(Ethylhexyl Acrylate) Films in a Large-Scale Batch Reactor," *Industrial & Engineering Chemistry Research*, vol. 58, no. 32, pp. 14795-14801, 2019/08/14 2019, doi: 10.1021/acs.iecr.9b02213.
- [25] K. K. Lau and K. K. Gleason, "Initiated chemical vapor deposition (iCVD) of poly (alkyl acrylates): an experimental study," *Macromolecules*, vol. 39, no. 10, pp. 3688-3694, 2006.
- [26] A. Khlyustova and R. Yang, "Initiated Chemical Vapor Deposition Kinetics of Poly (4-Aminostyrene)," *Frontiers in Bioengineering and Biotechnology*, p. 309, 2021.
- [27] M. E. Alf et al., "Chemical vapor deposition of conformal, functional, and responsive polymer films," *Advanced Materials*, vol. 22, no. 18, pp. 1993-2027, 2010.
- [28] J. Wu, Z. Feng, C. Dong, P. Zhu, J. Qiu, and L. Zhu, "Synthesis of sodium carboxymethyl cellulose/poly (acrylic acid) microgels via visible-light-triggered polymerization as a self-sedimentary cationic basic dye adsorbent," *Langmuir*, vol. 38, no. 12, pp. 3711-3719, 2022.
- [29] L. M. Sanchez, D. G. Actis, J. S. Gonzalez, P. M. Zélis, and V. A. Alvarez, "Effect of PAA-coated magnetic nanoparticles on the performance of PVA-based hydrogels developed to be used as environmental remediation devices," *Journal of Nanoparticle Research*, vol. 21, pp. 1-16, 2019.
- [30] T. Kavitha, I.-K. Kang, and S.-Y. Park, "Poly (acrylic acid)-grafted graphene oxide as an intracellular protein carrier," *Langmuir*, vol. 30, no. 1, pp. 402-409, 2014.
- [31] V. d. A. M. Gonzaga, B. A. Chrisostomo, A. L. Poli, and C. C. Schmitt, "Preparation, characterization and photostability of nanocomposite films based on poly (acrylic acid) and montmorillonite," *Materials Research*, vol. 21, 2018.
- [32] D. Lin-Vien, N. B. Colthup, W. G. Fateley, and J. G. Grasselli, *The handbook of infrared and Raman characteristic frequencies of organic molecules*. Elsevier, 1991.
- [33] P. K. Kashyap, Y. S. Negi, N. K. Goel, R. K. Diwan, and S. Rattan, "Chemical initiator-free synthesis of poly (acrylic acid-co-itaconic acid) using radiation-induced polymerization for application in

- dental cements," *Radiation Physics and Chemistry*, vol. 198, p. 110243, 2022.
- [34] J. Huang, F. Carpentier, F. Miserque, M. Ferry, and S. Esnouf, "Interaction between radio-oxidized polypropylene and gaseous HCl. Part 1. Qualitative evidence," *Polymer Degradation and Stability*, vol. 221, p. 110663, 2024/03/01/ 2024, doi: <https://doi.org/10.1016/j.polymdegradstab.2024.110663>.
- [35] W. E. Tenhaeff and K. K. Gleason, "Initiated and oxidative chemical vapor deposition of polymeric thin films: iCVD and oCVD," *Advanced Functional Materials*, vol. 18, no. 7, pp. 979-992, 2008.
- [36] M. Karaman et al., "Chemical and Physical Modification of Surfaces," in *Surface Treatments for Biological, Chemical, and Physical Applications*, 2017, pp. 23-66.
- [37] K. K. Gleason, "Nanoscale control by chemically vapour-deposited polymers," *Nature Reviews Physics*, vol. 2, no. 7, pp. 347-364, 2020/07/01 2020, doi: 10.1038/s42254-020-0192-6.
- [38] K. K. Gleason, "Designing organic and hybrid surfaces and devices with initiated chemical vapor deposition (iCVD)," *Advanced Materials*, p. 2306665, 2023.
- [39] F. Jabeen, M. Chen, B. Rasulev, M. Ossowski, and P. Boudjouk, "Refractive indices of diverse data set of polymers: A computational QSPR based study," *Computational Materials Science*, vol. 137, pp. 215-224, 2017, doi: 10.1016/j.commatsci.2017.05.022.
- [40] L.-Q. Chu, W.-J. Tan, H.-Q. Mao, and W. Knoll, "Characterization of UV-induced graft polymerization of poly (acrylic acid) using optical waveguide spectroscopy," *Macromolecules*, vol. 39, no. 25, pp. 8742-8746, 2006.
- [41] B. Liu, L. Wen, and X. Zhao, "The surface change of TiO₂ film induced by UV illumination and the effects on UV-vis transmission spectra," *Applied Surface Science*, vol. 255, no. 5, pp. 2752-2758, 2008.
- [42] M. Eita, L. Wågberg, and M. Muhammed, "Thin films of zinc oxide nanoparticles and poly (acrylic acid) fabricated by the layer-by-layer technique: A facile platform for outstanding properties," *The Journal of Physical Chemistry C*, vol. 116, no. 7, pp. 4621-4627, 2012.
- [43] S. Walheim, E. Schaffer, J. Mlynek, and U. Steiner, "Nanophase-separated polymer films as high-performance antireflection coatings," *Science*, vol. 283, no. 5401, pp. 520-522, 1999.
- [44] M. Gürsoy and B. Kocadayıoğulları, "Environmentally Friendly Approach for the Plasma Surface Modification of Fabrics for Improved Fog Harvesting Performance," *Fibers and Polymers*, vol. 24, no. 10, pp. 3557-3567, 2023.
- [45] S. M. Rumrill, V. Agarwal, and K. K. S. Lau, "Conformal Growth of Ultrathin Hydrophilic Coatings on Hydrophobic Surfaces Using Initiated Chemical Vapor Deposition," *Langmuir*, vol. 37, no. 25, pp. 7751-7759, Jun 29 2021, doi: 10.1021/acs.langmuir.1c00918.
- [46] K.-Y. Law, "Contact Angle Hysteresis on Smooth/Flat and Rough Surfaces. Interpretation, Mechanism, and Origin," *Accounts of Materials Research*, vol. 3, no. 1, pp. 1-7, 2022/01/28 2022, doi: 10.1021/accountsmr.1c00051.



UNCERTAINTY EVALUATION USING LAW OF PROPAGATION AND MONTE CARLO SIMULATION METHODS WITH THE AUTORFPOWER MEASUREMENT SOFTWARE

^{1,*} Erkan DANACI , ²Aliye KARTAL DOĞAN , ³Engin Can CİCEK , ⁴Anil CETINKAYA ,
⁵Muhammed Çağrı KAYA , ⁶M.S. Halit OGUZTUZUN , ⁷Gulsun TUNAY 

^{1,2}TUBITAK National Metrology Institute (UME), Kocaeli, TÜRKİYE

³ASELSAN Gölbaşı, Ankara, TÜRKİYE

⁴İskenderun Technical University, Hatay, TÜRKİYE

⁵Chalmers University of Technology Department of Computer Science and Engineering, Gothenburg, SWEDEN

⁶Middle East Technical University, Ankara, TÜRKİYE

⁷Spark Kalibrasyon Hizmetleri A.S., Ankara, TÜRKİYE

erkan.danaci@tubitak.gov.tr, aliye.dogan@tubitak.gov.tr, engcicek@aselsan.com.tr,

cetinkaya@ceng.metu.edu.tr, cagri.kaya@chalmers.se, oguztuzn@ceng.metu.edu.tr,

gulsun_e@hotmail.com

Highlights

- The Law of Propagation (LoP) and Monte Carlo Simulation (MCS) uncertainty calculation methods were briefly discussed.
- The details of the AutoRFPower software were presented, which was developed for performing LoP and MCS uncertainty calculations in automatic RF power measurement tasks.
- Measurement and uncertainty calculation results obtained using the AutoRFPower software were presented.
- A comparison was made between the uncertainty calculation results from the AutoRFPower software and those from a commercial uncertainty calculation simulation tool (Oracle Crystal Ball).
- The uncertainty calculation capabilities of the developed AutoRFPower software were validated.



UNCERTAINTY EVALUATION USING LAW OF PROPAGATION AND MONTE CARLO SIMULATION METHODS WITH THE AUTORFPOWER MEASUREMENT SOFTWARE

^{1,*} Erkan DANACI , ² Aliye KARTAL DOĞAN , ³ Engin Can CİCEK , ⁴ Anıl CETINKAYA ,
⁵ Muhammed Çağrı KAYA , ⁶ M.S. Halit OGUZTUZUN , ⁷ Gulsun TUNAY 

^{1,2}TUBITAK National Metrology Institute (UME), Kocaeli, TÜRKİYE

³ASELSAN Gölbaşı, Ankara, TÜRKİYE

⁴İskenderun Technical University, Hatay, TÜRKİYE

⁵Chalmers University of Technology Department of Computer Science and Engineering, Gothenburg, SWEDEN

⁶Middle East Technical University, Ankara, TÜRKİYE

⁷Spark Kalibrasyon Hizmetleri A.S., Ankara, TÜRKİYE

erkan.danaci@tubitak.gov.tr, aliye.dogan@tubitak.gov.tr, engcicek@aselsan.com.tr,

cetinkaya@ceng.metu.edu.tr, cagri.kaya@chalmers.se, oguztuzn@ceng.metu.edu.tr,

gulsun_e@hotmail.com

(Received: 29.10.2023; Accepted in Revised Form: 13.05.2024)

ABSTRACT: RF power measurement is essential in RF and microwave metrology. For reliable and accurate power measurement, automatic measurement is preferred. A software application in C#, named AutoRFPower, was developed for automatic RF power measurement and uncertainty calculations at this study. According to the GUM document, this application is enhanced for uncertainty calculations by utilizing the Law of Propagation method and the Monte Carlo Simulation method. Trial measurements were performed at different RF power levels and frequencies between 50 MHz and 18 GHz using the AutoRFPower software. Law of Propagation and Monte Carlo Simulation uncertainty calculations were carried out by AutoRFPower based on the trial measurements and by the Oracle Crystal Ball simulation application. All measurements and their uncertainty calculations were compared with each other, and this study validated the uncertainty calculation of AutoRFPower. In addition, it was observed that in the Monte Carlo Simulation, uncertainty calculation results were non-symmetrical normal distribution, contrary to the assumption of symmetrical normal distribution according to the Law of Propagation method. Moreover, it has been observed that the statistical distribution of uncertainty changes depending on the dominant component of the parameters in the model function used for the uncertainty calculation with the Monte Carlo Simulation method.

Keywords: Auto RF Power Measurement, Law of Propagation Method, Monte Carlo Simulation Method, Uncertainty Calculation

1. INTRODUCTION

RF power measurement is a vital topic at the RF and microwave metrology laboratory. To have reliable power measurement, operator mistakes should be decreased. To minimize those mistakes, the use of automatic measurement software is preferred.

Although it is crucial to carry out such good, successive measurements at RF and Microwave metrology, it is also essential to calculate the uncertainty of the measurement correctly according to the "Guide to the Expression of Uncertainty in Measurement (GUM)" document [1, 2]. Law of Propagation (LoP) and Monte Carlo Simulation (MCS) methods are used to evaluate measurement uncertainties in GUM [3, 4].

The LoP method is based on the central limit theory. It calculates uncertainty with all input parameters that contribute to uncertainty calculation having normal distribution, or those should be transformed from other distributions such as rectangular, triangular, and u-shape to normal distribution. The input

parameters that do not have normal distribution are assumed as symmetrical normal distribution when transformed into a normal distribution from their actual distributions. If the uncertainty component has rectangular, triangle, and u-shape distributions, it should be divided into $\sqrt{3}$, $\sqrt{6}$, and $\sqrt{2}$ for normal distribution transfer, respectively. This assumption causes the calculated uncertainty of the LoP method to have a balanced normal distribution. Combined uncertainty can be calculated using Equation (1) for the LoP method [1, 2].

$$u(k=1) = \sqrt{\sum_{i=1}^n c_i^2 \cdot u_i^2} \tag{1}$$

where $u(k=1)$ is the combined uncertainty with coverage factor one (68 % reliability), c_i is the sensitivity coefficient of each uncertainty component in the model function ($f(\cdot)$) and u_i is the uncertainty value of each component in the model function. The c_i can be calculated with partial derivative of the model function of the considered uncertainty component ($\partial f(\cdot)/\partial i$), and u_i is a related uncertainty which has normal distribution. Figure 1 shows the visualization of the calculation flow of the LoP method uncertainty.

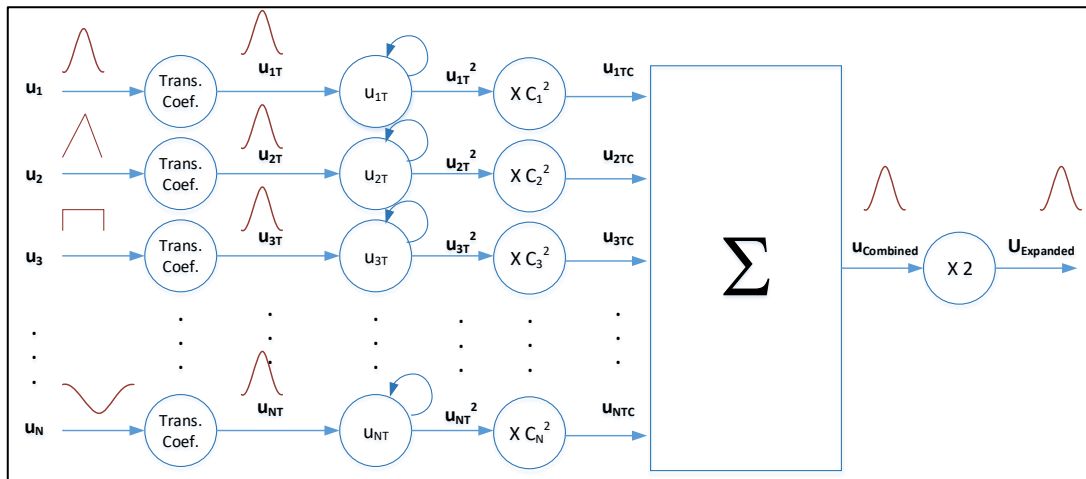


Figure 1. Uncertainty calculation flow chart of the LoP method

The MCS method is an analytical method used before and still in calculating measurement uncertainties. The MCS method is generally not preferred if LoP can be used because it is difficult to take many repetitive measurements such as 10^5 times or more [5-10]. Many repetitive measurements can be impossible for each uncertainty component. To simulate the real measurement, all the input parameters for uncertainty calculation is generated by randomized at least 10^5 times before uncertainty calculation. There is no symmetrical normal distribution transformation in the MCS method, and the input component's distribution effect can be seen in the combined uncertainty in the MCS method. The uncertainty calculation flow chart is given in Figure 2 for the MCS method in this study.

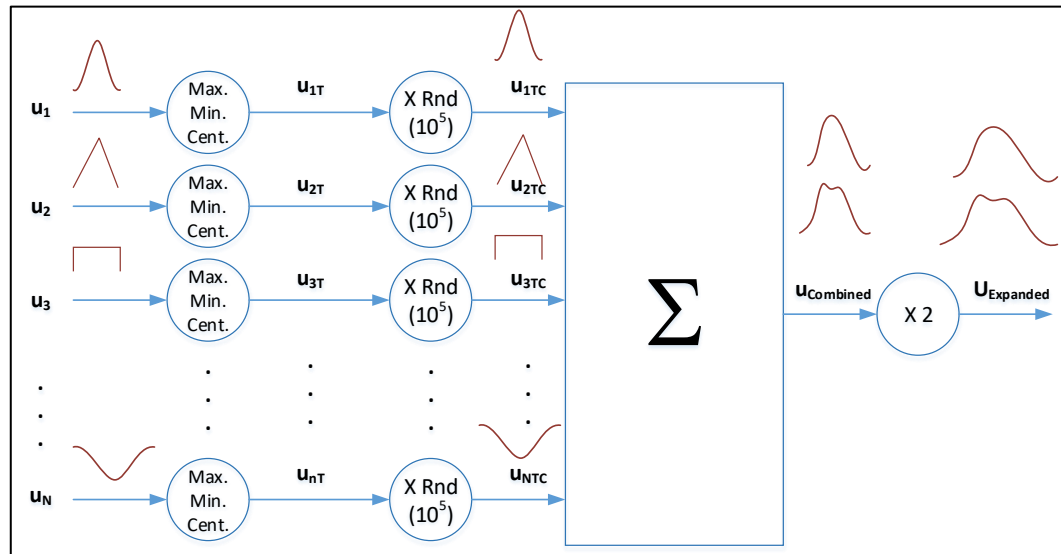


Figure 2. Uncertainty calculation flow chart of the MCS Method

Uncertainty calculation needs to be improved in the LoP method due to the normal distribution transformation of all parameters. The LoP method might have deficiencies when the model function has non-linear input parameters.

A software tool, called AutoRFPower, was developed on the C# platform with the collaboration of TUBITAK, SPARK, and METU [11, 12]. In this study, LoP and MCS methods calculated the uncertainties of the measurements taken using the enhanced automatic RF power measurement software (AutoRFPower). Also, the uncertainty calculation capabilities of the AutoRFPower software were validated. For validation, firstly, the uncertainty values calculated numerically according to the LoP method were compared with the uncertainty values produced by the AutoRFPower software, and the MCS uncertainty ability of the software was compared with the results of commercially available MCS software. This study compared and discussed all uncertainties calculated with the developed software and simulator.

2. MEASUREMENT BY AUTORFPOWER SOFTWARE AND UNCERTAINTY CALCULATION TECHNIQUES

An RF signal generator, a power sensor, and a power meter are used in a simple RF power measurement setup as shown in Figure 3. An attenuator is preferred for high power measurement with low power sensor and an adapter is preferred for adapting the different connectorized RF connectors in Figure 3. Depending on the measurement frequencies and RF power levels, various power sensors, such as thermocouples, semiconductor diodes, and thermistors, can be used as RF power sensors [13, 14]. In order to measure wide frequency range and wide power range, it is necessary to use an automatic measurement system.

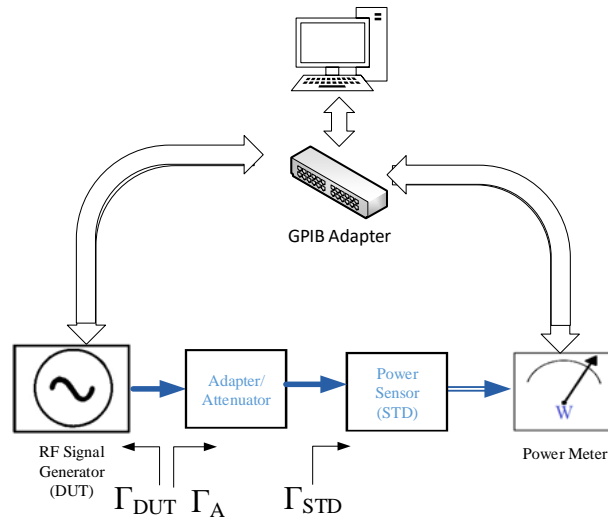


Figure 3. Automatic RF power measurement setup

For measuring RF power automatically, developed software is necessary to control the operations of the computer and the measurement system. In order to communicate with the computer and measurement devices, an interface bus should be used. As shown in Figure 3, the General Propose Interface Bus (GPIB) adapter and its protocol are used to communicate with the computer and the other measurement devices used for automatic RF power measurement [15].

The power value read by the power meters in RF power measurement systems cannot directly show the power given by RF signal sources due to impedance mismatches with non-ideal connectors and power sensor losses. Considering the losses and impedance mismatches in the RF power measurement system, it is necessary to calculate the actual RF power value of the RF signal source by writing a model function. The model function for the actual RF power of the signal generator is given with Equation (2) for the setup given at Figure 3.

$$P_{DUT} = \frac{P_{READ}}{CF_{STD}} \cdot \left| \frac{1}{S_{21A}} \right|^2 \cdot M \quad (2)$$

where;

P_{DUT} : Actual RF Power of Device Under Test (DUT) RF signal generator,

P_{READ} : Average RF power reading from power meter,

CF_{STD} : Calibration Factor of Standard (STD) power sensor,

S_{21A} : Forward transmission coefficient of the attenuator (complex),

M : Impedance mismatch due to the non-ideal RF connectors, it can be calculated with Equation (3),

$$M = |1 - \Gamma_A \cdot \Gamma_{DUT}|^2 \quad (3)$$

where;

Γ_A : Equivalent reflection coefficient of the input port of attenuator(s) shown in Figure 3 (complex). Γ_A is the reflection coefficient of the STD power sensor input (Γ_{STD}), if attenuator is not placed on the setup,

Γ_{DUT} : Complex reflection coefficient of DUT signal generator shown in Figure 3.

In this study, different RF power and frequency range measurements were tried with the AutoRFPower software, and the uncertainty calculation capabilities of the software were validated.

For the first experiment, the technical specifications of the power meter, the power sensor, and the RF signal source used in this measurement setup are given in Table 1.

Table 1. The equipment used in the measurement setup

Equipment	Model	Measurement Range
Power Meter	N1914A	-70 dBm -+44 dBm
Power Sensor	E4413A	50 MHz – 26.5 GHz
Signal Generator	E8257D	250 kHz – 40 GHz
10 dB Attenuator	8491B	10 MHz – 18 GHz

Measurements were performed by the measurement setup at the frequencies of 50 MHz, 1000 MHz, 5000 MHz, 10000 MHz, 15000 MHz and 18000 MHz, and at power levels of 0 dBm and 5 dBm. While taking the measurements by the developed software at the different frequencies and power levels, they were also successively recorded manually by the operator for software validation.

The actual RF power value (P_{DUT}) was calculated by taking into account the calibration factor of the power sensor, the forward transmission coefficient of the attenuator, and the complex equivalent reflection coefficient of the input port of the attenuator and also that of the DUT signal generator using the Equation (2).

Two different RF power values can be calculated depending on whether the DUT signal generator's reflection coefficient (Γ_{DUT}) is vectorial or only magnitude. If the Γ_{DUT} is known as vectorial (Case 1), the impedance mismatch is calculated by using Equation (3). In order to calculate the impedance mismatch numerically Equation (4) can be used as well. Mismatch uncertainty calculation has normal distribution when Equation (4) is used.

$$M = 1 + |\Gamma_A|^2 + |\Gamma_{DUT}|^2 - 2 \cdot |\Gamma_A| \cdot |\Gamma_{DUT}| \cdot \cos(\theta_A + \theta_{DUT}) \quad (4)$$

If only the magnitude of Γ_{DUT} is known (Case 2), the impedance mismatch (M) is assumed to be 1 (one). In this situation, the uncertainty of the impedance mismatch can be calculated using the magnitude of the reflection coefficient of the signal generator and the magnitude of the reflection coefficient of the power sensor. The magnitude of the reflection coefficient of the signal generator can be obtained by using the standing wave ratio of the signal generator, which is given into the data sheets of the signal generator. This mismatch uncertainty has a U-shaped distribution. In order to calculate the power uncertainty, the uncertainty of the mismatch, which has a U-shaped distribution, should be transformed into a normal distribution by dividing it by $\sqrt{2}$.

In this study, the measurement results taken by the AutoRFPower software and calculated actual powers are given in Table 2. The P_{DUT} values were calculated for both impedance mismatch calculation cases. The vectorial reflection coefficient measurement of the signal generator is so tricky. Most laboratories do not prefer the vectorial reflection coefficient measurement, and they like to use the standing wave ratio of the manufacturer in the manufacturer data sheets. The complex reflection coefficient of the signal generator was not measured in this study. A calibrated attenuator was connected to the output port of the signal generator. In order to check the AutoRFPower software's uncertainty calculation capability for this study at Case 1, the output reflection coefficient of the attenuator was accepted that the complex reflection coefficient of the signal generator. Impedance mismatch error was calculated by the output reflection coefficient of the attenuator (in complex) and the reflection coefficient of the DUT PS (in complex). Calculated P_{DUT} values are given for two different power levels as 0 dBm and 5 dBm and Case 1 and Case 2 in Figure 4 and Figure 5, respectively.

The reading powers (P_{READ}) differ from the calculated actual power (P_{DUT}) in Figure 4 and Figure 5. The P_{READ} contains the power sensor losses and the impedance mismatch errors. In order to eliminate these errors using Equation (2), P_{DUT} was obtained as a difference from P_{READ} . There is a slight difference between the calculated P_{DUT} for Case 1 and the calculated P_{DUT} for Case 2. These differences come from the different impedance mismatch calculations as given above.

Table 2. Calculated RF power values according to the mismatch calculation cases

Freq. (MHz)	Applied Power from Signal Generator (DUT) (dBm)	Reading Power P_{READ} (mW)	CF_{STD}	S_{21A} (Linear Magnitude)	Calculated Power P_{DUT} (mW) @ Case 1	Calculated Power P_{DUT} (mW) @ Case 2
50	0	0.092038	1.0000	0.3184366	0.98725	0.98580
1000	0	0.090822	0.9816	0.3176025	1.00163	1.00024
5000	0	0.080260	0.9592	0.3157301	0.93193	0.92623
10000	0	0.076380	0.9365	0.3132852	0.89847	0.90027
15000	0	0.071097	0.9210	0.3113364	0.88172	0.87236
18000	0	0.068634	0.9150	0.3108678	0.83852	0.82781
50	5	0.294230	1.0000	0.3184366	3.15470	3.15143
1000	5	0.288524	0.9816	0.3176025	3.18116	3.17756
5000	5	0.254833	0.9592	0.3157301	2.95980	2.94086
10000	5	0.242381	0.9365	0.3132852	2.85191	2.85686
15000	5	0.227139	0.9210	0.3113364	2.81639	2.78701
18000	5	0.220456	0.9150	0.3108678	2.69217	2.65898

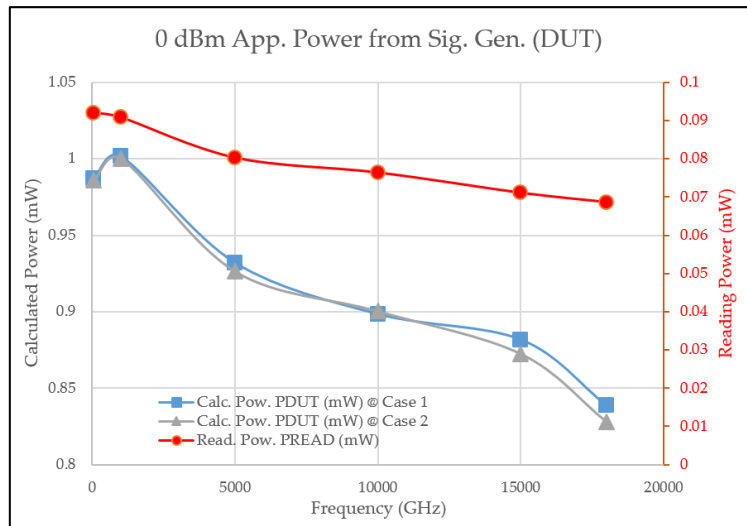


Figure 4. 0 dBm calculated DUT output powers for Case 1 and Case 2

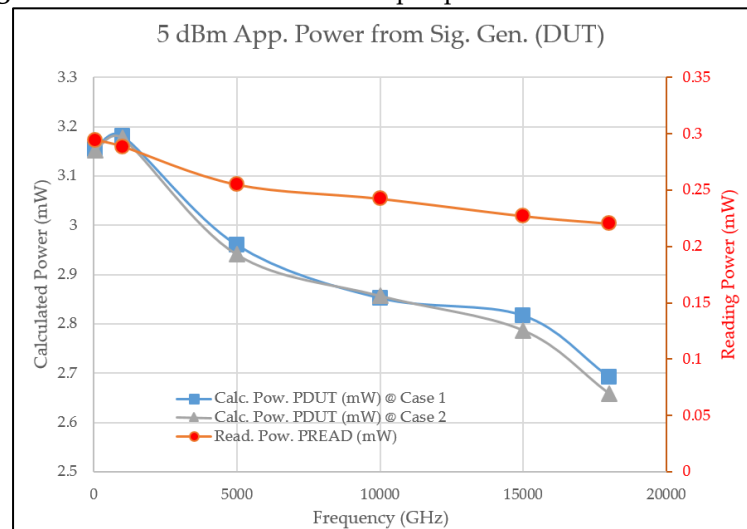


Figure 5. 5 dBm calculated DUT output powers for Case 1 and Case 2

3. COMPARISON OF UNCERTAINTY EVALUATION METHODS

To calculate uncertainty with the AutoRFPower software, two uncertainty calculation codes, implementing the LoP and MCS methods, were included in the software.

Combined uncertainties were calculated using Equation (1) and Equation (5) for LoP and MCS methods, respectively at this study.

$$u(k=1) = \sqrt{\sum_{i=1}^n u_{Ri}^2} \quad (5)$$

where $u(k=1)$ is the combined uncertainty with coverage factor one (68 % reliability), and u_{Ri} is the uncertainty value of each component in the model function randomly generated and u_{Ri} has different distribution.

Four uncertainty calculations given below were performed in this study.

1. According to the GUM LoP method, the first uncertainty calculation was done using manual measurement data and the MS Excel application.
2. The Oracle Crystal Ball application calculated the second uncertainty using the MCS method (OMm).
3. The third uncertainty calculation was made by AutoRFPower software. AutoRFPower can calculate the uncertainty using the GUM LoP method (ALm).
4. The fourth uncertainty calculation was made by AutoRFPower software alone. The AutoRFPower software can also calculate the uncertainty using the GUM MCS method (AMm).

For four uncertainty calculations, the same RF power measurement data were used for Case 1 and Case 2 determined in this study.

Uncertainty components and their statistical distributions are given below;

- u_{PREAD} – uncertainty of repeated power measurement, Gaussian
- u_{PMacc} – uncertainty of accuracy of the power meter, rectangular
- u_{PMres} – uncertainty of resolution of the power meter, rectangular
- u_{CFSTD} – uncertainty of CF of the STD PS, Gaussian
- u_{S21A} – uncertainty of the forward transmission coefficient of attenuator, Gaussian
- $u_{|\Gamma_A|}$ – uncertainty of the magnitude of Γ_A , Gaussian
- $u_{|\Gamma_{DUT}|}$ – uncertainty of the magnitude of Γ_{DUT} , Gaussian
- u_{θ_A} – uncertainty of the phase of Γ_A , Gaussian
- $u_{\theta_{DUT}}$ – uncertainty of the phase of Γ_{DUT} , Gaussian
- u_M – uncertainty of the impedance mismatch of connector where Γ_{DUT} is known as magnitude, U shape

In order to validate the LoP uncertainty calculation of AutoRFPower, manually calculated LoP uncertainty by using MS Excel and AutoRFPower LoP uncertainty calculation (ALm) were compared. There was a good agreement at the level of 10^{-4} differences. This difference is an acceptable value that the ALm could be used as a reference for comparisons.

In order to compare the uncertainty calculations at the first step in this study, ALm uncertainty were compared with AMm uncertainty. ALm uncertainty calculations, which were validated with MS Excel manual calculation, were used as a reference value for comparison.

In the second step of comparison, OMm uncertainty was compared with ALm uncertainty using the same measurement data. Calculated uncertainty values were given in Table 3 and Table 4 according to the cases with coverage factor two (95 %). Uncertainty differences from the reference uncertainty were given in Table 5. In this study, only the difference between the calculated uncertainties were given as evaluation method for comparison results.

Table 3. Calculated uncertainties according to the LoP and MCM with developed software and MC simulator application for Case 1

Frequency (MHz)	Calculated Power PDUT (mW) Case 1	ALm Unc. of Calculated Power (mW) Case 1	AMm Unc. of Calculated Power (mW) Case 1	OMm Unc. of Calculated Power (mW) Case 1
50	0.98725	0.01202	0.01203	0.01204
1000	1.00163	0.01243	0.01245	0.01243
5000	0.93193	0.01478	0.01481	0.01480
10000	0.89847	0.01426	0.01424	0.01427
15000	0.88172	0.03200	0.03201	0.03207
18000	0.83852	0.02267	0.02271	0.02268
50	3.15470	0.03837	0.03836	0.03843
1000	3.18116	0.03943	0.03938	0.03931
5000	2.95980	0.04689	0.04703	0.04683
10000	2.85191	0.04520	0.04520	0.04520
15000	2.81639	0.10220	0.10232	0.10215
18000	2.69217	0.07277	0.07276	0.07278

Table 4. Calculated uncertainties according to the LoP and MCM with developed software and MC simulator application for Case 2

Frequency (MHz)	Calculated Power PDUT (mW) Case 2	ALm Unc. of Calculated Power (mW) Case 2	AMm Unc. of Calculated Power (mW) Case 2	OMm Unc. of Calculated Power (mW) Case 2
50	0.98580	0.01206	0.01209	0.01209
1000	1.00024	0.01412	0.01411	0.01413
5000	0.92623	0.03606	0.03619	0.03610
10000	0.90027	0.02156	0.02159	0.02159
15000	0.87236	0.06486	0.06500	0.06488
18000	0.82781	0.09185	0.09188	0.09193
50	3.15143	0.03851	0.03845	0.03856
1000	3.17756	0.04481	0.04473	0.04470
5000	2.94086	0.11449	0.11445	0.11458
10000	2.85686	0.06840	0.06853	0.06844
15000	2.78701	0.20720	0.20712	0.20749
18000	2.65898	0.29503	0.29472	0.29510

Table 5. Calculated uncertainty differences from reference uncertainty

Frequency (MHz)	AMm-ALm @ Case 1	OMm-ALm @ Case 1	AMm-ALm @ Case 2	OMm-ALm @ Case 2
50	0.00001	0.00002	0.00003	0.00003
1000	0.00002	-0.00000	-0.00001	0.00001
5000	0.00003	0.00002	0.00013	0.00004
10000	-0.00002	0.00001	0.00003	0.00003
15000	0.00001	0.00007	0.00014	0.00002
18000	0.00004	0.00001	0.00003	0.00008
50	-0.00001	0.00006	-0.00006	0.00005
1000	-0.00005	-0.00012	-0.00008	-0.00011
5000	0.00014	-0.00006	-0.00004	0.00009
10000	-0.00000	-0.00000	0.00013	0.00004
15000	0.00012	-0.00005	-0.00008	0.00029
18000	-0.00001	0.00001	0.00003	0.00003

The uncertainties calculated with the MCS method using the uncertainty calculation module of the AutoRFPower software, were plotted for each frequency. Some selected graphics are given in Figures 6-7 for Case 1 and Case 2, respectively. It has been seen in the graphics that the uncertainties obtained by the MCS method calculation do not have a homogeneous normal distribution. Non-homogenous normal distribution can be seen using the triangles drawn in the figures, where the triangles are symmetrical, but the top corners of the triangles are not at the top of the histograms. In order to obtain the homogeneous normal distribution, more than 10^5 times power measurement should be performed instead of the generated randomized power values from 10 times power measurement.

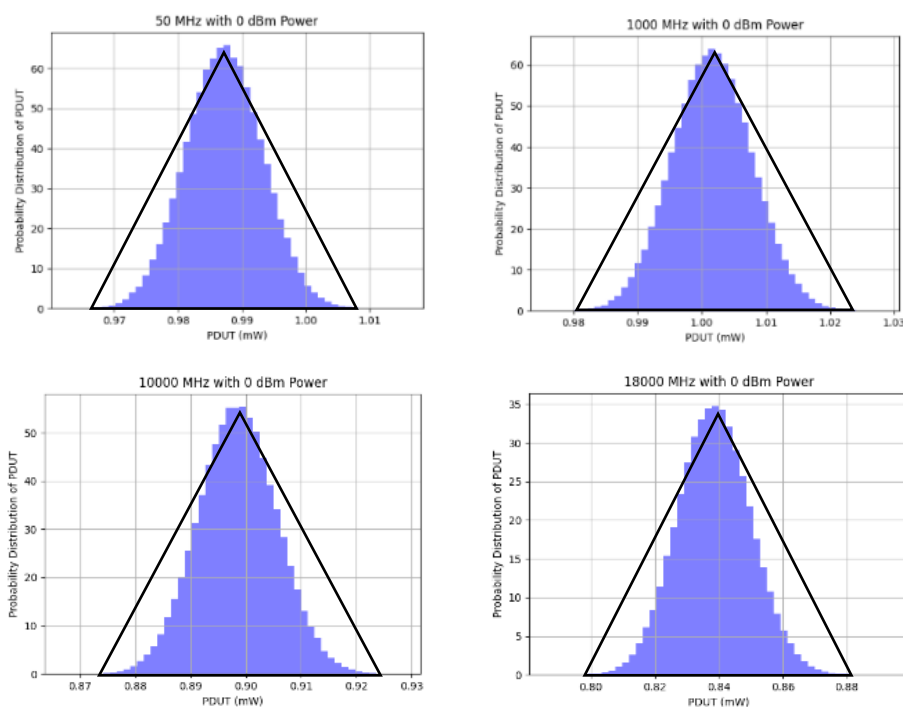


Figure 6. MCS Uncertainty values for Case 1 @ 0 dBm and different frequencies

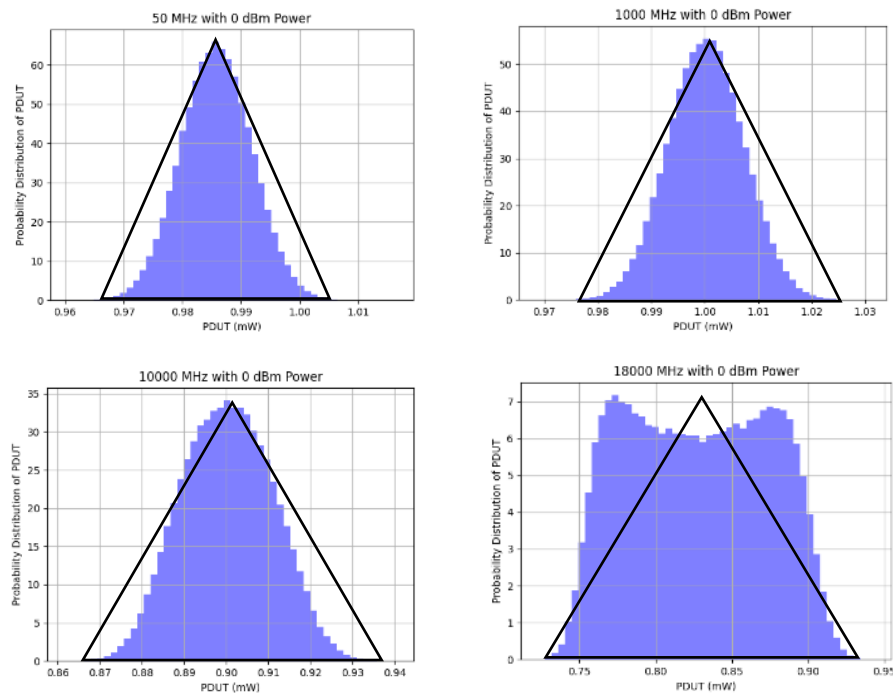


Figure 7. MCS Uncertainty values for Case 2 @ 0 dBm and different frequencies

4. CONCLUSION

This study validated the measurement results of the AutoRFPower software and uncertainty calculation results carried out by AutoRFPower according to the LoP and MCS methods. The AutoRFPower software was being tested with this study, and it will be available from SPARK (www.sparkmeasure.com). In addition, OMM uncertainties and AMM and ALM uncertainties calculated with AutoRFPower were compared.

In comparisons, it was observed that there was a 10^{-4} level difference between the LoP and the MCS method uncertainties.

When the uncertainty calculation results of the AutoRFPower software were compared with the OCB uncertainty results, it was observed the uncertainties obtained by MCS were the same as the OCB uncertainties. Moreover, it was noticed that the uncertainties evaluated according to the MCS method had a non-symmetrical normal distribution, contrary to the assumption of symmetrical normal distribution according to LoP GUM. On the other hand, in the uncertainty calculation by using the MSC method, it has been observed that the statistical distribution of the uncertainty changes depending on the dominant component of the parameters in the model function used for the uncertainty calculation.

AutoRFPower software was initially developed for the Keysight, Agilent, and HP brand mark devices. This software is being improved in other European-funded research projects by other National Metrology Institutes and designated institutes such as NSAI (Ireland), CMI (Czech Republic), Trescal (Denmark), IMBiH (Bosnia & Herzegovina), and SIQ (Slovenia). Additional measurement devices are being added to the software in an ongoing European-funded project. AutoRFPower software can calculate the ALM and AMM uncertainty with the new brand devices by new users in future.

Declaration of Ethical Standards

The authors of this article declare that the materials and methods used in this study do not require ethical committee permission and/or legal-special permission.

Credit Authorship Contribution Statement

CRedit (Contributor Roles Taxonomy) was introduced with the intention of recognizing individual author contributions, reducing authorship disputes and facilitating collaboration.

Declaration of Competing Interest

The authors declare that they have no known competing financial interests or personal relationships that could have appeared to influence the work reported in this paper.

Funding / Acknowledgements

This work is supported by The Scientific and Technological Research Council of Turkey (TÜBİTAK) under Grant No. 5200040 entitled "A New Method and Software Development for Automatic RF Power Measurement and RF Power Meter Calibration".

Data Availability

There is no any data from a data repository.

5. REFERENCES

- [1] BIPM, "Evaluation of measurement data – Guide to the expression of the uncertainty in measurement", Bureau Int. des Poids et Mesures, JCGM 100:2008, 1st ed., Sep. 2008. [Online]. Available: https://www.bipm.org/documents/20126/2071204/JCGM_100_2008_E.pdf/cb0ef43f-baa5-11cf-3f85-4dcd86f77bd6 [Accessed: August 06, 2024].
- [2] BIPM, "Evaluation of measurement data – Supplement 1 to the "Guide to the expression of uncertainty in measurement" – Propagation of distributions using a Monte Carlo method", Bureau Int. des Poids et Mesures, JCGM 101:2008, 1st ed., Sep. 2008. [Online]. Available: https://www.bipm.org/documents/20126/2071204/JCGM_101_2008_E.pdf/325dcaad-c15a-407c-1105-8b7f322d651c [Accessed: August 06, 2024].
- [3] P. R. G. Couto, J. Carretero, and S. P. de Oliveira, Monte Carlo Simulations Applied to Uncertainty in Measurement, Theory and Applications of Monte Carlo Simulations. Intech, March 06, 2013. [E-Book]. Available: <https://www.intechopen.com/chapters/43533>. doi: 10.5772/53014.
- [4] C.F. Dietrich, Uncertainty, calibration and probability, 2nd edition, Adam-Hilger (Bristol), 1991.
- [5] G. M. Mahmoud, and R. S. Hegazy, "Comparison of GUM and Monte Carlo methods for the uncertainty estimation in hardness measurements", International Journal of Metrology and Quality Engineering, vol. 8, no. 9, May 24, Article 14, 2017. <https://doi.org/10.1051/ijmqe/2017014>
- [6] O. Ibe, Markov Processes for Stochastic Modelling, Basic Concepts in Probability, 2nd edition, Elsevier, pp. 1-27, 2013.
- [7] J. Han, H. Chen, and Y. Cao, "Uncertainty Evaluation Using Monte Carlo Method with MATLAB", presented at IEEE 10th International Conference on Electronic Measurement & Instruments, vol. 2. August 2011, pp. 282-286.
- [8] C. E. Papadopoulos, H. Yeung, "Uncertainty estimation and Monte Carlo simulation method", Flow Measurement and Instrumentation, vol. 12, issue 4, 2001, pp. 291-298. [https://doi.org/10.1016/S0955-5986\(01\)00015-2](https://doi.org/10.1016/S0955-5986(01)00015-2).
- [9] M. Á. Herrador, A. G. Asuero, A. G. González, "Estimation of the uncertainty of indirect measurements from the propagation of distributions by using the Monte-Carlo method: An overview", Chemometrics and Intelligent Laboratory Systems, vol. 79, issue 1-2, 2005, pp. 115-122. <https://doi.org/10.1016/j.chemolab.2005.04.010>.

- [10] I. Farrance, R. Frenkel, "Uncertainty in measurement: a review of monte carlo simulation using microsoft excel for the calculation of uncertainties through functional relationships, including uncertainties in empirically derived constants", *Clin Biochem Rev.* vol. 35, no. 1, Feb. 2014, pp. 37-61. PMID: 24659835; PMCID: PMC3961998.
- [11] A. Yugruk, E. Danaci, A. K. Dogan and A. O. Salman, "The Effects of Sequential and Multiple Measurement on RF Power," 2021 29th Signal Processing and Communications Applications Conference (SIU), 2021, pp. 1-4, doi: 10.1109/SIU53274.2021.9477768.
- [12] A. Cetinkaya, A. K. Dogan, E. Danaci and H. Oguztuzun, "AUTORFPOWER: Automatic RF Power Measurement Software for Metrological Applications," 2021 2nd International Informatics and Software Engineering Conference (IISEC), 2021, pp. 1-4, doi: 10.1109/IISEC54230.2021.9672386.
- [13] A. Cetinkaya, M.C. Kaya, E. Danaci and H. Oguztuzun, "Uncertainty Calculation-As-A-Service: An IIoT Application For Automated RF Power Sensor Calibration", IMEKO TC6, International Conference on Metrology and Digital Transformation, September 2022, Berlin.
- [14] D. M. Pozar, *Microwave Engineering*, John Wiley & Sons 4th Edition, 2011. ISBN: 1118213637, 9781118213636.
- [15] J. Jia, J. Kuang, Z. He and J. Fang, "Design of automated test system based on GPIB," 2009 9th International Conference on Electronic Measurement & Instruments, 2009, pp. 1-943-1-948, doi: 10.1109/ICEMI.2009.5274384.



EFFECT OF CHEMICAL MODIFICATION OF MULTIWALL CARBON NANOTUBES ON THE PROPERTIES OF POLY(LACTIC ACID) COMPOSITE FILMS: SYNTHESIS AND CHARACTERIZATION

¹Figen ARSLAN , ^{2,*} Şükran Melda ESKİTOROS TOĞAY 

¹ Gazi University, Engineering Faculty, Chemical Engineering Department, Ankara, TÜRKİYE

² Health Sciences University, Gulhane Vocational School of Health Services, Pharmacy Services Department, Ankara, TÜRKİYE

[1figen.arslan@hotmail.com](mailto:figen.arslan@hotmail.com), [2melda.togay@sbu.edu.tr](mailto:melda.togay@sbu.edu.tr)

Highlights

- Unmodified and modified MWCNTs such as MWCNT-COOH, MWCNT-OH, and MA-g-MWCNT were incorporated into the PLA matrix.
- The nanocomposite films were successfully prepared by the solvent casting method.
- These nanocomposite films can be used for different applications due to their improved properties especially in biomedical.



EFFECT OF CHEMICAL MODIFICATION OF MULTIWALL CARBON NANOTUBES ON THE PROPERTIES OF POLY(LACTIC ACID) COMPOSITE FILMS: SYNTHESIS AND CHARACTERIZATION

¹Figen ARSLAN , ^{2,*} Şükran Melda ESKİTOROS TOĞAY 

¹ Gazi University, Engineering Faculty, Chemical Engineering Department, Ankara, TÜRKİYE

² Health Sciences University, Gulhane Vocational School of Health Services, Pharmacy Services Department, Ankara, TÜRKİYE

figen.arслан@hotmail.com, melda.togay@sbu.edu.tr

(Received: 10.01.2024; Accepted in Revised Form: 21.05.2024)

ABSTRACT: To enhance the properties of poly(lactic acid) (PLA) composite films, unmodified (MWCNT) and modified multiwall carbon nanotubes (MWCNT-COOH, MWCNT-OH, and MA-g-MWCNT) were incorporated into the polymer matrix followed by the solvent casting method. The success of the modification of MWCNT with maleic anhydride (MA) was verified by absorption transmission reflectance spectroscopy (ATR). The fabricated nanocomposite films were analyzed by Fourier transform infrared (FT-IR) spectroscopy, thermal analyses, atomic force microscopy (AFM), contact angle measurements, dynamic mechanical analysis (DMA), and electrical conductivity tests. ATR spectra showed that MA was covalently grafted to the surface of the MWCNT, which was well dispersed and homogeneously incorporated in the PLA matrix. The results of the thermal degradation demonstrated that the degradation value of the film increased from 328.91°C to 347°C with the addition of 0.5 wt% MA-g-MWCNT. Additionally, the MWCNT-OH/PLA films illustrated strongly hydrophilic nature due to the -OH groups. The surface resistance of 3 wt% of the MWCNT-COOH/PLA nanocomposite film decreased from 2.56×10^9 to $2.42 \times 10^3 \Omega$ (by 10^6 order). Therefore, the properties of PLA were increased with the addition of functionalized MWCNTs, which can be used for different applications such as biomedical, food packaging, and electronics.

Keywords: Nanocomposites, Multiwall Carbon Nanotube, Poly(Lactic Acid), Grafting, Maleic Anhydride

1. INTRODUCTION

Polymeric nanocomposites have gained much attention due to their significant mechanical, thermal, electrical, and biodegradable properties [1, 2]. Among these nanocomposites, biodegradable polymers have specific properties such as renewable, excellent biodegradable, and biocompatible [3, 4]. Therefore, biodegradable polymeric nanocomposites have been used in almost all areas such as food packaging, biomedical, solar cells, electronic components [5], and eco-friendly applications. These polymers such as poly(lactic acid) (PLA), poly(ethylene oxide) (PEO), poly(3-hydroxybutyrate) (PHB), and polycaprolactone (PCL) [2] have been extensively used in these nanocomposites [1]. Poly(lactic acid) (PLA), which is a biodegradable polyester [6], is derived from renewable resources such as corn and sugar [1]. However, poor mechanical properties, brittleness [7], low crystallization rate, low impact strength, low glass transition temperature, and poor electrical conductivity of PLA severely restrict its applications [4]. Therefore, blending PLA with other polymers or reinforced nanomaterials overcomes these drawbacks of PLA, and leads to the desired properties [8]. To enhance its properties, nanomaterials such as carbon nanotubes [9], montmorillonite [10], and graphene oxide [11] can be used to reinforce.

Multiwall carbon nanotubes (MWCNTs) have attracted a great deal of interest for material sciences due to their high physicochemical properties [12]. MWCNTs possess a large surface area, high elastic modulus, high mechanical and barrier properties, good thermal stability up to 2800°C in a vacuum, and high thermal and electrical conductivity [13]. Thus, they have been used as superior reinforced nanomaterials in polymeric nanocomposites [14]. Especially in the food industry, the studies showed that

*Corresponding Author: Şükran Melda ESKİTOROS TOĞAY, melda.togay@sbu.edu.tr

there were no harmful effects of the use of MWCNTs as nanofillers [15, 16]. Yu et al. [15] displayed the potential use of grafted MWCNTs in the PHBV films as food packaging. However, the interfacial interaction between polymer matrix and MWCNTs depends on the dispersion of nanofillers in matrices [17]. Seligra et al. [18] developed a technique to disperse MWCNTs in the PLA matrix by linking covalently the nanofiller with the polymer. Yinghui Zhou et al. [19] investigated the effects of the CNTs-COOH nanoparticles on the properties of PLA/CNTs-COOH nanocomposites. The most important issue of the MWCNT nanocomposites is the dispersion of them in the matrix. Therefore, the physical/chemical treatment can be used to improve the dispersion and the compatibility between MWCNT and the polymer matrix [1]. The mechanical performance of the materials can be improved by the strong interfacial adhesion between the matrix and the nanofiller [20] by the functionalization of MWCNT with a compatibilizer agent such as maleic anhydride [21] which is a popular and effective method to enhance this adhesion [22].

To improve the properties of MWCNT, some compatibilizer agents such as maleic anhydride (MA) can be selected. It is highly reactive [23], which enhances the adhesion between polymers and MWNT. MA grafted MWCNT showed better properties than pure MWNT nanoparticles [24]. Huang et al. [24] produced composite materials composed of MA grafted MWCNT and PMMA and investigated the electrical property and EMI shielding efficiency. Wu et al. [25] functionalized MWCNTs with maleic acid (MAA) and maleic anhydride (MA) by the free radical reaction and produced the nanocomposites by the hydrogen bonding with poly (urea urethane) (PUU). Both non-covalent and covalent modifications of the MWCNT surface have been used to improve the wetting and solubility of MWCNT. The advantage of non-covalent attachment is that the perfect structure of the MWCNT is not damaged, and its mechanical properties remain intact. The main disadvantage of this attachment is that the forces between the wrapping molecules and the MWCNT are very weak, which means that the load may not be transferred efficiently from the polymer matrix to the MWCNT filler [26].

Low amounts of MA-g-multi-walled carbon nanotubes (MWCNTs) and other functionalized MWCNT species such as carboxyl (-COOH) and hydroxyl (-OH) groups can indeed act as plasticizers in poly(lactic acid) (PLA) polymer matrices. Here are some literature references that elaborate on this topic specifically in the context of PLA. Zhou et al. [27] described a study where polylactic acid (PLA) was modified with poly(butylene adipate-co-terephthalate) (PBAT) and carbon nanotubes (CNTs-COOH) containing carboxyl groups using melt blending. A compatibilizer, ethylene-butyl acrylate-glycidyl methacrylate (E-BA-GMA), was employed to enhance the interaction between the CNTs-COOH nanoparticles and the PLA/PBAT matrix. The effects of varying CNTs-COOH content on mechanical properties, thermal properties, crystallinity, and morphology of PLA/CNTs-COOH nanocomposites were investigated. The results showed that incorporating CNTs-COOH nanoparticles led to simultaneous improvements in tensile strength, elongation at break, and impact strength of PLA. Additionally, PLA/CNTs-COOH nanocomposites exhibited higher thermal stability compared to pure PLA, with increases observed in glass transition temperature and initial degradation temperature as CNTs-COOH content increased. At low CNTs-COOH content (≤ 0.5 wt%), the nanoparticles dispersed uniformly in the PLA matrix. Overall, CNTs-COOH were found to be effective fillers for reinforcing and toughening PLA simultaneously, with the PLA/CNTs-COOH nanocomposite containing 0.5 wt% CNTs-COOH demonstrating a favorable combination of strength and toughness [27]. To enhance the performance of PLA (polylactic acid) composites, addressing the poor dispersion and adhesion of carbon nanotubes (CNT) is crucial. Zhang et al. [28] utilized sodium dodecylbenzene sulfonate to modify multi-walled CNT surfaces, improving interfacial adhesion with PLLA (levopolylactic acid) through melt blending. This modification reduced the composite's conductivity below the penetration threshold and enhanced its thermal stability. Additionally, Urtekin et al. [29] leveraged CNT's bridging effect to enhance PLA's interaction with polycarbonate (PC). They compounded variously functionalized multi-walled CNTs (MWCNT, MWCNT-OH, MWCNT-COOH, PC-g-MWCNT) with PC/PLA in a twin-screw extruder. This process facilitated effective grafting of PC onto MWCNT, resulting in improved composite properties. Notably, the addition of 5 wt% MWCNT-OH yielded the highest values for elongation at break, tensile strength, and modulus

in the PC/PLA composites. These studies collectively demonstrate that maleic anhydride-grafted MWCNTs, as well as MWCNTs functionalized with carboxyl and hydroxyl groups, can act as effective plasticizers in PLA polymer matrices, leading to improvements in crystallization behavior, mechanical properties, and thermal stability.

The novelty of this study is that not only the functionalization of MWCNT with MA and also the investigation of the effects of unmodified (MWCNT) and modified multiwall carbon nanotubes (MWCNT-COOH, MWCNT-OH, and MA-g-MWCNT) on the PLA nanocomposites followed by the solvent casting method. Thus, the thermal, mechanical, and electrical properties of nanocomposite materials were determined, and the results of the nanocomposites were compared with neat PLA film.

2. MATERIAL AND METHODS

2.1. Materials

MWCNTs were bought from Timesnano (Chinese Academy of Sciences (CAS)) with a diameter of 10 and 20 nm, a length of 30 μm , and >95 wt% of purity. MWCNT-OH composes of 3.06 wt% -OH content and MWCNT-COOH was 2.00 wt% -COOH content. Poly (L-lactic acid) (PLA) was supplied by Isochem. Chloroform (99%), tetrahydrofuran (99%), acetone (>99%), benzoyl peroxide (BPO) (99%), and maleic anhydride used for functionalization of MWCNTs were purchased from Sigma-Aldrich (St. Louis, USA). All the solvents were used without any further purification.

2.2. Functionalization of the MWCNTs

Maleic anhydride functionalized multiwalled carbon nanotubes (MA-g-MWCNT) were prepared by the following procedure [30]: 1 g of MWCNTs was mixed by refluxing with 2.6 g of maleic anhydride. MA was added into 50 mL of acetone and 50 mL of THF and mixed at 80°C for 4 h. 0.1 g of benzoyl peroxide (BPO) was used as an initiator of the free radical reaction in this procedure. In the last part, anhydrous acetone was used to wash the functionalized MWCNTs (MA-g-MWCNT), and MA-g-MWCNT was centrifuged.

2.3. Preparation of Samples

All the nanocomposite films were prepared by solvent casting method. 5% (w/v) of PLA was added into 100 mL of chloroform and stirred to get a homogenous mixture. Then, appropriate amounts of MWCNT, MWCNT-COOH, MWCNT-OH, and MA-g-MWCNT were separately mixed in this mixture to obtain 0.5, 1, 2, and 3 wt.% ratios of nanofillers. To produce unmodified and modified MWCNT nanocomposites, the solutions were sonicated for 4 h in a water bath at room temperature to enhance the dispersion of MWCNTs and functionalized-MWCNTs in the polymer matrix. The prepared solutions were cast on Petri dishes and put in a vacuum oven at room temperature to remove completely the residue solvent. Finally, the fabricated films were peeled, and the thicknesses were measured as approximately 130 μm . Table 1 shows the amounts of the polymer and nanofillers. 0.5% MWCNT/PLA, 1% MWCNT/PLA, 2% MWCNT/PLA, and 3% MWCNT/PLA nanocomposite films.

Table 1. The prepared polymer solutions for the solution casting method

Films	PLA %	MWCNT %	MWCNT- COOH %	MWCNT-OH %	MA-g-MWCNT %
PLA	5	-	-	-	-
MWCNT/PLA	5	0.5	-	-	-
	5	1.0	-	-	-
	5	2.0	-	-	-
	5	3.0	-	-	-
MWCNT-COOH/ PLA	5	-	0.5	-	-
	5	-	1.0	-	-
	5	-	2.0	-	-
	5	-	3.0	-	-
MWCNT-COOH/PLA	5	-	0.5	-	-
	5	-	1.0	-	-
	5	-	2.0	-	-
	5	-	3.0	-	-
MWCNT-OH/PLA	5	-	-	0.5	-
	5	-	-	1.0	-
	5	-	-	2.0	-
	5	-	-	3.0	-
MA-g-MWCNT /PLA	5	-	-	-	0.5
	5	-	-	-	1.0
	5	-	-	-	2.0
	5	-	-	-	3.0

2.4. Characterization of Samples

2.4.1. ATR spectroscopy

The grafting behavior of the maleic anhydride (MA) onto the MWCNT was analyzed by Absorption Transmission Reflectance (ATR) spectroscopy (Bruker Tensor 27, USA).

2.4.2. FTIR spectroscopy

The chemical bonding of the prepared films was investigated by the Fourier transform infrared (FTIR) spectrometry (Thermo Nicolet Avatar 370 spectrometer, USA). The examination covered a wavenumber range of 4000–400 cm^{-1} with a resolution of 4 cm^{-1} at ambient temperature.

2.4.3. Electrical conductivity

The electrical conductivity was measured using a standard four-point method. All conductivity measurements were determined at room temperature with a Keithley 2400 Source Meter (USA). Rectangular samples of 1 × 5 cm^2 dimensions were prepared for conductivity analysis of the nanocomposite films produced of different types and concentrations. The thickness and resistance values for each sample obtained were taken as the average of the five determined values. The electrical conductivity values of the nanocomposite films were calculated using the resistance values read with the help of the device. The averages of five measurements were reported for each composite.

2.4.4. Thermal characterizations

The thermal gravimetric analysis (TGA) was determined by Pyris 1 TGA device (Perkin Elmer Inc., USA). The samples were heated from 0 to 1000°C under a nitrogen atmosphere with a heating rate of 10°C min⁻¹. In addition, differential scanning calorimeter (DSC) analysis was carried out with the Scinco DSC N-650 instrument (Seoul, Korea). The samples were heated at a temperature range of 25-200°C under a nitrogen atmosphere at an increment of 10°C min⁻¹.

Crystallinity values of the PLA in the nanocomposite films were calculated from the following equation (1):

$$\text{Crystallinity (\%)} = \left(\frac{\Delta H_m}{93.7} \right) \times 100 \quad (1)$$

where ΔH_m is the melting enthalpy (J/g) and 93.7 J/g is the theoretical enthalpy of completely crystalline PLA [31].

2.4.5. Contact angle analysis

The surface nature of the materials was evaluated by the water contact angle analysis (WCA) using the Krüss DSA 100 instrument (Hamburg, Germany) at ambient temperature. The measurements involved applying a 5 µL water droplet with the sessile drop method, and the tests were repeated at least three times using deionized water.

2.4.6. Dynamic mechanical analysis

The dynamic mechanical analysis (DMA) was carried out with the Gabo Eplexor 100 N instrument (Germany) in tension mode for a rectangular specimen of dimension (10 × 35 × 2 mm³). The isochronal frequency of 10 Hz, static load at 1% strain, and dynamic load at 0.2 % strain were applied, and the storage modulus (E'), loss factor ($\tan \delta$), and loss modulus (E'') were recorded.

2.4.7. Atomic force microscopy

The atomic force microscopy (AFM) images of 0.5 wt% of the nanocomposite films were obtained using a Park System (XE-100 E instrument, Korea). The analysis covered a 5 × 5 µm² area at room temperature, employing a scanning rate of 0.5 Hz and operating in non-tapping mode.

3. RESULTS AND DISCUSSION

3.1. ATR Spectroscopy Analysis

Figure 1 shows the ATR spectra of the MWCNT and the MWCNT functionalized with maleic anhydride (MA), carboxyl (-COOH), and hydroxyl (-OH), respectively.

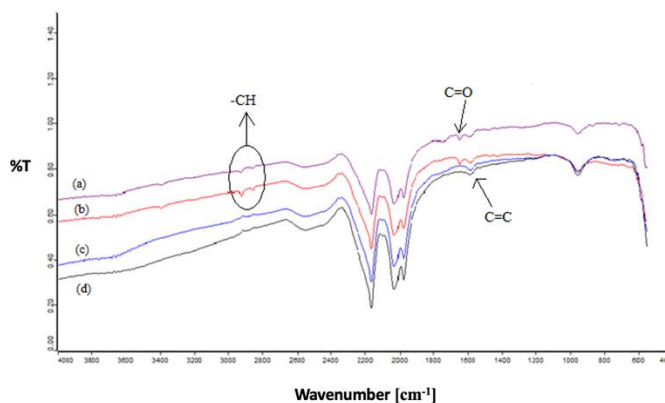


Figure 1. ATR spectrum of nanoparticles (a) MA-g-MWCNT, (b) MWCNT-COOH, (c) MWCNT-OH, (d) MWCNT

The characteristic peak of the aromatic ring (C=C) was obtained between 1600 and 1450 cm^{-1} in the spectra of all the MWCNTs. The stretching vibration of carbonyls (C=O) appeared at 1760-1690 cm^{-1} , which belonged to the carbonyl group (C=O) for MWCNT-COOH and MA-g-MWCNT particles. The C=O stretching at 1721 cm^{-1} , corresponds to the incorporated carboxylic acid groups (-COOH) due to the acid treatment process, characterized the MWCNT-COOH [1]. The C-H stretching at 2853 and 2925 cm^{-1} corresponded to alkyl groups, which comes from the carboxyl group [26]. After the functionalization of MWCNT with maleic anhydride, some organic groups in the chemical structure of maleic anhydride were attached to the surface of MWCNT via the chemical bonds. One of these organic groups, the carbonyl group (C=O), was observed in the spectrum of MA-g-MWCNT at a wavelength of 1740 cm^{-1} . Moreover, the transmittance band appears at 2848 and 2947 cm^{-1} corresponding to alkyl groups (-CH) which is regarding the maleic anhydride [30]. Alkyl groups (-CH) existed in carboxyl acid and maleic anhydride; thus, the stretching frequencies appeared at 2854 cm^{-1} and 2917 cm^{-1} . These peaks were nearly the same for MWCNT-COOH and MA-g-MWCNT.

3.2. FTIR Analysis

The FTIR spectra of nanocomposite films are shown in Figures 2 to 5.

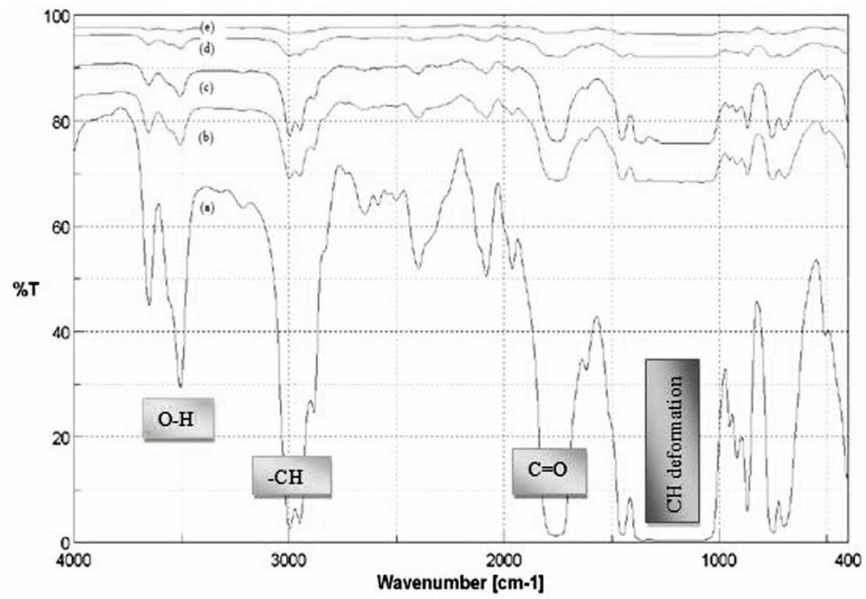


Figure 2. FTIR spectra of (a) neat PLA, (b) 0.5% MWCNT/PLA, (c) 1% MWCNT/PLA, (d) 2% MWCNT/PLA, (e) 3% MWCNT/PLA nanocomposite films

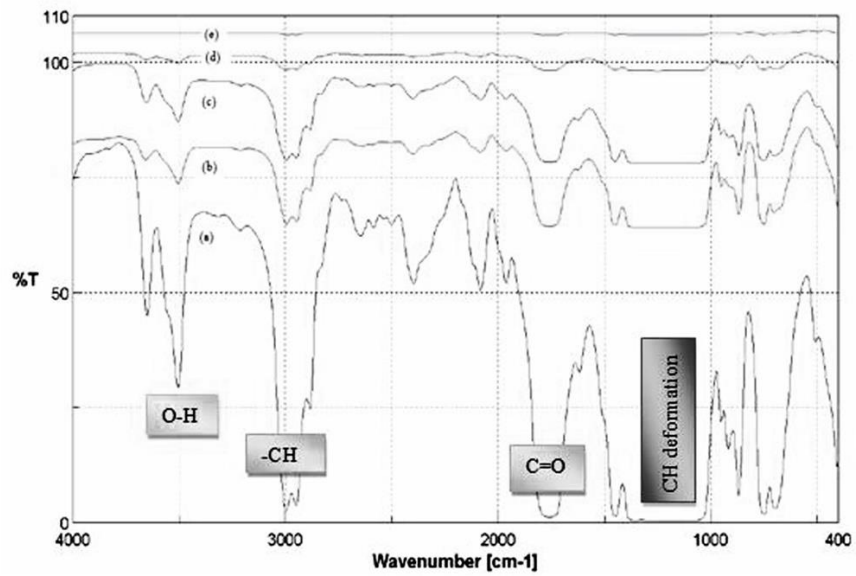


Figure 3. FTIR spectra of (a) neat PLA, (b) 0.5% MWCNT-COOH/PLA, (c) 1% MWCNT-COOH/PLA, (d) 2% MWCNT-COOH/PLA, (e) 3% MWCNT-COOH/PLA nanocomposite films

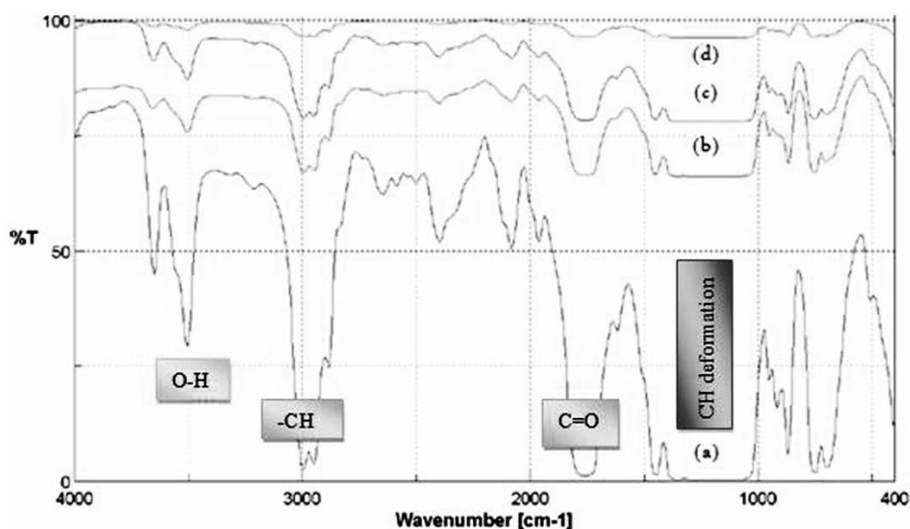


Figure 4. FTIR spectra of (a) neat PLA, (b) 0.5% MA-g-MWCNT/PLA, (c) 1% MA-g-MWCNT/PLA, (d) 2% MA-g-MWCNT/PLA, (e) 3% MA-g-MWCNT/PLA nanocomposite films

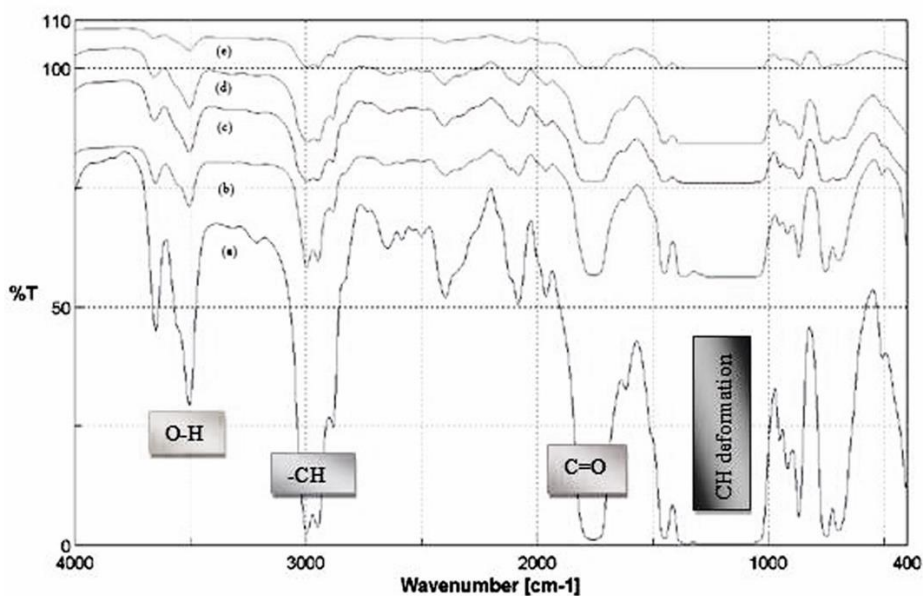


Figure 5. FTIR spectra of (a) neat PLA, (b) 0.5% MWCNT-OH/PLA, (c) 1% MWCNT-OH/PLA, (d) 2% MWCNT-OH/PLA, (e) 3% MWCNT-OH/PLA nanocomposite films

The peaks of pure PLA present CH stretching at 2900-3000 cm^{-1} , C=O carbonyl stretching vibration at 1760 cm^{-1} , CH bending vibrations at 1350-1460 cm^{-1} , and C-C stretching vibration at 870 cm^{-1} [32], as shown in Figures 2 to 5. Accordingly, these peaks were observed for the MWCNT/PLA, MWCNT-COOH/PLA, MA-g-MWCNT/PLA, and MWCNT-OH/PLA nanocomposite films with different amounts of MWCNTs and functionalized MWCNTs. It was clearly understood that when increasing the nanoparticle content of nanocomposite films, the peaks were not observed apparently due to the black color of MWCNT particles. These films were so opaque that they prevented the transmittance of FTIR measurements.

3.3. Electrical Conductivity Analysis

Electrical conductivity relies on the properties of nanofillers such as shape, size, concentration, and distribution of them in the polymer matrix. MWCNTs have a very high aspect ratio in the range of 100-

1000. Therefore, they can build new conductive paths at a low volume fraction [33]. It is well known that chemical functionalization interrupts the extended conjugation of nanotubes, leading to a decrease in the electrical conductivity of functionalized CNTs. Specifically, altering the nanotubes results in a significant reduction in conductivity. Therefore, the electrical conductivity of nanocomposites acquired using functionalized CNT nanoparticles is typically lower compared to those utilizing non-functionalized CNT nanoparticles. On the other hand, some researchers found that the electrical conductivity properties of the types of CNT particles that are functionalized with $-\text{COOH}$ or $-\text{OH}$ groups may have improved [34]. All the results of the electrical conductivity of the samples were determined by four-point electrical analysis, as shown in Table 2.

Table 2. Electrical conductivity of composites for different types of particles

Particle	Conc., %	R, ohm	ρ , ohm.cm	σ , ohm.cm ⁻¹
-	0	256*10 ⁷ ±0.5	6.8*10 ⁶	1.47*10 ⁻⁷
MWCNT	0.5	132*10 ⁷ ±0.2	3.2*10 ⁶	3.10*10 ⁻⁷
MWCNT	1	2.24*10 ⁷ ±3.5	4.9*10 ⁴	2.05*10 ⁻⁵
MWCNT	2	6.4*10 ⁶ ±1.5	1.3*10 ⁴	7.96*10 ⁻⁵
MWCNT	3	2720±0.5	7.18	0.14
MWCNT-COOH	0.5	6.4*10 ⁸ ±46.5	1.9*10 ⁶	5.08*10 ⁻⁷
MWCNT-COOH	1	478*10 ² ±6.1	182	0.005
MWCNT-COOH	2	4780±0.59	14.9	0.067
MWCNT-COOH	3	2420±0.24	6.1	0.163
MA-g-MWCNT	0.5	1.6*10 ⁹ ±0.19	2.9*10 ⁶	3.34*10 ⁻⁷
MA-g-MWCNT	1	1.2*10 ⁹ ±0.24	3.1*10 ⁶	3.21*10 ⁻⁷
MA-g-MWCNT	2	1.9*10 ⁶ ±0.38	5*10 ³	0.0002
MA-g-MWCNT	3	8.3*10 ⁵ ±109.8	2.3*10 ⁴	0.0004
MWCNT-OH	0.5	1.5*10 ⁹ ±0.2	5.4*10 ⁶	1.86*10 ⁻⁷
MWCNT-OH	1	69*10 ⁷ ±30.2	2*10 ⁶	4.90*10 ⁻⁷
MWCNT-OH	2	9.1*10 ⁴ ±5.5	207.7	0.005
MWCNT-OH	3	13*10 ³ ±1.6	36.09	0.03

As shown in Table 2, the electrical conductivity of the nanocomposite films was higher than the neat PLA film. In addition, when increased the amount of reinforcements from 0.5% to 3% for MWCNT, MWCNT-COOH, MA-g-MWCNT, and MWCNT-OH in the PLA polymer matrix, the electrical conductivity of the nanocomposite films increased. However, MWCNT-COOH/PLA composite films showed the highest conductivity value. It was observed that the electrical conductivity of the nanocomposite increases with the addition of CNTs to the PLA which has a very low electrical conductivity value due to the π -bonds present in the carbon nanotubes. The carbonyl (C=O) group in the carboxyl ($-\text{COOH}$) group has a π -bond; therefore, the highest increment in electrical conductivity was found in the MWCNT-COOH/PLA composite films.

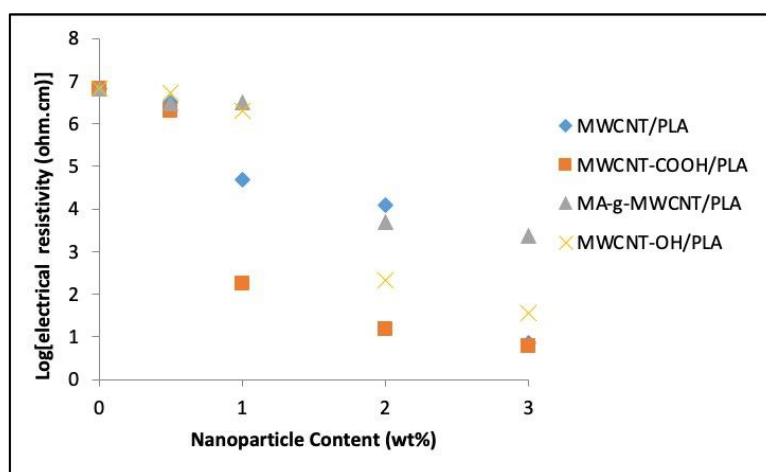


Figure 6. Comparison of electrical resistivity of the composite films

Figure 6 shows the variation of electrical resistivity with respect to the type of nanoparticles. A drastic decrease in the electrical resistivity was obtained at 1 wt.% for the MWCNT-COOH/PLA composite, which indicates that the percolation threshold for the formation of a conductive MWCNT-COOH network in the PLA matrix was reached. Moreover, the percolation threshold was gained at 1.5 wt% for MA-g-MWCNT/PLA and MWCNT-OH/PLA nanocomposites due to decreasing of electrical resistivity.

3.4. Thermal Analysis

Table 3 illustrates the thermal results such as initial thermal degradation temperature, final thermal decomposition temperature, and the percentage of the residue amount. The effect of MWCNT, MWCNT-COOH, MA-g-MWCNT and MWCNT-OH nanoparticles on the thermal degradation temperature and thermal stability of PLA was investigated by TG analysis.

Table 3. The thermal properties obtained by TGA analysis

Films	Conc. of nanoparticle, % wt	Initial decomposition temp, °C	Final decomposition temp, °C	Residue, % at 800°C
Neat PLA	—	328.9	370.3	1.635
MWCNT/PLA	0.5	325.7	371.3	1.531
MWCNT/PLA	1	332.1	371.7	1.820
MWCNT-COOH/PLA	0.5	344.8	377.6	1.986
MWCNT-COOH/PLA	1	343.2	379.2	0.595
MA-g-MWCNT/PLA	0.5	347.0	393.3	0.976
MA-g-MWCNT/PLA	2	340.6	386.7	1.752
MWCNT-OH/PLA	0.5	341.6	377.1	1.986
MWCNT-OH/PLA	2	345.8	378.9	1.492

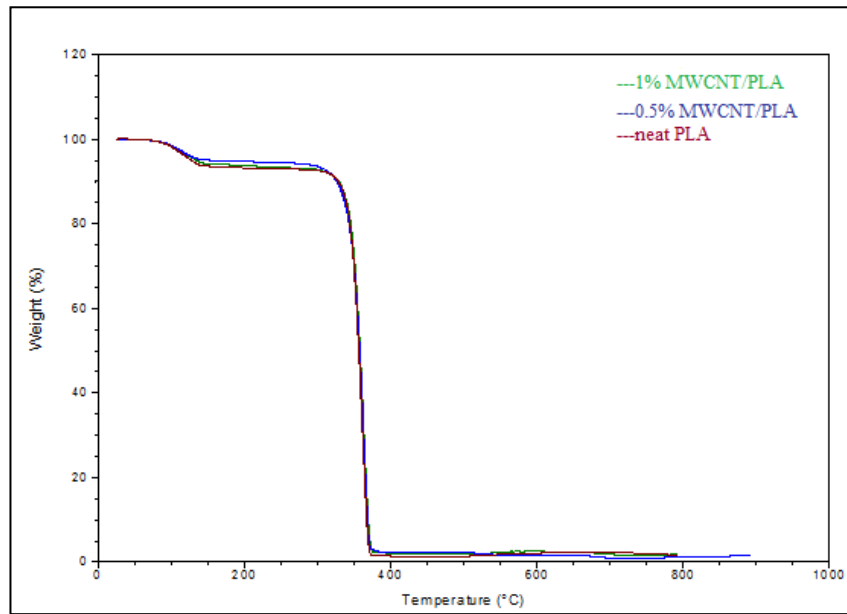


Figure 7. TGA curves of neat PLA, 0.5 wt% MWCNT/PLA and 1 wt% MWCNT/PLA composite films

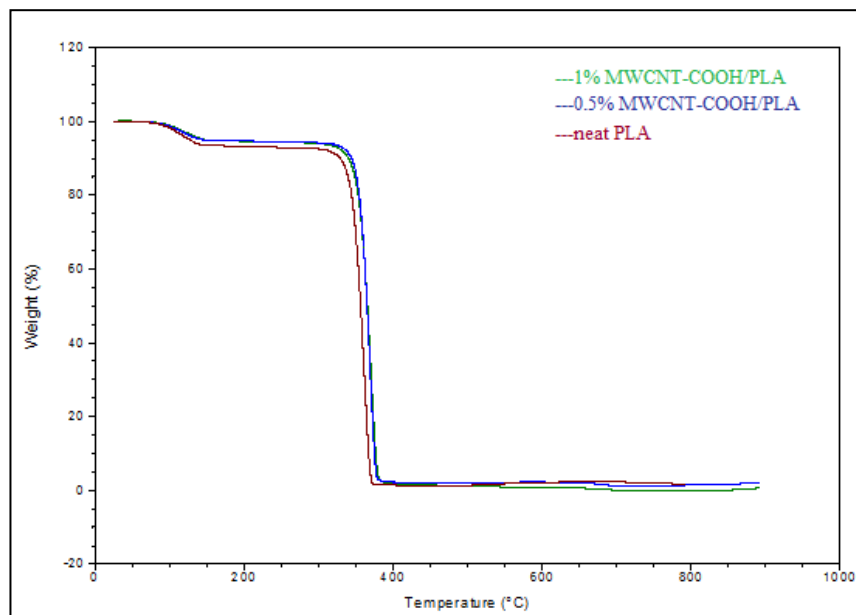


Figure 8. TGA curves of neat PLA, 0.5 wt% MWCNT-COOH/PLA and 1 wt% MWCNT-COOH/PLA composite films

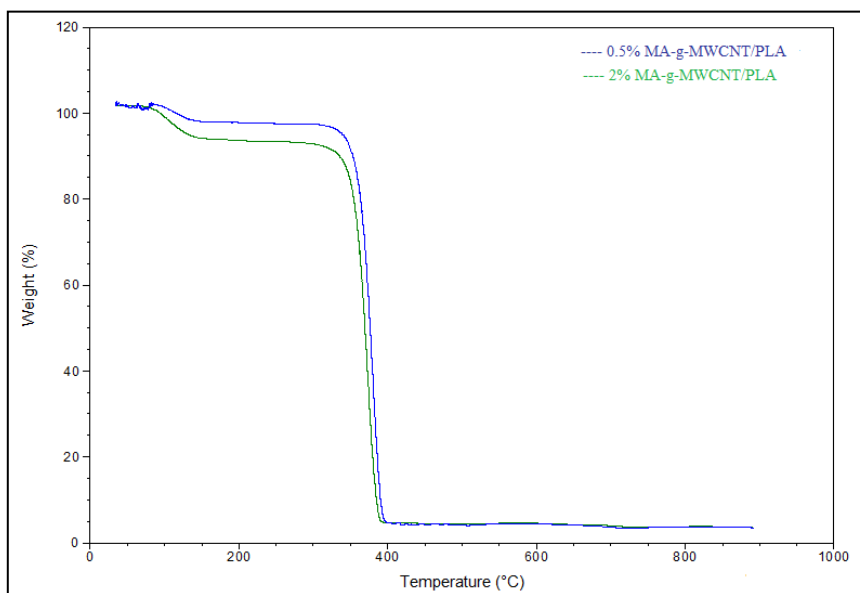


Figure 9. TGA curves of 0.5 wt% MA-g-MWCNT/PLA and 2 wt% MA-g-MWCNT/PLA composite films

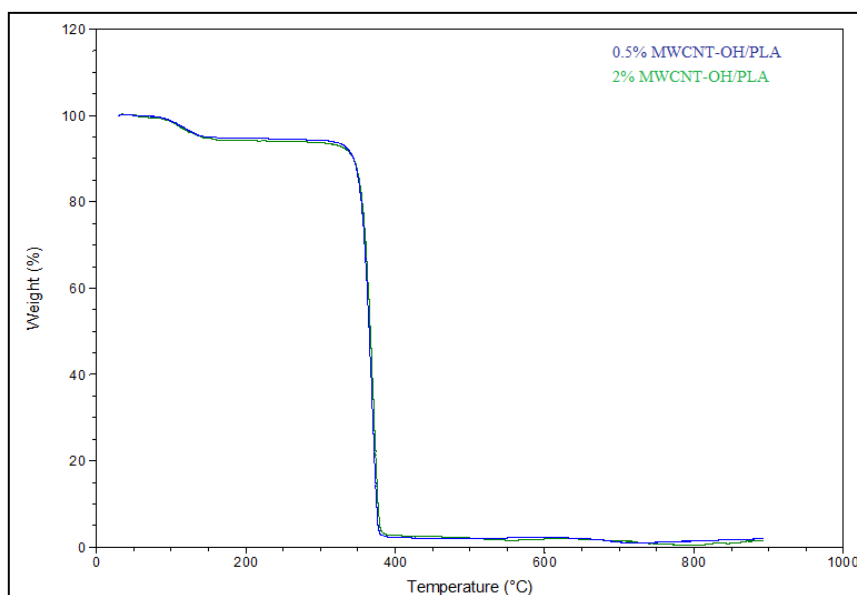


Figure 10. TGA curves of 0.5 wt% MWCNT-OH/PLA and 2 wt% MWCNT-OH/PLA composite films

As can be seen from TGA curves (Figure 7 to 10), the major weight loss was noticed in the temperature range between 300°C and 400°C. The nanocomposite films began to decompose and completed the decomposition at a higher temperature from neat PLA. This condition indicates the improved thermal stability of nanocomposite films due to the high thermal degradation of carbon nanotubes used as a nanofiller. Moreover, the primary purpose of employing a grafting technique is to improve the bonding at the interface between the polymer matrix and MWCNT. This circumstance facilitates efficient transmission of loads from the matrix to the nanoparticle, ultimately boosting thermal stability. As well, the most increment thermal stability of PLA was reached when the addition 0.5 wt% of MA-g-MWCNT with initial decomposition temperature increased from 328.91°C to 347°C due to the better interfacial bond between MA-g-MWCNT and PLA [35]. In the study of Chrissafis [36] on the thermal degradation kinetics of PLA reinforced with MWCNT-COOH and that of Kuan et al. [30] in which PLA polymer was reinforced with carbon nanotubes, the thermal degradation temperatures of nanocomposites were higher than the thermal degradation temperature of pure PLA. When the initial decomposition temperatures of 0.5 wt.% MWCNT-COOH/PLA and 1 wt.% MWCNT-COOH/PLA were compared, the 0.5 wt.% MWCNT-

COOH/PLA nanocomposite film began to decompose at a higher temperature. This is an indication that the addition of MWCNTs-COOH causes a substantial thermal enhancement of PLA, at least at the initial stages of decomposition. This improvement is mainly attributed to good matrix–nanotube interaction, good thermal conductivity of the nanotubes and also due to their barrier effect. The nanocomposite begins to decompose at higher temperatures, although the addition of MWCNTs-COOH seems to have little effect on the temperature which the maximum decomposition rate takes place.

Figure 11 and 12 show the effect of different types of 0.5 wt% and 2 wt% of MWCNTs n nanocomposite films on the glass transition temperature (T_g), melting temperature (T_m), and the melting enthalpy (ΔH_m) obtained by DSC analysis.

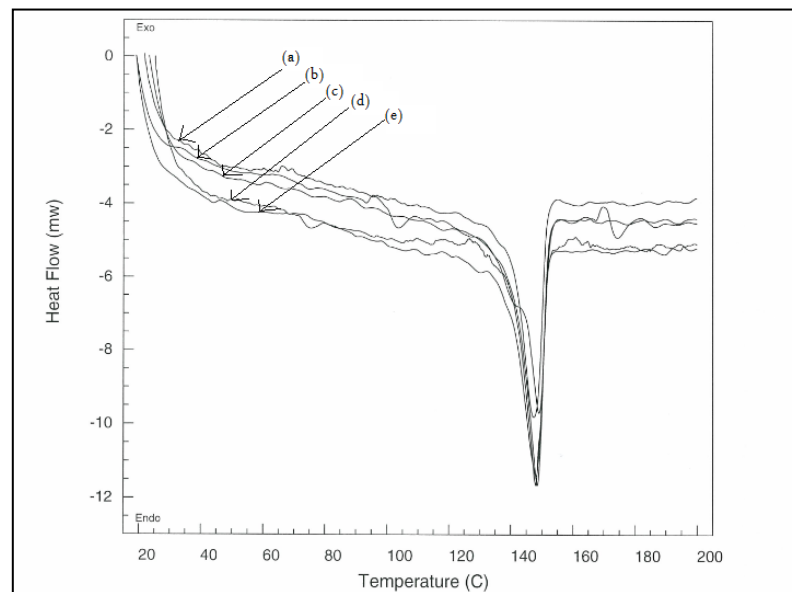


Figure 11. DSC curves of films of (a) 0.5 wt% MWCNT-COOH/PLA, (b) 0.5 wt% MWCNT/PLA, (c) neat PLA, (d) 2 wt% MWCNT/PLA, (e) 2 wt% MWCNT-COOH/PLA

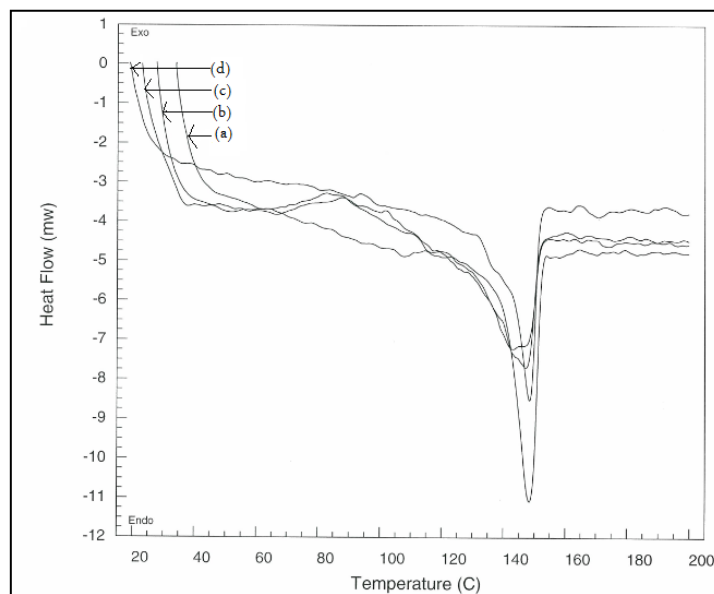


Figure 12. DSC curves of films of (a) 0.5 wt% MA-g-MWCNT/PLA, (b) 2 wt% MA-g-MWCNT/PLA, (c) 0.5 wt% MWCNT-OH/PLA, (d) 2 wt% MWCNT-OH/PLA

The nanocomposite films' glass transition temperature (T_g) is connected to the collective movement of lengthy chain segments, a process that might face obstacles due to MWCNT-OH presence.

Consequently, robust connections between the matrix and the strengthening component might impede the polymer chain's movement, resulting in an elevation in the Tg value [1].

It demonstrated that the Tg increased from 85.78 to 87.74 for the MWCNT-OH/PLA nanocomposite film, and it was higher than neat PLA (Table 4). Therefore, the highest increment was reached with the MWCNT-OH nanofiller. For all the nanocomposite films, when increasing the concentration of nanofillers in the polymer matrix, Tg increased. Conversely, the Tg values were lower than that of neat PLA, unlike MWCNT-OH/PLA nanocomposite film.

Table 4. The thermal properties of neat PLA and the nanocomposite films

Particle	Conc., %	Tg, °C	Tm, °C	ΔH_m , J/g	Xc, %
neat PLA	0	73.7	149.1	28.3	30.2
MWCNT/PLA	0.5	70.6	148.5	31.3	33.4
MWCNT/PLA	2	74.8	148.1	30.9	33.1
MWCNT-COOH/PLA	0.5	66.9	147.4	32.6	34.7
MWCNT-COOH/PLA	2	72.8	148.1	29.6	31.6
MA-g-MWCNT/PLA	0.5	68.6	148.3	32.9	35.2
MA-g-MWCNT/PLA	2	69.5	142.9	37.6	40.1
MWCNT-OH/PLA	0.5	85.8	147.2	46.7	49.8
MWCNT-OH/PLA	2	87.7	148.4	30.8	32.9

Table 3 summarizes the thermal property (Tg, Tm, ΔH_m , Xc) of different types of nanocomposite films. Generally, the melting temperatures (Tm) and melting enthalpy (ΔH_m) decreased with increasing the amount of nanoparticles in the nanocomposite films, and the lowest Tm value was attained at 2 wt% of MA-g-MWCNT/PLA. The Tm values of nanocomposite materials were lower than that of neat PLA. The lowest Tm value was found as 142.96 °C for 2wt% of MA-g-MWCNT/PLA. Wu and Liao [37] explained that the melting temperature (Tm) decreased markedly with an increasing MWNTs-OH content up to 1 wt% and then the effect was slight. The marked decrease in Tm of PLA-g-AA/MWNTs-OH is probably the result of the MWNTs-OH prohibiting the movement of the polymer segments, causing polymer chain arrangement to become more difficult, and also of the hydrophilic character of MWNTs-OH leading to poor adhesion with the hydrophobic PLA.

Moreover, the enthalpy of melting (ΔH_m) is a measure of the energy required to melt a material, and it is closely related to the crystallinity of a polymer composite. Higher ΔH_m values typically indicate greater crystallinity, as more energy is needed to break the ordered crystalline structure during melting. At 0.5% concentration of the MWCNT/PLA composite film, there was an increase in ΔH_m compared to neat PLA, indicating enhanced crystallinity. This suggests that the incorporation of MWCNT improved the crystalline structure of PLA. However, at 2% concentration, ΔH_m decreases slightly compared to the 0.5% concentration. This could indicate a saturation effect where higher concentrations of MWCNT might disrupt the crystalline structure, leading to a decrease in crystallinity despite still being higher than neat PLA. For MWCNT-COOH/PLA composites, at both 0.5% and 2% concentrations, ΔH_m values are lower compared to neat PLA. This suggests that the presence of MWCNT-COOH may not significantly enhance crystallinity in PLA composites. Both at 0.5% and 2% concentrations of the MA-g-MWCNT/PLA composites, there are substantial increases in ΔH_m compared to neat PLA. This indicates that the presence

of MA-g-MWCNT greatly enhances crystallinity in PLA composites, likely due to strong interactions between the grafted MWCNT and the PLA matrix. Additionally, at 0.5% concentration of the MWCNT-OH/PLA composite films, there's a significant increase in ΔH_m compared to neat PLA, indicating a substantial enhancement in crystallinity. This suggests that MWCNT-OH effectively promotes crystallization in PLA composites. However, at 2% concentration, ΔH_m decreases compared to the 0.5% concentration, which could indicate a disruption in crystalline structure at higher concentrations. Overall, the effects of MWCNT species on crystallinity, as indicated by ΔH_m , vary depending on the functional groups and concentrations. While some species enhance crystallinity at certain concentrations, others may exhibit diminishing returns or even disruption of crystalline structure at higher concentrations.

3.5. Dynamic Mechanical Analyzer (DMA)

Figure 13 and Figure 14 depict the mechanical analysis of the neat PLA, 3% MWCNT-COOH/PLA, 3% MA-g-MWCNT/PLA, and 3% MWCNT-OH/PLA samples. It is exactly known that in dynamic mechanical analysis (DMA), the storage modulus (E') and loss modulus (E'') are key parameters used to characterize the mechanical properties of materials over a range of temperatures. The storage modulus (E') measures the stored energy, relatively the elastic portion of materials. On the other side, the loss modulus (E'') assesses the energy dissipated as heat, relatively the viscous portion of materials. As well, E''/E' ratio gives the $\tan \delta$ values for DMA analysis.

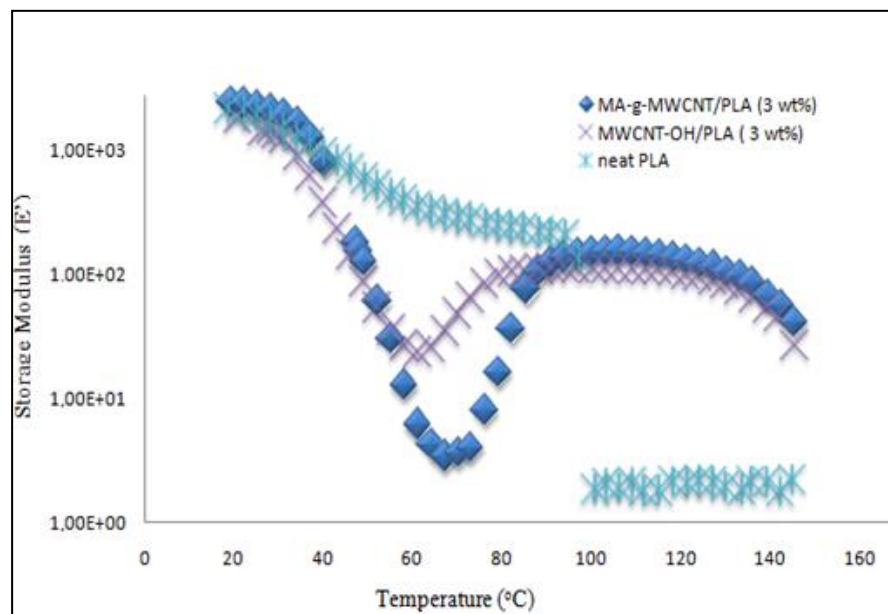


Figure 13. Relationship between the E' (storage modulus) and temperature

The storage modulus of PLA composites with MA-g-MWCNT showed an increase compared to neat PLA over a certain temperature range. This increase could indicate improved reinforcement effects and better load transfer between the MWCNT and PLA matrix. However, beyond a certain temperature, the storage modulus started to decrease as the material underwent softening or transition to a more viscoelastic state. On the other side, PLA composites with MWCNT-OH exhibited a slight increase in storage modulus compared to neat PLA over a wider temperature range. The presence of hydroxyl functional groups enhanced compatibility between MWCNT-OH and the PLA matrix, leading to improved stiffness and mechanical properties over a broader temperature range.

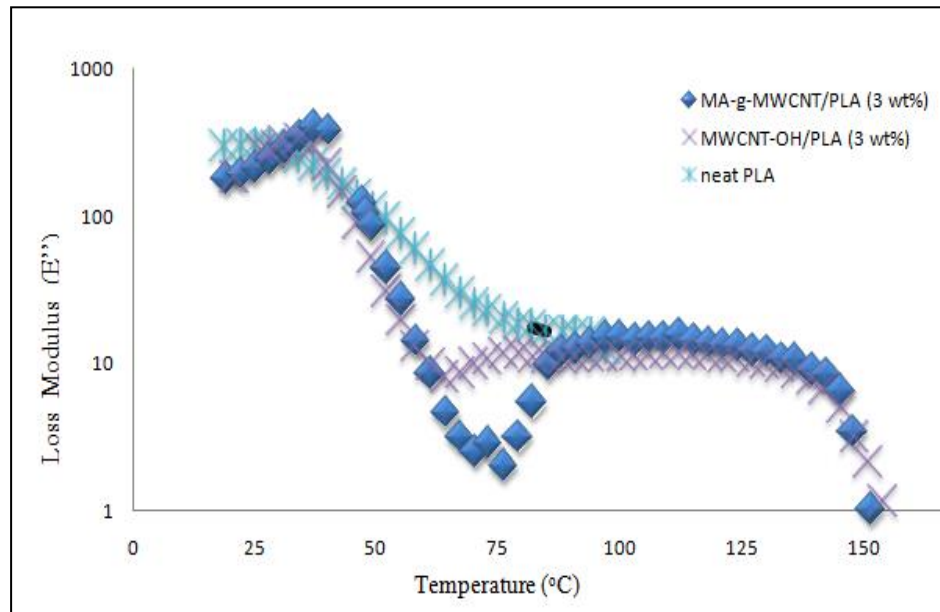


Figure 14. Relationship between the E'' (loss modulus) and temperature

The loss modulus of PLA composites with MA-g-MWCNT increased compared to neat PLA, indicating enhanced damping characteristics. This increase could be due to improved interfacial adhesion and viscoelastic behavior of the composite. Similarly, the loss modulus of PLA composites with MWCNT-OH also increased compared to neat PLA, indicating improved damping characteristics. The enhanced interfacial adhesion and reinforcement effects contribute to the increased loss modulus, especially at higher temperatures.

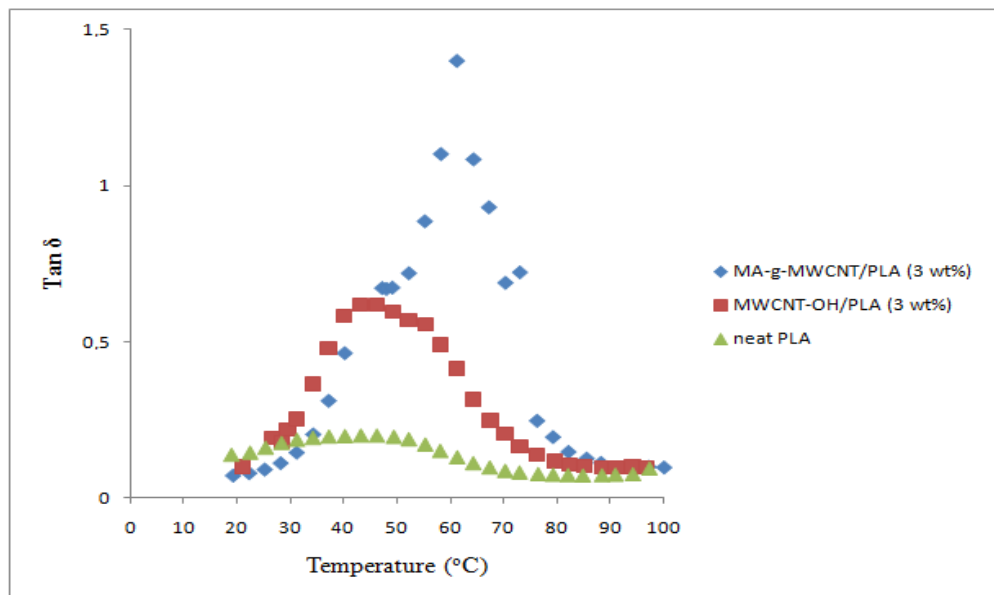


Figure 15. Variation of the $\tan \delta$ with temperature for MA-g-MWCNT/PLA, MWCNT-OH/PLA and neat PLA

The dynamic mechanical properties of neat PLA and modified-MWCNT/PLA nanocomposites such as MA-g-MWCNT/PLA and MWCNT-OH/PLA including 3 wt% of nanoparticles were measured and determined the compatibility between the matrix and filler. Fig. 15 illustrates variations of the loss tangent ($\tan \delta$) with the temperature of the MA-g-MWCNT/PLA, MWCNT-OH/PLA, and neat PLA.

An important observation is that $\tan \delta$ exhibits a rapid rise at a specific temperature, signifying the

initiation of segmental movement, followed by a subsequent decline.

Overall, the peak becomes wider and less intense as the filler content increases, as the presence of the inorganic network impedes the polymer chains' segmental mobility. The displacement of the $\tan \delta$ value towards higher temperatures implies the robust interfacial connection between the polymer matrix and the functionalized MWCNT nanoparticles [18]. Relatively, the most efficient bonding obtained in MA-g-MWCNT/PLA nanocomposite with 3 wt% of MA-g-MWCNT due to the shift to high temperature of $\tan \delta$ value. On the other hand, MWCNT/PLA and MWCNT-COOH/PLA nanocomposite films were very stiff and brittle; therefore, DMA analysis of these nanocomposites couldn't be done.

3.6. Contact angle analysis

Contact angle values for the neat PLA and all the nanocomposite films with concentrations from 0.5 wt% to 3 wt% were given in Figure 16. The water wettability of a material's surface plays a critical role in determining the biological response.

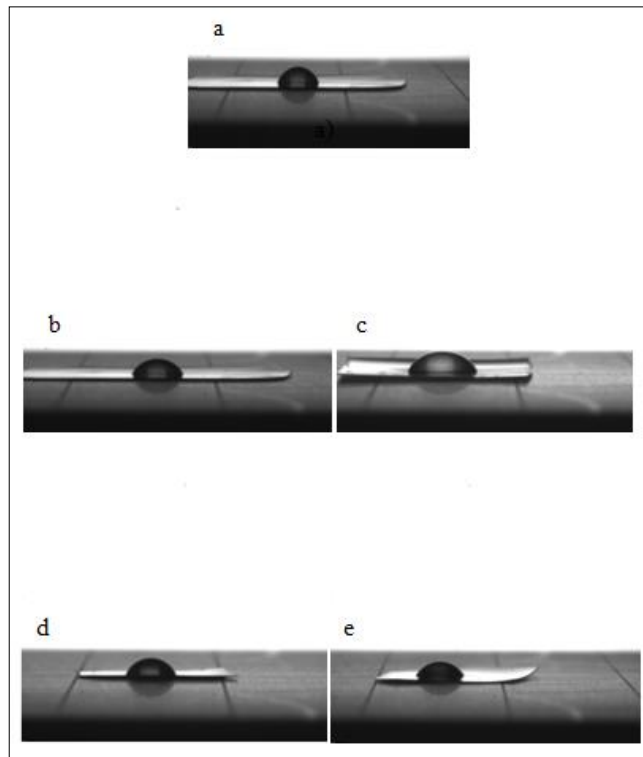


Figure 16. Contact angle images of neat PLA and nanocomposite films (a) neat PLA, (b) MWCNT/PLA, (c) MWCNT-COOH/PLA, (d) MA-g-MWCNT/PLA and (e) MWCNT-OH/PLA

The contact angle value of the neat PLA film was calculated as 82.55° ; therefore, PLA is a hydrophobic polymer [1]. After the modification of the surface of MWCNT with -OH group, the contact angle value of the films decreased and this film showed hydrophilic character. Table 5 shows the contact angle values with respect to various concentrations. The results indicated that the MWCNT-OH/PLA films were strongly hydrophilic compared to the other films due to the -OH groups. Moreover, MWCNT/PLA and MA-g-MWCNT/PLA films revealed more hydrophobic character.

Table 5. Contact angle values of neat PLA and its nanocomposite films

Films	Concentration (%)	Contact Angle (°)
Neat PLA	0	82.55 ± 6.72
MWCNT/PLA	0.5	79.65 ± 4.04
MWCNT/PLA	1	80.35 ± 7.06
MWCNT/PLA	2	87.46 ± 0.56
MWCNT/PLA	3	85.75 ± 5.95
MWCNT-COOH/PLA	0.5	79.9 ± 9.0
MWCNT-COOH/PLA	1	77.08 ± 9.30
MWCNT-COOH/PLA	2	70.4 ± 12.40
MWCNT-COOH/PLA	3	71.43 ± 6.64
MA-g-MWCNT/PLA	0.5	82.73 ± 2.03
MA-g-MWCNT/PLA	1	99.28 ± 8.42
MA-g-MWCNT/PLA	2	92.05 ± 13.01
MA-g-MWCNT/PLA	3	84.03 ± 9.41
MWCNT-OH/PLA	0.5	65.93 ± 2.34
MWCNT-OH/PLA	1	62.25 ± 6.25
MWCNT-OH/PLA	2	64.13 ± 2.05
MWCNT-OH/PLA	3	28.55 ± 2.54

3.7. Atomic force microscopy (AFM)

Figure 17 displays AFM images of the neat PLA and its nanocomposite films with the concentration of the nanoparticle of 0.5 wt%.

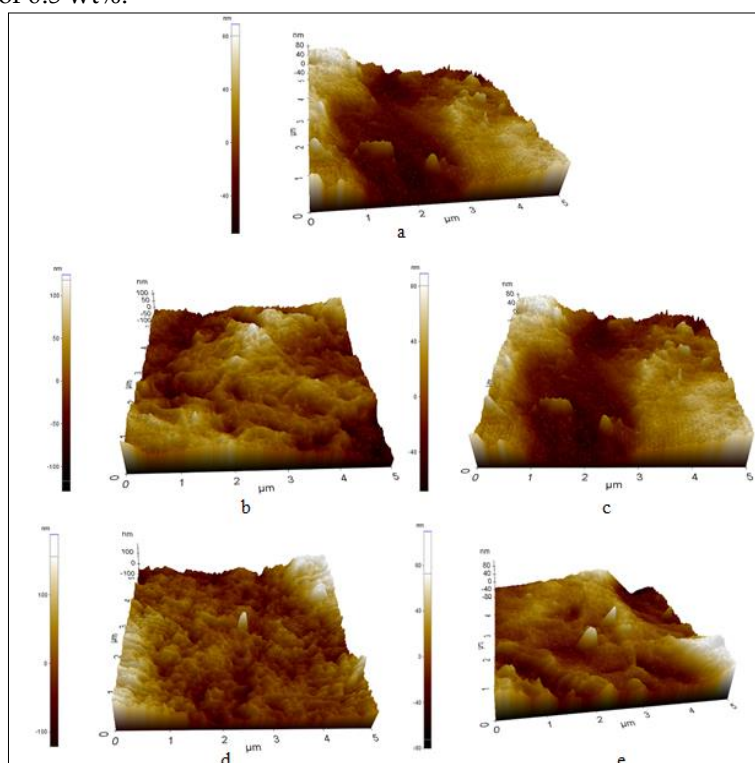


Figure 17. AFM images of neat PLA and its nanocomposite films (a) neat PLA, (b) MWCNT/PLA, (c) MWCNT-COOH/PLA, (d) MA-g-MWCNT/PLA and (e) MWCNT-OH/PLA

As shown in Figure 17, the dispersion of the nanoparticles in the PLA matrix was achieved homogeneously for MA-g-MWCNT/PLA. In Figure 17(b), there was no aggregation in the polymer matrix with MA-g-MWCNT nanoparticles. Therefore, the best interfacial bonding was obtained between the MA-g-MWCNT nanoparticle and PLA.

Table 6. Surface roughness of the neat PLA and its nanocomposite films

Films	Surface roughness value (R_z , nm)
Neat PLA	39.59
MWCNT/PLA	23.15
MWCNT-COOH/PLA	36.12
MWCNT-OH/PLA	20.51
MA-g-MWCNT/PLA	46.47

When the surface roughnesses of the nanocomposite films were compared, the MA-g-MWCNT/PLA films showed the roughest surface at 46.47 nm. While the neat PLA film had a surface roughness of 39.59 nm, it increased to 46.47 for the MA-g-MWCNT/PLA film. The reason is that the roughness increased with the addition of MA-g-MWCNT to the polymer matrix due to the good interaction between the particle and polymer.

4. CONCLUSIONS

The neat PLA and MWCNT/PLA, MWCNT-COOH/PLA, MA-g-MWCNT/PLA, and MWCNT-OH/PLA nanocomposite films were successfully prepared by the solvent casting method. ATR analysis showed that the maleic anhydride (MA) was strongly grafted onto the surface of MWCNT (MA-g-MWCNT). In addition, the dynamic mechanical analysis demonstrated good interfacial adhesion between 3% of the MA-g-MWCNT nanoparticle and the PLA matrix. Thermal analyses represented that the thermal stability of the nanocomposite films increased, and these films completely decomposed at a higher temperature compared to the neat PLA. The most increment of the thermal stability of the films was obtained by the addition of 0.5 wt% MA-g-MWCNT with initial decomposition temperature increased from 328.91°C to 347°C. The surface resistance of the nanocomposite film of 3 wt% MWCNT-COOH/PLA decreased from 2.56×10^9 to $2.42 \times 10^3 \Omega$ (by 10^6 order). Moreover, MWCNT-COOH/PLA composite films illustrated higher electrical conductivity than other nanocomposite films. For AFM analysis, the functionalized MWCNT particles were homogeneously dispersed in the PLA matrix. Consequently, these nanocomposite films can be used for electronic systems, biomedical applications, or as packaging materials due to the improved properties of the PLA polymer with MWCNTs.

Declaration of Ethical Standards

Authors declare to comply with all ethical guidelines including authorship, citation, data reporting, and publishing original research.

Credit Authorship Contribution Statement

F.A: Investigation, Experimental Section, Data Curation, Methodology, Investigation, Writing – original draft. **Ş.M.E.T:** Methodology, Conceptualization, Validation, Resources, Writing – original draft, Writing -review & editing, Supervision.

Declaration of Competing Interest

The authors declare that they have no known competing financial interests or personal relationships that could have appeared to influence the work reported in this paper.

Funding / Acknowledgements

The authors would like to thank Roketsan A.S. for the thermogravimetric analysis.

Data Availability

The data that support the findings of this study are available from the corresponding author upon reasonable request.

5. REFERENCES





- [1] C. S. Wu and H. T. Liao, "Study on the preparation and characterization of biodegradable polylactide/multi-walled carbon nanotubes nanocomposites", *Polymer*, vol. 48, no. 15, pp. 4449-4458, 2007.
- [2] S. Azizi, M. Azizi, and M. Sabetzadeh, "The role of multiwalled carbon nanotubes in the mechanical, thermal, rheological, and electrical properties of PP/PLA/MWCNTs nanocomposites", *Journal of Composites Science*, vol. 3, no. 3, pp. 64-79, 2019.
- [3] R. Scaffaro, F. Lopresti, A. Sutura, L. Botta, R. M. Fontana, and G. Gallo, "Plasma modified PLA electrospun membranes for actinorhodin production intensification in *Streptomyces coelicolor* immobilized-cell cultivations", *Colloids and Surfaces B: Biointerfaces*, vol. 157, pp. 233-241, 2017.
- [4] Y. Zare, H. Garmabi, and K. Y. Rhee, "Structural and phase separation characterization of poly (lactic acid)/poly (ethylene oxide)/carbon nanotube nanocomposites by rheological examinations", *Composites Part B: Engineering*, vol. 144, pp. 1-10, 2018.
- [5] H. M. Alghamdi, M. M. Abutalib, A. Rajeh, M. A. Mannaa, O. Nur, and E. M. Abdelrazek, "Effect of the Fe₂O₃/TiO₂ Nanoparticles on the Structural, Mechanical, Electrical Properties and Antibacterial Activity of the Biodegradable Chitosan/Polyvinyl Alcohol Blend for Food Packaging", *Journal of Polymers and the Environment*, vol. 30, no. 9, pp. 3865-3874, 2022.
- [6] J. Ahmed and S. K. Varshney, "Polylactides—chemistry, properties and green packaging technology: A review", *International Journal of Food Properties*, vol. 14, no. 1, pp. 37-58, 2011.
- [7] J. You, L. Lou, W. Yu, and C. Zhou, "The preparation and crystallization of long chain branching polylactide made by melt radicals reaction", *Journal of Applied Polymer Science*, vol. 129, no. 4, pp. 1959-1970, 2013.
- [8] X. Liu, C. Gao, P. Sangwan, L. Yu, and Z. Tong, "Accelerating the degradation of polyolefins through additives and blending", *Journal of Applied Polymer Science*, vol. 131, no. 18, pp. 40750, 2014.
- [9] X. Wang, H. Zhou, B. Liu, Z. Du, and H. Li, "Chain extension and foaming behavior of poly (lactic acid) by functionalized multiwalled carbon nanotubes and chain extender", *Advances in Polymer Technology*, vol. 33, no. S1, pp. 21444-21454, 2014.
- [10] D. S. Aldana, E. D. Villa, M. Hernández, D. Dios, G. G. Sanchez, Q. R. Cruz, S. F. Gallardo, H. P. Castillo, and L. B. Casarrubias, "Barrier Properties of Polylactic Acid in Cellulose Based Packages Using Montmorillonite as Filler", *Polymers*, vol. 6, pp. 2386-2403, 2014.
- [11] B. W. Chieng, N. A. Ibrahim, N. A., W. M. Z. Wan Yunus, M. Z. Hussein, Y. Y. Then, and Y. Y. Loo, "Effects of graphene nanoplatelets and reduced graphene oxide on poly (lactic acid) and plasticized poly (lactic acid): A comparative study", *Polymers*, vol. 6, no. 8, pp. 2232-2246, 2014.
- [12] Y. Gogotsi, *Nanotubes and Nanofibers*. Boca Raton, CRC Press, 2006.

- [13] B. Kumar, M. Castro, and J. F. Feller, "Poly (lactic acid)–multi-wall carbon nanotube conductive biopolymer nanocomposite vapour sensors", *Sensors and Actuators B: Chemical*, vol. 161, no.1, pp. 621-628, 2012.
- [14] S. W. Ko, M. K. Hong, B. J. Park, R. K. Gupta, H. J. Choi, and S. N. Bhattacharya, "Morphological and rheological characterization of multi-walled carbon nanotube/PLA/PBAT blend nanocomposites", *Polymer Bulletin*, vol. 63, pp. 125-134, 2009.
- [15] H. Y. Yu, Z. Y. Qin, B. Sun, X. G. Yang, and J. M. Yao, "Reinforcement of transparent poly (3-hydroxybutyrate-co-3-hydroxyvalerate) by incorporation of functionalized carbon nanotubes as a novel bionanocomposite for food packaging", *Composites Science and Technology*, vol. 94, pp. 96-104, 2014.
- [16] P. K. Tripathi, S. Durbach, and N. J. Coville, "Synthesis of multi-walled carbon nanotubes from plastic waste using a stainless-steel CVD reactor as catalyst", *Nanomaterials*, vol. 7, no. 10, pp. 284-301, 2017.
- [17] N. Thummarungsan, D. Pattavarakorn, and A. Sirivat, "Tuning rigidity and negative electrostriction of multi-walled carbon nanotube filled poly (lactic acid)", *Polymer*, vol. 196, pp. 122488-122499, 2020.
- [18] P. G. Seligra, F. Nuevo, M. Lamanna, and L. Famá, "Covalent grafting of carbon nanotubes to PLA in order to improve compatibility", *Composites Part B: Engineering*, vol. 46, pp. 61-68, 2013.
- [19] Y. Zhou, L. Lei, B. Yang, J. Li, and J. Ren, "Preparation and characterization of polylactic acid (PLA) carbon nanotube nanocomposites", *Polymer Testing*, vol. 68, pp. 34-38, 2018.
- [20] G. E. A. Verginio, T. L. D. A. Montanheiro, L. S. Montagna, J. Marini, and F. R. Passador, "Effectiveness of the preparation of maleic anhydride grafted poly (lactic acid) by reactive processing for poly (lactic acid)/carbon nanotubes nanocomposites", *Journal of Applied Polymer Science*, vol. 138, no. 12, pp. 50087, 2021.
- [21] N. F. Braga, H. M. Zaggo, T. L. Montanheiro, and F. R. Passador, "Preparation of maleic anhydride grafted poly (trimethylene terephthalate) (PTT-g-MA) by reactive extrusion processing", *Journal of Manufacturing and Materials Processing*, vol. 3, no. 2, pp. 37, 2019.
- [22] Y. Y. Lu, H. Li, and H. Z. Liu, "Maleic anhydride functionalization of multi-walled carbon nanotubes by the electron beam irradiation in the liquid media", *Physica E: Low-dimensional Systems and Nanostructures*, vol. 43, no. 1, pp. 510-514, 2019.
- [23] C. Y. Hong, Y. Z. You, and C. Y. Pan, "A new approach to functionalize multi-walled carbon nanotubes by the use of functional polymers", *Polymer*, vol. 47, no. 12, pp. 4300-4309, 2006.
- [24] Y. L. Huang, S. M. Yuen, C. C. M. Ma, C. Y. Chuang, K. C. Yu, C. C. Teng, H. W. Tien, Y. C. Chiu, S. Y. Wu, S. H. Liao, and F. B. Weng, "Morphological, electrical, electromagnetic interference (EMI) shielding, and tribological properties of functionalized multi-walled carbon nanotube/poly methyl methacrylate (PMMA) composites", *Composites Science and Technology*, vol. 69, no. 11-12, pp. 1991-1996, 2009.
- [25] H. L. Wu, C. H. Wang, C. C. M. Ma, Y. C. Chiu, M. T. Chiang, and C. L. Chiang, "Preparations and properties of maleic acid and maleic anhydride functionalized multiwall carbon nanotube/poly (urea urethane) nanocomposites", *Composites Science and Technology*, vol. 67, no. 9, pp. 1854-1860, 2017.
- [26] G. X. Chen, H. S. Kim, B. H. Park, and J. S. Yoon, "Controlled functionalization of multiwalled carbon nanotubes with various molecular-weight poly (L-lactic acid)", *The Journal of Physical Chemistry B*, vol. 109, no. 47, pp. 22237-22243, 2005.
- [27] Y. Zhou, L. Lei, B. Yang, J. Li, and J. Ren, "Preparation and characterization of polylactic acid (PLA) carbon nanotube nanocomposites", *Polymer Testing*, vol. 68, pp. 34-38, 2018.
- [28] Q. Zhang, H. Quan, J. Liu, D. Gao, and S. Zhang, *China Synthetic Resin and Plastics*, vol. 39, pp. 5, 2022.

- [29] G. Urtekin and A. Aytac, "The effects of multi-walled carbon nanotube additives with different functionalities on the properties of polycarbonate/poly (lactic acid) blend", *Journal of Polymer Research*, vol. 28, pp. 1, 2021.
- [30] C. F. Kuan, H. C. Kuan, C. C. M. Ma, and C. H. Chen, "Mechanical and electrical properties of multi-wall carbon nanotube/poly (lactic acid) composites", *Journal of Physics and Chemistry of Solids*, vol. 69, no. 5-6, pp. 1395-1398, 2008.
- [31] Y. Zare and K. Y. Rhee, "Formulation of tunneling resistance between neighboring carbon nanotubes in polymer nanocomposites", *Engineering Science and Technology, an International Journal*, vol. 24, no. 3, pp. 605-610, 2021.
- [32] N. Nakayama and T. Hayashi, "Preparation and characterization of poly (l-lactic acid)/TiO₂ nanoparticle nanocomposite films with high transparency and efficient photodegradability", *Polymer Degradation and Stability*, vol. 92, no. 7, pp. 1255-1264, 2007.
- [33] P. Pötschke, S. M. Dudkin, and I. Alig, "Dielectric spectroscopy on melt processed polycarbonate—multiwalled carbon nanotube composites", *Polymer*, vol. 44, no. 17, pp. 5023-5030, 2003.
- [34] N. G. Sahoo, S. Rana, J. W. Cho, L. Li, and S. H. Chan, "Polymer nanocomposites based on functionalized carbon nanotubes", *Progress in Polymer Science*, vol. 35, no. 7, pp. 837-867, 2010.
- [35] B. V. Basheer, J. J. George, S. Siengchin, and J. Parameswaranpillai, "Polymer grafted carbon nanotubes—Synthesis, properties, and applications: A review", *Nano-Structures & Nano-Objects*, vol. 22, pp. 100429, 2020.
- [36] K. Chrissafis, "Detail kinetic analysis of the thermal decomposition of PLA with oxidized multi-walled carbon nanotubes", *Thermochimica Acta*, vol. 511, no. 1-2, pp. 163-167, 2010.
- [37] C. S. Wu and H. T. Liao, "Study on the preparation and characterization of biodegradable polylactide/multi-walled carbon nanotubes nanocomposites", *Polymer*, vol. 48, no. 15, pp. 4449-4458, 2007.



A COMPARATIVE ANALYSIS OF LAND FRAGMENTATION, CONSOLIDATION PRACTICES AND POLICY RESPONSES IN TÜRKİYE AND KYRGYZSTAN

¹Ainura BATYKOVA , ^{2,*}Orhan ERCAN , ³Tamchybek TULEEV , ⁴Ahmet Hilmi ERCİYES 

¹ *Kyrgyz National Agrarian University, Bishkek, KYRGYZSTAN*

^{2,4} *Ankara University, Applied Sciences Faculty, Real Estate Development and Management Department, Ankara, TÜRKİYE*

³ *Agricultural Project Implementation Unit KR*

¹aj.batykova@gmail.com, ²orhanercan@ankara.edu.tr, ³tamchybek@gmail.com, ⁴aherciyes@ankara.edu.tr

Highlights

- The fragmentation holds significance from both policy-making and social perspectives
- Land consolidation is key to preventing fragmentation.
- Türkiye and Kyrgyzstan can solve fragmentation problems



A COMPARATIVE ANALYSIS OF LAND FRAGMENTATION AND CONSOLIDATION PRACTICES, POLICY RESPONSES IN TÜRKİYE AND KYRGYZSTAN

¹Ainura BATYKOVA , ^{2,*}Orhan ERCAN , ³Tamchybek TULEEV , ⁴Ahmet Hilmi ERCİYES 

¹ Kyrgyz National Agrarian University, Bishkek, KYRGYZSTAN

^{2,4} Ankara University, Applied Sciences Faculty, Real Estate Development and Management Department, Ankara, TÜRKİYE

³ Agricultural Project Implementation Unit, KYRGYZSTAN

¹ aj.batykova@gmail.com, ² orhanercan@ankara.edu.tr, ³ tamchybek@gmail.com, ⁴ aherciyes@ankara.edu.tr

(Received: 14.05.2024; Accepted in Revised Form: 28.05.2024)

ABSTRACT: Understanding agricultural land dynamics is imperative for sustainable development. This research presents a comparative analysis of land fragmentation and consolidation practices in Türkiye and Kyrgyzstan. Land fragmentation, a global issue, hinders agricultural modernization due to small, scattered parcels. Factors such as inheritance laws, population pressure, and economic shifts contribute to fragmentation. Land consolidation, a solution advocated by FAO and FIG, aims to redistribute land, enhance productivity, and achieve public objectives. While Türkiye demonstrates successful land consolidation efforts, Kyrgyzstan lacks legislation and institutional capacity, impeding progress. Recommendations include tailored legislation, institutional strengthening, and international collaboration. Türkiye's experience shows significant reductions in parcel numbers and increased access to resources. Addressing fragmentation requires simultaneous consolidation and land banking initiatives. By implementing these recommendations, both countries can overcome fragmentation challenges and foster sustainable agricultural development.

Keywords: Agricultural Dynamics, Comparative Study, Land Consolidation Practices, Land Fragmentation Analysis, Policy Responses

1. INTRODUCTION

Farm or parcel size is generally considered as the size of land within an operation. One of the barriers to agricultural development and modernization is land fragmentation. Land fragmentation refers to the situation where numerous parcels owned by an individual are small, spatially distant, and scattered in a way that hinders rational cultivation [1]. Land fragmentation is typically expressed in terms of the size of agricultural land, the number and size of parcels owned by an individual, the spatial distribution of parcels, and the shape of parcels [2, 3]. The primary issues associated with land fragmentation include the small size, irregular shape, and spatial distribution of parcels. Ownership of land or parcel size, and the effects of this size on land fragmentation and/or agricultural productivity, are common issues globally [4, 5].

The reasons for changes in land use and fragmentation of agricultural lands vary across countries. Generally, these reasons include factors such as inheritance laws and regulations, population pressure on agricultural lands, socio-economic factors like non-agricultural use, rapid urbanization, industrialization, and rural-to-urban migration, as well as environmental characteristics such as climate, soil, and topography. Additionally, agricultural activities such as crop patterns, types of crops, and alternative crops, along with increasing land prices, contribute to these changes [1, 3-8].

Land fragmentation can be categorized into two types: physical fragmentation (parcel sizes) and fragmentation of ownership (legal) [1, 5]. Within this framework, land fragmentation includes fragmentation of ownership due to legal reasons such as inheritance, fragmentation of land use by tenants and landowners, fragmentation of ownership and use, and internal fragmentation, which considers parcel shape, size, and distance between parcels [5, 9].

*Corresponding Author: Orhan ERCAN, orhanercan@ankara.edu.tr

As a result of the fragmentation of agricultural lands, numerous fragmented properties, irregularly shaped agricultural lands, and small, spatially distant parcels emerge. Fragmentation leads to high production costs, lack of access to fields due to inadequate or absent roads, limited access to water, and an agricultural infrastructure distant from agricultural technology, resulting in only subsistence-level production by low-capital farmers.

Although land fragmentation is often associated with Europe, it is documented as a worldwide issue. Countries such as Taiwan, Malaysia, Japan, the United States, Kenya, Uganda, Peru, and Mexico are recognized as experiencing fragmentation [10].

In former Soviet Union countries, agricultural land ownership is moderately to highly fragmented in all countries except for Belarus, Ukraine, and Russia, due to land reforms. Meanwhile, in countries such as Serbia, Bosnia and Herzegovina, North Macedonia, Croatia, Slovenia, Montenegro, Kosovo, and Poland, ownership of agricultural land is highly fragmented due to over 75% of agricultural land being privately and state-owned during the socialist era. Land reforms in Albania, Romania, Bulgaria, and Moldova resulted in fragmented land use due to the distribution of physical blocks/parcels. The average size of agricultural land in these countries is approximately 0,3 hectares, with agricultural enterprises typically ranging from 1 to 3 hectares in size [2]. In contrast, Western Europe generally grapples with land use and internal fragmentation issues [9].

In the 2000 World Census of Agriculture (WCA) report, the Asia-Pacific region is identified as having the highest degree of land fragmentation. The average size of farms in the region is one hectare, significantly below the average farm size of 5,5 hectares for FAO member countries. Agricultural land sizes in the Pacific Islands range from 0,6 to 3,6 hectares. In some Asian countries, the proportion of small farms, defined as those less than two hectares, can reach up to 90% of the country's agricultural land assets. Land fragmentation is also a concern for countries such as Bangladesh, Vietnam, China, Taiwan, Turkey, the United States, Nepal, India, Ethiopia, Ghana, Rwanda, Israel, South Asian countries, Jordan, Peru, and Syria [10]. In Ethiopia, approximately 92,26% of rural households operate on an average of 1,4 hectares of agricultural land, which constitutes 72% of the country's total agricultural land. The country's average agricultural land size is approximately 0,8 hectares [4].

In Central Asian countries like Kazakhstan, Tajikistan, Turkmenistan, and Uzbekistan, the fragmentation of agricultural lands has largely occurred with the transition from a planned economy to a market-oriented one. Since the 1990s, many large farms (sovkhozes and kolkhozes) have been disbanded and transformed into small plots [11]. In some transition countries, the privatization of agriculture is cited as a cause of land fragmentation and irregularities in the supply chain.

In the mid-1990s, the extensive land reforms implemented in Kyrgyzstan initiated the privatization of agriculture, making the Kyrgyz experience relatively different from other Central Asian countries. Through the land reform in Kyrgyzstan, approximately 2 million individuals, including owners of small-scale farms responsible for agricultural production and larger agricultural enterprises, were distributed 75% of agricultural land. While individual, privatized ownership was welcomed positively, the expected positive development in agricultural production could not be achieved due to the poor condition of irrigation channels and unequal distribution of irrigation water in the small plots resulting from land fragmentation, leading farmers to revert to subsistence farming.

Land consolidation (LC) has been defined by the Veršinskas, et al. [12] as a legally regulated procedure directed by public authorities, used to regulate property structures in rural areas, aiming to reduce land fragmentation through comprehensive redistribution of land, expand farms, and/or achieve other public objectives such as nature restoration and infrastructure. Similarly positioned as a land policy tool by Lisec, et al. [13], LC has been emphasized as a tool for implementing government policies related to agriculture, rural development, nature conservation, and the environment. It has been noted that the traditional goal of facilitating agricultural development by reducing land fragmentation has evolved into a multipurpose approach in modern times, becoming increasingly globally implemented.

Throughout history, LC has stood out as the most effective method of land management for addressing the challenge of land fragmentation and enhancing land use efficiency [14]. Increasing

agricultural productivity through the development of LC tools; improving the incomes of small-scale food producers; and legally establishing rights, responsibilities, and limitations related to land as a result of rural LC projects contribute to SDG 1.4. Additionally, LC contributes to SDG 5 by promoting gender equality, SDG 11 regarding sustainable cities and communities, SDG 13 addressing climate action and global warming, and SDG 15 in terms of determining, monitoring, and managing land use changes, LC, and rural land management.

One of the most important outcomes to be achieved through LC is a high rate of LC. With the expansion of LC programs in 2008, LC has become a significant tool for agricultural development in Turkey. The main objectives of LC projects include reducing land fragmentation, improving in field road infrastructure, mitigating irrigation and drainage issues, and providing land development services such as leveling and stone collection. Additionally, the implementation of LC in highways, motorways, intersections, airports, and organized industrial zones has increased, and environmental solutions such as the creation of ecological corridors and the registration of protected areas have accelerated. The significance of LC was further enhanced by a legal regulation in 2014 that prevents the fragmentation of agricultural lands through inheritance. With this legal regulation, the planning of land acquisition and LC projects together has been introduced. During this period, while LC efforts gained momentum, the number of stakeholders continued to increase due to inheritance division.

This research delves into the global causes and solutions of agricultural land fragmentation, with a comparative analysis between Turkey and Kyrgyzstan. It presents findings, conclusions, and recommendations for both countries. While emphasizing the need to prevent land fragmentation in Kyrgyzstan and improve practices in Turkey, it's evident that the persistence of land fragmentation in Turkey adversely affects project success and duration. Recommendations for Kyrgyzstan include prioritizing measures to prevent land fragmentation and integrating LC into the country's agricultural development strategies. Addressing these issues requires simultaneous implementation of LC and land banking practices, which can significantly contribute not only to LC but also to transitioning agriculture towards more organized enterprises.

2. THE REASONS FOR LAND FRAGMENTATION AND LAND CONSOLIDATION IN TÜRKİYE

2.1 Land Use Categories and Agricultural Population

Urban settlements, constituting 1,6% of Türkiye's surface area, accommodate 67,9% of the population. While in regions classified as rural, 17,3% of the population resides. In settlements classified as urban-rural, comprising 4,9% of the total, 14,8% of the population lives [6, 15]. According to the 2022 Turkstat data, 4,866 million people are employed in the agricultural sector.

Out of Türkiye's total approximate 78 million hectares of land area, 23,864 million hectares are agricultural land, 23,11 million hectares are forests, and 14,617 million hectares consist of pastures and meadows (Table 1). The fact that approximately one-third of the country's surface area is agricultural land reflects its status as an agricultural country.

Table 1. Land use categories and amounts in Türkiye

Class	Area (thousand hectares)
Total utilized agricultural land	38,482
Total arable land and land under permanent crops	23,864
Total arable land	20,194
Sown area	16,510
Fallow area	2,960
Areas of vegetables and gardens	718
Areas of fruits, beverages and spices crops, vineyards and olive trees	3,671
Land under permanent meadows and pastures	14,617
Forest area	23,110

Source: Turkstat 2016

2.2 Legal Framework

Article 44 of the Constitution of the Republic of Türkiye and Article 755 of the Turkish Civil Code provide for LC. Within this framework, it is stated that "Improvement works such as straightening waterways, irrigation, draining marshy areas, road construction, afforestation, and land LC can only be carried out with the joint initiatives of the relevant landowners, provided that more than half of the land is owned, and two-thirds of the owners decide in this way. Other owners must also comply with this decision. The decision taken is recorded in the declarations column of the land registry. Special legal provisions regarding these matters are reserved." Optional LC is defined in the LC regulation as "LC carried out by obtaining the signed consent of fifty-one percent of the landowners in terms of number and fifty-one percent of the area they own in the project area.

LC in Türkiye is regulated by Law No. 5403 on Soil Conservation and Land Use, Law No. 3083 on Land Arrangement in Irrigation Areas, and Law No. 7139. With a law amendment in 2018, the General Directorate of State Hydraulic Works (DSİ) was authorized as the implementing agency for LC and in-field development services. Other institutions and organizations, subject to DSİ's permission, are authorized to carry out LC and in-field development services as project administrators. Therefore, municipalities, institutions responsible for railway or highway construction, or other organizations can conduct LC activities. Most LC projects are requested by public authorities.

According to Law No. 5403 on Soil Conservation and Land Use and the Regulation on Conservation, Use, and Consolidation of Agricultural Lands, LC is defined as "preventing the degradation and fragmentation of agricultural lands due to natural and artificial factors, and in fragmented lands, combining multiple land parcels while considering their natural characteristics, usage integrity, and property rights to create economic, ecological, and more functional new parcels, determining the usage methods based on land characteristics and area, and providing land development services.

LC works are conducted in two separate forms: voluntary and compulsory, with the implementation principles being the same. While voluntary LC is generally prioritized in practice, compulsory LC is often carried out as well. In consolidation areas, participation fees of up to 10% are deducted from the lands belonging to individuals and public or private legal entities, depending on the nature of the project, for shared public areas such as roads and canals. Landowners are not required to pay additional taxes due to LC projects. Additionally, parcels newly formed according to block design are exempt from land registry fees and cadastre charges. All project-related costs are covered by the state budget.

LC projects are carried out in collaboration with other relevant institutions such as the General Directorate of Agricultural Reform (TRGM), the General Directorate of Highways and Railways (TCK and DDY), and the General Directorate of Land Registry and Cadastre (TKGM). Projects are implemented by private companies determined through open tender.

2.3 Land Fragmentation

In Türkiye, reasons for the fragmentation of agricultural enterprises include inheritance law, inheritance transmissions; fragmented cadastral parcels, scattered small lands (inheritance, commerce, public investment, spatial reasons); fragmented use (trade among farmers, leasing); sharecropping; lack of sufficient agricultural mechanization; rapid population growth, industrialization, and rapid urbanization; land markets, historical/cultural perspectives [16, 17]. Additionally, the absence of agricultural land use planning, even at the macro level, is also a significant factor.

In the country, there are 32,5 million agricultural parcels, more than 40 million shareholders [18-20], and 3,1 million agricultural enterprises. Regarding parcel numbers, a significant portion of the enterprises (98,2%) consist of lands ranging from 5 to 499 hectares, with 77,5% of these parcels being between 20 and 499 hectares in size. On average, each agricultural enterprise comprises 11 parcels, with an average parcel size of 5,9 hectares for agricultural lands [6, 21]. Additionally, on average, a parcel is jointly owned by 13 individuals, contributing to a fragmented ownership structure and a complex land use system. Consequently, agricultural lands are often small, scattered, and divided into numerous parcels that do not generate sufficient income. More than 50% of the existing parcels lack access roads to the fields, and for those that do, the quality of the in-field roads is low. Furthermore, 50% of the parcels are distant from irrigation channels [18]. For these reasons, the country's agricultural sector faces issues related to fragmentation, scale, inheritance, accessibility to parcels, and access to water in its land-related infrastructure [18-20].

As Küsek, et al. [22] have also pointed out, out of the 40 million shareholders, 37 million are not engaged in agriculture and reside in urban areas. This situation has two types of disadvantages:

- a) Shareholders engaged in agriculture in rural areas do not invest in agriculture or agricultural land because they do not own all of the land they use. They do not engage in agricultural development because they cannot obtain loans from banks or grants from the ministry for the agricultural land they use.
- b) The 37 million landowners who have shares in these parcels, usually residing in cities, cannot use, sell, or lease their agricultural land, even though they are shareholders.

In Türkiye, due to inheritance and other factors, land holdings are decreasing day by day. The amount of abandoned and unused land is approximately 2 million hectares [6, 19].

To prevent these disadvantages, in 2014, the inheritance law was revised to introduce rules for the buying and selling of agricultural lands and to establish the legal framework for land banking systems. Today, the failure to integrate land banking practices with LC practices reduces the success of the applications and increases objections. Field observations indicate that land banking practices need to be integrated with LC practices to enhance the effectiveness of LC efforts [17, 22].

2.4 Land Consolidation

The preparation phase of LC projects consists of determining the project area, conducting preliminary discussions with landowners, obtaining data from land registry and cadastre directorates, obtaining project data from public institutions, preparing a feasibility report for the LC project, obtaining the Presidential decree, the tender process, and handing over the site to the contractor firm (Figure 1).

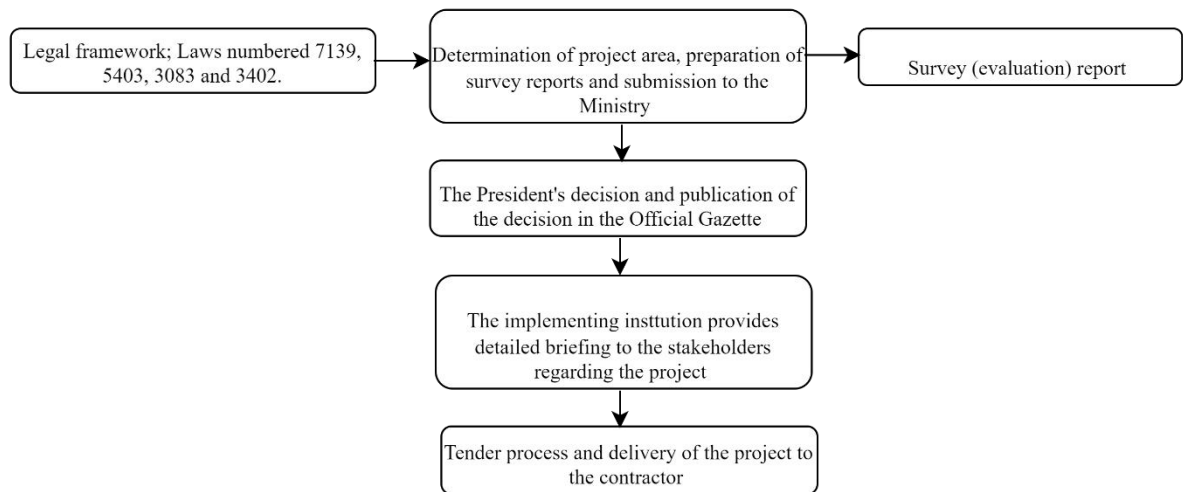


Figure 1. LC preparation works

During the project implementation phase, there are four main steps: creation of a project database using obtained land registry and cadastre data and orthophoto maps of the project area, conducting soil survey and land grading studies, preparing re-allotment planning, and conducting interviews with farmers.

Re-allotment planning aims to reduce both land ownership and land use fragmentation. Its goal is to promote the growth of agricultural enterprises. At this stage, the number of parcels is optimized for agricultural efficiency. This involves minimizing the distances between the farmer's 8-10 parcel fragments and consolidating them into one or more parcels with regular geometry.

After the project, parcels will have access to roads and irrigation and/or drainage. In the final stage, the re-allotment plan is approved by DSI or other public institution implementing the project. Necessary property checks are conducted by local cadastre and land registry offices to register the newly formed parcels. Construction works are carried out in the project area, and the project is completed (Figure 2).

The allocation of land of equal value through land grading studies, creating parcels suitable for agricultural production, displacement of parcels subject to LC, determination of farmer preferences, and participation in public services are among the key considerations in LC practices.

2.5 Land Consolidation Practices in Türkiye

The total area suitable for LC in the country is 14,3 million hectares (Table 2). As of 2022, a total of 8,78 million hectares of land have been awarded to the private sector for LC projects under 450 projects, with 6,78 million hectares of land projects completed (325 projects) and registered in the land registry. Efforts are ongoing to complete and register the remaining 2 million hectares covered by the remaining 125 projects [18]. In addition to soil classification and block design, LC projects also provide services such as reducing land fragmentation, improving agricultural road infrastructure, and addressing irrigation and drainage issues. Furthermore, they provide land development services such as removing unused channels and leveling parcels.

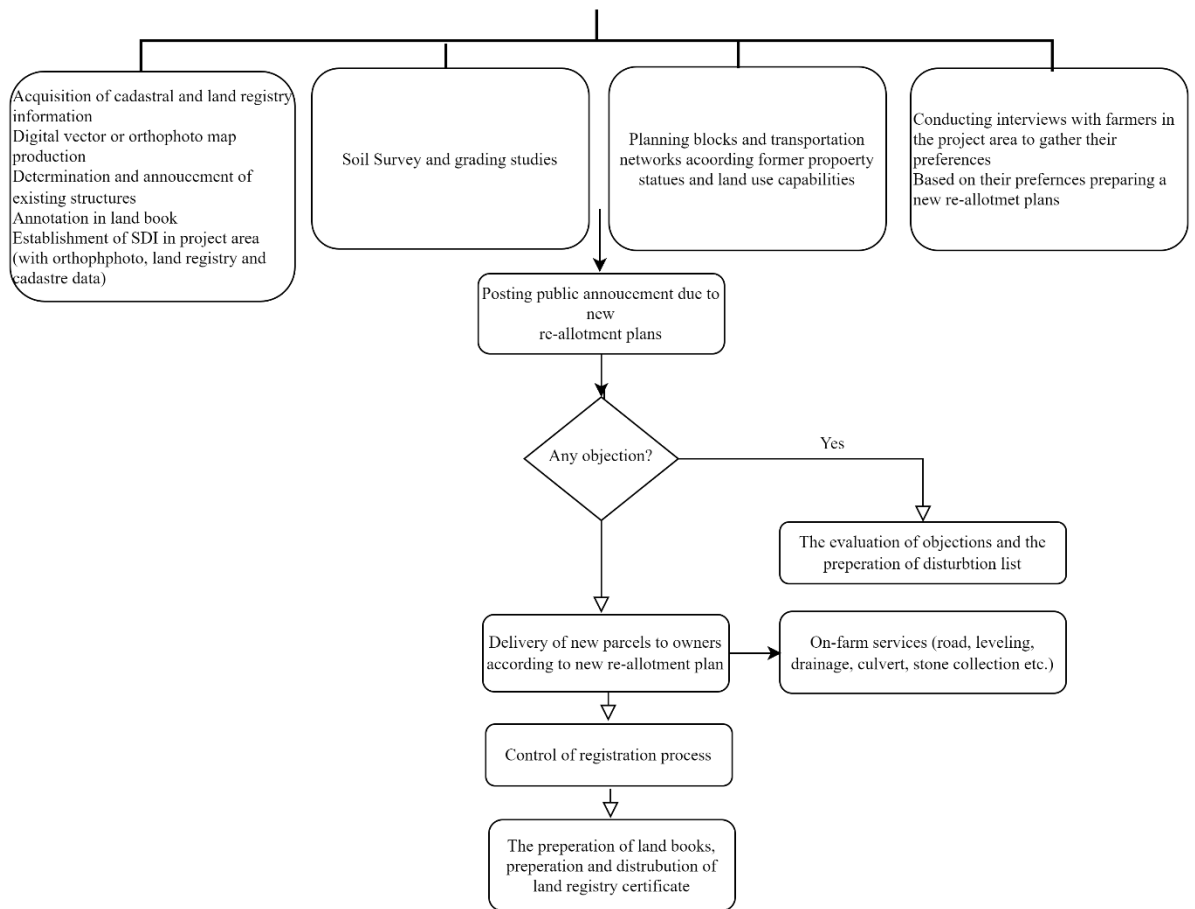


Figure 2. LC projects implementation process

Table 2. Lands suitable for LC and consolidation projects

LC and In-Farm Development	Area (ha)	Population
The area with completed projects registered	6.781.335	3.000.000
Area Under Ongoing LC Studies	1.998.900	1.150.000
Total Area Subject to LC Studies	8.780.235	4.150.000
Remaining Potential Area Suitable for LC	5.519.765	3.000.000
Total Area Suitable for LC	14.300.000	7.150.000

Source: Compiled from Demirbaş 2023

In Türkiye, LC projects typically cover an area of approximately 10.000-30.000 hectares [1, 17]. Re-allotment planning is generally integrated with public investments in agricultural infrastructure within the project area. Studies on the implementation of LC typically span 3 to 5 years [17, 18].

To assess the impact of LC on parcel numbers and sizes of newly formed parcels before and after LC across different years and geographical regions of the country, six LC projects were examined, totaling 64.998 hectares. As depicted in Table-2, there was an average decrease of 48% in parcel numbers and a remarkable increase of 136% in parcel areas. These findings underscore the pivotal role of LC not only in realizing various benefits but also in effectively mitigating land fragmentation (Table 3).

Table 3. Comparison of parcel numbers and parcel areas before and after LC

Project Name	Project Area (ha)	The Number of Parcels Before LC	New Parcel Count	Decrease in Parcel Count (%)	Average Parcel Size Before LC (m2)	New Average Parcel Size (m2)	Parcel Enlargement Rate (%)
Denizli Tavas							
Büyükkonak LC and In-Farm Services	1.050	11.342	2.745	76	1.000	4.000	300
Elazığ Uluova LC ve In-Farm Services	850	1.335	642	52	5.500	11.170	103
Karaman Ekinözü LC ve In-Farm Services	3.250	1.130	509	55	12.900	52.800	309
Kayseri Sarıoğlan LC and In-Farm Services	4.000	2.294	1.636	29	17.400	24.450	41
Niğde Misli 4. Kısım LC and In-Farm Services	3.500	2.591	1.863	28	13.500	19.000	41
Manyas Ovası ve Bereketli Pompaj Sulaması LC and In-Farm Services	23.348	19.097	10.120	47	12.340	14.800	20
Total	64.998	37.789	17.515	Avrg:48%	62.640	126.220	Avrg:136%

Source: Created from DSİ Projects

Between 2010 and 2012, the General Directorate of Agricultural Reform and the FAO conducted a joint pilot study to assess the impact of LC in Türkiye. The study focused on four primary objectives: reducing land fragmentation, improving access to agricultural parcels by roads, irrigation, and water, and assessing cost-effectiveness [23].

Key Findings:

- **Parcel Reduction and Size Increase:** The number of parcels in the project decreased from 2.531 to 1.559, representing a 38% reduction. Meanwhile, the average parcel size increased from 2,38 hectares to 3,87 hectares, reflecting a 1,5-hectare or 63% increase in size.
- **Farmers' Parcel Ownership:** Prior to LC, farmers owned an average of 7,1 parcels each. After LC, this decreased to an average of 2,7 parcels per farmer, indicating a 61% reduction in parcel ownership.
- **Satisfaction Levels:** A significant proportion of farmers, specifically 84%, expressed satisfaction with the LC process. Only 9% reported being either not satisfied at all or not very satisfied.
- **Road and Irrigation Infrastructure:** The total length of roads within the fields increased from 115.084 meters before LC to 193.729 meters after LC, marking a 68% increase. Similarly, the irrigation system length expanded from 111.023 meters to 152.880 meters, representing a 38% increase. Importantly, 100% of parcels within the project scope now have access to both road and irrigation infrastructure.
- **These findings underscore the effectiveness of LC in achieving its objectives, particularly in reducing land fragmentation and improving agricultural infrastructure. The study provides valuable insights for policymakers and stakeholders involved in land management and rural development initiatives in Türkiye.**

3. THE REASONS FOR LAND FRAGMENTATION AND LAND CONSOLIDATION INITIATIVES IN KYRGYZSTAN

3.1 Land Use Categories and Agricultural Population

Kyrgyzstan has a land area of 19.994.928 hectares, with an estimated population of 7.037.600 people as of 2023. More than 65% of Kyrgyzstan's population resides in rural areas. The number of the agricultural population amounts to 4.584.000 people.

As presented in Table 4, agricultural lands, which account for 34% of the country's total area, serve as an indicator of the country's agricultural productivity. Forested areas make up 13%, while water-covered areas constitute 4% of the country's land area.

Table 4. Land use categories and their areas

Categories of the land fund	Area, hectares	Percentage
Agricultural lands;	6.753.418	34
Settlement lands (cities, villages) lands;	277.934	1
Lands designated for industrial, transport, communication, defense, and other purposes;	230.778	1
Lands of specially protected natural areas;	1.187.277	6
Forest lands;	2.530.390	13
Water lands;	767.292	4
Reserve lands	8.247.839	41
Total:	19.994.928	100

Source: Compiled from Soil Code of Kyrgyzstan

The total area of agricultural lands is 10.461.666 hectares. Among these: the area of arable lands is 1.212.375 hectares, permanent plantations cover 37.236 hectares, fallow lands occupy 34.771 hectares, pasture areas span 169.788 hectares, and meadows encompass 9.007.496 hectares (Table 5).

Table 5. Classification and sizes of agricultural lands

Names of agricultural lands:	Area, hectares	Percentage
Arable lands	1.212.375	11,5
Perennial plantations	37.236	0,4
Fallow lands	34.771	0,4
Highlands	169.788	1,6
Pastures	9.007.496	86,1
Total	10.461.666	100

According to the Constitution of Kyrgyzstan and land laws, lands can be classified as state-owned, municipal-owned, privately owned, and other forms of ownership. Agriculture is predominantly carried out on privately owned lands. Lands under state ownership mostly consist of pastures and highlands.

Table 6. Ownership types and distribution to agricultural areas

Forms of Ownership	Total Area, thousand ha	Of which, agricultural lands, thousand ha				
		Arable lands	Perennial plantation	Highlands	Pastures	Fallow lands
State	18.653,4	246,7	14,9	83,2	9.027,8	28,6
Municipal	206,1	135,6	14,4	7,1	28,5	1,5
Private	57,3	0,9	0,8	0,04	3,6	0,02
Nationwide	6,5	0,8	0,9	0,02	0,03	0
State	1.203,6	955,9	21,2	86,3	1,6	9,2
Municipal	811,1	658,1	21,1	1,5	0,3	0,6
Private	19.994,9	1.203,5	36,9	169,5	9.033	37,8
Nationwide	1.023,7	794,5	36,3	8,7	28,8	2,1

In Kyrgyzstan, the agricultural sector is an important part of the economy. The agricultural sector accounts for 14,7% of the country's gross domestic product (GDP), with approximately 417.195 people employed in this sector (Ministry of Agriculture, 2022). According to the International Labor Organization (ILO) data in 2019, 19,3% of the workforce is employed in the agricultural sector. There are 360 existing agricultural cooperatives in Kyrgyzstan. Of these, 91% are private peasant farms, 3% are collective peasant farms, 5% are agricultural cooperatives, and 1% are joint-stock companies (Figure 3).

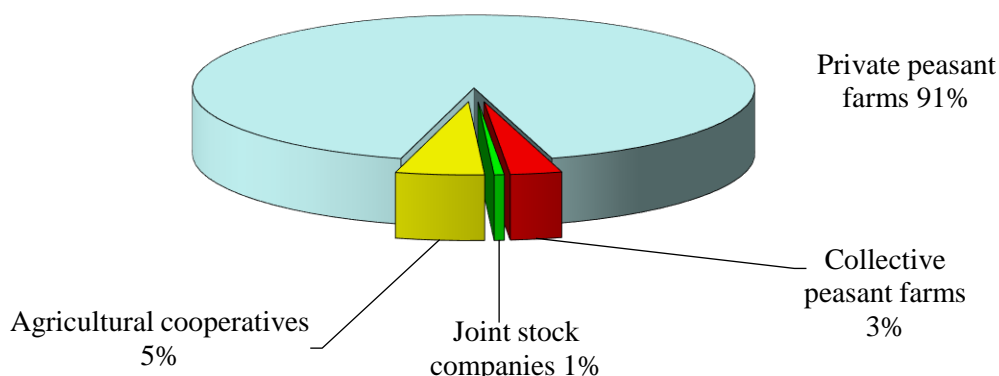


Figure 3. Usage structure of private agricultural land by farm types in Kyrgyzstan

Cooperatives and other agricultural organizations account for only 4,5% of the total agricultural production volume in the country. 75% of plant products are produced by farms and individual farm enterprises. Small-scale farmers are not integrated into modern supply chains. Low investment, limited mechanization, and land fragmentation in the agricultural sector pose a growth-inhibiting challenge for all stakeholders in the supply chain.

Within the framework of the Directive on Leasing State-Owned Agricultural Land, the Agricultural Land State Fund offers economically attractive agricultural lands for lease to farmers, local individuals, or institutions through auction.

3.2 Legal Framework

Previously, all lands in Kyrgyzstan were owned by the state and were dominated by large-scale socialist farms managing thousands of hectares of agricultural land and employing hundreds of workers. The transformation of the agricultural sector began in the early 1990s, initially focusing on the liberalization of agricultural markets and prices. Due to the absence of private ownership, land use certificates were issued to peasants using the land. These certificates provided five legal rights to individual farmers, including transferring, exchanging, selling, leasing, and using the land as collateral

for credit [24]. Land reforms were implemented in two phases between 1991 and 1996. The first phase, initiated between 1991 and 1993, led to the enactment of agricultural and land reform in the Kyrgyz Republic between 1994 and 1996, with the issuance of the Presidential Decree in 1994, and continues to this day. The first phase of the reforms was characterized by leasing of lands from collective farms (kolkhozes) and Soviet state farms (sovkhozes) for up to 49 years. During this period, farm enterprises based on state ownership and leased collective farms emerged. This phase marked the emergence and development of the land market through leasing and led to the formation of new management practices.

In 1998, with the new Constitution providing a legal basis, the transition of land ownership to private ownership before the second phase of the reform laid the groundwork for market circulation. In 1999, with the adoption of the New Land Law in Kyrgyzstan, regulations were introduced to contribute to the development of the land market through buying and selling [25]. Another significant change was the establishment of collective action institutions such as water user associations responsible for operating, maintaining, and regulating water allocation for farm irrigation facilities.

In 2013, within the framework of international cooperation, action plans were developed for 21 sectors to support long-term and sustainable initiatives and to lay the groundwork for political and economic reforms [26]. Within this framework, sub-sectors such as water management and LC were also addressed.

The National Development Program of Kyrgyzstan until 2026 includes actions aimed at developing the agricultural sector. These actions encompass:

- Reconstruction of irrigation systems (2018-2022)
- Expansion of irrigation agriculture in the Issyk-Kul and Naryn Regions under common ownership (2021-2024)
- Implementation of a national traceability system for agricultural products
- Establishment of a single value chain
- Creation of agricultural marketing and e-commerce centers
- Establishment of an agro-smart database [27].

Regarding LC, while the Kyrgyzstan Constitution doesn't contain specific provisions, the Civil Code Articles 41, 42, and 43 regulate conditions for land division and management of lands not subject to common ownership. The country's Land Law addresses issues related to cadastre and LC. Despite no separate law specifically covering LC, aspects of it are addressed within land use, protection, and management regulations.

In March 2022, the "Regulation of Land Law of the Kyrgyz Republic" was enacted, which also regulates land relations in the country. Issues concerning land are managed by a Land Resources Service within the Cabinet of Ministers of the Kyrgyz Republic.

In Kyrgyzstan, discussions and planning are underway regarding LC, which involves combining fragmented parcels of land for better management and utilization. Among the methods being considered are simple LC, where smaller plots are merged, comprehensive consolidation, which involves larger-scale integration, and multipurpose consolidation, which aims to address various needs simultaneously.

It's recognized that establishing a robust legal framework at the national level is essential to facilitate effective LC programs. This framework would provide clarity on property rights, streamline administrative processes, and ensure fair treatment of all stakeholders involved. Such clarity is crucial for guiding the implementation of LC projects and resolving any disputes that may arise.

3.3 Land Fragmentation

In Kyrgyzstan, farms are classified into three main organizational categories according to official classification: household plots, peasant farms, and state & collective farms. State & cooperative farms are generally referred to as "agricultural enterprises" and encompass both state-owned and cooperative farms. Household plots and peasant farms vary significantly in their commercial tendencies, sizes, and legal statuses. Household plots are typically smaller and subsistence-oriented. Legally, household plots are considered as physical assets, while peasant farms are registered as legal entities. Household plots consist of primary agricultural land, often a small parcel of land associated with rural residences. Peasant farms

typically operate on family-owned land but may also utilize additional leased land from other farms (Table 7).

Table 7. Main characteristics of the farm types in Kyrgyzstan, 2007

	Household plots	Peasant farms	State & collective farms
Number, thousand	924,1	323,6	1,3
Average size of arable land holdings, hectares	0,11	2,9	58,9
Total sown area, thousand Hectares	101,2	951,5	76,1
Share in total sown area, %	9	84,3	6,7

Source: NSC of the Kyrgyz Republic 2008

The land use patterns of state and cooperative farms in Kyrgyzstan have undergone significant changes as part of the land reform process. Initially, there was a reduction in the amount of agricultural land allocated to these farms, which began with the transition period and was further accelerated by government directives issued after 1995.

During this process, there was a notable shift in land ownership from corporate farms to peasant farms. These peasant farms, numbering over 300.000 across the country, typically manage smaller plots of land, averaging about 2,9 hectares each. Despite their smaller size, they collectively control around 90% of the total cultivable land in the country.

On the other hand, traditional household plots, which are even smaller in size, averaging about 0,11 hectares each, control the remaining 10% of cultivable land. This fragmentation of land ownership is a significant characteristic of the land reform process in Kyrgyzstan.

To illustrate, imagine a scenario where a corporate farm that previously controlled a large tract of land has now been divided into numerous smaller plots managed by individual peasant farmers. This redistribution of land has led to a more decentralized ownership structure, with a larger number of smaller-scale farmers actively participating in agricultural production.

Table 7 also indicates a significant decrease of approximately 165.000 hectares in total cultivated agricultural land between 1991 and 2007. This decline is noteworthy as it signifies that over 13% of the land used for agricultural purposes in 1991 was either converted to non-agricultural use or left unused. It's important to note that one negative consequence of land reform in Kyrgyzstan was its contribution to the fragmentation of land use and its impact on collective action in the rural economy [24].

Land reforms, coupled with unsustainable land use practices and a lack of capacity and finance, have led to increased land fragmentation. These issues pose significant barriers to long-term investment and the efficient utilization of agricultural land. LC, by preventing land fragmentation and allowing farmers to expand their land holdings, can help make them more competitive.

These data not only reveal the presence of land fragmentation in Kyrgyzstan but also underscore the importance of distinguishing between fragmentation in land use and fragmentation in land ownership. Continued or increasing fragmentation can impede the economically efficient management of land, leading to adverse effects on agricultural productivity.

Therefore, it's crucial to address both land use and land ownership fragmentation to ensure sustainable agricultural practices and maximize productivity. By promoting initiatives that encourage LC of fragmented land parcels and streamline land management processes, policymakers can support more efficient and productive agricultural systems.

3.4 Land Consolidation

In Kyrgyzstan, LC has emerged as a crucial objective to bolster agricultural development. Typically, these LC efforts are implemented alongside the enhancement of local agricultural infrastructure, with a specific focus on areas suitable for irrigation or planned irrigation projects. The primary goals of LC

projects include reducing land fragmentation, improving local road networks, addressing irrigation and drainage challenges, and providing essential infrastructure services like land leveling and stone collection. Despite the introduction of the simple LC concept, Kyrgyzstan lacks experience in implementing such initiatives, and progress has been limited.

Pilot projects have been carried out on a voluntary basis, utilizing a model that focuses solely on combining parcels to enhance agricultural productivity. However, there's a concern that this approach may disproportionately benefit wealthier farmers or agricultural enterprises. To address this, it's essential to consider compulsory LC, led by the government, to establish necessary agricultural infrastructure and ensure equitable access to resources.

Moving forward, Kyrgyzstan could benefit from incorporating lessons learned from pilot projects and international best practices to develop effective LC strategies tailored to its specific needs. This may involve engaging with local communities, fostering partnerships between public and private stakeholders, and providing support and incentives for smallholder farmers to participate in LC efforts.

LC pilot projects were conducted with USAID support. In selecting the pilot project areas, the presence of fragmented, unused land and investor interest in the projects were considered primary factors [28]. Three investors were selected for three project areas with different characteristics:

- In Sailyk AO, an area consisting of a total of 56 parcels covering 63,8 hectares,
- In Arashan AO, an area of approximately 130 hectares consisting of 78 parcels of privately owned agricultural land, which were not irrigated,
- In Uch-Korgon AO, an area of 328,18 hectares covering a total of 867 parcels of traditional privately-owned irrigated land.

It is stated that these projects, implemented on a voluntary LC basis, have been successfully completed as a result of their implementation.

In addition to these, LC projects were carried out in the ayil aimaks of Zhany-Nookat and Zulpui in the Nookat district of Osh region with USAID financing. A LC project covering 50 parcels on 33,5 hectares of land was implemented in the Zulpui ayil aimak. Examples of before and after LC are shown in Figure 4.



Figure 4. Zhany-Nookat ayil aimak of the Nookat before (left) and after (right) LC

In Figure 5, LC is seen in Zulpuev Municipality, Osh Oblast. Original, fragmented parcels (left); LC after months later (right)

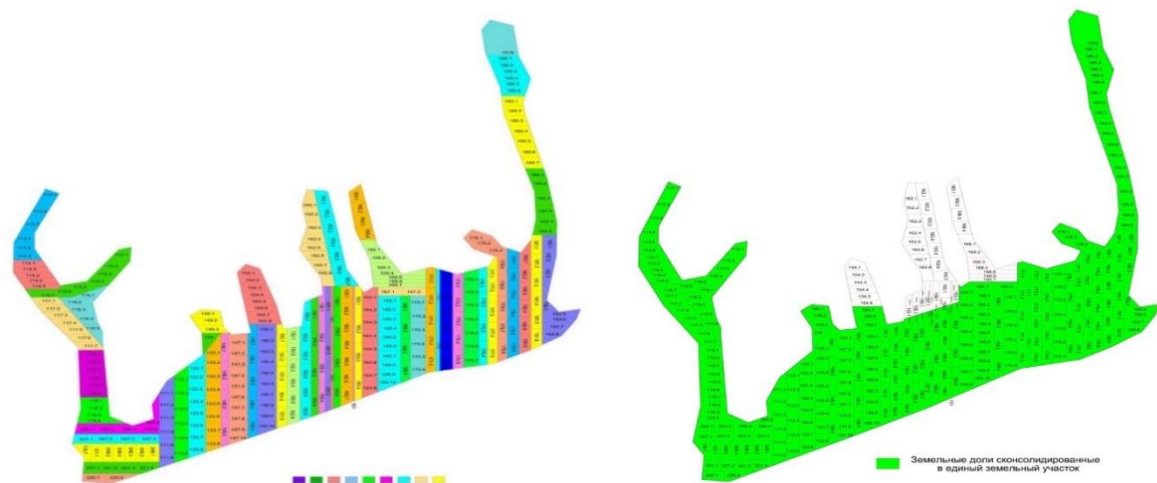


Figure 5. Zulpui aiyl aimak before (left) and after (right) LC

4. DISCUSSION AND RESULTS

4.1 Discussion

LC is a planning and management process that affects agricultural lands. It draws attention due to its various aspects such as improving productivity and sustainability, managing land use, planning infrastructure and services, protecting the environment, utilizing natural resources, and evaluating social and economic impacts.

Having knowledge of agricultural population data is crucial as it helps in making agriculture more attractive and enhancing the sustainability of agricultural enterprises through LC. Furthermore, considering that large and fertile agricultural lands generally provide more job opportunities and increase income prospects in the agricultural sector, they have the potential to offer better living conditions and job opportunities for rural populations.

Although Türkiye's land area is approximately four times larger than that of Kyrgyzstan, its population is approximately twelve times larger. 93,5% of the country consists of rural areas, with agricultural land accounting for 48,9% of the total. This includes 63% of total arable land and land under permanent crops. 17,3% of the population resides in rural areas, while urban-rural mixed settlements constitute 4,9% of the country's land area, accommodating 14,8% of the population. In Kyrgyzstan, 65% of the population resides in rural areas, with cultivated agricultural land covering 18% of the country's land area.

In Türkiye, 18% of the population is engaged in agriculture, with an employment rate of 5,66% and the agricultural sector's share in GDP being 5,4%. In Kyrgyzstan, 19,3% of the population is employed in the agricultural sector, with the GDP rate approximately at 14,7%.

Comparison of agricultural population, share in GDP, and employment in the agricultural sector between Türkiye and Kyrgyzstan reveals that Kyrgyzstan is indeed primarily an agricultural country (Table 8).

Table 8. Comparing the agricultural land use categories, population and economic indicators

TÜRKİYE	KYRGYZSTAN
The countries' Area and population?	
Area:780.000 km2 Population: 86.011.789	Area: 199.949 km2 Population: 7.037.600
Rural Area and Rural Population (rural/urban-rural)?	
17,3% of the population resides in rural areas, which cover 93,5% of the country. In urban-rural mixed settlements, constituting 4,9% of the total, 14,8% of the population lives.	More than 65% of the population resides in rural areas, which account for 34% of the country's land area.
Agricultural land amounts?	
Total utilized agricultural land is 38.000.482 ha, out of which total arable land covers 23.864.000 ha. This means that 63% of the total agricultural land used is arable land.	Total utilized agricultural land is 6.753.418 hectares, with total arable land covering 1.212.375 ha. This indicates that 18% of the total agricultural land used is arable land.
The countries' agricultural population?	
14.705.000 (18%)	4.584.000 (65%)
Agricultural parcel numbers?	
32.500.000	N/A
The share of the agricultural sector in the country's gross domestic product (GDP)?	
5,4%	14,7%
Employment in the agricultural sector?	
4.866.000 (5,66%)	417.195 (19,3%)

Türkiye is a highly experienced country in the field of LC. In this regard, LC is addressed in the Constitution and the Civil Code. There are laws and regulations concerning the subject and its implementation. Cadastre studies, which constitute the technical and legal infrastructure of LC, have been completed nationwide. The DSİ is authorized as the implementing agency for LC and on-farm development services. Other institutions are authorized to carry out LC and on-farm development services as project administrators subject to the approval of DSİ. Farmers are exempt from taxes, fees, and charges within the scope of LC projects. However, farmers may be required to contribute a maximum of 10% to common facilities Table 9.

In Kyrgyzstan, apart from the three articles in the Civil Code related to LC, no legal framework has been established, and therefore, there is no public institution directly responsible for LC. Consequently, it is believed that turning LC into a state policy by establishing its legal framework would contribute to the country's agriculture and economy, considering Kyrgyzstan's readiness in terms of cadastral infrastructure and its classification as an agricultural country.

Table 9. Comparing the legal framework

TÜRKIYE	KYRGYZSTAN
Are there any articles regarding LC both in the Constitution and Civil Code?	
Yes, LC is mentioned in Article 44 of the Turkish Civil Code and Article 755 of the Turkish Civil Code.	It is not included in the Constitution. Articles 41, 42, and 43 of the Civil Code are related to the conditions for the division of lands.
What are the main legal codes related with LC in the country?	
Law No. 3083 on Land Arrangement in Irrigation Areas No. 3083, Law No. 7139 on the Organization and Duties of the General Directorate of State Hydraulic Works, Law No. 5403 on Soil Conservation and Land Use, Law No. 2644 on Land Registry, Law No. 3402 on Cadastre, Law No. 6831 on Forestry, Law No. 4342 on Pastures, Law No. 3213 on Mining, Law No. 442 on Villages, Law No. 6360 on Metropolitan Municipalities, Law No. 3194 on Zoning, Law No. 2863 on the Protection of Cultural and Natural Resources, Law No. 3202 on Services for Villages, along with related Ministry Regulations.	In Kyrgyzstan, there is a Land Law that regulates issues related to land ownership, cadastre, and LC. The "Regulation on Land Law of the Kyrgyz Republic," which also regulates land relations in the country, was enacted in March 2022.
Is there a Land Policy in the country that covers topics such as property, cadastre, and LC?	
Yes, Land policy is clearly stated in the Turkish Civil Code.	Yes, issues related to land ownership, cadastre, and LC are regulated by the Land Law.
Has the cadastre been completed in your country?"	
Yes	Yes
Is there a LC Law in the country?	
Yes	There is no separate law that directly and entirely covers LC.
Is there public institution directly responsible LC?	
Yes	No
The institutions where LC is carried out collaboratively?	
DSİ is authorized as the implementing agency for LC and on-farm development services. Other institutions and organizations outside of DSİ are authorized to carry out LC and on-farm development services as project administrators subject to the approval of DSİ.	No
Are farmers required to pay taxes, fees, or similar charges for LC?	
No, Farmers are exempt from such taxation in LC.	There is no legislation or implementation regarding the matter.
Is there a deduction made from farmers as deduction for participation in common facilities in LC, and if so, what is the deduction rate?	
Max: 10%	There is no legislation. No project has been initiated yet.

Rural land fragmentation can arise from historical, cultural, social, economic, and environmental factors. Among these factors, land fragmentation through inheritance may be one of the most significant. Globally, land is inherited and fragmented from one generation to the next. Over time, with each succession, land is divided among multiple heirs, leading to increased fragmentation and the emergence of smaller parcels of land with multiple stakeholders. However, factors such as rapid population growth, urbanization, infrastructure development, and land speculation contribute to increased pressure on land resources, necessitating the subdivision of land into even smaller parcels to support the livelihoods of the growing population. This process poses a significant challenge to one of today's most pressing issues: ensuring food security. Topics like this, as well as similar ones, are on the agenda of countries like Türkiye

and Kyrgyzstan

In Türkiye, the number of agricultural holdings is 3,1 million. Due to inheritance, there are 40 million shareholders of these holdings. As a result of this fragmentation caused by inheritance, the average number of agricultural parcels per holding is approximately 11, and the parcel size is slightly less than six hectares. Due to land fragmentation, scale issues, inheritance, parcel access, and water access deeply affect agricultural infrastructure and agricultural production. LC programs, land use planning, land ownership reform, supporting sustainable agricultural practices, community-based natural resource management initiatives, and conducting LC and land banking activities together are considered as measures that can be taken against land fragmentation.

Consequently, the privatization of large agricultural enterprises in Kyrgyzstan has led to individual ownership arising from land fragmentation, resulting in parcel sizes averaging approximately (estimated) 1.200.000 holdings, with parcel sizes in 90% of them averaging 2,9 hectares and the remaining 10% falling as low as 0,11 hectares (Table 10).

Ultimately, although the reasons may differ, it is understood that both Türkiye and Kyrgyzstan are significantly affected by land fragmentation, and LC is perceived as the solution to this issue.

Table 10. Land fragmentation: a comparison of its causes and solutions

TÜRKİYE	KYRGYZSTAN
The number of agricultural holdings?	
3.100.000	1.200.000 (The estimate; with more than 300.000 peasant farms averaging 2,9 ha of agricultural land and over 900.000 traditional household parcels averaging 0,11 ha)
The average number of parcels on a holding?	
On average, each agricultural holding consists of 11 parcels.	There is no statistical information
The average size of agricultural parcels?	
5,9 ha	More than 300.000 peasant farms averaging 2,9 ha of agricultural land and over 900.000 traditional household parcels averaging 0,11 ha
What are the primary drivers of land fragmentation in the country?	
The primary reason is inheritance. Additionally, the absence of a clear definition of a farmer, migration from rural to urban areas due to social, economic, educational reasons, and the uncertain status of siblings who remain in the village and engage in agriculture in terms of agricultural significance.	The fragmentation of agricultural lands in Kyrgyzstan largely began with the transition to a market-oriented economy, leading to the dissolution of sovkhoses and kolkhozes and the transformation of agriculture into smaller units managed by individual farmers.
What are the problems caused by fragmentation in your country?	
Scale issues, inheritance, parcel access, and access to water are deeply affecting agricultural infrastructure and agriculture.	It has a negative impact on agricultural development.
Is there an unused (abandoned) land in the country? If any, its size?	
Approximately 2.100.000 ha	In 1991, more than 13% of the total area used for agricultural purposes was converted to non-agricultural uses.
What could be the solution to land fragmentation?	
LC programs, Land use planning, Land ownership reform, Supporting sustainable agricultural practices, Community-based natural resource management initiatives, Conducting LC and land banking activities together can be included.	Preventing fragmentation through inheritance Land Law reform, LC, Improvement of cadastre records to identify and reclaim abandoned agricultural lands, Infrastructure development and farmer support.

When comparing Türkiye and Kyrgyzstan's approaches and implementations to LC projects,

Türkiye's extensive experience over the years stands out, contrasting with Kyrgyzstan's relatively nascent involvement in this field. Table 11 has examined the differences and similarities in the understanding and processes of LC in both countries. As seen, while Türkiye is highly experienced in LC practices, Kyrgyzstan is still in the early stages. However, both countries have the fundamental data for LC, including soil databases and digital land registry-cadastre data.

Table 11. Land fragmentation: a comparison of its causes and solutions

TÜRKİYE	KYRGYZSTAN
Is voluntary LC or compulsory LC being implemented?	
There are also examples of voluntary LC alongside significant compulsory LC.	In the pilot project conducted with international aid institutions, voluntary LC has been implemented.
Are land registry and cadastre data in digital format?	
Yes	Yes
Are orthophotos used as base maps in LC projects?	
Yes	There is currently no implementation of actual LC projects
Are interviews conducted to gather farmers' preferences?	
Yes	The pilot project was conducted with the participation of a few large farmers, and their opinions were taken into account.
Is there a soil database with sufficient accuracy in the country?	
Is it produced as a stage of soil classification LC projects?	
Yes. However, land classification is carried out according to the Storie index in the projects.	Yes, there is a soil database
Are pasture lands being included in LC?	
Yes	No information
Are there enough qualified experts in the country to work on LC projects?	
Yes	There is no personnel with experience in LC.
Are LC projects carried out through private sector tenders?	
Yes, all	There is no LC project.

4.2 Results

In this research, it has been observed that within the framework of land fragmentation, consolidation practices, and policy responses, there are both similarities and differences between the two countries. According to the findings obtained, the results of the research can be summarized as follows:

- 1) Kyrgyzstan is more agriculturally oriented compared to Türkiye.
- 2) Both countries have nearly identical proportions of their populations engaged in agriculture.
- 3) Türkiye stands as a highly experienced country in LC. As of 2023, it has undertaken LC projects covering 8,78 million hectares of land and continues to do so. Conversely, Kyrgyzstan is still in the phase of research, discussion, and strategy development.
- 4) Despite differing motivations, both countries suffer from land fragmentation. High parcel numbers per farm and low average parcel counts prevent households from generating sufficient income from agriculture.
- 5) Consequently, both countries have areas of unused, abandoned, or misused lands.
- 6) Turkish and Kyrgyz academics concur that LC is essential for preventing land fragmentation and enhancing agricultural productivity
- 7) Both countries possess soil databases and digital land registry-cadastre systems, forming the foundation of LC.

- 8) Both countries have responded to the needs by developing policy responses in line with the legal, social, economic, and environmental conditions of the country. Examples of policy responses can be seen in Kyrgyzstan with the law enacted in 2022, and in Türkiye with the changes in laws regarding agricultural land sales in 2014 and institutional restructuring in 2018.
- 9) In Kyrgyzstan,
 - a) there is an understanding of the need for legislative work to reduce administrative barriers and simplify the re-registration processes of property rights within the scope of LC. This way, conducive conditions for LC can be established.
 - b) The design and execution of strategies, such as land auctions and exchanges, are crucial for ensuring transparency in land transactions and facilitating the establishment of the actual market worth of land parcels. Consequently, proficient land users can competitively obtain extra land parcels to broaden their economic endeavors.
 - c) Conducting training initiatives for land users covering topics such as market economics, legal intricacies of land ownership and utilization, and cutting-edge agricultural technologies is essential. By raising awareness, farmers can make informed choices regarding the LC and effective utilization of land resources.
- 10) In Türkiye;
 - a) Türkiye has completed its legal framework and institutional development regarding LC.
 - b) LC in Türkiye is conducted through tendering processes involving the private sector.
 - c) LC projects are predominantly carried out by public institutions under compulsory LC regulations. Farmers are exempt from taxes, fees, and duties in LC projects.
 - d) Land fragmentation poses a scalability issue in agricultural production, hindering access to water and in field roads. These factors necessitate LC in Türkiye.
 - e) LC projects are executed by experienced personnel utilizing modern technology. There is a substantial number of qualified LC experts in public, academic, and private sectors.

5. CONCLUSION

This research aimed to facilitate the understanding of agricultural land dynamics in Türkiye and Kyrgyzstan through a comparative analysis of land fragmentation and consolidation practices and policy responses. The ultimate goal was to develop recommendations for enhanced practices in both countries.

The foremost conclusion of the study is the absence of legislation concerning LC in Kyrgyzstan. To address this gap, it is imperative to develop LC legislation tailored to the specific conditions of the country. This lack of legal framework poses a significant barrier to effective LC efforts and hinders progress in addressing land fragmentation issues.

Enhancing institutional structures to fulfil the responsibilities outlined in the LC legislation constitutes another significant outcome. Developing institutional capacity, incorporating modern technology, and embracing digitalization are vital areas that need to be addressed within this scope. Strengthening institutional frameworks will enable more efficient and effective implementation of LC projects and ensure their long-term sustainability.

Given that LC involves direct participation of farmers and leads to changes in property ownership, it is paramount for policymakers, public institutions, and farmers to deeply understand the content, implementation, contribution to farmer welfare, and agricultural development aspects of the project to ensure their support and success. Prioritizing public awareness on these matters stands as a crucial outcome and recommendation. Engaging stakeholders in the planning and implementation process will foster greater buy-in and ownership of LC initiatives, leading to more successful outcomes.

Initiating pilot projects for LC through international collaboration at the outset, followed by their widespread dissemination across the country based on the resulting outcomes, highlights a pivotal result deserving thorough investigation. Collaborating with international partners can provide valuable expertise, resources, and support for implementing LC projects effectively.

The analysis conducted within the study has demonstrated that the number of parcels involved in LC efforts in Türkiye has decreased by approximately 50%, while parcel areas have enlarged by around 130%. Moreover, it has been observed that each parcel now benefits from access to water and field access roads. These findings are further verified by a study conducted by the FAO in collaboration with relevant Turkish government agencies. The revelation of the achievement of the technical objectives of LC projects in Türkiye represents a valuable outcome derived from this study.

In conclusion, the persistence of the problem of land fragmentation in Türkiye negatively impacts the success and duration of projects. Addressing this issue requires the simultaneous implementation of LC and land banking practices. Land banking can significantly contribute not only to LC but also to the transition of agriculture towards more organized enterprises. By implementing the recommendations outlined in this study, both Turkey and Kyrgyzstan can take significant steps towards overcoming the challenges posed by land fragmentation and promoting sustainable agricultural development.

Declaration of Ethical Standards

Authors declare that all ethical standards have been complied with.

Credit Authorship Contribution Statement

Orhan ERCAN Originated the fundamental concept, made a substantial contribution to its development, and spearheaded the manuscript drafting process.

Ainura BATYKOVA Assisted in shaping the research design, conducting analysis, and refining the manuscript, actively engaging in result discussions and contributing to the final version.

Tamchybek TULEEV Gathered and presented data on land fragmentation in Kyrgyzstan.

Ahmet Hilmi ERCİYES Compiled and structured information on land consolidation practices in Türkiye, contributing to shaping the final form of the research.

Declaration of Competing Interest

The authors declare that there are no declarations of interest.

Funding / Acknowledgements

The authors have not disclosed any funding.

Data Availability

Due to the nature of this study, no statistical or formula-based data were utilized.

REFERENCES

- [1] M. B. Hartvigsen, Land reform and land consolidation in Central and Eastern Europe after 1989: Experiences and perspectives. 2015.
- [2] M. Hartvigsen, "Land reform and land fragmentation in Central and Eastern Europe," Land use policy, vol. 36, pp. 330-341, 2014.
- [3] I. Markuszewska, "The outlook of land consolidation in Poland: Stakeholdersdilemmas and policy weaknesses," 2016.
- [4] G. T. Alemu, Z. Berhanie Ayele, and A. Abelieneh Berhanu, "Effects of land fragmentation on productivity in Northwestern Ethiopia," Advances in Agriculture, vol. 2017, 2017.
- [5] D. Balcı and A. S. Gün, "Toprak Yönetiminde Toprak Toplulaştırması Süreci (Land Consolidation Process in Land Management)," Turkish Journal of Agriculture-Food Science and Technology, vol. 12, no. 3, pp. 462-469, 2024.

- [6] O. Ercan, "Agricultural land-based functional model for effective rural land management in Türkiye," *Journal of Agricultural Sciences*, n.d., doi: <https://doi.org/10.15832/ankutbd.1342935>.
- [7] L. Luo, C. Yang, R. Chen, and W. Liu, "Comprehensive Land Consolidation Zoning Based on Minimum Cumulative Resistance Model—A Case Study of Chongqing, Southwest China," *Land*, vol. 12, no. 10, p. 1935, 2023.
- [8] B. Paudel, J. Pandit, and B. Reed, "Fragmentation and conversion of agriculture land in Nepal and Land Use Policy 2012," 2013.
- [9] K. O. Asiama, R. Bennett, and J. Zevenbergen, "Land consolidation for Sub-Saharan Africa's customary lands: The need for responsible approaches," *American Journal of Rural Development*, vol. 5, no. 2, pp. 39-45, 2017.
- [10] R. Beltramo, A. Rostagno, and A. Bonadonna, "Land consolidation associations and the management of territories in harsh Italian environments: A review," *Resources*, vol. 7, no. 1, p. 19, 2018.
- [11] C. Raab and M. Spies, "Characterising cropland fragmentation in post-Soviet Central Asia, using Landsat remote-sensing time series data," *Applied Geography*, vol. 156, p. 102968, 2023.
- [12] T. Veršinskis, M. Vidar, M. Hartvigsen, K. Mitic Arsova, F. Van Holst, and M. Gorgan, *Land Consolidation (Legal Brief, no. 1)*. Rome, Italy: FAO, 2021, p. 10.
- [13] A. Lisec, M. Louwsma, and W. Krupowicz, "Public participation," in *Land Consolidation – The Fundamentals to Guide Practice*. Denmark: International Federation of Surveyors (FIG), 2022, ch. 3, pp. 25-33.
- [14] S. Li and W. Song, "Research progress in land consolidation and rural Revitalization: Current status, characteristics, regional differences, and evolution laws," *Land*, vol. 12, no. 1, p. 210, 2023.
- [15] TURKSTAT. [Online]. Available: <https://www.tuik.gov.tr/>
- [16] İ. Arıcı and Ş. T. Akkaya Aslan, "Arazi Toplulaştırmada Çok Amaçlı Proje Geliştirmenin Yararları ve Zorlukları," in *Biyosistem Mühendisliği III*, A. Atılğan, H. Değirmenci, V. Demircan, and Ç. Tanrıverdi Eds.: Akademisyen Kitabevi, 2022, pp. 9-16.
- [17] F. T. Z. Gülsever, O. Özkan, and U. Büyükhataipoğlu, "The Land Consolidation Implementation Studies In Turkey," in *Symposium on Land Consolidation and Land Readjustment for Sustainable Development*, Apeldoorn, 2016: FIG, in *Symposium on Land Consolidation and Land Readjustment for Sustainable Development Proceedings* [Online]. Available: https://fig.net/resources/proceedings/2016/Symposium_LCLR_Apeldoorn_2016_Proceedings.pdf [Online]. Available: https://fig.net/resources/proceedings/2016/Symposium_LCLR_Apeldoorn_2016_Proceedings.pdf
- [18] S. Demirbaş, "Türkiye'de Arazi Toplulaştırma Çalışmaları," in *III. International Conference on Real Estate Development and Management*, Ankara, 2023, Ankara: Ankara Üniversitesi Yayınevi, 2024.
- [19] M. Türker, "In Turkey Land Abandonment and the Combat Activities (Land Banking Services)," Santiago, 2019.
- [20] M. Türker, "Türkiye'de Tarımsal Arazi Yönetimi ve Geleceği (Agricultural Land Management and its Future in Türkiye)," in *III. International Conference on Real Estate Development and Management*, Ankara, 2023, Ankara: Ankara Üniversitesi Yayınevi, 2024.
- [21] TURKSTAT. [Online]. Available: <https://www.tuik.gov.tr/>
- [22] G. Küsek, Ş. Akdemir, and I. S. Ismaila, "Land consolidation in Turkey-a multipurpose/discipline land consolidation in Turkey with ICT support 2023," *Scientific Papers Series Management, Economic Engineering in Agriculture & Rural Development*, vol. 23, no. 2, 2023.
- [23] M. Kvistgaard, "Pilot evaluation: Land Consolidation in Konya Region, Cumra District, villages Inli and Dinlendik (2010-2012)," *Ministry of Food, Agriculture and Livestock of Turkey & FAO.*, 2015. [Online]. Available:

- https://www.fao.org/fileadmin/user_upload/reu/europe/documents/Events2015/LN7/Konya_en.pdf
- [24] K. Akramov and N. Omuraliev, "Institutional change, rural services, and agricultural performance in Kyrgyzstan," 2009.
- [25] Land Code of the Kyrgyz Republic, 1999.
- [26] USAID, "Kyrgyzstan Local Development Program A Task Order Under The Segir/Gbtı Iı Iqc Final Report," United States Agency for International Development, 2014. [Online]. Available: <https://urban-links.org/wp-content/uploads/Kyrgyzstan-%E2%80%93-Local-Economic-Development-Program.pdf>
- [27] Kırgızistan Tarım Sektörü Ülke Yatırımcı Rehberi, 2022. [Online]. Available: <https://www.tarimorman.gov.tr/ABDGM/Belgeler/Ulke%20Masalar%C4%B1/K%C4%B1rg%C4%B1zistan.pdf>
- [28] USAID, "Land Reform And Market Development Project Iı Final Report Kyrgyzstan 2008–2010," United States Agency for International Development, 2010. [Online]. Available: https://pdf.usaid.gov/pdf_docs/PDACR659.pdf



TRAJECTORY TRACKING CONTROL OF A TWO WHEELED SELF-BALANCING ROBOT BY USING SLIDING MODE CONTROL

^{1,*} Mustafa DOĞAN , ² Ümit ÖNEN 

¹AVL Research and Engineering, Istanbul, TÜRKİYE

²Necmettin Erbakan University, Engineering Faculty, Mechatronics Engineering Department, Konya, TÜRKİYE

¹mustafa.dogan@avl.com, ²uonen@erbakan.edu.tr

Highlights

- Trajectory tracking control of a two wheeled self-balancing robot by using Sliding Mode Control (SMC) was realized.
- The performance of the SMC controller has been examined under five different cases including external disturbance and various parameter uncertainties and compared with PID and LQR methods.
- Chattering problem inherent in the SMC method was eliminated by employing tangent hyperbolic (tanh) switching function instead of signum function.
- Results showed that, PID control is extremely sensitive to disturbance inputs and parameter changes, and the LQR controller provides a much better performance than the PID control in terms of response speed and robustness. The results also showed that the proposed SMC controller not only offer as good performance as the LQR controller in terms of response speed, but it is extremely robust and almost insensitive to disturbance inputs and excessive parameter changes.



TRAJECTORY TRACKING CONTROL OF A TWO WHEELED SELF-BALANCING ROBOT BY USING SLIDING MODE CONTROL

^{1,*} Mustafa DOĞAN , ² Ümit ÖNEN 

¹AVL Research and Engineering, Istanbul, TÜRKİYE

²Necmettin Erbakan University, Engineering Faculty, Mechatronics Engineering Department, Konya, TÜRKİYE

¹mustafa.dogan@avl.com, ²uonen@erbakan.edu.tr

(Received: 26.01.2024; Accepted in Revised Form: 30.05.2024)

ABSTRACT: Two-Wheeled Self-Balancing Robots are widely used in various fields today. These systems have a highly unstable nature due to their underactuated structures. On the other hand, parameter uncertainties and external disturbances significantly affect their control performance. The best way to deal with parameter uncertainties that can easily lead controllers to instability is to use robust control methods. Dealing with these uncertainties is particularly crucial in control of underactuated and unstable systems such as Two-Wheeled Self-Balancing Robots. In this study, trajectory tracking control of a two wheeled self-balancing robot by using Sliding Mode Control (SMC) was realized. The chattering problem inherent in the SMC method was eliminated by employing tangent hyperbolic (\tanh) switching function instead of signum function. The performance of the SMC controller has been examined under five different cases including external disturbance and various parameter uncertainties and compared with PID and LQR methods. The results showed that the SMC method is much more insensitive to parameter changes than the PID and LQR methods. It has also been observed that all three controllers maintain their stability against disturbance inputs, but the SMC method offers a better control performance.

Keywords: Sliding Mode Control, Two Wheeled Self Balancing Robot, Trajectory Tracking

ÖZ: İki Tekerlekli Kendini Dengeleyen Robotlar günümüzde çeşitli alanlarda yaygın olarak kullanılmaktadır. Bu sistemler eksik tahrikli yapıları nedeniyle oldukça kararsız bir yapıya sahiptirler. Öte yandan parametre belirsizlikleri ve dış etkenler, kontrol performanslarını önemli ölçüde etkilemektedir. Kontrolcülerini kolayca kararsızlığa sürükleyebilecek parametre belirsizlikleri ile başa çıkmanın en iyi yolu gürbüz kontrol yöntemleri kullanmaktır. Bu belirsizliklerle başa çıkmak, özellikle İki Tekerlekli Kendini Dengeleyen Robotlar gibi eksik-tahrikli ve kararsız sistemlerin kontrol problemlerinde çok önemlidir. Bu çalışmada, bozucu giriş ve parametre belirsizliklerine karşı Kayan Kipli Kontrol (KKK) yöntemi ile yörünge takibi üzerinde çalışılmıştır. KKK yönteminin yapısından kaynaklanan çatırtı problemi, işaret fonksiyonu yerine tanjant hiperbolik (\tanh) anahtarlama fonksiyonu kullanılarak ortadan kaldırılmıştır. KKK kontrolcüsünün performansı, bozucu giriş ve farklı parametre belirsizliklerini içeren beş farklı senaryo için incelemiş, PID ve LQR yöntemleri ile karşılaştırılmıştır. Sonuçlar, KKK yönteminin parametre değişimlerine karşı PID ve LQR yöntemlerinden çok daha duyarsız olduğunu göstermiştir. Ayrıca bozucu girişlere karşı üç kontrolcüsünün de kararlılığını koruduğu ancak KKK yönteminin daha iyi bir kontrol performansı sunduğu görülmüştür.

Anahtar Kelimeler: Kayan Kipli Kontrol, İki Tekerlekli Denge Robotu, Yörünge Takibi.

1. INTRODUCTION

Underactuated systems refer to systems equipped with a limited number of actuators or sensors. In such systems, the number of degrees of freedom is greater than the number of actuators or sensors used. Despite their advantages such as low cost, energy efficiency and simplicity, underactuated systems have some disadvantages in terms of control.

*Corresponding Author: Mustafa DOĞAN, mustafa.dogan@avl.com

Two-wheeled self-balancing robots have a highly unstable dynamics with their nonlinear structure. In addition, other factors such as parameter changes, damping, friction, external disturbances make the control of such systems more difficult. The best way to overcome these challenges is to use robust controllers. In the relevant literature, several different approaches have been proposed for the control of two-wheeled self-balancing robots.

Linear control methods with simple mathematical models are frequently preferred due to their easy applicability. Linear controllers such as PID controller [1], Linear Quadratic Regulator (LQR) [2], Linear Quadratic Gaussian (LQG) [3], State-Feedback [4], Cascade controller [5] can be used to control two-wheeled self-balancing robots. These controllers can provide very satisfactory performance in some systems under certain conditions. However, since these controllers use linearised models, they are very sensitive to parameter uncertainties. In addition, due to their structure, they may be insufficient against external disturbances.

As an alternative to classical linear controllers, smart control methods such as Fuzzy Logic Controller (FLC) [6], FLC-PID [7], FLC-LQR [8] are widely using. Smart control methods can provide more adaptivity than classic approaches. However, they still cannot provide robustness in parameter uncertainty conditions.

Adaptive control algorithms have been presented to adapt to changing conditions over time. Various adaptive control methods such as Reinforcement Learning [9], Machine Learning [10], Artificial Neural Networks [11], Fuzzy Logic Neural Networks NN-FLC [12] stand out with less model dependency and adaptive structure. Despite their advantages, design and training of large networks in these approaches can be quite complex. High computational power and large data set requirements during training of artificial neural networks make it difficult to apply these methods.

Model Predictive Control (MPC) [13] which is based on predicting system behaviour using system models, can provide robustness against system uncertainties in the control of complex systems. However, the success of this approach depends on very precisely modelled system dynamics. Difficulties in modelling complex and nonlinear systems limit the success of the controller. Optimisation-based H_2 [14], H_∞ [15] approaches can provide robustness against the disturbances and parameter uncertainties with an accurate model. The biggest disadvantage of these controllers is that they can be effective in a limited working area with defined cost functions.

Lyapunov Controllers [16] are successful in stability; however, they may not be satisfactory enough to meet performance expectations for systems that require precise control. Backstepping Control [17] and Active Disturbance Rejection Control (ADRC) [18] are also have robust characteristics.

The Sliding Mode Control (SMC) approach is a control method known for its robustness against the disturbances and system uncertainties. Although the Conventional SMC method is insensitive to matched disturbances, but it is sensitive to unmatched disturbances. The state observer-based SMC [19] can ensure the robustness of the controller against the unmatched disturbances. The major disadvantage of the SMC is chattering problem. In the most general definition, chattering is the rapid changes of the control signal in high-frequency sawtooth form. This is caused by the switching function in the structure of the SMC. The chattering problem can be eliminated with Neural Network based SMC [20]. However, high computational demanding and the need for a comprehensive dataset are disadvantages of this approach.

In this study, the trajectory tracking control of a two-wheeled self-balancing robot was discussed. First, kinematic and dynamic models of the system are presented. Then, a Sliding Mode controller with tangent hyperbolic switching function was designed. In order to evaluate the response speed and robustness of the designed controller, simulation studies were carried out using five different scenarios with different disturbance inputs and parameter changes. For comparing the performance of the SMC controller, PID and LQR control were also applied to the system and the results were presented comparatively.

2. MATERIAL AND METHODS

Simplified model of a two-wheeled self-balancing robot is seen in Figure 1. The system consists of a chassis and a pendulum-shaped body balanced by two wheels. It is an underactuated system with two

inputs and three outputs. The right and left wheel torques are the system inputs while the x - y coordinates and θ angle of the body relative to vertical (z) axis are the system outputs. This system is quite difficult to control since the position, orientation and vertical angle of the body must be controlled only by the torques applied to wheels. In order to achieve a precise control, the kinematic and dynamic models of the system must be obtained accurately.

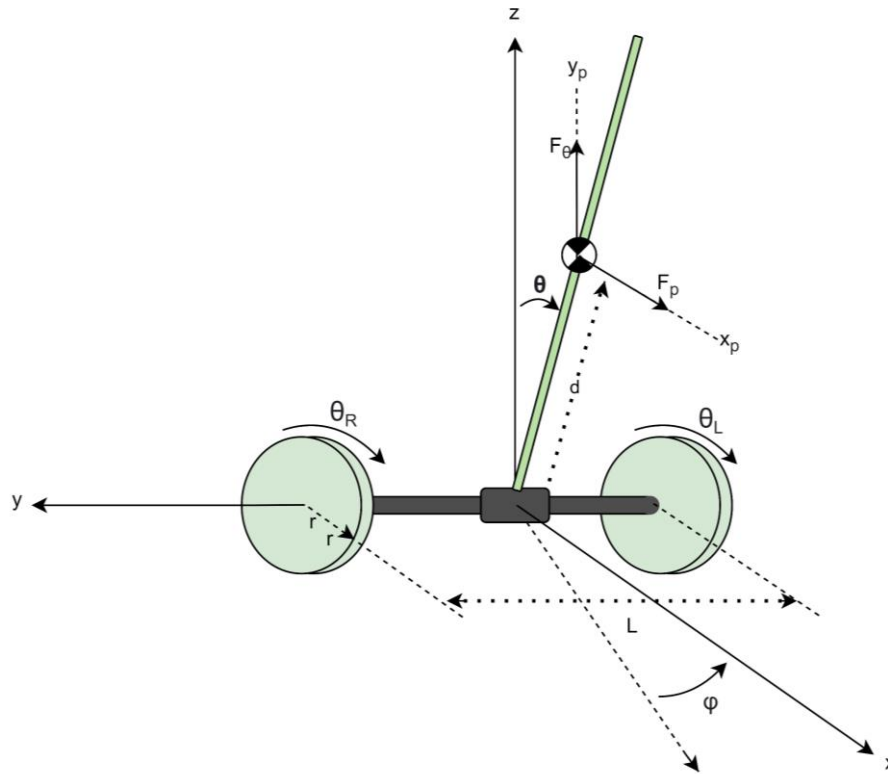


Figure 1. Simplified model of a two-wheeled self-balancing robot

2.1. Kinematic Model of The Two-Wheeled Self-Balancing Robot

In order to describe all movements of the system, generalized coordinates can be selected as follows.

$$q = [X_c \ Y_c \ \varphi \ \theta \ \theta_R \ \theta_L]^T \quad (1)$$

In this expression, X_c and Y_c , are the position of the centre of mass, φ is the angle of the robot in the x - y plane, θ is the angle between the body and the vertical (z) axis, θ_R and θ_L are the right and left wheel angles, respectively. These coordinates are clearly seen in Figure 2.

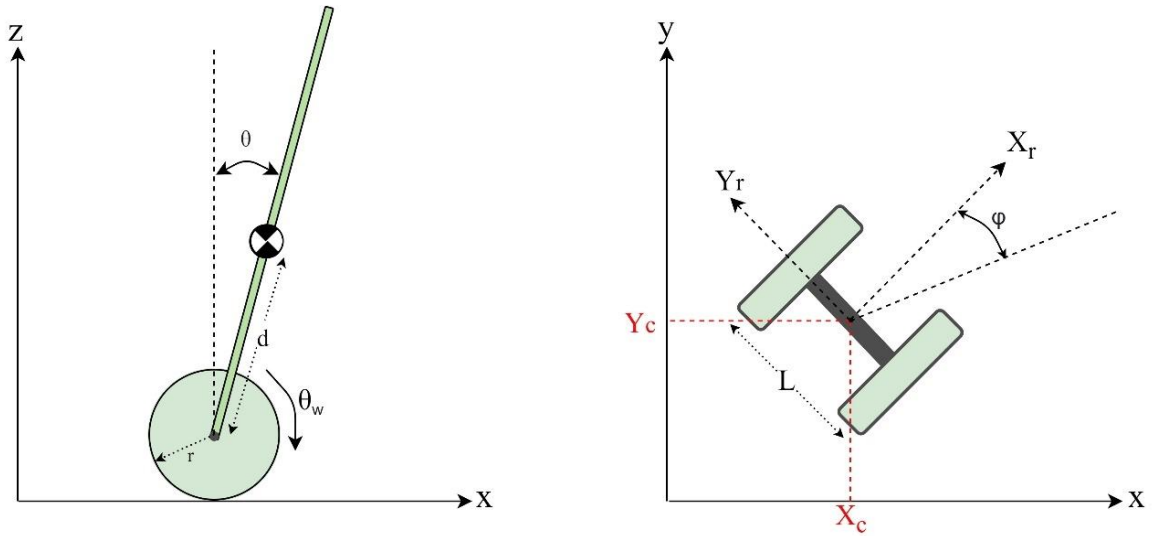


Figure 2. Generalized coordinates of the two-wheeled self-balancing robot

There are two different constraints for the system considered in this study. First, the wheels do not slide laterally. Secondly, the wheels are in pure rolling, that is, the entire rotational movement turns into translation. Therefore, by defining $l=L/2$, the constraint equations can be written as follows.

$$\dot{y} \cos\varphi - \dot{x} \sin\varphi = 0 \tag{2}$$

$$\begin{aligned} \dot{x} \cos\varphi - \dot{y} \sin\varphi + l\dot{\varphi} - r\dot{\theta}_r &= 0 \\ \dot{x} \cos\varphi - \dot{y} \sin\varphi - l\dot{\varphi} - r\dot{\theta}_l &= 0 \end{aligned} \tag{3}$$

Linear and angular velocities of the system can be defined respectively as; $v = r(\dot{\theta}_r + \dot{\theta}_l)/2$ and $\omega = r(\dot{\theta}_r - \dot{\theta}_l)/L$. If the necessary arrangements are made in (2) and (3) using these definitions, the kinematic model of the system is obtained as follows.

$$\begin{bmatrix} \dot{x} \\ \dot{y} \\ \dot{\varphi} \end{bmatrix} = \begin{bmatrix} \cos\varphi & 0 \\ \sin\varphi & 0 \\ 0 & 1 \end{bmatrix} \begin{bmatrix} v \\ \omega \end{bmatrix} \tag{4}$$

2.2. Dynamic Model of The Two-Wheeled Self-Balancing Robot

In this study, the dynamic model of two-wheeled self-balancing robot presented by Junfeng and Wangying [21] was used. State-space representation of the system can be defined as $\dot{x} = Ax + Bu$ and shown as follow,

$$x = \begin{bmatrix} \dot{x}_r \\ \dot{x}_l \\ \dot{\theta} \\ \dot{\varphi} \\ \dot{\varphi} \end{bmatrix} = \begin{bmatrix} 0 & 1 & 0 & 0 & 0 & 0 \\ 0 & 0 & A_{23} & 0 & 0 & 0 \\ 0 & 0 & 0 & 1 & 0 & 0 \\ 0 & 0 & A_{43} & 0 & 0 & 0 \\ 0 & 0 & 0 & 0 & 0 & 1 \\ 0 & 0 & 0 & 0 & 0 & 0 \end{bmatrix} \begin{bmatrix} x_r \\ x_l \\ \theta \\ \varphi \\ \dot{\varphi} \end{bmatrix} + \begin{bmatrix} 0 \\ B_2 \\ 0 \\ B_4 \\ 0 \\ B_6 \end{bmatrix} \begin{bmatrix} C_l \\ C_r \end{bmatrix} \tag{5}$$

where C_l and C_r are the left end right wheel torques respectively. This wheel torques can be transformed into the C_θ and C_φ for decoupling purpose as follow.

$$\begin{bmatrix} C_l \\ C_r \end{bmatrix} = \begin{bmatrix} 0.5 & 0.5 \\ 0.5 & -0.5 \end{bmatrix} \begin{bmatrix} C_\theta + u_d \\ C_\varphi \end{bmatrix} \tag{6}$$

In this equation, u_d is the external disturbance. The matrix elements in Equation (5) can be defined as follows:

$$\begin{aligned} A_{23} &= g \left(1 - \frac{4}{3} d \frac{M_p}{Q} \right), & A_{43} &= g \frac{M_p}{Q} \\ B_2 &= \frac{4dP}{3Q} - \frac{1}{M_p d}, & B_4 &= -\frac{P}{Q} \\ B_6 &= \frac{6}{(9M_r + M_p)RL} \end{aligned} \quad (7)$$

where

$$Q = \frac{1}{3} \frac{M_p(M_p + 6M_r)d}{(M_p + \frac{3}{2}M_r)R}, \quad P = \frac{1}{d} + \frac{M_p}{M_p + \frac{3}{2}M_r}$$

In these equations, M_w and M_p is the mass of the wheel and body respectively, R is the wheel radius, d is the distance between the wheel axis and centre of mass and L is the distance between wheels.

2.3. Kinematic Controller

Controllers that calculate the kinematic movements required for a robot to reach the desired position are called kinematic controllers. A kinematic controller is needed to perform of trajectory control. The kinematic controller calculates the movements required for a robot to reach the desired position by converting the desired trajectory motions into new outputs in terms of angular and linear velocity. Kinematic controller design is based on the kinematic model. Equation (4) can be rearranged as follows:

$$\begin{bmatrix} v \\ \omega \end{bmatrix} = \begin{bmatrix} \cos\varphi & \sin\varphi \\ -\frac{1}{d} \sin\varphi & \frac{1}{d} \cos\varphi \end{bmatrix} \begin{bmatrix} \dot{x} \\ \dot{y} \end{bmatrix} \quad (8)$$

By defining $\tilde{x} = x_d - x$ and $\tilde{y} = y_d - y$ and adding the controller gains $k_x, k_y > 0$ and saturation constants $I_x, I_y \in \mathbb{R}$ into equation, the kinematic controller can be obtained as below [22].

$$\begin{bmatrix} v_d \\ \omega_d \end{bmatrix} = \begin{bmatrix} \cos\varphi & \sin\varphi \\ -\frac{1}{d} \sin\varphi & \frac{1}{d} \cos\varphi \end{bmatrix} \begin{bmatrix} \dot{x}_d + I_x \tanh\left(\frac{k_x}{I_x} \tilde{x}\right) \\ \dot{y}_d + I_y \tanh\left(\frac{k_y}{I_y} \tilde{y}\right) \end{bmatrix} \quad (9)$$

2.4. Sliding Mode Controller

In applied control problems, there is always mismatching between the real system and the mathematical model. It's caused by factors such as unmodelled system dynamics, uncertainties in system parameters and disturbing external forces. In addition to model mismatches, if the system is exposed to intense disturbing forces, it will be very difficult to control such systems with classical closed-loop methods. At this point, robust controllers come into play [23].

SMC is a robust control approach that can provide stability guarantee against system uncertainties and disturbances. Before starting the SMC design, some arrangements should be made on the system model. By defining $f_1 = A_{23}$, $f_2 = A_{43}$, $f_3 = \dot{\varphi}$, $g_1 = B_2$, $g_2 = B_4$, $g_3 = B_6$, $T_v = C_\theta$, $T_\omega = C_\varphi$ in Equation

(5) and making the necessary arrangements, the dynamic equation of the system can be written in a new form as follows.

$$\begin{aligned}\ddot{x} &= f_1\theta + g_1T_v \\ \ddot{\theta}_p &= f_2\theta + g_2T_v \\ \ddot{\varphi} &= f_3 + g_3T_\omega\end{aligned}\quad (10)$$

Where T_v and T_ω corresponds to control inputs for separated subsystems, and x_d, y_d, φ_d are desired positions, so the error dynamics of the system can be expressed as follows:

$$\begin{aligned}\dot{e}_1 &= e_2 \\ \dot{e}_2 &= \ddot{x} - \ddot{x}_d \\ \dot{e}_3 &= e_4 \\ \dot{e}_4 &= \ddot{\theta} - \ddot{\theta}_d \\ \dot{e}_5 &= e_6 \\ \dot{e}_6 &= \ddot{\varphi} - \ddot{\varphi}_d\end{aligned}\quad (11)$$

The SMC method will move the system dynamics towards the defined sliding surface. This movement of the controller is called reaching mode. The time until the reaching mode is called the reaching time. As soon as the system dynamics reaches the sliding surface, it starts the sliding motion. Sliding motion is called sliding mode. Sliding surfaces that move e_2, e_4 and e_6 errors towards to zero when $t \rightarrow \infty$ can be defined as follows.

$$\begin{aligned}s_1 &= c_1e_1 + e_2 \\ s_2 &= c_2e_3 + e_4 \\ s_3 &= c_3e_5 + e_6\end{aligned}\quad (12)$$

The coefficients $c_1, c_2, c_3 > 0$ in the defined sliding surfaces are called slope constants. The reaching time is related to the slope of the sliding surfaces. Therefore, these coefficients directly affect the control performance and should be chosen carefully. In order to obtain control signals, derivation of the Equation (12) can be written as follow.

$$\begin{aligned}\dot{s}_1 &= c_1\dot{e}_1 + \dot{e}_2 = \ddot{x} - \ddot{x}_d + c_1\dot{e}_1 \\ \dot{s}_2 &= c_2\dot{e}_3 + \dot{e}_4 = \ddot{\theta} - \ddot{\theta}_d + c_2\dot{e}_3 \\ \dot{s}_3 &= c_3\dot{e}_5 + \dot{e}_6 = \ddot{\varphi} - \ddot{\varphi}_d + c_3\dot{e}_5\end{aligned}\quad (13)$$

A SMC consists of two parts which called switching and equivalent. Switching part is a signum function, and is responsible for moving the system variables towards to sliding surface. $\dot{s}_1, \dot{s}_2, \dot{s}_3$ terms in Equation (13) correspond to switching function. Switching function can be premised with defining controller gains as $\eta_1, \eta_2, \eta_3 > 0$ as follow.

$$\begin{aligned}u_{sw1} &= \dot{s}_1 = -\eta_1 \text{sgn}(s_1) \\ u_{sw2} &= \dot{s}_2 = -\eta_2 \text{sgn}(s_2) \\ u_{sw3} &= \dot{s}_3 = -\eta_3 \text{sgn}(s_3)\end{aligned}\quad (14)$$

Equivalent control occurs in condition when the system has reached to the sliding phase. This condition can be also defined as $\dot{s}_1, \dot{s}_2, \dot{s}_3 = 0$. Equation (11) and Equation (13) can be re-written as follow.

$$\begin{aligned}c_1\dot{e}_1 + \ddot{x} - \ddot{x}_d &= 0 \\ c_2\dot{e}_3 + \ddot{\theta} - \ddot{\theta}_d &= 0 \\ c_3\dot{e}_5 + \ddot{\varphi} - \ddot{\varphi}_d &= 0\end{aligned}\quad (15)$$

If Equation (15) arranged by using the Equation (10) then,

$$\begin{aligned} c_1 \dot{e}_1 + f_1 \theta + g_1 T_{v1} - \ddot{x}_d &= 0 \\ c_2 \dot{e}_3 + f_2 \theta + g_2 T_{v2} - \ddot{\theta}_d &= 0 \\ c_3 \dot{e}_5 + f_3 \varphi + g_3 T_\omega - \ddot{\varphi}_d &= 0 \end{aligned} \quad (16)$$

where T_{v1} and T_{v2} corresponds to torque forces related with coupled x and θ inputs. The equivalent control term can be obtained by re-arranging Equation (16) as follows,

$$\begin{aligned} u_{eq1} &= \frac{\ddot{x}_d - c_1 \dot{e}_1 - f_1 \theta}{g_1} \\ u_{eq2} &= \frac{\ddot{\theta}_d - c_2 \dot{e}_3 - f_2 \theta}{g_2} \\ u_{eq3} &= \frac{\ddot{\varphi}_d - c_3 \dot{e}_5 - f_3 \varphi_p}{g_3} \end{aligned} \quad (17)$$

Finally, SMC control signal can be obtained with re-arrange Equation 10, 13 and 15 as follow.

$$\begin{aligned} T_{v1} &= \frac{\ddot{x}_d - c_1 \dot{e}_1 - \eta_1 \operatorname{sgn}(s_1) - f_1 \theta}{g_1} \\ T_{v2} &= \frac{\ddot{\theta}_d - c_2 \dot{e}_3 - \eta_2 \operatorname{sgn}(s_2) - f_2 \theta}{g_2} \\ T_\omega &= \frac{\ddot{\varphi}_d - c_3 \dot{e}_5 - \eta_3 \operatorname{sgn}(s_3) - f_3 \varphi}{g_3} \end{aligned} \quad (18)$$

Control signals with control gains $\eta_1, \eta_2, \eta_3 > 0$ can be obtained as above. It can be expressed as $T_v = k_{VCSMC}(T_{v2} - T_{v1})$ and $T_\omega = k_{\omega CSMC} T_\omega$ where k_{VCSMC} and $k_{\omega CSMC}$ are the controller gain constants. Tangent hyperbolic (tanh) function is used instead of sign to prevent chattering. The obtained control signals can be modelled on Simulink as shown in Figure 3.

A Lyapunov function candidate in the form of $V = \frac{1}{2}s$ is defined to perform stability analyse. According to the Lyapunov theorem, for a system to be stable, the condition $\dot{V} \leq 0$ must be ensured.

$$\begin{aligned} \dot{V}_1 &= s_1 \dot{s}_1 = s_1(\ddot{x} - \ddot{x}_d + c_1 \dot{e}_1) = -\eta_1 |s_1| \leq 0 \\ \dot{V}_2 &= s_2 \dot{s}_2 = s_2(\ddot{\theta} - \ddot{\theta}_d + c_2 \dot{e}_3) = -\eta_2 |s_2| \leq 0 \\ \dot{V}_3 &= s_3 \dot{s}_3 = s_3(\ddot{\varphi} - \ddot{\varphi}_d + c_3 \dot{e}_5) = -\eta_3 |s_3| \leq 0 \end{aligned} \quad (19)$$

Equation (19) shows that all three controller signals ensure the Lyapunov stability condition. In other words, the designed controllers will lead the error signal in the system to zero in time. Sliding Mode Control strategy and general schematic of the closed loop system is given in Figure 3.

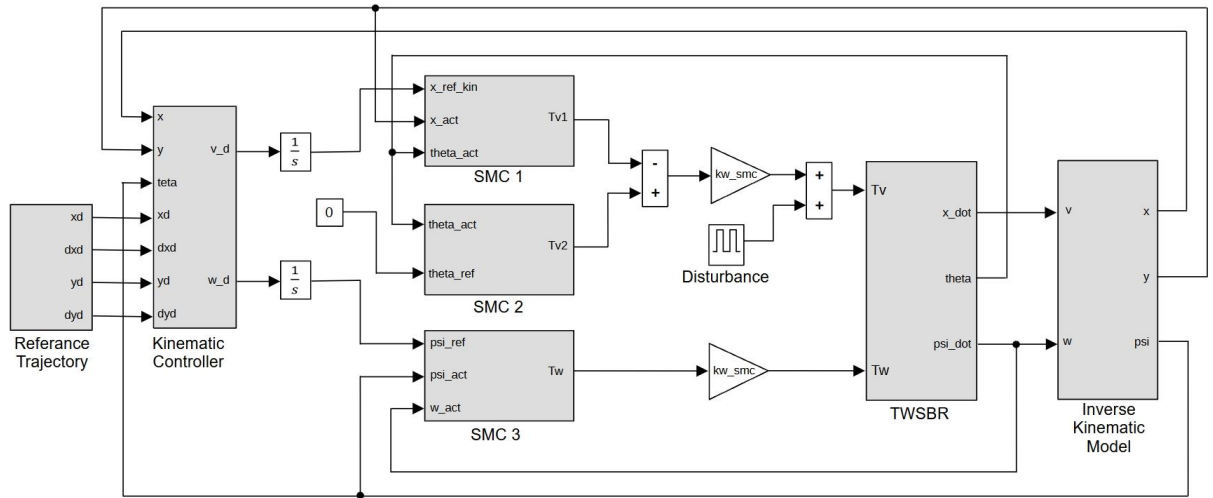


Figure 3. SMC - Closed Loop Block Diagram of the System

\dot{x} , θ , and φ control variables are controlling respectively with SMC 1, SMC 2 and SMC 3 given in Figure 3. Detailed block diagram for SMC 1, SMC 2 and SMC 3 can be seen in Figure 4.

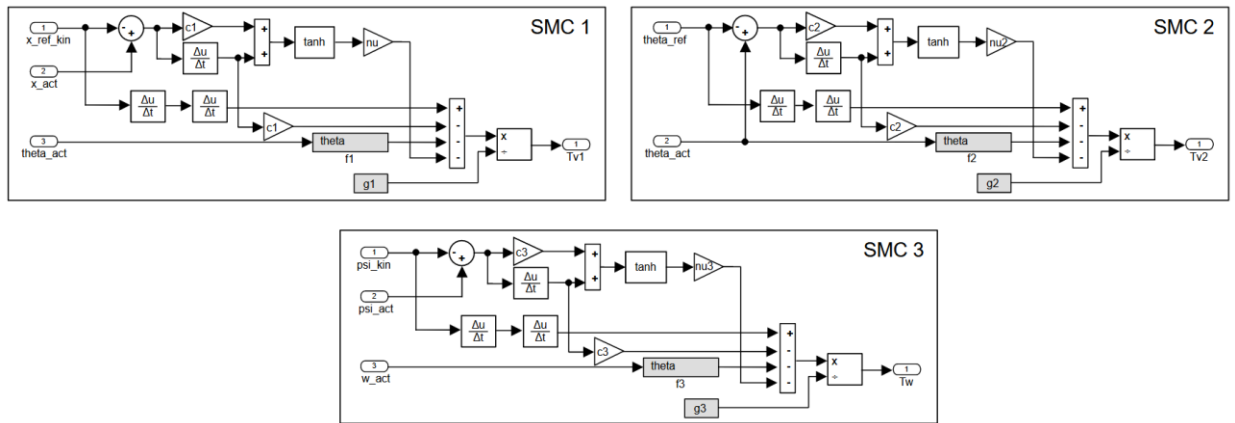


Figure 4. SMC Control Scheme

2.5. PID Control

PID is the abbreviation of “Proportional-Integral-Derivative” terms. While PID control can give good control performance in linear systems, it is not very satisfactory in dealing with non-linear systems. However, it is one of the most frequently used methods due to its easy design and applicability. The mathematical representation of the PID controller can be expressed as follows [24].

$$u(t) = K_p e(t) + K_i \int e(t) dt + K_d \frac{de}{dt} \tag{20}$$

In the Eq. 21. K_p , K_i ve K_d gains respectively corresponds to proportional, integral and derivative part of the controller. $e(t)$ corresponds to error inputs by time. The integral term corresponds to the integral of the error value and produces a control signal that corrects the total error. The term derivative refers to the derivative of the error value and produces a control signal that responds to rapidly changing errors. In other words, the proportional term refers to the current error, the integral term refers to the sum of past errors, and the derivative term refers to the prediction of future errors [25]. PID controller schematics can be seen in Figure 5.

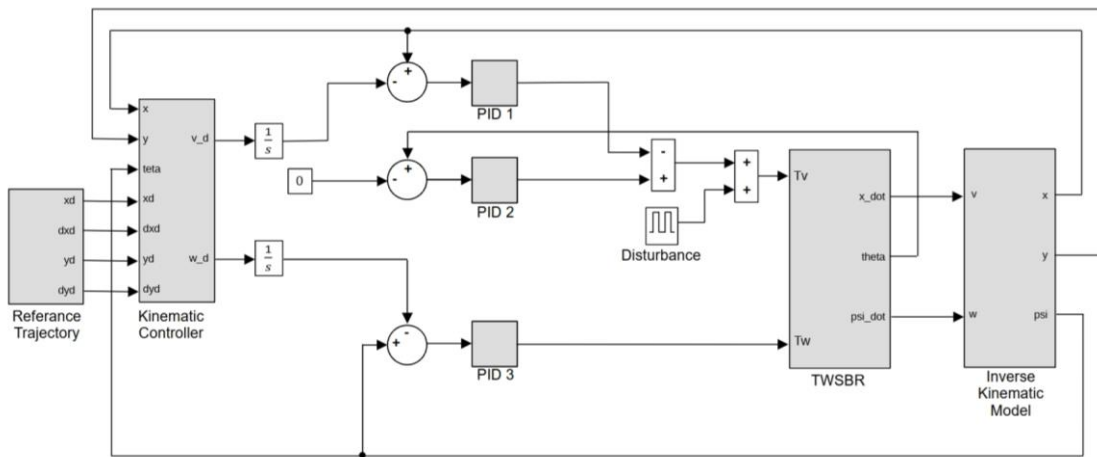


Figure 5. PID Closed Loop Control Schematic

2.6. LQR Control

The Linear Quadratic Regulator (LQR) is one of the optimal control methods frequently used today. In the LQR method, it is aimed to obtain an optimum control signal by using the performance index and the state variables of the system [26].

$$J = \frac{1}{2} \int_0^{\infty} (x^T Q x + u^T R u) dt \tag{21}$$

Performance index J which obtained using system state variables as $\dot{x} = Ax + Bu$ and $u = -Kx$ system inputs is given in Eq. 21. K is gain matrice and define as $K = R^{-1}B^T P$. Q and R diagonal matrices and P is a symmetrical matrix which can be obtained from Ricatti Equation given in Eq. 22.

$$PA + A^T - PBR^{-1}P + Q = 0 \tag{22}$$

The aim of the LQR method is to minimize the performance index J with using Q and R parameters. The Q matrix represents the speed of reaching the reference and the R parameter represents the amount of energy to be consumed. LQR control schematics can be seen in Figure 6.

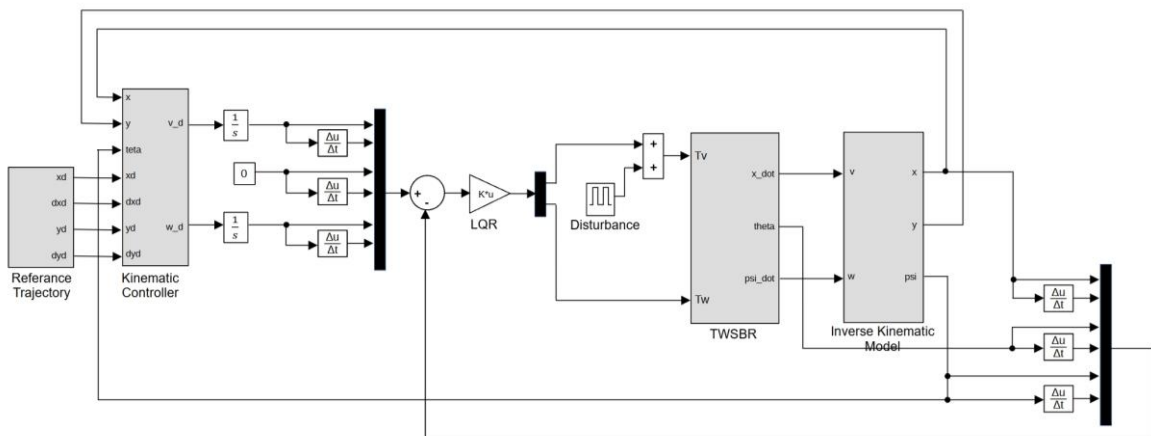


Figure 6. LQR Closed Loop Control Schematic

3. RESULTS AND DISCUSSION

In order to evaluate the response speed and robustness of the designed controller, simulation studies were carried out using five different scenarios having different disturbance inputs and parameter changes. PID and LQR control are also applied to the system to compare the performance of the proposed SMC controller. Simulation studies were carried out in MATLAB/Simulink. An infinite type of trajectory was used as a reference and the simulation time was determined as 150 seconds. System parameters are given in Table 1. All the SMC, PID and LQR controller parameters are determined by using trial-and-error method and given in Table 2.

Table 1. Physical Parameters of the System

Parameter	Description	Value
R	Wheel diameter	0.1 m
L	Distance between wheels	0.3 m
D	Distance of pendulum centre of gravity to shaft	0.45 m
g	Gravity force	9.8 m/s ²
M _p	Mass of the pendulum	3 kg
M _w	Mass of the wheels	0.5 kg

Table 2. Controller Parameters

Kinematic Controller	$k_x, k_y = 4, I_x, I_y = 0.025$		
SMC	$k_{vCSMC} = 50, k_{\omega CSMC} = 1$	$C_1 = 1, C_2 = 10, C_3 = 5$	$\eta_1 = 3.5, \eta_2 = 11, \eta_3 = 1$
PID	$K_{P1} = -2, K_{I1} = -4, K_{D1} = -4$	$K_{P2} = -2, K_{I2} = -4, K_{D2} = -4$	$K_{P3} = -2, K_{I3} = -4, K_{D3} = -4$
LQR	$K = \begin{bmatrix} -27 & -51 & -334 & -23 & 0 & 0 \\ 0 & 0 & 0 & 0 & 10 & 1 \end{bmatrix}$		

Case 1: In the first simulation study, performances of the controllers are tested under ideal conditions without any disturbance or parameter changes and the results are given in Figure 5 – Figure 8. All the controllers showed a successful trajectory tracking performance by quickly providing the desired position and orientation as seen in Figure 7 and Figure 8. However, while the SMC and LQR controllers reached the reference velocity quickly at the beginning of the movement, the PID controller gave a very oscillatory and late response as seen in Figure 9. For the PID control, this fluctuation in the velocity caused the body to make an oscillatory movement and reach the equilibrium quite late as seen in Figure 10. Although the LQR control gave a successful result in terms of body angle, the SMC control showed the best performance. On the other hand, the SMC control produced much more aggressive torques than the others at the beginning of the movement, but it quickly stabilized as seen in Figure 10. Moreover, thanks to tanh switching function, there is no chattering in the SMC control signal.

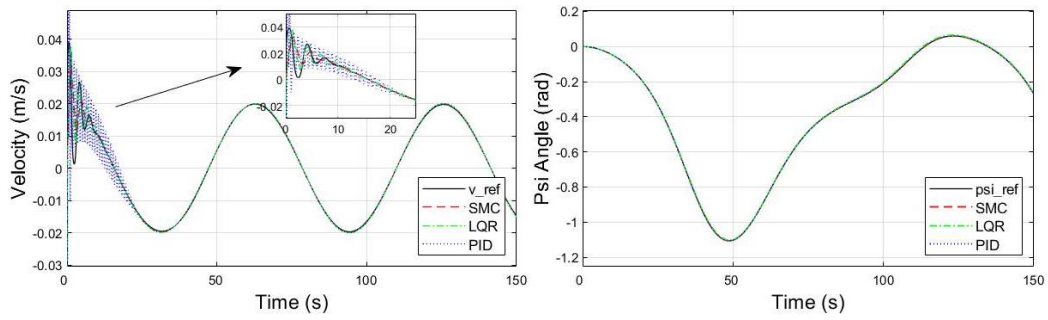


Figure 7. Velocity and movement angle (ψ) of the robot (Case 1)

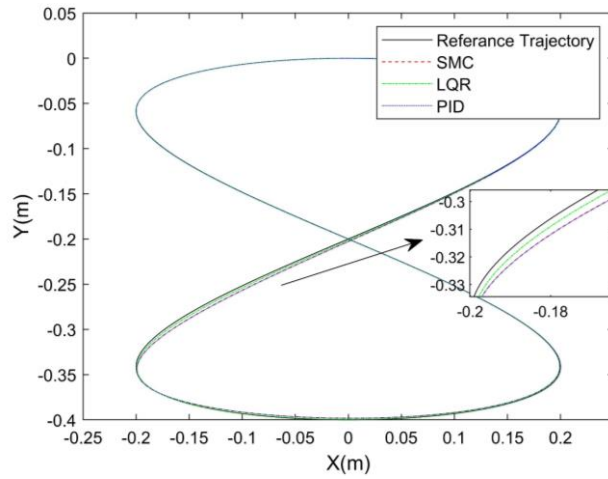


Figure 8. Trajectory tracking (Case 1)

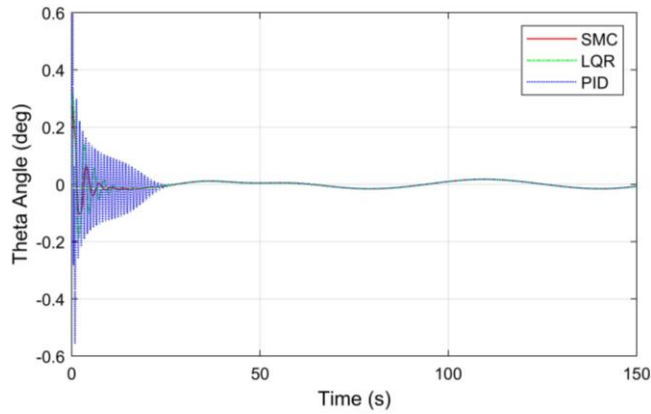


Figure 9. Body (θ) Angle (Case 1)

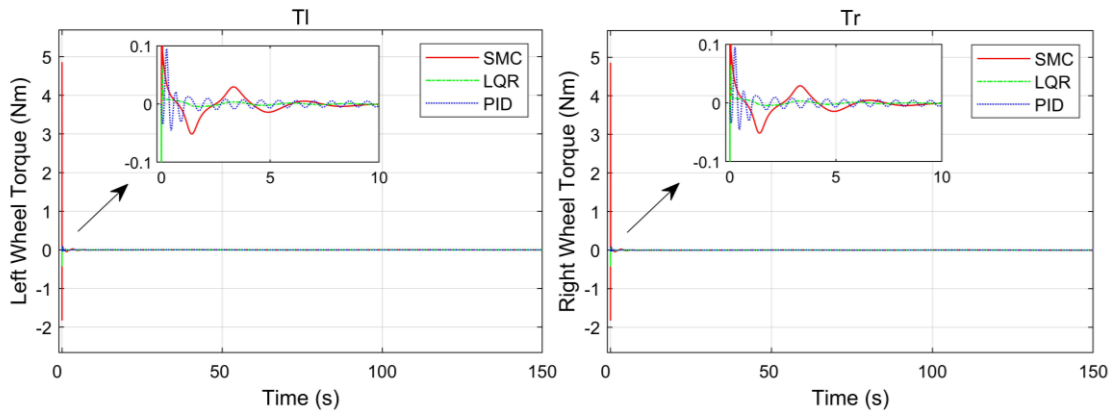


Figure 10. Wheel torques (Case 1)

In the following cases, disturbance input and parameter changes were applied to the system to examine the robustness of the controllers.

Case 2: In this case, only the 0.5 Nm impulse signal seen in Figure 11 was applied to the control input of the system for 1 second as a disturbance and no changes have been made to the system parameters. Disturbance input applied in coupled \dot{x} and $\dot{\theta}$ control output and can be seen in Figure 3.

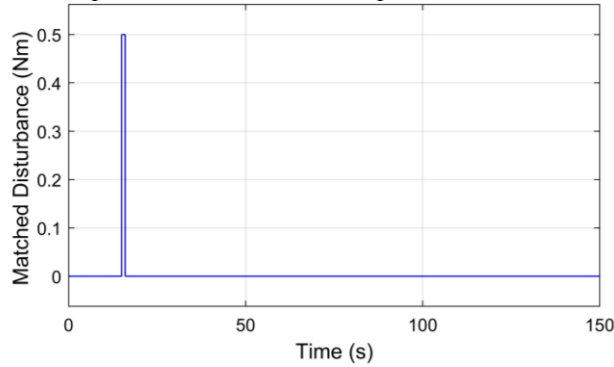


Figure 11. Disturbance signal applied to the system

In the presence of the disturbance, the trajectory tracking performance of the SMC and LQR control methods are quite close to each other. It can be seen from Figure 13 that the SMC and LQR controllers are much more insensitive to disturbance input than the PID controller. Additionally, while a limited speed fluctuation occurs in the LQR and SMC controllers after the disturbance input, these fluctuations are quite high in the PID controller as seen in Figure 12. As a result of velocity fluctuations, the maximum body angle reaches 1.5 degrees in the PID control, while it is around 0.25 degrees in the LQR control. Furthermore, the proposed SMC controller is almost not affected by the disturbance input.

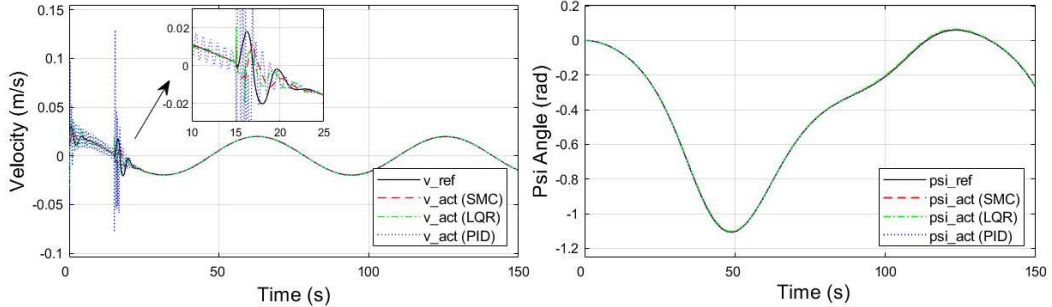


Figure 12. Velocity and movement angle (φ) of the robot (Case 2)

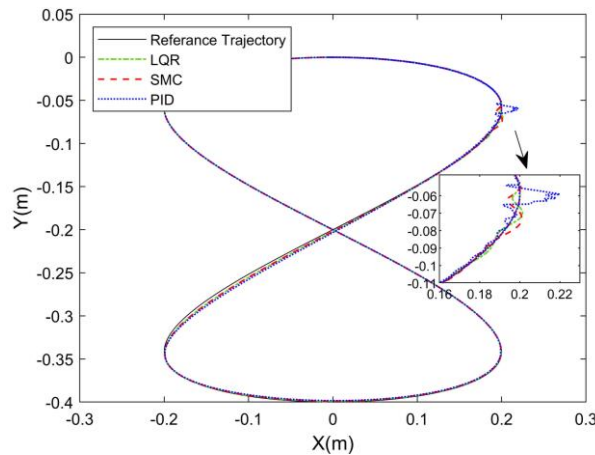


Figure 13. Trajectory Tracking (Case 2)

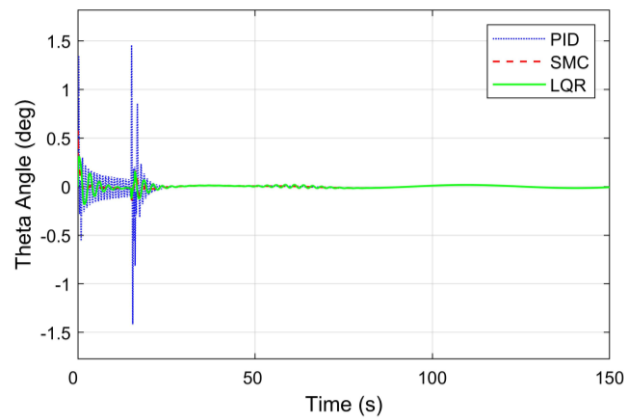


Figure 14. Body (θ) Angle (Case 2)

As seen in Figure 15, although the SMC controller applies much higher torques at the beginning of the movement, it applies much less torque than the PID and LQR controllers against the disturbance input.

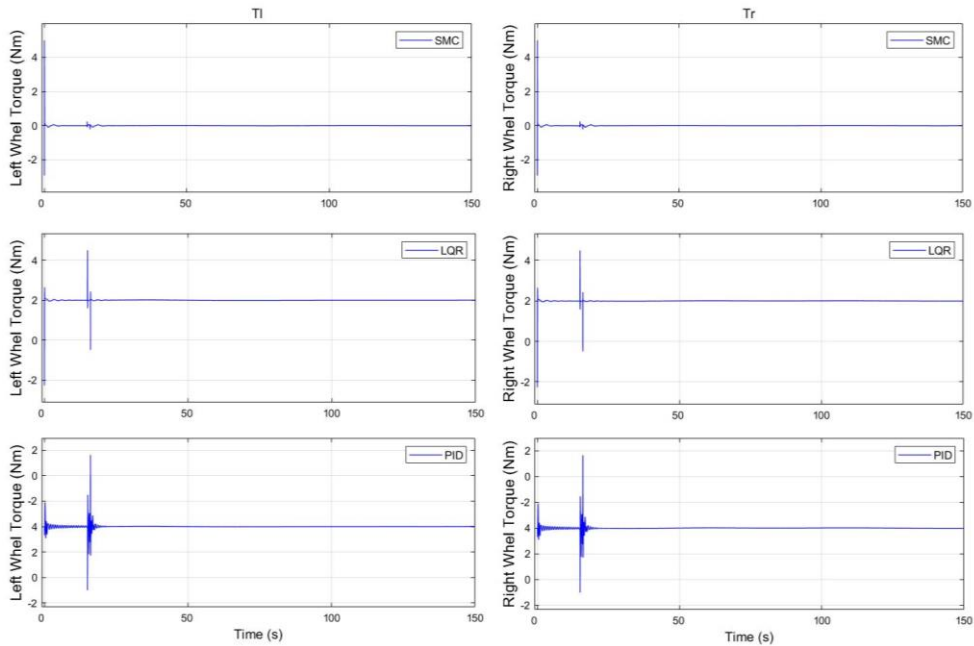


Figure 15. Wheel torques (Case 2)

Parameter uncertainty is a factor affecting the stability of many controllers. In order to test the robustness of the controllers against to parameter uncertainties, simulations were performed by changing the body mass M_p in three different ways, 6 kg, 10 kg, 50 kg respectively.

Case 3: In this case, the body weight M_p was increased from 3 kg to 6 kg. The PID controller is negatively affected by parameter changes, and it almost lost its stability. Large oscillations in speed, trajectory, and body angle for PID control can be seen in Figure 16- Figure 18.

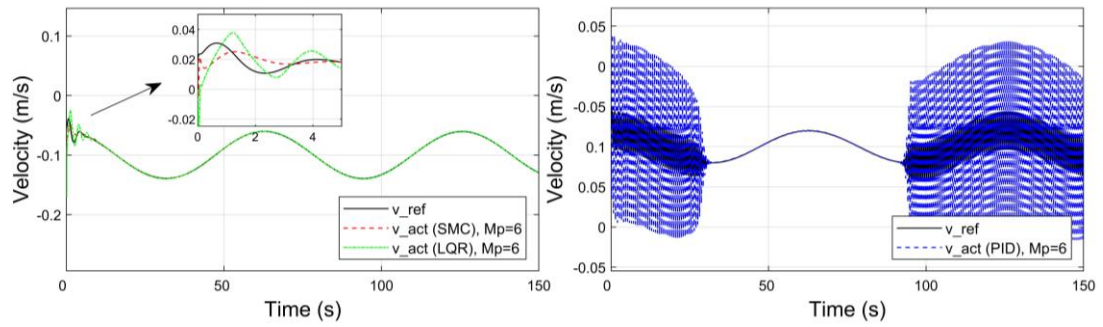


Figure 16. Velocity of the robot (Case 3)

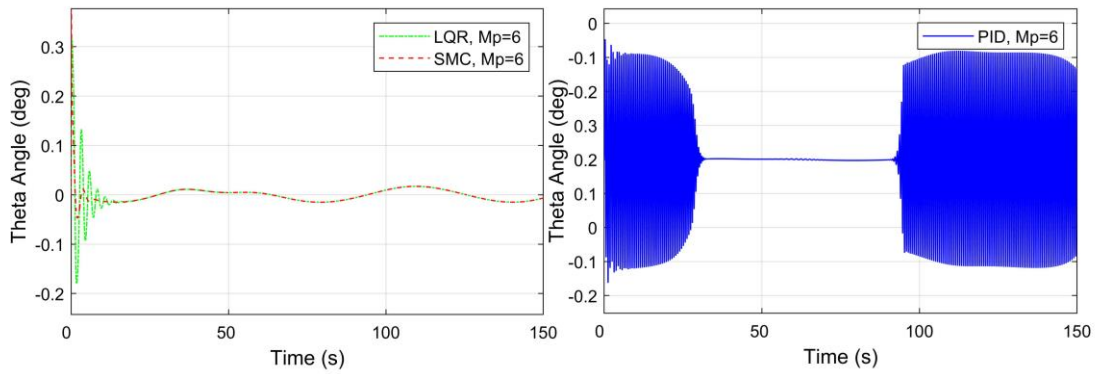


Figure 17. Body (θ) Angle (Case 3)

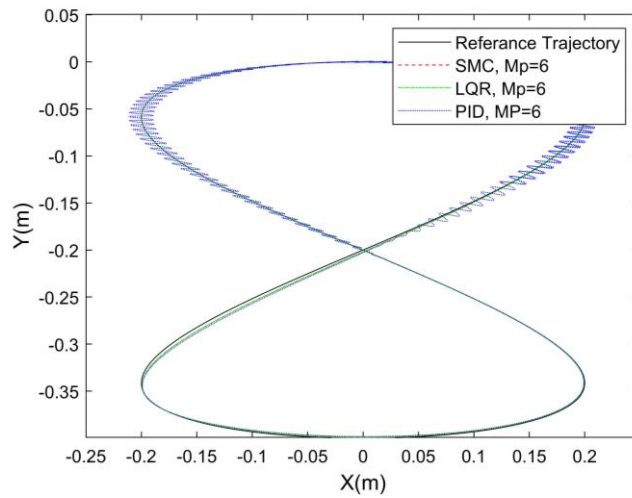


Figure 18. Trajectory Tracking (Case 3)

Case 4: Body weight M_p increased to 10 kg. In this case the PID control response became completely unstable and was therefore not shown in the graphs. On the other hand, it can be seen in Figure 19-Figure 21 that SMC and LQR controllers continue to maintain their stability and offer successful trajectory tracking performance. However, SMC control offers a much more successful performance than LQR in balancing the body angle as seen in Figure 21.

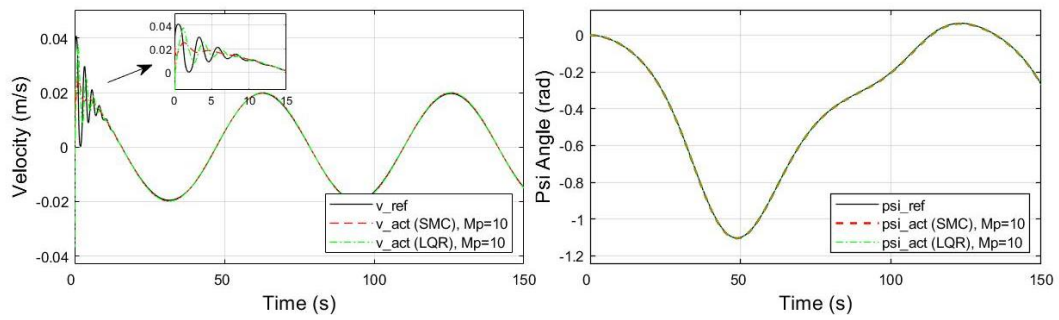


Figure 19. Velocity and movement angle (φ) of the robot (Case 4)

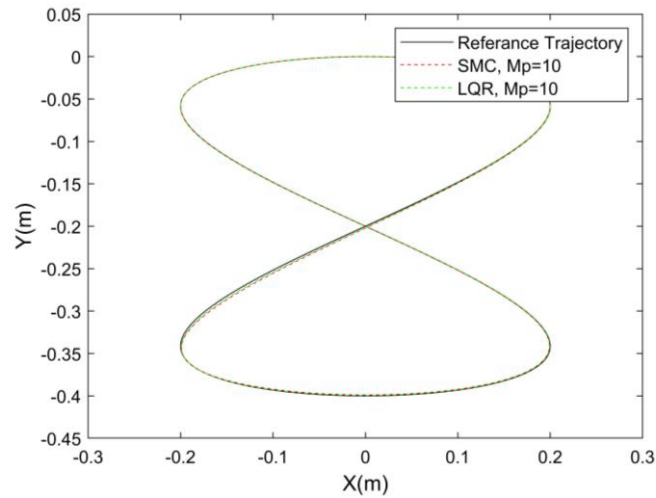


Figure 20. Trajectory Tracking (Case 4)

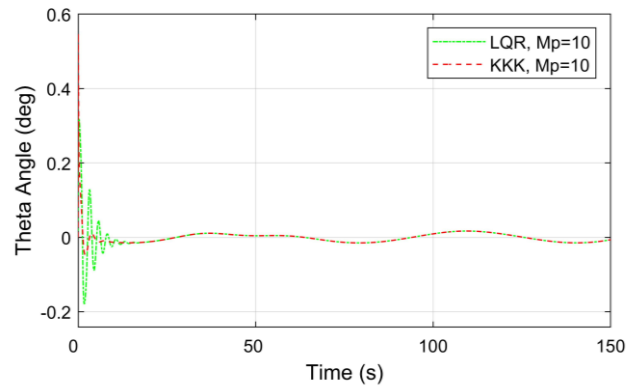


Figure 21. Body (θ) Angle (Case 4)

Case 5: In this case the robustness of the proposed controller against to parameter variations was tested under an extreme condition by increasing the body weight M_p from 3 kg to 50 kg. Under these conditions, it is seen in Figure 22 – Figure 25 that the LQR controller begins to become unstable and excessive oscillations occur in trajectory tracking and body angle. On the other hand, it is seen that the proposed SMC controller maintains its stability even in this extreme case and provides a very successful response in trajectory tracking and balancing the body angle.

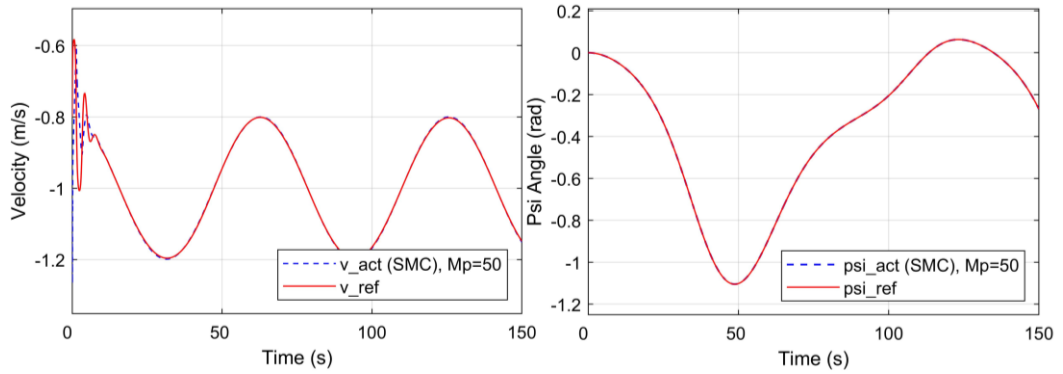


Figure 22. Velocity and movement angle (φ) of the robot for SMC (Case 5)

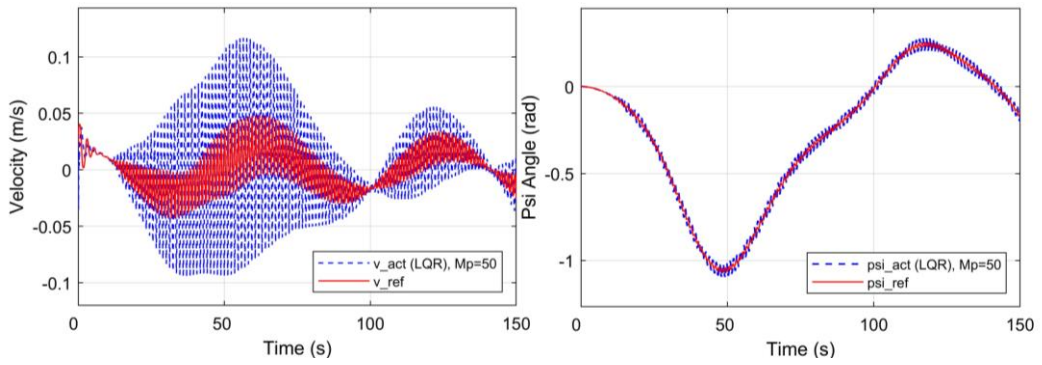


Figure 23. Velocity and movement angle (φ) of the robot for LQR (Case 5)

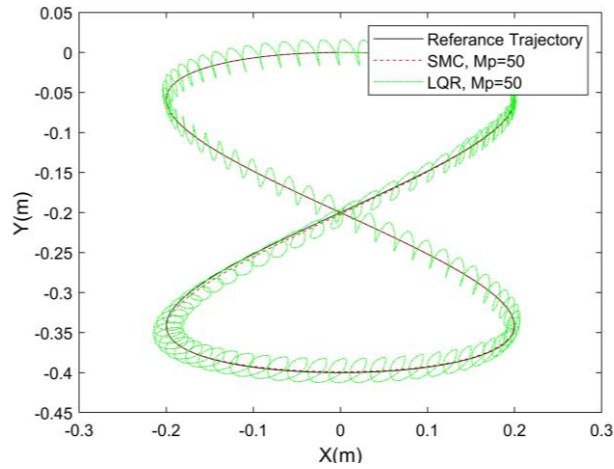


Figure 24. Trajectory Tracking (Case 5)

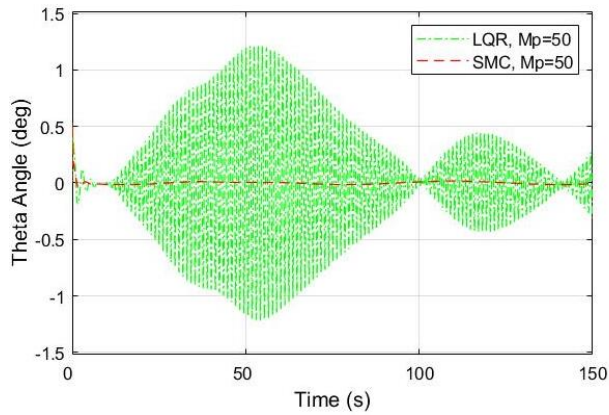


Figure 25. Body (θ) Angle (Case 5)

4. CONCLUSIONS

Parameter uncertainties and external disturbances negatively affect the stability of controllers. In this study, a robust SMC method against to uncertainties and disturbances for trajectory tracking of a two-wheeled self-balancing robot is investigated. In the proposed method, the chattering problem is eliminated by using a tangent hyperbolic switching function. The performance of the proposed method is tested for five different scenarios having different disturbance inputs and parameter changes and compared with LQR and PID controllers. The results showed that the PID control is extremely sensitive to disturbance inputs and parameter changes, and the LQR controller provides a much better performance than the PID control in terms of response speed and robustness. The results also showed that the proposed SMC controller not only offer as good performance as the LQR controller in terms of response speed, but it is extremely robust and almost insensitive to disturbance inputs and excessive parameter changes.

Declaration of Ethical Standards

The authors of this article declare that the materials and methods used in this study do not require ethical committee permission and/or legal-special permission.

Credit Authorship Contribution Statement

M. DOĞAN: Methodology, Conceptualization, Resources, Investigation, Writing.

U. ÖNEN: Methodology, Conceptualization, Resources, Investigation, Writing -review & editing, Supervision.

Declaration of Competing Interest

The authors declare that they have no known competing financial interests or personal relationships that could have appeared to influence the work reported in this paper.

Funding / Acknowledgements

The author(s) received no financial support for the research.

Data Availability

Data available on request from the author.

5. REFERENCES

- [1] D. Nemeč, D. Adamković, M. Hrubos, R. Pirnik, ve M. Mihalik, "Fast Two-Wheeled Balancing Robot", ss. 1-9, Haz. 2021, doi: 10.1109/ICCC51557.2021.9454659.
- [2] G. C. M. Santo ve C. Garcia, "Construction, Control Design and Bluetooth Trajectory Control of a Self-Balancing Robot", içinde *SBAI 2019*, 2019. doi: 10.17648/sbai-2019-111151.
- [3] K. Prakash ve K. Thomas, "Study of controllers for a two wheeled self-balancing robot", 2016 *International Conference on Next Generation Intelligent Systems, ICNGIS 2016*, Şub. 2017, doi: 10.1109/ICNGIS.2016.7854009.
- [4] F. Grasser, A. D'Arrigo, S. Colombi, ve A. C. Rufer, "JOE: A mobile, inverted pendulum", *IEEE Transactions on Industrial Electronics*, c. 49, sy 1, ss. 107-114, Şub. 2002, doi: 10.1109/41.982254.
- [5] M. Velazquez, D. Cruz, S. Garcia, ve M. Bandala, "Velocity and Motion Control of a Self-Balancing Vehicle Based on a Cascade Control Strategy", *Int J Adv Robot Syst*, c. 13, sy 3, Haz. 2016, doi: 10.5772/63933.

- [6] J. X. Xu, Z. Q. Guo, ve T. H. Lee, "Design and implementation of a takagi-sugeno-type fuzzy logic controller on a two-wheeled mobile robot", *IEEE Transactions on Industrial Electronics*, c. 60, sy 12, ss. 5717-5728, 2012, doi: 10.1109/TIE.2012.2230600.
- [7] M. El-Bardini ve A. M. El-Nagar, "Interval type-2 fuzzy PID controller for uncertain nonlinear inverted pendulum system", *ISA Trans*, c. 53, sy 3, ss. 732-743, 2014, doi: 10.1016/J.ISATRA.2014.02.007.
- [8] O. Begovich, E. N. Sanchez, ve M. Maldonado, "Takagi-Sugeno fuzzy scheme for real-time trajectory tracking of an underactuated robot", *IEEE Transactions on Control Systems Technology*, c. 10, sy 1, ss. 14-20, Oca. 2002, doi: 10.1109/87.974334.
- [9] L. Guo, S. A. A. Rizvi, ve Z. Lin, "Optimal control of a two-wheeled self-balancing robot by reinforcement learning", *International Journal of Robust and Nonlinear Control*, c. 31, sy 6, ss. 1885-1904, Nis. 2021, doi: 10.1002/RNC.5058.
- [10] A. Unluturk ve O. Aydogdu, "Machine Learning Based Self-Balancing and Motion Control of the Underactuated Mobile Inverted Pendulum with Variable Load", *IEEE Access*, c. 10, ss. 104706-104718, 2022, doi: 10.1109/ACCESS.2022.3210540.
- [11] H. M. Omar, A. M. Elalawy, ve H. H. Ammar, "Two-wheeled Self balancing robot Modeling and Control using Artificial Neural Networks (ANN)", *NILES 2019 - Novel Intelligent and Leading Emerging Sciences Conference*, ss. 196-200, Eki. 2019, doi: 10.1109/NILES.2019.8909311.
- [12] J. Wu ve S. Jia, "T-S adaptive neural network fuzzy control applied in two-wheeled self-balancing robot", *Proceedings of the 6th International Forum on Strategic Technology, IFOST 2011*, c. 2, ss. 1023-1026, 2011, doi: 10.1109/IFOST.2011.6021194.
- [13] M. Önkol ve C. Kasnakoğlu, "Adaptive model predictive control of a two-wheeled robot manipulator with varying mass", *Measurement and Control (United Kingdom)*, c. 51, sy 1-2, ss. 38-56, Mar. 2018, doi: 10.1177/0020294018758527/ASSET/IMAGES/LARGE/10.1177_0020294018758527-FIG20.JPEG.
- [14] M. S. Mahmoud ve M. T. Nasir, "Robust control design of wheeled inverted pendulum assistant robot", *IEEE/CAA Journal of Automatica Sinica*, c. 4, sy 4, ss. 628-638, Eki. 2017, doi: 10.1109/JAS.2017.7510613.
- [15] G. V. Raffo, V. Madero, ve M. G. Ortega, "An application of the underactuated nonlinear \mathcal{H}_∞ controller to two-wheeled self-balanced vehicles", *Proceedings of the 15th IEEE International Conference on Emerging Technologies and Factory Automation, ETFA 2010*, 2010, doi: 10.1109/ETFA.2010.5641024.
- [16] N. Uddin, "Lyapunov-based control system design of two-wheeled robot", *Proceedings - 2017 International Conference on Computer, Control, Informatics and its Applications: Emerging Trends In Computational Science and Engineering, IC3INA 2017*, c. 2018-January, ss. 121-125, Tem. 2017, doi: 10.1109/IC3INA.2017.8251752.
- [17] S. Cheng, H. Liu, ve M. Yao, "An Adaptive Backstepping-Based Controller for Trajectory Tracking of Wheeled Robots", *2021 4th IEEE International Conference on Industrial Cyber-Physical Systems (ICPS)*, ss. 539-544, May. 2021, doi: 10.1109/ICPS49255.2021.9468124.
- [18] L. Jiang, H. Qiu, Z. Wu, ve J. He, "Active disturbance rejection control based on adaptive differential evolution for two-wheeled self-balancing robot", *Proceedings of the 28th Chinese Control and Decision Conference, CCDC 2016*, ss. 6761-6766, Ağu. 2016, doi: 10.1109/CCDC.2016.7532214.
- [19] U. Onen, "Model-Free Controller Design for Nonlinear Underactuated Systems with Uncertainties and Disturbances by Using Extended State Observer Based Chattering-Free Sliding Mode Control", *IEEE Access*, c. 11, ss. 2875-2885, 2023, doi: 10.1109/ACCESS.2023.3234864.
- [20] V. T. Nguyen, C. Y. Lin, S. F. Su, ve Q. V. Tran, "Adaptive Chattering Free Neural Network Based Sliding Mode Control for Trajectory Tracking of Redundant Parallel Manipulators", *Asian J Control*, c. 21, sy 3, ss. 1-16, Mar. 2019, doi: 10.1002/ASJC.1789.

- [21] W. Junfeng ve Z. Wanying, "Research on control method of two-wheeled self-balancing robot", *Proceedings - 4th International Conference on Intelligent Computation Technology and Automation, ICICTA 2011*, c. 1, ss. 476-479, 2011, doi: 10.1109/ICICTA.2011.132.
- [22] F. N. Martins, M. Sarcinelli-Filho, ve R. Carelli, "A Velocity-Based Dynamic Model and Its Properties for Differential Drive Mobile Robots", *Journal of Intelligent and Robotic Systems: Theory and Applications*, c. 85, sy 2, ss. 277-292, Şub. 2017, doi: 10.1007/S10846-016-0381-9/METRICS.
- [23] D. Qian ve J. Yi, *Hierarchical Sliding Mode Control for Under-actuated Cranes*. Springer Berlin Heidelberg, 2015. doi: 10.1007/978-3-662-48417-3.
- [24] M. Tinkir, U. Onen, M. Kalyoncu, ve F. M. Botsali, "Pid and interval type-2 fuzzy logic control of double inverted pendulum system", *2010 The 2nd International Conference on Computer and Automation Engineering, ICCAE 2010*, c. 1, ss. 117-121, 2010, doi: 10.1109/ICCAE.2010.5451988.
- [25] O. Çakır, ve S. Tekin, "Oransal İntegral Türevsel Denetleyici Parametrelerinin Sezgisel Optimizasyon Yöntemleri ile Ayarlanması", *Avrupa Bilim ve Teknoloji Dergisi*, sy 23, ss. 9-21, Nis. 2021, doi: 10.31590/EJOSAT.830467.
- [26] Ü. Önen, A. Çakan, ve İ. İlhan, "Particle Swarm Optimization Based LQR Control of an Inverted Pendulum", *ETJ Engineering and Technology Journal*, c. 2, ss. 2456-3358, 2017, doi: 10.18535/etj/v2i5.01.



A 3D U-NET BASED ON EARLY FUSION MODEL: IMPROVEMENT, COMPARATIVE ANALYSIS WITH STATE-OF-THE-ART MODELS AND FINE-TUNING

^{1,*}Beyza KAYHAN , ²Sait Ali UYMAZ 

^{1,2} Konya Technical University, Engineering and Natural Sciences Faculty, Computer Engineering Department,
Konya, TÜRKİYE

¹bkayhan@ktun.edu.tr, ²sauymaz@ktun.edu.tr

Highlights

- A review on deep learning based multi-organ segmentation.
- Using the two-stage U-Net model
- Improving fusion approach combining different color channels for segmentation of CT images
- Performing parameter optimization
- Comparison of performances of different models in segmentation of abdominal organs



A 3D U-NET BASED ON EARLY FUSION MODEL: IMPROVEMENT, COMPARATIVE ANALYSIS WITH STATE-OF-THE-ART MODELS AND FINE-TUNING

^{1,*}Beyza KAYHAN , ²Sait Ali UYMAZ 

^{1,2}Konya Technical University, Engineering and Natural Sciences Faculty, Computer Engineering Department, Konya, TÜRKİYE

¹bkayhan@ktun.edu.tr, ²sauymaz@ktun.edu.tr

(Received: 15.12.2023; Accepted in Revised Form: 20.06.2024)

ABSTRACT: Multi-organ segmentation is the process of identifying and separating multiple organs in medical images. This segmentation allows for the detection of structural abnormalities by examining the morphological structure of organs. Carrying out the process quickly and precisely has become an important issue in today's conditions. In recent years, researchers have used various technologies for the automatic segmentation of multiple organs. In this study, improvements were made to increase the multi-organ segmentation performance of the 3D U-Net based fusion model combining HSV and grayscale color spaces and compared with state-of-the-art models. Training and testing were performed on the MICCAI 2015 dataset published at Vanderbilt University, which contains 3D abdominal CT images in NIfTI format. The model's performance was evaluated using the Dice similarity coefficient. In the tests, the liver organ showed the highest Dice score. Considering the average Dice score of all organs, and comparing it with other models, it has been observed that the fusion approach model yields promising results.

Keywords: Computed Tomograph, Multi Organ Segmentation, Deep Learning, Fusion Model, U-Net

1. INTRODUCTION

Segmentation of organs in medical images is of crucial importance for diagnosing diseases, planning treatment, and locating target organs for radiotherapy [1]. Automated multi-organ segmentation is difficult because of structural complexity and volumetric differences of organs. In recent years, there has been a growing interest in using deep learning methods to address these difficulties [2]. These methods automatically extract feature vectors, which are used for tasks such as object detection and classification. This feature vector extraction is achieved through non-linear layers. By using multiple layers, deep learning can learn different features from the data. For example, basic features like edges and patterns are learned in the first layers, while more complex features are learned in subsequent layers [3], [4]. Deep learning has been successfully applied in various fields, including face recognition [5], voice recognition [6], robotic applications [7], and particularly in the biomedical applications [8]. This is due to the increasing availability of medical images and the ability of deep learning architectures to provide fast and reliable results [9].

In this study, a 3D U-Net based fusion model combining different color spaces was used to overcome the limitations of traditional methods in multi-organ segmentation and compared with state-of-the-art approaches. Roth et al. [10] increased the segmentation success by combining image inputs of different resolutions. This success shows that fusion models are an effective strategy, and based on this, the fusion model used in this study combines different color spaces. In combining different color spaces, Ghosh et al. (2018) was effective. Ghosh et al. [11] also found that combining different color spaces was effective in detecting bleeding areas in endoscopy images, with the HSV color space performing the best. This highlights the impact of color spaces on model performance. Additionally, using different color spaces can improve segmentation accuracy and reliability by highlighting different features in images [12]. One of the important aspects of this study is the inclusion of optimizations and fine-tuning to enhance the performance of the fusion model. Another crucial part is the integration of different slice selection methods to better capture contextual information from the 3D data. This approach aims to augment the data and

*Corresponding Author: Beyza KAYHAN, bkayhan@ktun.edu.tr

ultimately improve the accuracy and reliability of the segmentation.

2. RELATED WORK

Automatic segmentation of organs in computed tomography images is difficult due to differences in shape and size. Improving segmentation accuracy by overcoming these challenges has become an active area of research. When deep learning methods were not widespread, traditional and atlas-based methods were used in multi-organ segmentation. In these methods, mathematical and techniques methods are used to perform the segmentation process. Their differences in organs complicated the segmentation process. In recent years, deep learning-based methods that address organ differences more effectively have been used and have been observed to yield successful results [13].

Trullo et al. [14] proposed two common deep architectures to jointly separate all organs, including aorta, heart, esophagus, and trachea, instead of separating them separately. The second deep architecture, using the Sharp Mask network, is trained to distinguish each target organ from the background. In this study, initial segmentation was found to be useful for the segmentation of target organs. Larsson et al. [15] proposed a two-stage convolutional neural network for organ segmentation. In this network, each organ is segmented independently. The central voxel of the organ is obtained using the feature-based multiple atlas approach, and a prediction mask is placed around it. Subsequently, a 3D convolutional neural network (CNN) is applied for voxel-wise classification. This initialization method enables the training of regional networks, where the voxel only needs to distinguish between a specific organ and the background.

Roth et al. [16] propose a stepwise approach using a 3D fully convolutional network (FCN) trained on CT images. In the first stage, a mask of the patient's internal structure is obtained by applying simple thresholding with morphological operations. The FCN architecture is then trained using this mask, resulting in a reduction in the number of voxels required to calculate the loss function of the network. Additionally, the number of regions in the 3D image input to the convolutional neural network (CNN) is reduced by approximately 40%. In the second stage, the FCN architecture is trained with the mask obtained from the first stage. This architecture was tested on 150 CT images containing three organs (liver, spleen, and pancreas). Roth, Sugino, et al. [10] propose a multi-scale 3D FCN approach for high-resolution segmentation. The 3D FCN predictions of low-resolution inputs are combined with high-resolution 3D FCN inputs.

Shen et al. [17] show that the performance of multi-organ segmentation depends on the loss function as well as the network architecture. They compared the effects of Dice-based loss functions on CT images for multi-organ segmentation. In addition, they examined the impact of three different weighting types (uniform, simple, and square) and initial learning rates on segmentation using a 3D FCN. The models were evaluated on a random subset of 340 training and 37 test patients. The network produced a predictive map with eight classes, including seven organs (liver, stomach, spleen, gallbladder, artery, portal vein, and pancreas) and background.

Kekeya et al. [18] proposed a new deep learning model using transfer learning for automatic multi-organ segmentation. This model, called 3D U-JAPA-Net, in addition to the raw CT data, also uses a probability atlas of organs (PA), which provides information about the positions of the organs. The 3D U-JAPA-Net model utilizes transfer learning to effectively incorporate PA information. During the model training process, a 3D U-JAPA-Net with nine output classes (including eight organs and a background class) is trained using data from organs in their bounding boxes.

Vesal et al. [19] utilized a deep learning architecture to segment organs at risk (OARs) in thoracic CT images. The architecture combines a 2D U-Net and Dense Residual (DR) network, consisting of four downsampling and upsampling convolution blocks in the encoder and decoder branches. Due to limited sample size, a deeper 2D version of the network was used. In each block, two 3x3 convolutions and ReLU activation function were applied.

Mietzner and Mastmeyer [20] have developed an automated method for detecting and segmenting abdominal organs in CT scans. It is challenging to detect the pancreatic organ in particular. Using a

combination of the random forest regression method and the 2D U-Net architecture, the segmentation mask and bounding box of five organs, namely liver, kidneys, spleen, and pancreas were detected. A dataset of 50 CT scans was used in this study. Rister et al. [21] trained a deep neural network to perform multi-organ segmentation. 140 CT scans were used, including six organs: liver, lung, bladder, kidney, bone, and brain. First, the lungs and bones were segmented a 3D Fourier transform, followed by the use of a 3D U-Net architecture to segment the remaining organs. Liu et al. [22] aimed to develop a deep learning-based method for multi-organ segmentation. Eight organs, namely the large intestine, small intestine, duodenum, left kidney, right kidney, liver, spinal cord, and stomach, were labeled by experts in CT images. The segmentation process was performed using a 3D U-Net architecture. Fang and Yan [23] performed multi-organ segmentation using a multi-scale neural network. The system with pyramid input is integrated into the U-Net network to combine features at different scales. Finally, the pyramid outputs are combined to achieve improved segmentation. This proposed network is called PIPO-FAN. Zhang et al. [24] proposed a full volume-based method, the efficientSegNet network, for multi-organ segmentation. This method takes full advantage of the 3D context and aims to reduce computational costs.

Kaur et al. [25] present a systematic literature review for multi-organ segmentation in the study. Previous studies have shown that the most used architectures for abdominal multi-organ segmentation are CNN, FCN, and U-Net. Generally, segmentation of large organs such as liver, kidney and spleen has been performed. It is not preferred due to the difficulty of segmenting small organs such as duodenum, esophagus, pancreas, and gallbladder. More research is needed to segment small organs and improve segmentation accuracy in the future.

3. MATERIAL AND METHODS

In this study, the Python (3.6) programming language was utilized for automatic multi-organ segmentation. The Simple ITK library was used to read and process 3D tomography images, The Numpy library was used for numerical operations. The Pytorch library was also utilized for developing deep learning models. The fusion model used in this study was executed on NVidia GeForce RTX 2070 with 8 GB of memory.

In this section, the dataset used for training the model is discussed. The data preprocessing and data augmentation processes performed on this data set are explained. Additionally, details of the fusion model used for multi-organ segmentation are given.

3.1. Dataset

In this study, the dataset containing abdominal CT images provided by Vanderbilt University Medical Center (VUMC) was used. The dataset consists of 30 images. Volume dimensions of CT images are $512 \times 512 \times 85$ and $512 \times 512 \times 198$, resolution $0.54 \times 0.54 \text{ mm}^2$ and $0.98 \times 0.98 \text{ mm}^2$ and slice thickness 2.5 mm and 5.0 mm varies between. Trained individuals labeled a total of 13 organs in each CT image, which were then validated by a radiologist. Some patients do not have a right kidney or gallbladder. For this reason, it was not labeled. The data was recorded in the NIfTI file format [26]. Figure 1 shows each labeled organ.

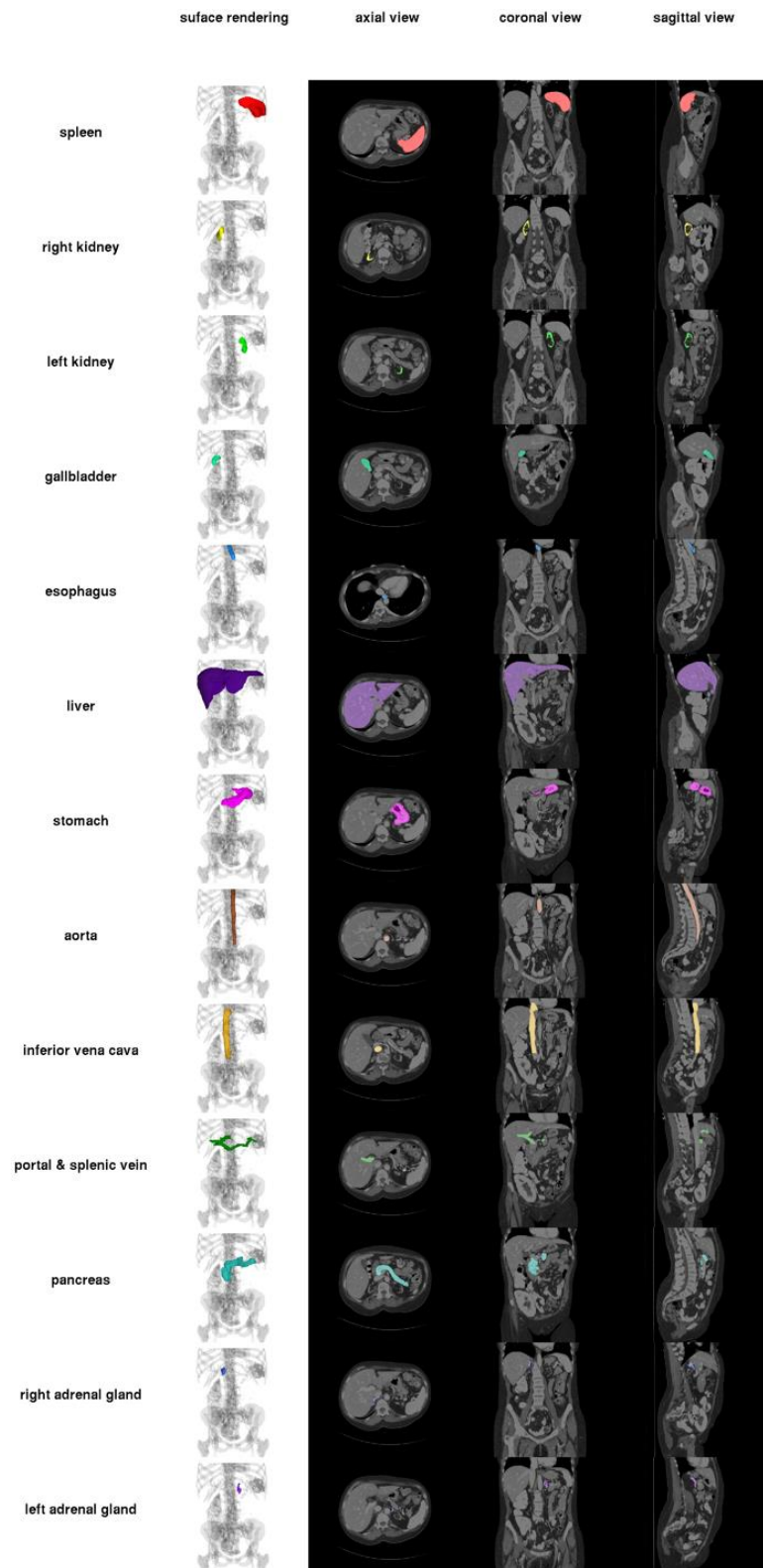


Figure 1. CT images of organs [26]

3.2. Data Preprocessing and Augmentation

Each CT image in the dataset varies in size from $512 \times 512 \times 85$ and $512 \times 512 \times 195$. Training with three-

dimensional data requires expensive hardware resources. Therefore, resizing images can help overcome this challenge. Due to GPU limitations, the image sizes in the x and y planes were reduced by 1/4 and the number of slices of each image was set to 64. However, to compensate for the information lost during this resizing process and to diversify our training set, different slices were selected from the same image. Five different methods were used for this slice selection process:

1. The first 64 slices of each image were selected.
2. The last 64 slices of each image were selected.
3. Each image was divided into two subsets based on the first slice. Subset 1 (0,2,4...,126) and subset 2 (1,3,5...,127) contain [27].
4. Each image was divided into two subsets based on the last slice. Subset 1 (69...191,193,195) and subset 2 (68...190,192,194) contain.
5. A random start slice was determined in the depth of each image, and 64 consecutive slices was selected from the start slice.

As a result, the input image size for the network was set to 128x128x64. Additionally, a random rotation between -5 and 5 degrees was applied to the images obtained with the 5th method to increase the diversity of the data. As a result of these processes, the number of images to be trained was increased from 24 to 192. In Table 1, the dimensions of the raw data, the preprocessing steps to equalize the slice sizes, the data augmentation process, and the result data are given. 'x' represents the random starting point selected from the slices, and 'z' represents the number of slices.

Table 1. Data obtained as a result of preprocessing and data augmentation of raw data

	Steps	Width	Height	Slice Number Range	Number of Data	Selected Slices	Rotation
Raw Data		512	512	85-195	24	-	-
Preprocessing Steps	1	128	128	64	24	(0...64)	-
	2	128	128	64	24	(z-63 ...z-2, z-1, z)	-
	3	128	128	64	24	z>125 (0,2,4...,126)	-
						z<125 (x,x+1,x+2...x+63)	
						z>126 (1,3,5...,127)	
4	128	128	64	24	(69...191,193,195)	-	
5	128	128	64	24	(68...190,192,194)	-	
Data Augmentation	6	128	128	64	24	(x, x+1, x+2...x+63)	-
						(x, x+1, x+2...x+63)	-5,5
Result Data		128	128	64	192		

The model used in this study has two stages. In the first stage, the gray images in the dataset were converted to images with HSV (Hue, Saturation, Value) [28] color space with the colormap function in the Simple ITK library. With this function, single channel images are normalized between 0 and 1 and a color map is used to assign colors to pixels in the image, pixels with a value of 1 are assigned the first color in the color map. The result is three-channel images with RGB (Red-Green-Blue) [28] color space. Images converted to RGB color space are converted to desired color space (HSV). In Eq. (1), 'Δ' represents the difference between the maximum (Cmax) and minimum (Cmin) values of the R, G, B components. To convert RGB images to the HSV color space, the maximum and minimum values of the R, G and B components are found, and the difference between them is calculated. In Eq. (2), 'H' represents the Hue,

which is calculated based on difference between color components (Δ) and the maximum component (C_{max}). In Eq. (3), 'S' represents the Saturation, which is calculated based on the maximum component (C_{max}). In Eq. (4), 'V' represents the Value or Brightness, which directly corresponds to the value of the maximum component.

$$\begin{aligned} C_{max} &= \max(R, G, B) \\ C_{min} &= \min(R, G, B) \\ \Delta &= C_{max} - C_{min} \end{aligned} \quad (1)$$

$$H = 0, \Delta = 0$$

$$H = \begin{cases} 60x \left(\frac{G-B}{\Delta} \text{Mod} 6 \right) & , C_{max} = R' \\ 60x \left(\frac{B-R}{\Delta} + 2 \right) & , C_{max} = G' \\ 60x \left(\frac{R-G}{\Delta} + 4 \right) & , C_{max} = B' \end{cases} \quad (2)$$

$$S = \begin{cases} 0 & , C_{max} = 0 \\ \frac{\Delta}{C_{max}} & , C_{max} \neq 0 \end{cases} \quad (3)$$

$$V = C_{max} \quad (4)$$

3.3. A 3D U-Net based on Early Fusion Model

The model used in this study is based on the two-stage 3D U-Net with early fusion approach using different color spaces proposed by Kayhan [12]. The 3D U-Net model with early fusion approach uses 3D U-Net with the same layers in both stages. The model uses two different color maps (Grayscale and HSV) of CT images. In both stages, the proposed 3D U-Net network is trained with HSV images, and an output of 15 channels is obtained by combining the output of the first stage (13 organs and one background) with the grayscale image. The image obtained is determined as the input to the 2nd stage. This merging process is called early fusion. In this way, it is aimed to make the features of the organs more evident. These combined images are again trained with the proposed 3D U-Net architecture, and predictive segmentation results are obtained. The general structure of this model is given in Figure 2 [12].

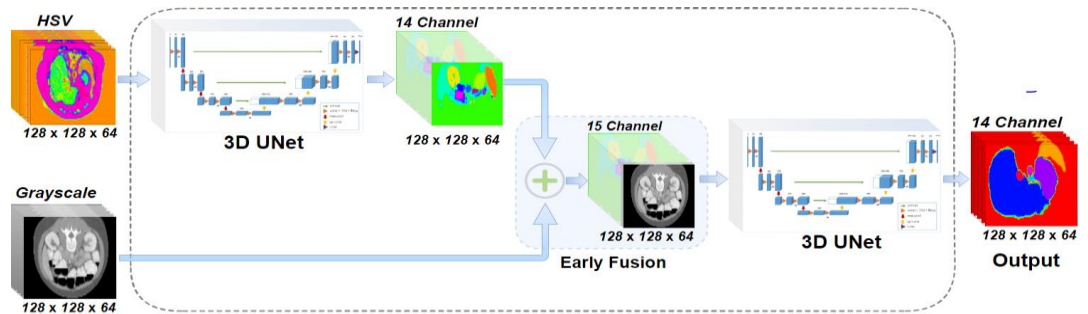


Figure 2. Fusion model [12]

Kayhan [12], proposed a 3D U-Net model consisting of encoder and decoder stages. In the first step of this model, images are fed into the encoder network. At each level, two 3x3x3 convolution operations are performed on the input images. Batch Normalization and ReLU activation function are used after each convolution operation. Maximum pooling and two-step 2x2x2 convolution are applied to the feature map obtained while transitioning from one level to another. The outputs obtained as a result of these processes are merged. In the decoding network, upsampling is performed with a two-step 2x2x2 transpose convolution until the input image size is obtained. Batch Normalization and ReLU activation function are

implemented after each transpose convolution. The feature map at each level in the decoding network and the feature map obtained from the corresponding encoder section are combined. Then, two 3x3x3 convolutions are applied to this combined feature map. In the last layer, because of the 1x1x1 convolution operation, a 128x128x48 size feature map with 14 channels is obtained. Three-dimensional multi-organ segmentation was performed by applying the softmax activation function to the output feature map.

In this study, the 3D U-Net model proposed by Kayhan [12] was fine-tuned to improve multi-organ segmentation performance. The two-step 2x2x2 convolution layer used for downsampling in the encoder network was removed, and a dropout layer was added after each inter-level transition in both the encoder and decoder networks. These fine-tuning operations were implemented to prevent overfitting of the model. Additionally, the number of slices was increased from 48 to 64 so that this model could learn more features from images and better capture context information. Figure 3 shows the 3D U-Net based model used in this study, and Table 2 shows the layers of this 3D U-Net model and the filter, input and output dimensions used in these layers.

Table 2. 3D U-Net based model layers, input and output values

Layers	Input Size		Output Size	Encoder	Layers	Input Size	Output Size	Decoder
	HSV Image	Gray Image						
Convolution	128x128x64x3	128x128x64x1	128x128x64x32	3x3x3 conv padding 1	Deconvolution	16x16x8x256	32x32x16x128	2x2x2 Transposed conv
		128x128x64x32	128x128x64x32		Concatenate Dropout	32x32x16x128 32x32x16x128	32x32x16x256	50%
Pooling		128x128x64x32	64x64x32x32	2x2x2 max pooling	Convolution	32x32x16x256	32x32x16x128	3x3x3 conv padding 1
Dropout		64x64x32x32	64x64x32x32	50%		32x32x16x128	32x32x16x128	
Convolution		64x64x32x32	64x64x32x64	3x3x3 conv padding 1	Deconvolution	32x32x16x128	64x64x32x64	2x2x2 Transposed conv
		64x64x32x64	64x64x32x64		Concatenate Dropout	64x64x32x64 64x64x32x64	64x64x32x128	50%
Pooling		64x64x32x64	32x32x16x64	2x2x2 max pooling	Convolution	64x64x32x128	64x64x32x64	3x3x3 conv padding 1
Dropout		32x32x16x64	32x32x16x64	50%		64x64x32x64	64x64x32x64	
Convolution		32x32x16x64	32x32x16x128	3x3x3 conv padding 1	Deconvolution	64x64x32x64	128x128x64x32	2x2x2 Transposed conv
		32x32x16x128	32x32x16x128		Concatenate Dropout	128x128x64x32 128x128x64x32	128x128x64x64	50%
Pooling		32x32x16x128	16x16x8x128	2x2x2 max pooling	Convolution	128x128x64x64	128x128x64x32	3x3x3 conv padding 1
Dropout		16x16x8x128	16x16x8x128	50%		128x128x64x32	128x128x64x32	
Convolution		16x16x8x128	16x16x8x256	3x3x3 conv padding 1	Convolution	128x128x64x32	128x128x64x14	1x1x1 conv
		16x16x8x256	16x16x8x256					

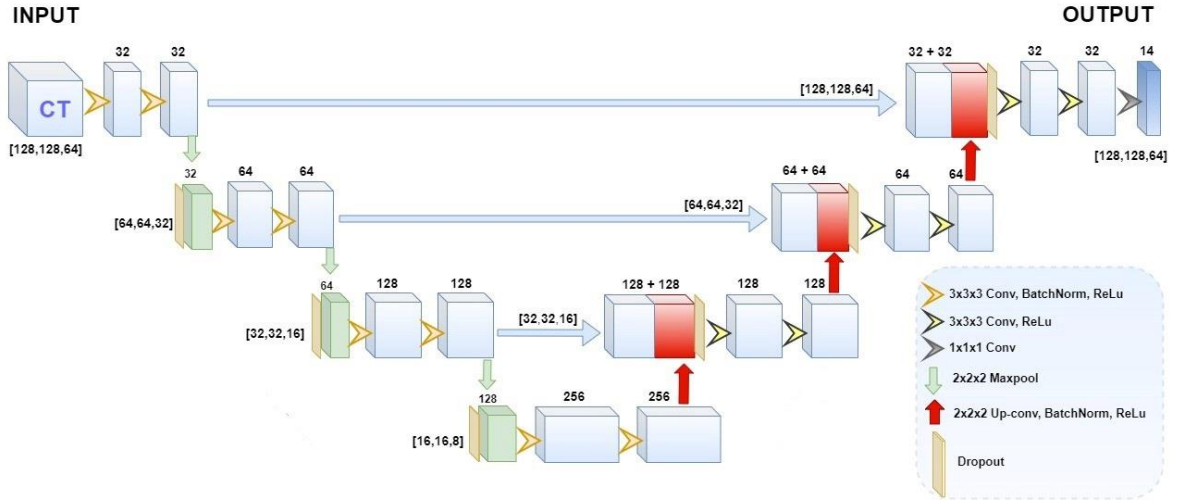


Figure 3. 3D U-Net based model

3.4. Hyperparameter Optimization

Hyperparameter optimization was carried out to improve the performance of the fusion model used in this study. To optimize the fusion model, training was conducted using various parameter sets. The data was split into 80% for training and 20% for testing. The dice score was used as the evaluation metric. In Table 3, the dice score results of different parameter sets on the test data set are given. When Table 3 is examined, batch size two was used in all samples, and the Adam optimization algorithm was used. Different learning rate values, dropout rates, activation functions and epoch numbers used with these parameters were compared. The dropout layer had a positive effect on the dice score result. The learning rate that gives the highest dice score is $1e-3$, the activation function is ReLU, the dropout rate is 0.5, and the epoch number is 200. As a result of this optimization, the parameter set giving the best result was determined.

3.5. Performance Evaluation Metric

The segmentation process performed in this study was evaluated using the Dice similarity coefficient. This metric evaluates the level of similarity in two images by measuring the number of matching pixels. Dice similarity coefficient formula is given in Eq. (5). The meaning of the symbols used in this equation is explained below [29].

- Y : Actual labels
- \hat{Y} : Predicted labels
- \hat{y}_{ij} : Elements in \hat{Y}
- y_{ij} : Elements in Y
- n : Row elements
- m : Column elements

$$DC = \frac{2|\hat{Y} \cap Y|}{|\hat{Y}| + |Y|} = \frac{2 \sum_{i=1}^n \sum_{j=1}^m \hat{y}_{ij} \cdot y_{ij}}{\sum_{i=1}^n \sum_{j=1}^m \hat{y}_{ij} + \sum_{i=1}^n \sum_{j=1}^m y_{ij}} \quad (5)$$

Table 3. Test dice results of different parameter sets

Batch size	Optimization algorithm	Learning rate	Activation function	Epoch	Dropout	Spleen	Right kidney	Left kidney	Esophagus	Gallbladder	Liver	Stomach	Aorta	Inferior vena cava	Portal and splenic vein	Pancreas	Right adrenal gland	Left adrenal gland	Average
2	Adam	1e-3	ReLU	100	-	0.934	0.944	0.937	0.619	0.665	0.958	0.869	0.851	0.814	0.709	0.754	0	0.583	0.741
					0.1	0.93	0.924	0.924	0.675	0.941	0.941	0.857	0.864	0.788	0.72	0.734	0.579	0.559	0.779
					0.2	0.914	0.944	0.91	0.754	0.663	0.958	0.861	0.846	0.78	0.732	0.745	0.609	0.588	0.793
					0.3	0.890	0.937	0.905	0.738	0.744	0.955	0.858	0.864	0.808	0.742	0.689	0.63	0.626	0.799
					0.4	0.943	0.942	0.925	0.511	0.70	0.95	0.866	0.844	0.788	0.711	0.683	0.584	0.635	0.775
					0.5	0.922	0.942	0.924	0.711	0.656	0.953	0.869	0.872	0.807	0.751	0.755	0.641	0.639	0.803
					0.954	0.948	0.949	0.743	0.719	0.96	0.885	0.881	0.80	0.764	0.779	0.641	0.632	0.82	
	200	0.947	0.95	0.949	0.723	0.713	0.964	0.882	0.882	0.82	0.744	0.765	0.641	0.629	0.816				
	300	0.947	0.95	0.949	0.723	0.713	0.964	0.882	0.882	0.82	0.744	0.765	0.641	0.629	0.816				
	5e-4	ReLU	200	ReLU	0.5	0.96	0.951	0.948	0.718	0.707	0.964	0.876	0.872	0.809	0.742	0.787	0.591	0.545	0.805
						0.938	0.94	0.91	0.724	0.698	0.96	0.87	0.876	0.813	0.74	0.745	0.619	0.621	0.804
						0.943	0.95	0.946	0.636	0	0.961	0.872	0.879	0.819	0.744	0.741	0.627	0.634	0.75

4. RESULTS

The fusion model used in this study was evaluated on the MICCIA 2015 dataset. Train and test performance results of the best parameter set determined because of hyperparameter optimization are given in Table 4. In multi-organ segmentation, the training and test dice results are 0.932 and 0.82, respectively. The curves of the results obtained during the training and test set are given in Figure 4, and the final test set results for each organ are given in Figure 5.

Table 4. Training and test dice results of each organ

SET	Dice Coefficient													
	Spleen	Right kidney	Left kidney	Esophagus	Gallbladder	Liver	Stomach	Aorta	Inferior vena cava	Portal and splenic vein	Pancreas	Right adrenal gland	Left adrenal gland	Average
Train set	0.962	0.951	0.95	0.935	0.922	0.968	0.945	0.932	0.914	0.881	0.887	0.939	0.931	0.932
Test set	0.954	0.948	0.949	0.743	0.719	0.96	0.885	0.881	0.80	0.764	0.779	0.641	0.632	0.82

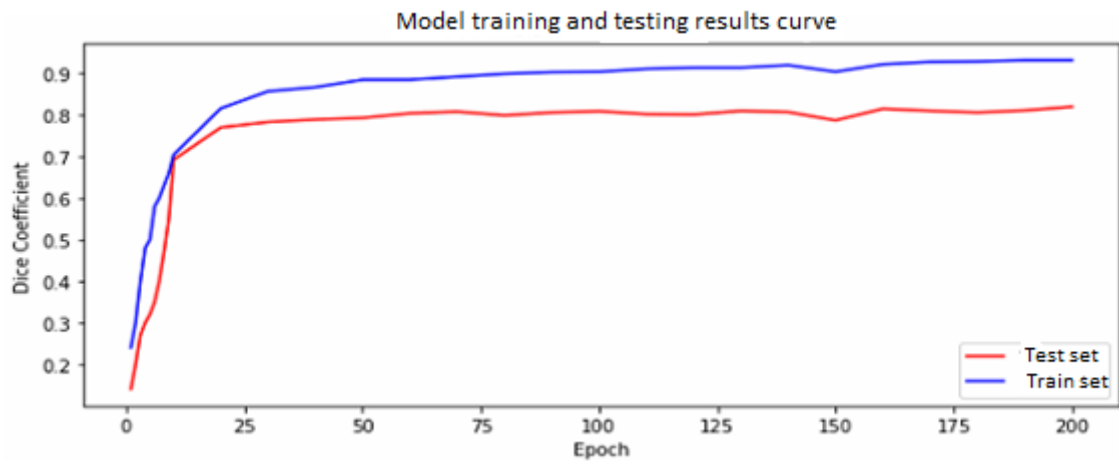


Figure 4. Multi-organ segmentation training and test result curves

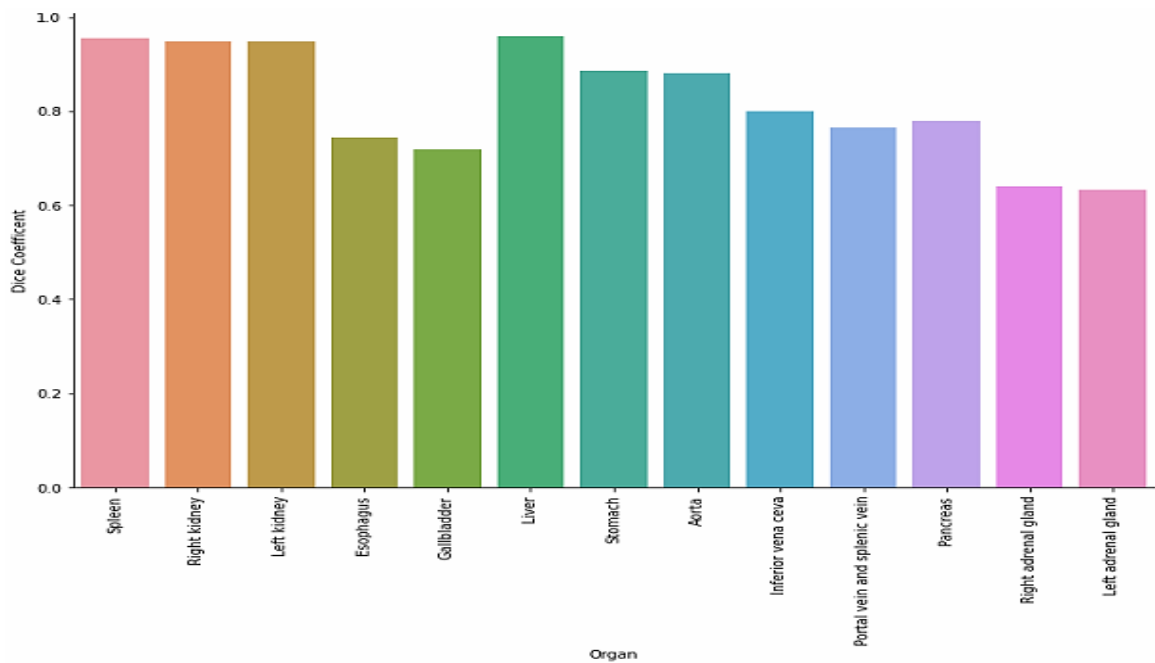


Figure 5. Test dice results of each organ

Figure 6 shows the predicted segmentation mask images and actual mask images of the final test results. These images are slices of a CT image. In addition, each organ is numbered. The confusion matrix of the fusion model is given in Figure 7. The confusion matrix shows the number of correct and incorrect pixels of each organ. Precision recall, f1 score and accuracy results of the fusion model are given in Table 5. These metrics were calculated for each organ using the pixel counts from the confusion matrix.

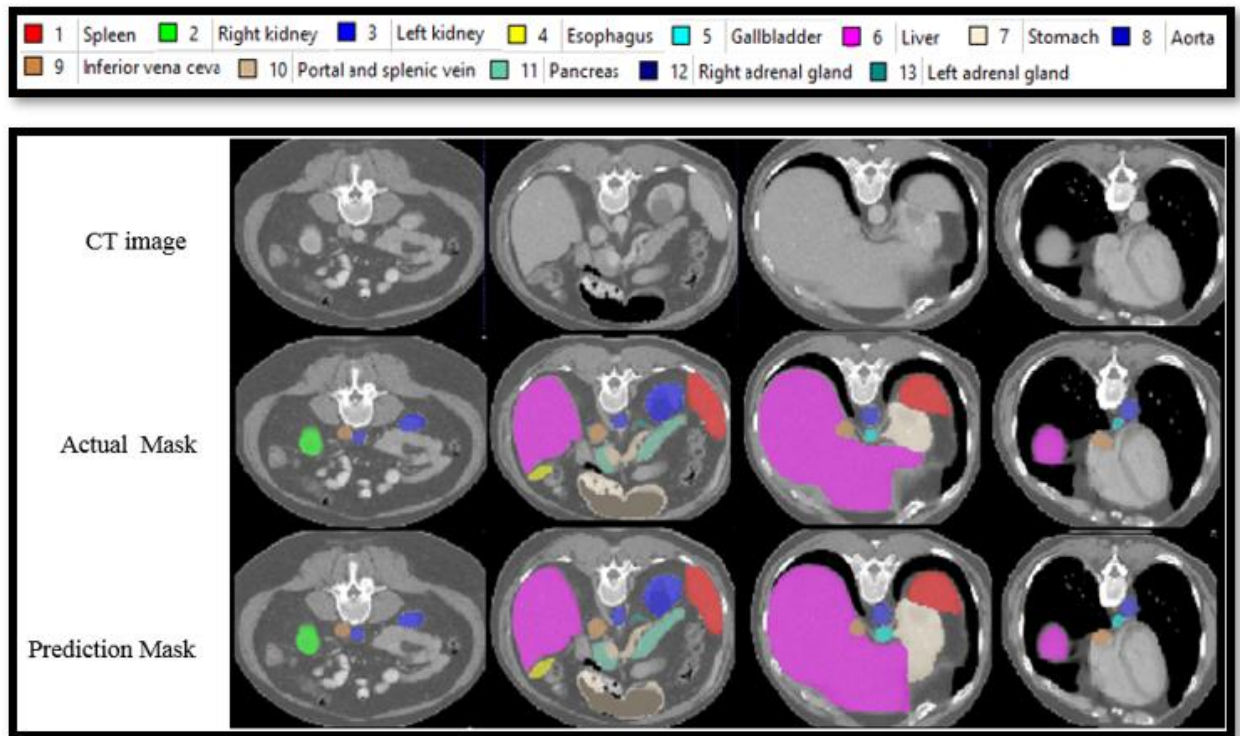


Figure 6. CT Image, actual mask and prediction mask

Confusion Matrix

0	11921437	1755	1646	984	559	532	13277	3743	1703	2206	581	1610	161	210
1	1314	40132	0	1	0	0	2	84	0	0	3	8	0	0
2	941	0	27027	4	0	0	31	0	0	0	0	0	0	0
3	1703	10	0	27878	0	0	0	0	0	0	0	0	0	0
4	265	0	0	0	1832	0	248	1	0	0	0	0	0	0
5	736	0	0	0	0	2235	55	125	8	0	0	0	0	0
6	4060	0	5	0	107	0	266471	894	0	320	175	1	30	0
7	9384	512	0	0	0	117	887	62034	0	0	0	131	0	0
8	3150	0	0	0	0	0	0	0	13704	37	0	0	0	0
9	1879	0	0	0	0	0	1804	0	0	11314	1	182	3	0
10	479	18	0	0	0	0	857	6	0	0	3854	197	0	0
11	2753	10	0	0	0	0	111	117	0	0	121	9775	0	0
12	158	0	0	0	0	0	34	0	0	11	0	0	363	0
13	258	0	0	0	0	0	0	5	0	0	1	4	0	459
	0	1	2	3	4	5	6	7	8	9	10	11	12	13

Actual pixel label

Predicted pixel label

Figure 7. Confusion matrix for multi-organ segmentation

Table 5. Precision, recall, f1-score, accuracy results of each organ

Evaluation metrics	Spleen	Right kidney	Left kidney	Esophagus	Gallbladder	Liver	Stomach	Aorta	Inferior vena cava	Portal and splenic vein	Pancreas	Right adrenal gland	Left adrenal gland	Average
Precision	0.966	0.965	0.942	0.78	0.707	0.979	0.849	0.811	0.745	0.712	0.758	0.641	0.631	0.806
Recall	0.945	0.942	0.965	0.733	0.774	0.939	0.981	0.889	0.814	0.813	0.82	0.65	0.686	0.842
F1 -Score	0.955	0.953	0.953	0.755	0.738	0.958	0.91	0.848	0.777	0.759	0.787	0.645	0.657	0.823
Accuracy	0.954	0.948	0.949	0.743	0.719	0.96	0.885	0.881	0.80	0.764	0.779	0.641	0.632	0.82

5. DISCUSSION

The dataset was initially trained using a single-stage 3D U-Net based model. This model was trained separately on both grayscale images and HSV images. Finally, the dataset was trained with a fusion model combining different color spaces (HSV and grayscale). In Table 6, the test results of the 3D U-Net with HSV, 3D U-Net with Grayscale, and the fusion model are compared.

Table 6. Comparison of 3D U-Net with grayscale, 3D U-Net with HSV, and fusion model

Model	Dice Coefficient													
	Spleen	Right kidney	Left kidney	Esophagus	Gallbladder	Liver	Stomach	Aorta	Inferior vena cava	Portal and splenic vein	Pancreas	Right adrenal gland	Left adrenal gland	Average
3D U-Net with Grayscale	0.92	0.936	0.895	0.587	0.709	0.956	0.857	0.87	0.82	0.735	0.718	0.642	0.588	0.787
3D U-Net with HSV	0.938	0.932	0.927	0.71	0.72	0.956	0.832	0.896	0.817	0.703	0.644	0.583	0.554	0.786
Fusion Model	0.954	0.948	0.949	0.743	0.719	0.96	0.885	0.881	0.80	0.764	0.779	0.641	0.632	0.82

In Table 7, the fusion model is compared with the results presented in Larsson et al. [15] and with the results of the model proposed by Kayhan[12]. The fusion model used in this study is a fine-tuned version of the 3D U-Net model proposed by Kayhan. The model results presented in the study of Larsson et al. and Kayhan were obtained from the MICCIA 2015 data set used in this study. The CNN and FCN architectures in Table 7 were developed by Larsson et al. [15]. IMI and CLS models are the two models that gave the best results in the "Multi-Atlas Abdomen Labeling Challenge" competition. The fusion model outperformed other models in terms of segmentation accuracy for all organs except two (inferior vena cava and right adrenal gland). The IMI model had the highest correct prediction rate for the inferior vena cava, while the FCN model had the highest correct prediction rate for the right adrenal gland. The fusion model ranks 2nd in accuracy of the Inferior vena cava and right adrenal gland organs. In addition, the fusion model gave the highest segmentation result in the mean of all organs, and it was observed that the

fine-tuning made to the 3D U-Net model proposed by Kayhan increased the performance.

Table 7. Comparison of the results of the fusion model with the results of other models

Dice Coefficient															
Model	Spleen	Right kidney	Left kidney	Esophagus	Gallbladder	Liver	Stomach	Aorta	Inferior vena cava	Portal and splenic vein	Pancreas	Right adrenal gland	Left adrenal gland	Average	Number of successful organs
CNN[15]	0.93	0.866	0.911	0.624	0.662	0.946	0.775	0.860	0.776	0.567	0.602	0.631	0.583	0.75	-
FCN[15]	0.936	0.897	0.911	0.613	0.588	0.949	0.764	0.87	0.72	0.758	0.715	0.646	0.63	0.767	1
CLS (MICCAI 2015)	0.911	0.893	0.901	0.375	0.607	0.940	0.704	0.811	0.76	0.649	0.643	0.557	0.582	0.723	-
IMI (MICCAI 2015)	0.919	0.901	0.914	0.604	0.692	0.948	0.805	0.857	0.828	0.754	0.74	0.615	0.623	0.790	1
Kayhan's Model[12]	0.94	0.934	0.937	0.698	0.703	0.951	0.847	0.873	0.816	0.698	0.774	0.611	0.558	0.796	-
Fusion Model	0.954	0.948	0.949	0.743	0.719	0.96	0.885	0.881	0.80	0.764	0.779	0.641	0.632	0.82	11

The fusion model results in Table 8 are compared with the results of the state-of-the-art models (Swin-Unet [30], TransUNet [31], LeViT-UNet [32], MISSFormer [33], CoTr [34], nnFormer [35], nnU-Net [36], UNETR [37], Swin UNETR [38]) on the MICCAI 2015 dataset. When the results are examined, it is seen that the fusion model is at a level to compete with state-of-the-art models.

Table 8. Comparison of the results of fusion model with the results of state-of-the-art models

Model	Spleen	Right kidney	Left kidney	Gallbladder	Liver	Stomach	Aorta	Pancreas
Swin-Unet	0.906	0.796	0.832	0.665	0.942	0.766	0.854	0.565
TransUNet	0.936	0.77	0.818	0.631	0.94	0.764	0.872	0.558
LeViT-UNet	0.888	0.802	0.846	0.622	0.931	0.727	0.873	0.59
MISSFormer	0.919	0.82	0.852	0.686	0.944	0.808	0.869	0.656
CoTr	0.922	0.864	0.853	0.814	0.968	0.76	0.921	0.802
nnFormer	0.898	0.87	0.875	0.781	0.954	0.825	0.89	0.819
nnU-Net	0.923	0.897	0.848	0.806	0.971	0.823	0.928	0.82
UNETR	0.861	0.797	0.813	0.698	0.942	0.762	0.889	0.589
Swin UNETR	0.887	0.891	0.852	0.765	0.969	0.797	0.927	0.772
Fusion Model	0.954	0.948	0.949	0.719	0.96	0.885	0.881	0.779

Multi organ segmentation was performed in this study. However, this study has limitations. The small size of the dataset may restrict the model's ability to accurately detect certain organ. Additionally, the

fusion model, which combines different color spaces, may increase computational costs. However, this approach has provided a unique perspective in the literature by allowing for more comprehensive image analysis and improved detection of organ boundaries. This approach could be a roadmap for similar applications in the future.

6. CONCLUSION

In this study, a model with early fusion approach is used to automatically perform multi-organ segmentation on CT images. Experimental studies and fine tuning were carried out to determine the model that gives better results. Firstly, a single-stage 3D U-Net model was trained for multi-organ segmentation with only Grayscale and only HSV images with the selected parameter set. The performance of the 3D U-Net model with grayscale, the 3D U-Net model with HSV, and the fusion model were compared. The 3D U-Net test set accuracy rate with grayscale is 0.787, the 3D U-Net test set accuracy rate with HSV is 0.786, and the test set accuracy rate of the fusion model is 0.82. In the fusion model, segmentation accuracy of the spleen, right kidney, left kidney, and liver is 90%, stomach, aorta, and inferior vena cava segmentation accuracy is 80%, esophagus, gallbladder, portal, and spleen vein, and pancreas segmentation accuracy is over 70%. The right and left adrenal glands, which give the lowest segmentation result among the organs, are over 60%. The fusion model achieved a high segmentation success rate in large-volume organs. It has been observed that the success of segmentation is low in small volume organs (right adrenal gland and left adrenal gland).

When this study is evaluated in general, the segmentation of organs is the first step to examining the internal structure of the organs. As a result of segmentation, various diseases can be diagnosed. However, the segmentation and classification of organs by radiologists is difficult and time-consuming because the shapes of the organs vary. In addition, since it requires knowledge and experience, the rate of making mistakes is high. To overcome these difficulties, a fusion model based on 3D U-Net combining different color spaces was used for automatic multi-organ segmentation on CT images. In addition, this fusion model was compared with state-of-the-art models made in this field. As a result, successful and promising results were obtained.

For future work, increasing the diversity of data used in multi-organ segmentation and incorporating attention mechanisms may improve the performance for small-sized organs. Additionally, using computers with high hardware capabilities to increase the resolution and number of slices in the images may also lead to better segmentation results.

Declaration of Ethical Standards

The authors conducted this study in accordance with all ethical standards.

Declaration of Competing Interest

The authors declare that they have no conflict of interest.

Data Availability

The datasets analyzed during the current study are available in the [syn3193805] repository, [<https://www.synapse.org/#!/Synapse:syn3193805/wiki/217760>].

Acknowledgement

This manuscript has been prepared from Beyza Kayhan's master's thesis supervised by Sait Ali UYMAZ and was approved by the Graduate Education Institute of Konya Technical University on January 7, 2022. Beyza KAYHAN designed the model and the computational framework and carried out the experiment and wrote the manuscript with support from Sait Ali UYMAZ. Sait Ali UYMAZ designed




and supervised the project.

7. REFERENCES

- [1] N. Shen *et al.*, "Multi-organ segmentation network for abdominal CT images based on spatial attention and deformable convolution," *Expert Systems with Applications*, vol. 211, p. 118625, 2023.
- [2] Y. Wang, Y. Zhou, W. Shen, S. Park, E. K. Fishman, and A. L. Yuille, "Abdominal multi-organ segmentation with organ-attention networks and statistical fusion," *Medical image analysis*, vol. 55, pp. 88-102, 2019.
- [3] Y. LeCun, Y. Bengio, and G. Hinton, "Deep learning," *nature*, vol. 521, no. 7553, pp. 436-444, 2015.
- [4] A. Şeker, B. Diri, and H. H. Balık, "A review about deep learning methods and applications," *Gazi J Eng Sci*, vol. 3, no. 3, pp. 47-64, 2017.
- [5] G. Guo and N. Zhang, "A survey on deep learning based face recognition," *Computer vision and image understanding*, vol. 189, p. 102805, 2019.
- [6] H.-S. Bae, H.-J. Lee, and S.-G. Lee, "Voice recognition based on adaptive MFCC and deep learning," in *2016 IEEE 11th Conference on Industrial Electronics and Applications (ICIEA)*, 2016: IEEE, pp. 1542-1546.
- [7] S. Caldera, A. Rassau, and D. Chai, "Review of deep learning methods in robotic grasp detection," *Multimodal Technologies and Interaction*, vol. 2, no. 3, p. 57, 2018.
- [8] G. Litjens *et al.*, "A survey on deep learning in medical image analysis," *Medical image analysis*, vol. 42, pp. 60-88, 2017.
- [9] M. Toğaçar and B. Ergen, "Biyomedikal Görüntülerde Derin Öğrenme ile Mevcut Yöntemlerin Kıyaslanması," *Fırat Üniversitesi Mühendislik Bilimleri Dergisi*, vol. 31, no. 1, pp. 109-121, 2019.
- [10] H. R. Roth *et al.*, "A multi-scale pyramid of 3D fully convolutional networks for abdominal multi-organ segmentation," in *Medical Image Computing and Computer Assisted Intervention—MICCAI 2018: 21st International Conference, Granada, Spain, September 16-20, 2018, Proceedings, Part IV 11*, 2018: Springer, pp. 417-425.
- [11] T. Ghosh, L. Li, and J. Chakareski, "Effective deep learning for semantic segmentation based bleeding zone detection in capsule endoscopy images," in *2018 25th IEEE International Conference on Image Processing (ICIP)*, 2018: IEEE, pp. 3034-3038.
- [12] B. Kayhan, "Deep learning based multiple organ segmentation in computed tomography images," Master's thesis, Konya Technical University, 2022.
- [13] B. Kayhan and S. A. Uymaz, "Multi Organ Segmentation in Medical Image.," *Current Studies in Healthcare and Technology* pp. 59-72, 2023.
- [14] R. Trullo, C. Petitjean, D. Nie, D. Shen, and S. Ruan, "Joint segmentation of multiple thoracic organs in CT images with two collaborative deep architectures," in *Deep Learning in Medical Image Analysis and Multimodal Learning for Clinical Decision Support: Third International Workshop, DLMIA 2017, and 7th International Workshop, ML-CDS 2017, Held in Conjunction with MICCAI 2017, Québec City, QC, Canada, September 14, Proceedings 3*, 2017: Springer, pp. 21-29.
- [15] M. Larsson, Y. Zhang, and F. Kahl, "Robust abdominal organ segmentation using regional convolutional neural networks," *Applied Soft Computing*, vol. 70, pp. 465-471, 2018.
- [16] H. R. Roth *et al.*, "Deep learning and its application to medical image segmentation," *Medical Imaging Technology*, vol. 36, no. 2, pp. 63-71, 2018.
- [17] C. Shen *et al.*, "On the influence of Dice loss function in multi-class organ segmentation of abdominal CT using 3D fully convolutional networks," *arXiv preprint arXiv:1801.05912*, 2018.
- [18] H. Takeya, T. Okada, and Y. Oshiro, "3D U-JAPA-Net: mixture of convolutional networks for abdominal multi-organ CT segmentation," in *Medical Image Computing and Computer Assisted Intervention—MICCAI 2018: 21st International Conference, Granada, Spain, September 16-20, 2018, Proceedings, Part IV 11*, 2018: Springer, pp. 426-433.

- [19] S. Vesal, N. Ravikumar, and A. Maier, "A 2D dilated residual U-Net for multi-organ segmentation in thoracic CT," *arXiv preprint arXiv:1905.07710*, 2019.
- [20] O. Mietzner and A. Mastmeyer, "Automatic multi-object organ detection and segmentation in abdominal CT-data," *medRxiv*, p. 2020.03.17.20036053, 2020.
- [21] B. Rister, D. Yi, K. Shivakumar, T. Nobashi, and D. L. Rubin, "CT-ORG, a new dataset for multiple organ segmentation in computed tomography," *Scientific Data*, vol. 7, no. 1, p. 381, 2020.
- [22] Y. Liu *et al.*, "CT-based multi-organ segmentation using a 3D self-attention U-net network for pancreatic radiotherapy," *Medical physics*, vol. 47, no. 9, pp. 4316-4324, 2020.
- [23] X. Fang and P. Yan, "Multi-organ segmentation over partially labeled datasets with multi-scale feature abstraction," *IEEE Transactions on Medical Imaging*, vol. 39, no. 11, pp. 3619-3629, 2020.
- [24] F. Zhang, Y. Wang, and H. Yang, "Efficient context-aware network for abdominal multi-organ segmentation," *arXiv preprint arXiv:2109.10601*, 2021.
- [25] H. Kaur, N. Kaur, and N. Neeru, "Evolution of multiorgan segmentation techniques from traditional to deep learning in abdominal CT images—A systematic review," *Displays*, vol. 73, p. 102223, 2022.
- [26] Z. Xu. "Multi-atlas labeling beyond the cranial vault - workshop and challenge." <https://www.synapse.org/#!/Synapse:syn3193805/wiki/217760>. (accessed 6.3.2021).
- [27] X. Gao, Y. Qian, and A. Gao, "COVID-VIT: Classification of COVID-19 from CT chest images based on vision transformer models," *arXiv preprint arXiv:2107.01682*, 2021.
- [28] V. Chernov, J. Alander, and V. Bochko, "Integer-based accurate conversion between RGB and HSV color spaces," *Computers & Electrical Engineering*, vol. 46, pp. 328-337, 2015.
- [29] L. Wang, C. Wang, Z. Sun, and S. Chen, "An improved dice loss for pneumothorax segmentation by mining the information of negative areas," *IEEE Access*, vol. 8, pp. 167939-167949, 2020.
- [30] H. Cao *et al.*, "Swin-unet: Unet-like pure transformer for medical image segmentation," in *European conference on computer vision*, 2022: Springer, pp. 205-218.
- [31] J. Chen *et al.*, "Transunet: Transformers make strong encoders for medical image segmentation," *arXiv preprint arXiv:2102.04306*, 2021.
- [32] G. Xu, X. Wu, X. Zhang, and X. He, "Levit-unet: Make faster encoders with transformer for medical image segmentation," *arXiv preprint arXiv:2107.08623*, 2021.
- [33] X. Huang, Z. Deng, D. Li, and X. Yuan, "Missformer: An effective medical image segmentation transformer," *arXiv preprint arXiv:2109.07162*, 2021.
- [34] Y. Xie, J. Zhang, C. Shen, and Y. Xia, "Cotr: Efficiently bridging cnn and transformer for 3d medical image segmentation," in *Medical Image Computing and Computer Assisted Intervention—MICCAI 2021: 24th International Conference, Strasbourg, France, September 27–October 1, 2021, Proceedings, Part III 24*, 2021: Springer, pp. 171-180.
- [35] H.-Y. Zhou, J. Guo, Y. Zhang, L. Yu, L. Wang, and Y. Yu, "nnformer: Interleaved transformer for volumetric segmentation," *arXiv preprint arXiv:2109.03201*, 2021.
- [36] F. Isensee, P. F. Jaeger, S. A. Kohl, J. Petersen, and K. H. Maier-Hein, "nnU-Net: a self-configuring method for deep learning-based biomedical image segmentation," *Nature methods*, vol. 18, no. 2, pp. 203-211, 2021.
- [37] A. Hatamizadeh *et al.*, "Unetr: Transformers for 3d medical image segmentation," in *Proceedings of the IEEE/CVF winter conference on applications of computer vision*, 2022, pp. 574-584.
- [38] A. Hatamizadeh, V. Nath, Y. Tang, D. Yang, H. R. Roth, and D. Xu, "Swin unetr: Swin transformers for semantic segmentation of brain tumors in mri images," in *International MICCAI Brainlesion Workshop*, 2021: Springer, pp. 272-284.

SYNTHESIS OF P(N-ISOPROPYL ACRYLAMIDE - HYDROXYPROPYL METHACRYLATE) THERMO RESPONSIVE COPOLYMER FILMS BY INITIATED CHEMICAL VAPOR DEPOSITION METHOD

^{1,*} Emine SEVGİLİ MERCAN , ²Kurtuluş YILMAZ , ³Mustafa KARAMAN 

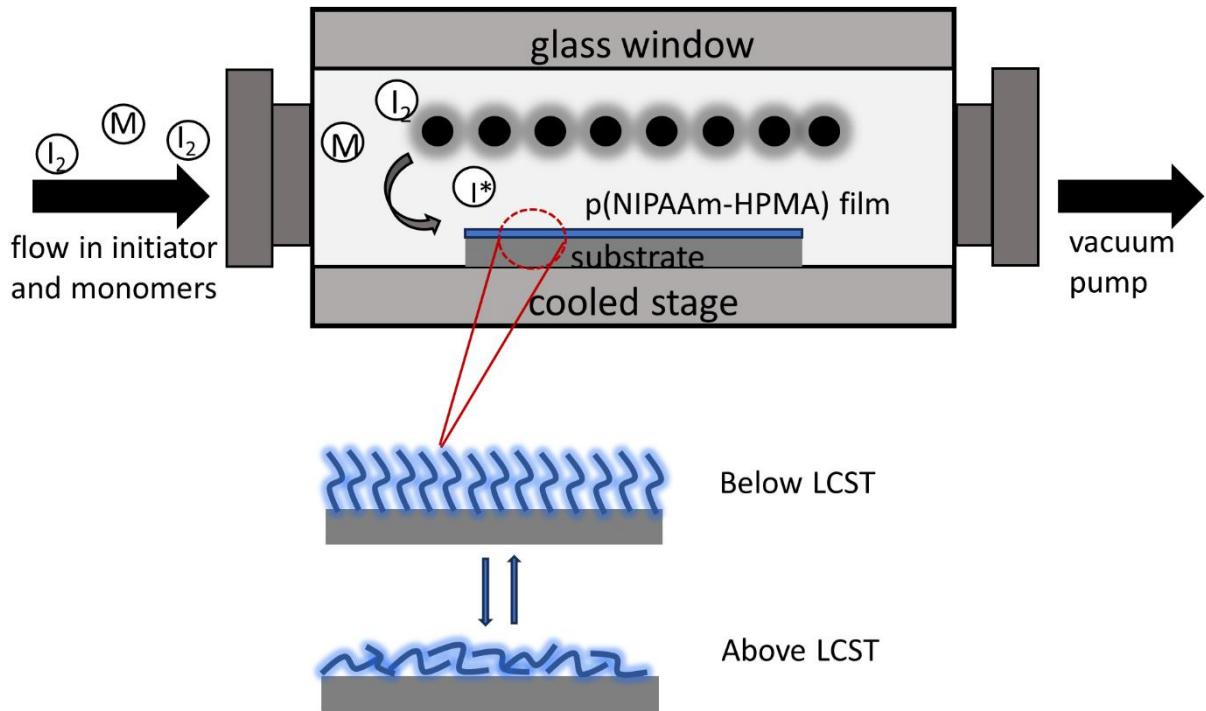
Konya Technical University, Engineering and Natural Sciences Faculty, Chemical Engineering Department,
Konya, TÜRKİYE

[1^{esmercan@ktun.edu.tr}](mailto:esmercan@ktun.edu.tr), [2^{kurtulusyilmaz3@gmail.com}](mailto:kurtulusyilmaz3@gmail.com), [3^{mkaraman@ktun.edu.tr}](mailto:mkaraman@ktun.edu.tr)

Highlights

- P(NIPAAm-HPMA) thermo-responsive copolymer thin films were synthesised by iCVD method.
- The LCST temperature of the copolymers was determined by temperature-dependent contact angle measurement.
- The LCST range obtained for the copolymers was found to be significantly lower (19-23°) than the value reported in the literature for pNIPAAm (~32°).




Graphical Abstract



Schematic illustration of iCVD p(NIPAAm-HPMA) film synthesis



SYNTHESIS OF P(N-ISOPROPYL ACRYLAMIDE - HYDROXYPROPYL METHACRYLATE) THERMO RESPONSIVE COPOLYMER FILMS BY INITIATED CHEMICAL VAPOR DEPOSITION METHOD

^{1,*} Emine SEVGİLİ MERCAN , ²Kurtuluş YILMAZ , ³Mustafa KARAMAN 

*Konya Technical University, Engineering and Natural Sciences Faculty, Chemical Engineering Department,
Konya, TÜRKİYE*

[1esmercan@ktun.edu.tr](mailto:esmercan@ktun.edu.tr), [2kurtulusyilmaz3@gmail.com](mailto:kurtulusyilmaz3@gmail.com), [3mkaraman@ktun.edu.tr](mailto:mkaraman@ktun.edu.tr)

(Received: 23.12.2023; Accepted in Revised Form: 24.06.2024)

ABSTRACT: This study illustrates the deposition of thermo responsive p(N-isopropyl acrylamide-hydroxypropyl methacrylate) p(NIPAAm-HPMA) copolymer thin films by initiated chemical vapor deposition (iCVD) method using tert-butyl peroxide (TBPO) as the initiator. Copolymers were deposited at three different HPMA flow rates and the effects of NIPAAm/HPMA flow rate ratio on the deposition rate, structure and responsive properties of the as-deposited films were investigated. The highest deposition rate of 50 nm/min was observed for the copolymer deposited using lowest NIPAAm/HPMA monomer ratio studied. The deposition rate showed a significant increase with decreasing NIPAAm/HPMA flow ratio. Results of FTIR and XPS spectroscopy analyses revealed a significant preservation of structural retention in iCVD p(NIPAAm-HPMA) thermo-responsive films. Lower critical solution temperatures (LCST) of p(NIPAAm-HPMA) films were determined by carrying out a temperature-dependent contact angle analysis. Accordingly, it was shown that LCST was varied between 19 and 23 °C, which was observed to be dependent on the NIPAAm/HPMA monomer ratio. That LCST range is considerably below the literature-reported values for pNIPAAm, which makes the as-deposited copolymer suitable for applications that require thermos-responsive properties at lower temperatures.

Keywords: *Thermo-responsive, iCVD, LCST, Polymeric Thin Film, Hydrogel*

1. INTRODUCTION

Polymers that respond to stimuli undergo alterations in their properties based on the external conditions. Physical or chemical stimuli like temperature [1], pH [2], electric or magnetic field [3], light intensity [4], and biological molecules [5] induce macroscopic reactions such as swelling/collapse or transformation from solution to gel in stimuli responsive polymer materials. Temperature is the most studied stimulus for stimuli-responsive polymers. Thermo-responsive polymers are structures that show a volume phase transition at a specific temperature [6]. While various temperature-sensitive polymers exist, including shape memory materials [7] and liquid crystal materials, the most commonly utilized types are polymer solutions that respond to liquid-liquid phase transitions triggered by changes in temperature. In this phase transition, a change from a transparent solution to a turbid solution is often observed, resulting from the difference in refractive index after the transition from a low-concentration polymer solution to a high-concentration polymer solution. The temperature where this phase transition occurs upon heating beyond a specific point is termed as LCST, while the temperature marking the onset of the opposite phase behavior is referred to as upper critical solution temperature (UCST) [8]. Polymers that undergo an LCST phase transition in water dissolve in water at low temperatures, and phase separation occurs as the temperature increases. Polymer chains transition from helix to sphere to aggregate at this point.

Poly(N-isopropylacrylamide) (pNIPAAm) stands out as one of the temperature-stable polymers that has been thoroughly investigated [9-11]. The thermal phase transition behavior of pNIPAAm was first reported in 1968 [12]. When pNIPAAm is immersed in an aqueous solution, it undergoes an abrupt shift

in volume-phase upon reaching temperatures above the lower critical solution temperature (LCST) of approximately 32°C. Below this temperature, hydrogen bonding predominates and the polymer chains are completely saturated with water and swell; above this temperature, hydrophobic interactions predominate and the polymer chains collapse by expelling water. Nevertheless, altering the lower critical solution temperature (LCST) of a thermosensitive hydrogel is achievable through the incorporation of suitable monomer units [13, 14]. Coating solid supports like silicon substrates with thin films of heat-shrinkable polymers enables expansion and contraction exclusively perpendicular to the substrate [15]. This gives rise to a temperature-responsive hydrogel structure with promising applications in sensors, actuators, and smart surfaces within the fields of biotechnology and medicine. [16-21].

Various techniques, whether solution-based or vapor-based, have been suggested for the synthesis of thin films of pNIPAAm. [22-25]. Methods used to produce polymeric thin films can be categorized into two groups.: solution-based or gas-based methods. Solution-based processes such as ATRP, dip coating, sol-gel, and layer-by-layer coating are among the frequently used techniques because they do not require special equipment and are easy to apply [26, 27]. On the other hand, the use of solvents in these processes may damage fragile substrates and the need for steps such as purification and drying may cause losses in terms of energy and cost [28]. Additionally, the porous or three-dimensional nature of the substrate used may make it difficult to obtain a conformal coating. In vapor-based methods such as CVD, the problems caused by solvent-based methods are minimized by eliminating the use of solvents [29-31]. With vapor-based techniques, materials with complex geometries that are difficult to coat with liquid phase methods or delicate surfaces such as paper and textiles can be coated conformally [32, 33]. Different types of CVD are used to obtain polymeric thin films [34-36]. In the iCVD process, alongside the monomer, an initiator species is introduced into the reactor. This initiator readily dissociates into reactive chemical species with minimal energy input, thanks to the presence of weak peroxide bonds, thereby lowering the heat energy needed to initiate the reaction. [37-39]. Thus, undesirable side reactions are prevented and chemical functionality is preserved. Another advantage of the system is that the coatings are applied at low surface temperatures and all-dry vapor environment.

2-hydroxypropyl methacrylate (HPMA) is a hydrogel with high biocompatibility. While HPMA is highly soluble in water, its polymer is not soluble. Copolymers of biocompatible HPMA hydrogels with various vinyl monomers have been used for medical applications [40]. The objective of this study was to deposit p(NIPAAm-HPMA) copolymer films using with iCVD and to investigate the LCST behavior of copolymers. Di-tertbutyl peroxide (TBPO) was used as the initiator. Kinetic studies were conducted to explore the impact of HPMA flow rate on the deposition rate. Higher deposition rates were observed with increasing HPMA flow rate at copolymers compared to the deposition rate of pNIPAAm. The contact angle measurement was used to determine the LCST temperatures of p(NIPAAm-HPMA) films at different substrate temperatures. The LCST range obtained for the copolymers was found to be considerably lower than the value reported in the literature for pNIPAAm. The high deposition rate of uniform p(NIPAAm-HPMA) thin films with the iCVD process and the tunability of the LCST value may lead to new possibilities for the use of this thermo-responsive hydrogel in different applications.

2. MATERIAL AND METHODS

2.1 Material

The depositions took place in a specially designed iCVD reactor. Si wafers (University wafer, 100, P-type), approximately 4x3 cm² in size, were placed in the reactor to perform depositions. Before coating, the Si wafers were cleaned in an acetone and 2-propanol mixture and dried with nitrogen. The synthesis of p(NIPAAm-HPMA) copolymer thin films was carried out using N-isopropyl acrylamide (NIPAAm) (Aldrich, %98), hydroxypropyl methacrylate (HPMA) (Aldrich, %98) and di-tert-butyl peroxide (TBPO) (Luperox, %97) as monomers and initiator, respectively. The precursors were utilized without undergoing any purification or modifications. The polymerization structures p(NIPAAm-HPMA) are shown in Figure 1.

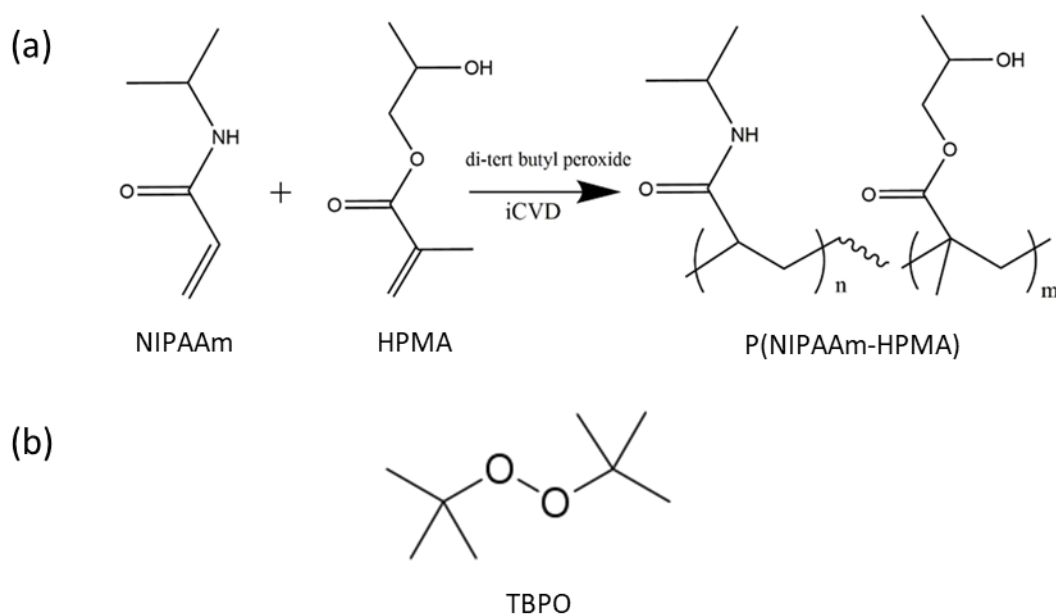


Figure 1. a) The polymerization structure of P(NIPAAm-co-HPMA) films b) the initiator used during the iCVD

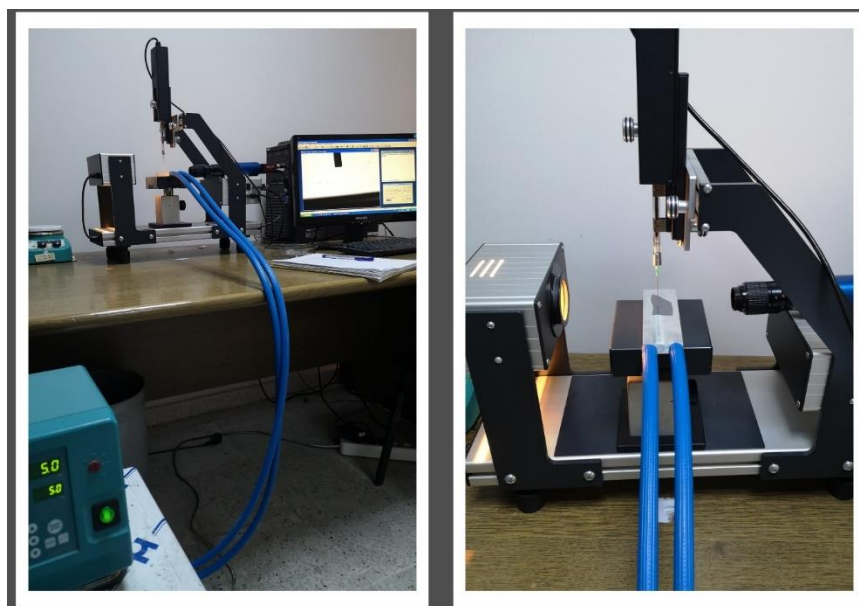
2.2 iCVD of P(NIPAAm-HPMA) Copolymer Films

Initiator and monomer vapors were introduced into the chamber via distinct lines. The NIPAAm monomer was heated to 80 °C and supplied to the reactor through a line kept at 95 °C. The HPMA monomer was heated to 60 °C and directed into the reactor through a line held at 95 °C. TBPO was vaporized at room temperature (25 °C). The flow rates of the monomer and initiator were controlled using needle valves. Depositions were made at three different HPMA flow rates and carried out until reaching 200 nm coating thickness. The deposition process included the real-time monitoring of film thickness using a laser interferometer, which was equipped with a 650 nm diode laser source and a laser power meter. The pressure inside the reactor was managed through a downstream pressure controller (MKS), which was fitted with a Baratron vacuum gauge (MKS). A dry vacuum pump (Edwards XDS-10) coupled with a liquid-nitrogen cold trap was employed to attain the vacuum. The substrate was cooled with water from a recirculating chiller (Thermo Neslab). Table 1 shows detailed deposition conditions.

Table 1: Deposition conditions of p(NIPAAm-HPMA) polymeric films

	p(NIPAAm-HPMA)-1	p(NIPAAm-HPMA)-2	p(NIPAAm-HPMA)-3
Initiator Flowrate	1 sccm	1 sccm	1 sccm
NIPAAm Flowrate	0.5 sccm	0.5 sccm	0.5 sccm
HPMA Flowrate	0.21 sccm	0.27 sccm	0.36 sccm
(NIPAAm/HPMA) monomer ratio	2.38	1.85	1.39
Substrate Temperature	30 °C	30 °C	30 °C
Filament Temperature	240 °C	240 °C	240 °C
Reactor Pressure	200 mtorr	200 mtorr	200 mtorr
Deposition rate	9 nm/min	30 nm/min	50 nm/min

To determine the LCST by contact angle measurement, films deposited on Si wafers were placed on a temperature-controlled aluminum plate. The contact angle measurement setup is shown in Figure 2. The temperature of the plate was varied between 5 degrees and 48 degrees at regular intervals. After the temperature of the plate reached the set value, it was allowed to reach thermal equilibrium for at least 20 minutes before contact angle measurements and at least three measurements were taken at each temperature.

**Figure 2.** Water contact angle measurement set-up

2.3 Film Characterization

The chemical structure of the deposited films was analyzed using Fourier-transform infrared (FTIR, Bruker, Vertex 70) and X-ray photoelectron (FTIR, ThermoScientific) spectroscopy techniques. FTIR measurements were conducted with a reflectance accessory in the range of 4000–400 cm^{-1} , employing an average resolution of 4 cm^{-1} over 64 scans. A 100 nm-thick aluminum layer was applied to the surfaces of glass substrates for reflectance-FTIR measurements, creating an IR-reflective surface. XPS analysis was carried out using a monochromatized aluminum X-ray source at a measurement take-off angle of 60

degrees. The water contact angles of p(NIPAAm-HPMA) were determined using microliter sessile drop contact angle analysis (Kruss Easy Drop). 5.0 μ L of distilled water was used in the experiments. The contact angle measuring device was used to determine the LCST temperatures of p(NIPAAm-HPMA) copolymer films by carrying out the measurements at different temperatures. The experiment employed an aluminum heating plate as the substrate holder, and temperature control was accomplished by connecting it to a recirculating chiller (Lab. Companion, RW-0525G).

3. RESULTS AND DISCUSSION

Firstly, the effect of changing HPMA flow rate on the deposition rate of p(NIPAAm-HPMA) copolymers was investigated. For the iCVD of pNIPAAm homopolymer, the deposition rate is usually quite low [40]. The deposition rate exhibited a significant increase with the synthesis of pNIPAAm as a copolymer with pHPMA. First, pNIPAAm was coated as a homopolymer and the deposition rate was measured at 4 nm/min. Later, the deposition rate of p(NIPAAm-HPMA)-1 copolymer, where the HPMA flow rate is the lowest, was found to be 8 nm/min. In subsequent experiments, the rates for p(NIPAAm-HPMA)-2 and p(NIPAAm-HPMA)-3 were found as 25 nm/min, and 50 nm/min respectively. Figure 3 shows the change in deposition rates versus monomer HPMA flow rate in the copolymer. Compared to the deposition rate of homopolymer pNIPAAm, it is seen that high deposition rates are achieved with increasing HPMA flow rate in copolymers. The 82 nm/min deposition rate was reported for iCVD of PHPMA homopolymer in literature, which may be the reason for achieving a high deposition rate for the copolymers deposited using this monomer [41].

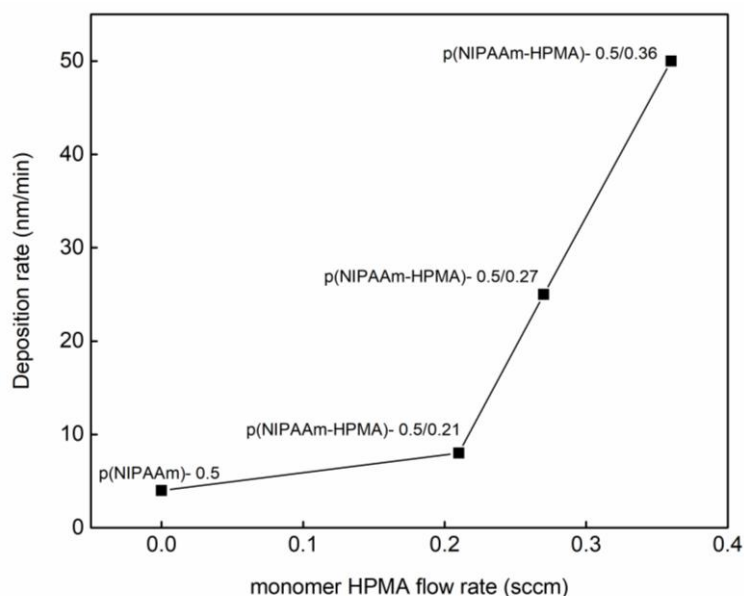


Figure 3: Effect of HPMA flow rate on deposition rate

The FTIR spectra of p(NIPAAm), p(HPMA) and copolymer films are shown in Figure 4. From the FTIR spectra, it can be seen that the characteristic absorption peaks of pNIPAAm and pHPMA appear also in the spectra of p(NIPAAm-HPMA) copolymer films. The peaks at 3280 cm^{-1} and 1650 cm^{-1} , seen only in pNIPAAm and copolymers, are attributed to secondary amide N-H stretching and primary amide C=O stretching peaks, respectively. The peak at 1730 cm^{-1} seen in the spectra of pHPMA and copolymers shows the stretching (C=O) peak of carbonyl groups [41, 42]. The N-H bond at 3280 cm^{-1} , the characteristic peak for pNIPAAm, which indicates bonded water molecules within the polymers, became less pronounced with increasing HPMA flow rate. It was also observed that the C-O stretching bond at 1270 cm^{-1} was more pronounced at copolymer with the increasing HPMA flow rate.

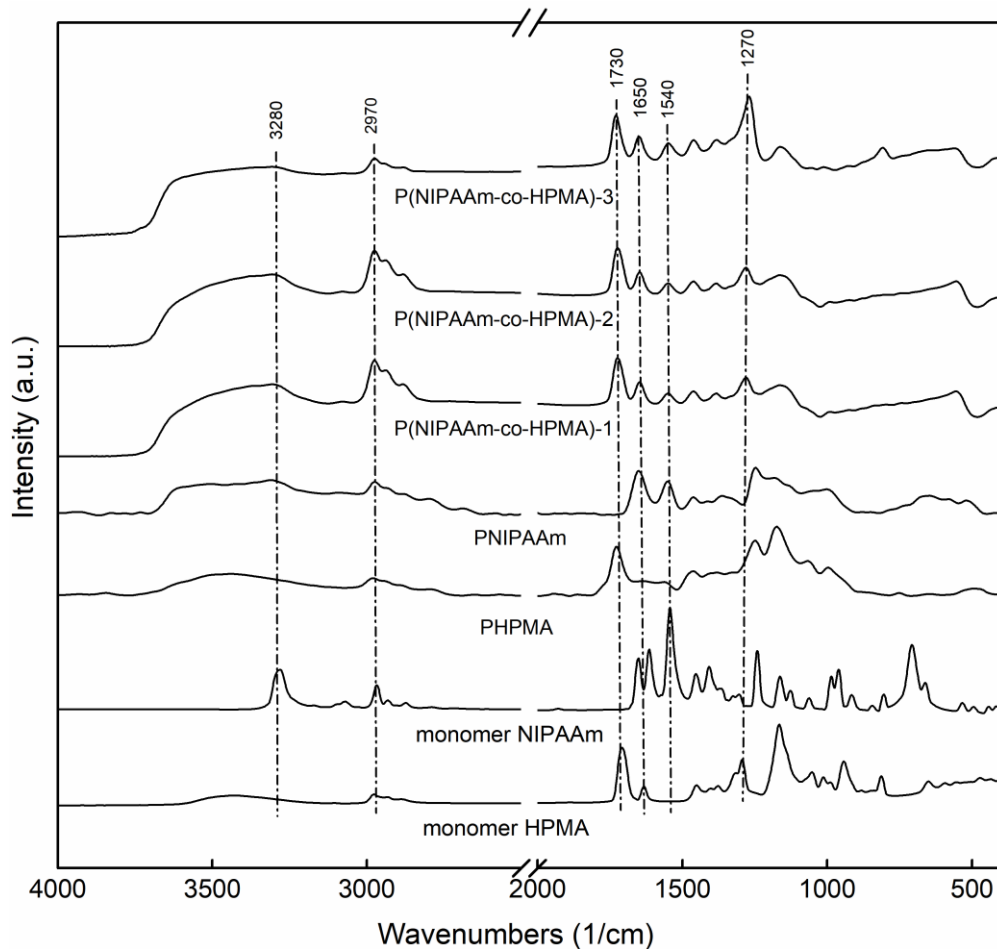


Figure 4: The FTIR spectrum of monomers, pNIPAAm, pHPMA and p(NIPAAm-co-HPMA) films

XPS analysis was performed for a detailed investigation of the composition of p(NIPAAm-HPMA) copolymer films. Figure 5 shows the XPS survey scan and high-resolution C1s spectra of the films. According to the survey scan results, C1s, O1s and N1s peaks were observed in all copolymer spectra, as expected from the chemical structures of HPMA ($C_7H_{12}O_3$) and NIPAAm ($C_6H_{11}NO$) monomers. The elemental compositions of the films are given in Table 2. Looking at the atomic percentage results given in Table 2, it was observed that the percentage of nitrogen in the structure decreased while the percentage of oxygen increased in parallel with the increase in the HPMA flow rate in the copolymer. A more comprehensive chemical analysis of p(NIPAAm-HPMA) polymer films was conducted through the examination of the high-resolution C1s spectrum. The C1s spectrum can be analyzed by fitting it with five primary peak components corresponding to $-CH_3$, $-CH_2$, $-C$, $-CH_2-N$, $-O-CH_2-$, and $-O-C^*C=O^*$, respectively [43]. Table 3 shows the binding energy values seen in the high-resolution C1s spectra of the films. In the copolymer film sample (fig 4c), the intensity of the C=O peak increases with increasing HPMA flow rate, indicating a higher incorporation of carbonyl groups into the structure. This observation is consistent with expectations, given the higher concentration of carbonyl groups inherent in the structure of the HPMA monomer. Consistent with the findings from XPS and FTIR analyses, it can be inferred that the iCVD technique allows for the production of conventionally polymerized p(NIPAAm-HPMA) copolymer thin films that closely resemble the structural characteristics of the initial monomers.

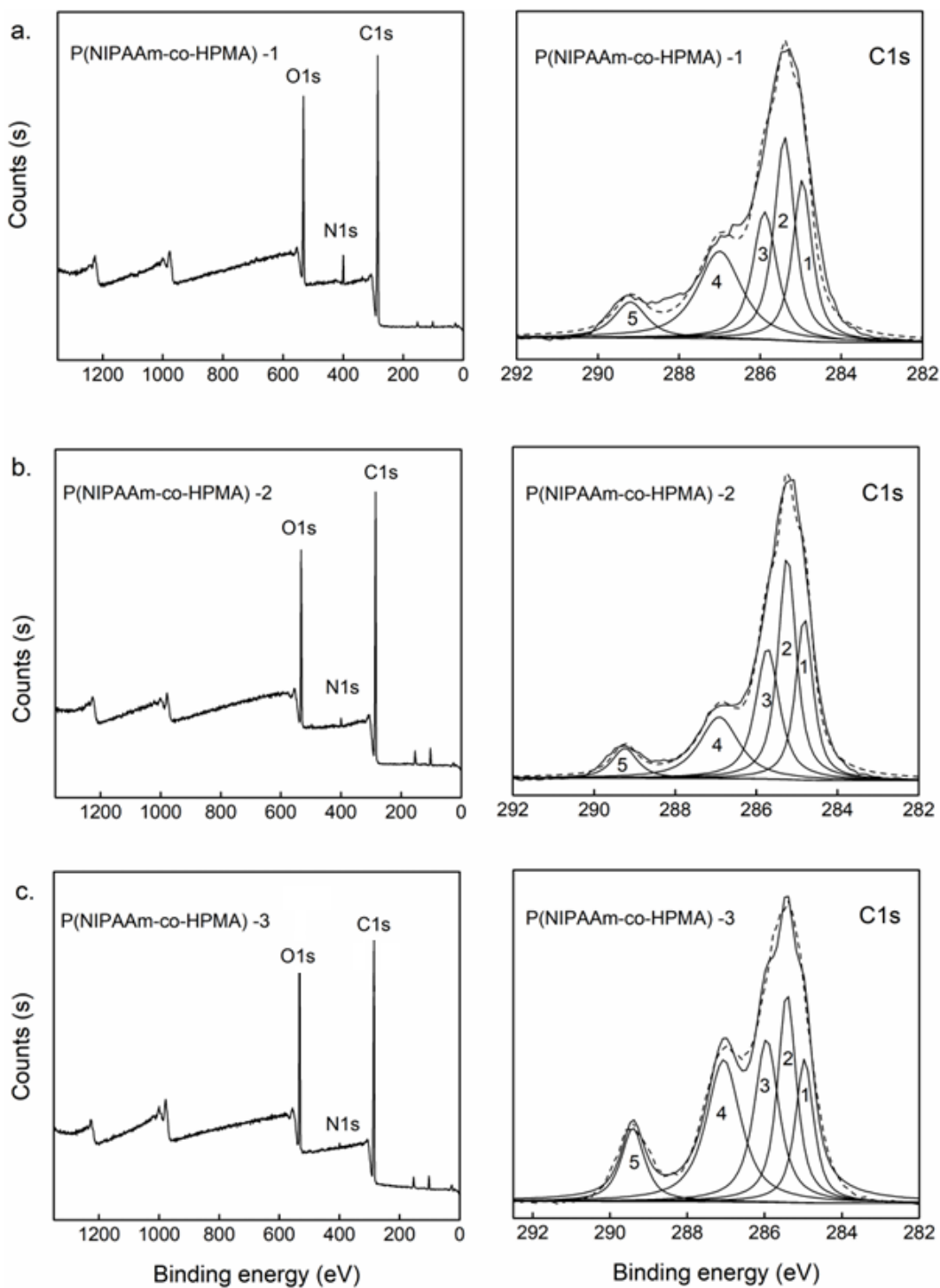


Figure 5: XPS survey scan and high-resolution C1s spectrum of the p(NIPAAm-HPMA) films a) p(NIPAAm-HPMA)-1 b) p(NIPAAm-HPMA)-2 c) p(NIPAAm-HPMA)-3

Table 2: Elemental composition of p(NIPAM-HPMA) films

	Carbon (%)	Oxygen (%)	Nitrogen (%)
p(NIPAAm-HPMA)-1	73.02	22.00	4.98
p(NIPAAm-HPMA)-2	71.54	24.08	4.38
p(NIPAAm-HPMA)-3	66.78	30.09	3.13

Table 3: High-resolution XPS scan data of the p(NIPAAm-HPMA) films

	Core level	Peak	Origin	iCVD films Binding energy (eV)	reference [43] Binding energy (eV)
p(NIPAAm-HPMA)-1	C 1s	1	-C*H ₃ , -C*H ₂ -C	284.96	285.00
		2	-C*H ₂ -N	285.40	285.75
		3	-O-C*H ₂ -	286.00	286.50
		4	-O-C*	287.03	287.00
		5	C=O*	289.10	289.15
p(NIPAAm-HPMA)-2	C 1s	1	-C*H ₃ , -C*H ₂ -C	284.82	285.00
		2	-C*H ₂ -N	285.24	285.75
		3	-O-C*H ₂ -	285.95	286.50
		4	-O-C*	286.91	287.00
		5	C=O*	289.24	289.15
p(NIPAAm-HPMA)-3	C 1s	1	-C*H ₃ , -C*H ₂ -C	284.97	285.00
		2	-C*H ₂ -N	285.42	285.75
		3	-O-C*H ₂ -	286.30	286.50
		4	-O-C*	287.06	287.00
		5	C=O*	289.21	289.15

The LCST value of iCVD copolymer films deposited with different HPMA flow rates was investigated using contact angle measurements. The literature research concluded that the temperature should be changed in a wide range to determine the contact angle and the LCST value. For each coated surface, first heating and then cooling measurements were done and the obtained results are given in Figure 6.

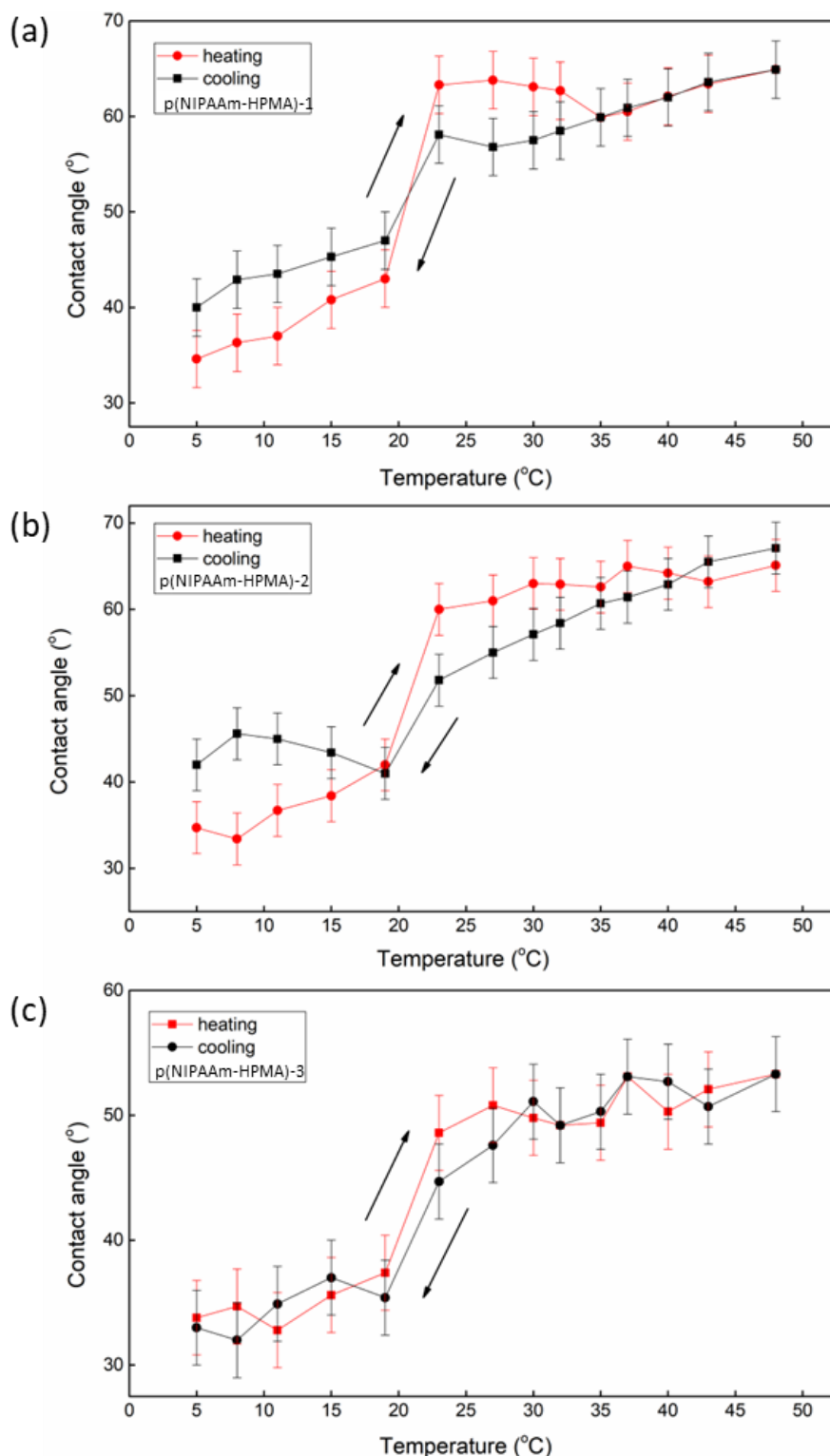


Figure 6: Effect of change in substrate temperature on water contact angle values in p(NIPAAm-HPMA) copolymer films a) p(NIPAAm-HPMA)-1 b) p(NIPAAm-HPMA)-2 c) p(NIPAAm-HPMA)-3

Based on the results, it was observed that the LCST values for the p(NIPAAm-HPMA) films varied within the range of 19 to 23 degrees. Notably, this range is considerably lower than the LCST value of pNIPAAm alone, which is 32 degrees [44]. It is established that the copolymerization of NIPAAm with a comonomer exhibiting greater hydrophobicity leads to a reduction in the LCST, whereas copolymerization with a more hydrophilic comonomer results in an increase in the LCST [9, 45, 46]. The

decline in LCST observed in this context can be anticipated, given the relatively heightened hydrophobicity of HPMA, which incorporates a methyl group. A contact angle alteration of around 30° corresponding to the thermo responsive transition between hydrophilicity and hydrophobicity was observed on the flat substrate modified with p(NIPAAm-HPMA) film; this aligns with the conclusions found in the literature [47]. This effect is clarified by the interplay between intermolecular and intramolecular hydrogen bonds below and above the LCST, which is approximately 32°C.

4. CONCLUSIONS

P(NIPAAm-HPMA) thermo-responsive hydrogel thin films were deposited by iCVD method on Si wafer surfaces. The effect of NIPAAm/HPMA flow rate on the deposition rate, structure and responsive properties of the as-deposited p(NIPAAm-HPMA) copolymers were revealed. The highest deposition rate of 50 nm/min was observed for the copolymer deposited using lowest NIPAAm/HPMA monomer ratio studied. The deposition rate showed a significant increase with decreasing NIPAAm/HPMA flow ratio. Results of the FTIR and XPS analyzes showed that the iCVD technique was able to tune the composition of the copolymers easily by just changing the monomer flow ratios. The LCST values of p(NIPAAm-HPMA) copolymer films on Si wafer surfaces, which were determined by monitoring the temperature dependence of the water contact angle values on temperature, was shown to vary between 19 and 23 °C. The LCST, as expected, was observed to be dependent on the NIPAAm/HPMA monomer ratio. That LCST range is considerably below the literature- reported values for pNIPAAm, which makes the as-deposited copolymer suitable for applications that require thermos-responsive properties at lower temperatures.

Declaration of Ethical Standards

The authors declare that all ethical guidelines including authorship, citation, data reporting, and publishing original research are followed.

Declaration of Competing Interest

The authors declare that there is no conflict of interest.

Acknowledgements

This project was supported by the Scientific Research Projects of Konya Technical University with a grant number of 18201085.

Data Availability

The data that support the findings of this study are available from the corresponding author upon reasonable request.

5. REFERENCES

- [1] D. Crespy and R. M. Rossi, "Temperature-responsive polymers with LCST in the physiological range and their applications in textiles," *Polymer International*, vol. 56, no. 12, pp. 1461-1468, 2007.
- [2] S. Dai, P. Ravi, and K. C. Tam, "pH-Responsive polymers: synthesis, properties and applications," *Soft Matter*, vol. 4, no. 3, pp. 435-449, 2008.
- [3] Y. Li et al., "Magnetic hydrogels and their potential biomedical applications," *Advanced Functional Materials*, vol. 23, no. 6, pp. 660-672, 2013.
- [4] J. S. Katz and J. A. Burdick, "Light-Responsive Biomaterials: Development and Applications," *Macromolecular Bioscience*, vol. 10, no. 4, pp. 339-348, 2010, doi: <https://doi.org/10.1002/mabi.200900297>.

- [5] R. V. Ulijn, "Enzyme-responsive materials: a new class of smart biomaterials," *Journal of Materials Chemistry*, vol. 16, no. 23, pp. 2217-2225, 2006.
- [6] M. A. Ward and T. K. Georgiou, "Thermoresponsive polymers for biomedical applications," *Polymers*, vol. 3, no. 3, pp. 1215-1242, 2011.
- [7] P. T. Mather, X. Luo, and I. A. Rousseau, "Shape memory polymer research," *Annual Review of Materials Research*, vol. 39, pp. 445-471, 2009.
- [8] I. Tokarev and S. Minko, "Stimuli-responsive hydrogel thin films," *Soft Matter*, Review vol. 5, no. 3, pp. 511-524, 2009, doi: 10.1039/b813827c.
- [9] M. E. Alf, T. A. Hatton, and K. K. Gleason, "Novel N-isopropylacrylamide based polymer architecture for faster LCST transition kinetics," *Polymer*, vol. 52, no. 20, pp. 4429-4434, 2011/09/12/2011, doi: <https://doi.org/10.1016/j.polymer.2011.07.051>.
- [10] H. H. Nguyen, B. Payre, J. Fitremann, N. Lauth-de Viguerie, and J.-D. Marty, "Thermoresponsive properties of PNIPAM-based hydrogels: effect of molecular architecture and embedded gold nanoparticles," *Langmuir*, vol. 31, no. 16, pp. 4761-4768, 2015.
- [11] W. Wei et al., "A novel thermo-responsive hydrogel based on salean and poly (N-isopropylacrylamide): Synthesis and characterization," *Colloids and Surfaces B: Biointerfaces*, vol. 125, pp. 1-11, 2015.
- [12] M. Heskins and J. E. Guillet, "Solution properties of poly (N-isopropylacrylamide)," *Journal of Macromolecular Science—Chemistry*, vol. 2, no. 8, pp. 1441-1455, 1968.
- [13] A. Pena-Francesch, L. Montero, and S. Borrós, "Tailoring the LCST of thermosensitive hydrogel thin films deposited by iCVD," *Langmuir*, vol. 30, no. 24, pp. 7162-7167, 2014.
- [14] K. Jain, R. Vedarajan, M. Watanabe, M. Ishikiriya, and N. Matsumi, "Tunable LCST behavior of poly (N-isopropylacrylamide/ionic liquid) copolymers," *Polymer Chemistry*, vol. 6, no. 38, pp. 6819-6825, 2015.
- [15] W. Wang et al., "Thin films of poly (N-isopropylacrylamide) end-capped with n-butyltrithiocarbonate," *Macromolecules*, vol. 41, no. 9, pp. 3209-3218, 2008.
- [16] Y. Guan and Y. Zhang, "PNIPAM microgels for biomedical applications: from dispersed particles to 3D assemblies," *Soft Matter*, vol. 7, no. 14, pp. 6375-6384, 2011.
- [17] M. R. Islam, A. Ahiabu, X. Li, and M. J. Serpe, "Poly (N-isopropylacrylamide) microgel-based optical devices for sensing and biosensing," *Sensors*, vol. 14, no. 5, pp. 8984-8995, 2014.
- [18] X. Xu et al., "Poly (N-isopropylacrylamide)-based thermoresponsive composite hydrogels for biomedical applications," *Polymers*, vol. 12, no. 3, p. 580, 2020.
- [19] J. Liu, L. Jiang, S. He, J. Zhang, and W. Shao, "Recent progress in PNIPAM-based multi-responsive actuators: A mini-review," *Chemical Engineering Journal*, vol. 433, p. 133496, 2022.
- [20] Z. Ayar, M. Shafieian, N. Mahmoodi, O. Sabzevari, and Z. Hassannejad, "A rechargeable drug delivery system based on pNIPAM hydrogel for the local release of curcumin," *Journal of Applied Polymer Science*, vol. 138, no. 40, p. 51167, 2021.
- [21] M. Cao et al., "Reversible thermoresponsive peptide–PNIPAM hydrogels for controlled drug delivery," *Biomacromolecules*, vol. 20, no. 9, pp. 3601-3610, 2019.
- [22] X. Lu, L. Zhang, L. Meng, and Y. Liu, "Synthesis of poly (N-isopropylacrylamide) by ATRP using a fluorescein-based initiator," *Polymer Bulletin*, vol. 59, no. 2, pp. 195-206, 2007.
- [23] M. Gürsoy, "Fabrication of Poly (N-isopropylacrylamide) with Higher Deposition Rate and Easier Phase Transition by Initiated Plasma Enhanced Chemical Vapor Deposition," *Plasma Chemistry and Plasma Processing*, pp. 1-17, 2020.
- [24] G. Conzatti, S. Cavalie, C. Combes, J. Torrisani, N. Carrère, and A. Tournette, "PNIPAM grafted surfaces through ATRP and RAFT polymerization: Chemistry and bioadhesion," *Colloids and Surfaces B: Biointerfaces*, vol. 151, pp. 143-155, 2017.
- [25] S. J. McInnes et al., "Fabrication and characterization of a porous silicon drug delivery system with an initiated chemical vapor deposition temperature-responsive coating," *Langmuir*, vol. 32, no. 1, pp. 301-308, 2016.

- [26] C. Wang et al., "Reversible ion-conducting switch by azobenzene molecule with light-controlled sol-gel transitions of the PNIPAm ion gel," *ACS Applied Materials & Interfaces*, vol. 12, no. 37, pp. 42202-42209, 2020.
- [27] J. E. Wong, A. K. Gaharwar, D. Müller-Schulte, D. Bahadur, and W. Richtering, "Dual-stimuli responsive PNiPAM microgel achieved via layer-by-layer assembly: Magnetic and thermoresponsive," *Journal of colloid and interface science*, vol. 324, no. 1-2, pp. 47-54, 2008.
- [28] B. Şimşek and M. Karaman, "Initiated chemical vapor deposition of poly (hexafluorobutyl acrylate) thin films for superhydrophobic surface modification of nanostructured textile surfaces," *Journal of Coatings Technology and Research*, vol. 17, no. 2, pp. 381-391, 2020.
- [29] G. Ozaydin-Ince, A. M. Coclite, and K. K. Gleason, "CVD of polymeric thin films: applications in sensors, biotechnology, microelectronics/organic electronics, microfluidics, MEMS, composites and membranes," *Reports on Progress in Physics*, vol. 75, no. 1, p. 016501, 2011.
- [30] K. K. Gleason, *CVD Polymers: Fabrication of Organic Surfaces and Devices (CVD Polymers: Fabrication of Organic Surfaces and Devices)*. 2015, pp. 1-461.
- [31] R. Sreenivasan and K. K. Gleason, "Overview of strategies for the CVD of organic films and functional polymer layers," *Chemical Vapor Deposition*, vol. 15, no. 4-6, pp. 77-90, 2009.
- [32] E. Çıtak, B. İstanbullu, H. Şakalak, M. Gürsoy, and M. Karaman, "All-Dry Hydrophobic Functionalization of Paper Surfaces for Efficient Transfer of CVD Graphene," *Macromolecular Chemistry and Physics*, vol. 220, no. 22, p. 1900277, 2019.
- [33] F. Z. Pour, H. Karimi, and V. M. Avargani, "Preparation of a superhydrophobic and superoleophilic polyester textile by chemical vapor deposition of dichlorodimethylsilane for Water-Oil separation," *Polyhedron*, vol. 159, pp. 54-63, 2019.
- [34] H. Şakalak, K. Yılmaz, M. Gürsoy, and M. Karaman, "Roll-to roll initiated chemical vapor deposition of super hydrophobic thin films on large-scale flexible substrates," *Chemical Engineering Science*, vol. 215, 2020, doi: 10.1016/j.ces.2019.115466.
- [35] K. Yılmaz, H. s. Şakalak, M. Gürsoy, and M. Karaman, "Initiated Chemical Vapor Deposition of Poly (Ethylhexyl Acrylate) Films in a Large-Scale Batch Reactor," *Industrial & Engineering Chemistry Research*, vol. 58, no. 32, pp. 14795-14801, 2019.
- [36] M. Gürsoy and M. Karaman, "Hydrophobic coating of expanded perlite particles by plasma polymerization," *Chemical Engineering Journal*, vol. 284, pp. 343-350, 2016.
- [37] M. N. Subramaniam, P. S. Goh, E. Sevgili, M. Karaman, W. J. Lau, and A. F. Ismail, "Hydroxypropyl methacrylate thin film coating on polyvinylidene fluoride hollow fiber membranes via initiated chemical vapor deposition," *European Polymer Journal*, vol. 122, 2020, doi: 10.1016/j.eurpolymj.2019.109360.
- [38] M. Karaman and N. Çabuk, "Initiated chemical vapor deposition of pH responsive poly (2-diisopropylamino) ethyl methacrylate thin films," *Thin Solid Films*, vol. 520, no. 21, pp. 6484-6488, 2012.
- [39] E. Çıtak et al., "Vapor deposition of quaternary ammonium methacrylate polymers with high antimicrobial activity: Synthetic route, toxicity assessment, and durability analysis," *Journal of Vacuum Science & Technology A: Vacuum, Surfaces, and Films*, vol. 38, no. 4, p. 043203, 2020.
- [40] M. E. Alf, "Functional and responsive surfaces via initiated chemical vapor deposition (iCVD)," *Massachusetts Institute of Technology*, 2011.
- [41] E. Sevgili and M. Karaman, "Initiated chemical vapor deposition of poly (Hydroxypropyl methacrylate) thin films," *Thin Solid Films*, vol. 687, p. 137446, 2019.
- [42] M. Kurečić, M. Sfiligoj-Smole, and K. Stana-Kleinschek, "UV polymerization of poly (N-isopropylacrylamide) hydrogel," *Materiali in tehnologije*, vol. 46, no. 1, pp. 87-91, 2012.
- [43] G. Beamson and D. Briggs, "High resolution monochromated X-ray photoelectron spectroscopy of organic polymers: a comparison between solid state data for organic polymers and gas phase data for small molecules," *Molecular Physics*, vol. 76, no. 4, pp. 919-936, 1992.

- [44] J.-F. Lutz, Ö. Akdemir, and A. Hoth, "Point by point comparison of two thermosensitive polymers exhibiting a similar LCST: is the age of poly (NIPAM) over?," *Journal of the American Chemical Society*, vol. 128, no. 40, pp. 13046-13047, 2006.
- [45] H. G. Schild, "Poly(N-isopropylacrylamide): experiment, theory and application," *Progress in Polymer Science*, vol. 17, no. 2, pp. 163-249, 1992/01/01/ 1992, doi: [https://doi.org/10.1016/0079-6700\(92\)90023-R](https://doi.org/10.1016/0079-6700(92)90023-R).
- [46] E. S. Gil and S. M. Hudson, "Stimuli-reponsive polymers and their bioconjugates," *Progress in Polymer Science*, vol. 29, no. 12, pp. 1173-1222, 2004/12/01/ 2004, doi: <https://doi.org/10.1016/j.progpolymsci.2004.08.003>.
- [47] T. Sun et al., "Reversible switching between superhydrophilicity and superhydrophobicity," *Angewandte Chemie International Edition*, vol. 43, no. 3, pp. 357-360, 2004.

A DEEP LEARNING ENSEMBLE APPROACH FOR X-RAY IMAGE CLASSIFICATION

¹Engin ESME , ^{2,*}Mustafa Servet KIRAN 

¹Konya Technical University, Engineering and Natural Sciences Faculty, Software Engineering Department,
Konya, TÜRKİYE

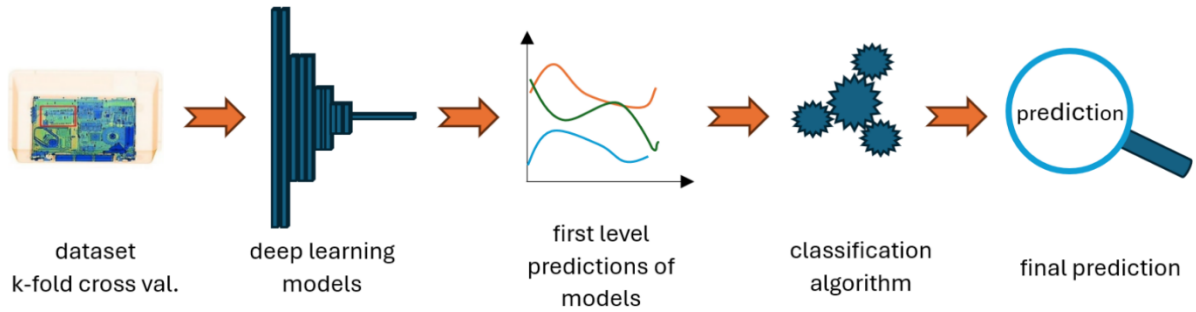
²Konya Technical University, Engineering and Natural Sciences Faculty, Computer Engineering Department,
Konya, TÜRKİYE

eesme@ktun.edu.tr, mskiran@ktun.edu.tr

Highlights

- Automating X-ray imaging using deep learning methods to overcome time and personnel constraints.
- Training deep learning models on X-ray images for detecting hidden explosive circuits.
- Developing an ensemble approach to enhance classification success.

Graphical Abstract





A DEEP LEARNING ENSEMBLE APPROACH FOR X-RAY IMAGE CLASSIFICATION

¹Engin ESME^{ID}, ^{2,*}Mustafa Servet KIRAN^{ID}

¹Konya Technical University, Engineering and Natural Sciences Faculty, Software Engineering Department, Konya,
TÜRKİYE

²Konya Technical University, Engineering and Natural Sciences Faculty, Computer Engineering Department, Konya,
TÜRKİYE

eesme@ktun.edu.tr, mskiran@ktun.edu.tr

(Received: 23.01.2024; Accepted in Revised Form: 19.07.2024)

ABSTRACT: The application of deep learning-based intelligent systems for X-ray imaging in various settings, including transportation, customs inspections, and public security, to identify hidden or prohibited objects are discussed in this study. In busy environments, x-ray inspections face challenges due to time limitations and a lack of qualified personnel. Deep learning algorithms can automate the imaging process, enhancing object detection and improving safety. This study uses a dataset of 5094 x-ray images of laptops with hidden foreign circuits and normal ones, training 11 deep learning algorithms with the 10-fold cross-validation method. The predictions of deep learning models selected based on the 70% threshold value have been combined using a meta-learner. ShuffleNet has the highest individual performance with 83.56%, followed by InceptionV3 at 81.30%, Darknet19 at 78.92%, DenseNet201 at 77.70% and Xception at 71.26%. Combining these models into an ensemble achieved a remarkable classification success rate of 85.97%, exceeding the performance of any individual model. The ensemble learning approach provides a more stable prediction output, reducing standard deviation among folds as well. This research highlights the potential for safer and more effective X-ray inspections through advanced machine learning techniques.

Keywords: Deep Learning, Ensemble Learning, Object Classification, X-Ray

1. INTRODUCTION

Passenger and cargo transportation, customs inspections, public buildings, and public areas commonly use X-ray imaging devices to detect hidden or prohibited objects and identify potential hazards. However, in places with heavy traffic, X-ray inspections can become inefficient and even unsafe due to time limitations, caseload, and lack of qualified personnel. Especially when items are stacked on each other, the images become complex, and it becomes challenging for operators to focus on the scanning screen for long periods. Moreover, situations like detecting explosive materials and related circuits require additional expertise. As a result, the problem of identifying threat objects concealed inside electronic devices arises. In this context, deep learning-based intelligent systems can automate the imaging process and object detection, making inspections safer. Deep learning algorithms are being explored in some research to evaluate X-ray security images since they can automatically extract high-level features compared to traditional image processing methods. Akçay, Kundegorski et al. examine transfer learning by applying Convolutional Neural Networks (CNNs) to the image classification problem used in X-ray luggage screening. Due to less training data, fully training CNN is difficult. Therefore, the last layers of the network are frozen, and only the initial layers are fine-tuned and optimized. The proposed method achieves more successful results than previous studies and is effective in detecting firearms [1]. Benedykciuk, Denkowski et al. address the material detection problem in the X-ray scanners used for security purposes. Scanner images are divided into six main categories based on whether organic or metallic. Feature extraction and classification are performed using deep learning methods. During

*Corresponding Author: Mustafa Servet KIRAN, mskiran@ktun.edu.tr

training, the images are split into parts representing six different material types, and a multi-scale network structure consisting of five sub-networks is used to handle size variations. Additionally, the effects of regularization and activation approaches such as (Exponential Linear Unit) ELU and Rectified Linear Units (RELU) on the architecture are also investigated [2]. Miao, Xie et al. conduct research on the detection of prohibited items in X-ray images. For this purpose, they create a dataset called SIXray, which is 100 times larger and resembles real-world data. The dataset contains approximately 1% of prohibited items. They develop an algorithm to hierarchically and iteratively enhance features to suppress the number of overlapping objects and irrelevant information in X-ray images. To improve the efficiency of the slow-working iterative algorithm, they limit forward and backward passes with a pruning mechanism. Additionally, they introduce a new loss function to address the data imbalance between positive and negative classes and achieve impressive results by testing it with different network frameworks [3]. Chang, Zhang et al. address the object detection problem in X-ray security imaging using a two-stage network. This method aims to reduce false alarms by considering the physical size of prohibited items. They also apply a method called "Hard-negative-example selection" to reduce the low performance caused by the imbalance between positive and negative examples. In the developed solution, they conduct experiments on SIXray and OPIXray datasets using the Feature Pyramid Network method and the Faster R-CNN method, along with the physical size and hard-negative selection mechanism [4]. Shao, Liu et al. separate prohibited objects from background images by highlighting the problem of object overlapping in X-ray scanning. In this method, they obtain features using Cross Stage Partial Darknet53 (CSPDarknet53), spatial pyramid pooling, and yolov4-tiny networks, and then separate foreground and background [5].

As revealed in these studies, the performance of deep learning models varies depending on network architectures and applications, and each network may exhibit different individual performances in different scenarios. In this regard, instead of designing a new network architecture in this research, we propose applying a method that takes advantage of using multiple deep learning networks. Ensemble learning is the general expression of approaches that aim to create a better model with improved generalization capability by bringing together a set of learners. The cumulative decision-making of multiple models on a problem highlights their strengths while compensating for their weaknesses, leading to enhanced performance. Each model is trained with different algorithms, parameters, or datasets to provide different perspectives on the problem. This way, the ensemble model becomes more reliable, producing consistent results while revealing relationships in a broader pattern space [6, 7]. Ensemble learning methods may involve various techniques for combining predictions, such as majority voting, weighting, or using an optimized machine learning model on the predictions. These methods target different objectives, including ensuring learning diversity, statistical stability, minimizing errors, and improving generalization performance [7, 8]. Ensemble approaches are widely used in the processing of X-ray images, particularly in the medical field [9-11] and biochemistry [12, 13] and physics [14, 15]. Nevertheless, the utilization of ensemble techniques on X-ray images is restricted within the realm of security. Kolte et al. use an architecture called Skip-GANomaly to overcome the problem of limited data in X-ray security applications and design an updated version using a UNet++ style generator. Then, they combine these two architectures using an ensemble method. It is reported that the ensemble method learns better features to distinguish the abnormal class from the normal class compared to individual architectures [16]. Kong et al. propose an approach that benefits from a classifier ensemble using multi-modal information from X-ray images of a single-view object. They use deep neural networks to learn a good representation for each method used to train the base classifiers. To achieve high overall classification performance, they estimate the reliabilities of the base classifiers by considering natural properties of an object in an X-ray image, such as color and shape. They perform tests on a dataset with 15 classes to evaluate the method's competitive performance [17]. Zhou et al. develop an adaptive weighted ensemble model for carotid ultrasound image segmentation, bringing together the advantages of different CNN models. During the joint training of ensemble networks, model weights and sample weights are combined to improve segmentation

performance. The method evaluates three different UNet++ models (ResNet152, DenseNet169, and VGG19) on carotid ultrasound images and achieves higher accuracy compared to other methods [18]. Ahmad et al. propose an ensemble-based classification network for classifying baggage X-ray images. The method utilizes joint learning of a deep CNN combined with a Principal Component Analysis (PCA)-based Support Vector Machine (SVM) classifier. The suggested method exhibits high performance in classifying baggage X-ray images [19]. The summarised studies are listed in Table 1 with their salient features. These studies demonstrate that the use of ensemble based deep learning networks can enhance the classification accuracy in X-ray security images compared to a single network.

It is seen that deep learning models have high success in subjects related to X-Ray images. In the methods and datasets available in the literature, object detection (gun, scissors, knife, etc.) is generally performed. Since the relevant datasets consist of images of these objects, their functions are limited to the detection of these objects. In very few of these studies, anomalies etc. are detected. In this study, a unique dataset was created by embedding the electronic circuits potentially belonging to explosives in laptops. The dataset contains different combinations of laptops and circuits. In this way, anomaly detection of electronic circuits can also be provided.

This study aims to efficiently differentiate a series of laptops, some containing a foreign circuit and others normal, in X-ray security image analysis using deep learning algorithms to determine whether they contain hazardous substances. For this purpose, an ensemble methodology is adopted to achieve more accurate and reliable detection of prohibited substances. In the proposed approach, individual outputs of each model are combined with an optimized machine learning algorithm which is a meta-learner. The individual performances of a total of 11 different deep learning models are compared and evaluated against the results of the community approach. The goal of using ensemble learning is to achieve more effective results in prohibited substance detection and provide a more efficient solution for security applications.

The project contributes to both security and deep learning literature in the following aspects.

- Detecting an explosive circuit hidden inside a laptop is a challenging problem for both human operators and deep learning models. Current X-ray devices do not have such detection software/hardware.
- There is a gap in the intersection between deep learning models and X-ray image analysis, especially the topic of X-ray image analysis as it relates to security.
- The existence of such a problem is not mentioned in the scientific literature.
- With this project, the problem is treated as a classification problem and a dataset is created to train the classification methods.
- In addition, an ensemble system with higher accuracy is developed.

2. MATERIALS AND METHODS

2.1. Ensemble Learning

Ensemble learning is a machine learning approach that aims to combine multiple individual models or learners to create a model with higher generalization capability. The fundamental idea behind ensemble learning is that relying on the predictions of various individual learners makes the final prediction more stable, reliable, and generalized compared to a single model. The main ensemble learning approaches can be listed as follows [7, 20]:

Table 1. Related research in the literature

Reference	Task	Methods	Notes
Akçay et al. [1]	Object Classification	Transfer learning using convolutional neural networks	Two class (gun/no gun) handgun detection problem, 98.92% detection accuracy.
Benedykciuk et al. [2]	Object Classification Material Detection	Multi-scale convolutional neural network	The method classify the materials into six groups: background, light organic, heavy organic, light metals, heavy metals and impenetrable. 95.5% detection accuracy.
Miao et al. [3]	Object Classification Threat Detection	The class-balanced hierarchical refinement is applied to ResNet, Inception, DenseNet.	Security Inspection Xray dataset is presented, it consists of 1,059,231 X-ray images, in which 6 classes of 8,929 prohibited items.
Chang et al. [4]	Object Classification Threat Detection	Faster R-CNN	The proposed method consists of convolutional feature maps, the reconstructed feature maps, binary masks. The physical size constraint formulated as a regularization term during the process of training the proposed detection network.
Shao et al. [5]	Object Classification Threat Detection	Foreground and background separation, YOLOv4	On the GDTIPXray, OPIXray, SIXray datasets, higher success was achieved than the other methods compared.
Zhao et al. [6]	Object Classification	Ensemble Learning, BoostForest, RandomForest, Extra-Trees, XGBoost, LightGBM, GBDT-PL	The research compares the performances of 7 different ensemble approaches on 30 different datasets.
Nasser and Akhloufi [9]	Image Classification Disease Detection	Deep Learning Models, Ensemble Learning	The review article summarizes the approaches and data sets used to diagnose chest disease with xray images.
Radak et al. [10]	Image Classification Disease Detection	Machine Learning, Deep Learning Models,	The review article summarizes the approaches and data sets used to diagnose breast cancer with medical images.
Khan et al. [11]	Image Classification Disease Detection	Machine Learning, Deep Learning Models, Ensemble Methods	The review article summarizes the approaches and data sets used to diagnose chest disease with xray images.
Wang et al. [12]	Classification and Segmentation	DenseNet, ResNet, Random Forest, CNN, Deep Neural Networks, xgBoost	Six feature extraction methods are integrated into proposed deep learning method respectively to form six baseline models. The weighted voting strategy is used to integrate the results from six different classifiers.
Putin et al. [13]	Prediction	Deep Neural Networks, Stacking Ensemble Model	The best performing DNN in the ensemble demonstrated 81.5% accuracy, while the entire ensemble achieved 83.5% accuracy.
Xie and Marsili [14]	Image Classification	Ensemble of Deep Belief Networks	Random energy model applied to the deep learning.
Hoffmann et al. [15]	Prediction	Ensemble of Deep Neural Networks	The paper applies the deep learning hybrid approach to measurement data from a real specimen of an asphere.
Kolte et al. [16]	Object classification Threat detection	GAN based ensembles	Proposed ensemble-based architecture achieved a 75.3% AUC on the SIXray dataset.
Kong et al. [17]	Object Recognition	Deep Neural Networks Based Ensemble Learning	The research reports the comparative results using a dataset with 15 classes.
Zhou et al. [18]	Image Segmentation	CNN, Adaptively weighted ensemble algorithm	Training multiple networks in the ensemble algorithm costs greater computational resources than a single network.
Ahmed et al. [19]	Object classification Threat detection	Deep Neural Networks, PCA, SVM	CNN-based classification models are hybridized with classical machine learning models.

1) **Bagging**

Data sets are randomly created, and learners are trained in parallel. The models' predictions are combined using majority voting.

2) **Boosting**

It is a method where each learner is trained to compensate for the errors of the previous learner. Learners are trained sequentially.

3) **Stacking**

A machine learning model learns from the outputs of individual learners. This meta-model combines the outputs of individual models to make the final prediction.

Commonly used ensemble techniques include bagging, boosting, and stacking, as shown in Figure 1 [21].

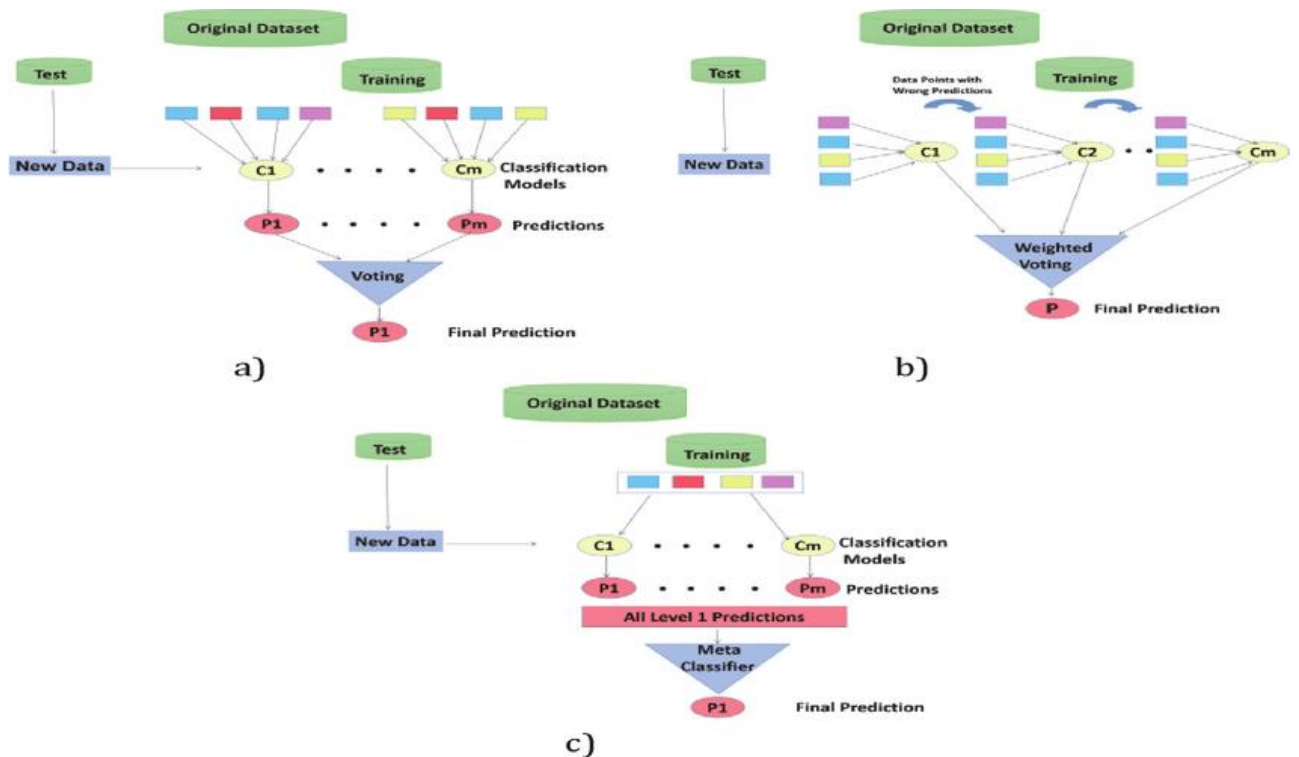


Figure 1. Ensemble techniques a) Bagging, b) Boosting, c) Stacking.

2.2. Deep Learning Models

1) **SuffleNet**

ShuffleNet is designed by Zhang et al. in 2018, specifically for mobile devices with limited computational capability. The cost is reduced with operations such as point group convolution and channel shuffling. The group convolution method, which is first used with AlexNet, is introduced as a new method in ShuffleNet architecture by using it together with the shuffling process [22].

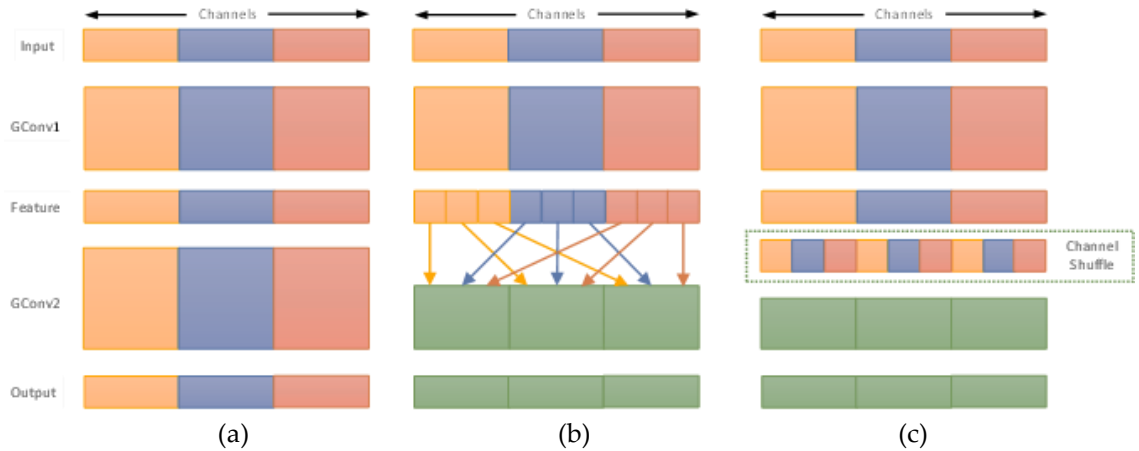


Figure 2. The channel diagrams for convolution a) Group convolution with no cross-talking b) Group convolution with cross talking c) Shuffled channels.

As shown in Figure 2(a), the input value inside group convolution is processed independently on different graphics processing units through convolution and batch normalization. In this case, only the filters in the relevant group affect the output result. However, kernels from a different group than the relevant group may have a significant impact on some outputs. Therefore, in some methods, the groups in the relevant outputs are applied to the next convolution process. As shown in Figure 2(b), each sub-group is mixed in a way to contribute to a different group, which improves performance. Instead of this, in Figure 2(c), the mixing process is performed using matrix transpose and flattening operations. This way, compared to Figure 2(b), a less costly mixing process is achieved. The most significant advantage of these processes in ShuffleNet is the ability to achieve similar classification performance with much less complexity in models.

2) DarkNet

DarkNets are deep learning architectures designed for single-shot tasks, incorporating YOLOv2 and YOLOv3 in their backbone structures. There are two DarkNet models available: DarkNet-19 [23] and DarkNet-53 [24], comprising 19 and 53 convolution layers, respectively. DarkNet-53, in addition to its extensive convolution layers, also employs residual connections to address degradation issues. The configuration of layers for DarkNet-19 are illustrated in Figure 3.

Layer	Filters	Size/Stride	Output
Convolutional	32	3x3	224x224
MaxPool		2x2/2	112x112
Convolutional	64	3x3	112x112
MaxPool		2x2/2	56x56
Convolutional	128	3x3	56
Convolutional	64	1x1	56
Convolutional	128	3x3	56
MaxPool		2x2/2	28x28
Convolutional	256	3x3	28x28
Convolutional	128	1x1	28x28
Convolutional	256	3x3	28x28
MaxPool		2x2/2	14x14
Convolutional	512	3x3	14x14
Convolutional	256	1x1	14x14
Convolutional	512	3x3	14x14
Convolutional	256	1x1	14x14
Convolutional	512	3x3	14x14
MaxPool		2x2/2	7x7
Convolutional	1027	3x3	7x7
Convolutional	512	1x1	7x7
Convolutional	1024	3x3	7x7
Convolutional	512	1x1	7x7
Convolutional	1024	3x3	7x7
Convolutional	1000	1x1	7x7
Avgpool		Global	7x7
Softmax			1000

Figure 3. The layers of DarkNet-19

3) Inception

The first CNN model that increased the network's width using modules called "Inception" is introduced by Szegedy et al. in 2015. The inception architecture aims to approximately mimic the optimal local sparse structure within a convolutional network. It performs 1x1, 3x3, and 5x5 convolutions, as well as 3x3 maximum pooling, in parallel within the convolutional layers. To reduce computational complexity, 1x1 convolution layers are added before the parallel Inception convolutional layers which are shown in Figure 4 [25].

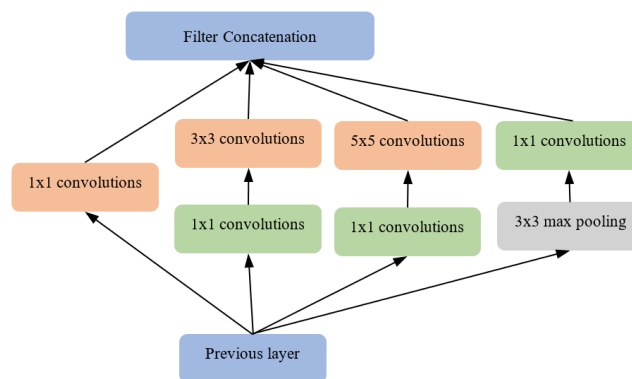


Figure 4. Inception convolutional layers

4) DenseNet

DenseNet, is an architecture introduced by Gao Huang et al. in 2017. It is specifically designed to tackle the vanishing gradient problem and enhance feature reuse within deep neural networks. This is achieved

through the utilization of dense connections, where each layer is directly connected to every other layer in a feed-forward manner. Within the Dense Blocks depicted in Figure 5, each layer is linked with corresponding feature map sizes. Every layer not only forwards its feature maps to subsequent layers but also receives supplementary inputs from the preceding layers, ensuring the preservation of an uninterrupted information flow. These attributes contribute to making DenseNet a robust and effective type of CNN, showcasing outstanding performance across diverse computer vision tasks [26].

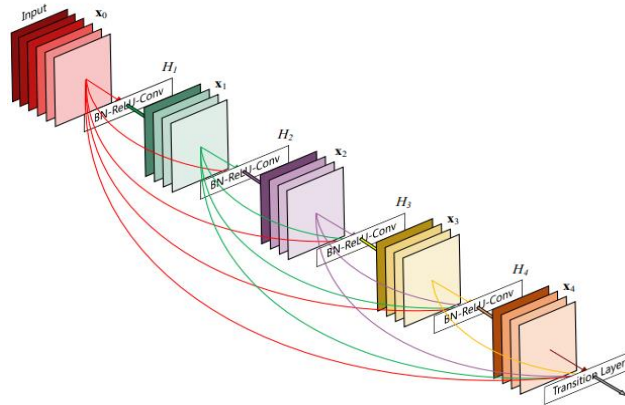


Figure 5. Dense Blocks

5) Xception

Xception is a deep learning model introduced by François Chollet in 2016. The name "Xception" means Extreme Inception, indicating that it is an extension of the Inception architecture. Instead of spatial filters, depthwise separable convolutions are developed to separate spatial and channel-wise filtering, aiming to enhance the performance of CNNs. The convolution process, as shown in Figure 6, consists of deep convolution where each channel evolves independently and pointwise convolution is applied for inter-channel interactions using a 1x1 convolution [27].

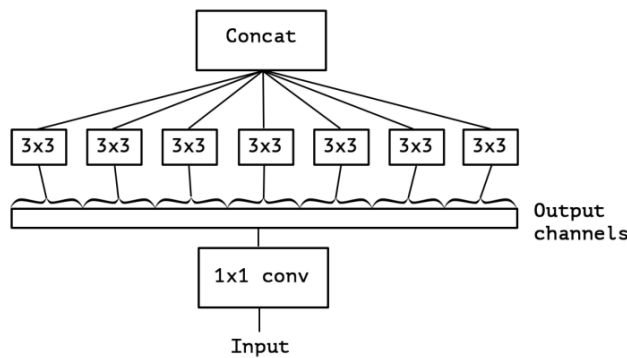


Figure 6. Xception Module

2.3. Dataset

The aim of the research is to use deep learning methods to detect circuits hidden in laptops. In this context, a dataset is needed to train and test deep learning methods. For this reason, the data set was created by us. Arduino uno, nano, bluetooth boards that are easily available in the market were preferred as circuits. Since

many different laptops were needed, second-hand laptops were purchased from the market. X-ray images of 60 laptops in different configurations were obtained by using the X-ray devices at the airport with the permission of the Konya Airport Administrative Authority. X-ray images of the laptops taken from different perspectives are given in Figure 7. The areas enclosed in red rectangles in images contain hidden circuits that do not belong to the computer motherboard.

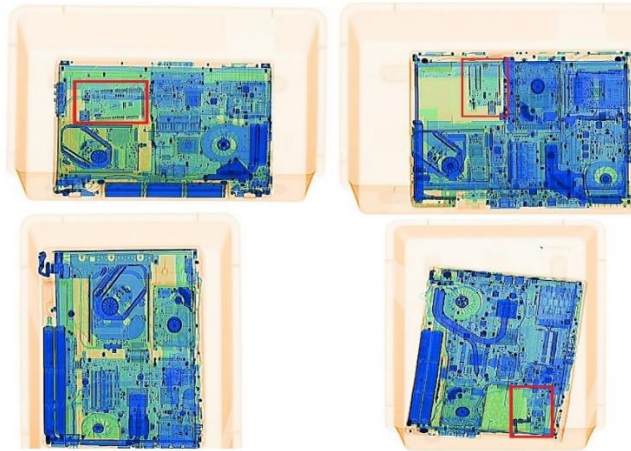


Figure 7. X-ray images of the laptops

In a period of 5 months, a total of 6395 X-ray images were taken. Of these, 2545 have hidden circuitry and 3850 do not. In order to keep the data balanced, the number of images without circuitry was reduced to 2549 and a total of 5094 X-ray images were used in the experiments. Since the problem is considered as a classification problem, it is necessary to have the labels of the images during the training and testing process with deep learning methods. The 5094 X-ray images were labeled as normal or abnormal and stored in different folders. The background and object images were segmented and the clean image shown in Figure 8 was obtained. Since deep learning architectures have different input sizes, all images were resized for each deep learning algorithm to match the input size of the images. Since the number of images was sufficient to train the deep learning models, no data augmentation was performed.

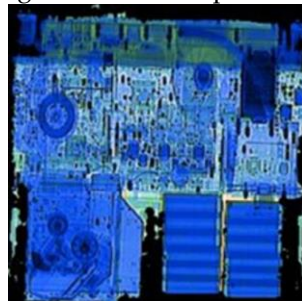


Figure 8. Preprocessed image sample

2.4. Proposed Method

The dataset consists of a total of X-ray images of 5094 laptops, including 2545 images of laptops with foreign circuits hidden inside and 2549 images of normal laptops without any modifications. A total of 11 deep learning algorithms were trained with Adaptive Moment Estimation optimizer. Adam is more efficient

in situations where gradient-based optimization algorithms have problems such as local minima and slow training speed. Since Adam is a more efficient and faster optimization algorithm, it is often the default optimization algorithm in deep learning models. In the experimental study, 100 epochs and 3000 iterations were sufficient to determine whether the deep learning models trained or not. The batchsize value of all models was set to 32 depending on the hardware used. The 10-fold cross-validation method was applied, and the training and test sets for each fold were recorded.

To ensure the effectiveness of the ensemble learning approach, algorithms with validation accuracy above 70% were preferred, as very poorly performing learners could negatively impact the ensemble result. The individual decisions of learners were combined using an optimized machine learning method. The choice and optimization of the machine learning algorithm (meta-learner) were performed using the `fitcauto` function with options for all learners and all `OptimizeHyperparameters` in Matlab software. `fitcauto` automatically tries different classification models with various settings. It uses Bayesian optimization to select the best model and cross-validation to evaluate their performance, ultimately determining the best model for predictions. The applied method is illustrated in Figure 9.

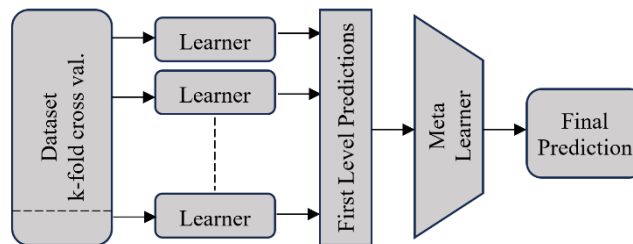


Figure 9. Proposed ensemble method

This ensemble learning model is based on a meta-model that learns from the output of individual learners. Deep learning models with high classification accuracy are used as individual learners. The predictions of the deep learning models provide the first level predictions. Based on these predictions, a machine learning model is optimized on the problem as a meta-learner. The `fitcauto` function includes the following classifiers: Discriminant analysis classifier, Ensemble classification model, Kernel classification model, k-nearest neighbor model, Linear classification model, Naive Bayes classifier, Neural network classifier, Support vector machine classifier, Binary decision classification tree. The Linear Classification model was used as a meta-learner since it provides higher correct classification success than the others.

3. RESULTS

In the study, X-ray images containing normal and abnormal classes were trained on 11 deep learning models listed in Table 2. The table presents the validation accuracy values of each model during the training process for each fold.

Table 2. Individual classification accuracy of deep learning algorithms

Model	k-fold										Avg.
	1	2	3	4	5	6	7	8	9	10	
efficientnetb0	59.49	63.35	59.05	57.38	58.55	60.87	59.45	60.65	58.28	56.47	59.35
resnet18	63.27	65.16	63.93	67.49	64.65	63.42	64.46	64.58	67.44	63.88	64.83
resnet50	59.64	60.51	64.87	60.36	61.02	61.24	61.85	60.29	67.08	63.81	62.07
resnet101	64.29	62.33	61.96	63.05	59.71	62.18	61.77	62.18	63.88	59.96	62.13
darknet19	77.60	77.96	77.02	75.64	79.20	78.55	80.31	75.35	79.36	76.38	77.74
darknet53	68.58	67.42	61.82	65.53	62.76	64.58	68.39	69.53	66.86	68.60	66.41
mobilenetv2	61.53	59.71	61.38	62.25	60.51	60.00	61.63	60.22	62.21	61.56	61.10
shufflenet	82.76	83.13	83.64	82.25	80.80	85.24	80.67	83.56	83.28	83.94	82.93
inceptionv3	82.04	80.73	77.45	81.38	80.15	84.51	85.10	84.15	83.94	82.41	82.19
densenet201	74.84	78.40	79.64	76.73	80.80	78.76	79.43	79.85	76.67	76.74	78.19
xception	71.93	74.04	70.04	69.60	68.80	70.04	69.91	71.64	75.73	70.42	71.21

Using 10-fold cross validation, the results on the validation set obtained during the training process are presented with averages. The model with the lowest performance is efficientnetb0. The average accuracy is 59.35%. The highest performing model is shufflenet. The average accuracy is 82.93%. Among the other models, resnet18, resnet50, darknet19, darknet53, inceptionv3, and densenet201 perform quite competitively. On the other hand, models such as resnet101, mobilenetv2, and xception perform slightly worse. They have accuracy rates in the low 60% range.

The problem of very low-performing learners can negatively impact the ensemble decision since they do not learn the problem effectively. Therefore, a threshold value of 70% was set based on the individual results of deep learning models, and models belonging to DarkNet19, Shufflenet, InceptionV3, DenseNet201, and Xception architectures were selected for use in the ensemble approach. Table 3 provides the individual accuracy of the correct classification performances of the top learners and the accuracy of the correct classification performances of the predictions produced by the meta-learner on the test set. Table 4 provides the evaluation metrics as an average of 10 folds.

Table 3. The classification accuracy of top models and meta-learner on test set

Model	k-fold										Avg.	σ
	1	2	3	4	5	6	7	8	9	10		
darknet19	80.35	77.60	81.53	78.19	77.60	78.98	81.93	71.32	81.14	80.55	78.92	2.95
shufflenet	83.10	83.89	86.05	81.14	81.93	88.80	80.55	82.51	84.09	83.50	83.56	2.30
inceptionv3	81.93	77.60	78.19	80.16	80.94	84.68	84.68	79.96	83.50	81.34	81.30	2.34
densenet201	74.66	77.01	77.41	72.89	82.12	78.59	78.98	78.98	75.83	80.55	77.70	2.61
xception	75.25	70.33	68.57	68.57	69.35	70.73	71.91	69.16	75.64	73.08	71.26	2.50
ensemble	86.64	83.89	86.64	82.12	86.25	87.62	88.02	85.46	85.66	87.43	85.97	1.72

The ensemble model is the highest with an average accuracy of 85.97%. Darknet19, shufflenet and inceptionv3 models also performed quite well, but no deep learning model achieved a higher percentage accuracy than the ensemble model. This indicates that an ensemble model performs better than the others on the test set. Although densenet201 and xception have a lower average accuracy percentage, they still perform reasonably well. Furthermore, the standard deviation (σ) value shows how consistent the performance of each

model is. The Ensemble model has the lowest standard deviation, indicating that its performance is more consistent.

Table 4. Evaluation metrics of top models and meta-learner on test set

	Accuracy	Specificity	Precision	Recall	F-Measure	G-mean
darknet19	78.92	80.75	80.27	76.98	78.48	78.76
shufflenet	83.56	85.33	84.93	81.99	83.23	83.53
inceptionv3	81.30	84.44	83.69	77.96	80.62	81.06
densenet201	77.70	78.81	78.43	76.58	77.41	77.63
xception	71.26	71.81	71.75	70.84	71.00	71.08
ensemble	85.97	84.54	84.98	87.37	86.12	85.92

Table 4 presents the accuracy, specificity, precision, precision, recall, F-Measure and G-mean metrics for assessing model performance [28]. Proposed ensemble learning achieved better correct classification performance than the individual highest performing ShuffleNet model in 9 out of 10 folds. When looking at the average accuracy values, the ensemble approach showed 14.72% higher performance compared to the worst model and 2.42% higher performance compared to the best model. Additionally, it provided a more stable prediction output according to the standard deviation (σ). Ensemble method shows the highest accuracy, precision, and F-measure, indicating superior performance compared to individual models. Table 5 shows the confusion matrix of the average of the 10-fold cross-validation results of the ensemble model.

Table 5. Confusion matrix of the ensemble model

		Normal	Abnormal
True Class	Normal	219	39
	Abnormal	32	219
		Predicted Class	

4. CONCLUSION

In environments where security controls are tightened, X-ray devices are commonly used with human operators. X-ray systems become inefficient in high-traffic areas or when expertise is required for the recognition of a threat object. Applications such as classification or anomaly detection on X-ray images using deep learning have been widely used, especially in the medical field, but have not received sufficient attention for security purposes. In this research, deep learning methods were examined on laptop X-ray images, some of which contain threat objects, in terms of both individual correct classification performance and proposing an ensemble approach instead of designing a new model architecture. The ensemble approach highlighted the advantages of existing models, resulting in a more stable output with 1.72 lower standard deviation and 87.43% higher correct classification performance compared to all individual models.

There is a limited number of studies in the literature that focus on the ensemble approach for forbidden object detection in X-ray images. In addition to developing new architectures on this topic, different ensemble methods can also be applied.

Declaration of Ethical Standards

The authors declare that they have carried out this completely original study by adhering to all ethical

rules including authorship, citation and data reporting.

Credit Authorship Contribution Statement

Engin EŞME: Methodology, Conceptualization, Resources, Investigation, Writing.
Mustafa Servet KIRAN: Methodology, Conceptualization, Resources, Investigation, Writing, Supervision.

Declaration of Competing Interest

The authors declared that they have no conflict of interest.

Funding / Acknowledgment

This study has been supported by The Scientific and Technological Research Council of Türkiye under Grant 122E024. The authors thank the council for the institutional supports.

Data Availability

Data supporting the findings of this study can be obtained from the corresponding author with reasonable requests to assist in scientific studies.



REFERENCES

- [1] S. Akçay, M. E. Kundegorski, M. Devereux, and T. P. Breckon, "Transfer learning using convolutional neural networks for object classification within X-ray baggage security imagery," in 2016 IEEE International Conference on Image Processing (ICIP), 25-28 Sept. 2016 2016, pp. 1057-1061, doi: 10.1109/ICIP.2016.7532519.
- [2] E. Benedykciuk, M. Denkowski, and K. Dmitruk, "Material classification in X-ray images based on multi-scale CNN," *Signal, Image and Video Processing*, vol. 15, no. 6, pp. 1285-1293, 2021/09/01 2021, doi: 10.1007/s11760-021-01859-9.
- [3] C. Miao et al., "Sixray: A large-scale security inspection x-ray benchmark for prohibited item discovery in overlapping images," in *Proc. IEEE/CVF Conference on Computer Vision and Pattern Recognition (CVPR) 2019*, pp. 2119-2128.
- [4] A. Chang, Y. Zhang, S. Zhang, L. Zhong, and L. Zhang, "Detecting prohibited objects with physical size constraint from cluttered X-ray baggage images," *Knowledge-Based Systems*, vol. 237, p. 107916, 2022.
- [5] F. Shao, J. Liu, P. Wu, Z. Yang, and Z. Wu, "Exploiting foreground and background separation for prohibited item detection in overlapping X-Ray images," *Pattern Recognition*, vol. 122, p. 108261, 2022.
- [6] C. Zhao et al., "BoostTree and BoostForest for ensemble learning," *IEEE Transactions on Pattern Analysis and Machine Intelligence*, 2022.
- [7] Z.-H. Zhou, *Ensemble learning*. Springer, 2021.
- [8] I. H. Witten, E. Frank, and M. A. Hall, "Data mining: Practical machine learning tools and techniques," ed: Morgan Kaufmann, 2016.
- [9] A. Ait Nasser and M. A. Akhloufi, "A review of recent advances in deep learning models for chest disease detection using radiography," *Diagnostics*, vol. 13, no. 1, p. 159, 2023.

- [10] M. Radak, H. Y. Lafta, and H. Fallahi, "Machine learning and deep learning techniques for breast cancer diagnosis and classification: a comprehensive review of medical imaging studies," *Journal of Cancer Research and Clinical Oncology*, pp. 1-19, 2023.
- [11] W. Khan, N. Zaki, and L. Ali, "Intelligent pneumonia identification from chest x-rays: A systematic literature review," *IEEE Access*, vol. 9, pp. 51747-51771, 2021.
- [12] H. Wang, H. Li, W. Gao, and J. Xie, "PrUb-EL: A hybrid framework based on deep learning for identifying ubiquitination sites in *Arabidopsis thaliana* using ensemble learning strategy," *Analytical Biochemistry*, vol. 658, p. 114935, 2022.
- [13] E. Putin et al., "Deep biomarkers of human aging: application of deep neural networks to biomarker development," *Aging (Albany NY)*, vol. 8, no. 5, p. 1021, 2016.
- [14] P. Peng, C. Marceau, and D. M. Villeneuve, "Attosecond imaging of molecules using high harmonic spectroscopy," *Nature Reviews Physics*, vol. 1, no. 2, pp. 144-155, 2019.
- [15] R. Xie and M. Marsili, "A random energy approach to deep learning," *Journal of Statistical Mechanics: Theory and Experiment*, vol. 2022, no. 7, p. 073404, 2022.
- [16] S. Kolte, N. Bhowmik, and Dhiraj, "Threat Object-based anomaly detection in X-ray images using GAN-based ensembles," *Neural Computing and Applications*, pp. 1-16, 2022.
- [17] Q. Kong, N. Akira, B. Tong, Y. Watanabe, D. Matsubara, and T. Murakami, "Multimodal Deep Neural Networks Based Ensemble Learning for X-Ray Object Recognition," 2019: Springer, pp. 523-538.
- [18] R. Zhou, F. Wang, X. Fang, A. Fenster, and H. Gan, "An adaptively weighted ensemble of multiple CNNs for carotid ultrasound image segmentation," *Biomedical Signal Processing and Control*, vol. 83, p. 104673, 2023.
- [19] A. H. Ahmed, M. Al Radi, and N. Werghi, "An Ensemble Learning Method Based on Deep Neural and Pca-Based Svm Network for Baggage Threat and Smoke Recognition," in *Proc. Advances in Science and Engineering Technology International Conferences, Dubai, 2023*, pp. 1-6.
- [20] A. Kumar and J. Mayank, "Ensemble learning for AI developers," *BAPress: Berkeley, CA, USA*, 2020.
- [21] E. O. Kiyak, "Data Mining and Machine Learning for Software Engineering," *Data Mining-Methods, Applications and Systems*, 2020.
- [22] X. Zhang, X. Zhou, M. Lin, and J. Sun, "Shufflenet: An extremely efficient convolutional neural network for mobile devices," in *Proc. IEEE conference on computer vision and pattern recognition*, 2018, pp. 6848-6856.
- [23] J. Redmon and A. Farhadi, "YOLO9000: better, faster, stronger," in *Proc. IEEE conference on computer vision and pattern recognition*, 2017, pp. 7263-7271.
- [24] J. Redmon and A. Farhadi, "Yolov3: An incremental improvement," *arXiv preprint arXiv:1804.02767*, 2018.
- [25] C. Szegedy et al., "Going deeper with convolutions," in *Proc. IEEE conference on computer vision and pattern recognition*, 2015, pp. 1-9.
- [26] G. Huang, Z. Liu, L. Van Der Maaten, and K. Q. Weinberger, "Densely connected convolutional networks," in *Proc. IEEE conference on computer vision and pattern recognition*, 2017, pp. 4700-4708.
- [27] F. Chollet, "Xception: Deep learning with depthwise separable convolutions," in *Proc. IEEE conference on computer vision and pattern recognition*, 2017, pp. 1251-1258.
- [28] Ž. Vujović, "Classification model evaluation metrics," *International Journal of Advanced Computer Science and Applications*, vol. 12, no. 6, pp. 599-606, 2021.



REFRACTIVE INDEX BASED DETECTION WITH A HIGH SENSITIVITY BIOSENSOR ENHANCED BY GRAPHENE

¹Ahmet Murat ERTURAN , ^{2,*}Seyfettin Sinan GÜLTEKİN 

^{1,2}Konya Technical University, Engineering and Natural Sciences Faculty, Electrical and Electronics Engineering
Department, Konya, TÜRKİYE

amerturan@ktun.edu.tr, ssgultekin@ktun.edu.tr

Highlights

- A highly sensitive biosensor based on graphene has been proposed.
- The achievement of 96.2% high transmission resonance mode was made possible by the strip gap created to enhance the excitation of graphene plasmons.
- The findings indicate that when analytes with varying refractive indices are exposed to the sensor surface, the sensor's sensitivity is 6282 nm/RIU.



REFRACTIVE INDEX BASED DETECTION WITH A HIGH SENSITIVITY BIOSENSOR ENHANCED BY GRAPHENE

¹Ahmet Murat ERTURAN^{ORCID}, ^{2,*} Seyfettin Sinan GÜLTEKİN^{ORCID}

*Konya Technical University, Engineering and Natural Sciences Faculty, Electrical and Electronics Engineering
Department, Konya, TÜRKİYE*

amerturan@ktun.edu.tr, ssgultekin@ktun.edu.tr

(Received: 02.05.2024; Accepted in Revised Form: 28.07.2024)

ABSTRACT: Over the past decade, optical sensors have made significant advances. An optical sensor examines the environmental impact through the change of an optical signal and offers advantages such as low cost and label-free detection. In this study, a sensor consisting of a single graphene layer and a slit positioned on the substrate is proposed. The strip gap made to improve the excitation of graphene plasmons allowed to achieve 96.2% high transmission resonance mode. This demonstrates the ability of the sensor surface to detect changing environmental conditions. The results show that the sensitivity of the sensor is 6282 nm/RIU when the sensor surface is exposed to analytes with different refractive indices. The use of a single graphene sheet eliminates the need for a metal resonator and achieves a higher sensitivity compared to some experiments recently published in the literature. Thus, the disadvantage of significant ohmic losses in metal resonators is avoided. Furthermore, a thorough discussion of various factors, including the modification of the strip gap width on the graphene layer and electrical tunability, led to the achievement of optimal sensitivity.

Keywords: *Graphene, Biosensor, Refractive Index Sensing, Plasmonics, Metamaterials*

1. INTRODUCTION

Early diagnosis of diseases and monitor the environment has grown in importance in recent years, and biosensors have made this possible [1], [2]. Biosensors are used in the detection of disease, studying the results obtained through the influence of target biomolecules on the sensor response [3]. These measurable signals play an important role in detecting the presence of biomolecules. In recent years, optical sensors capable of making high-precision measurements have attracted great attention [4], [5], [6]. Another issue that is as important as accurate early diagnosis is that this detection can be made with high sensitivity. Metamaterial-based plasmonic biosensors have great advantages in making these sensitive measurements [7]. These structures are basically obtained by dielectric and metal layers placed on a thin metal film, and this causes the interaction of light with matter along with high-energy surface plasmons developing at the dielectric-metal interface [8]. This movement at the interface changes the behavior of light and allows biomolecules to be detected sensitively depending on the collective refractive index difference. In contrast to these advantages, the most important disadvantage of metal-structured plasmonic biosensors is their high electrical loss [9]. There are also limitations such as production difficulties, cost, volume and oxidation by interference with bioanalytes [10]. In addition, their plasmonic properties are fixed and they provide spectral responses that cannot be changed after fabrication process. For a different spectral response, the design, fabrication and characterization steps must be redone for the specific spectral range.

In recent years, graphene has become an important cornerstone for biosensing. It is very desirable due to its amazing electrical qualities, versatility, and ease of production [11], [12], [13]. Graphene consists of carbon atoms arranged in a two-dimensional structural honeycomb pattern and has the advantages of strong electrical conductivity and chemical tunability [14]. These graphene-based biosensors have been used in many sensing studies, from detection of cancer cells to DNA Detection [15], [16]. Graphene's high electron mobility and chemical tunability can be integrated into different

*Corresponding Author: Seyfettin Sinan GÜLTEKİN, ssgultekin@ktun.edu.tr

optical devices, enabling the optical sensor to operate in various spectral ranges [17]. Metals such as gold and silver are used in plasmonic sensors to improve the light-matter interaction by increasing collective electron emission at the surface; nevertheless, a significant disadvantage of these materials is their high dielectric constant and ohmic losses [18]. Surface plasmons, which are based on the optical characteristics of graphene, can be employed to offer strong confinement and large-area augmentation of electromagnetic waves in order to get over this drawback.

This article proposes a low-cost, high-performance, electrically tunable biosensor that is derived from solely graphene layers, as opposed to conventional metal-based biosensors. The graphene layer was completely coated on the substrate and a slit was formed at the center position to enhance the surface plasmon polariton effect. The impact of this slit on the transmission spectrum was investigated using numerical analysis, and a comprehensive discussion was held on the influence of graphene plasmons surrounding the slit. Furthermore, the spectrum response of the sensor at various fermi energies in the terahertz frequency range resulting from graphene's chemical tunability was investigated. In addition, the effect of the relaxation time of graphene on the spectral response is also discussed in detail. Finally, the spectrum response to environmental refractive index was investigated using bioanalytes with varying refractive indices on the sensor surface. These samples showed a high sensitivity detection capacity at 6282 nm/RIU.

2. MATERIAL AND METHODS

The proposed graphene-based biosensor's single-cell image and spectral transmission response are displayed in Figure 1. There is a single-layer graphene sheet on the SiN substrate and a longitudinal slit in the middle of the graphene sheet. The excitation of graphene plasmons is intended to be amplified around this slit. The period of the single-cell along the x and y axis was determined as $P=600$ nm. Thus, the left and right portions of the graphene slit include graphene layers that were the same height and width. The width of the graphene slit was determined as $g=60$ nm and the width of the layers around the slit along the x-axis was determined as $L=270$ nm. Numerical analysis of the single layer graphene biosensor was performed using the Finite Difference Time Domain (FDTD) method. Periodic boundary conditions were employed along the x and y axes and Perfectly Matched Layer (PML) boundary conditions were used along the z axis to determine the simulation boundary conditions. The illumination is directed at a zero-degree angle along the z-axis towards the sensor surface under x-polarized light. The transmission signal shown in Figure 1b illustrates the spectral response of the graphene-based biosensor, revealing a transmission resonance mode of 96.2% at a wavelength of 37.37 μm with a 60 nm graphene slit. The changes in both the rate and bandwidth of the transmission signal caused by the slit created on the graphene layer are discussed in the following sections. However, it should be noted that in each part where the width of the graphene slit is not specified, the width is 60 nm, which is optimized to give the result in Figure 1b.

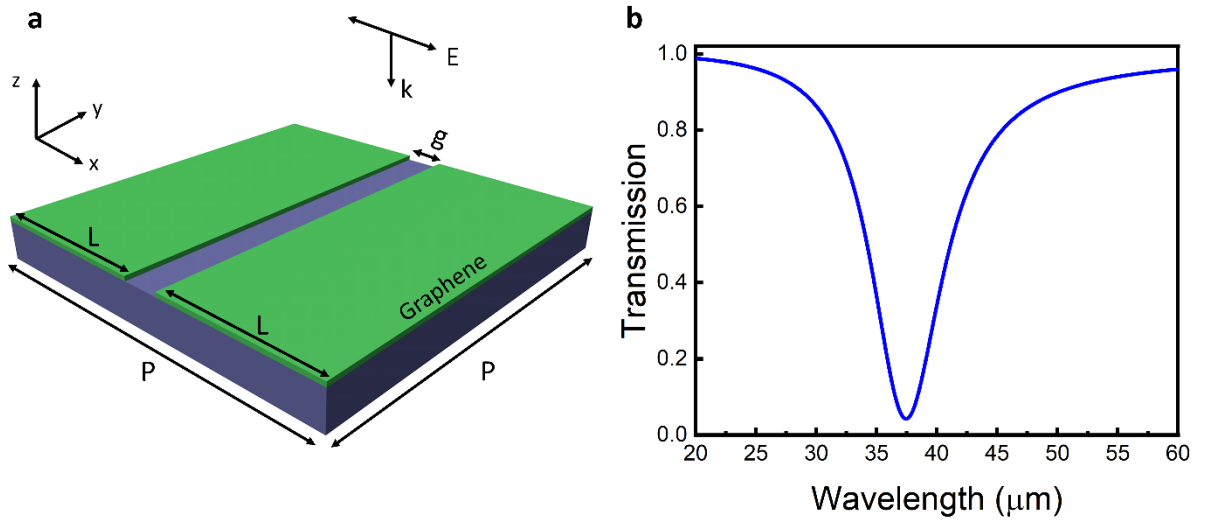


Figure 1. (a) The perspective view of a graphene-based biosensor. L refers to the size of the graphene plate, g to the gap, and P to the single-cell period. (b) Transmission signal graph of graphene biosensor ($g=40$ nm, $Ef=0.4$ eV, $\tau=0.5$).

Graphene is modeled using the Kubo formula in the computational study carried out to investigate the optical properties of the suggested single-layer graphene-based biosensor. To describe the light-matter interaction in metal-based structures, the Drude (and later Lorentz) model is used, which describes in a simple and intuitive way how electrons are transported, and this model underlies the definition of electrical permittivity [19]. In graphene-based structures, this definition is made using the Kubo formula and the isotropic surface conductivity of graphene is expressed as intra-band and inter-band transitions (Eq-1) [20]. This model allows analysis of the conductivity, permeability, chemical potential, plasma frequency, and relaxation time of graphene.

$$\sigma = \sigma_{\text{int } ra}(\omega, \mu_c, \Gamma, T) + \sigma_{\text{int } er}(\omega, \mu_c, \Gamma, T) \quad (1)$$

According to Equation 1, graphene's conductivity depends on the light's energy and the electron-hole pair [20]. Graphene's extraordinary properties can be modified depending on external factors. Particularly, the application of electrostatic fields can change graphene's electronic structure, influencing the antenna resonance mode. Additionally, changes in the relaxation time determined by conductivity affect the optical response. The surface conductivity of graphene based on the Kubo formula is shown in Equations 2 and 3.

$$\sigma_{\text{int } ra}(\omega, \mu_c, \Gamma, T) = i \frac{e^2 k_B T}{\pi \hbar^2 (\omega + 2i\Gamma)} \left(\frac{\mu_c}{k_B T} + 2 \ln \left(e^{-\frac{\mu_c}{\hbar k_B T}} + 1 \right) \right) \quad (2)$$

$$\sigma_{\text{int } er}(\omega, \mu_c, \Gamma, T) = i \frac{e^2}{4\pi \hbar} \ln \frac{2|\mu_c| - (\omega + 2i\Gamma)\hbar}{2|\mu_c| + (\omega + 2i\Gamma)\hbar} \quad (3)$$

Here, μ_c represents the chemical potential, Γ is the scattering rate, T is temperature, e is the electron charge, $\hbar = h/2\pi$ is the reduced Planck's constant, and k_B is the Boltzmann constant. Figure 2 shows the electrical field and charge distribution graphs of the graphene-based biosensor operating in transmission resonance mode. The change in the electric field and charge density along the slit on the single-layer graphene structure showed a distinct behavior. The structure where the electric field distribution is studied in Figure 2a shows that the field distribution along the slit is severely restricted, whereas the field distribution along the left and right graphene plates is significantly decreased. Graphene plasmons evolving across the gap can explain the effect of confining this field on the gap. Figure 2b shows the charge distribution graph along the slit. This graph illustrates how the oscillation of oppositely charged

plasmons at the left and right borders of the slit results in a dipolar charge distribution. This dipolar effect spread strongly across the slit and strengthened the spectral response. In Figure 2c, the electric field effect developing along the slit of the graphene-based biosensor is shown along the z axis. This graph demonstrates the electric field's concentration at the slit's boundaries, providing support for Figure 2a. These physical concepts provide an understanding of the biosensor's strong resonant transmission mode.

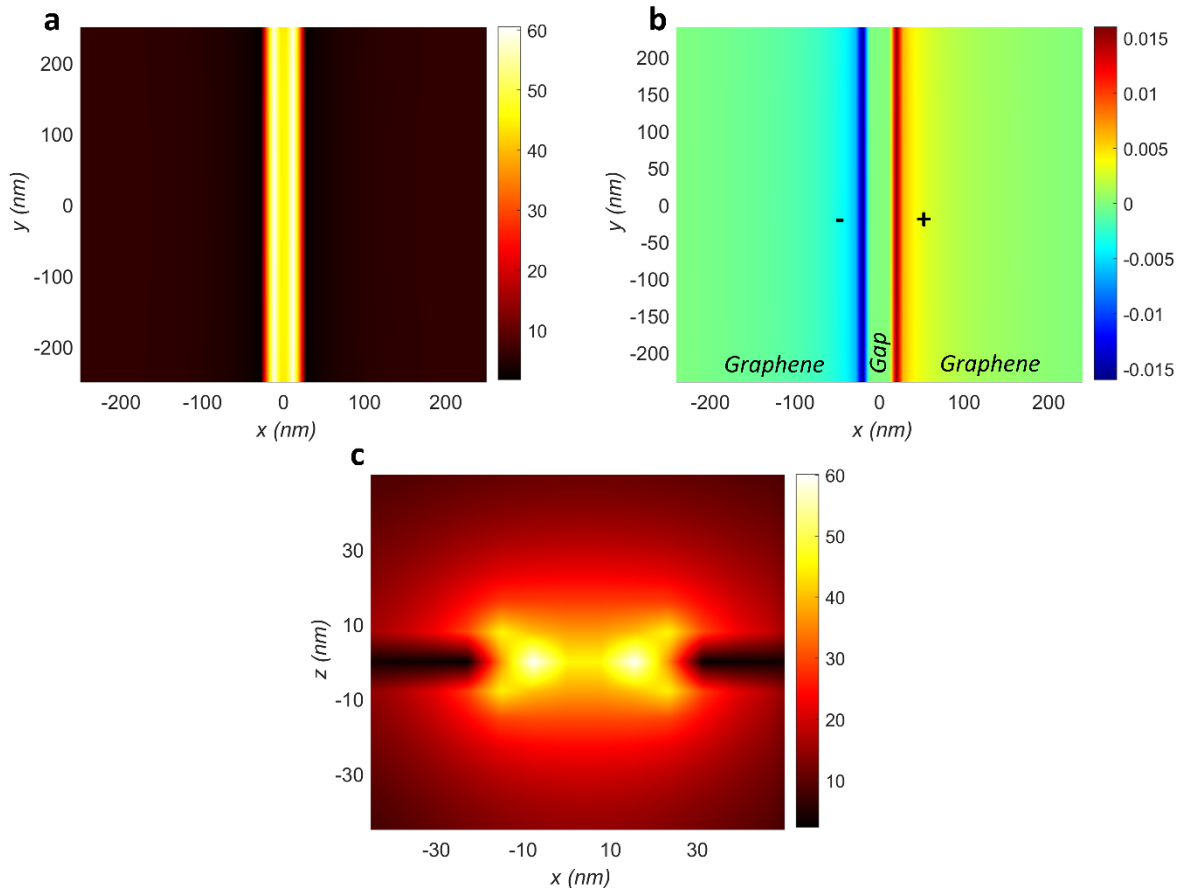


Figure 2. (a) The electric field developing in the graphene slit (gap) is shown in the x-y plane. (b) Charge distribution graph in which the dipole distribution occurs around the graphene slit (gap). (c) Representation of the electric field in the slit in the x-z plane.

Figure 3 demonstrates how altering the slit width in the suggested graphene-based biosensor affects the transmission resonance mode. It has been observed that the resonance mode of the transmission signal shifts to lower wavelengths as the gap between graphene plates increases. This effect in the resonance mode can be explained as an effect of the spatial distribution of graphene plasmons. Another effect is the bandwidth change in the resonant signal with increasing slit width. As the slit width increased, the bandwidth of the resonance mode decreased. Figure 3b uses a scatter plot to further investigate the shift in resonant transmission modes from Figure 3a. This graph indicates that a bigger resonance peak shift was initially produced by increasing the slit width, but that the resonance peak shift decreased as the slit width reached the threshold value. The wide-area dispersion of graphene plasmons is observed to continue at a certain rate, and the effect shown here is compatible with the effects reported in the relevant studies [21], [22]. The numerical analyses presented here illustrate how the size of the split between graphene plates affects the resonance mode, which allows for the optimization of this effect.

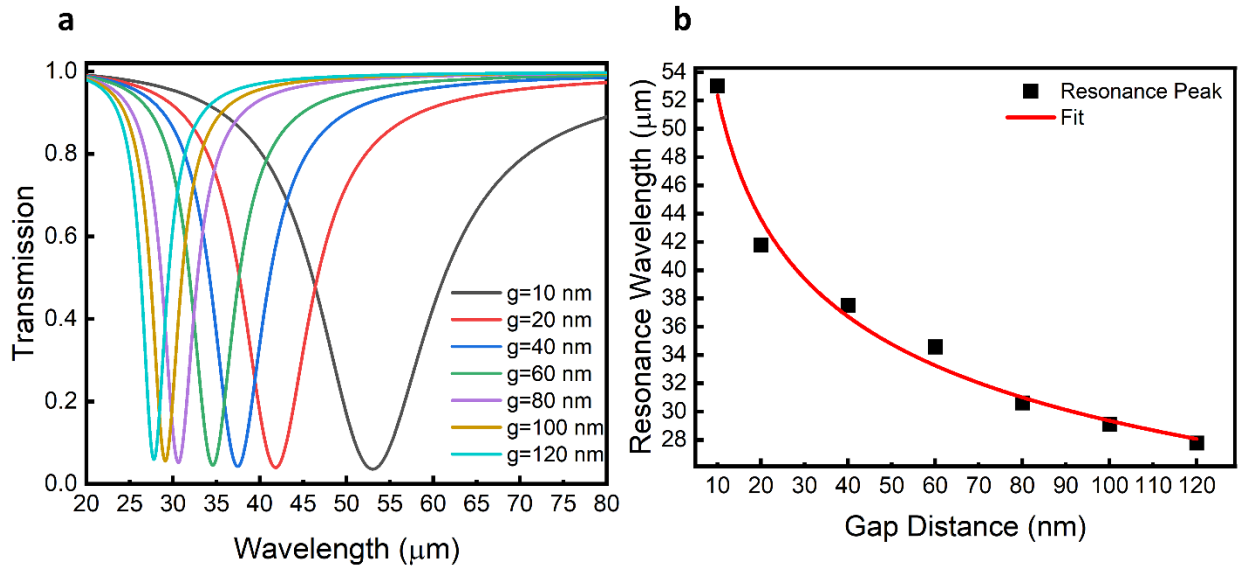


Figure 3. (a) The resonance mode is demonstrated to shift to various wavelengths in response to variations in the gap width(g). (b) The resonance wavelength variation as a function of slit width is demonstrated.

Figure 4 examines how variations in the Fermi energy level affect the resonance wavelength and transmission rate of the graphene-based biosensor. In Figure 4a, the Fermi energy level varied in 0.1 eV increments between 0.1 eV and 0.7 eV, and the signal underwent a blue shift as the Fermi energy level increased. Furthermore, at 0.1 eV energy level, the transmission rate was approximately 75%, but at 0.7 eV energy level, it increased to approximately 99%. The strong interaction in graphene plasmons due to the increase in the charge carrier density of graphene explains this increase. The increase in the transported charge density allows electrostatic gating, shifting the signal to lower wavelengths, increasing the transmission rate and reducing the bandwidth. Figure 4b is illustrated in order to more clearly analyze the effect of this change in the Fermi energy level on the wavelength shift. This graph indicates that while the growing charge density resulting from an increase in Fermi energy level initially exhibited a dramatic wavelength shortening tendency, as it approached the limit values of the graphene charge carrier, it began to exhibit a decreasing trend. This negative correlation between the Fermi energy level and the wavelength explains that graphene plasmons oscillate more strongly and the wavelength becomes shorter with the increase in the fermi energy level. Because greater charges correspond in higher electron density, which expands the space that the graphene layer can enclose. The primary benefit of this is that its static tunability eliminates the need for remanufacturing, allowing it to be utilized in differentiable applications. Thanks to its electrical tunability without changing the physical structure, it can suit different requirements and be integrated into different systems. In addition, changing the Fermi energy can improve the performance of graphene-based sensors and transistors by adjusting the electron transition path. While electrically non-tunable devices require extensive materials for different functions, an electrically tunable graphene-based sensor has a flexible application capability without the need for material changes. This results in a highly flexible tunable sensor platform that can achieve resonance modes at different wavelengths without the need for re-fabrication. In addition to increasing the electrical and optoelectronic flexibility of the sensor, it also eliminates the additional cost burden arising from refabrication.

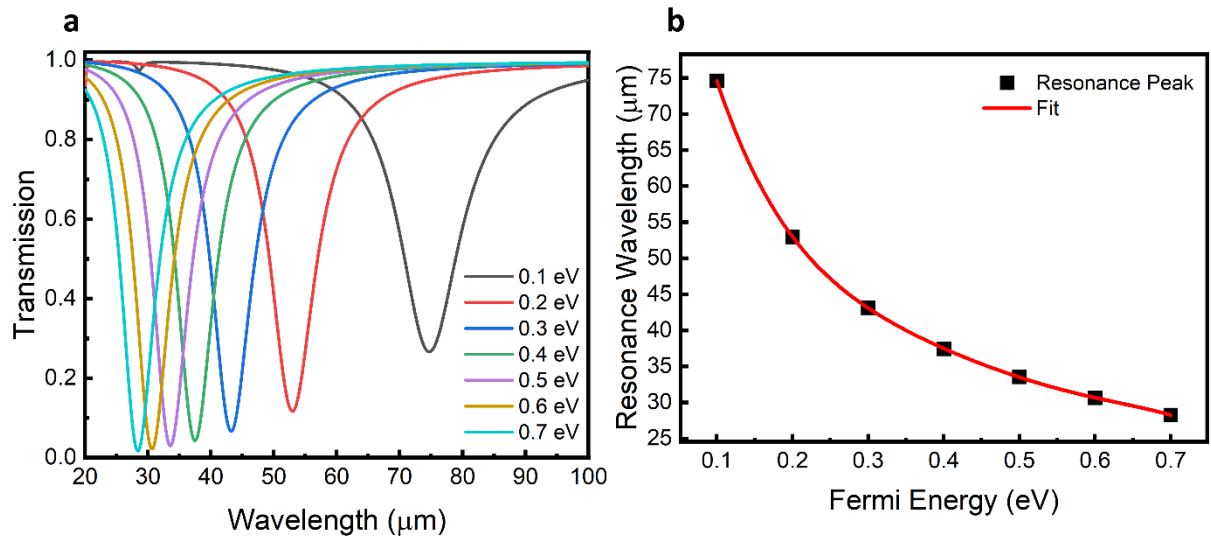


Figure 4. (a) The change in resonance mode due to gradually changing the Fermi energy level. (b) The tendency of the Fermi energy level to switch all resonance modes

Electron mobility is one of the most significant characteristics of graphene. The interaction between electron mobility and chemical potential depends on the relaxation dynamics of electrons within the unique two-dimensional structure of graphene. There is a mean time during the movement of electrons in graphene caused by collisions or scattering. This time indicates the resistance to the mobility of electrons in graphene and the elapsed time. Figure 5a clearly shows that despite the varying relaxation time, the transmission resonance peak remains at the same wavelength. Figure 5b illustrates the effect of changing relaxation time on the transmission percentage. The decreasing carrier density reduces collective oscillations, pulling the transmission rate down from 96% to 74%.

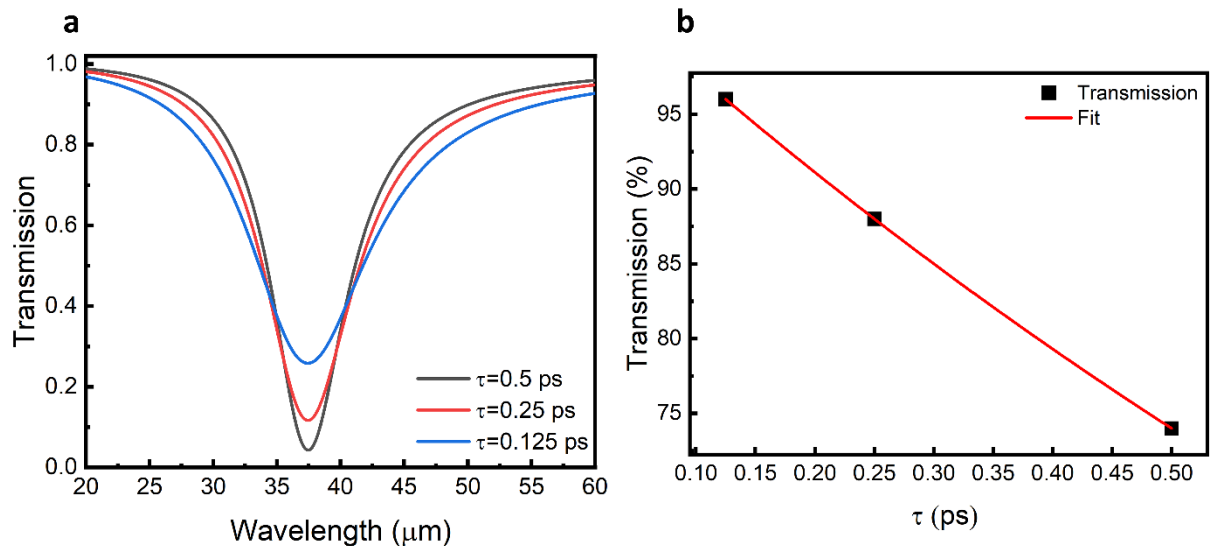


Figure 5. (a) The effect of relaxation time on resonance mode. (b) The variation in transmission strength as a function of relaxation time is demonstrated.

Finally, the sensitivity of the sensor to biomolecular detection was examined. Figure 6a shows the response of the graphene structure with a gap to the changing refractive index of the medium in terms of the transmission resonance mode. In this instance, the medium's refractive index (RI) was changed from 1 to 2, which allowed for the analysis of the transmission spectrum. The characteristic shift of the transmission resonance mode towards longer wavelengths is noticed when RI values grow. This change

affects the coupling conditions of plasmonic excitations and is a direct result of the dielectric shift in the environment surrounding graphene. The increase in the refractive index on the sensor surface is an indicator of an increase in density, and with this increase, a shift to longer wavelengths occurs in order to maintain the resonance mode. The relationship between an increase in refractive index and a rise in resonance wavelength is graphically depicted in Figure 6b. The graph indicates that there is a linear rise in behavior for the 11 points that were obtained in 0.1 increments from $n=1$ to $n=2$. The graph, which is represented by the equation $y=9.535x+27.44$, demonstrates that the wavelength increases linearly with each unit change in RI values. The sensitivity of biosensors can be expressed as a function between the refractive index change per unit and the resonance wavelength change. The sensitivity of the biosensor proposed in this study is computed and expressed with the formula $S=\Delta\lambda/\Delta n$. As a result, 6282 nm/RIU was determined to be the sensor's sensitivity based on the resonance mode caused by $n=1$ refractive index and the resonance mode variation caused by $n=1.1$ refractive index. The sensor sensitivity was computed and the wavelength magnitudes based on the resonant mode peaks were established during this measurement. The graph in Figure 6b shows the linear increase of each point and proves that the sensor will show similar sensitivity at all increments. This level of sensitivity is very sensitive and can be used in biosensing applications.

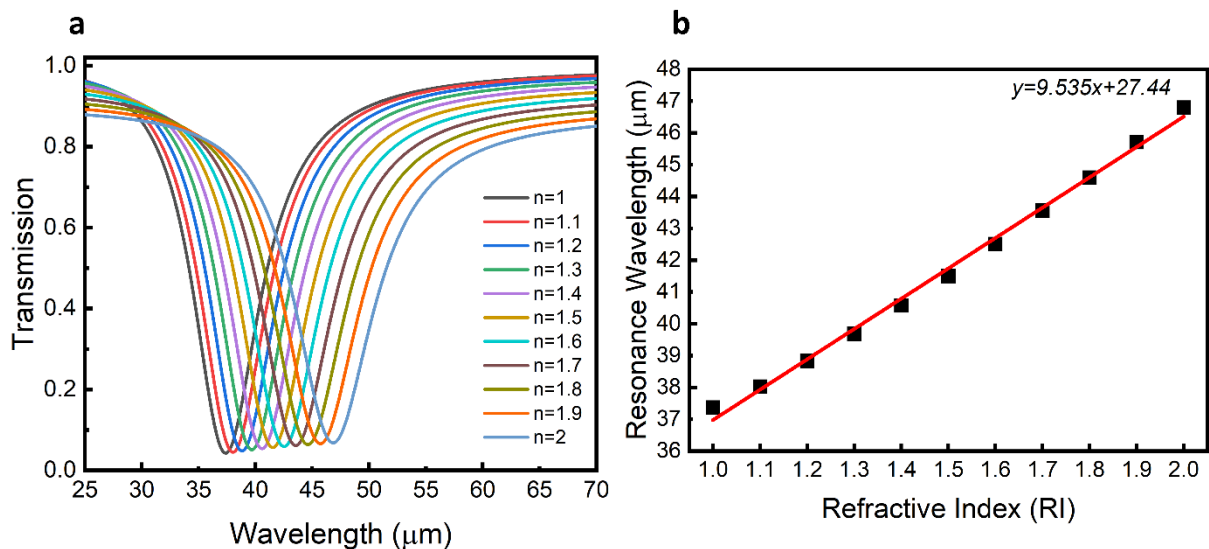


Figure 6. (a) The spectral response of graphene sensor for varying refractive index. (b) The linear relation between the resonance mode of the sensor and the change in refractive index surrounding it.

Table 1 shows recent plasmonic biosensors along with sensor types, materials, and sensitivity data. Sensitivity conditions for biosensors have a direct impact on the sensor's accuracy of detection. Especially for label-free sensing, measuring the resonance mode response due to different refractive indices determines the sensitivity [[23], [24], [25], [26], [27], [28], [29], [30]]. In the literature, metal-based biosensors have been shown to achieve sensitivity rates as high as 2610 nm/RIU. However, biosensors with these metal structures have serious disadvantages due to their cost, difficulty in production and oxidation by bioanalytes. In addition, the high ohmic loss of metals limits the propagation and reduces the impact of evolving plasmons. They also require remanufacturing after they are built since they cannot be statically adjusted to different resonance modes. On the other hand, graphene offers benefits including strong field restrictions, minimal losses, and low prices because of its exceptional electrical and optical properties. These benefits have led to discussions on graphene-based sensors and the proposal of highly sensitive sensors like 2900 nm/RIU. The graphene-based biosensor proposed in this article has been shown to have a stronger detection ability compared to similar studies, showing a sensitivity rate of 6282 nm/RIU. In addition to the advantage of high sensitivity, the proposed biosensor structure also offers advantages such as low cost and static tunability. In this way, it becomes easier to

integrate into different sensing applications that require different resonance modes.

The fabrication of this graphene-based biosensor, which exhibits strong detection ability in numerical analysis, is carried out by following several different nanofabrication steps. Graphene is grown using methods such as chemical vapor deposition (CVD) and can be transferred to any desired surface. Graphene grown on a copper foil is transferred to the surface with a support layer such as polymethyl methacrylate (PMMA) in order to be transferred safely. Then, the copper foil on the surface is removed using Ferric Chloride solid. Single-layer graphene transfer is achieved by cleaning the dissolved PMMA layer. Electron beam lithography (EBL) and reactive ion etching (RIE) methods can be used to create a 40 nm wide slit in the middle of the monolayer graphene layer on the surface. The surface is coated with EBL positive resistivity PMMA, baked, and the 40 nm wide gap is subjected to electron bombardment. Then, the chip is kept in Methyl isobutyl ketone (MIBK) liquid and the area exposed to the electron beam is developed. The sensor is immersed in IPA and rinsed, and a 40 nm wide slit is opened up to the graphene layer. Subsequently, RIE is utilized to etch the graphene layer, creating a precise 40 nm wide strip.

Table 1. The sensitivity values obtained from recent literature articles

	Year	Sensor structure type	Material	S (nm/RIU)
[23]	2016	Plasmonic Au Sensor	Au	623
[24]	2017	Plasmonic Ag Sensor	Ag	2610
[25]	2018	Metal-insulator-metal (MIM) waveguide coupled with concentric double rings resonator (CDRR)	Ag	1060
[26]	2019	Plasmonic Graphene Ribbon	Graphene	2900
[27]	2020	Plasmonic Ag Sensor	Ag	1380
[28]	2021	Plasmonic Sensor	Si/Au	1320
[29]	2022	Plasmonic Perfect Absorber	LiNbO3/Graphene/Au	981
[30]	2023	Plasmonic Ring Resonator	Si/Graphene	2200
This work	2024	Plasmonic Graphene Sensor	SiO2/Graphene	6282

4. CONCLUSIONS

In this paper, a graphene-based biosensor is proposed to eliminate the disadvantages of metal-based plasmonic biosensors. The graphene monolayer is placed on the substrate and a cavity is formed in the center of this layer. This graphene cavity has a high transmission resonance mode of 96.2% due to the limited propagation of graphene plasmons around it. The excellent electrical and optical capabilities of graphene have been exploited with this evolving resonance mode. The effects of the width of the graphene cavity and the relaxation time of the graphene on the transmission resonance mode are discussed in detail and the optimum transmission mode is determined. In addition, the electrical tunability of graphene is exploited to show that the antenna shifts to different resonant modes at varying fermi energy levels, resulting in static tunability. The variation of the sensor resonance mode against the changing refractive index on the sensor surface is thoroughly examined after the optimal transmission

mode with all of these parameters has been found. The results show that the sensor has a high sensitivity of 6282 nm/RIU.

Declaration of Ethical Standards

Authors declare to comply with all ethical guidelines including authorship, citation, data reporting, and publishing original research.

Declaration of Competing Interest

The authors declare that they have no known competing financial interests or personal relationships that could have appeared to influence the work reported in this paper.

Funding / Acknowledgements

No funding is available for this research.

Data Availability

Data will be made available on request.

5. REFERENCES

- [1] A. Jarahi Khameneh *et al.*, "Trends in electrochemical biosensors for the early diagnosis of breast cancer through the detection of relevant biomarkers," *Chemical Physics Impact*, vol. 8, no. September 2023, p. 100425, 2024, doi: 10.1016/j.chphi.2023.100425.
- [2] S. Mummareddy, S. Pradhan, A. K. Narasimhan, and A. Natarajan, "On demand biosensors for early diagnosis of cancer and immune checkpoints blockade therapy monitoring from liquid biopsy," *Biosensors (Basel)*, vol. 11, no. 12, 2021, doi: 10.3390/bios11120500.
- [3] J. Yoon, M. Shin, T. Lee, and J. W. Choi, "Highly sensitive biosensors based on biomolecules and functional nanomaterials depending on the types of nanomaterials: A perspective review," *Materials*, vol. 13, no. 2, pp. 1–21, 2020, doi: 10.3390/ma13020299.
- [4] D. Bhatia, S. Paul, T. Acharjee, and S. S. Ramachairy, "Biosensors and their widespread impact on human health," *Sensors International*, vol. 5, no. July 2023, p. 100257, 2024, doi: 10.1016/j.sintl.2023.100257.
- [5] N. Bontempi *et al.*, "Highly sensitive biosensors based on all-dielectric nanoresonators," *Nanoscale*, vol. 9, no. 15, pp. 4972–4980, 2017, doi: 10.1039/c6nr07904k.
- [6] A. A. Smith, R. Li, and Z. T. H. Tse, "Reshaping healthcare with wearable biosensors," *Sci Rep*, vol. 13, no. 1, pp. 1–16, 2023, doi: 10.1038/s41598-022-26951-z.
- [7] M. E. Hamza, M. A. Othman, and M. A. Swillam, "Plasmonic Biosensors: Review," *Biology (Basel)*, vol. 11, no. 5, 2022, doi: 10.3390/biology11050621.
- [8] H. Yu, Y. Peng, Y. Yang, and Z. Y. Li, "Plasmon-enhanced light–matter interactions and applications," *NPJ Comput Mater*, vol. 5, no. 1, pp. 1–14, 2019, doi: 10.1038/s41524-019-0184-1.
- [9] H. A. Elsayed *et al.*, "High-performance biosensors based on angular plasmonic of a multilayer design: new materials for enhancing sensitivity of one-dimensional designs," *RSC Adv*, vol. 14, no. 11, pp. 7877–7890, 2024, doi: 10.1039/d3ra08731j.
- [10] Y. V. Stebunov, D. I. Yakubovsky, D. Y. Fedyanin, A. V. Arsenin, and V. S. Volkov, "Superior Sensitivity of Copper-Based Plasmonic Biosensors," *Langmuir*, vol. 34, no. 15, pp. 4681–4687, 2018, doi: 10.1021/acs.langmuir.8b00276.

- [11] M. E. E. Alahi, M. I. Rizu, F. W. Tina, Z. Huang, A. Nag, and N. Afsarimanesh, "Recent Advancements in Graphene-Based Implantable Electrodes for Neural Recording/Stimulation," *Sensors*, vol. 23, no. 24, 2023, doi: 10.3390/s23249911.
- [12] Y. Bai, T. Xu, and X. Zhang, "Graphene-based biosensors for detection of biomarkers," *Micromachines (Basel)*, vol. 11, no. 1, 2020, doi: 10.3390/mi11010060.
- [13] J. Peña-Bahamonde, H. N. Nguyen, S. K. Fanourakis, and D. F. Rodrigues, "Recent advances in graphene-based biosensor technology with applications in life sciences," *J Nanobiotechnology*, vol. 16, no. 1, pp. 1–17, 2018, doi: 10.1186/s12951-018-0400-z.
- [14] V. B. Mbayachi, E. Ndayiragije, T. Sammani, S. Taj, E. R. Mbuta, and A. ullah khan, "Graphene synthesis, characterization and its applications: A review," *Results Chem*, vol. 3, p. 100163, 2021, doi: 10.1016/j.rechem.2021.100163.
- [15] H. N. K. AL-Salman *et al.*, "Graphene oxide-based biosensors for detection of lung cancer: A review," *Results Chem*, vol. 7, no. November 2023, p. 101300, 2024, doi: 10.1016/j.rechem.2023.101300.
- [16] M. T. Hwang *et al.*, "Ultrasensitive detection of nucleic acids using deformed graphene channel field effect biosensors," *Nat Commun*, vol. 11, no. 1, 2020, doi: 10.1038/s41467-020-15330-9.
- [17] D. L. P. and M. F. Ashok K. Sood, Isaac Lund, Yash R. Puri, Harry Efstathiadis, Pradeep Haldar, Nibir K. Dhar, Jay Lewis, Madan Dubey, Eugene Zakar, Priyalal Wijewarnasuriya, "Review of Graphene Technology and Its Applications for Electronic Devices," in *Graphene - New Trends and Developments*, 2015.
- [18] S. H. Oh *et al.*, "Nanophotonic biosensors harnessing van der Waals materials," *Nat Commun*, vol. 12, no. 1, pp. 1–18, 2021, doi: 10.1038/s41467-021-23564-4.
- [19] A. Alabastri *et al.*, "Molding of plasmonic resonances in metallic nanostructures: Dependence of the non-linear electric permittivity on system size and temperature," *Materials*, vol. 6, no. 11, pp. 4879–4910, 2013, doi: 10.3390/ma6114879.
- [20] S. Cynthia, R. Ahmed, S. Islam, K. Ali, and M. Hossain, "Graphene based hyperbolic metamaterial for tunable mid-infrared biosensing," *RSC Adv*, vol. 11, no. 14, pp. 7938–7945, 2021, doi: 10.1039/d0ra09781k.
- [21] R. B. Hwang, "A theoretical design of evanescent wave biosensors based on gate-controlled graphene surface plasmon resonance," *Sci Rep*, vol. 11, no. 1, pp. 1–10, 2021, doi: 10.1038/s41598-021-81595-9.
- [22] Y. Wu, Q. Nie, C. Tang, B. Yan, F. Liu, and M. Zhu, "Bandwidth tunability of graphene absorption enhancement by hybridization of delocalized surface plasmon polaritons and localized magnetic plasmons," *Discover Nano*, vol. 19, no. 1, 2024, doi: 10.1186/s11671-024-03961-6.
- [23] Y. Liang, M. Lu, S. Chu, L. Li, and W. Peng, "Tunable Plasmonic Resonances in the Hexagonal Nanoarrays of Annular Aperture for Biosensing," *Plasmonics*, vol. 11, no. 1, pp. 205–212, 2016, doi: 10.1007/s11468-015-0041-0.
- [24] M. R. Rakhshani and M. A. Mansouri-Birjandi, "Utilizing the Metallic Nano-Rods in Hexagonal Configuration to Enhance Sensitivity of the Plasmonic Racetrack Resonator in Sensing Application," *Plasmonics*, vol. 12, no. 4, pp. 999–1006, 2017, doi: 10.1007/s11468-016-0351-x.
- [25] Z. Zhang *et al.*, "Plasmonic refractive index sensor with high figure of merit based on concentric-rings resonator," *Sensors (Switzerland)*, vol. 18, no. 1, 2018, doi: 10.3390/s18010116.
- [26] H. Yang *et al.*, "High-sensitivity plasmonics biosensor based on graphene ribbon arrays," *2019 7th International Conference on Information, Communication and Networks, ICICN 2019*, pp. 105–108, 2019, doi: 10.1109/ICICN.2019.8834950.
- [27] M. R. Rakhshani, "Optical refractive index sensor with two plasmonic double-square resonators for simultaneous sensing of human blood groups," *Photonics Nanostruct*, vol. 39, no. August 2019, p. 100768, 2020, doi: 10.1016/j.photonics.2020.100768.
- [28] L. Hajshahvaladi, H. Kaatuzian, and M. Danaie, "A high-sensitivity refractive index biosensor based on Si nanorings coupled to plasmonic nanohole arrays for glucose detection in water

- solution," *Opt Commun*, vol. 502, no. August 2021, p. 127421, 2022, doi: 10.1016/j.optcom.2021.127421.
- [29] M. Irfan, Y. Khan, A. U. Rehman, M. A. Butt, S. N. Khonina, and N. L. Kazanskiy, "Plasmonic Refractive Index and Temperature Sensor Based on Graphene and LiNbO₃," *Sensors*, vol. 22, no. 20, 2022, doi: 10.3390/s22207790.
- [30] S. K. Patel, J. Surve, J. Parmar, K. Aliqab, M. Alsharari, and A. Armghan, "SARS-CoV-2 detecting rapid metasurface-based sensor," *Diam Relat Mater*, vol. 132, no. November 2022, p. 109644, 2023, doi: 10.1016/j.diamond.2022.109644.



INVESTIGATION OF THE EFFECT OF ANNUAL AVERAGE TEMPERATURE AND PRECIPITATION CHANGES ON CORS-TR STATIONS: THE CASE OF KSTM STATION

¹Alparslan ACAR , ^{2,*}Sercan BÜLBÜL , ³Fuat BAŞÇİFTÇİ , ⁴Ömer YILDIRIM 

^{1,4} *Gaziosmanpaşa University, Geomatics Engineering Department, Tokat, TÜRKİYE*

² *Konya Technical University, Geomatics Engineering Department, Konya, TÜRKİYE*

³ *Karamanoglu Mehmetbey University, Mapping and Cadastre Programme, Karaman, TÜRKİYE*

¹alparslan.acar@gop.edu.tr, ²sbulbul@ktun.edu.tr, ³fuatbasciftci@kmu.edu.tr, ⁴omer.yildirim@gop.edu.tr

Highlights

- Annual average temperature and precipitation changes
- CORS-TR stations covering the whole of Turkey are effectively used in earthquake researches to determine point positioning.
- GNSS is one of the most effective methods for determining point position by utilizing space technology.



INVESTIGATION OF THE EFFECT OF ANNUAL AVERAGE TEMPERATURE AND PRECIPITATION CHANGES ON CORS-TR STATIONS: THE CASE OF KSTM STATION

¹Alparslan ACAR , ^{2,*}Sercan BÜLBÜL , ³Fuat BAŞÇİFTÇİ , ⁴Ömer YILDIRIM 

^{1,4} Gaziosmanpaşa University, Geomatics Engineering Department, Tokat, TÜRKİYE

² Konya Technical University, Geomatics Engineering Department, Konya, TÜRKİYE

³Karamanoglu Mehmetbey University, Mapping and Cadastre Programme, Karaman, TÜRKİYE

¹alparslan.acar@gop.edu.tr, ²sbulbul@ktun.edu.tr, ³fuatbasçiftci@kmu.edu.tr, ⁴omer.yildirim@gop.edu.tr

(Received: 17.07.2024; Accepted in Revised Form: 02.08.2024)

ABSTRACT: In this study, the effects of meteorological changes on the point positioning of CORS-TR stations were investigated. For this purpose, KURU, SINP, BOYT, CORU, CANK, CMLD, KRBK, KSTM stations were selected. The KSTM station was taken as unknown and adjusted based on other stations. Seasonal normal values of KSTM station in Kastamonu province covering the years 2016-2020 were examined in terms of temperature and precipitation amount. These values were determined according to the minimum, maximum and average value criteria by using Türkiye State Meteorological Service data. For the calculations, IGS-standardized RINEX data of the stations for 5 years and 12 months between 2016 and 2020 and for 10 days on the 11th and 20th days of each month were used. All calculations were processed with Leica Geo Office v8.x. The calculated coordinates were compared with the current coordinates of CORS-TR at the same epoch and examined according to annual temperature and precipitation. In the analyzes, it was tested by statistical method whether all measurements were compatible. When it was examined whether the temperature changes were statistically significant, it was observed that the test values were calculated according to the temperature changes were below the test distribution limit at 95% confidence interval. When it was examined whether the precipitation changes were statistically significant, it was observed that the test values were calculated according to the precipitation changes were below the test distribution limit at 95% confidence interval.

Keywords: CORS-TR, GNSS, Leica Geo Office v8.x, Precipitation, Temperature

1. INTRODUCTION

The Global Navigation Satellite System (GNSS), which is based on the principle of determining the location of a point on the Earth using instantaneous or different techniques, is becoming increasingly important in all areas of our lives. Here, while trying to obtain location information, many error sources that will affect the positioning accuracy may also occur. These; satellite clock and orbit errors, antenna phase center and receiver clock errors, atmospheric errors with ionospheric, tropospheric effects, errors due to signal reflection effect, etc. can be counted as. Elimination of these errors allows instantaneous and highly accurate position and velocity determination of a point on the earth.

GNSS technique applications in increasingly differentiated and diversified application areas such as navigation and transportation applications, meteorological studies, agriculture and hydrology fields, geodetic measurements, data collection for geographic information systems, remote sensing, geoscience studies have become a global monitoring system for collecting, evaluating and delivering data to many users for different methods in certain standards [1].

In addition to enabling both instant and post-process research on the subjects of study, these networks provide users with information such as ionosphere, troposphere corrections, time corrections, satellite orbital ephemeris, etc. The networks are improved, protected and maintained by different institutions/organizations. These networks include International GNSS Service (IGS), which is used globally, and the Continuously Operation Reference Stations-Türkiye (CORS-TR), which is used regionally in Türkiye and allows both post-process and continuously point positioning [2].

*Corresponding Author: Sercan BÜLBÜL, sbulbul@ktun.edu.tr

In recent years, numerous studies have focused on the relationship between GNSS and meteorological changes under Space Weather Conditions (SWCs). The following citations are examples of some of such studies: Bilgen et al., [3], investigated the effect of Meteorological Weather Events on Precise Point Positioning at CORS-TR Stations. In the international paper prepared by Bos et al., [4], coordinates and velocities of 4 GNSS stations with continuous observations were found using time series. It is stated that the coordinates and velocities found have seasonal effects and what these effects are caused by.

Zumberge et al., [5] later proposed Precise Point Positioning (PPP) analysis in GNSS solutions. Nakamura et al., [6] mentioned that the Japanese GPS Earth Observation Network (GEONET) of more than 1200 GPS stations established for earthquake research has been expanded to include scientific applications, meteorology and ionospheric research, and GEONET contributes to the assimilation of GPS precipitable water vapor data into the Japan Meteorological Agency (JMA) Mesoscale Numerical Prediction Model. In the world, studies are ongoing to determine the appropriate model to be selected to obtain high-resolution water vapor distribution in small-scale areas for GNSS tomography [7-9].

Increasingly changing climatic conditions are discussed in national and international policies. In this context, studies are being carried out in various countries on the design and implementation of optimum systems for the prediction of meteorological disasters. This platform provides an overview into weather forecasting processes. This and similar studies will contribute to the identification of natural disasters related to meteorological events. National Center for Atmospheric Research and National Oceanic and Atmospheric Administration (NOAA) Forecast Systems Laboratory, Boulder, USA [10-12] and Department of Meteorology, Florida State University [13], Nottingham University and Met Office UK [14-15], Various meteorological institutions around the world, such as MeteoSwiss in Switzerland [16], the German Weather Service [17], the Danish Meteorological Institute, [18], the Finnish Meteorological Institute, [19], the French Meteorological Office [20], in Italy [21], and at the Shanghai Meteorological Center and the State Main Laboratory for Extreme Weather in collaboration with universities in China [22].

In this study, the effect of meteorological weather events on the location accuracy of the KSTM station between 2016 and 2020 was investigated. For this purpose, the coordinate change of the KSTM station for 5 years (11th - 20th days of each month) was analyzed by comparing space weather conditions and meteorological events.

2. MATERIAL AND METHOD

2.1. Space Weather Conditions and Indices

2.1.1. Space weather conditions

Unexpected irregular variations in the ionosphere of solar or extrasolar origin create space weather conditions. These include galactic cosmic rays, solar radiation storms, ionospheric scintillation, solar extreme ultraviolet (EUV) radiation, auroras, traveling ionospheric disturbance, coronal holes, geomagnetic storms, coronal mass ejection, radiation belts, solar flares and solar wind [23, 24]. These conditions are described in the subsections below and Figure 1 shows some of the space weather conditions and their effects [25].

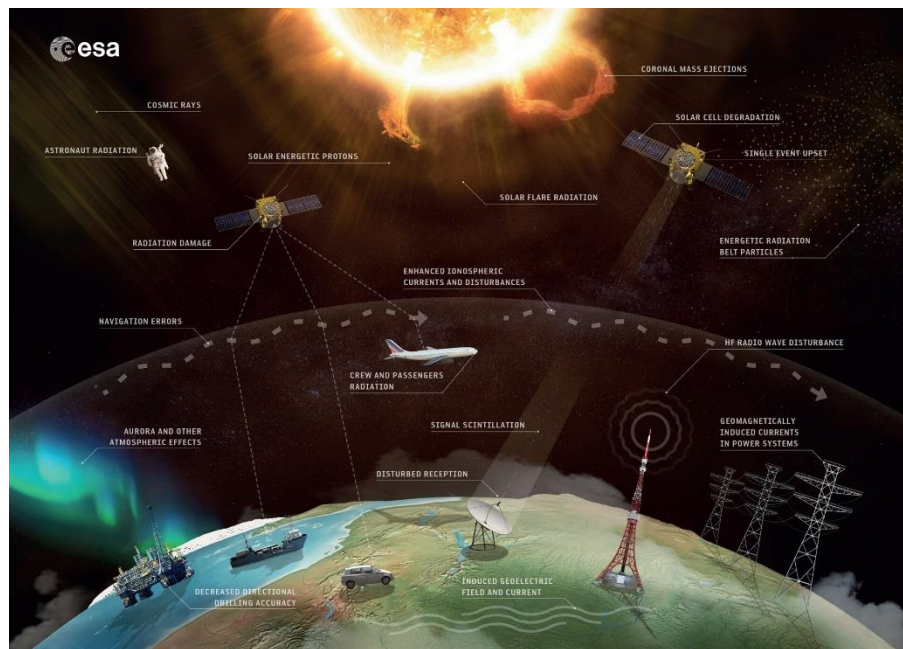


Figure 1. The effects of space weather conditions [25]

2.1.1.1. Solar activity indices

The most widely used index of solar activity, F10.7, has a wavelength of 10.7 cm (2800 MHz) and its unit is Solar Flux Units (sfu) [26]. As one of the most established records of solar activity, F10.7 has been measured since 1947 [27]. The F10.7 index is related to the Sunspot Number (SSN) [28]. F10.7 values vary over a wide range. It can be as low as 50 sfu during sunspot minimum periods and as high as 300 sfu during sunspot maximum periods. The threshold value of this index is 150 sfu, and if it exceeds this value, there is a situation of high solar activity ($1 \text{ sfu} = 10^{-22} \text{ Wm}^{-2} \text{ Hz}^{-1}$) [24].

2.1.1.2. Geomagnetic storm and geomagnetic activity indices

The geomagnetic storm (Kp) index, which stands for planetary index (planetarische Kennziffer), is used to measure and monitor changes in the Earth's magnetic field and to indicate the severity of disturbances in this field. It is also used to study the underlying causes of geomagnetic activity. The Kp index represents the average value of geomagnetic disturbance levels in two horizontal magnetic field components derived at 3-hour intervals, monitored by 13 ground-based magnetic observatories [29, 30]. The Kp index ranges from 0 to 9, where a value of 0 indicates minimal geomagnetic activity and a value of 9 indicates extreme geomagnetic storms [31].

One of the most common indices used to characterize geomagnetic activity is Disturbance storm time (Dst) and its unit is nanoTesla (nT). The index is a measure of the changes in the geomagnetic field during magnetic storms due to the influence of ring current originating in the terrestrial magnetosphere, which leads to a decrease in the horizontal component of the magnetic field. The Dst is obtained from the average of the distortions of the horizontal component (H component) of the Earth's magnetic field strength in the hourly range [32]. The Dst index, which determines whether a storm is occurring, is calculated from data from 4 observatories, Honolulu ($21^{\circ}19'1.2''$ North, 202° East), Kakioka ($36^{\circ}13'8''$ North, $140^{\circ}11'20.4''$ East), San Juan ($18^{\circ}6'39.6''$ North, $293^{\circ}51'00''$ East) and Hermanus ($34^{\circ}25'26.4''$ South, $19^{\circ}13'30''$ East) [33- 35].

2.2. Geolocations

There are two types of point positioning methods: absolute position and relative position determination.

Absolute position is the time elapsed between the signal time from the satellite and the arrival time at the receiver multiplied by the speed of light. Point positioning in this way is called absolute point positioning. The point positioning is calculated as follow;

$$\rho_a^u = \sqrt{(x_u - x_a)^2 + (y_u - y_a)^2 + (z_u - z_a)^2} = c \cdot \Delta\delta_a^u \quad (1)$$

Here; x_u, y_u, z_u are satellite coordinates, x_a, y_a, z_a are the receiver coordinates and $\Delta\delta_a^u$ refers to the time difference between the receiver and the satellite.

The main purpose of the relative point positioning method is to eliminate common errors such as receiver clock errors, satellite clock errors and integer phase ambiguity. This is done by using a differencing approach between observations. The most commonly used differencing methods are single and double differencing (Figure 2).

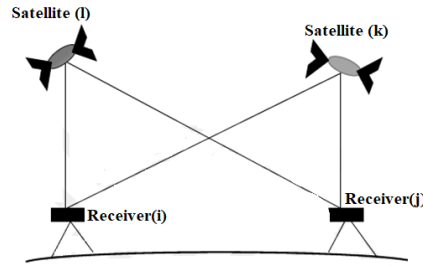


Figure 2. Observations between two receivers and two satellites

Single Differencing (SD) is a method that is performed by taking measurement differences between two receivers measuring to the same satellite or between two satellites and one receiver. This method eliminates clock errors. Single differences between two receivers and one satellite is obtained as;

$$\begin{aligned} \Delta L_{a_{ij}}^{u_l} &= L_{a_i}^{u_l} - L_{a_j}^{u_l} = \Delta\rho_{a_{ij}}^{u_l} + c\Delta\delta_{a_{ij}}^{u_l} + \Delta I_{a_{ij}}^{u_l} + \Delta\rho_{a_{ij}}^{u_l} + \Lambda\Delta N_{a_{ij}}^{u_l} + \varepsilon_{L_{ij}}^k \\ \Delta P_{a_{ij}}^{u_l} &= P_{a_i}^{u_l} - P_{a_j}^{u_l} = \Delta\rho_{a_{ij}}^{u_l} + c\Delta\delta_{a_{ij}}^{u_l} + \Delta I_{a_{ij}}^{u_l} + \Delta\rho_{a_{ij}}^{u_l} + \varepsilon_{P_{ij}}^k \end{aligned} \quad (2)$$

This single differencing method between different receivers of the same satellite eliminates satellite clock errors. For short baselines up to a few kilometers, the ionospheric and tropospheric delay can be neglected due to the differential to the same satellite. A receiver is a single difference between two satellites is obtained as

$$\begin{aligned} \nabla L_{a_i}^{u_{kl}} &= L_{a_i}^{u_k} - L_{a_i}^{u_l} = \nabla\rho_{a_i}^{u_{kl}} + c\nabla\delta_{a_i}^{u_{kl}} + \nabla I_{a_i}^{u_{kl}} + \Delta\rho_{a_i}^{u_{kl}} + \Lambda\nabla N_{a_i}^{u_{kl}} + \varepsilon_{L_i}^{lk} \\ \nabla P_{a_i}^{u_{kl}} &= P_{a_i}^{u_k} - P_{a_i}^{u_l} = \nabla\rho_{a_i}^{u_{kl}} + c\nabla\delta_{a_i}^{u_{kl}} + \nabla I_{a_i}^{u_{kl}} + \Delta\rho_{a_i}^{u_{kl}} + \varepsilon_{P_i}^{lk} \end{aligned} \quad (3)$$

Receiver clock errors are eliminated by single differencing between different satellites and the same receiver [36].

3. DATASET

In this study, the effect of meteorological changes on the positions obtained from CORS-TR was investigated. The study area of the application was selected to cover a total of 8 CORS-TR, including KSTM

(Kastamonu) station in the center and other stations CMLD (Çamlıdere), KRBK (Karabük), KURU (Kurucaşile), SINP (Sinop), BOYT (Boyabat), CORU (Çorum), CANK (Çankırı) (Figure 3).



Figure 3. Application area and selected stations

While investigating the effect of meteorological changes on the positioning of CORS-TR in the study area, changes that may occur due to earthquake movements are not included in the analysis and evaluation.

The meteorological time intervals of the KSTM station (data are associated with Kastamonu province) in the study area were analyzed in two stages: temperature and precipitation. For this purpose, data on the monthly average temperature and monthly total precipitation amounts of the KSTM station point between 2016 and 2020 were obtained on the Meteorological data information presentation system (MEVBIS) of Türkiye State Meteorological Service (Figure 4-5).

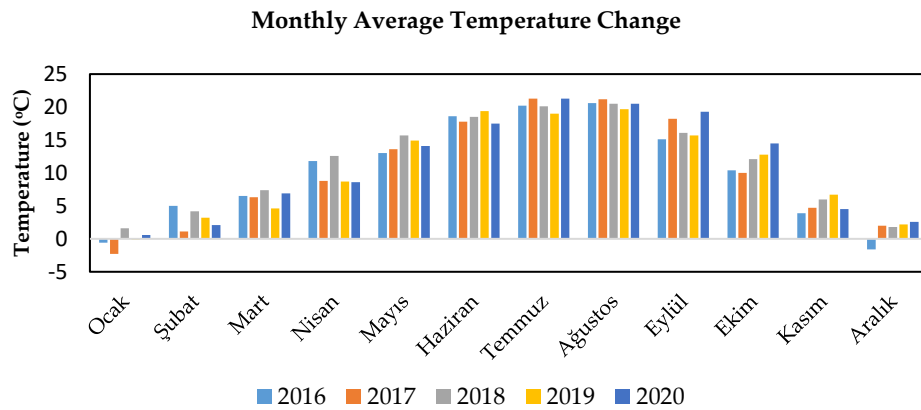


Figure 4. Monthly average temperature change between 2016 and 2020 for KSTM station

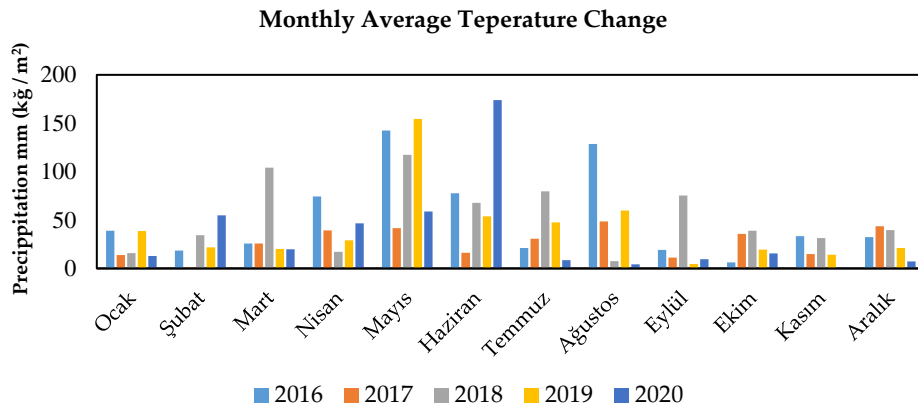


Figure 5. Monthly total precipitation change between 2016 and 2020 for KSTM station

When Figure 4-5 is analyzed, it is determined that January is the month with the lowest temperature and August is the month with the highest temperature between 2016 and 2020. In terms of monthly total precipitation amounts, it was observed that November was the month with the lowest precipitation and May was the month with the highest precipitation.

F10.7, Dst and Kp indices were obtained from <https://omniweb.gsfc.nasa.gov/form/dx1.html>.

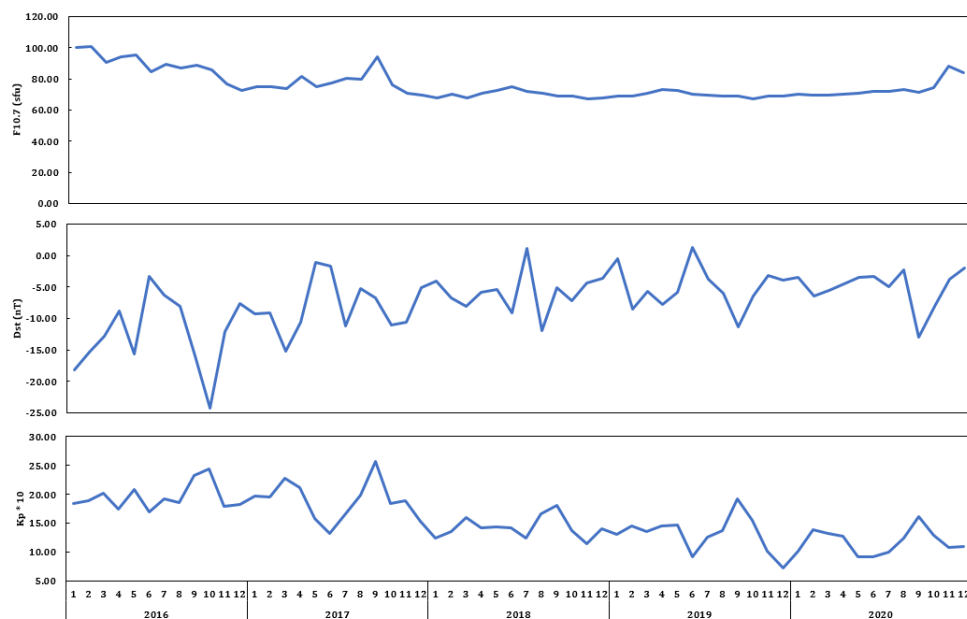


Figure 6. Space weather conditions between 2016 and 2020

When Figure 6 is analyzed, it is concluded that there is no disturbing activity on GNSS measurements in terms of space weather conditions in the selected date range and there is no other effect on coordinate calculations other than GNSS measurement errors.

In the analysis of position changes, 30-second, 24-hour RINEX data of CORS-TR and precise orbital information of GPS and GLONASS satellites (sp3) were used and daily solutions were obtained by processing GNSS data for the selected date range with Leica GeoOffice version 8.1 (LGO v8.1) software. Time series of daily solutions are given in Figure 7.

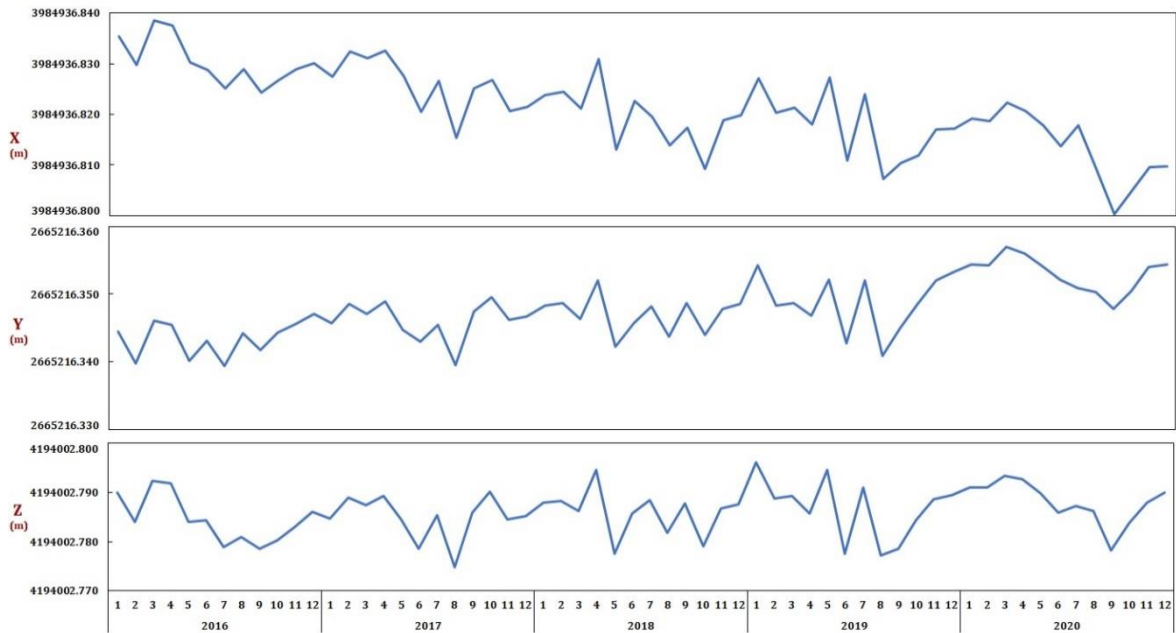


Figure 7. Coordinates of KSTM station between 2016 and 2020 (2005.0)

When Figure 7 is examined, it is seen that the X coordinate changed between 3984936.800 m - 3984936.839 m and there is a negative movement, the Y coordinate changed between 2665216.339 m - 2665216.357 m and there is a positive movement, and the Z coordinate changed between 4194002.775 m - 4194002.796 m.

4. RESULTS

The calculated coordinates of the KSTM station and the CORS-TR coordinates published by the General Directorate of Land Registry and Cadastre (TKGM) (2005.00 epoch) were compared and subjected to statistical testing at 95% confidence interval.

Using calculated coordinates and real coordinates (2005.00 epoch); differences of coordinates,

$$D_{x_{year}} = X_{i_{year}} - X_{2005.00} \quad D_{y_{year}} = Y_{i_{year}} - Y_{2005.00} \quad D_{z_{year}} = Z_{i_{year}} - Z_{2005.00} \quad (4)$$

root mean squared errors (RMSE) of the measures,

$$m_{x_{year}} = \sqrt{\frac{(\sum D_{x_{year}})^2}{n}} \quad m_{y_{year}} = \sqrt{\frac{(\sum D_{y_{year}})^2}{n}} \quad m_{z_{year}} = \sqrt{\frac{(\sum D_{z_{year}})^2}{n}} \quad (5)$$

RMSEs of the differences

$$\begin{aligned} m_{DX} &= \sqrt{(m_{x_{2016}})^2 + (m_{x_{2017}})^2 + (m_{x_{2018}})^2 + (m_{x_{2019}})^2 + (m_{x_{2020}})^2} \\ m_{DY} &= \sqrt{(m_{y_{2016}})^2 + (m_{y_{2017}})^2 + (m_{y_{2018}})^2 + (m_{y_{2019}})^2 + (m_{y_{2020}})^2} \\ m_{DZ} &= \sqrt{(m_{z_{2016}})^2 + (m_{z_{2017}})^2 + (m_{z_{2018}})^2 + (m_{z_{2019}})^2 + (m_{z_{2020}})^2} \end{aligned} \quad (6)$$

and test values;

$$T_X = \frac{D_X}{m_{DX}} \quad T_Y = \frac{D_Y}{m_{DY}} \quad T_Z = \frac{D_Z}{m_{DZ}} \quad (7)$$

calculated with the equations.

Figure 8 shows the calculated Cartesian coordinate differences of the KSTM station, and Tables 2-4 show the test values and RMSE of the measurements and differences.

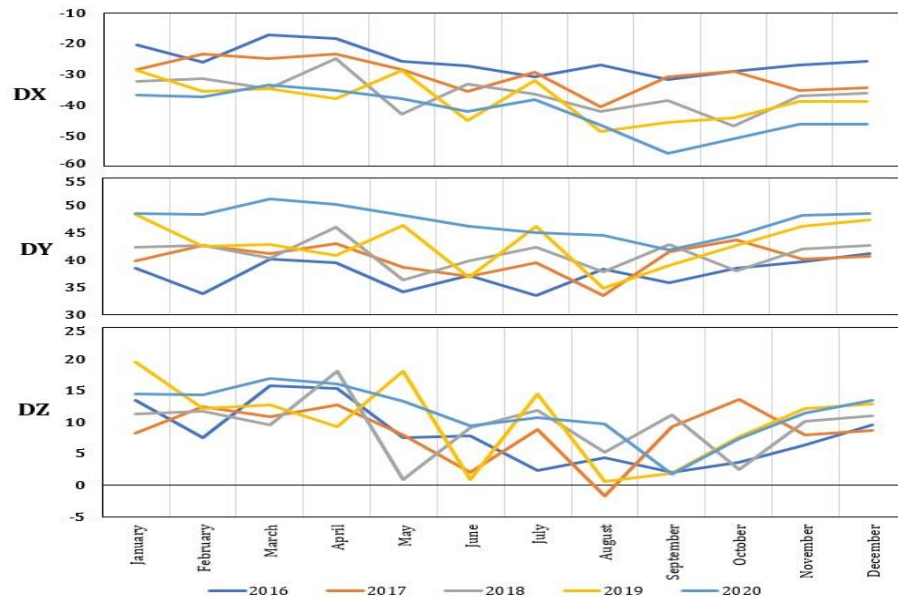


Figure 8. Cartesian coordinate differences (mm) for KSTM station

Table 1. KSTM station between 2016 and 2020 D_X statistical values of the coordinate difference

	2016		2017		2018		2019		2020	
	D_X (mm)	T_X	D_X (mm)	T_X	D_X (mm)	T_X	D_X (mm)	T_X	D_X (mm)	T_X
January	-20.64	0.26	-28.54	0.36	-32.24	0.41	-28.84	0.36	-36.84	0.46
February	-26.17	0.33	-23.57	0.30	-31.57	0.40	-35.67	0.45	-37.37	0.47
March	-17.40	0.22	-24.95	0.31	-34.85	0.44	-34.75	0.44	-33.70	0.42
April	-18.53	0.23	-23.48	0.30	-25.08	0.32	-37.98	0.48	-35.33	0.44
May	-25.81	0.32	-28.45	0.36	-42.98	0.54	-28.75	0.36	-38.11	0.48
June	-27.24	0.34	-35.58	0.45	-33.28	0.42	-45.18	0.57	-42.24	0.53
July	-30.92	0.39	-29.46	0.37	-36.56	0.46	-31.96	0.40	-38.22	0.48
August	-27.05	0.34	-40.69	0.51	-42.19	0.53	-48.79	0.61	-46.65	0.59
September	-31.78	0.40	-30.92	0.39	-38.72	0.49	-45.62	0.57	-55.68	0.70
October	-29.25	0.37	-29.20	0.37	-46.80	0.59	-44.10	0.55	-51.05	0.64
November	-27.09	0.34	-35.33	0.44	-37.13	0.47	-39.03	0.49	-46.39	0.58
December	-25.96	0.33	-34.51	0.43	-36.21	0.46	-38.81	0.49	-46.26	0.58
m_{dx_i}	26.02		30.81		36.89		38.81		42.83	
m_{DX}						79.55				

Table 2. KSTM station between 2016 and 2020 D_Y statistical values of the coordinate difference

	2016		2017		2018		2019		2020	
	D_Y (mm)	T_Y	D_Y (mm)	T_Y	D_Y (mm)	T_Y	D_Y (mm)	T_Y	D_Y (mm)	T_Y
January	38.61	0.49	39.81	0.50	42.41	0.53	48.31	0.61	48.51	0.61
February	33.87	0.43	42.67	0.54	42.77	0.54	42.47	0.53	48.37	0.61
March	40.19	0.51	41.22	0.52	40.42	0.51	42.82	0.54	51.09	0.64
April	39.55	0.50	42.98	0.54	46.08	0.58	40.88	0.51	50.15	0.63
May	34.24	0.43	38.76	0.49	36.36	0.46	46.26	0.58	48.24	0.61
June	37.19	0.47	37.12	0.47	39.82	0.50	36.82	0.46	46.19	0.58
July	33.48	0.42	39.51	0.50	42.31	0.53	46.11	0.58	44.98	0.57
August	38.34	0.48	33.56	0.42	37.86	0.48	34.96	0.44	44.44	0.56
September	35.80	0.45	41.52	0.52	42.82	0.54	39.02	0.49	41.90	0.53
October	38.48	0.48	43.61	0.55	38.11	0.48	42.71	0.54	44.58	0.56
November	39.64	0.50	40.27	0.51	41.97	0.53	46.17	0.58	48.14	0.61
December	41.22	0.52	40.76	0.51	42.66	0.54	47.36	0.60	48.52	0.61
$m_{d_{y_i}}$	37.63		40.24		41.21		43.02		47.16	
m_{D_Y}	93.85									

Table 3. KSTM station between 2016 and 2020 D_Z statistical values of the coordinate difference

	2016		2017		2018		2019		2020	
	D_Z (mm)	T_Z	D_Z (mm)	T_Z	D_Z (mm)	T_Z	D_Z (mm)	T_Z	D_Z (mm)	T_Z
January	13.38	0.17	8.18	0.10	11.28	0.14	19.48	0.24	14.38	0.18
February	7.46	0.09	12.46	0.16	11.76	0.15	12.16	0.15	14.36	0.18
March	15.78	0.20	10.80	0.14	9.60	0.12	12.70	0.16	16.88	0.21
April	15.26	0.19	12.68	0.16	18.08	0.23	9.18	0.12	16.06	0.20
May	7.46	0.09	7.88	0.10	0.88	0.01	18.08	0.23	13.26	0.17
June	7.74	0.10	1.96	0.02	9.06	0.11	0.86	0.01	9.34	0.12
July	2.34	0.03	8.86	0.11	11.86	0.15	14.46	0.18	10.74	0.14
August	4.32	0.05	-1.76	0.02	5.14	0.06	0.64	0.01	9.72	0.12
September	2.00	0.03	9.32	0.12	11.12	0.14	1.92	0.02	1.70	0.02
October	3.60	0.05	13.62	0.17	2.42	0.03	7.72	0.10	7.30	0.09
November	6.38	0.08	8.00	0.10	10.10	0.13	12.10	0.15	11.38	0.14
December	9.48	0.12	8.70	0.11	11.00	0.14	12.90	0.16	13.38	0.17
$m_{d_{z_i}}$	9.15		9.39		10.36		11.85		12.23	
m_{D_Z}	23.86									

The test distribution limit of the calculated test magnitudes at 95% confidence interval $t_{f,1-0.05/2} = 2.5706$ with the limit value. When Table 1-3 is examined, it is seen that all test values are compared with the limit value $t_{f,1-0.05/2}$ and it was observed that it remained smaller than table value.

5. CONCLUSION

The meteorological time intervals of the KSTM station located in the study area were evaluated in two stages: temperature and precipitation. For this purpose, data on the monthly average temperature and monthly total precipitation amounts of Kastamonu province between 2016-2020, where KSTM station is located, were obtained from the MEVBIS. As a result of the study, when the average temperature is examined periods between 2016-2020, it was concluded that the month with the lowest temperature was January with -0.16 °C, the month with the highest temperature was August with 20.5 °C, and when the monthly total precipitation amounts were examined; the month with the lowest amount of precipitation was November with 18.94 (mm) and the month with the highest amount of precipitation was May with 102.90 (mm).

When Figure 6 is analyzed again, it is concluded that there is no disturbing activity on GNSS measurements in terms of space weather conditions in the selected date range and there is no other effect on coordinate calculations other than GNSS measurement errors. The data were processed in LGO v8.1

software by using 30-s and 24-hour RINEX data of CORS-TR for ten days starting from the 11th day of the month for the months of January, May, August and November and the precise orbit ephemeris information of GPS and GLONASS satellites. In the next stage, velocity vector were calculated and the coordinates of the KSTM station were shifted to the reference epoch (ITRF96 2005.00 Epoch). These coordinates were compared with the real coordinates published by the TKGM and subjected to statistical test at 95% confidence interval.

When it was examined whether the temperature changes were statistically significant, it was observed that the test values were calculated according to the temperature changes were below the test distribution limit $t_{f,1-0.05/2} = 2.5706$ at 95% confidence interval. As a result, it is seen that the positioning changes of the KSTM station within the study boundary are not affected by the temperature changes during the selected years.

When it was examined whether the precipitation changes were statistically significant, it was observed that the test values were calculated according to the precipitation changes were below the test distribution limit $t_{f,1-0.05/2} = 2.5706$ at 95% confidence interval. As a result, it is seen that the positioning changes of the KSTM station within the study boundary are not also affected by the precipitation during the years.

As a result of this study, it was observed that temperature and precipitation changes did not have any negative effect on positioning with CORS-TR stations. As a result, it was found that the measurements made based on the CORS-TR network in all weather conditions give equal accuracy. In this study, the fact that the selected days did not exceed the limit values in any space weather conditions could not reveal the relationship between GNSS and positioning. In order to guide future studies, it would be appropriate to investigate the possible effects of different space weather conditions on GNSS position accuracy.

Declaration of Ethical Standards

The authors declare that the study complies with all applicable laws and regulations and meets ethical standards.

Declaration of Competing Interest

The authors declare that they have no known competing financial interests or personal relationships that could have appeared to influence the work reported in this paper.

Funding / Acknowledgements

The authors declare that no funding was used in the study.

Data Availability

No data are associated in the manuscript.

6. REFERENCES

- [1] F. Pektaş, "Gerçek zamanlı ulusal ve yerel Sabit GNSS ağlarına dayalı kinematik konumlama (TUSAGA-Aktif – İSKİ-UKBS ağlarının yerel ölçekte karşılaştırılması)," M. S. thesis, Yıldız Technical University, Istanbul, 2010.
- [2] S. Bülbül, "TUSAGA-Aktif noktalarında renkli gürültülerden arındırılmış hız bileşenlerinin belirlenmesi," Ph. D. thesis, Konya Technical University, Konya, 2018.
- [3] B. Bilgen, S. Bülbül, and C. İnal C. "TUSAGA-Aktif istasyonlarındaki meteorolojik hava olaylarının hassas nokta konumlamaya etkisi," *Afyon Kocatepe Üniversitesi Fen ve Mühendislik Bilimleri Dergisi*, vol. 21, no. 6, pp. 1393-1403, 2021.

- [4] M. S. Bos, L. Bastos, and R.M.S. Fernandes, "The influence of seasonal signals on the estimation of the tectonic motion in short continuous GPS time-series," *Journal of Geodynamics*, vol. 49, pp. 205-209, 2010.
- [5] J.F. Zumberge, M.B. Heflin, D. C. Jefferson, M.M. Watkins, and F.H. Webb, "Precise point processing for the efficient and robust analysis of GPS data from large networks," *Journal of Geophysical Research*, vol. 102, pp. 5005-5017, 1997.
- [6] H. Nakamura, K. Koizumi, and N. Mannoji, "Data Assimilation of GPS precipitable water vapor into the jma mesoscale numerical weather prediction model and its impact on rainfall forecasts," *Journal of the Meteorological Society of Japan*, vol. 82, no. 1, pp. 441-452, 2004.
- [7] G. Möller, and D. Landskron, "Atmospheric bending effects in GNSS tomography," *Atmospheric Measurement Techniques*, vol. 12, no. 1, pp. 23-34, 2019.
- [8] A. Garcia Vieira de Sá, "Tomographic determination of the spatial distribution of water vapour using GNSS observations for real-time applications," Ph. D. thesis, Wrocław University of Environmental and Life Sciences, 2018.
- [9] H. Brenot, W. Rohm, M. Kačmařík, G. Möller, A. Sá, D. Tondaš, L. Rapant, R. Biondi, T. Manning, and C. Champollion, "Cross-comparison ve methodological improvement in GPS tomography," *Remote Sensing*, vol. 12, no. 1, pp. 30, 2020.
- [10] Y. H. Kuo, Y.R. Guo, and E.R. Westwater, "Assimilation of precipitable water measurements into a mesoscale numerical model," *Monthly Weather Review*, vol. 121, no. 4, pp. 1215-1238, 1993.
- [11] T. L. Smith, S. G. Benjamin, S. I. Gutman, and S. Sahn, "Short-range forecast impact from assimilation of GPS-IPW observations into the rapid update cycle," *Monthly Weather Review*, vol. 135, no.8, pp. 2914-2930, 2007.
- [12] M.S. F. V. De Pondeva, and X. Zou, "A case study of the variational assimilation of GPS zenith delay observations into a mesoscale model," *Journal of Applied Meteorology and Climatology*, vol. 40, no. 9, pp. 1559-1576, 2001.
- [13] S. Q. Peng, and X. Zou, "Impact on short-range precipitation forecasts from assimilation of ground-based GPS zenith total delay and rain gauge precipitation observations," *Journal of the Meteorological Society of Japan*, vol. 82, no. 1B, pp. 491-506, 2004.
- [14] H.C. Baker, A. H. Dodson, N.T. Penna, M. Higgings, and D. Offiler, "Ground-based GPS water vapour estimation: potential for meteorological forecasting," *Journal of Atmospheric and Solar-Terrestrial Physics*, vol. 63, no. 12, pp. 1305-1314, 2001.
- [15] D. Jerrett, and J. Nash, "Potential uses of surface based GPS water vapour measurements for meteorological purposes," *Physics and Chemistry of the Earth, Part A: Solid Earth and Geodesy*, vol. 6, no. 6-8, pp. 457- 461, 2001.
- [16] G. Guerova, "Application of GPS derived water vapour for numerical weather prediction in switzerland," Ph. D. thesis, University of Bern, 2003.
- [17] G. Gendt, G. Dick, C. Reigber, M. Tomassini, Y. Liu, and M. Ramatschi, "Near real time GPS water vapor monitoring for numerical weather prediction in Germany," *Journal of the Meteorological Society of Japan*, vol. 82, no. 1B, pp. 361-370, 2004.
- [18] H. Vedel, and X. Y. Huang, "Impact of ground based GPS data on numerical weather prediction," *Journal of the Meteorological Society of Japan*, vol. 82, no. 1B, pp. 459-472, 2004.
- [19] R. Eresmaa, H. Järvinen, and K. Salonen, "Potential of ground-based GPS slant delays for numerical weather prediction," *Atmos. Chem. Phys.*, vol. 7, pp. 3143-3151, 2006.
- [20] P. Poli, P. Moll, F. Rabier, G. Desroziers, B. Chapnik, L. Berre, S. B. Healy, E. Andersson, and F. Z. ElGuelai, "Forecast impact studies of zenith total delay data from european near real-time GPS stations in météo France 4DVAR," *Journal of Geophysical Research: Atmospheres*, vol. 112, pp. D06114, 2007.
- [21] C. Faccani, R. Ferretti, R. Pacione, T. Paolucci, F. Vespe, and L. Cucurull, "Impact of a high density GPS network on the operational forecast," *Advances in Geosciences*, vol. 2, pp. 73-79, 2005.

- [22] M. Zhang, Y. Ni, and F. Zhang, "Variational assimilation of GPS precipitable water vapor ve hourly rainfall observations for a Meso- β scale heavy precipitation event during the 2002 Mei-Yu Season," *Advances in Atmospheric Sciences*, vol. 24, no. 3, pp. 509-526, 2007.
- [23] National Oceanic and Atmospheric Administration, "Space Weather Prediction Center," [Online]. Available: <https://www.swpc.noaa.gov/phenomena> [Accessed: Apr. 20, 2024].
- [24] F. Başçiftçi, C. Inal, Ö. Yildirim, and S. Bulbul, "Comparison of regional and global TEC values: Turkey model," *International Journal of Engineering and Geosciences*, vol. 3, no. 2, pp. 61-72, 2018.
- [25] ESA Space Weather Service Network, [Online]. Available: <https://swe.ssa.esa.int/what-is-space-weather> [Accessed: May. 15, 2024].
- [26] R. Mukesh, V. Karthikeyan, P. Soma, and P. Sindhu, "Cokriging based statistical approximation model for forecasting ionospheric VTEC during high solar activity and storm days," *Astrophysics and Space Science*, vol. 364, pp. 131, 2019.
- [27] Space Weather Prediction Center (2024). F10.7 cm radio emissions, [Online]. Available: <https://www.swpc.noaa.gov/phenomena/f107-cm-radio-emissions> [Accessed: May. 16, 2024].
- [28] Australian Space Weather Forecasting Centre [Online]. Available: <https://www.sws.bom.gov.au/> [Accessed: May. 16, 2024].
- [29] International Service of Geomagnetic Indices, "Kp index," [Online]. Available: https://isgi.unistra.fr/indices_kp.php [Accessed: May. 16, 2024].
- [30] F. Basciftci, and S. Bulbul, "Investigation of ionospheric TEC changes potentially related to Seferihisar-Izmir earthquake (30 October 2020, MW 6.6)," *Bulletin of Geophysics & Oceanography*, vol. 63, no. 3, pp. 4382-4400, 2022.
- [31] B. Lemmerer, S. Unger, "Modeling and pricing of space weather derivatives," *Risk Management*, vol. 21, pp. 265-291, 2019.
- [32] N. Myagkova, V. R. Shirokii, R. D. Vladimirov, O. G. Barinov, and S. A. Dolenko, "Prediction of the Dst geomagnetic index using adaptive methods," *Russian Meteorology and Hydrology*, vol. 46, pp. 157-162, 2021.
- [33] International Service of Geomagnetic Indices "Dst index", [Online]. Available: https://isgi.unistra.fr/indices_dst.php [Accessed: May. 16, 2024].
- [34] Banerjee, A. Bej, and T. N. Chatterjee, "On the existence of a long range correlation in the Geomagnetic Disturbance storm time (Dst) index," *Astrophysics and Space Science*, vol. 337, pp. 23-32, 2012.
- [35] S. Bulbul, and F. Basciftci, "TEC anomalies observed before and after Sivrice-Elaziğ earthquake (24 January 2020, Mw: 6.8)," *Arabian Journal of Geosciences*, vol. 14, no. 12, pp. 1077, 2021.
- [36] R. Dach, S. Lutz, P. Walser, and P. Fridez, *Bernese GNSS Software Version 5.2. User manual*, Astronomical Institute, University of Bern, Bern Open Publishing, 2015.

THEORETICAL INVESTIGATION FOR YTTERBIUM EFFECT ON RADIATION SHIELDING CHARACTERISTICS OF 50Bi₂O₃-15Li₂O-15PbO-(20-X)B₂O₃-Yb₂O₃ BORATE GLASSES

¹Murat AYGÜN^{ID}, ^{2,*}Zeynep AYGÜN^{ID}, ³İbrahim HAN^{ID}, ⁴Emine NARMANLI HAN^{ID}

¹ Bitlis Eren University, Arts&Sciences Faculty, Physics Department, Bitlis, TÜRKİYE

^{2*} Bitlis Eren University, Vocational School of Technical Sciences, Bitlis, TÜRKİYE

³ Ağrı İbrahim Cecen University, Arts&Sciences Faculty, Physics Department, Ağrı, TÜRKİYE

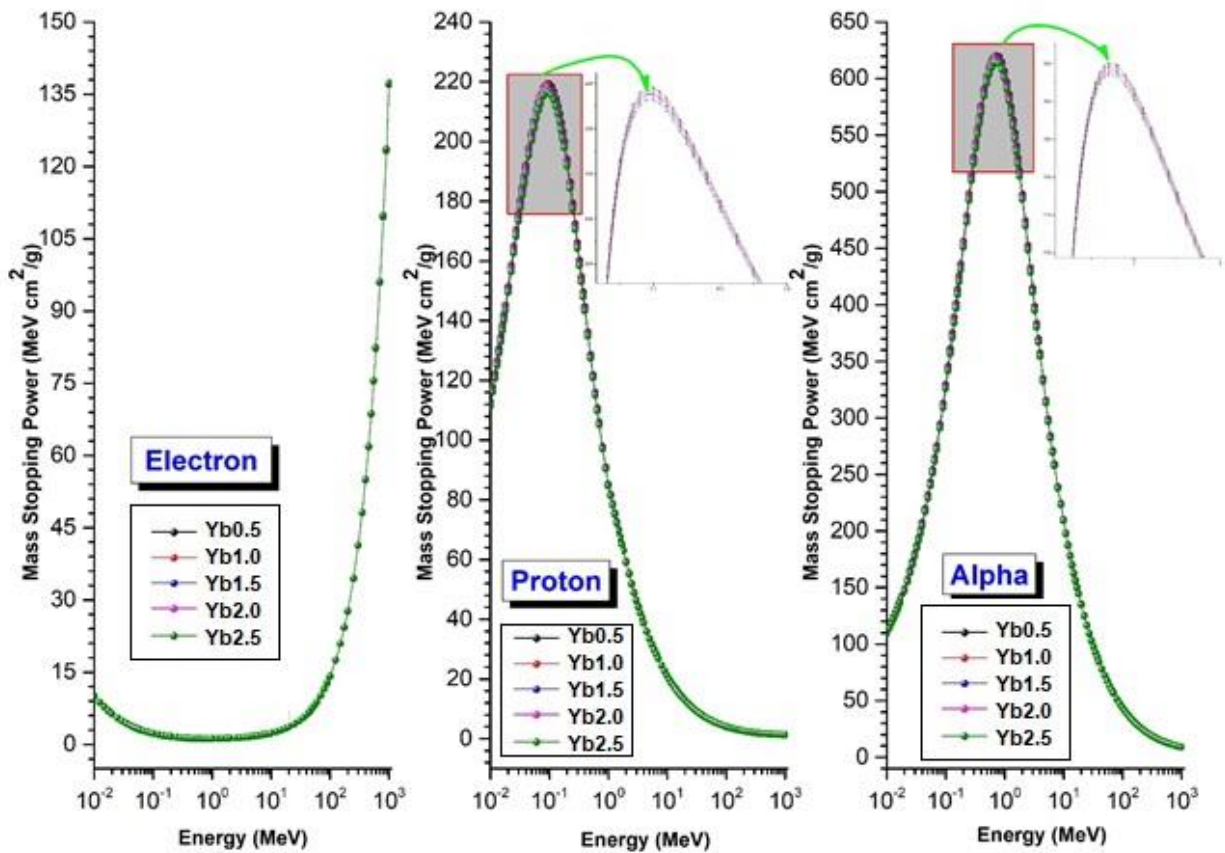
⁴ Ağrı İbrahim Cecen University, Vocational School, Ağrı, TÜRKİYE

¹maygun@beu.edu.tr, ²zaygun@beu.edu.tr, ³ihan@agri.edu.tr, ⁴enhan@agri.edu.tr

Highlights

- Radiation shielding characteristics of ytterbium doped glasses have been studied.
- Phy-X/PSD, PAGEX, ESTAR, and SRIM codes have been used.
- Increasing amount of ytterbium exhibited higher shielding performances.

Graphical Abstract



Dependence of MSP values of alpha, proton and electron particles versus the energy.



THEORETICAL INVESTIGATION FOR YTTERBIUM EFFECT ON RADIATION SHIELDING CHARACTERISTICS OF $50\text{Bi}_2\text{O}_3\text{-}15\text{Li}_2\text{O}\text{-}15\text{PbO}\text{-}(20\text{-X})\text{B}_2\text{O}_3\text{-Yb}_2\text{O}_3$ BORATE GLASSES

¹Murat AYGÜN^{ID}, ^{2,*}Zeynep AYGÜN^{ID}, ³İbrahim HAN^{ID}, ⁴Emine NARMANLI HAN^{ID}

¹ Bitlis Eren University, Arts&Sciences Faculty, Physics Department, Bitlis, TÜRKİYE

^{2*} Bitlis Eren University, Vocational School of Technical Sciences, Bitlis, TÜRKİYE

³ Ağrı İbrahim Cecen University, Arts&Sciences Faculty, Physics Department, Ağrı, TÜRKİYE

⁴ Ağrı İbrahim Cecen University, Vocational School, Ağrı, TÜRKİYE

¹maygun@beu.edu.tr, ²zaygun@beu.edu.tr, ³ihan@agri.edu.tr, ⁴enhan@agri.edu.tr

(Received: 06.06.2024; Accepted in Revised Form: 07.08.2024)

ABSTRACT: As the nuclear industry has developed and radiation technologies have become more widely used, the dose of radiation from both synthetically produced sources and radioisotopes has increased, as has the number of people being irradiated. It is of the utmost importance to utilise appropriate shielding materials in order to reduce the negative effects of radiation sources. Doped glasses are among the most significant candidate materials in the field of radiation shielding. To this end, it was aimed to investigate the charged particle, gamma-ray and neutron shielding characteristics of ytterbium doped glasses with composition of $50\text{Bi}_2\text{O}_3\text{-}15\text{Li}_2\text{O}\text{-}15\text{PbO}\text{-}(20\text{-x})\text{B}_2\text{O}_3\text{-Yb}_2\text{O}_3$ (where $x = 0.5, 1.0, 1.5, 2.0$ and 2.5). In this regard, the radiation shielding parameters were estimated by using Phy-X/PSD, PAGEX, ESTAR, and SRIM codes. Furthermore, the results were compared comprehensively and comparatively. Charged particle (alpha, proton and electron), gamma ray and neutron shielding efficiencies were found to be proportional to ytterbium content. The glasses with the increasing amount of ytterbium exhibited higher shielding performances. It can be said that all the studied glasses and particularly Yb2.5 sample could be used as shielding materials in many radiation related applications.

Keywords: Borate Glass, Charged Particle Shielding, Gamma Shielding, Neutron Shielding, Yb

1. INTRODUCTION

The group of rare earth elements (REs) is widely used in glass, ceramics, metallurgical industry, laser production, magnet production, oil catalyst and high-tech devices [1-6]. Ytterbium (Yb^{3+}), a rare earth (RE) element, has the potential to be utilized in the refinement of grains and the improvement of mechanical features of stainless steel products. With the half-life of 32 days, the radioactive isotope ^{169}Yb is sometimes employed as a radiation source in the area of nuclear medicine. Alloys of ytterbium-iron-cobalt-manganese are appropriate for the production of high-quality permanent magnets. Similarly, ytterbium-doped crystals have the ability to act as dopant materials in lasers.

Glass is a material of great interest to researchers due to its many benefits, including its perfect corrosion resistance, hardness, optical properties and ease of processing by various techniques. Rare earth doped glass matrices can be a valuable alternative to glass materials for potential use as scintillators and non-lead shields due to their low fabrication cost, chemical resistance, ease of fabrication and thermal stability properties [1-4]. Bismuth glass is in demand because of its extraordinary properties in amplifiers, lasers, optical data storage devices, etc. It is evident that the bismuth-borate matrix represents an ideal host matrix for REs, with applications spanning a range of disciplines including optical fibers, optical data storage devices, display technology, lasers, medical diagnostics and sensors [5-8]. Thus, Bi-doped glasses attract great attention from researchers [9-11]. Bi_2O_3 doped silica borotellurite glasses were studied by Geidam et al. [9] and it is suggested that the glasses are mechanically and thermally stable for applications in radiation shielding. Also, effect of Bi_2O_3 on gamma ray shielding and structural properties of borosilicate glasses recycled from high pressure sodium lamp glass was investigated and it was reported that good results were obtained [10]. Additionally, the Yb^{3+} ions present within the glasses serve as

*Corresponding Author: Zeynep AYGÜN, zaygun@beu.edu.tr

sensitizers for the various RE³⁺ ions, imparting the energy to increase the efficiency of emission, thereby imparting a dielectric nature to the glasses [8].

The use of glass doped with REs has become a key component in the development of photonic applications in modern life. In recent decades, there has been extensive investigation into the synthesis of materials doped with REs for application within lighting technologies. This is because of the necessity of improving the performance of solid-state devices, LEDs, lasers etc. [12]. It is also important to examine the influence of the external ionizing radiation on the glassy structures' microstructure. Learning about the interaction between radiation and glasses gives us enlightening information for the reaction of the glassy matrices to the radiation. The radiation features of the RE-doped glass matrix are strongly influenced by the composition of the host material and these features were commonly studied by the researchers [12-16]. In particular, it has been demonstrated in numerous studies that the addition of Yb³⁺ ions into glasses significantly enhances their capacity for effective protection [17-19]. The role of Yb₂O₃ in the radiation shielding properties of B₂O₃-TiO₂-BaO glasses was studied by Negm et al. [18], and it was obtained that this type of glass with low concentrations of Yb₂O₃ shows good shielding properties. Tamam et al. [19] reported that the photon shielding ability and dosimetry potential of the glass system improved with Yb³⁺ weight content of the glasses and they are recommended for gamma radiation inhibition functions such as nuclear waste container, structural and source shields.

In countries with developing economies, nuclear energy has become a significant aspect of the energy production landscape. The operation of the nuclear reactor will result in the release of highly penetrating and dangerous radiation. Accordingly, it is essential that the reactor site is safeguarded by an appropriate layer of protection. With the growth of the nuclear industry and the increasing utilisation of radiation technologies, it is therefore evident that the attenuation of radiation levels to ensure safety has become a crucial requirement. For this purpose, the goal of the study is to analyze the radiation-glasses interaction characteristics and to obtain the radiation attenuation parameters (RAP), which are significant to have the knowledge of attenuating abilities of the glasses, including the mass and linear attenuation coefficient values (MACVs and LACVs), mean free path value (MFPV), half value layer value (HVLV), electronic and atomic cross sections (ECS and ACS), effective and equivalent atomic number (Z_{eff} and Z_{eq}), effective electron density and conductivity (N_{eff} and C_{eff}), buildup factors (BUF), KERMA, fast neutron removal cross section value (FNRCVS), the mass stopping power (MSP) and projected range (R_p). In this context, the RAP of 50Bi₂O₃-15Li₂O-15PbO-(20-x)B₂O₃-Yb₂O₃ ($x = 0.5, 1.0, 1.5, 2.0$ and 2.5 mol%) glasses are evaluated by Phy-X/PSD [20], SRIM [21], PAGEX [22] and ESTAR (Institute) codes in different energies.

2. MATERIAL AND METHODS

The knowledge necessary for the computations of glass samples were taken from Ref. Bhemarajam et al. [8] to ascertain their potential for radiation shielding. The glasses with a composition of 50Bi₂O₃-15Li₂O-15PbO-(20-x)B₂O₃-Yb₂O₃ ($x = 0.5, 1.0, 1.5, 2.0$ and 2.5 mol%) have been obtained using the melt quenching technique. In melt quenching technique, firstly, the chemicals were weighted according to mol percent, then, they were ground to homogeneity using an agate mortar and placed into an alumina crucible. The obtained mixture is melted in an electric furnace at high temperatures. The desired melts were then quenched using a preheated brass plate and a quencher to produce a glass sample. Glass samples were annealed to avoid unwanted thermal stress and air bubbles in the synthesised glass [8]. Table 1 presents the densities, chemical compositions and molar volumes of the chosen glasses. The samples are labeled as Yb0.5, Yb1.0, Yb1.5, Yb2.0 and Yb2.5 for $x = 0.5, 1.0, 1.5, 2.0$ and 2.5 mol%, respectively. The study [8] outlines the methodology employed to prepare and assess the physical characteristics of the studied samples.

Table 1. The elemental components and density of the glasses [8].

Sample	Bi	O	B	Li	Pb	Yb	Density (g/cm ³)
Yb0.5	0.7295	0.1340	0.0147	0.0073	0.1085	0.0060	5.302
Yb1.0	0.7253	0.1333	0.0143	0.0072	0.1079	0.0120	5.403
Yb1.5	0.7213	0.1325	0.0138	0.0072	0.1073	0.0179	5.523
Yb2.0	0.7173	0.1318	0.0134	0.0071	0.1067	0.0238	5.635
Yb2.5	0.7133	0.1311	0.0129	0.0071	0.1061	0.0295	5.794

2.1. Radiation protection parameters for the interaction of charged and uncharged particles with matter

The Beer–Lambert statement can be written to determine MACVs,

$$I = I_0 e^{-\mu t} \tag{1}$$

$$\mu_m = \frac{\mu}{\rho} = \frac{\ln(I_0/I)}{\rho t} = \frac{\ln(I_0/I)}{t_m} \tag{2}$$

LACVs and MACVs are accepted as μ (cm⁻¹) and μ_m (cm²/g), respectively. The MACV is the potential for interaction between photons and the mass per unit area of a material, which provides insight into the absorption characteristics of the material in question. LACV is the fraction of incident photons attenuated per unit material thickness.

The HVLV refers to the capacity of radiation to penetrate a given substance. MFPV quantifies the average length traversed by radiation between two consecutive collisions within a given medium. HVLV and MFPV are calculated with the following equations

$$\text{HVLV} = \frac{\ln(2)}{\mu} , \quad \text{MFPV} = \frac{1}{\mu} \tag{3}$$

The interaction possibilities of electrons and atoms in a given volume of any given material is denoted by the symbols ECS and ACS, respectively. ACS (σ_a) and ECS (σ_e) can be acquired with the help of equations [23]

$$\text{ACS} = \sigma_a = \frac{N}{N_A} (\mu/\rho) , \quad \text{ECS} = \sigma_e = \frac{\sigma_a}{Z_{\text{eff}}} \tag{4}$$

A compound's atomic number is constituted by several elements; a compound with more than one element is referred to as an effective atomic number (Z_{eff}). Z_{eff} is obtained by [24]

$$Z_{\text{eff}} = \sigma_a / \sigma_e \tag{5}$$

The N_{eff} parameter is associated with the effective conductivity of the relevant material, which is dependent upon the excitatory photon energy. C_{eff} is in proportion to N_{eff} . N_{eff} and C_{eff} values can be written as

$$N_{\text{eff}} = \frac{\mu_m}{\sigma_e} , \quad C_{\text{eff}} = \left(\frac{N_{\text{eff}} \rho e^2 \tau}{m_e} \right) \times 10^3 \tag{6}$$

The N_{eff} value of the charged particles (CPs) can be determined by replacing MAC with the MSP value [21].

BUF, energy absorption build up factor (EABF) and exposure build up factor (EBF), can be found by the following equations below [25-27].

$$Z_{\text{eq}} = \frac{Z_1(\log R_2 - \log R) + Z_2(\log R - \log R_1)}{\log R_2 - \log R_1} \tag{7}$$

$$F = \frac{F_1(\log Z_2 - \log Z_{eq}) + F_2(\log Z_{eq} - \log Z_1)}{\log Z_2 - \log Z_1} \quad (8)$$

$$B(E, x) \begin{cases} 1 + \frac{(b-1)(K^x-1)}{(K-1)} & \text{for } K \neq 1 \\ 1 + (b-1)x & \text{for } K = 1 \end{cases} \quad (9)$$

$$K(E, x) = cx^a + d \frac{\tanh\left(\frac{x}{K_k} - 2\right) - \tanh(-2)}{1 - \tanh(-2)} \quad \text{for } x \leq 40 \text{ mfp} \quad (10)$$

The R1 and R2 values represent the ratio of Compton scattering to total attenuation for adjacent elements with atomic numbers Z1 and Z2, measured in micrometres. F is a set of G-P FP (a, b, c, d, and XK coefficients) for the sample. F1 and F2 are the G-P FP for atomic numbers Z1 and Z2 at a specific energy. x and E refer to the penetration depth and primary photon energy, respectively.

In the case of glass systems, the KERMA with reference to air can be expressed as follows: [28]

$$\text{KERMA} = \frac{(\mu_{en}/\rho)_{\text{glass}}}{(\mu_{en}/\rho)_{\text{air}}} \quad (11)$$

The FNRC SV (ΣR) quantifies a material's potential capacity to attenuate neutrons and can be found by [20]

$$\Sigma R = \sum_i \rho_i (\Sigma R / \rho)_i \quad (12)$$

where ρ_i and $(\Sigma R / \rho)_i$ are the partial density of the glass and the mass removal cross-section of the *i*th constituent element, respectively.

SP can be formulated as [29]

$$\frac{dE}{dx} = 4\pi r_0^2 z^2 \frac{mc^2}{\beta^2} NZ \left[\ln \left(\frac{2mc^2}{I} \beta^2 \gamma^2 \right) - \beta^2 \right] \quad (13)$$

and for electrons the SP formula is

$$\frac{dE}{dx} = 4\pi r_0^2 \frac{mc^2}{\beta^2} NZ \left\{ \ln \left(\frac{\beta \gamma \sqrt{\gamma - 1}}{I} mc^2 \right) + \frac{1}{2\gamma^2} \left[\frac{(\gamma - 1)^2}{8} + 1 - (\gamma^2 + 2\gamma - 1) \ln 2 \right] \right\} \quad (14)$$

The Rp value is assumed as

$$\text{Rp}(E) = \int_0^E \frac{1}{\left(-\frac{dE}{dx} \right)} dE \quad (15)$$

3. RESULTS and DISCUSSION

3.1. Radiation shielding analysis of charged and uncharged particles

The MACVs varied with photon energies were illustrated in Fig. 1(a). The MACRs exhibited a sharp reduction due to the photoelectric (PE) process at low energies (1-100 keV). At mid-energies (100 keV-5 MeV), they exhibited a slight change due to Compton scattering (CS). With increasing energy, the MACRs exhibited an increase due to pair production (PP) at high energies (>5 MeV) [30]. It can be said that the glasses protect well and Yb2.5 is slightly better than other results. The glasses shield equally well. Additionally, the LACVs that vary with photon energies were presented in Fig. 1(b), and the same shielding feature was found for the glasses. In Fig. 2, it is demonstrated that the MACVs of the glasses have better shielding features especially at low energies than the previously investigated shield materials [31].

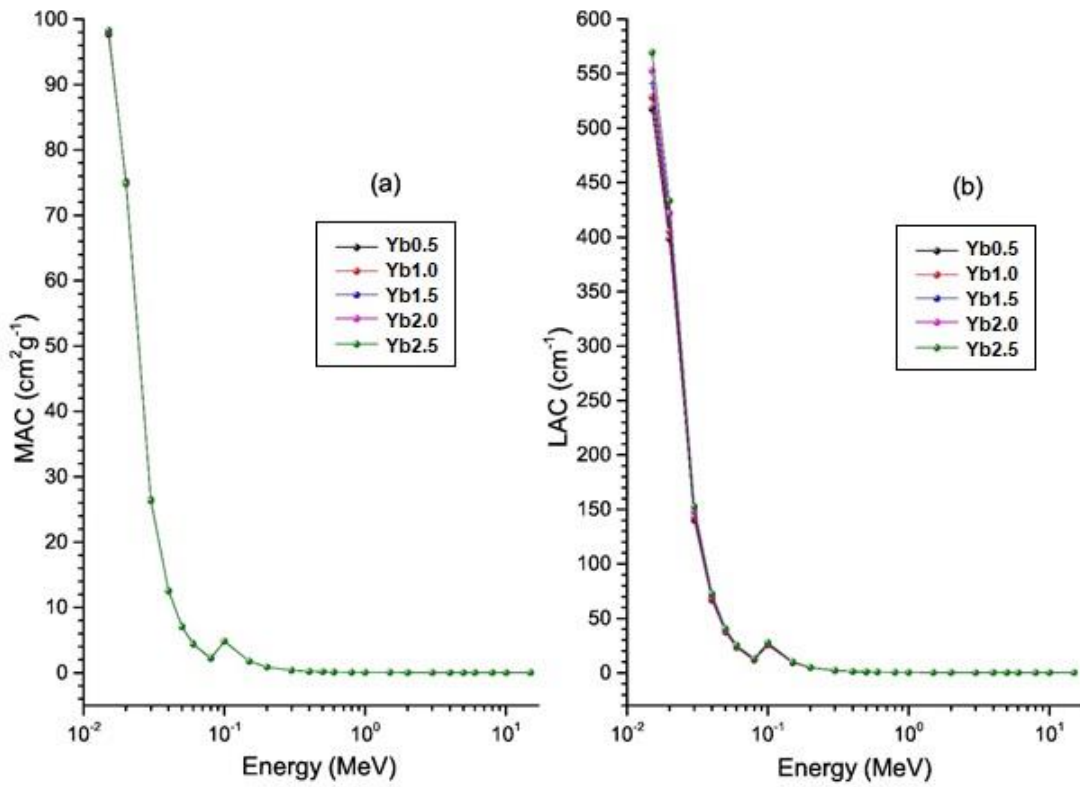


Figure 1. Variations of MAC (a) and LAC (b) values with photon energies.

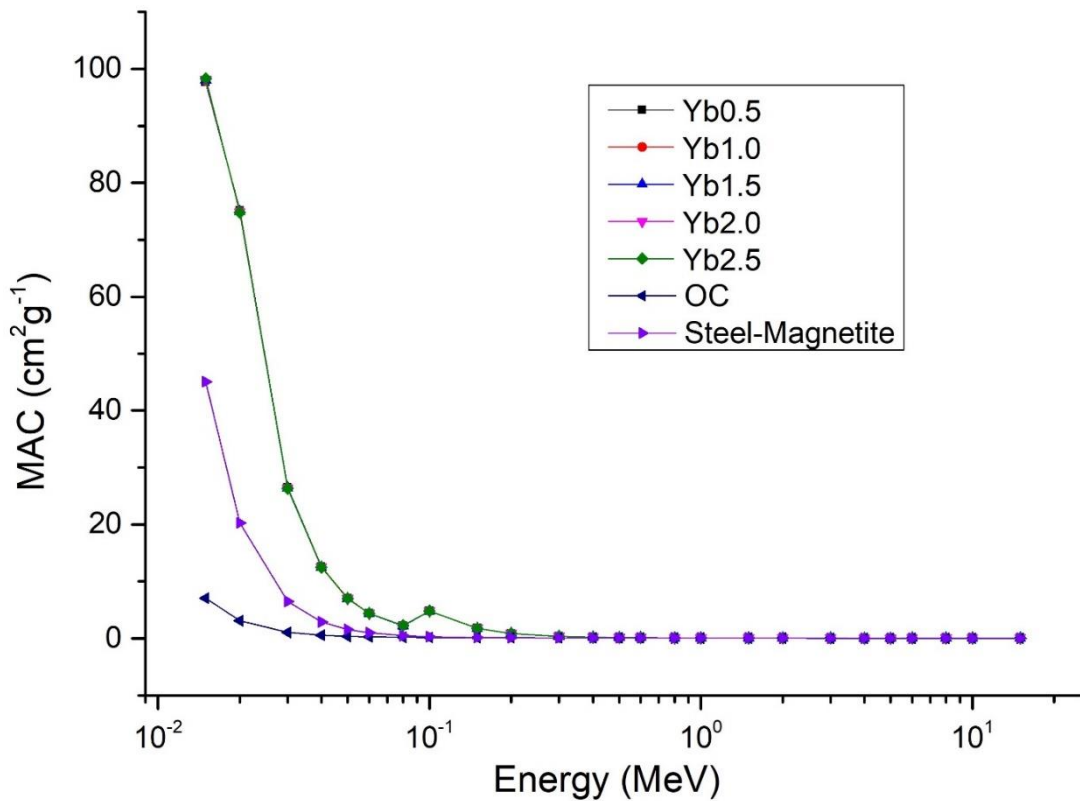


Figure 2. Comparison of MAC values of the glasses with previously studied shields.

The MFP and HVL results were exhibited in Figs. 3(a)-(b). At energies dominated by CS, photons were observed to exhibit a high probability of scattering. Consequently, thicker materials were found to be necessary, as they exhibited a lower probability of absorption and a greater photon MFPV. In the high energy region, lower HVL and MFP results were observed to be beneficial for enhanced shielding capability. In the high-energy region, lower HVL and MFP values are required, while in the lower energy region, thicker materials are necessary. In this regard, the MFP and HVL results are ordered as follows: $Yb2.5 < Yb2.0 < Yb1.5 < Yb1.0 < Yb0.5$. It is worth noting that glass Yb0.5 has the lowest level of shielding ability due to its high HVLVs and MFPVs, and Yb2.5 may offer the highest level of shielding among the glasses due to the lowest values. As seen in Fig. 4, the HVLVs of the studied glasses are lower than those of the materials reported before [31], so it can be said that the glasses are better protection materials.

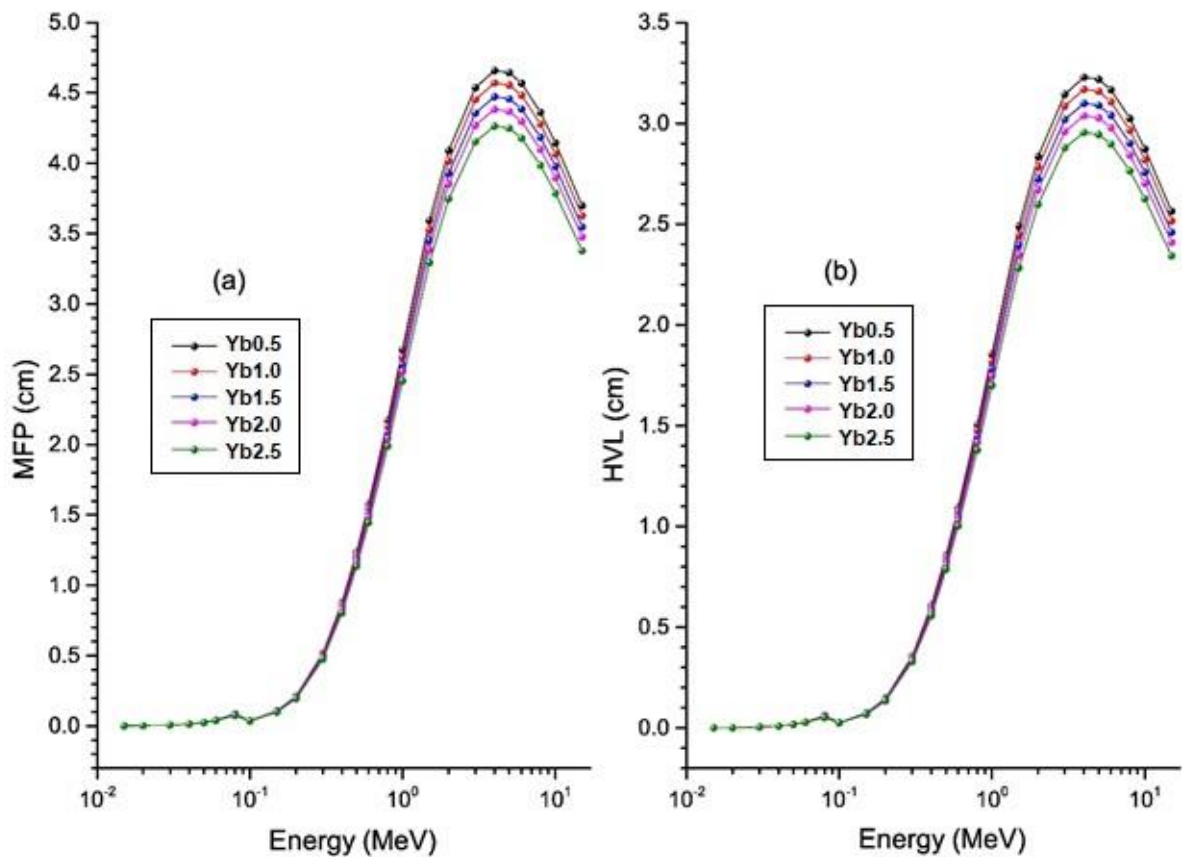


Figure 3. Variations of MFP (a) and HVL (b) values with photon energies.

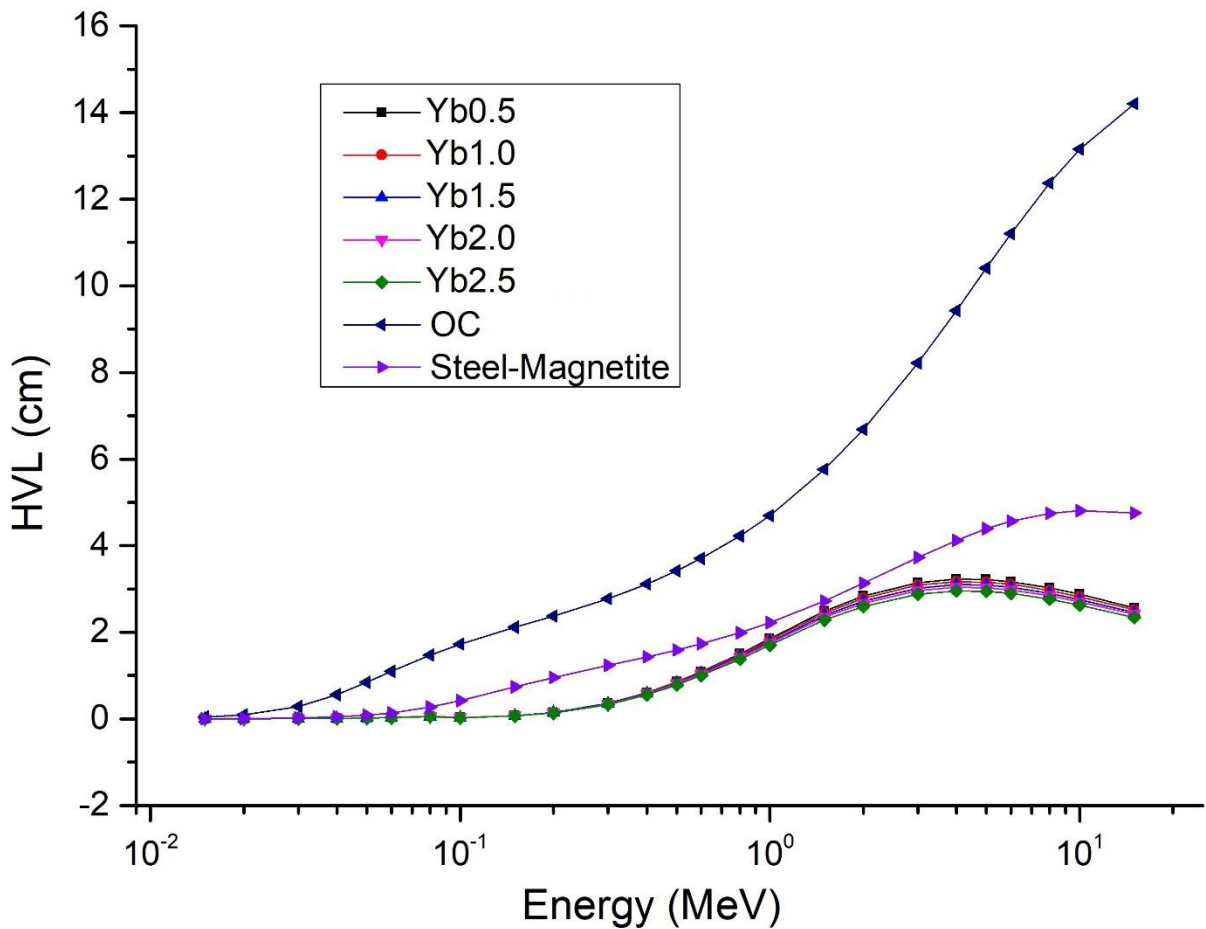


Figure 4. Comparison of HVLs of the glasses with previously studied shields.

It can be of interest to enquire further into the interaction probabilities of a material, which are shown by ACS and ECS in Figs. 5(a) and (b). The results demonstrate that the ACS and ECS values exhibited a correlation with the energy of the photon. It can be postulated that the higher ACS and ECS results point to a better protective glass. It would appear that Yb2.5 has the highest protection character among all the glasses, based on the ACS and ECS values.

The Z_{eff} results, which is displayed in Fig. 6(a), gave the highest values because of the PE at low energy levels. The results exhibited a sharp decline and subsequent increase as the energy increases, before stabilizing at high energies. Glass with Yb2.5 composition, which contains a higher amount of Yb, shows the highest Z_{eff} values and thus the highest shielding performance. On the other hand, Yb0.5 with a lower Yb content show the lowest Z_{eff} values and the lowest protection ability. The Z_{eq} values of the glasses are displayed in Fig. 6(b). Yb2.5 presents a greater interaction, while Yb0.5 shows the least interaction between radiation and matter. The obtained values indicate that Yb2.5 exhibits a more pronounced interaction with radiation than Yb0.5, which demonstrates the least interaction among the glasses investigated. The Z_{eff} values of the glasses are also compared with those of the previous results reported for widely used shielding materials by Bashter [31]. The values are higher than the ordinary concrete (OC) and steel-magnetite, thus the protection abilities are higher.

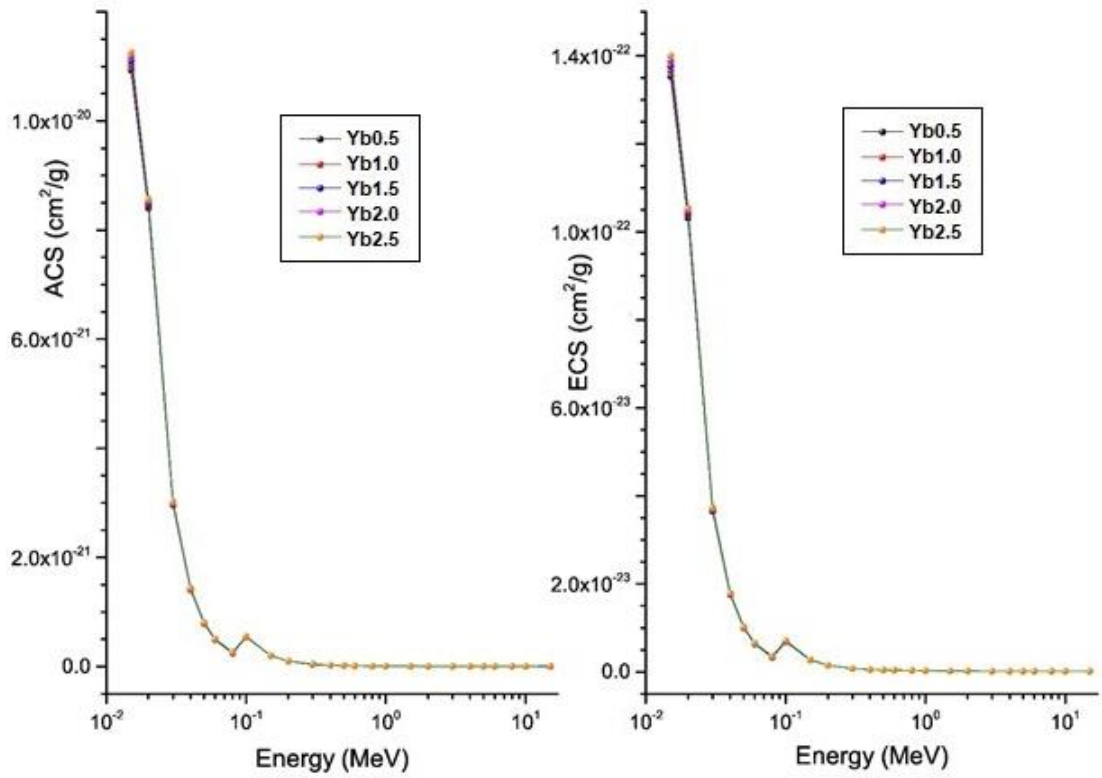


Figure 5. Variations of ACS (a) and ECS (b) values with photon energies.

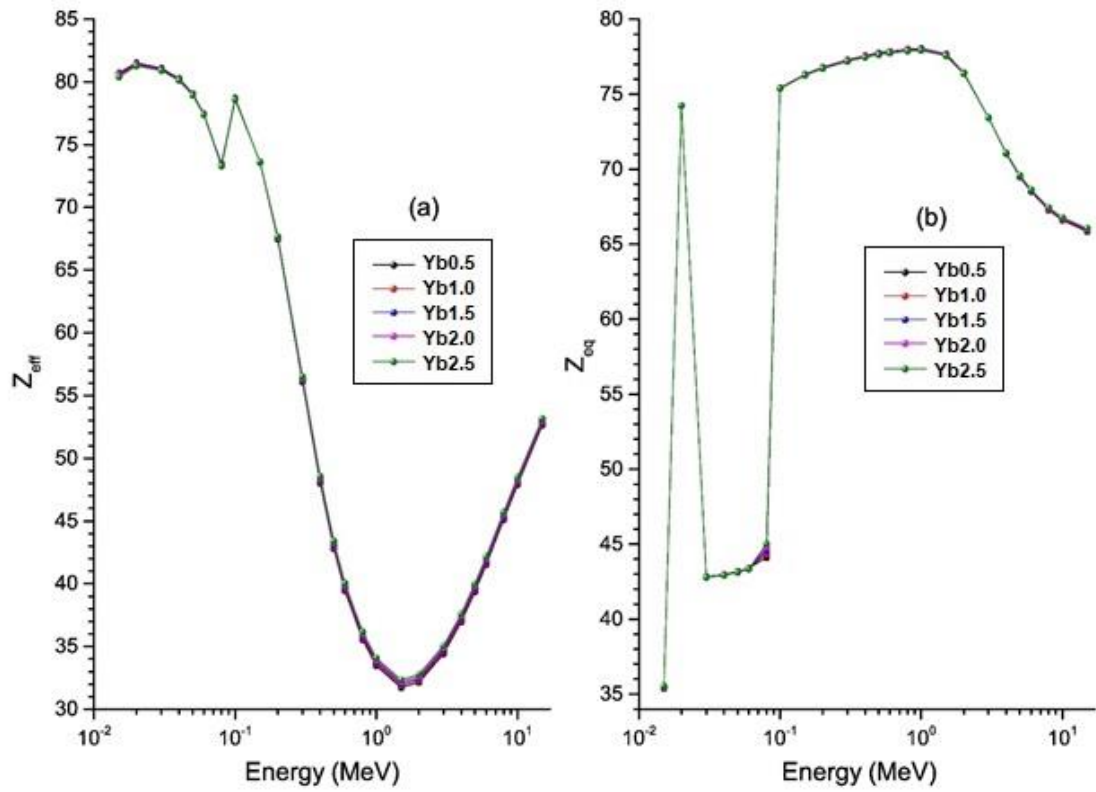


Figure 6. Changes of Z_{eff} (a) and Z_{eq} (b) values with photon energies.

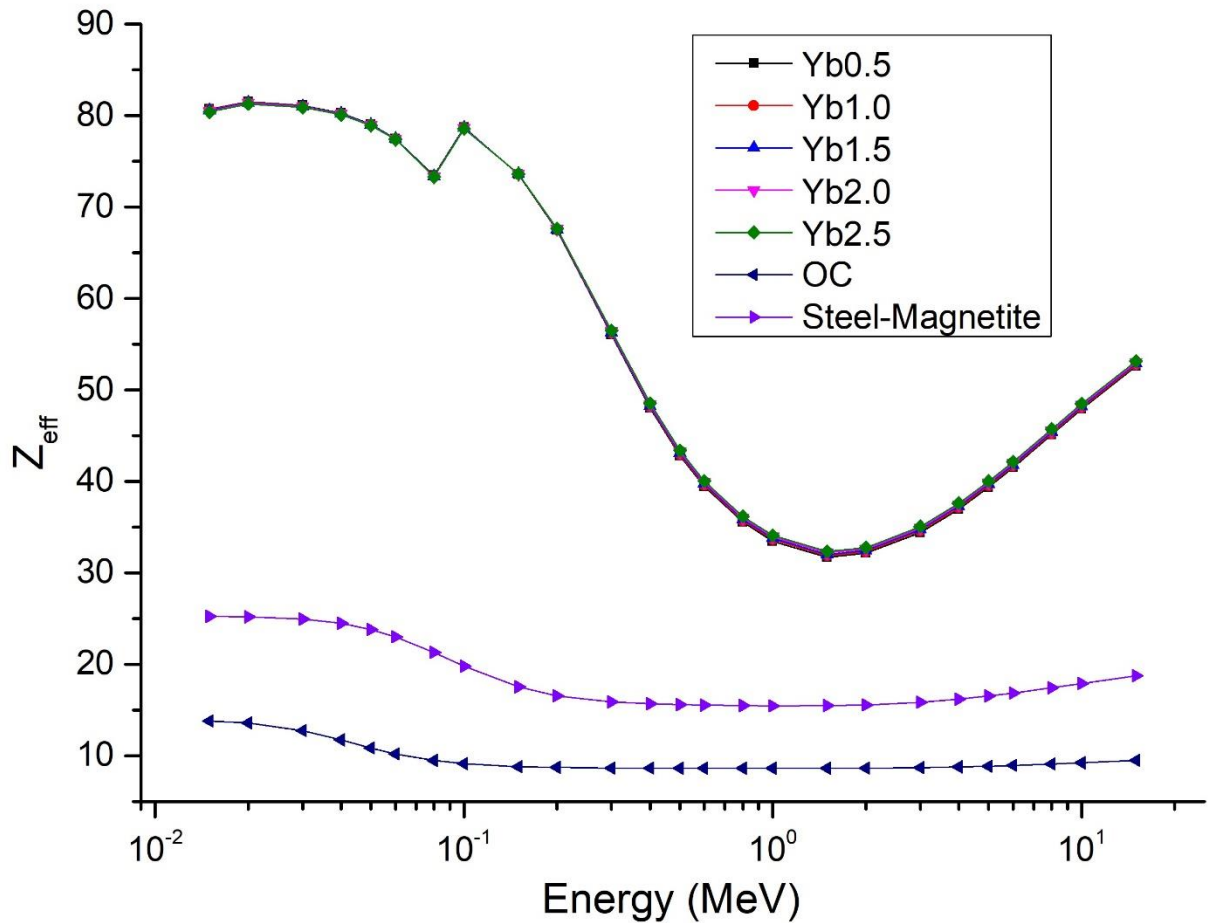


Figure 7. Comparison of Z_{eff} values of the glasses with previously studied shields.

Photon-material interactions result in alterations to the number of free electrons within the material, influenced by PE, CS, and PP interactions. This change is contingent upon the N_{eff} results, which correspond to the number of conduction electrons within the material. Consequently, C_{eff} is proportional to the N_{eff} of the glasses. The alterations in C_{eff} and N_{eff} results according to photon energies are illustrated in Figs. 8(a)-(b). It is noticed that Yb2.5 exhibits the highest C_{eff} and N_{eff} results among the glasses. The very sharp peak seen for Z_{eff} , C_{eff} and N_{eff} around 0.1 MeV can be attributed to the K absorption edges of the Bi and Pb elements [32].

The EABF and EBF of the glasses for 16 penetration depths were defined by the help of Phy-X/PSD and their changes with the incident energy are shown in Figs. 9 and 10, respectively. In the PE region, all energies absorb lower energy photons, resulting in small buildup factors. A large number of scattered photons in the CS region can cause the photon accumulation to increase, causing the factors to reach the highest values in the mid-energy region. The photon absorption rate is high in the PP region, which results in lower buildup factors in higher energy regions. The results indicate that the photon cluster for Yb0.5 is higher than that of the other glasses, as evidenced by the values obtained for EBF and EABF. Additionally, sharp increases in the energies at ≈ 0.03 and 0.1 MeV can be explained as L1 and K absorption edges of Bi [32].

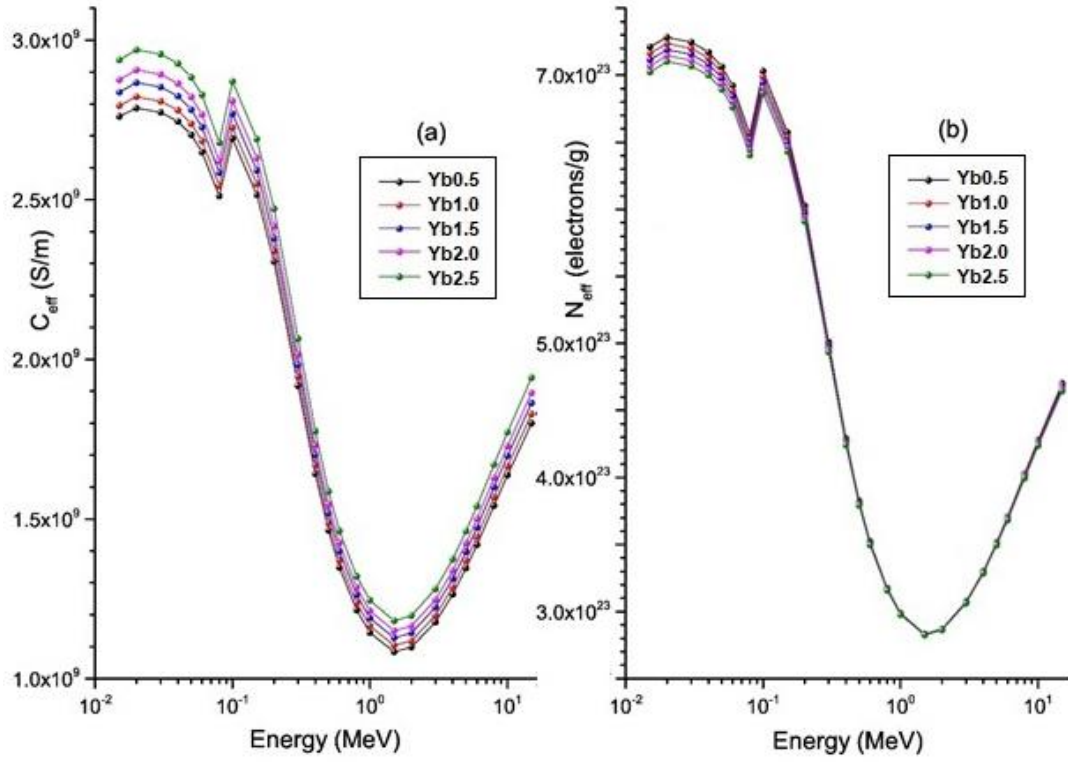


Figure 8. Changes of C_{eff} (a) and N_{eff} (b) values with photon energies.

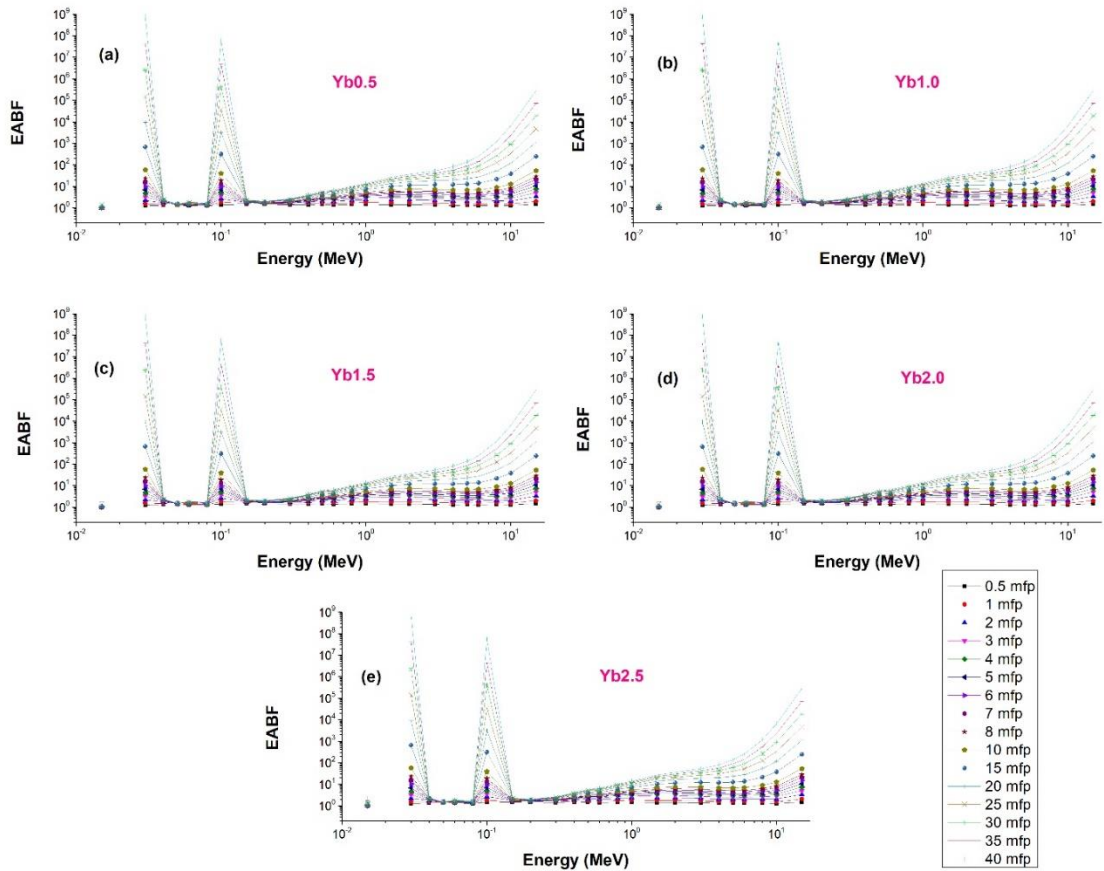


Figure 9. Variations of EABF values with photon energies.

The μ_{en} values are estimated and demonstrated in Fig. 11(a). The results (in cm²/g) are in the range 0.022946 - 2266.293, 0.022941 - 2261.435, 0.022936 - 2256.637, 0.022932 - 2251.895 and 0.022927 - 2247.195 for Yb0.5, Yb1.0, Yb1.5, Yb2.0 and Yb2.5, respectively. The findings follow this order: Yb2.5 < Yb2.0 < Yb1.5 < Yb1.0 < Yb0.5. Additionally, the KERMA values are determined and shown in Fig. 11(b). At low energies, KERMA values are at their minimum, and begins to increase and reaches its highest value at 0.04 MeV. The data then demonstrated a rapid decline, followed by an average behavior. Yb0.5 achieved the greatest KERMA at 0.04 MeV while Yb2.5 had the lowest KERMA.

The neutron attenuation of the glasses is determined by means of the thermal and FNRCS values and shown in Fig. 12. Yb2.5 has the highest value and Yb0.5 the lowest for fast neutrons. The FNRCS values are compared with some shielding materials such as Bi₂O₃ glass, graphite and borogypsum reported previously and illustrated in Fig. 12 [30,33,34]. Unlike fast neutrons, thermal ones have the lowest value for Yb2.5 and the highest for Yb0.5. This phenomenon can be explained by the high content of heavy elements, for example bismuth, which do not have the capacity to absorb fast neutrons effectively within the glass composition. Given that B is an effective thermal neutron absorber [35], the elevated B₂O₃ concentration in the glass Yb0.5 has resulted in a notable enhancement in the glass's thermal neutron absorption capacity. It can be also seen that thermal neutron attenuation is better for Yb⁺³ doped glasses than that of cement mortar with 10% and 20%, replacement of borosilicate glass powder studied by Jang et al. [36].

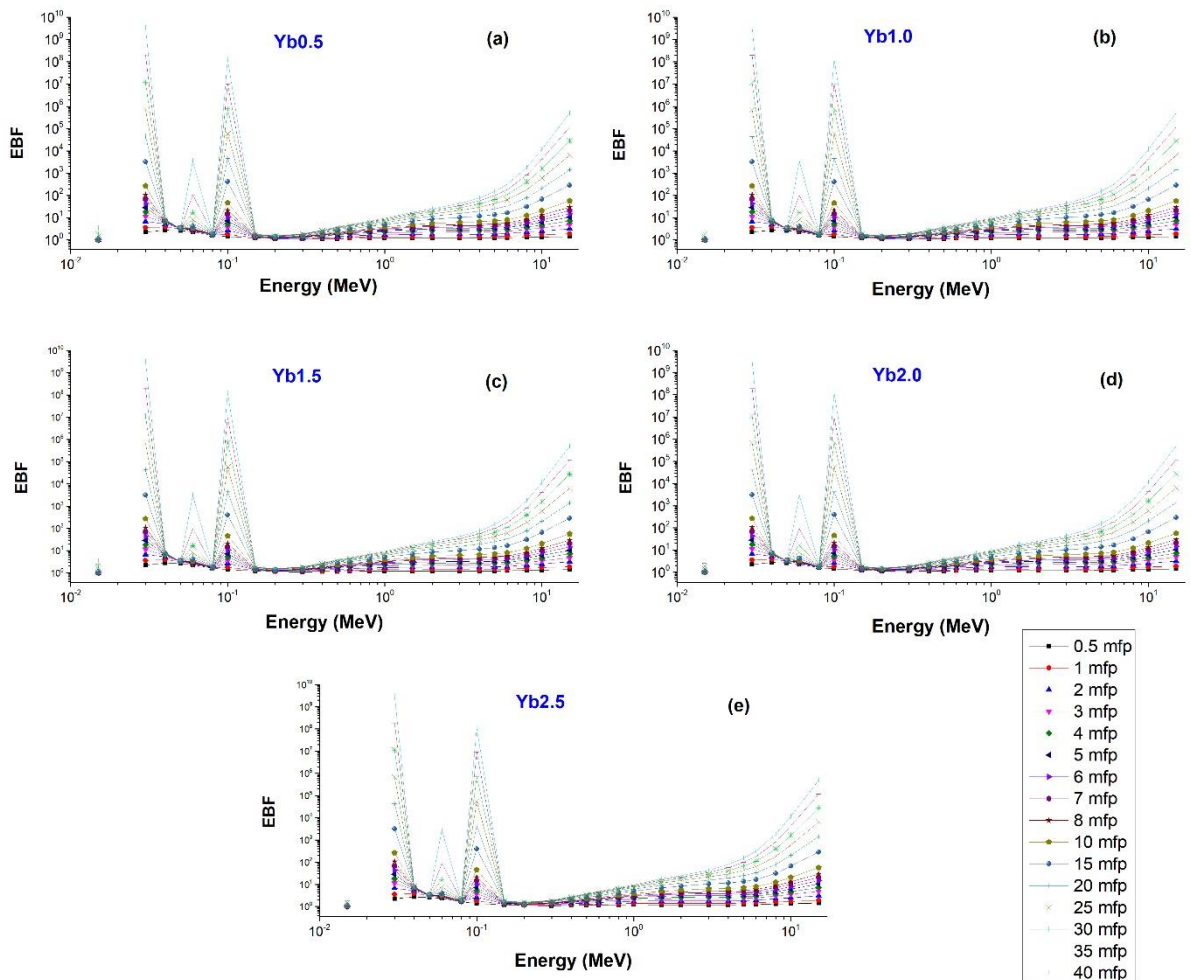


Figure 10. Variations of EBF values with photon energies.

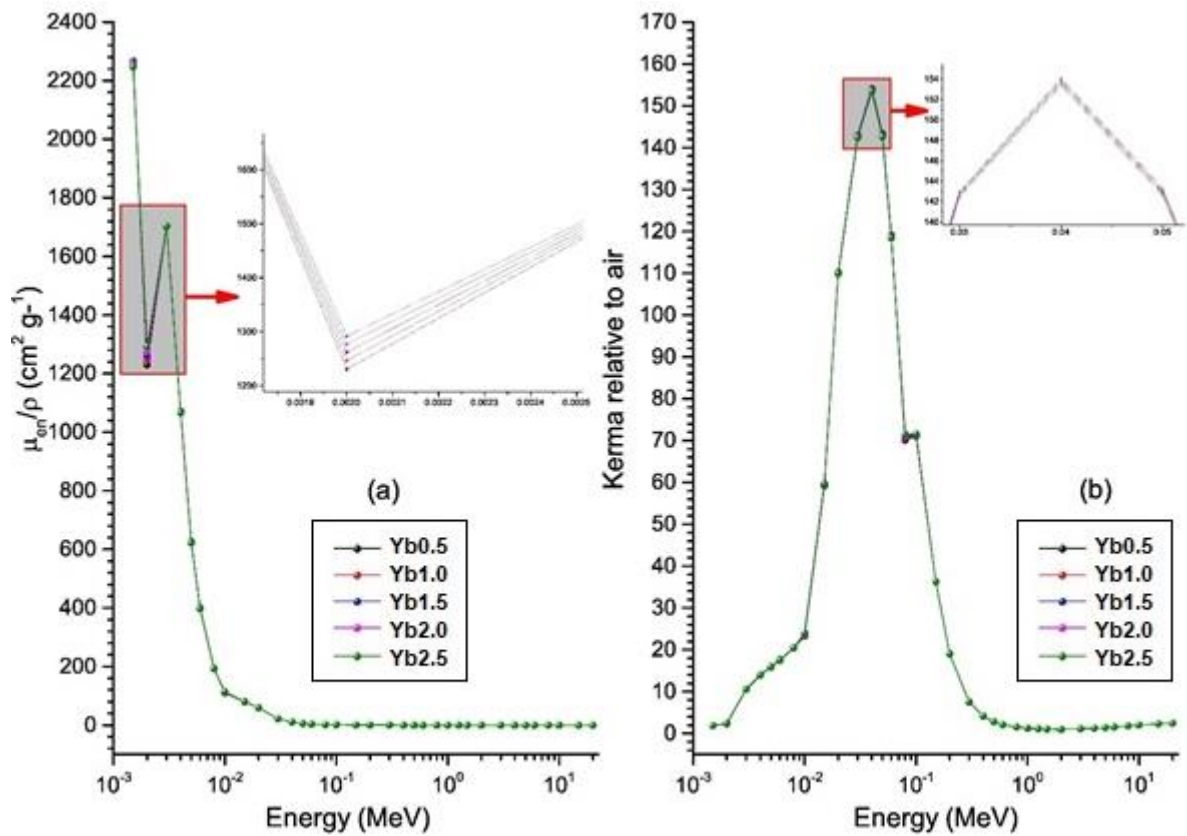


Figure 11. Variations of μ_{en}/ρ (a) and KERMA relative to air (b) values with photon energies.

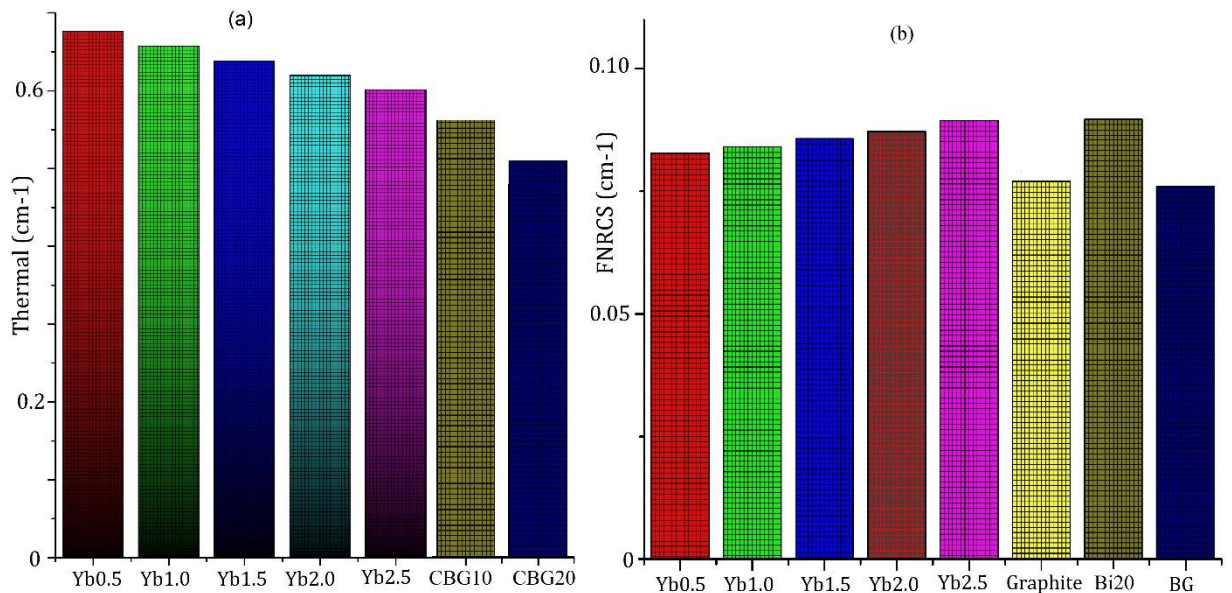


Figure 12. Comparison of thermal and FNRCS values of the glasses as comparative with previously reported materials.

The interaction of CPs with glasses is of paramount importance in radiation therapy. In order to ascertain the suitability of glasses for this aim, the MSP values of the electron, alpha and proton have been estimated for the glasses in question and the results have been presented in Fig. 13. The MSP values of electrons exhibit a decrease with increasing energy, followed by a gradual increase. In this case, the energy

loss mechanism of electrons is taken into account. It is supposed that electrons experience Coulomb interactions and bremsstrahlung. The MSP values (in MeV cm²/g) of electrons are among 1.196 – 137.0, 1.195 – 137.1, 1.194 – 137.2, 1.193 – 137.3 and 1.192 – 137.3 for Yb0.5, Yb1.0, Yb1.5, Yb2.0 and Yb2.5, respectively. MSP values for protons, increase with energy and subsequently, the value reduces in a gradual manner until the maximum is reached. The MSP results (in MeV cm²/g) of proton are among 1.306 – 219.136, 1.306 – 218.436, 1.305 – 217.735, 1.304 – 217.034 and 1.304 – 216.334 for Yb0.5, Yb1.0, Yb1.5, Yb2.0 and Yb2.5, respectively. The MSP for alpha particle exhibits an increase in energy prior to a subsequent decrease. It should be noted that the behavior of proton and alpha particles can be affected by the dependence of their electronic and nuclear energy losses, that in turn, can be influenced by the kinetic energy of the particles in question. The MSP values (in MeV cm²/g) of alpha are among 8.881 – 620.172, 8.877 – 618.671, 8.872 – 617.169, 8.868 – 615.668 and 8.863 – 614.166 for Yb0.5, Yb1.0, Yb1.5, Yb2.0 and Yb2.5, respectively. The MSP values for the glasses are given in the following order for the CPs: MSP_{electrons} < MSP_{protons} < MSP_{alpha}.

The Rp results are calculated by performing the SRIM and the ESTAR codes at 0.01 - 30 MeV, and are displayed in Fig. 14. The Rp values (in μm) for electron are among 1.1976 – 22180, 1.1765 – 21765, 1.1522 – 21310, 1.1306 – 20887 and 1.1007 – 20331 for Yb0.5, Yb1.0, Yb1.5, Yb2.0 and Yb2.5, respectively. The Rp results (in μm) for proton are among 0.1082 – 3380, 0.1063 – 3320, 0.1042 – 3250, 0.1022 – 3180 and 0.0995 – 3100 for Yb0.5, Yb1.0, Yb1.5, Yb2.0 and Yb2.5, respectively. The Rp results (in μm) for alpha are among 0.0713 – 157, 0.0701 – 152, 0.0686 – 148, 0.0673 – 144 and 0.0655 – 125 for Yb0.5, Yb1.0, Yb1.5, Yb2.0 and Yb2.5, respectively. The order of Rp values for the glasses is as follows: R_{alpha} < R_{proton} < R_{electron}. Additionally, the largest Rp values of CPs follow the following order: Yb0.5 > Yb1.0 > Yb1.5 > Yb2.0 > Yb2.5. It is of significant importance to note that the glass with the highest density exhibits a lower Rp value, while the glass with the lowest density exhibits the greatest Rp value.

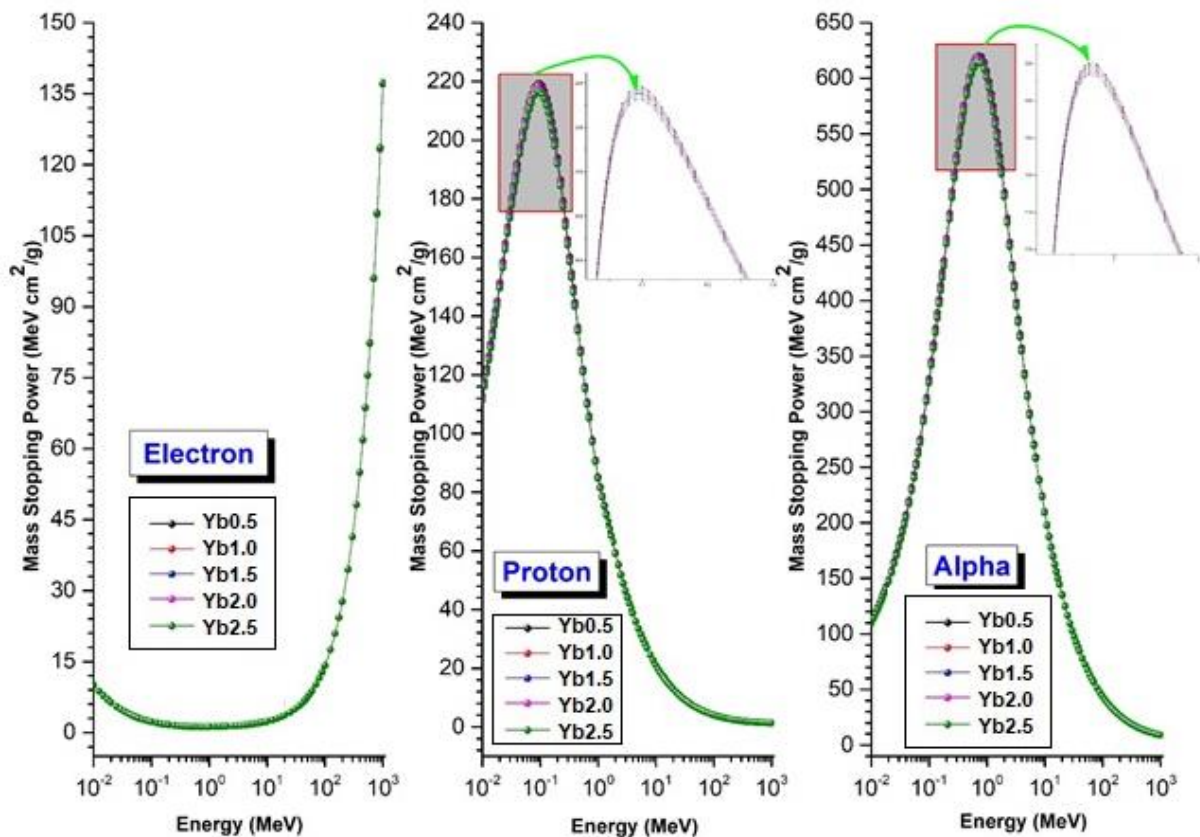


Figure 13. Dependence of MSP values of alpha, proton and electron particles versus the energy.

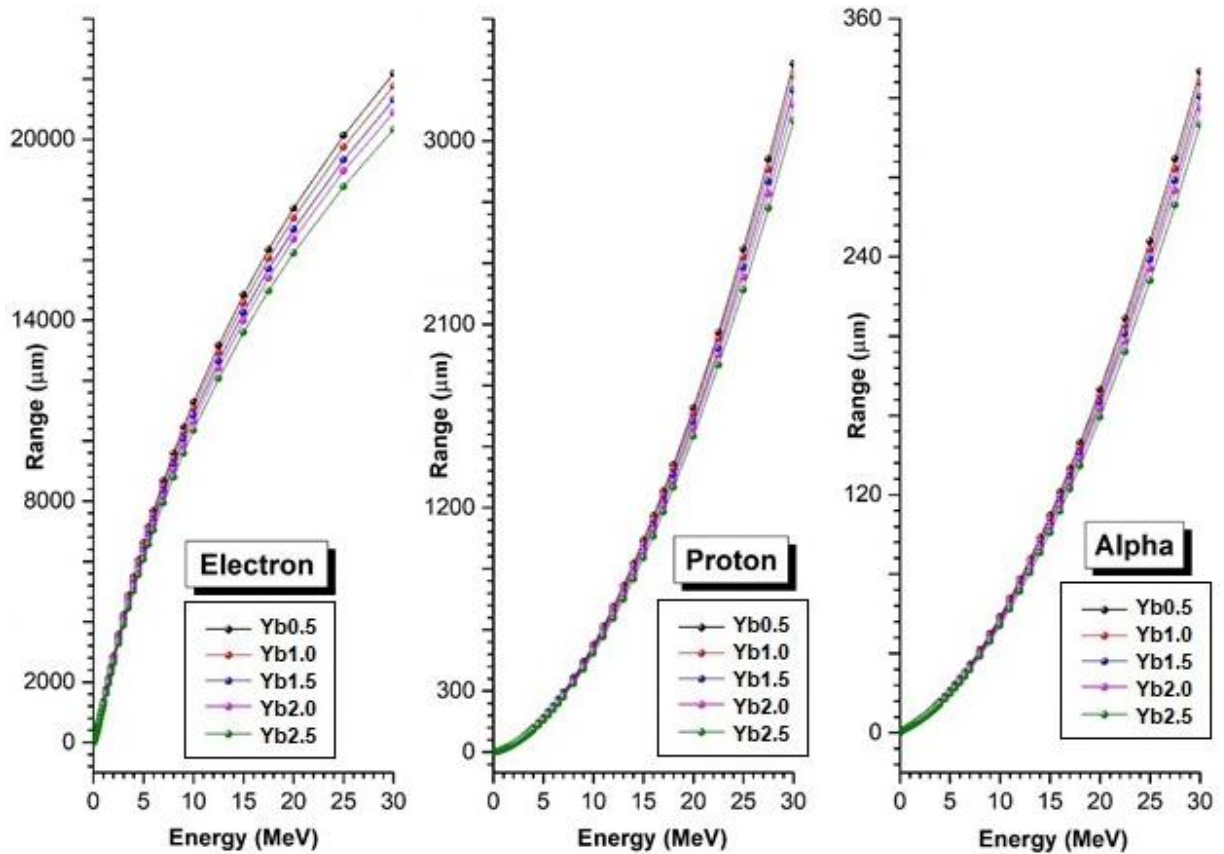


Figure 14. Changes of R_p values of alpha, proton and electron particles versus energy.

The Z_{eff} results of the glasses are illustrated in Fig. 15. The Z_{eff} values for electron are among 21.422 - 40.659, 21.623 - 40.804, 21.778 - 40.948, 21.925 - 41.091, 22.069 - 41.217 for Yb0.5, Yb1.0, Yb1.5, Yb2.0 and Yb2.5, respectively. The Z_{eff} values for proton are among 12.185 - 24.951, 12.191 - 25.814, 12.196 - 26.041, 12.202 - 26.164, 12.207 - 26.265 for Yb0.5, Yb1.0, Yb1.5, Yb2.0 and Yb2.5, respectively. The Z_{eff} results for alpha are among 13.447 - 38.556, 13.469 - 38.566, 13.703 - 38.576, 13.726 - 38.586, and 13.749 - 38.596 for Yb0.5, Yb1.0, Yb1.5, Yb2.0 and Yb2.5, respectively. From the results, the largest Z_{eff} values of the glasses for all the CPs give the following order: Yb0.5 < Yb1.0 < Yb1.5 < Yb2.0 < Yb2.5. The Z_{eff} values for electrons increase gradually with the kinetic energy for each sample. It has been documented that there is a non-monotonic variation in the behavior of alpha particles and protons in both low- and high-energy contexts. Furthermore, Z_{eff} values tend to increase with increasing glass density.

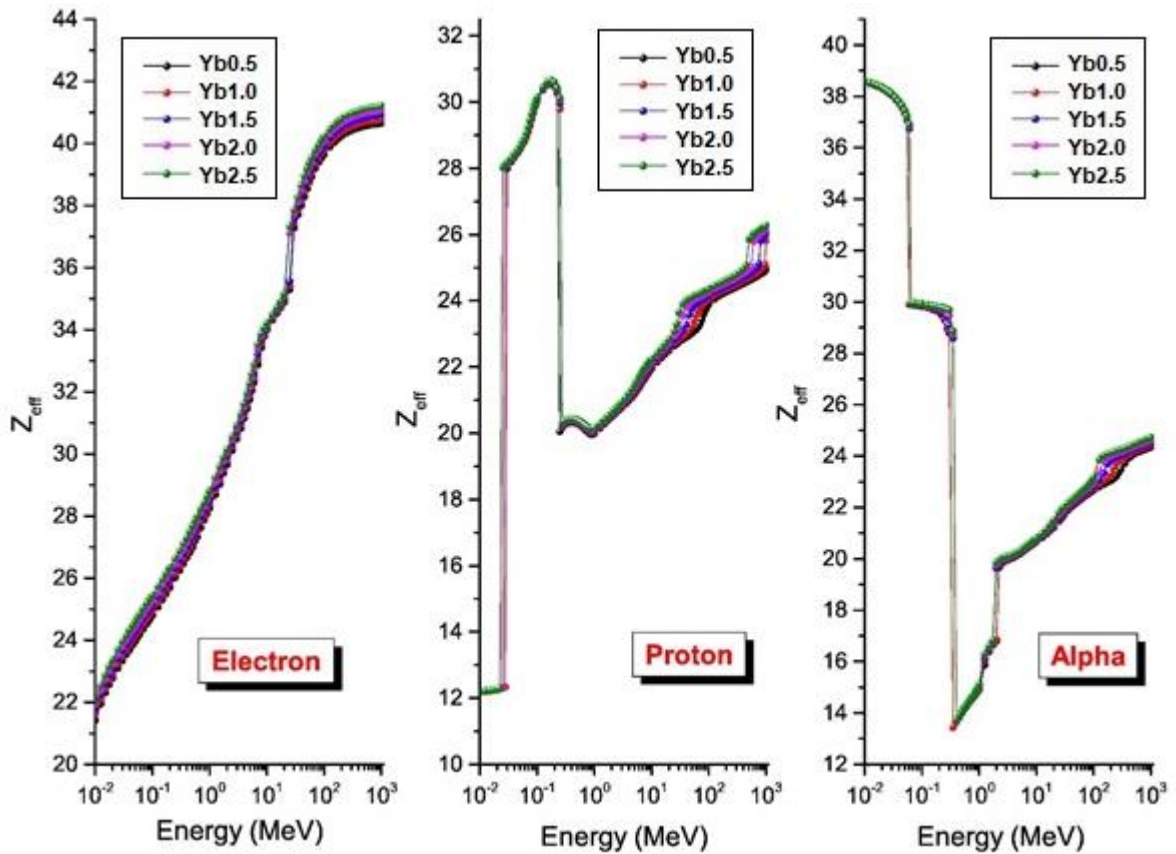


Figure 15. Variations of Z_{eff} values for alpha, proton and electron interactions with the studied glasses.

Also, the N_{eff} results of the glasses for the CPs are calculated and demonstrated in Fig. 16. The N_{eff} results (electrons/g) of electron are among $1.913 \times 10^{23} - 3.632 \times 10^{23}$, $1.921 \times 10^{23} - 3.624 \times 10^{23}$, $1.923 \times 10^{23} - 3.617 \times 10^{23}$, $1.926 \times 10^{23} - 3.609 \times 10^{23}$, $1.927 \times 10^{23} - 3.600 \times 10^{23}$ for Yb0.5, Yb1.0, Yb1.5, Yb2.0 and Yb2.5, respectively. The N_{eff} values (electrons/g) of proton are among $1.088 \times 10^{23} - 2.729 \times 10^{23}$, $1.083 \times 10^{23} - 2.716 \times 10^{23}$, $1.077 \times 10^{23} - 2.703 \times 10^{23}$, $1.071 \times 10^{23} - 2.691 \times 10^{23}$, $1.066 \times 10^{23} - 2.678 \times 10^{23}$ for Yb0.5, Yb1.0, Yb1.5, Yb2.0 and Yb2.5, respectively. The N_{eff} values (electrons/g) of alpha are among $1.201 \times 10^{23} - 3.444 \times 10^{23}$, $1.196 \times 10^{23} - 3.426 \times 10^{23}$, $1.210 \times 10^{23} - 3.407 \times 10^{23}$, $1.205 \times 10^{23} - 3.389 \times 10^{23}$, $1.201 \times 10^{23} - 3.371 \times 10^{23}$ for Yb0.5, Yb1.0, Yb1.5, Yb2.0 and Yb2.5, respectively. A similar pattern is observed in the N_{eff} values as Z_{eff} for electrons, which increase gradually with increasing kinetic energy for each glass sample. It is observed that non-monotonic variations in N_{eff} values for alpha and proton are present in both low and high-energy regions.

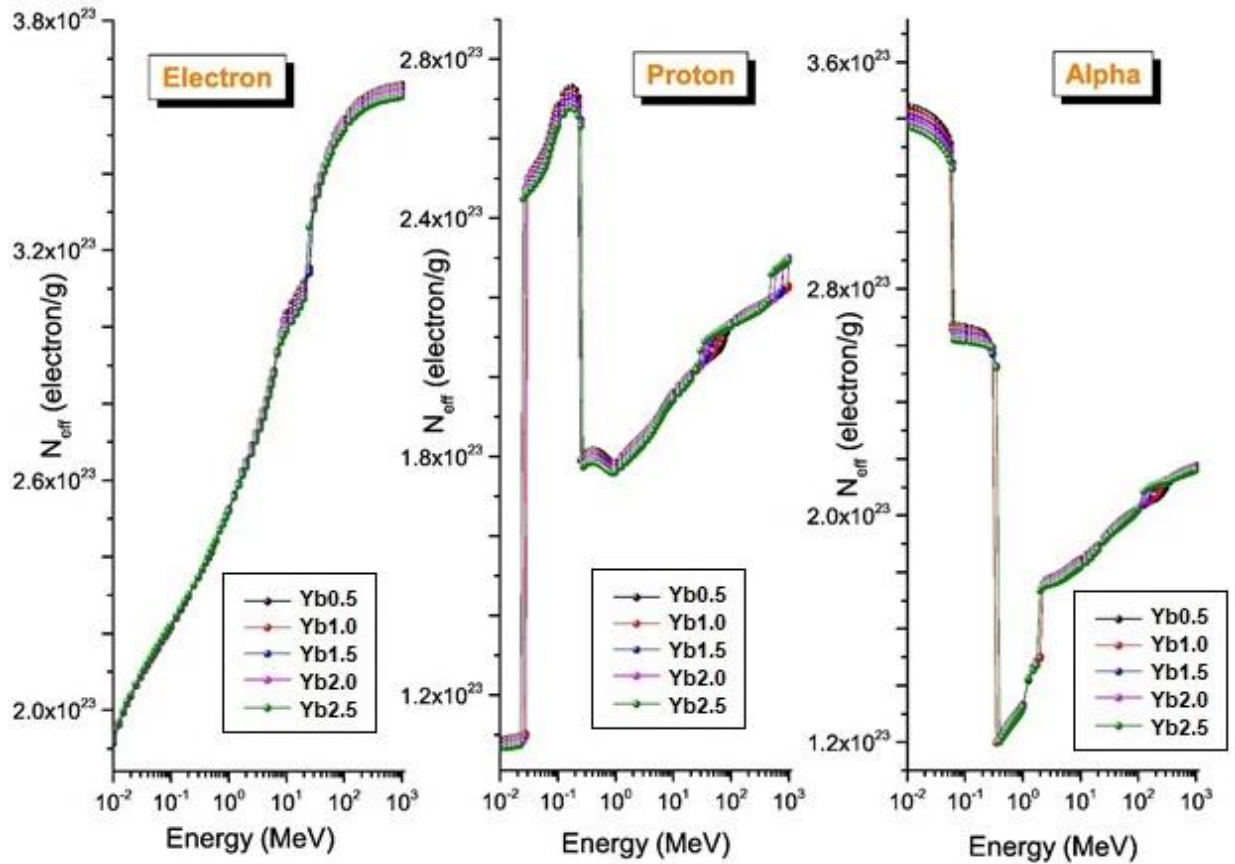


Figure 16. Variations of N_{eff} values for alpha, proton and electron interactions with the studied glasses.

4. CONCLUSIONS

In the paper, the radiation protection properties of Yb³⁺ doped glasses with contents of 50Bi₂O₃-15Li₂O-15PbO-(20-x)B₂O₃-Yb₂O₃ (x = 0.5, 1.0, 1.5, 2.0 and 2.5 mol%) were examined for fast neutron, CPs and gamma-ray by Phy-X/PSD, PAGEX, ESTAR and SRIM codes. The MACVs, LACVs, MFP, HVL, ACS, ECS and Z_{eff} values were evaluated and it was observed that these parameters exhibited energy-dependent behavior due to the photon interaction processes occurring across a broad spectrum of energies. In addition, the highest and lowest MACVs, LACVs, ACS, ECS, Z_{eff} and μ_{en} values were found for Yb_{2.5} and Yb_{0.5} while those of MFPVs and HVLVs were determined for Yb_{0.5} and Yb_{2.5} glasses, respectively. Since the best neutron shielding value was obtained for Yb_{2.5} that has the highest FNRCs value among the glass samples, it can be explained that it is the glass with the best neutron shielding feature. The CPs' MSP results for the glasses are obtained in the order of alpha>proton>electron. The glass with the Yb_{0.5} composition recorded the longest R_p values for CPs, while the glass with Yb_{2.5} gave the shortest values. This difference can be assigned to the necessity of minimum thickness. The glasses subjected to investigation displayed an enhanced capability to shield against a range of CPs when Yb³⁺ was introduced. The study revealed that Yb_{2.5} offers the highest level of protection against gamma rays, neutrons and CPs, while Yb_{0.5} demonstrated the least effective performance among the glasses. It can be concluded that glasses with a higher proportion of Yb³⁺ provide a superior level of protection, while those with a lower proportion of Yb³⁺ offer a lesser degree of protection. As a result of this, it can be said that Yb³⁺ activated glasses with a composition of 50Bi₂O₃-15Li₂O-15PbO-(20-x)B₂O₃-Yb₂O₃ can be applied as good shields for use in a wide range of applications. The results suggest that the investigated glasses with high Bi (Bi50) content and Yb³⁺ addition may have excellent radiation attenuation properties making them a promising option for radiation shielding applications. The attenuation of the RE-doped glasses is

a notable factor in achieving enhanced shielding, which in turn makes them appropriate for use in lighting technologies. It can thus be posited that Yb³⁺-doped glasses will prove instrumental in the advancement of material designs.

Declaration of Ethical Standards

Not applicable

Credit Authorship Contribution Statement

M. AYGUN: Conceptualization, Methodology, Writing original draft, Visualization, Investigation.

Z. AYGUN: Methodology, Writing original draft, Visualization, Investigation.

I. HAN: Writing original draft, Visualization, Investigation.

E. NARMANLI HAN: Writing- review, Visualization and editing.

Declaration of Competing Interest

The authors declare that they have no known competing financial interests or personal relationships that could have appeared to influence the work reported in this paper.

Funding

Not applicable

Data Availability

Data of this study are available from the corresponding author on responsible request.

5. REFERENCES

- [1] M. Ahmadi, Z. Vahid, N. Darush, "Investigated mechanical, physical parameters and Gamma-Neutron radiation shielding of the rare earth (Er₂O₃/CeO₂) doped barium borate glass: Role of the melting time and temperature," *Radiat. Phys. Chem.*, vol. 217, p. 111450, 2024. <https://doi.org/10.1016/j.radphyschem.2023.111450>
- [2] N. Almousa, S.A.M. Issa, A.S. Abouhaswa, H.M.H. Zakaly, "Improved radiation shielding efficiency and optical properties of borate glass by incorporating dysprosium(III) oxide," *Mater. Today Commun.*, vol. 39, p. 109198, 2024. <https://doi.org/10.1016/j.mtcomm.2024.109198>
- [3] H.Al-Ghamdi, N.A.M. Alsaif, Z.Y. Khattari, A.A. El-Hamalawy, R. S. Diab, et al., "Development of Ce³⁺- and Yb³⁺-doped borate glasses for optical and radiation protection materials," *J. Mater. Sci.: Mater. Electron*, vol. 34, p. 1272, 2023. <https://doi.org/10.1007/s10854-023-10687-1>
- [4] M. Aygun, "Gamma-ray, fast neutron and charged particle shielding performance of 15Li₂O-25BaO-(40-x)B₂O₃-20P₂O₅-xDy₂O₃ glass system," *Radiat. Phys. Chem.*, vol. 219, p. 111671, 2024. <https://doi.org/10.1016/j.radphyschem.2024.111671>
- [5] P. Ramesh, Vinod Hegde, A.G. Pramod, B. Eraiah, D.A. Agarkov, G.M. Eliseeva, M.K. Pandey, K. Annapurna, G. Jagannath, M.K. Kokila, "Compositional dependence of red photoluminescence of Eu³⁺ ions in lead and bismuth containing borate glasses," *Solid State Sci.*, vol. 107, p. 106360, 2020. <https://doi.org/10.1016/j.solidstatesciences.2020.106360>.
- [6] M. Pokhrel, G. A. Kumar, D. K. Sardar, "Highly efficient NIR to NIR and VIS upconversion in Er³⁺ and Yb³⁺ doped in M₂O₂S (M = Gd, La, Y)," *J. Mater. Chem. A*, vol. 38, pp. 11595-11606, 2013. <https://doi.org/10.1039/C3TA12205K>
- [7] C. Wang, Xueqiang Liu, Kuan Peiwen, Peng Wang, Liyan Zhang, Danping Chen, "~1µm laser output based on heterogeneous fiber with Yb³⁺-doped fluorophosphate core and phosphate

- cladding," *Mater. Letters*, vol. 179, pp. 9-11, 2016. <https://doi.org/10.1016/j.matlet.2016.05.033>.
- [8] J. Bhemarajam, M. Varkolu, P. Syam Prasad, M. Prasad, "Effect of Yb³⁺ ions on spectroscopic and optical properties of Bi₂O₃-B₂O₃-Li₂O-PbO glass system," *Results in Optics*, vol. 14, p. 100582, 2024, <https://doi.org/10.1016/j.rio.2023.100582>
- [9] I.G. Geidam, K.A. Matori, M.K. Halimah, K.T. Chan, et al., "Thermo-physical and elastic properties of Bi₂O₃ doped silica borotellurite glasses," *Optik*, vol. 248, p. 168201, 2021. <https://doi.org/10.1016/j.jjleo.2021.168201>
- [10] M. Kurudirek, N. Chutithanapanon, R. Laopaiboon, C. Yenchai, C. Bootjomchai, "Effect of Bi₂O₃ on gamma ray shielding and structural properties of borosilicate glasses recycled from high pressure sodium lamp glass," *J. Alloys Compd.*, vol. 745, pp. 355-364, 2018. <https://doi.org/10.1016/j.jallcom.2018.02.158>
- [11] K.A. Naseer, K. Marimuthu, M.S. Al-Buriah, A. Alalawic, H.O. Tekin, "Influence of Bi₂O₃ concentration on barium-telluro-borate glasses: Physical, structural and radiation-shielding properties," *Ceramics Inter.*, vol. 47, pp. 329-340, 2021. <https://doi.org/10.1016/j.ceramint.2020.08.138>
- [12] E.V. Malchukova, A.I. Nepomnyashchikh, B. Boizot, and E.I. Terukov, "Radiation Effects and Optical Properties of Aluminoborosilicate Glass Doped with RE Ions," *Glass Phys. Chem.*, vol. 44, no. 4, pp. 356-363, 2018. <https://doi.org/10.1134/S1087659618040090>
- [13] E.V. Malchukova, and B. Boizot, "Reduction of Eu³⁺ to Eu²⁺ in aluminoborosilicate glasses under ionizing radiation", *Mater. Res. Bull.*, vol. 45, pp. 1299-1303, 2010. <https://doi.org/10.1016/J.MATERRESBULL.2010.04.027>
- [14] G. Lakshminarayana, Ashok Kumar, H.O. Tekin, Shams A.M. Issa, M.S. Al-Buriah, Dong-Eun Lee, Jonghun Yoon, Taejoon Park, "Binary B₂O₃-Bi₂O₃ glasses: scrutinization of directly and indirectly ionizing radiations shielding abilities," *J. Mater. Res. Technol.*, vol. 9, no. 6, pp. 14549-14567, 2020. <https://doi.org/10.1016/j.jmrt.2020.10.019>.
- [15] P. Vani, G. Vinitha, M.I. Sayyed, Maha M. AlShammari, N. Manikandan, "Effect of rare earth dopants on the radiation shielding properties of barium tellurite glasses," *Nucl. Engineer. Technol.*, vol. 53, no. 12, pp. 4106-4113, 2021. <https://doi.org/10.1016/j.net.2021.06.009>.
- [16] E.M. Abou Hussein, A. Sobhy, "Experimental investigation of new rare earth borosilicate glasses from municipal waste ash as high-dose radiation dosimeters," *Ceramics Inter.*, vol. 50, no. 13, pp. 23012-23024, 2024. <https://doi.org/10.1016/j.ceramint.2024.04.023>.
- [17] K.G. Mahmoud, M.I. Sayyed, A.S. Abouhaswa, "Optical and γ -ray absorption characteristics of Yb₂O₃-doped borate based glasses: a step towards understanding the substitution of B₂O₃/Yb₂O₃ in the lead borate glass system," *Physica Scripta*, vol. 98(11), 2023. <http://dx.doi.org/10.1088/1402-4896/ad00e7>
- [18] H.H. Negm, A.A. Sdeek, A.A. Ebrahim, "The Role of Ytterbium (Yb₂O₃) in the Radiation Shielding Properties of Barium Titanium Borate Glasses (B₂O₃-TiO₂-BaO) in Terms of γ and β Radiations," *J. Electronic Mater.*, vol. 53, pp. 3965-3979, 2024. <https://doi.org/10.1007/s11664-024-11073-1>
- [19] N. Tamam, Z.A. Alrowaili, I.O. Olarinoye, A. Hammoud et al., "Fabrication and characterisation of TeO₂-based composite doped with Yb³⁺ and Bi³⁺ for enhanced radiation shielding safety," *Radiat. Phys. Chem.*, vol. 215, p. 111315, 2024. <https://doi.org/10.1016/j.radphyschem.2023.111315>
- [20] E. Şakar, Ö.F. Özpolat, B. Alim, M.I. Sayyed, M. Kurudirek, "Phy-X / PSD: Development of a user friendly online software for calculation of parameters relevant to radiation shielding and dosimetry," *Radiat. Phys. Chem.*, vol. 166, p. 108496, 2020. <https://doi.org/10.1016/j.radphyschem.2019.108496>
- [21] J.F. Ziegler, "SRIM-The Stopping and Range of Ions in Matter,". <http://www.srim.org>.
- [22] S. Prabhu, S. Jayaram, S.G. Bubbly, S.B. Gudennavar, "A simple software for swift computation of photon and charged particle interaction parameters: PAGEX," *Appl. Radiat. Isotopes*, vol. 176, p. 109903, 2021. <https://doi.org/10.1016/j.apradiso.2021.109903>

- [23] I. Han, L. Demir, "Studies on effective atomic numbers, electron densities from mass attenuation coefficients in TixCo1-x and CoxCu1-x alloys," *Nucl. Instr. Methods in Phys. Res. Section B*, vol. 267, pp. 3505–3510, 2009. <https://doi.org/10.1016/j.nimb.2009.08.022>
- [24] H.C. Manjunatha, "A study of gamma attenuation parameters in poly methyl methacrylate and Kapton," *Radiat. Phys. Chem.*, vol. 137, pp. 254–259, 2017. <https://doi.org/10.1016/j.radphyschem.2016.01.024>
- [25] Y. Harima, "An historical review and current status of buildup factor calculations and applications," *Radiat. Phys. Chem.*, vol. 41, pp. 631–672, 1993.
- [26] Y. Harima, Y. Sakamoto, S. Tanaka, M. Kawai, "Validity of the Geometric-Progression Formula in Approximating Gamma-Ray Buildup Factors," *Nucl. Sci. Engineer.*, vol. 94, pp. 24–35, 1986.
- [27] ANSI/ANS 6.4.3 Gamma-ray Attenuation Coefficients and Buildup Factors for Engineering Materials. American Nucl Soc, La Grange Park, Illinois, 1991.
- [28] K.R.M. Abdelgawad, G.S.M. Ahmed, A.T.M. Farag, A.A. Bendary, B.A. Tartor, I.I. Bashter, S.M. Salem, "Eco-friendly transparent glass prepared from rice straw ash for neutron and charged particle radiation shielding," *Annl. Nucl. Energy*, vol. 191, p. 109939, 2023. <https://doi.org/10.1016/j.anucene.2023.109939>
- [29] M.F. L'Annunziata, "Nuclear Radiation, Its Interaction With Matter And Radioisotope Decay," *Handbook of Radioactivity Analysis*, pp. 1-122, 2003.
- [30] M. Aygun, Z. Aygun., "A comprehensive analysis on radiation shielding characteristics of borogypsum (boron waste) by Phy-X/PSD code," *Revista Mexicana de Fisica*, vol. 69, pp. 1–7, 2023. <https://doi.org/10.31349/RevMexFis.69.040401>
- [31] I.I. Bashter, "Calculation of radiation attenuation coefficients for shielding concretes," *Annl. Nucl. Energy*, vol. 24, pp. 1389-1401, 1997. [https://doi.org/10.1016/S0306-4549\(97\)00003-0](https://doi.org/10.1016/S0306-4549(97)00003-0)
- [32] G. Lakshminarayana, Y. Elmahroug, A. Kumar, H.O. Tekin, et al., "Detailed Inspection of γ -Ray, Fast and Thermal Neutrons Shielding Competence of Calcium Oxide or Strontium Oxide Comprising Bismuth Borate Glasses," *Mater.* vol. 14, p. 2265, 2021. <https://doi.org/10.3390/ma14092265>
- [33] K.M. Kaky, M.I. Sayyed, M.K. Hamad, S. Biradar, M.H.A. Mhareb, U. Altimari, M.M. Taki, "Bismuth Oxide Effects on Optical, Structural, Mechanical, and Radiation Shielding Features of Borosilicate glasses," *Optical Mater.* <https://doi.org/10.1016/j.optmat.2024.115853>.
- [34] M. Al-Buriahi, A. Abouhaswa, H. Tekin, C. Sriwunkum, F. El-Agawany, T. Nutaro, et al., "Structure, optical, gamma-ray and neutron shielding properties of NiO doped B₂O₃-BaCO₃-Li₂CO₃ glass systems," *Ceram. Int.*, vol. 46, pp. 1711–1721, 2020. <https://doi.org/10.1016/j.ceramint.2019.09.144>.
- [35] Y.S. Rammah, F.I. El-Agawany, A. Gamal, I.O. Olarinoye, E.M. Ahmed, A.S. Abouhaswa, "Responsibility of Bi₂O₃ Content in Photon, Alpha, Proton, Fast and Thermal Neutron Shielding Capacity and Elastic Moduli of ZnO/B₂O₃/Bi₂O₃ Glasses," *J. Inorganic Organometallic Polymers Mater.*, vol. 31, pp. 3505–3524, 2021. <https://doi.org/10.1007/s10904-021-01976-5>
- [36] B.K. Jang, J.C. Lee, J.H. Kim, C.W. Chung, "Enhancement of thermal neutron shielding of cement mortar by using borosilicate glass powder," *Appl. Radiat. Isot.*, vol. 123, pp. 1-5, 2017. <https://doi.org/10.1016/j.apradiso.2017.01.047>

ESTIMATING THE SOLAR EXERGY POTENTIAL OF SURFACES WITH DIFFERENT TILT ANGLES

^{1,*}Ahmet KABUL , ²Fatih YİĞİT , ³Aslı DURAN 

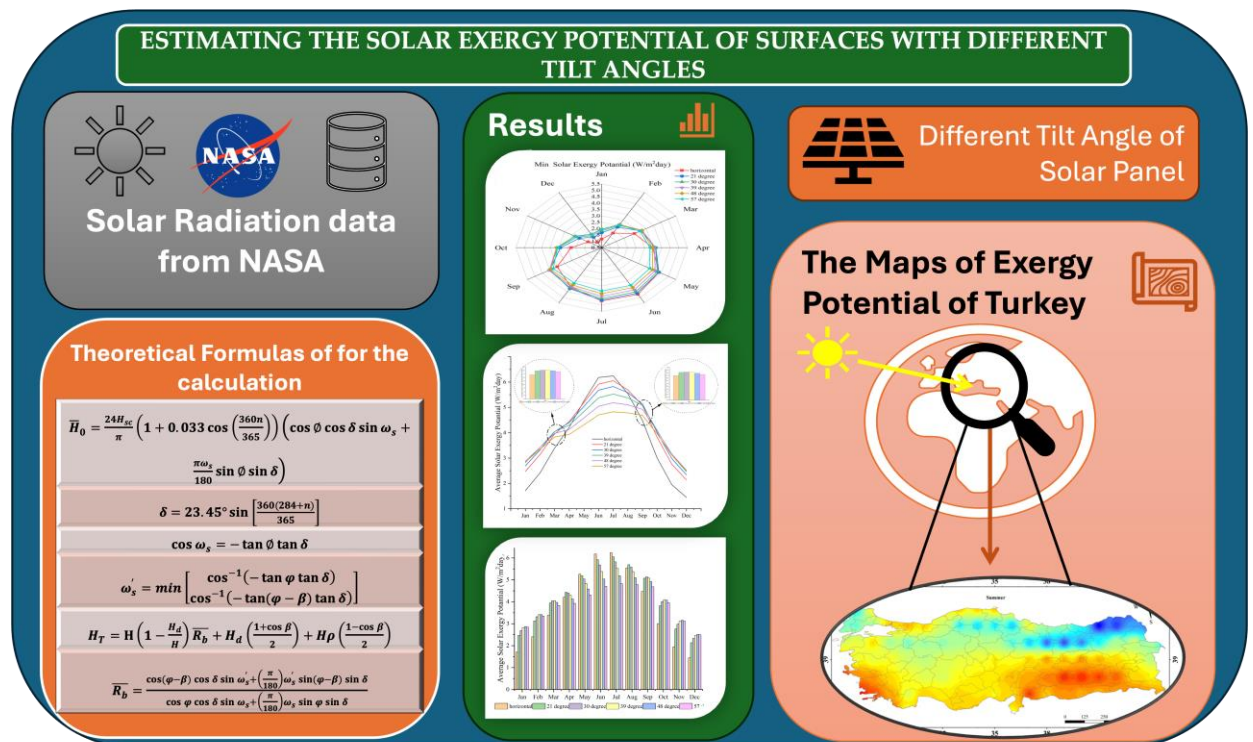
Isparta University of Applied Science, Technology Faculty, Mechanical Engineering Department, Isparta, TÜRKİYE

ahmetkabal@isparta.edu.tr, fatihyigit@isparta.edu.tr, y12230640027@isparta.edu.tr

Highlights

- The importance of utilizing Turkey's solar energy potential
- The effect of different tilt angles on solar energy potential
- Determination of the exergy potential of solar energy at different tilt angles
- Solar exergy maps of Turkey at the optimum tilt angle

Graphical Abstract





ESTIMATING THE SOLAR EXERGY POTENTIAL OF SURFACES WITH DIFFERENT TILT ANGLES

^{1,*} Ahmet KABUL , ²Fatih YİĞİT , ³Aslı DURAN 

Isparta University of Applied Science, Technology Faculty, Mechanical Engineering Department, Isparta, TÜRKİYE

ahmetkabal@isparta.edu.tr, fatihyigit@isparta.edu.tr, yl2230640027@isparta.edu.tr

(Received: 24.04.2024; Accepted in Revised Form: 19.08.2024)

ABSTRACT: Solar energy, which is a clean, unlimited, and environmentally friendly energy source, has critical importance in sustainable energy management. The usable potential of energy is expressed in terms of exergy, and the determination of the exergy potential of solar energy ensures the correct utilization of this potential. Turkey has a very high solar energy potential, and this potential should be utilized in the most efficient way possible to achieve sustainable energy targets. The tilt angle of solar panels has a significant effect on efficiency. Efficient operation of solar panels can be achieved by determining the optimum tilt angle. In this study, Turkey's solar exergy potential was calculated for the horizontal plane and five different tilt angles (21°, 30°, 39°, 48°, and 57°). Thus, it was tried to determine the appropriate panel angle to get the highest efficiency from solar panels that can be used in different regions of Turkey. The calculations are based on 22-year average solar energy potential data obtained from NASA. The exergy potential was determined for the coordinates where Turkey is located, and the potential for the regions between the coordinates was determined by the interpolation method. With the interpolation method used, an approximate estimation for the areas where there is no measurement is also provided, and it is aimed at saving the time and cost required for long-term measurements. Among the tilt angles analyzed, the optimum angle for the whole year was determined to be 30 degrees. The exergy potential for 30° inclined surfaces in all coordinates of Turkey is given as a seasonal map. With the use of the maps, it is thought that the optimum angle and exergy potential for different regions and seasons of Turkey will be predicted, and thus it will be easier for new investors to determine the high-potential regions of Turkey.

Keywords: Exergy Potential, Optimum Tilt Angle, Solar Energy, Solar Exergy Potential Maps

1. INTRODUCTION

Energy is essential for sustaining human existence, providing comfort, and meeting needs. The sustainable management of energy is necessary to meet all these demands, keep the economy and industry running, and preserve a habitable environment [1], [2]. Conventional energy sources, especially fossil fuels, provide much of the energy needed by the modern world. However, the exploitation of these resources causes pollution, such as greenhouse gas emissions, which accelerate climate change and damage ecosystems. The use of renewable energy sources might help to lessen these detrimental impacts on the environment. Renewable energy sources are essential for a sustainable future, and solar energy is particularly notable among them [3], [4]. Solar energy is essential to meeting our energy demands since it is a clean, endless, and environmentally friendly energy source. Determining solar energy's potential is crucial to its efficient utilization. Utilizing Turkey's abundant solar energy resources is essential to achieving sustainable energy targets and expanding the country's energy portfolio [5]. Several studies have explored Turkey's solar energy potential, focusing on various regions and employing different methodologies to evaluate and optimize solar energy applications.

Turkey's solar energy potential has been the subject of several studies. Research conducted in the province of Karabük aimed to evaluate local solar energy applications and examine the benefits and drawbacks of this energy source [6]. An efficiency map was made using the Analytical Hierarchy Process

*Corresponding Author: Ahmet KABUL, ahmetkabal@isparta.edu.tr

(AHP) technique to evaluate the solar energy potential of Gaziantep province [7]. In the province of Kars, potential sites for solar power plant projects were identified by the application of AHP methodologies and CSB investigations [8]. An attempt was made to determine which of the three accessible alternative provinces—Istanbul, Nevşehir, and Bilecik—is the best location for a solar power plant (SPP) to be established in Turkey using the Multi-Criteria Decision Making (MCDM) approach [9]. Several studies have been conducted to evaluate Turkey's energy situation, renewable energy resources, and solar energy [10], [11], [12], [13].

A fundamental concept in thermodynamic analysis and performance evaluation of energy systems is the determination of energy potential. Exergy is a unit of measurement for energy quality that describes an energy form's capacity for work. In addition to energy analysis, exergy analysis provides a more accurate and efficient means of evaluating energy conversion or distribution processes and systems. Energy is wasted during recycling in real processes, whereas it is saved during ideal processes. Consequently, exergy can be employed to calculate the thermal losses and inefficiencies of each energy system unit, as well as a useful indicator of possible environmental effects. Researchers have carried out studies on the exergy of Turkey's solar energy potential. The exergy of global solar radiation was investigated using measurement data for Erzurum province [14]. In another study, horizontal-plane solar radiation data were taken from 8 measurement stations in Turkey, and energy and exergy research were carried out for these regions [15]. The researchers analyzed Turkey's solar radiation exergy and the environmental-economic analysis of solar radiation incidents on the horizontal plane [16].

The tilt angle of solar panels with respect to the surface can have a substantial impact on their efficiency. By ensuring that the sun's rays reach the panels at their highest level, the optimal tilt angle increases the amount of energy produced. According to studies, altering the tilt angles can have a significant impact on the amount of energy that solar panels can capture annually [17], [18], [19], and [20]. For instance, a study conducted in Kayseri revealed that positioning solar panels with an optimal monthly tilt angle yielded 4.11% more energy than a constant annual tilt angle. Additionally, it was demonstrated that adjusting seasonal and semi-annual tilt angles could enhance energy efficiency, although this increase was less pronounced than that observed with monthly adjustments [21].

The Photovoltaic Geographic Information System (PVGIS) [22] and the Hottel & Woertz (HW) methods are two of the techniques used to calculate the tilt angles. The optimal tilt angles for the panels are determined using these techniques, considering the region and climate data currently available. The PVGIS approach employs satellite-interactive meteorological data to simulate the ideal hourly, daily, monthly, and annual solar radiation levels based on the desired geographic location and panel tilt angle.

A study conducted in Ardahan province demonstrated that surfaces with the optimal tilt angle for each day exhibited an increase of up to 17% in annual total solar radiation values when compared to horizontal surfaces. The minimum increase was 3.4% on surfaces with a $\beta = \phi + 15^\circ$ tilt angle [23]. A comprehensive evaluation of solar collectors at various tilt angles has been conducted for the province of Erzincan, with particular focus on energy and exergy considerations [24]. These studies demonstrate the importance of solar collector tilt and orientation in optimizing solar radiation energy harvesting. Identifying the optimal tilt angles is crucial for enhancing the efficiency of solar energy systems and reducing energy costs. Furthermore, these studies present a scientific approach for planning and arranging solar collectors, enabling a more effective utilization of renewable energy sources.

Despite these efforts, a gap remains in understanding the exergy potential of solar energy in Turkey, particularly concerning the optimal tilt angles for solar panels. This study addresses this gap by calculating the solar energy potential for different tilt angles and providing detailed seasonal maps. The primary contributions of this study are the identification of the optimum tilt angle for maximizing solar energy potential and the presentation of energy potential maps that can guide future solar energy investments in Turkey.

In this study, the exergy potential of surfaces with varying tilt degrees can be quantified, providing valuable insights for solar collector design and optimization. This knowledge can be used to inform the design of solar energy collectors, enabling more effective use of solar energy. The data set utilized for this

study comprised the 22-year average total average daily irradiation to the horizontal plane, diffuse average daily irradiation to the horizontal plane, and outdoor temperatures at 10 m height. These data were obtained from NASA for 140 coordinate points located between 26° and 45° east. As a general approach, it is recommended to position the solar panels so that the latitude angle of the panels is 15 degrees below the latitude angle in summer and 15 degrees above the latitude angle in winter. Therefore, considering Turkey's smallest latitude angle of 36 degrees and the largest latitude angle of 42 degrees, angles that will cover 15 degrees more (57 degrees) and 15 degrees less (21 degrees) were studied. The calculations of Turkey's solar energy potential were made for both horizontal and five different inclination angles (21°, 30°, 39°, 48°, and 57°), covering a latitude range of 36°–42° north parallel.

The long-term NASA data and IDW interpolation method used in this study allow us to make accurate forecasts even in missing data regions. This is one of the innovative aspects of our study. In addition, the detailed examination of the performance of specific tilt angles in different seasons provides a more comprehensive analysis compared to other studies in this field.

The organization of this paper is as follows: Section 2 describes the materials and methods used in this study, including the exercise analysis and the determination of solar potential. Section 3 presents the results and discussion, including seasonal exercise potential maps and an analysis of different tilt angles. Finally, Section 4 concludes the study and suggests directions for future research.

2. MATERIAL AND METHODS

To optimize the utilization of solar radiation in solar energy system design, it is of paramount importance to accurately calculate the tilt angles of the solar collectors. By ensuring that the sun's rays are perpendicular to the collector surface, these angles enhance the efficiency of energy collection. The optimal tilt angle of the collectors is significantly influenced by variations in solar incidence angles due to seasonal variations and geographic locations.

The following equations are employed to determine the inclination angles of 21°, 30°, 39°, 48°, and 57° on a horizontal plane, with the objective of illustrating the impacts of these angles on the exergy potential of solar energy. To determine the solar exergy potential, the diffuse average daily irradiance to the horizontal plane, the 22-year average total average daily irradiance to the horizontal plane, and the outdoor temperatures at a height of 10 meters were taken into consideration for 140 coordinate points between the 26°–45° east latitudes and the 36°–42° north parallels in Turkey.

2.1. Exergy Analysis

Exergy is the portion of the thermodynamic potential that can be transformed into the greatest amount of work. It is a key concept in determining the amount of work that thermodynamic systems can produce. It is frequently used to evaluate the energy quality of thermodynamic systems and to identify potential flaws or issues. When a system moves from its current thermodynamic equilibrium to one of reversible processes and reaches equilibrium with its external environment, that state is referred to as exertion. When there is no exchange of matter or energy between a thermodynamic system and its environment, or in the case of reversible processes, the maximum amount of work that can be produced from the system is measured. In this case, the external work of the system is maximized, but its internal energy and entropy are constant. Exergy is the name given to this maximum theoretical work [25], [26].

In Equation 1, the ratio of the maximum work (W) that can be achieved using radiation to the energy "E" of the solar source can be used to mathematically describe the conversion efficiency of thermal radiation into real work [27].

$$\eta = \frac{W}{E} \quad 1$$

This useful work from radiation will be maximized for a reversible process. The highest formula efficiency is given in Equation 2 below.

$$\eta_{c,max} = \frac{W_{max}}{E} \quad 2$$

The exergy of the system is the maximum amount of work that can be extracted, and the exergy efficiency is the maximum system efficiency. Exergy efficiency can be expressed as in Equation 3:

$$\psi = \frac{H_{g,ex}}{H} \quad 3$$

The exergy efficiency “ ψ ” in Equation 3 replaces $\eta_{c,max}$ in Equation 2. Similarly, $H_{g,ex}$ represents the solar radiation exergy W_{max} term, while H (incoming solar radiation) is used instead of the energy input E . According to Petela, ψ represents the highest percentage of solar radiation that can be converted into work (Petela, 2003). Petela developed the concept of exergy of solar radiation to assess the efficiency and reversibility of all energetic processes involving heat radiation. To estimate the exergy of heat radiation, formulas have been proposed that consider the ratio of exergy to radiation energy.

The exergy of solar energy is determined by the model given by Petela, [28] as follows (Equation 4).

$$\psi_i = 1 + \frac{1}{3} \left(\frac{T_0}{T_s} \right)^4 - \frac{4 T_0}{3 T_s} \quad 4$$

Here, ψ_i represents the relative potential of the maximum output from solar radiation, T_s is the solar temperature and its value is 1459.5 K for diffuse solar radiation and T_s 5760 K for beam (or direct) solar radiation. T_0 is the monthly average air temperature (in Kelvin) for the considered location. The Petela model gives similar results to the Jeter and Spanner model, so the choice of the Petela model is reasonable and leads to acceptable results.

As the outside temperature increases, the efficiency of both radiant and diffuse solar energy decreases. This implies that less work can be produced from incoming radiation when the ambient temperature rises. Equations 5 and 6 can be used to determine the exergy values of the highest relative energy availability potential ψ , diffuse $H_{d,ex}$ and direct $H_{b,ex}$ solar radiation [29], [30].

$$H_{d,ex} = \psi_d H_d \quad 5$$

$$H_{b,ex} = \psi_b H_b = \psi_b (H_g - H_d) \quad 6$$

The exergy of global solar radiation is calculated using Equation 7 or Equation 8. Global solar energy efficiency can be calculated using Equation 9 or Equation 10 [29].

$$H_{g,ex} = H_{b,ex} + H_{d,ex} \quad 7$$

$$H_{g,ex} = \psi_g H_g \quad 8$$

$$\psi_g = \frac{H_{g,ex}}{H_g} = \frac{\psi_b H_b + \psi_d H_d}{H_g} \quad 9$$

$$\psi_g = \psi_b \left(1 - \frac{H_d}{H_g} \right) + \psi_d \left(\frac{H_d}{H_g} \right) \quad 10$$

2.2. Determination of Solar Potential

To optimize the use of solar energy, it is necessary to ascertain the capacity of the sun for solar energy. Solar radiation intensity at a specific location is defined as the quantity of solar energy received per unit area. This is influenced by the angle at which sunlight strikes an item, the atmospheric condition, and

obstructions such as clouds or buildings. A region with a higher solar radiation intensity also has a larger solar energy potential. Several factors must be considered when calculating solar energy potential, including the quantity and duration of solar radiation, the environment, and the location. The potential for solar energy is also affected by the length of time exposed to sunshine. Regions with longer daylight hours or generally more sunny days may have greater solar energy potential. Seasonal fluctuations in daylight length should also be considered when assessing solar energy potential.

Geographical location is one of the most crucial elements in determining solar energy potential. Areas situated closer to the equator receive a greater quantity of direct sunlight throughout the year than those situated at a greater distance from the equator. This phenomenon enhances the potential for solar energy generation in these regions. The angle and orientation of solar panels with respect to the sun are also influenced by latitude, and this has an impact on the effectiveness of energy capture. Equation 11 provides the formula for calculating solar radiation from extraterrestrial sources [29], [31].

$$\frac{H_0}{\pi} = \frac{24H_{sc}}{\pi} \left(1 + 0.033 \cos \cos \left(\frac{360n}{365} \right) \right) \left(\cos \cos \varnothing \cos \cos \delta \sin \sin \omega_s + \frac{\pi \omega_s}{180} \sin \sin \varnothing \sin \sin \delta \right) \quad 11$$

Here \varnothing is the degree of latitude (north (+), south (-), $-90 < \varnothing < 90$), δ is the solar declination angle, ω_s is the solar hour angle and H_{sc} is the solar constant (1367 W/m^2). The solar declination angle δ and the solar hour angle ω_s are calculated using Equation 12 and Equation 13, respectively [29], [31]

$$\delta = 23.45^\circ \sin \sin \left[\frac{360(284+n)}{365} \right] \quad 12$$

$$\cos \cos \omega_s = -\tan \tan \varnothing \tan \tan \delta \quad 13$$

2.3. Monthly Average Solar Radiation Incident on A Given Area in The Horizontal Plane

(Klein, 1977) simplified the calculation of H_0 in Equation 11 by defining for each month a typical day when the daily extraterrestrial solar radiation value is extremely close to the monthly average value. The monthly average solar radiation (H) incident on a given area on a horizontal plane can be determined by Equation 14.

$$\frac{H}{H_0} = \left(a + b \frac{n}{N} \right) \quad 14$$

Here, a and b are region-dependent constants, and $\frac{n}{N}$ is the relative insolation time (insolation time/day length). The region-dependent constants a and b in Equation 14 are given in Equation 15 and Equation 16 below for Turkey, depending on the latitude angle (φ), declination angle (δ) and location height (Z) in meters above sea level ([31], [32]).

$$a = 0.103 + 0.000017Z + 0.198 \cos \cos (\varphi - \delta) \quad 15$$

$$b = \cos \cos (\varphi - \delta) \quad 16$$

Conditions associated with climate, like humidity, cloud cover, and air pollution, have an impact on the amount of solar energy that is accessible. In locations with poor sky conditions, solar energy potential may be lower than in areas with clear skies. It is therefore necessary to comprehend local climate trends in order to make an appropriate assessment of solar energy potential. Based on the clarity index (CT), Equation 17 can be used to calculate the ratio of daily horizontal plane diffuse radiation to total radiation [31], [32].

$$\frac{H_d}{H} = 0.173 - 0.414K_T - 0.428K_T^2 \tag{17}$$

Based on the relative insolation time and clarity index of Equation 18, the equation calculates the monthly average daily solar radiation to the horizontal unit plane on Earth.

$$K_T = \frac{H}{H_0} \tag{18}$$

Several variables, such as solar radiation intensity, sunlight duration, geographic location, climate, and technical infrastructure, should be considered when estimating solar energy potential. By carefully weighing these variables, stakeholders may identify the best sites for solar projects and maximize the efficient use of this renewable resource.

2.4. Average Daily Total Radiation Falling on The Sloping Surface

On the inclined plane, there is a difference between the dawn angle of the incident radiation and the first-hour angle of first fall (ω_s) Equation 19 yields the first hour angle of first fall (ω'_s) The equation's usage of the word "min" designates that the smaller of these two integers will be chosen [29], [32].

$$\omega'_s = \min[(-\tan \varphi \tan \delta) \quad (-\tan(\varphi - \beta) \tan \delta)] \tag{19}$$

The average daily total radiation falling on the sloped surface is found using equation 20. R_b is defined as the ratio of daily direct radiation (H_b) falling on the horizontal surface to daily direct radiation (H_{bT}) falling on the inclined surface. Equation 21 establishes it for the northern hemisphere's south-facing surface ($\gamma=0^\circ$) [31], [32].

$$H_T = H \left(1 - \frac{H_d}{H} \right) R_b + H_d \left(\frac{1 + \cos \delta \cos \beta}{2} \right) + H \rho \left(\frac{1 - \cos \delta \cos \beta}{2} \right) \tag{20}$$

$$R_b = \frac{\cos \varphi \cos(\varphi - \beta) \cos \delta \sin \omega'_s + \left(\frac{\pi}{180}\right) \omega'_s \sin(\varphi - \beta) \sin \delta}{\cos \varphi \cos \delta \sin \omega_s + \left(\frac{\pi}{180}\right) \omega_s \sin \varphi \sin \delta} \tag{21}$$

2.5. Study Area and Data

Turkey was selected as the research site for this study to evaluate the potential for solar energy. Turkey is located between the 26°–45° east meridians and the 36°–42° north parallels. For each coordinate between the 26°–45° east meridians and the 36°–42° north parallel, NASA has supplied solar energy data. For each coordinate, the exergy potential of solar energy was calculated using the formulas presented in the initial section of this website. The resulting exergy potential was then visualized using IDW (inverse distance weighting) interpolation.

2.6. IDW Interpolation Method

The fields of geographic information systems (GIS) and geology are two contexts in which IDW is applied. It is commonly used to depict point data on a regular surface or to fill in missing data. The interpolation of point data to create a map is a typical use case for IDW. Using this method, a point's value is determined by weighing it based on the separation between known points. IDW's fundamental principle is that a point's estimated value is calculated by inversely weighting its distances to known points. This means that points that are closer together weigh more than points that are further away. The value of a point should ideally be determined by weights proportional to the distances to that location. The mathematical model of IDW interpolation is given in Equation 22 [33],[34].

$$Z(x, y) = \frac{\sum_{i=1}^n \frac{Z_i}{d_i^p}}{\sum_{i=1}^n \frac{1}{d_i^p}}$$

22

Here, $Z(x, y)$, is the value of the point with the estimated value, Z_i is the value of one of the known points, and d_i is the distance of the known points to the target point p is the weighting factor (usually taken as 2 or 3).

Among the benefits of IDW are the following:

- It is fast and easy.
- Non-linear relationships are modeled by it.
- Since it is based on point data, it can work with irregular or incomplete data.

However, IDW has several disadvantages.

- It requires a homogeneous distribution of known points to work properly.
- When data from close points is weighted too heavily compared to data from other points, it can lead to the problem of overscoring.
- If the weighting factor is not chosen correctly, the results can be negatively affected.

3. RESULTS AND DISCUSSION

This study calculates the solar exergy potential of Turkey for both the horizontal plane and five specific tilt angles (21°, 30°, 39°, 48°, and 57°). These angles were selected to cover a broad range of possible panel orientations, reflecting both practical and theoretical considerations for optimizing solar energy capture. Previous studies have indicated varying efficiency gains at different tilt angles, and the study aims to identify the most effective angle for maximizing exergy potential. Calculations were made using 22-year average solar energy potential data obtained from NASA, ensuring a robust and comprehensive analysis.

The exergy potentials of Turkey in the horizontal plane and five different tilt angles (21, 30, 39, 48, and 57) were calculated, and seasonal maps were created. For Turkey, the winter season is considered December, January, and February; the spring season is March, April, and May; the summer season is June, July, and August; and the autumn season is September, October, and November, respectively.

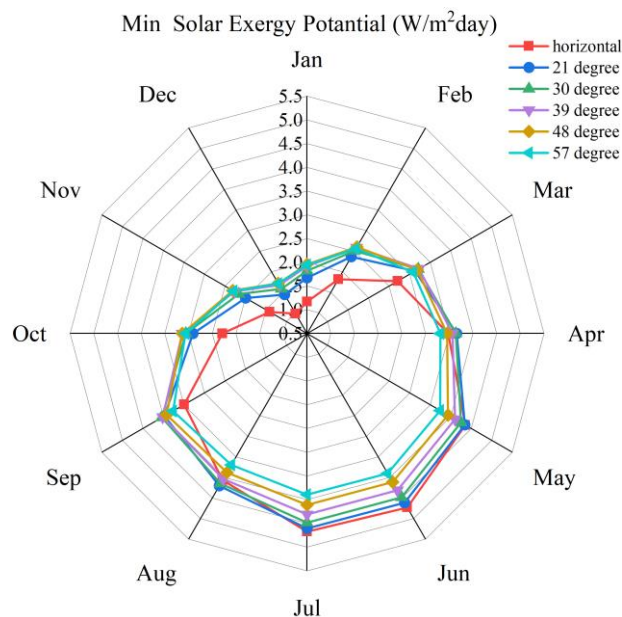


Figure 1. Minimum solar exergy potential of different tilt angles for each month

Figure 1 shows the variation of the average lowest solar exergy potential for different inclination angles according to the months. In Figure 1, it is seen that the lowest solar exergy potential in the winter months is seen on the horizontal plane with 1.324 W/m²day and the highest with 2.094 W/m²day on the surface inclined at 48°. In the spring months, the lowest solar exergy potential is 3.381 W/m²day with a 57° inclined plane, and the highest solar exergy potential is 3.711 W/m²day with a 21° inclined surface. In summer, the lowest solar exergy potential was 3.383 W/m²day at a 57° inclined plane, and the highest solar exergy potential was 4.490 W/m²day at a horizontal surface. In autumn, the lowest solar exergy potential was 2.400 W/m²day on the horizontal plane, and the highest solar exergy potential was 3.141 W/m²day on the surface inclined at 39°.

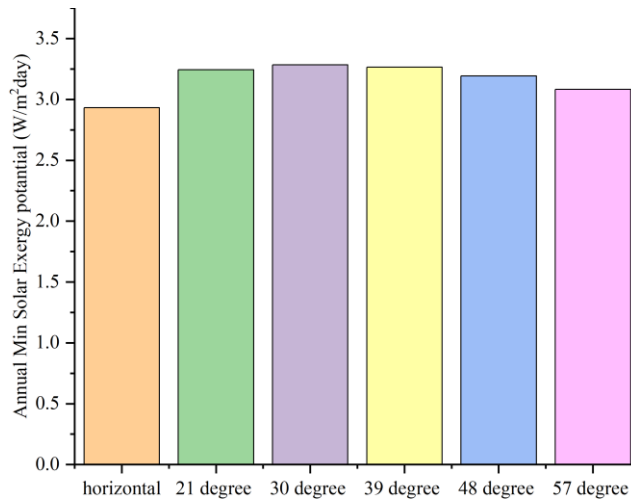


Figure 2. Average minimum annual solar energy potential of different tilt angles

Figure 2 shows the annual average minimum solar exergy potential for different tilt angles. Although the highest and lowest exergy potentials are observed at different inclination angles (Figure 1), when the annual average solar exergy potential is considered (Figure 2), it is determined that the highest potential is on 30° inclined surfaces (3.283 W/m²day) and the lowest potential is on horizontal planes (2.932 W/m²day).

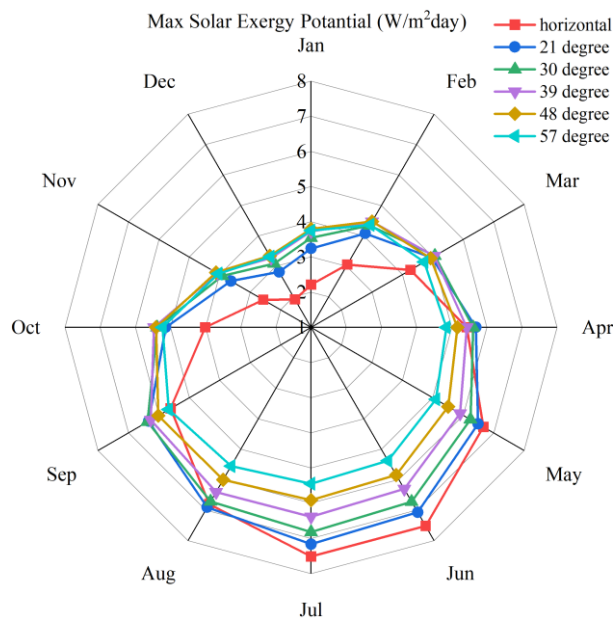


Figure 3. Maximum solar exergy potential of different tilt angles for each month

The average maximum solar energy potential fluctuation per month for various inclinations is displayed in Figure 3. Figure 3 shows that the solar energy potential is highest on the surface inclined at 48°, with 3.871 W/m²day, and lowest on the horizontal plane, at 2.396 W/m²day. During the spring season, the solar energy potential ranged from 4.888 W/m²day on a 57° inclined plane to 5.713 W/m²day on a 21° inclined surface. During summer, the solar energy potential ranged from 5.460 W/m²day at a 57° inclined plane to 7.281 W/m²day at a flat surface. Autumn solar exergy potentials were as low as 4.064 W/m²day on the horizontal plane and as high as 5.272 W/m²day on the 39-° inclined surface.

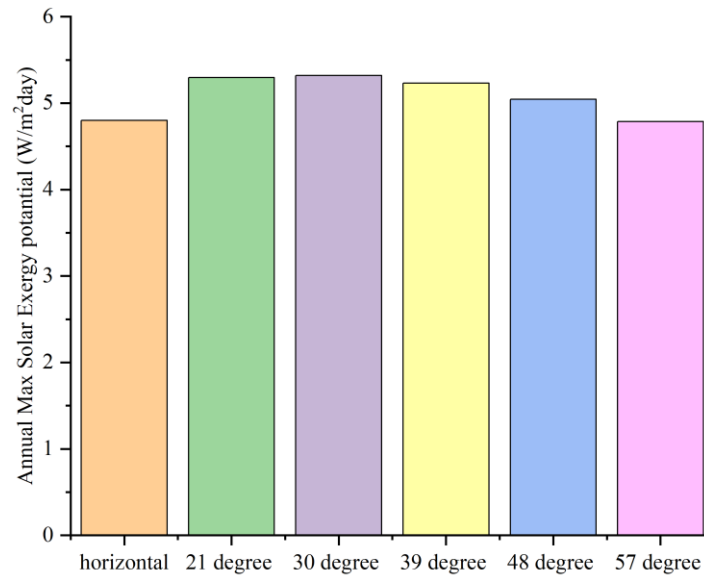


Figure 4. Average maximum annual solar energy potential of different tilt angles

The yearly average maximum solar energy potential for various tilt degrees is displayed in Figure 4. The annual average solar exergy potential (Figure 4) shows that, despite the highest and lowest exergy potentials being observed at different inclination angles (Figure 3), the highest potential is at 30° inclined surfaces (5.319 W/m²day) and the lowest potential is at 57° inclined planes (4.785 W/m²day).

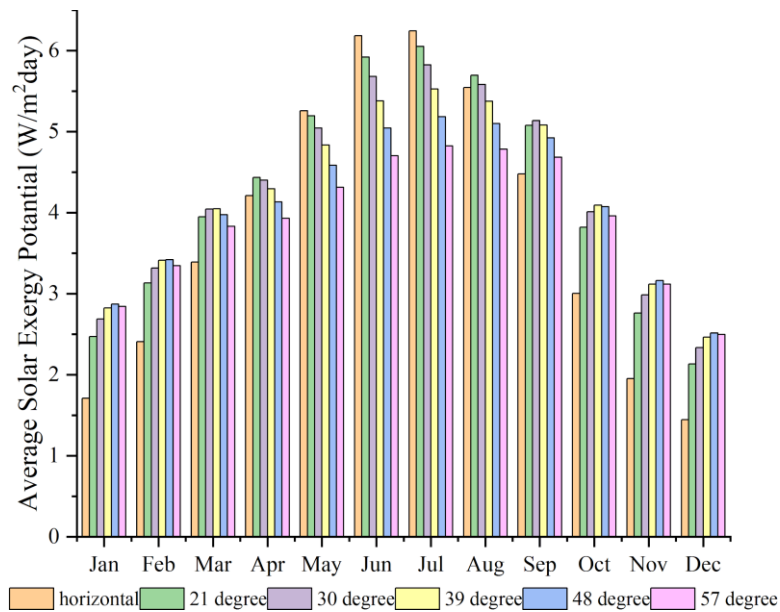


Figure 5. Average solar exergy potential of different tilt angles for each month

The average solar energy potential variation according to month for various inclination degrees is depicted in Figure 5. Figure 5 shows that during the winter, the solar energy potential is lowest on the horizontal plane (1.855 W/m²day) and maximum on the surface inclined at 48° (2.936 W/m²day). During the spring season, the solar energy potential ranged from 4.026 W/m²day on a 57° inclined plane to 4.527 W/m²day on a 21° inclined surface. During the summer, the solar energy potential ranged from 4.771 W/m²day at a 57° inclined plane to 5.990 W/m²day at a horizontal surface. During the fall season, the solar exergy potential reached its maximum on an inclined surface at 39° and its lowest on a level plane at 3.145 W/m²day.

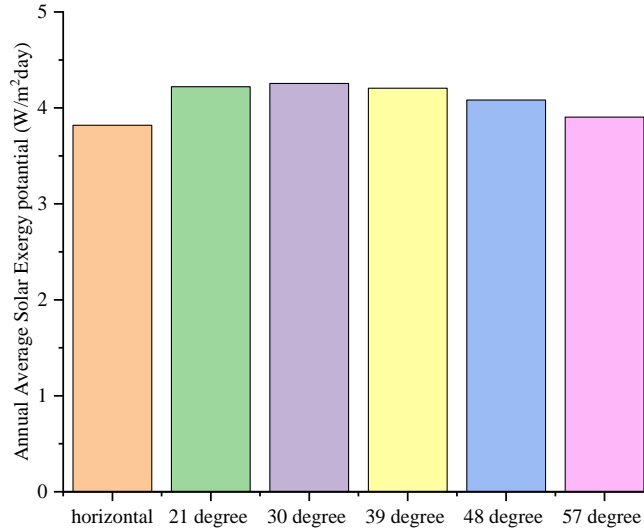


Figure 6. Average annual solar energy potential of different tilt angles

Figure 6 shows the annual average solar exergy potential for different tilt angles. Although the highest and lowest exergy potentials are observed at different inclination angles (Figure 5), when the annual average solar exergy potential is considered (Figure 6), it is determined that the highest potential is on 30° inclined surfaces (4.255 W/m²day) and the lowest potential is on horizontal planes (3.819 W/m²day).

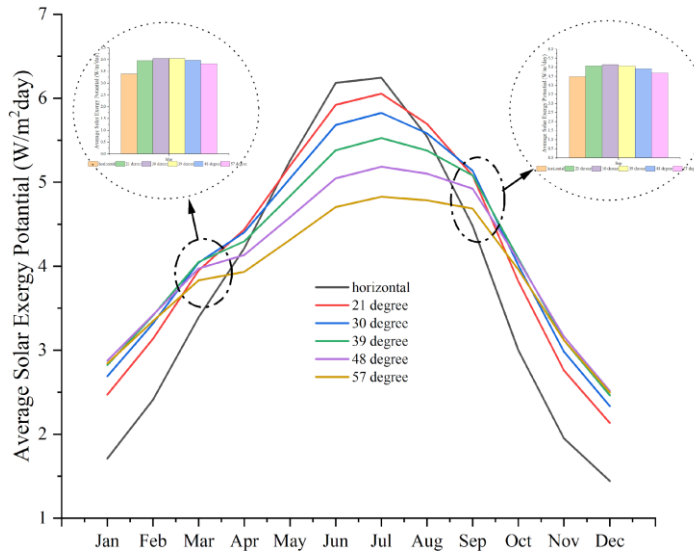


Figure 7. Detailed representation of the average solar energy potential of different tilt angles for the equinox

The equinoxes are two special days when the angle between the plane of the Earth's ecliptic and the plane of the equator is zero. Due to the Earth's axis tilt, the angle of its orbit around the sun changes

according to the seasons. On the days of the equinoxes, the Earth's obliquity to the sun is at its minimum, and the sun's rays come at a right angle to the equator. On these days, the duration of day and night is approximately equal. The equinox periods are called the vernal equinox (in March) and the autumnal equinox (in September). At these times, the angle at which the sun's rays fall changes depending on the position of the Earth in its orbit around the sun. Equinox days are the times when this change is most pronounced. Figure 7 shows the average solar energy potential of different inclination angles for the equinox in detail. Considering the equinox days, it is observed that the solar exergy potential decreases approximately with the increase in the inclination angle after March, which includes the spring equinox, while the solar exergy potential increases approximately with the increase in the inclination angle after September, which includes the autumn equinox. It was found that the effect of tilt angle on solar exergy potential in the equinox months is less compared to other months.

Between Figures 8 and 11, the four-season solar exergy potential of the 30° sloping surfaces that provide the highest solar exergy potential is given in the form of a map. The color scales in the figures are arranged separately for each season to reveal the differences according to the regions more clearly. In the maps, the change of the exergy potential from low to high is colored from blue to red.

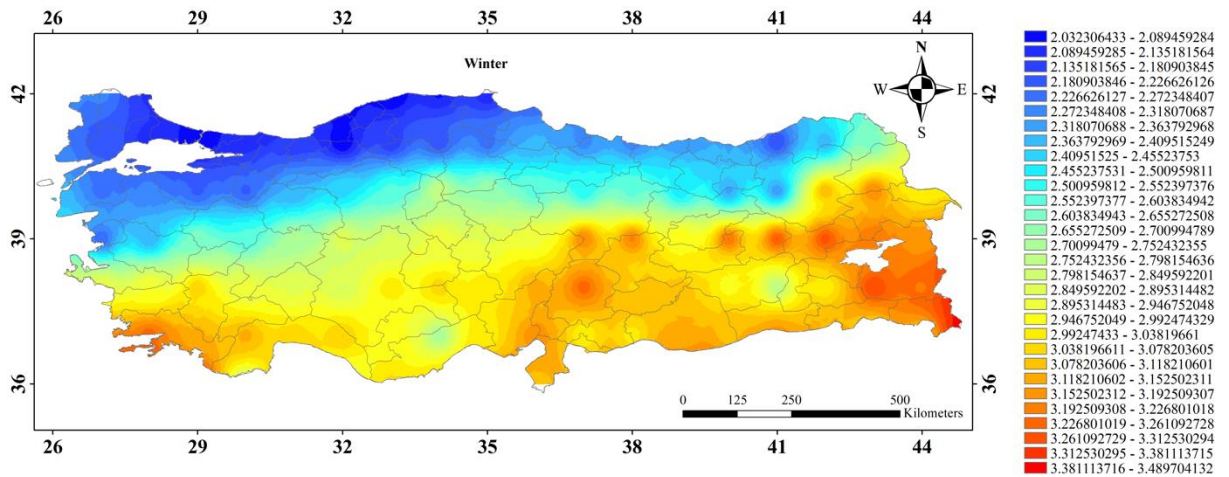


Figure 8. Solar exergy potential in winter for 30° inclined surfaces

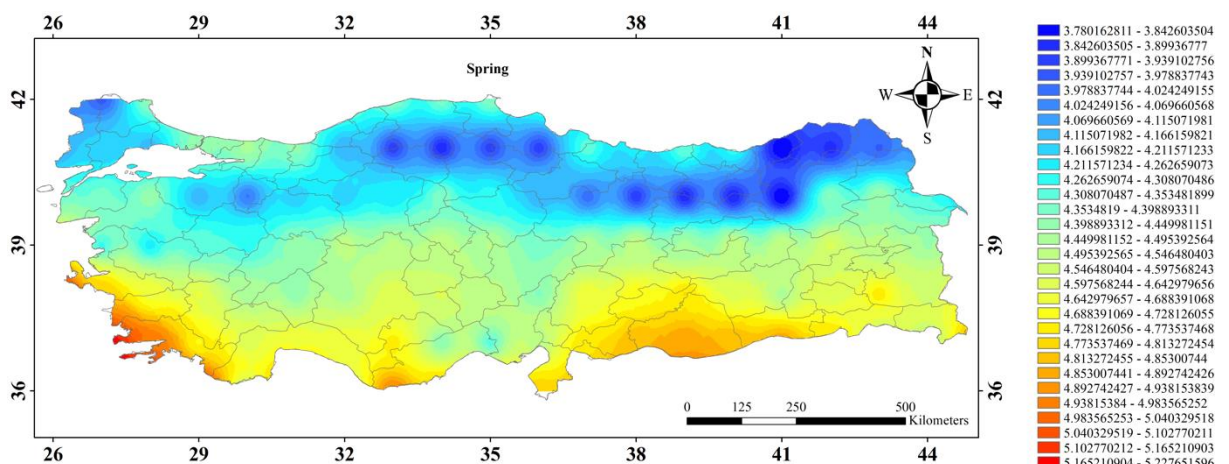


Figure 9. Solar exergy potential in spring for 30° inclined surfaces

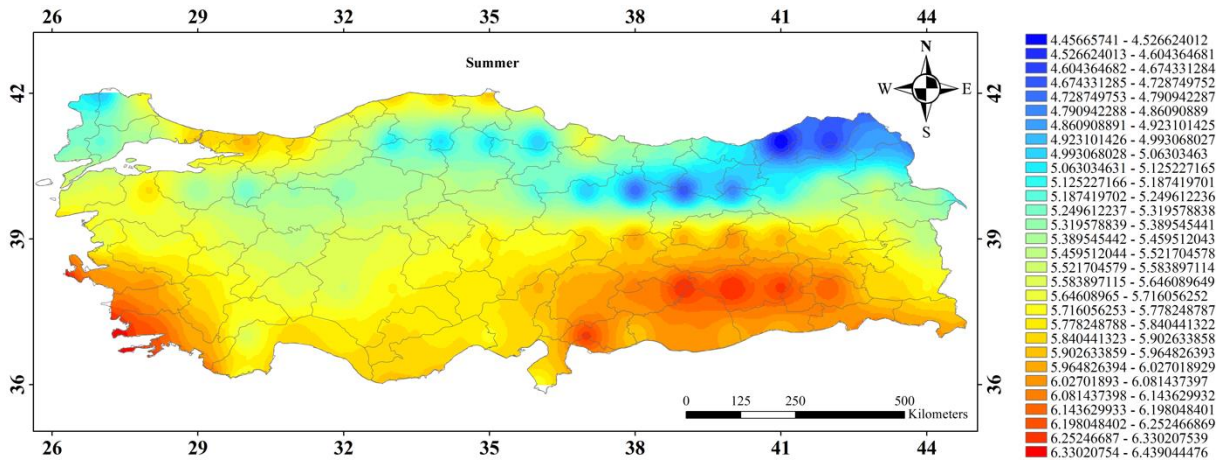


Figure 10. Solar exergy potential in summer for 30° inclined surfaces

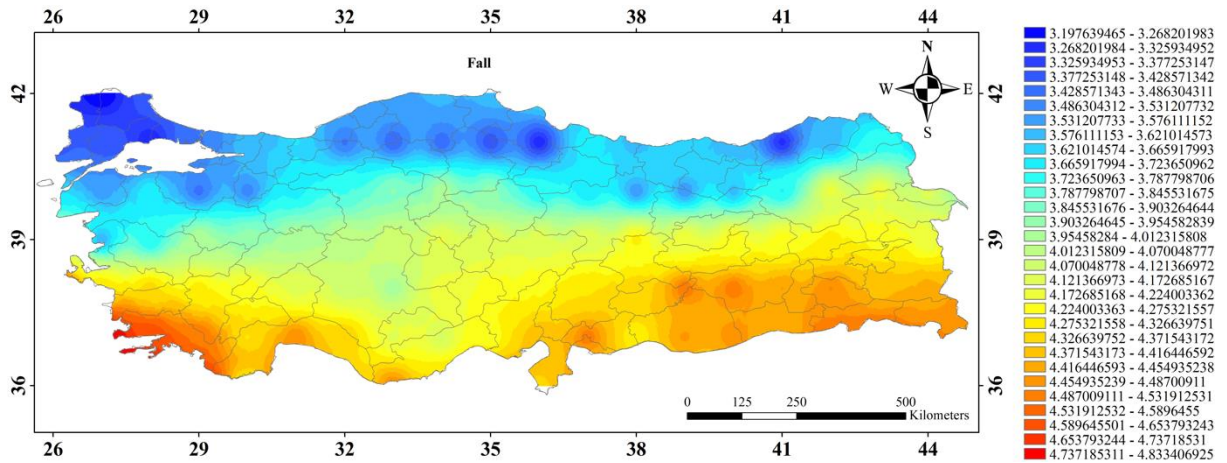


Figure 11. Solar exergy potential in autumn for 30° inclined surfaces

The findings of the study showed that the 30° slope angle provided the highest value for the annual average exergy potential (4.255 W/m²/day). This value is 10% higher than the potential of horizontal surfaces. Furthermore, the seasonal performance of the different tilt angles was also analyzed. For example, it was found that the 48° slope angle provided the highest exergy potential in winter (2.936 W/m²/day), while in summer, the horizontal surfaces provided the highest potential (5.990 W/m²/day).

The study was compared with previous studies in terms of data source, methodology, results and innovative approaches, and common and different aspects were revealed. In the comparisons, firstly the studies conducted for the cities of Turkey and then similar studies conducted for different countries and cities were taken into consideration. A comparison chart is given in Table 1.

Table 1. Comparison with previous studies

Name of the Study	Bibliography	Working area	Tilt Angles	Data Source	Methodology of the Study	Results of the Study	Innovative Approaches of the Study
Solar Energy Potential Assessment for Karabük, Turkey	[6]	Karabük	Various (e.g., optimal monthly, seasonal)	Solar energy potential data from local meteorological stations	AHP, GIS-based analysis	Identification of optimal locations for solar energy plants	Use of AHP and GIS for optimal site selection, focus on local conditions
Solar Energy Potential Evaluation in Gaziantep, Turkey	[7]	Gaziantep	Various (monthly, seasonal)	Solar energy data from local sources, NASA data	AHP analysis	Evaluation of solar energy potential using AHP methodology	AHP methodology to evaluate regional solar potential
Solar Energy Potential in Kars, Turkey	[8]	Kars	Various (seasonal)	Local solar radiation data and GIS analysis tools	AHP, GIS-based analysis	Identification of potential areas for solar power plants	Combining AHP and GIS for detailed spatial analysis
Solar Energy Potential and Optimal Tilt Angles in Istanbul, Turkey	[21]	Istanbul	Monthly, seasonal, annual	Solar irradiance data from local meteorological stations, NASA data	Experimental analysis, tilt angle optimization	Optimal monthly and seasonal tilt angles identified	Focus on experimental validation of tilt angle optimization
Solar Energy Potential and Optimal Site Selection in Nevşehir, Turkey	[9]	Nevşehir	Various (annual)	Solar energy potential data from local sources and meteorological stations	AHP-VIKOR hybrid method	Identification of optimal sites for solar power plants using AHP-VIKOR	Use of hybrid AHP-VIKOR method for comprehensive site selection analysis
Estimating the Optimum Tilt Angles for South-Facing Surfaces in Palestine	[35]	Palestine	Various (e.g., optimal monthly, seasonal, semi-annual, annual)	PVGIS, PVWatts, mathematical models	Mathematical models, software tools (PVGIS, PVWatts)	Monthly adjustments yield 17% more energy, yearly optimal tilt angle around 29°	Use of PVGIS and PVWatts tools, focus on efficiency gains from tilt adjustments
Solar irradiance estimation models and optimum tilt angles	[36]	General studies	Various	Mathematical models	Mathematical models	Optimal tilt angles identified for various conditions	Use of various mathematical models for irradiance estimation
Assessment of potential solar energy with the models for optimum tilt angles	[37]	General studies	Various	Mathematical models	Mathematical models	Potential energy gains with optimal tilt angles	Comprehensive model-based analysis of solar potential
Estimation of ideal tilt angle for solar-PV panel surfaces facing south	[38]	General studies	Various	Mathematical models	Mathematical models	Ideal tilt angles significantly improve energy capture	Focus on ideal tilt angles for maximum energy capture

In this study, the whole of Turkey was selected as the study area and the optimum tilt angle was tried to be determined by Interpolation method (IDW) and exergy analysis methods considering NASA 22-year average solar energy data for horizontal, 21°, 30°, 39°, 48°, 57° angles. Detailed seasonal exergy potential maps were created and IDW interpolation was used for missing data regions. The findings of our study show the reliability and accuracy of our method and the data used when compared with similar studies conducted in provinces such as Karabük, Gaziantep and Kars. For example, studies conducted in Karabük evaluated the benefits and challenges of local solar energy applications [6]. In another study conducted in Gaziantep, solar energy potential was evaluated using the Analytic Hierarchy Process (AHP) method [7]. Similarly, potential areas for solar power plants in Kars province were identified using AHP methodology and GIS analyses [8]. This comparison shows that our study is compatible with other studies and the methodology used gives reliable results. While the Karabük study focussed on the evaluation of local applications, the Gaziantep study made a potential assessment with the AHP method. The Kars study identified potential areas with AHP and GIS analyses. In this study, NASA's long-term data and IDW interpolation method provide a comprehensive analysis across Turkey by making accurate predictions even in missing data regions.

In this study, NASA's 22-year average solar energy data were used. Other studies used data obtained from PVGIS, PVWatts, local meteorological stations and various meteorological sources. While IDW interpolation method and exergy analysis were used in this study, other studies used mathematical models, optimisation techniques and efficiency analyses. In this study, it is stated that the optimum tilt angle is 30° throughout the year and seasonal maps are provided. Other studies have presented results on how seasonal and annual adjustments can improve energy efficiency. This study presented detailed seasonal exergy potential maps using the IDW interpolation method to make accurate predictions in missing data regions. Other studies have utilised tools such as PVGIS and PVWatts, and have presented detailed seasonal exergy potential maps based on climatic conditions. These findings are an important guide for solar energy investments in Turkey and will contribute to increasing energy efficiency and reducing energy costs by determining optimal tilt angles for the design and layout of solar collectors.

4. CONCLUSIONS

The aim of this study is to determine the solar energy exergy potential for different tilt angles in different regions of Turkey and to determine the most suitable panel tilt angles. In this context, NASA's 22 years of solar energy data were used to accurately determine the solar energy potential of Turkey. The IDW interpolation method is preferred for estimating the exergy potential in regions with data deficiency, which provides advantages in terms of cost and time. In this study, to utilize solar energy more, the exergy potential incident on the horizontal surface was calculated, and the effect of the panel tilt angle on the exergy potential was investigated. The average solar exergy potential varies according to months and seasons at different tilt angles. The results obtained in the study are as follows:

- Considering the annual average solar exergy potential, it was determined that the highest potential for the horizontal, 21° inclination, 30° inclination, 39° inclination, 48° inclination, and 57° inclined surfaces was found to be on the 30° inclined surface.
- Solar exergy potential was found to be less in January, February, March, October, November, and December and more in April, May, June, July, August, and September compared to the year average.
- In January, February, November, and December, as the slope angle increases, it is observed that the solar exergy potential increases up to a 48° slope and decreases at higher slope angles.
- In the months of May, June, and July, it was determined that the solar exergy potential decreases as the slope angle increases.
- As the slope angle increases in March and October, it is observed that the solar exergy potential increases up to 39° slope and decreases at higher slope angles.

- As the slope angle increases in April and August, it is observed that the solar exergy potential increases up to a 21° slope and decreases at higher slope angles.
- In September, as the inclination angle increases, it is observed that the solar exergy potential increases up to 30° inclination and decreases at higher inclination angles.

These results provide an important guide for solar energy investments in Turkey. By determining the optimal tilt angles for the design and layout of solar collectors, energy efficiency can be increased, and energy costs can be reduced. Future research in this area may benefit from the application of additional machine learning techniques to more accurately determine the exergy potential outside of the measurement locations, considering the assessments conducted. Furthermore, the solar energy exergy potential map may be updated using software that integrates newly measured data, which undergoes annual changes.

The solar maps developed in this study are thought to provide information on total solar radiation levels that can be used as a database for future investments in the solar energy sector in Turkey. The results of this study can be used as a guide for solar panel manufacturers and installation companies for exergy potential-based evaluation methods, unlike the method that allows investment decisions to be made based only on the energy potential of the sun.

Declaration of Ethical Standards

Authors declare to comply with all ethical guidelines including authorship, citation, data reporting, and publishing original research.

Credit Authorship Contribution Statement

AUTHOR-1: Methodology, Conceptualization, Supervision.

AUTHOR-2: Resources, Investigation, Writing -review & editing,

AUTHOR-3: Methodology, Conceptualization, Resources, Investigation, Writing -review & editing,

Declaration of Competing Interest

The authors declared that they have no conflict of interest.

Funding / Acknowledgements

The author(s) received no financial support for the research.

Data Availability

The data that support the findings of this study are available from the corresponding author upon reasonable request.

REFERENCES

- [1] Ü. Ağbulut, G. Yıldız, H. Bakır, F. Polat, Y. Biçen, A. Ergün and A.E. Gürel, "Current practices, potentials, challenges, future opportunities, environmental and economic assumptions for Türkiye's clean and sustainable energy policy: A comprehensive assessment," *Sustainable Energy Technologies and Assessments*, vol. 56, Mar. 2023, Doi: 10.1016/j.seta.2023.103019.
- [2] H. N. D. Senyapar, "Renewable Energy Literature in Turkey: Mapping Analysis of the Field and Future Study Suggestions on Overlooked Issues," *International Journal of Renewable Energy*

- Research*, vol. 13, no. 1, pp. 221–235, Mar. 2023, Doi: 10.20508/ijrer. v13i1.13810.g8677.
- [3] S. Keleş and S. Bilgen, "Renewable energy sources in Turkey for climate change mitigation and energy sustainability," *Renewable and Sustainable Energy Reviews*, vol. 16, no. 7. pp. 5199–5206, Sep. 2012. Doi: 10.1016/j.rser.2012.05.026.
- [4] S. Bilgen, S. Keleş, A. Kaygusuz, A. Sari, and K. Kaygusuz, "Global warming and renewable energy sources for sustainable development: A case study in Turkey," *Renewable and Sustainable Energy Reviews*, vol. 12, no. 2. pp. 372–396, Feb. 2008. Doi: 10.1016/j.rser.2006.07.016.
- [5] M. A. Peçe, S. Ceyhan, A. Kamacı, and V. Cengiz, "The effects of renewable energy sources on Türkiye's economic growth: ARDL estimation," *Environmental Science and Pollution Research*, vol. 30, no. 15, pp. 45112–45122, Mar. 2023, doi: 10.1007/s11356-023-25479-7.
- [6] D. Arca and H. Keskin Çıtroğlu, "Güneş enerjisi santral (GES) yapım yerlerinin CBS dayalı çok kriterli karar analizi ile belirlenmesi: Karabük örneği," *Journal of Geomatics*, vol. 7, no. 1, pp. 17–25, Apr. 2022, doi: 10.29128/geomatik.803200.
- [7] G. Kum, M. E. Sönmez, and M. Karabaş, "Determination of Solar Energy Potential in Gaziantep Province by Analytical Hierarchy Process Method (AHP)," *Journal of Geography*, pp. 61–72, Dec. 2019, doi: 10.26650/jgeog2019-0031.
- [8] M. Demir, "Kars İlinde Güneş Enerjisi Santrali Kurulum Potansiyeli Taşıyan Alanların, CBS Analizleri ve AHP Yöntemi Kullanılarak Belirlenmesi," *Journal of Geography*, vol. 0, no. 46, pp. 93–109, Jul. 2023, doi: 10.26650/jgeog2023-1168805.
- [9] M. C. Urgan and E. D. Göbelioğlu, "AHP-VİKOR hibrit yöntemi ile güneş enerjisi santrali yer seçimi" *Sakarya Üniversitesi İşletme Enstitüsü Dergisi*, vol. 5, no. 2, pp. 95–109, Dec. 2023, doi: 10.47542/sauied.1388986.
- [10] K. B. Varınca and M. T. Gönüllü, "Türkiye'de Güneş Enerjisi Potansiyeli ve Bu Potansiyelin Kullanım Derecesi, Yöntemi ve Yaygınlığı Üzerine Bir Araştırma," in *I. Ulusal Güneş ve Hidrojen Enerjisi Kongresi*, Eskişehir, Jun. 2006, pp. 270-275.
- [11] E. A. Yılmaz, "Türkiye'nin Yenilenebilir Enerji Potansiyeli ve Gelecek Hedefleri Renewable Energy Potential and Future Aims of Turkey," *Ordu Üniversitesi Sosyal Bilimler Araştırmaları Dergisi*, vol. 8, no. 3, pp. 525–535, 2018, doi: 10.2018/Kabul.
- [12] F. Ç. Kılıç, "Solar Energy, Its Recent Status in Turkey and Production Technologies," *Mühendis ve Makina*, vol. 671, pp. 28–40, 2015.
- [13] M. Yılmaz, "The energy potential of Turkey and its importance of renewable energy sources in terms of electricity production," *Ankara Üniversitesi Çevre Bilimleri Dergisi*, vol. 4, no. 2, pp. 33–54, 2012.
- [14] G. Kaltakkıran, "Exergy Analysis of Solar Radiation Based on Measurement Data: A Study in Erzurum Province," *Journal of Studies in Advanced Technologies*, vol. 1, no. 2, pp. 94–104, 2023, doi: 10.5281/zenodo.10445102.
- [15] A. Çelik, "Uzun Süreli Verilere Dayalı Güneş Radyasyonunun Ekserji Ve Enerji Analizi," *M. S. thesis, University of Karamanoğlu Mehmetbey, Karaman*, 2021.
- [16] Y. Kurtgoz, E. Deniz, and I. Turker, "Solar radiation exergy and enviroeconomic analysis for Turkey," *International Journal of Exergy*, vol.24 no.2, pp. 281-300, 2017.
- [17] J. Kaldellis and D. Zafirakis, "Experimental investigation of the optimum photovoltaic panels' tilt angle during the summer period," *Energy*, vol. 38, no. 1, pp. 305–314, 2012, doi: 10.1016/j.energy.2011.11.058.
- [18] W. D. Lubitz, "Effect of manual tilt adjustments on incident irradiance on fixed and tracking solar panels," *Appl Energy*, vol. 88, no. 5, pp. 1710–1719, 2011, doi: 10.1016/j.apenergy.2010.11.008.
- [19] K. Ülgen, "Optimum tilt angle for solar collectors," *Energy Sources, Part A: Recovery, Utilization and Environmental Effects*, vol. 28, no. 13, pp. 1171–1180, Sep. 2006, doi: 10.1080/00908310600584524.
- [20] S. Roberts and N. Guariento, *Building Integrated Photovoltaics A Handbook*. Berlin, Germany.: Birkhauser Press, 2009.
- [21] A. R. Dal, "Investigation of the Effect of Optimum Tilt Angle on Yield in Solar Energy Panels,"

- Bilecik Şeyh Edebali Üniversitesi Fen Bilimleri Dergisi*, vol. 8, no. 1, pp. 241–250, Jun. 2021, doi: 10.35193/bseufbd.878795.
- [22] Anonim, "Photovoltaic Geographical Information System." Accessed: Apr. 19, 2024. [Online]. Available: https://re.jrc.ec.europa.eu/pvg_download/map_index.html
- [23] G. Kaltakkıran and K. Bakirci, "Effect of Surface Inclines to Solar Energy Potential," *Tesisat Mühendisliği Dergisi*, vol. 175, pp. 30–38, 2020, [Online]. Available: <https://www.researchgate.net/publication/340351509>
- [24] M. Y. Kaba, A. K. Seyhan, P. Celen, and A. Celen, "Energy and Exergy Analysis of Solar Collectors Having Different Tilt Angles: Case Study of Erzincan City," *Konya Journal of Engineering Sciences*, vol. 10, no. 3, pp. 634–648, Sep. 2022, doi: 10.36306/konjes.1096936.
- [25] N. Arslanoğlu, "Evaluation and establishment of diffuse solar radiation models for Bursa, Turkey," *Energy Sources, Part A: Recovery, Utilization and Environmental Effects*, vol. 38, no. 18, pp. 2788–2797, Sep. 2016, doi: 10.1080/15567036.2016.1214640.
- [26] S. Bilgen and I. Sarıkaya, "Exergy for environment, ecology and sustainable development," *Renewable and Sustainable Energy Reviews*, vol. 51. Elsevier Ltd, pp. 1115–1131, Jul. 30, 2015. doi: 10.1016/j.rser.2015.07.015.
- [27] N. Arslanoğlu, "Empirical modeling of solar radiation exergy for Turkey," *Appl Therm Eng*, vol. 108, pp. 1033–1040, Sep. 2016, doi: 10.1016/j.applthermaleng.2016.08.002.
- [28] R. Petela, "Exergy of undiluted thermal radiation," *Solar Energy*, vol. 74, no. 6, pp. 469–488, 2003, doi: 10.1016/S0038-092X(03)00226-3.
- [29] A. Yiğit and I. Atmaca, *Güneş Enerjisi Mühendislik Uygulamaları*, 2. baskı. Bursa: DORA Basım-Yayın, 2018.
- [30] S. A. Kalogirou, *Solar energy engineering: processes and systems*. Elsevier, 2023.
- [31] G. N. Tiwari, *Solar energy: fundamentals, design, modelling and applications*. Alpha Science Int'l Ltd, 2002.
- [32] A. Yiğit and N. Arslanoğlu, "Anlık Işınım Şiddeti Ve Çevresel Faktörlere Bağlı Optimum Pv Panel Açısı, Verim, Güç Üretiminin İncelenmesi," *Uludağ University Journal of The Faculty of Engineering*, pp. 301–314, Apr. 2021, doi: 10.17482/uumfd.824582.
- [33] M. Demircan, İ. Alan, and S. Şensoy, "Coğrafi Bilgi Sistemleri Kullanılarak Sıcaklık Haritalarının Çözünürlüğünün Artırılması," in *TMMOB Harita ve Kadastro Mühendisleri Odası 13. Türkiye Harita Bilimsel ve Teknik Kurultayı*, 2011.
- [34] C. D. Lloyd, *Local Models for Spatial Analysis*, 2nd ed. CRC Press, 2010.
- [35] A. Juaidi, S. Abdel-Fattah, and F. Manzano-Agugliaro, "Estimating the Optimum Tilt Angles for South-Facing Surfaces in Palestine," *Energies*, vol. 13, no.3, pp. 1-29, 2020, doi.org/10.3390/en13030623
- [36] M. A. Danandeh, "Solar irradiance estimation models and optimum tilt angle approaches: A comparative study," *Renewable and Sustainable Energy Reviews*, vol.92, pp. 319-330, 2018.
- [37] Q. Hassan, M.K. Abbas, A.M. Abdulateef, J. Abdulateef, and A. Mohamad, "Assessment the potential solar energy with the models for optimum tilt angles of maximum solar irradiance for Iraq," *Case Studies in Chemical and Environmental Engineering*, vol 4, pp. 100-140, 2021
- [38] S. Alqaed, J. Mustafa, F. A. Almeahadi, and B. Jamil, "Estimation of ideal tilt angle for solar-PV panel surfaces facing south: a case study for Najran City, Saudi Arabia," *Journal of Thermal Analysis and Calorimetry*, vol. 148, no.16, pp. 8641-8654, 2023.

ADVANCING MEMORY DENSITY: A NOVEL DESIGN FOR MULTIPLE-BIT-PER-CELL PHASE CHANGE MEMORY

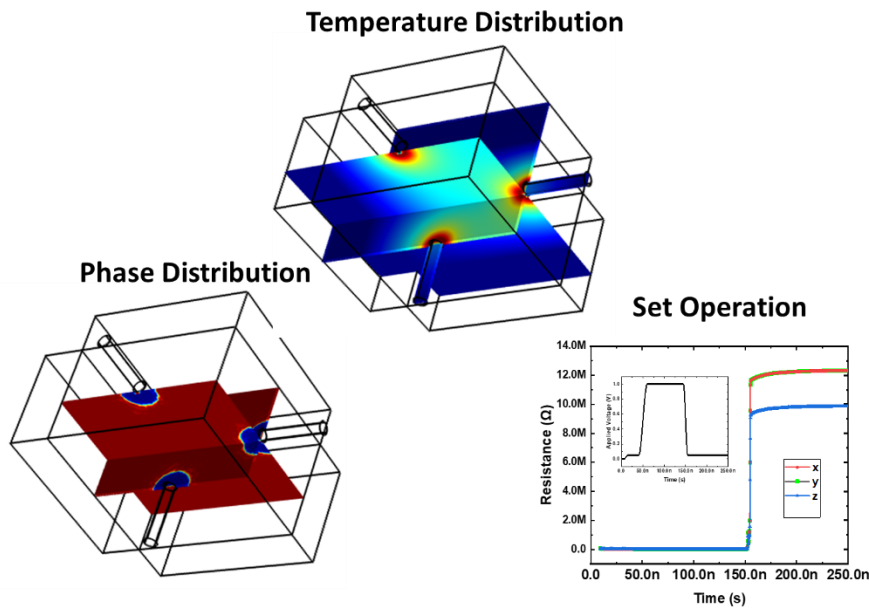
* Ibrahim CINAR 

Karamanoglu Mehmetbey University, Medical Services and Techniques Department, Karaman, TÜRKİYE
icinar@kmu.edu.tr

Highlights

- Innovative Multiple-Bit-Per-Cell PCM Design
- Use of GST for Superior Performance
- Detailed 3D Temperature and Phase Distribution Analysis
- Significant Resistance Modulation
- Optimized Design for Enhanced Device Performance

Graphical Abstract



Design Concepts	Resistance level	Storage information
General design (REF)	2 states	1 bit
Middle resistance level device(REF)	3 and/or 4 states	1 or 2 bit
New design	2 states (x3 from direction)	1 bit x 3 = 3 bit



ADVANCING MEMORY DENSITY: A NOVEL DESIGN FOR MULTIPLE-BIT-PER-CELL PHASE CHANGE MEMORY

*Ibrahim CINAR 

Karamanoglu Mehmetbey University, Medical Services and Techniques Department, Karaman, TURKIYE
icinar@kmu.edu.tr

(Received: 01.07.2024; Accepted in Revised Form: 20.08.2024)

ABSTRACT: Multiple-bit-per-cell phase-change memory (MPCM) has emerged as a promising solution to address the escalating demands for high-density, low-power, and fast-access memory in modern computing and data storage systems. This paper presents a novel device design aimed at enabling multiple bits per cell in phase-change memory, thereby significantly enhancing memory density while maintaining performance and reliability. Leveraging innovative material compositions and advanced fabrication techniques, the proposed design demonstrates the potential to push the boundaries of memory capacity, efficiency, and scalability. Through comprehensive simulation analysis and performance evaluations, we showcase the feasibility and advantages of the new device design, highlighting its potential to revolutionize memory architectures and meet the evolving needs of next-generation computing systems.

Keywords: *Phase Change Memory, Multiple-Bit-Per-Cell, Finite Element Modeling, Novel Design, Memory Architecture*

1. INTRODUCTION

As the demand for high-density, low-power, and fast-access memory continues to escalate in modern computing and data storage systems, researchers are exploring novel avenues to meet these ever-growing requirements [1-6]. Among the promising contenders in this landscape, multiple-bit-per-cell phase-change memory (PCM) stands out as a transformative technology with the potential to revolutionize memory architectures [7-9]. Traditional PCM technology, known for its non-volatile characteristics and scalability, has already demonstrated its prowess in various applications [10-13]. However, to further enhance its storage capacity and efficiency, researchers have turned their attention towards enabling multiple bits per cell, thereby exponentially increasing the memory density without compromising on performance [14-19]. For this purpose, common strategies have included modifying the phase change properties through graded doping and the use of multilayer stacks of phase change alloys. Graded doping involves the incorporation of elements such as nitrogen in $\text{Ge}_2\text{Sb}_2\text{Te}_5$ [20], selenium in GeSb [21], and the formulation of $\text{Ga}_2\text{Te}_2\text{Sb}_5$ [22], each of which adjusts the material properties to optimize switching behavior. Alternatively, multilayer stacks combine different phase change materials with varying phase transition characteristics, such as Sb_2Te_3 with $\text{Ge}_2\text{Sb}_2\text{Te}_5$ [23, 24], GeTe with $\text{Ge}_2\text{Sb}_2\text{Te}_5$ [25], and InSe with $\text{Ge}_2\text{Sb}_2\text{Te}_5$ [26].

Through a comprehensive analysis of the underlying principles, fabrication processes, and performance characteristics, this study explores the potential of a novel multiple-bit-per-cell phase change memory (MPCM) device, specifically utilizing $\text{Ge}_2\text{Sb}_2\text{Te}_5$ (GST) as the base phase change material. Over the years, various PCM devices utilizing different phase change alloys have been constructed and placed, demonstrating the diverse approaches in phase change memory technology, however, GST has emerged as the most extensively used and studied due to its exceptional thermal and electrical properties. The widespread adoption and research interest in GST highlight its effectiveness in delivering reliable and efficient performance for PCM applications. By presenting simulation results and performance evaluations, we demonstrate that our innovative design achieves higher storage capacities while maintaining reliability and endurance. The multiple-bit-per-cell capability, facilitated by the superior

*Corresponding Author: Ibrahim ÇINAR, icinar@kmu.edu.tr

phase change characteristics of GST, represents a significant advancement in memory technology. This advancement provides a promising pathway to meet the increasing demands of modern computing and data storage applications. Our study aims to contribute to this evolving field by introducing a groundbreaking device design based on GST and offering insights into its potential impact on future memory architectures, thereby paving the way for next-generation data-centric solutions.

2. MATERIAL AND METHODS

2.1. Device Structure

A 50 nm-thick active layer based on phase-change material GST is encapsulated between three heater-metal electrodes made of 30 nm WTi. These electrodes are strategically positioned from three distinct directions: x , y , and z , as depicted in Figure 1 b). Each heater electrode corresponds to a bottom contact, which acts as the ground terminal. During current distribution, the electrodes also serve as thermal reservoirs. Adjacent to the WTi layer, a stack of Ta and Au layers is utilized. Additionally, Al_2O_3 serves as an isolation barrier to protect the device from environmental influences. This sophisticated layered architecture ensures efficient performance, management of the heat distribution, and enhanced durability of the device from the all directions.

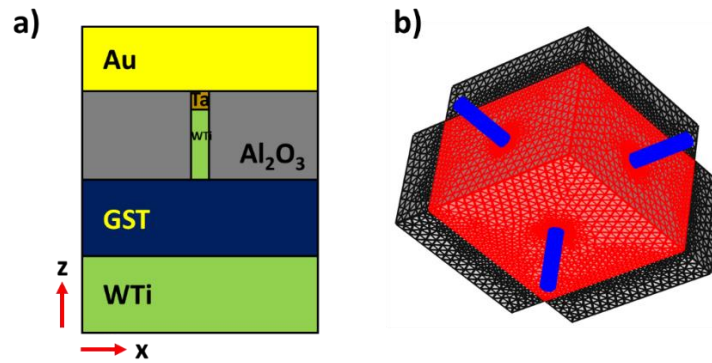


Figure 1. a) General phase change memory cell structure: 6 nm diameter circular heater contact and 80x80x50 nm GST layer. Ta/Au stack acts as the contact electrode for devices, and Al_2O_3 is used as isolation. b) 3-D structure of PCM cell (blue circulars are WTi heater contacts, red rectangular is GST and blacks are WTi bottom contacts)

2.2. Finite Element Model

In the realm of reset operation of phase-change simulation, traditional approaches have largely relied on two-dimensional electro-thermal and crystallization models [27-29]. However, for the nuanced requirements of a PCM device, we have innovatively developed a 3-D finite element simulation. This advanced model also emphasizes the significance of the top contact shape in modifying a mixture phase level, a concept elaborated further by Cinar in 2015[30]. In the present study, aimed at the design of a multi-bit-per-cell memory device, we employed 3D finite element simulations within a cell featuring a single active layer of GST with three heater electrodes. These simulations intricately incorporate phase-change kinetics, electrical properties, thermal characteristics, and percolation phenomena. The simulation framework is built upon an iterative approach, utilizing coupled differential equations that are temperature-dependent. Additionally, the inclusion of the Seebeck coefficient allows for the consideration of thermoelectric effects[31, 32], as well as adding Peltier effect [33]. The dynamics of the switching process exhibit a high sensitivity to both the programming current distribution and defect density. This is attributed to the inhomogeneous current flow and varying crystallite distribution during the phase-change process. To accurately capture these effects within the simulation, optimization of nucleation and

growth rates becomes imperative, as highlighted by Cinar (2015). Furthermore, our simulation framework employs adaptive meshing strategies. Specifically, the mesh elements for the phase-change layer ranges of $1 \times 1 \times 1 \text{ nm}^3$, while the contact regions (not for heater) are represented with a maximum mesh size of $2 \times 2 \times 2 \text{ nm}^3$. This granularity ensures a comprehensive understanding of the entire switching process. Boundary conditions are meticulously defined; the top and bottom surfaces of the metal electrodes, along with all external surfaces, are set as Dirichlet boundary conditions. Conversely, Neumann boundary conditions are applied to the interface surfaces. Given the field insulation properties of the Al_2O_3 layer, which is considered a near-perfect insulator, our simulation predominantly focuses on the top and bottom electrodes in the three specified directions, along with the GST layer, to depict the simulation results effectively. The simulation model is modular, comprising distinct submodels for electrical, thermal, and phase-change phenomena. This multiphysics approach allows for the nonlinear interactions between these submodels to be accurately represented. Each submodel is assigned specific tasks: the electrical model encompasses temperature and phase-dependent electrical conductivity variations; the thermal model addresses heat diffusion equations to calculate joule heating from electrical current, incorporating temperature and phase-dependent thermal conductivity; and finally, the phase-change model evaluates temperature-dependent nucleation and growth kinetics of crystallites, both homogeneous and heterogeneous.

Within the submodels, distinct equations are addressed based on the temperature and phase states of the materials under consideration. In the electrical submodel, the Laplace equation $\nabla \cdot [\sigma \nabla F] = 0$ is iteratively solved, employing 10 ps time steps, for each mesh element. This is executed in tandem with the thermal submodel to derive the spatial electrical potential distribution, represented as $F(x,y,z)$. Here, σ denotes the electrical conductivity of the materials. At ambient temperature, the electrical conductivities σ are reported as 2770 S/m for the crystalline phase and 3 S/m for the amorphous phase, as documented by Reifenberg et al. (2006). It is noteworthy that the electrical conductivity σ exhibits a temperature-dependent nature, which is further influenced by the structural phase of the GST layer. Consequently, as the temperature rises, the GST layer demonstrates increased conductivity, regardless of its phase, primarily due to the temperature-dependent σ values, with a more pronounced effect observed in the amorphous phase, as highlighted by Cinar et al. (2015).

In the thermal submodel, the electrical potential within the device gives rise to two significant parameters contributing to the heat generation, expressed as $Q = (JA) 2R\Delta t$, where A represents the cross-sectional area and Δt denotes the simulation time step. These parameters are the electrical current density, J , and the resistance value, R , of the material. The heat diffusion equation is employed to determine how temperature is distributed within the materials. Consequently, this heat equation is solved iteratively to derive the temperature distribution, represented as $T(x,y,z)$.

$$C \frac{\partial T}{\partial t} - \nabla \cdot [\kappa \nabla T] = Q + Q_{th} \quad (1)$$

Here, C represents the heat capacity and κ denotes the thermal conductivity. The term $Q_{th} = -TJ\nabla S$ incorporates the influence of the thermoelectric effect on heating. In this expression, S signifies the temperature-dependent Seebeck coefficient, and ∇S is defined as dS/dT , as referenced in studies by Cinar et al. (2015) and Fiflis et al. (2013)[34].

For the GST material, the thermal conductivity κ values at room temperature are reported as 0.7 W/(Km) for the crystalline phase and 0.3 W/(Km) for the amorphous phase, as documented by Won et al. (2012). Additionally, the Seebeck coefficient, S , is specified as 47 $\mu\text{V/K}$ for the crystalline phase and 380 $\mu\text{V/K}$ for the amorphous phase, as cited in studies by Cinar et al. (2015) and Fiflis et al. (2013). In the simulation, the heat capacity of GST remains consistent at 202 J/(kg K) for both crystalline and amorphous phases when $T < 800 \text{ K}$. To account for the phase transition, latent heat is incorporated into the calculations using a smooth Gaussian function centered on the melting point ($T_m = 892 \text{ K}$), as outlined by Reifenberg et al. (2006) and Peng et al. (1997)[35]. It is evident from the equations and the units of the parameters that the majority of the simulation parameters are temperature-dependent. Consequently, the temperature

distribution within the device significantly influences the phase change kinetics and ultimately determines the final phases of the materials.

When a programming pulse is applied to a PCM device, several key parameters critically influence the phase transition within a specific mesh element. These parameters include local temperature, temperature-dependent activation energy, and the state of adjacent cells. Considering the factors, the mesh element undergoes a phase transition randomly within the active region, leading to the formation of crystal nuclei. These nuclei can then grow, resulting in either a homogeneous or heterogeneous phase configuration within the active region. Because of temperature differences between the active region and its surroundings, crystallization outside the active region has minimal impact on the switching process. To model the probability rate of the crystallization process, the following equation is used, which depends on the nucleation rate, I_n , and the growth velocity of the nuclei, V_g ,

$$dP/dt = I_n(T) (1-P/N) + V_g(T) (1-P/a_0) \quad (2)$$

In the given equation, P represents the probability of crystallization, N stands for the number of molecules per unit volume, and a_0 denotes the atomic jump distance. The terms $I_n(T)$ and $V_g(T)$ correspond to the temperature-dependent nucleation and growth rates, respectively. For a deeper understanding of their influence on the phase change of the material, refer to the study by Cinar (2015). In general, to ascertain the comprehensive physical properties of semiconductors, encompassing both the crystalline and amorphous phases within, the Bruggeman effective medium approximation (EMA) proves to be a valuable method for application. Utilizing this approach, we can compute the electrical conductivity and thermal conductivity. Specifically, the electrical conductivity can be determined using the equation proposed by Bruggeman et al. (1935)[36].

$$(f, \sigma_a \sigma_c) = 0.25\{(2\sigma_p - \sigma'_p) + (2\sigma_p - \sigma'_p)^2 + (8\sigma_a \sigma_c)\}^{1/2} \quad (3)$$

In the provided equation, σ_a and σ_c represent the electrical conductivities of the amorphous and crystalline phases, respectively, while f denotes the crystallization fraction. Also, $\sigma_p = (1-f) \sigma_a + f \sigma_c$ and $\sigma'_p = (1-f) \sigma_c + f \sigma_a$. By integrating all submodels and formulas, we can obtain a comprehensive understanding of the electrical, thermal, and phase change profiles within the device, particularly for both GST layers. Once the crystallization fractions within the volume of the GSTs are determined, the device resistance during and/or after the application of a pulse can be computed.

3. RESULTS AND DISCUSSION

The innovative design of our phase change memory (PCM) device incorporates a sophisticated temperature control mechanism that ensures homogeneous temperature changes in three distinct directions, dictated by the applied voltage. This precision temperature management is crucial for the reliable operation of the switching mechanism, which transitions the phase change material between different states to store data. By carefully controlling the voltage, the device can induce temperature gradients along the x , y , and z axes, allowing for the precise manipulation of the material's phase. This multi-directional temperature modulation enables the PCM to achieve clear and distinct phase states, essential for accurately representing multiple data levels within each cell. The homogeneous temperature distribution across all three directions ensures consistent and repeatable phase transitions, thereby enhancing the reliability and efficiency of the data storage process. This advanced thermal management approach not only improves the device's performance and data integrity but also contributes to its ability to store a higher density of information, pushing the boundaries of current memory technology.

A detailed 3-D illustration of temperature distribution is presented in Figure 2. These simulations reveal the temperature distribution within the GST layer when subjected to distinct programming voltage pulses: Figure 2a) 1 V applied in the z direction ($T_{max} = 1029$ °C), 0.8 V in the x direction ($T_{max} = 658$ °C), and 0.6 V in the y direction ($T_{max} = 532$ °C), Figure 2b) 1 V applied in the x and z directions ($T_{max} =$

1061 °C) and 0.6 V in the y direction ($T_{\max} = 519$ °C), and Figure 2c) 1 V applied uniformly in the x, y, and z directions, ($T_{\max} = 1077$ °C).

Each voltage pulse maintains a duration of 100 nanoseconds with a trailing edge of 10 nanoseconds. The simulations indicate that the temperature distribution within the GST layer is homogeneous in all directions due to contact shape, ensuring even thermal management across the material. Notably, the maximum observed temperature varies with the amplitude of the applied voltage, reflecting how different voltage pulse configurations affect the thermal profile. Higher voltages result in higher peak temperatures, which, in turn, influence the phase change behavior within the GST layer. Consequently, each voltage configuration leads to distinct temperature distributions and maximum temperature values, inducing various phase transitions in the GST material. This comprehensive analysis underscores the critical relationship between applied voltage amplitude and thermal behavior in phase change memory devices, providing significant insights into how these variations impact the material's phase state and overall device performance.

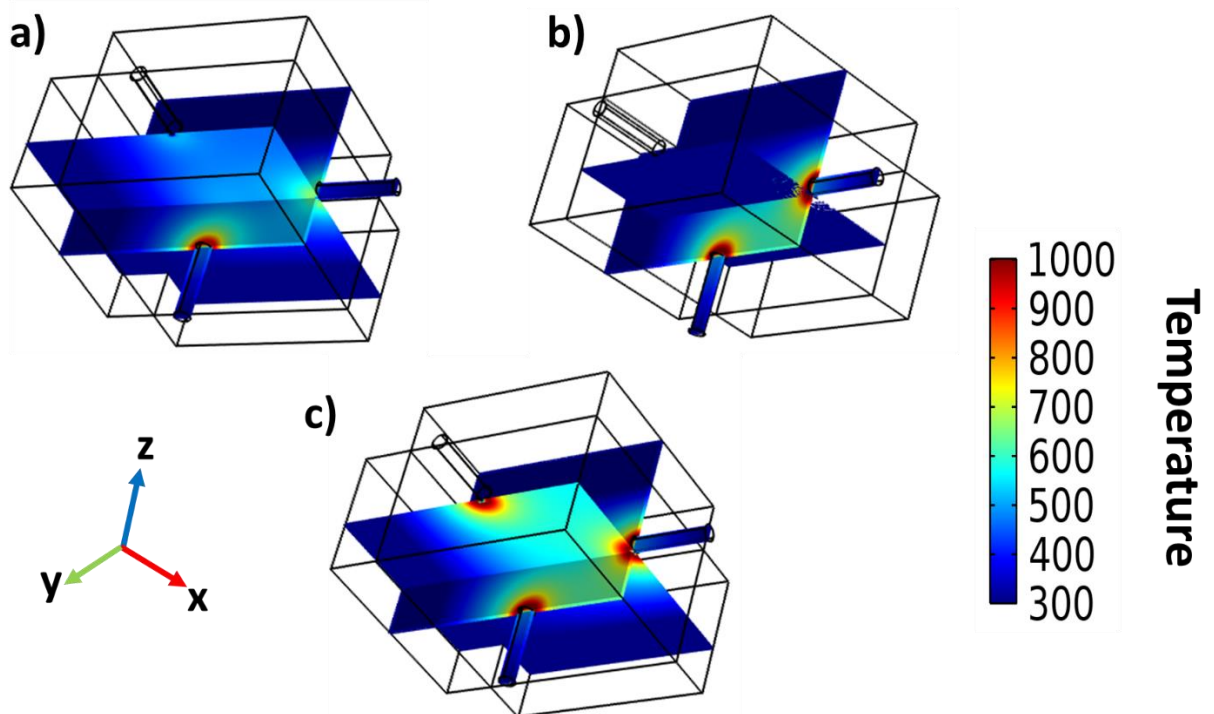


Figure 2. 3-D illustration of temperature distribution is plotted in three 6 nm circular top contact heaters device. The simulations depict the temperature distribution within the GST layer during programming voltage pulses with the following configurations: a) 1 V in the z direction, 0.8 V in the x direction, and 0.6 V in the y direction b) 1 V applied in the z and x directions and 0.6 V in the y direction, and c) 1 V applied in all three directions,. Each pulse has a duration of 100 ns with a trailing edge of 10 ns. This comprehensive analysis provides insights into how different voltage conditions affect the thermal profile within the GST layer.

As voltage is applied, it generates a corresponding temperature gradient within the material. When the temperature reaches specific thresholds, it causes the material to switch between amorphous and crystalline phases. Each phase has distinct electrical properties, such as different resistances, which can be reliably read and written to represent multiple bits of data. Due to the design concept and thermoelectric effects, these short-range thermal interactions are crucial for the performance of such devices.

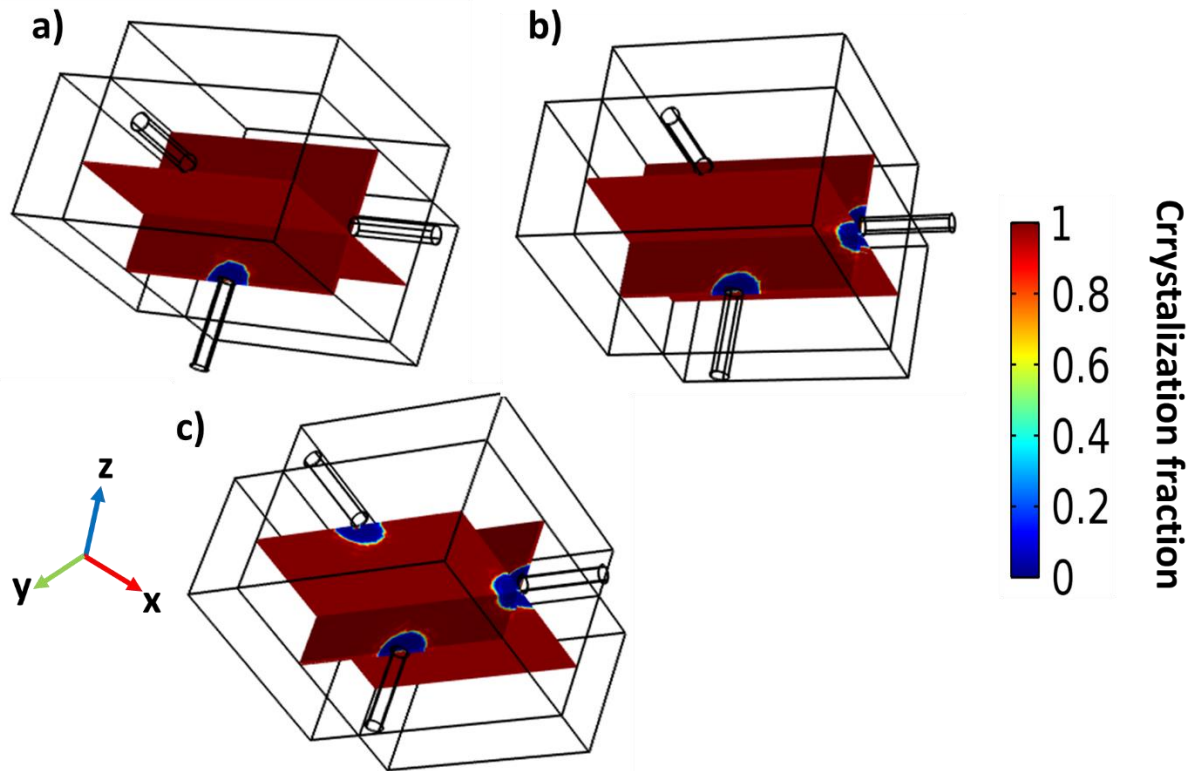


Figure 3. The crystallization fraction, f within the PCM layer of circular top contacts PCM cells is depicted after applying distinct programming voltage pulses: a) 1 V in the z direction, 0.8 V in the x direction, and 0.6 V in the y direction b) 1 V applied in the z and x directions and 0.6 V in the y direction, and c) 1 V applied in all three directions, using a 100 ns reset pulse with a 10 ns trailing edge. The color scale represents $f = 1$ (red) for crystalline phases and $= 0$ (blue) for amorphous phases. A vertical and horizontal cross-sections of the device, taken through the center, illustrates how different pulse amplitudes result in varying device resistances, namely phase differences.

From the simulation results depicted in Figure 3, it is evident that the phase distribution varies significantly depending on the applied voltage pulse amplitude. The crystallization fraction, f within the PCM layer is illustrated after applying three distinct programming voltage sequences: Figure 3a) 1 V in the z direction, 0.8 V in the x direction, and 0.6 V in the y direction, Figure 3b) 1 V applied in the z and x directions, and 0.6 V in the y direction and Figure 3c) 1 V applied uniformly in all three directions. Each programming pulse has a duration of 100 ns with a trailing edge of 10 ns. Vertical and horizontal cross-sections of the device, taken through the center, visually demonstrate how these different pulse amplitudes lead to varying device resistances, reflecting differences in phase distribution. This analysis underscores the impact of applied voltage pulse characteristics on the crystallization behavior of the PCM layer, highlighting its importance in optimizing device performance and functionality.

The switching process is highly sensitive and controlled, ensuring that the phase change occurs uniformly across the entire memory cell. This uniformity is crucial for maintaining data integrity and preventing partial switching, which could lead to data errors. By fine-tuning the voltage and, consequently, the temperature, we achieve precise control over the phase state of the material. This capability allows for rapid and repeatable switching between phases, enabling efficient data storage and retrieval at high speeds. The ability to reliably control phase switching through temperature changes not only enhances the performance and density of the PCM device but also underscores its potential for next-generation memory applications.

After obtaining the phase distribution, the calculated resistance values in the three directions of the device for a 1 V applied voltage pulse with a duration of 100 ns with a trailing edge of 10 ns are illustrated in Figure 4. The simulation results depict the Set operation with Figure 4a) a constant 1 V pulse and Figure 4b) varying programming voltages for a 100 ns pulse width with a 10 ns trailing edge. Figure 4a) shows

the resistance vs. time for the three directions, while Figure 4b) presents the resistance vs. applied voltage for the three directions. The obtained resistances in the x and y directions are similar, whereas the z direction exhibits different resistance values due to the thinner phase change material in the z direction.

Before the voltage was applied, the device resistance was measured at 30 kΩ in the x and y directions and 19 kΩ in the z direction. After applying the 1 V voltage pulse, the resistance increased to 12.5 MΩ in the x and y directions and 9.6 MΩ in the z direction. This represents a resistance change of approximately 420-fold in the x and y directions and 500-fold in the z direction. The data revealed that the z direction exhibited a notably lower resistance compared to the x and y directions. This lower resistance in the z direction is attributed to its reduced thickness, which facilitates a more efficient phase change due to the shorter path for current flow and heat dissipation. Consequently, the phase change material in the z direction undergoes a more uniform and complete transition, resulting in lower overall resistance.

Additionally, we conducted a detailed analysis of resistance as a function of the applied voltage (Figure 4b)). The resistance vs. voltage graph showed a characteristic abrupt switching behavior, clearly demarcating the transition from the crystalline to the amorphous state. This sharp switching is indicative of the rapid phase change occurring within the material, where a small increase in voltage induces a significant rise in resistance, marking the transformation from a highly conductive crystalline phase to a much more resistive amorphous phase. This abrupt switching is essential for the reliable operation of PCM devices, as it allows for distinct and stable data states that can be precisely controlled and detected. The ability to obtain clear resistance characteristics in multiple directions and to observe abrupt switching behavior underscores the effectiveness of our PCM device design in achieving efficient and high-density data storage.

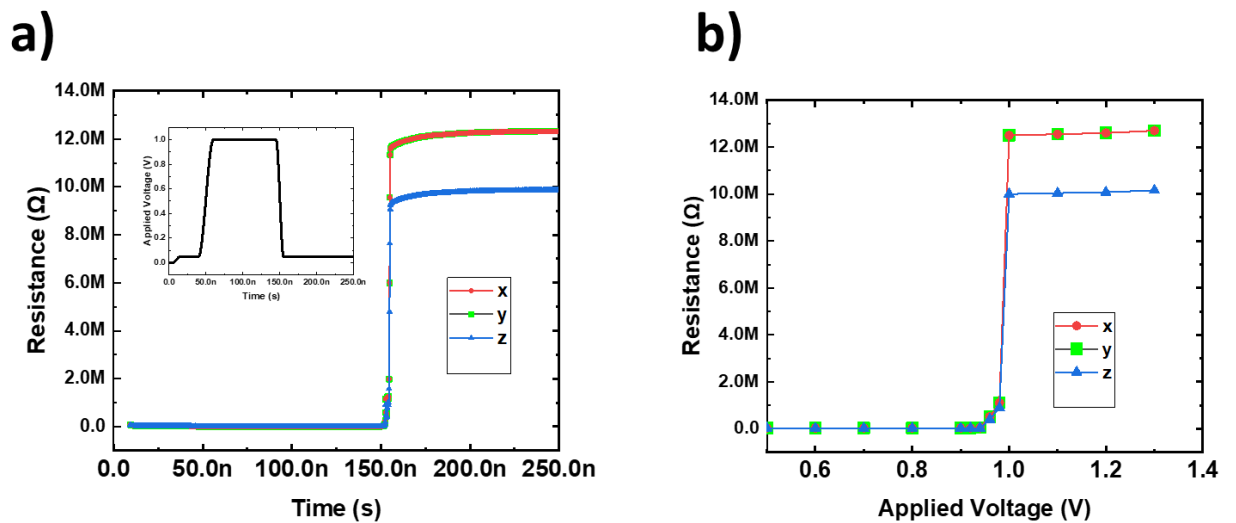


Figure 4. Simulation results of Set operation for a) 1 V and b) increasing programming voltages for a 100 ns width pulse with 10 ns trailing edge. a) Resistance vs Time for three directions and b) Resistance vs Applied Voltage in three directions.

The novel design of our phase change memory (PCM) device introduces an innovative approach to data storage, enabling significant advancements in memory technology. Unlike traditional PCM systems that store a single bit per cell by differentiating between two phases, our design utilizes a unique three-directional phase change mechanism. This approach allows each memory cell to represent three distinct levels, corresponding to 0, 1, and 2, effectively enabling the storage of three bits per cell. As a result, the device can store information at a much higher density, significantly increasing data capacity without increasing the physical footprint. Simulations confirm the clear distinction between these levels, ensuring reliable data encoding and retrieval. This breakthrough in PCM technology not only enhances storage efficiency but also paves the way for faster data access and reduced power consumption, marking a

significant leap forward in the development of high-performance, scalable memory solutions for a wide range of applications.

4. CONCLUSIONS

In summary, the introduction of our novel multiple-bit-per-cell phase-change memory (PCM) device design marks a significant step forward in memory technology. Through meticulous engineering and innovative approaches, we have demonstrated the feasibility of achieving higher memory densities while maintaining performance and reliability. This advancement holds great promise for addressing the escalating demands of modern computing and data storage systems, offering enhanced efficiency and scalability. As we continue to refine and optimize this design, we anticipate further breakthroughs in memory architectures and the realization of even more powerful computing capabilities.

Declaration of Ethical Standards

The authors declare that they have carried out this completely original study by adhering to all ethical rules including authorship, citation and data reporting.

Credit Authorship Contribution Statement

Ibrahim Çınar conceived and designed the study, conducted the experiments, analyzed the data, and wrote the manuscript.

Declaration of Competing Interest

The authors declared that they have no conflict of interest.

Funding / Acknowledgements

The author(s) received no financial support for the research.

Data Availability

Data supporting the findings of this study can be obtained from the corresponding author with reasonable requests to assist in scientific studies.

5. REFERENCES

- [1] H. S. P. Wong et al., "Phase Change Memory," *Proceedings of the IEEE*, vol. 98, no. 12, pp. 2201-2227, 2010, doi: 10.1109/jproc.2010.2070050.
- [2] M. Wuttig and N. Yamada, "Phase-change materials for rewriteable data storage," *Nature materials*, vol. 6, no. 11, pp. 824-832, 2007.
- [3] S. Raoux, W. Welnic, and D. Ielmini, "Phase change materials and their application to nonvolatile memories," *Chemical reviews*, vol. 110, no. 1, pp. 240-267, 2010.
- [4] A. Pirovano, A. L. Lacaita, A. Benvenuti, F. Pellizzer, and R. Bez, "Electronic switching in phase-change memories," *IEEE Transactions on Electron Devices*, vol. 51, no. 3, pp. 452-459, 2004.
- [5] G. W. Burr et al., "Phase change memory technology," *Journal of Vacuum Science & Technology B*, vol. 28, no. 2, pp. 223-262, 2010.
- [6] S. G. Sarwat, "Materials science and engineering of phase change random access memory," *Materials science and technology*, vol. 33, no. 16, pp. 1890-1906, 2017.
- [7] P. Fantini, "Phase change memory applications: the history, the present and the future," *Journal of Physics D: Applied Physics*, vol. 53, no. 28, p. 283002, 2020.

- [8] M. Le Gallo and A. Sebastian, "An overview of phase-change memory device physics," *Journal of Physics D: Applied Physics*, vol. 53, no. 21, p. 213002, 2020.
- [9] B. Kim et al., "Current status and future prospect of phase change memory," in 2011 9th IEEE International Conference on ASIC, 2011: IEEE, pp. 279-282.
- [10] O. Zilberberg, S. Weiss, and S. Toledo, "Phase-change memory: An architectural perspective," *ACM Computing Surveys (CSUR)*, vol. 45, no. 3, pp. 1-33, 2013.
- [11] K. Jiang, S. Li, F. Chen, L. Zhu, and W. Li, "Microstructure characterization, phase transition, and device application of phase-change memory materials," *Science and Technology of Advanced Materials*, vol. 24, no. 1, p. 2252725, 2023.
- [12] F. Ding et al., "A review of compact modeling for phase change memory," *Journal of Semiconductors*, vol. 43, no. 2, p. 023101, 2022.
- [13] D. Ielmini, S. Lavizzari, D. Sharma, and A. L. Lacaita, "Physical interpretation, modeling and impact on phase change memory (PCM) reliability of resistance drift due to chalcogenide structural relaxation," in 2007 IEEE International Electron Devices Meeting, 2007: IEEE, pp. 939-942.
- [14] J. Tominaga, "The Design and Application on Interfacial Phase-Change Memory," *physica status solidi (RRL)–Rapid Research Letters*, vol. 13, no. 4, p. 1800539, 2019.
- [15] A. Ehrmann, T. Blachowicz, G. Ehrmann, and T. Grethe, "Recent developments in phase-change memory," *Applied Research*, vol. 1, no. 4, p. e202200024, 2022.
- [16] A. Lotnyk, M. Behrens, and B. Rauschenbach, "Phase change thin films for non-volatile memory applications," *Nanoscale Advances*, vol. 1, no. 10, pp. 3836-3857, 2019.
- [17] M. S. Arjunan, S. Durai, and A. Manivannan, "Multilevel Switching in Phase-Change Photonic Memory Devices," *physica status solidi (RRL)–Rapid Research Letters*, vol. 15, no. 11, p. 2100291, 2021.
- [18] A. Gokce et al., "Toward multiple-bit-per-cell memory operation with stable resistance levels in phase change nanodevices," *IEEE Transactions on Electron Devices*, vol. 63, no. 8, pp. 3103-3108, 2016.
- [19] İ. Çinar, "Finite element modelling of a nanoscale semiconductor device to develop multiple bit per cell media," *Avrupa Bilim ve Teknoloji Dergisi*, no. 19, pp. 84-91, 2020.
- [20] B. Liu, T. Zhang, J. Xia, Z. Song, S. Feng, and B. Chen, "Nitrogen-implanted Ge₂Sb₂Te₅ film used as multilevel storage media for phase change random access memory," *Semiconductor science and technology*, vol. 19, no. 6, p. L61, 2004.
- [21] Y. Gu, Z. Song, T. Zhang, B. Liu, and S. Feng, "Novel phase-change material GeSbSe for application of three-level phase-change random access memory," *Solid-state electronics*, vol. 54, no. 4, pp. 443-446, 2010.
- [22] K. F. Kao, C. M. Lee, M. J. Chen, M. J. Tsai, and T. S. Chin, "Ga₂Te₃Sb₅— A Candidate for Fast and Ultralong Retention Phase-Change Memory," *Advanced materials*, vol. 21, no. 17, pp. 1695-1699, 2009.
- [23] F. Rao, Z. Song, L. Wu, B. Liu, S. Feng, and B. Chen, "Investigation on the stabilization of the median resistance state for phase change memory cell with doublelayer chalcogenide films," *Applied Physics Letters*, vol. 91, no. 12, 2007.
- [24] F. Rao et al., "Multilevel data storage characteristics of phase change memory cell with doublelayer chalcogenide films (Ge₂Sb₂Te₅ and Sb₂Te₃)," *Japanese journal of applied physics*, vol. 46, no. 1L, p. L25, 2007.
- [25] S.-H. Hong, H. Lee, K.-I. Kim, Y. Choi, and Y.-K. Lee, "Fabrication of multilevel switching high density phase change data recording using stacked GeTe/GeSbTe structure," *Japanese journal of applied physics*, vol. 50, no. 8R, p. 081201, 2011.
- [26] S.-H. Hong, H. Lee, Y. Choi, and Y.-K. Lee, "Fabrication of multi-level switching phase change nano-pillar device using InSe/GeSbTe stacked structure," *Current Applied Physics*, vol. 11, no. 5, pp. S16-S20, 2011.

- [27] J. Reifenberg, E. Pop, A. Gibby, S. Wong, and K. Goodson, "Multiphysics modeling and impact of thermal boundary resistance in phase change memory devices," in *Thermal and Thermomechanical Proceedings 10th Intersociety Conference on Phenomena in Electronics Systems, 2006. IThERM 2006.*, 2006: IEEE, pp. 106-113.
- [28] A. Cywar, J. Li, C. Lam, and H. Silva, "The impact of heater-recess and load matching in phase change memory mushroom cells," *Nanotechnology*, vol. 23, no. 22, p. 225201, 2012.
- [29] D.-H. Kim, F. Merget, M. Först, and H. Kurz, "Three-dimensional simulation model of switching dynamics in phase change random access memory cells," *Journal of Applied Physics*, vol. 101, no. 6, 2007.
- [30] I. Cinar et al., "Three dimensional finite element modeling and characterization of intermediate states in single active layer phase change memory devices," *Journal of Applied Physics*, vol. 117, no. 21, 2015.
- [31] C. Ma, J. He, J. Lu, J. Zhu, and Z. Hu, "Modeling of the temperature profiles and thermoelectric effects in phase change memory cells," *Applied Sciences*, vol. 8, no. 8, p. 1238, 2018.
- [32] J. Lee, M. Asheghi, and K. E. Goodson, "Impact of thermoelectric phenomena on phase-change memory performance metrics and scaling," *Nanotechnology*, vol. 23, no. 20, p. 205201, 2012.
- [33] A. Faraclas, G. Bakan, F. Dirisaglik, N. E. Williams, A. Gokirmak, and H. Silva, "Modeling of thermoelectric effects in phase change memory cells," *IEEE Transactions on Electron Devices*, vol. 61, no. 2, pp. 372-378, 2014.
- [34] P. Fflis, L. Kirsch, D. Andruczyk, D. Curreli, and D. N. Ruzic, "Seebeck coefficient measurements on li, sn, ta, mo, and w," *Journal of nuclear materials*, vol. 438, no. 1-3, pp. 224-227, 2013.
- [35] C. Peng, L. Cheng, and M. Mansuripur, "Experimental and theoretical investigations of laser-induced crystallization and amorphization in phase-change optical recording media," *Journal of Applied Physics*, vol. 82, no. 9, pp. 4183-4191, 1997.
- [36] V. D. Bruggeman, "Berechnung verschiedener physikalischer Konstanten von heterogenen Substanzen. I. Dielektrizitätskonstanten und Leitfähigkeiten der Mischkörper aus isotropen Substanzen," *Annalen der physik*, vol. 416, no. 7, pp. 636-664, 1935.



DETERMINATION OF THE CARBON FOOTPRINT OF ANIMAL WASTE AND CLIMATE CHANGE; KARAMAN EXAMPLE

¹Yusuf Alparslan ARGUN^{ID}, ^{2,*}Özgür ÇAKMAKCI^{ID}

Karamanoglu Mehmetbey University, Kazım Karabekir Vocational School, Karaman, TURKIYE

yusufargun@kmu.edu.tr, ozgurcakmakci@kmu.edu.tr

Highlights

- The results obtained using Tier 1 and Tier 2 approaches are as follows: 0.4924-0.5014 kg CO₂e per 1 liter of milk for Cattle. For sheep, it is 4.5167-6.5627 kg CO₂e per 1 kg of meat. For goat, it is 5.0813-6.0231 kg CO₂e per 1 kg of meat. These results can be taken into account when creating strategies to reduce methane gas emissions.
- According to the findings of the study, it was observed that there were significant differences in carbon footprint values between animal categories and subcategories. When the Tier 2 approach was used, carbon footprint values were higher than the Tier 1 approach.
- Another finding of the study is that the manure management system also contributes to the carbon footprint.



DETERMINATION OF THE CARBON FOOTPRINT OF ANIMAL WASTE AND CLIMATE CHANGE; KARAMAN EXAMPLE

¹Yusuf Alparslan ARGUN^{ID}, ^{2,*}Özgür ÇAKMAKCI^{ID}

Karamanoglu Mehmetbey University, Kazım Karabekir Vocational School, Karaman, TÜRKİYE
¹yusufargun@kmu.edu.tr, ²ozgurcakmakci@kmu.edu.tr

(Received: 22.01.2024; Accepted in Revised Form: 24.08.2024)

ABSTRACT: Climate change is a major concern around the world. In this context, the carbon footprint of animal waste is of critical importance for sustainability and climate change management. The aim of this study is to estimate the carbon footprint resulting from animal breeding and animal waste in the Karaman region. In the study, 2022 data was used and there are 1019277 sheep and 81368 cattle for Karaman. In the study, Tier 1 and Tier 2 approaches were used to estimate methane gas emissions related to both enteric fermentation resulting from animal digestive processes and manure management. According to the results of the study, the results obtained using Tier 1 and Tier 2 approaches are as follows: 0.4924-0.5014 kg CO₂e per 1 liter of milk for Cattle. For sheep, it is 4.5167-6.5627 kg CO₂e per 1 kg of meat. For goat, it is 5.0813-6.0231 kg CO₂e per 1 kg of meat. These results can be taken into account when creating strategies to reduce methane gas emissions. It is recommended to add better quality and high energy content foods to the feed ration, especially to reduce enteric fermentation. In addition, this study is a resource for relevant researchers working in the field in calculating the carbon loads of animal waste and is thought to be a guide for decision makers and practitioners.

Keywords: Carbon Footprint, Greenhouse Gas, Tier Approaches, Carbon Emission, Karaman

1.INTRODUCTION

Increasing world population and human needs have led to resource depletion and environmental problems, including global warming and climate change. The Kyoto Protocol specifies greenhouse gases and emission sources responsible for global warming as carbon dioxide (CO₂), methane (CH₄), nitrogen oxide (N₂O), hydrofluorocarbons (HFCs), perfluorocarbons (PFCs), and sulfur hexafluoride (SF₆) [1], [2]. The carbon footprint is a measure of these emissions in terms of carbon dioxide and is divided into primary and secondary categories. This study focuses on the firstly carbon footprint.

The Intergovernmental Panel on Climate Change (IPCC) has developed Tier 1-2-3 methods for calculating greenhouse gas emissions [3, 4]. According to the Food and Agriculture Organization (FAO), 18% of total greenhouse gas emissions originate from agricultural activities, with 14.5% of this figure attributed to livestock production. Livestock farms are significant sources of CH₄ and N₂O emissions. These gases have a much higher global warming potential than CO₂ [5, 6]. In the USA, the livestock sector accounts for 28% of antropogenic methane emissions [7]. Methane gas is produced as a result of the anaerobic decay of organic compounds found in the feces and manure of farm animals, posing a global problem. The annual methane gas emission from this source is estimated at 9.3 teragrams (Tg), contributing to 5% of the total global methane emissions [8, 9].

The livestock sector significantly contributes to global greenhouse gas emissions [10]. During milk production, the major greenhouse gas released is methane (CH₄), mainly produced by microbial fermentation in the digestive tracts of ruminant animals like cattle and sheep [11]. Methane is a greenhouse gas 25 times more potent than carbon dioxide (CO₂) and lingers in the atmosphere for approximately 12 years [12]. Therefore, the livestock sector must develop strategies to reduce methane emissions and decrease its carbon footprint [6].

*Corresponding Author: Özgür ÇAKMAKCI, ozgurcakmakci@kmu.edu.tr

The life cycle analysis (LCA) method can evaluate the carbon footprint of the livestock industry, calculating environmental impacts throughout a product or service's life cycle. LCA covers various stages of milk production, including feed production, animal care, manure management, milk processing, and distribution, measuring greenhouse gas emissions throughout these stages [13].

Numerous studies in the literature calculate the carbon footprint of milk production in different countries and production systems. These studies demonstrate that the carbon footprint of milk production varies depending on regional and systemic factors. For instance, studies by [4], [14-31] have reported that the carbon footprint of milk production varies depending on factors such as feed efficiency, animal productivity, manure management, energy use, transportation distance, and climatic conditions.

In conclusion, the carbon footprint of milk production is a crucial aspect of the battle against global warming. The LCA method is employed to calculate and reduce the carbon footprint of milk production. It is evident from the literature that the carbon footprint of milk production varies based on regional and systemic factors, and various strategies have been proposed to decrease methane emissions. Implementing these strategies can contribute to the sustainability of dairy production, but their cost-effectiveness, socioeconomic, and environmental impacts must also be considered.

The goal of this study is to estimate the carbon footprint resulting from animal activities in the Karaman region using Tier 1 and Tier 2 approaches.

2.MATERIAL AND METHODS

2.1. Current Situation of Karaman Province

Karaman Province is located in the south of Turkey and is situated between 37°-11' north latitude and 33°-13' east longitude. It is bordered by Mersin and Antalya to the south, and Konya to the west, north, and east. The city center is situated on a plain, with extensions of the Taurus Mountains to the south. The province is divided into 6 districts, 10 towns, and 154 villages. The geographical landscape of Karaman Province exhibits a unique characteristic where the northern part is covered with steppe vegetation, while the southern part is abundant in forests. Although the majority of the province's land is mountainous, the city center is located in a flat area [32].

The total land area of the province covers 885,100 hectares, with 39% dedicated to agricultural lands, 23% to meadow pasture areas, 27% to forested areas, and 11% to other uses. Crop production spans across 346,848 hectares throughout the province, with 62% of these areas allocated to field crops and 15% reserved for fallow lands. Specialized products such as fruit orchards cover 8.7% of agricultural lands, vineyards 1.4%, and vegetable cultivation 3.9%. Agriculture and animal husbandry are the primary sources of income for the regional economy in Karaman Province, highlighting the importance of this sector in the region [33, 34].

2.2. Data Collection

For this study, data regarding the number of animals in villages and neighborhoods were acquired from the provincial directorate of agriculture and forestry to determine the quantity of animal waste in Karaman Province and its districts. Human population and animal number data for the districts are presented in Table 1.

The geographical coordinates of Karaman Province, its districts, neighborhoods, and villages were recorded using the ArcMap 10.5 software.

The distribution of the number of animals in Karaman Province's districts was analyzed to calculate the potential carbon footprint resulting from animal waste. This data was then transferred to the ArcMap 10.5 software for density analysis.

Table 1. Population and Animal Number Data for DistrictsTable

District	Number of Cattle	Number of Sheep	Number of Goats	Human Population
AYRANCI	7138	258738	21875	7859
ERMENEK	5372	14684	35335	27417
BAŞYAYLA	1457	3681	4859	3508
KAZIMKARABEKİR	3541	24828	6219	4404
SARIVELİLER	3005	5620	7205	11232
CENTRAL DISTRICT	60855	479890	156343	247334

2.3. Business Status

In this section, the factors that are effective in the formation of climatic environmental conditions in the livestock barns where the study was conducted are explained. Additionally, various variables such as barn types, capacities, ventilation systems, manure removal methods and barn layouts vary among livestock facilities. More extensive livestock farming is done than commercial livestock farming. Therefore, the number of places where animal husbandry is carried out within the framework of a certain system is low density.

For this reason, Tier-2 data for places where livestock activities are carried out were included in the calculations based on average range values (Table 2).

Table 2 Acceptances regarding livestock activities used in Tier-2

Ym	Value			Source
	Cow	Sheep	Goat	
Ym	6,5	4,5	4,5	[35]
ASH	8%	9%	9%	[36]; [37]; [38]
Livestock weight	550 kg	45 kg	40 kg	[39]; [40]
Ca	0.17 MJ d ⁻¹ kg ⁻¹	0.009MJd ⁻¹ /kg ⁻¹	0.009MJd ⁻¹ /kg ⁻¹	[35]
Daily milk production	3,2 ton/year	0,8 ton/year	0,8 ton/year	[41]; [42]
Milk Fat percentage	%3,5	%6	%4,5	[43]; [44]; [45]; [46]
C _p	0,1	0,126	0,077	[35]
Wool/Fleece quantity	-	3,6kg/yıl	-	[47]
Feed Ration	12 kg/day	0,9 kg/day	0,9 kg/day	[48]; [49]; [50]; [51]

2.4. Carbon Footprint Calculation

In this study, Tier methods published by IPCC were used to examine methane (CH₄) and carbon dioxide (CO₂) emissions caused by dairy cattle farming, sheep and goat breeding sub-sectors within the livestock sector [35]. The IPCC 2006 National Greenhouse Gas Inventory Guide provides methodologies to be used in estimating national inventories and is the main methodological source for this study. In our study, sector and technology data were the main deciding factors when choosing the calculation method. Tier approaches determined by the IPCC are divided into three, but Tier 1 and Tier 2 approaches were used in this study.

When we calculate carbon footprint, the calculation is made per specific functional unit. For example, for dairy cattle farming, functional units such as 1 kg of processed milk or 1 hectare of agricultural land are taken as basis. This choice has been important in interpreting the results in regions where production is concentrated [52, 53, 4].

The carbon footprint calculation process, which is the main purpose of our study, was made on a per kg product basis. Emissions are typically corrected based on factors such as kg live weight or carcass weight for meat production systems and solids content per kg milk for dairy production systems. However, it is important to note that these rules do not apply to some special cases. In particular, different approaches are required for boneless meat and protein. Additionally, some studies also present a measure of output per domain [54, 55].

Therefore, this study calculated the carbon footprint through functional units such as 1 liter of milk in cattle enterprises and 1 kg of meat in sheep enterprises.

2.4.1. Tier 1 approach

The Tier 1 method is one of the simplest and most basic calculation methods, and in this method equations and default parameter values (e.g. emissions and stock change factors) are provided. The Tier 1 approach is based on country-specific activity data, but often sources of estimates for various parameters are available worldwide (e.g. deforestation rates, agricultural production statistics, global land cover maps, fertilizer use, animal population data, etc.) and specific values may not be available [35].

In carbon footprint calculations related to fertilizer management, the emission factor according to the Tier 1 method varies depending on the physical conditions (indoor or outdoor) and temperature conditions of the place where the manure are stored or preserved [56]. In accordance with the IPCC guidance, the Tier 1 approach is a simplified method for estimating emissions that only includes selected data for specific animal species, subcategories and climate zones or temperature ranges, together with the default emission factors found in the guidance [35]. In this study, equation 2.1 was used to calculate the carbon footprint resulting from manure management.

$$\text{CH4}_{\text{Fertilizer}} = \sum_T \frac{(\text{EF}_T \cdot \text{N}_T)}{10^6} \quad (2.1)$$

In this equality;

$\text{CH4}_{\text{Fertilizer}}$: Methane emissions from manure management (Gg CH₄/year)

$\text{EF}_{(T)}$: Emission factor for the defined livestock sector (kgCHVhead/year)

$\text{N}_{(T)}$: Number of animals in the population

T : Animal type

EF(T) values were determined using emission factors selected from Table 10.14 and Table 10.15 based on the subcategories specified in the IPCC 2006 guidance. These tables were created taking into account the differences in the development levels of the countries and the fertilizer management systems used. Additionally, another important parameter such as temperature was also taken into account. It has been noted that Turkey is evaluated in the category of developing countries and the average temperature of Karaman province is 12°C according to measurements between 1991-2020 [57]. Therefore, emission factor selections were made from the intersections of these values. Based on the data provided as reference in the IPCC guideline, methane emission factor tables resulting from manure management varying with temperature values for the Tier 1 approach are given below (Tables 3 and Tables 4).

Table 3. Methane emission factor from manure management for cattle [35].

	Cold			Temperate										Hot					
	<10°C	11°C	12°C	13°C	14°C	15°C	16°C	17°C	18°C	19°C	20°C	21°C	22°C	23°C	24°C	25°C	26°C	27°C	>28°C
Dairy Cattle	11	12	13	14	15	20	21	22	23	25	27	28	30	33	35	37	42	45	46
Other Cattle	6	6	7	7	8	9	10	11	11	12	13	14	15	16	18	19	21	23	23

Table 4. Methane emission factor due to manure management for small ruminants that varies with temperature values [35].

	Cold (<15°C)	Temperate (15°C-25°C)	Hot (>25°C)
Sheep			
Developed countries	0.19	0.28	0.37
Developing countries	0.10	0.15	0.20
Goat			
Developed countries	0.13	0.20	0.26
Developing countries	0.11	0.17	0.22

In the methane emission factor tables due to manure management, in this study, it was determined as 13 kg CH/head.year for cattle, 0.13 kg CH/head.year for goat enterprises and 0.13 kg CH/head.year for sheep pen enterprises.

Another important source of methane originating from livestock subcategories is the rumination process that animals carry out during digestion. Methane is a byproduct produced as a result of enteric fermentation that occurs in the digestive system of grazing animals. Enteric fermentation is carried out by microorganisms that carry out the digestive process by breaking down carbohydrate molecules in the bloodstream of the grazing animal into simple molecules [56]. The amount of methane produced varies depending on the animal's digestive system type, age, weight, and the quality and quantity of feed consumed [35].

In this study, the Tier 1 approach specified in the IPCC guideline was used to calculate methane (CH4) emissions from enteric fermentation. This approach uses default emission factors to estimate emissions and includes key data such as animal species, diets and annual milk yields. Additionally, equation 2.2 was used for the calculations, which is a mathematical formula used to estimate CH4 emissions from enteric fermentation. This equation is a useful tool for calculating emissions, taking into account the characteristics and feeding habits of animals [35].

$$\text{Emissions} = (EF_T) \times \left(\frac{N_T}{10^6}\right) \tag{2.2}$$

In this equality;

- Emissions : Methane emissions from enteric fermentation (Gg CH4/year)
- EF(T) : Emission factor for the defined livestock sector (kgCH4.head/year)
- N(T) : Number of animals in the population
- T : Animal type

EF(T) values are calculated using emission factors selected from Table 10.10 and Table 10.11 based on subcategories in the IPCC 2006 guidance. These tables take into account the differences in the development levels of the countries and the feed compositions used. For the Tier 1 approach, enteric fermentation-derived methane emission factor tables, which vary according to temperature values, were created as stated in Tables 5 and Tables 6.

Table 5. Methane emission factor from enteric fermentation for cattle [35].

	Animal Category	Emission Factor	Description
Eastern European Country Category	Dairy Cattle	99	Average Milk Production 2550
	Other Cattle	58	Includes cattle, bulls and young animals

Table 6. Methane emission factor from enteric fermentation for sheep [35]

Animal Category	Developed country	Developing country	Live weight
Koyun	8	5	65 kg - developed 45 kg-developing country
Keçi	5	5	40 kg

In the study, using Table 4 and Table 5, the methane emission factor originating from enteric fermentation was selected as 99 kg CH₄/head.year for dairy cattle and 5 kg CH₄/head.year for goat and sheep pen enterprises.

2.4.2 Tier 2 approach

The Tier 2 approach follows a similar methodological approach as Tier 1, but the key difference is the use of emission factors based on country- or region-specific data. Country-specific emission factors better adapt to factors such as climate zones, land use systems and livestock categories in that country and allow for a more accurate carbon footprint estimate. The Tier 2 approach is also more suitable for specific regions or land use/livestock categories, using more detailed data and subcategorized activity data [35].

Determining the Tier 2 approach is based on estimating the gross energy intake when calculating the enteric emissions of a particular animal species in the animal population. Gross energy is calculated by several factors and includes:

1. Net energy required for maintenance
2. Net energy required for daily activities
3. Net energy required for growth
4. Net energy required for lactation (milk production)
5. Net energy required for operation
6. Net energy required for wool production
7. Net energy required for pregnancy
8. Ratio of net energy available in the feed to digestible energy consumed (REM)
9. Ratio of net energy available for growth in nutrition to digestible energy consumed (REG)

Calculation of these factors is used to determine gross energy. In this study, equation 2.3 was used for gross energy calculation. This approach provides more detailed data to obtain more precise results and estimate enteric emissions for specific animal species [58].

$$GE = \left[\left(\frac{NE_m + NE_a + NE_l + NE_w + NE_p}{REM} \right) + \left(\frac{NE_g + NE_{wool}}{REG} \right) \right] / \left(\% \frac{DE}{100} \right) \quad (2.3)$$

In this equality;

GE : Gross Energy (MJ/day)

Nem	: Net energy needed by the animal for care (MJ/day)
Nea	: Net energy required by the animal for activity (MJ/day)
NEl	: Net energy required by the animal for lactation (MJ/day)
New	: Net energy required by the animal for work (MJ/day)
NEp	: Net energy required by the animal for pregnancy (MJ/day)
NEg	: Net energy required by the animal for growth (MJ/day)
NEwool	: Net energy required by the animal for wool production (MJ/day)
REM	: The ratio of the net energy available in the feed to the digestible energy consumed
REG	: The ratio of net energy available for growth in nutrition to digestible energy consumed
DE	: Digestible energy expressed as a percentage of gross energy (%)

Tables used to determine gross energy for dairy cattle, sheep and goat enterprises are included in Annex 10A.1 of Chapter 10 of the IPCC 2006 guide. These tables present variables such as gross energy intake, metabolizable energy, net energy maintenance and net energy production by animal categories and subcategories. These variables can be used to calculate the values of the parameters in the formulas used to determine gross energy. For gross energy calculation, separate tables and values were taken into account for dairy cattle enterprises, separate tables for sheep farming enterprises and separate tables for goat enterprises.

After gross energy calculations were completed, equation 2.4 was used in this study to calculate methane emissions from enteric fermentation for selected livestock categories. This approach helps the study obtain more precise and specific results and aims to estimate the carbon footprint more accurately [4].

$$EF = \frac{GE \times \left(\frac{Y_m}{100}\right) \times 365}{55,65} \quad (2.4)$$

In this equality;

EF : Emission factor from enteric fermentation (kg CH₄/head.year)

GE : Gross energy (MJ/day)

Y_m : Methane conversion factor (percentage of gross energy in feed converted to methane)

55.65 : Methane energy content (MJ/kg CH₄)

Dairy cattle, sheep and goats vary significantly from country to country in terms of management characteristics and manure management systems. In the Tier 2 method, the calculation of methane emission factors from manure depends on the manure properties and manure management system features [35]. In this study, equation 2.5 was used to calculate the methane emission factor from fertilizer.

$$EF = (VST \times 365) \times [Bo(T) \times 0,67 \times \left(\sum \frac{MCF_{s,k}}{100}\right) \times MSt, s, k] \quad (2.5)$$

In this equality;

EF : Annual CH₄ emission factor for the livestock category

VST : Volatile solids excreted daily from the animal category (kg dry matter/head.day)

Bo(T) : Maximum methane production capacity for fertilizer produced by animal category (m³ CH₄/kg)

0.67 : m³ CH₄ in kg CH₄ conversion factor

MCF(s,k) : Methane conversion factor (%) for each manure management system according to climate zone

MS(T,S,K) : Animal category, manure management system, climate zone fraction (dimensionless)

There is another equation that should also be used for the VS(T) parameter used in this equation. The equation to be used in the calculation is given in 2.6.

$$VS = (GE \times (1 - \frac{\%DE}{100}) + (UE \times GE)) \times (\frac{1-ASH}{18,45}) \quad (2.6)$$

In this equality;

VS : Volatile solids (kg VS/day)

GE : Gross energy (MJ/day)

DE% : Percentage of digestible food. It will be selected according to mortar categories and feeding diversity in Table 10.2.

(UE*GE) : Urinary energy is expressed as a fraction of gross energy. Typically 0.04GE can be considered the urinary energy excretion by most ruminants.

ASH : Ash content of manure.

18.45 : Conversion factor for gross energy per kg dry matter (MJ/kg).

The numerical data obtained in this study are the results of emission factors calculated using Tier approaches. In order for this data to be used for carbon footprint estimation, it must be multiplied by CO₂ equivalent (CO₂e) conversion factors. The IPCC uses equivalence factors to convert greenhouse gas emissions into CO₂e. These factors are calculated based on the 100-year global warming potential of different greenhouse gases. According to IPCC data in 1997, the 100-year global warming potential of CH₄ was accepted as 21, N₂O as 310 and CO₂ as 1 [59]. However, in subsequent updates, the equivalence factors were changed according to the update made by the IPCC [35]. After this update, the 100-year global warming potential of CH₄ is accepted as 25, N₂O as 298, and CO₂ as 1 [55]. CO₂ equivalence conversion rates are given in Table 7.

Table 7. Greenhouse gases CO₂ equivalent conversion factors [55].

Greenhouse Gas	Name	CO ₂ e [59]	CO ₂ eq [35]	Main Source
CO ₂	Carbon dioxide	1	1	Fossil fuels, deforestation
CH ₄	Methane	21	25	Rice fields, animal stomachs, biomass burning, landfills, leaks in natural gas pipelines, mines
N ₂ O	Nitroxide	310	298	Chemical fertilizers, fossil fuels, nylon production

In addition to methane emissions from enteric fermentation and fertilizer management, other emissions also occur in the businesses in the study area for various reasons. These reasons include emissions resulting from ventilation, heating, cooling, lighting, electricity and fuel consumption used in businesses. In the dairy cattle enterprises and sheep barn enterprises covered by the study, various operations such as milking, heating, manure cleaning and manure removal are carried out even if natural ventilation is used [6].

When calculating the carbon footprint, conversion factors used for electricity and fuel consumption are also taken into account. The emission factors used in this study are as follows: 2.66 kg CO₂e/kg for diesel fuel, 2.86 kg CO₂e/kg for coal heating and 0.40 kg CO₂e/kW/hour for electricity used in various production activities within the enterprise (Table 8) [25].

This information was used to take into account the full scope of emissions to calculate the carbon footprint of the study. In this way, the contributions of businesses to greenhouse gas emissions are evaluated from a more holistic perspective.

Table 8. Electricity and fuel emission factors used in carbon footprint [25]

Emission Source	Coefficient	Unit
Diesel	2,66	kg CO ₂ eq/ kg
Electric	0,40	kg CO ₂ eq kW/h
Coal	2,86	kg CO ₂ eq/ kg

3. RESULTS AND DISCUSSION

In this study, Tier 1 and Tier 2 approaches developed by IPCC were used to calculate the carbon footprint for selected livestock facilities. The aim is to estimate the greenhouse gas emissions and carbon footprint caused by cattle and sheep farming activities in Karaman city center, districts, villages and neighborhoods. Calculating the carbon footprint and evaluating the results is important to understand the potential of animal production enterprises in Karaman province to reduce greenhouse gas emissions and to determine these measures. This study can help create and implement policies and practices to reduce greenhouse gas emissions.

The results of the study can be used to determine which livestock activities create the most emissions and in which regions these emissions are concentrated. This information can be used to identify areas where measures to reduce carbon footprint should be focused. It may also be useful to evaluate the effectiveness of measures to reduce the environmental impact of livestock enterprises.

As a result, this study should be seen as an important step to understand and reduce the environmental impacts of the animal production sector in Karaman province. This can contribute to promoting a sustainable livestock sector.

3.1. Carbon Footprint According to Tier 1 Approach

In the study, carbon footprints of livestock activities within the borders of Karaman province were determined using the Tier 1 approach of the IPCC guide. This calculation approach was made taking into account the geographical location of the region and annual average temperature data. The carbon footprint per 1 liter of milk for cattle is calculated as 0.4924 kg CO₂e, and the annual total carbon footprint of these animals is determined as 227830.4 tons CO₂e.

In study [58], it was mentioned that a carbon footprint of 0.4215 kg CO₂e per 1 liter of milk was determined for dairy cattle in Bursa, and the total annual carbon footprint of the dairy cattle enterprise was 461 tons of CO₂e. In this study, it was stated that the carbon footprint of a dairy cattle enterprise consists of four components: enteric fermentation, manure management system, fuel and electricity consumption within the enterprise. Additionally, it was stated that the values used to calculate the carbon footprint resulting from dairy farming in Ireland. In study were close to other similar studies [60], greenhouse gas emissions were expressed as CO₂ equivalents. Emissions per hectare for dairy farming were calculated as 6,835 kg CO₂e/year, and for beef production as 4,859 kg CO₂e/year. These emission values are associated with all land areas within the scope of the study. In [23] study, Canada's dairy sector was examined and a model was developed to estimate the carbon footprint of dairy products. The carbon footprint of raw milk varies in different regions and is calculated as 0.93 kg CO₂e/1 L milk in the western regions and 1.12 kg CO₂e/1 L milk in the eastern regions.

All these studies show that different approaches can be used to determine and reduce the carbon footprint of the livestock sector and that geographical, climatic and operating differences can affect the results. The carbon footprint amounts calculated at the end of the study are similar to studies conducted in similar regions.

According to calculations made for Karaman province, 4.52 kg CO₂e is emitted per 1 kg of meat production for sheep barns, and 5.08 kg CO₂e is emitted per 1 kg of meat production for goat barns. These results show that the factors that contribute to the carbon footprint of cattle also apply to sheep and goat

pens. The annual carbon footprint for sheep pens was calculated as 160,047.4 tons CO₂e, and for goat pens it was determined as 47,120.7 tons CO₂e.

These results are consistent with previous studies. The study conducted revealed that sheep pens emit 0.0912 kg of CO₂e per 1 kg of meat production and the annual carbon footprint of the enterprise is 329 tons of CO₂e [58]. This study indicates that the factors that contribute to the carbon footprint of dairy cattle enterprises are also valid for sheep enterprises. It divided carbon footprint calculations in sheep farms in Australia into two: methane emissions from manure and methane emissions from enteric fermentation [61]. According to this study, methane emissions from manure were calculated as 0.00076 kg CO₂e per 1 kg of meat production, and methane emissions from enteric fermentation were calculated as 4.6 kg CO₂e per 1 kg of meat production. In the research conducted by [17], a literature review was conducted on the factors affecting the size of emissions and surveys were conducted on two farms with a more intensive production system and a larger system. In the farm with a more intensive production system, 0.4 kg of methane emission per kg of sheep meat was detected, and in the farm with a larger production system, 0.9 kg of methane emission per kg of sheep meat was detected. These differences have been attributed to factors such as lambs remaining on pasture longer and the addition of more forage. The study also showed that emission amounts may vary depending on various factors such as feed composition, feed quality, age of the animals, the duration they are active, breed and gender.

The carbon footprint amounts obtained using the Tier 1 approach are given in Table 9 and the Karaman-wide CO₂ distribution map is given in Figure 1.

Calculations show that the carbon footprint amounts of livestock activities in Karaman province are at different levels. These results help to identify the main reasons why emission amounts vary between livestock subcategories. Two main reasons stand out: Enteric fermentation of ruminant animals and differences in manure management systems. This information can form an important basis for developing environmental sustainability strategies and reducing emissions at the regional level. Additionally, these data can contribute to the development of better practices to reduce the environmental impact of livestock farming enterprises.

Table 9. CO₂ equivalent amounts of Districts in terms of animal waste (Tier-1)

District	Cattle Total tons CO ₂ eq	Sheep Total tons CO ₂ eq	Goat Total tons CO ₂ eq	Grand Total tonnes CO ₂ eq
AYRANCI	19986,4	52588,4985	4446,09375	77020,99225
ERMENEK	15041,6	2984,523	7181,83875	25207,96175
BAŞYAYLA	4079,6	748,16325	987,59175	5815,355
KAZIMKARABEKİR	9914,8	5046,291	1264,01175	16225,10275
SARIVELİLER	8414	1142,265	1464,41625	11020,68125
CENTRAL DISTRICT	170394	97537,6425	31776,71475	299708,3573
Total	227830,4	160047,3833	47120,667	434998,4503

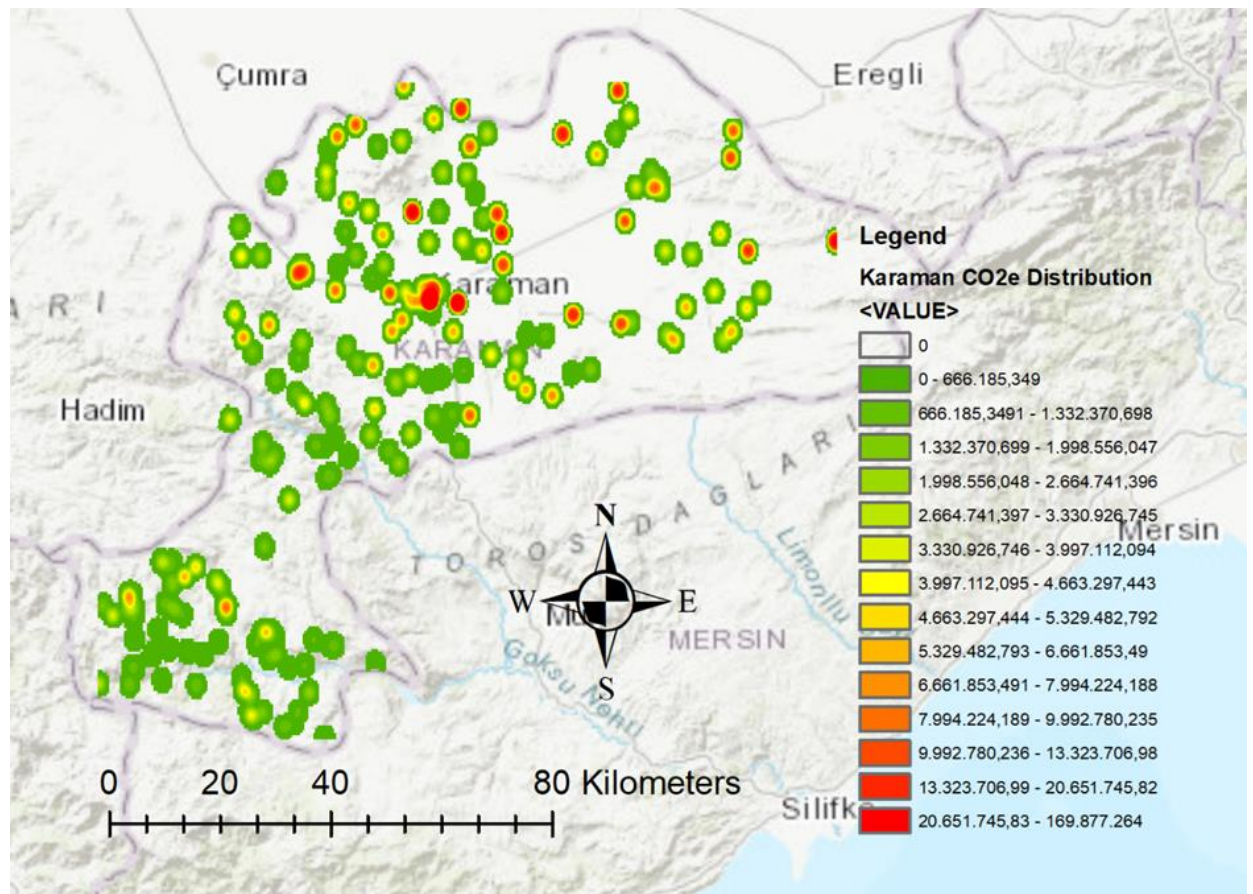


Figure 1 CO₂eq distribution map across Karaman using Tier 1 approach

3.2. Carbon Footprint According to Tier 2 Approach

In this study, the carbon footprint of livestock enterprises operating in Karaman province was determined with the Tier 2 approach included in the guide published by [35]. The Tier 2 approach takes into account parameters that vary depending on the species, age group, nutritional level and climatic conditions of the animals. These parameters include factors such as live weight of the animals, daily feed consumption, nutritional value of the feed, type of digestive system of the animals, and manure management system. In this study, carbon footprint calculations were made for cattle, sheep and goats using parameters selected in accordance with the geographical location and climatic characteristics of Karaman province. According to the results of the study, the carbon footprint of milk obtained from cattle was determined as 0.5013 kg CO₂e/1 L. The total annual carbon footprint of cattle was found to be 231995.7 tons CO₂e. 88% of this amount comes from enteric fermentation (204,000 tons CO₂e) and 12% comes from fertilizer management (27,995.7 tons CO₂e). The carbon footprint of meat obtained from sheep and goats was determined as 6.5627 kg CO₂e / 1 kg meat and 6.0231 kg CO₂e / 1 kg meat, respectively. The annual total carbon footprint of sheep and goats was found to be 232548.1 tons CO₂e and 55854.67 tons CO₂e, respectively. Of these amounts, 93% (216.169% tons CO₂e and 51.954% tons CO₂e) comes from enteric fermentation, and 7% (16.379% tons CO₂e and 5.900% tons CO₂e) comes from manure management (Table 10). It has been observed that a large part of the carbon footprint originates from enteric fermentation, while manure management has a smaller share. Detailed results of the study obtained using the Tier 2 approach are presented in Table 11 and the CO₂ equidistribution map of Karaman province is presented in Figure 2.

Table 10 Methane formation amounts from fertilizer and fermentation in the districts in terms of animal waste

District	CH4 from cattle manure	CH4 from SHEEP manure	CH4 from GOAT manure EF(annual)(methane)(kg)	CH4 from cattle fermentati on	CH4 from SHEEP fermentatio n	CH4 from GOAT fermentatio n-
AYRANCI	96109,374	192809,08 3	13298,39 3	717962,606	2863624,955	197509,419
ERMENEK	72331,123	10942,376	21481,08 4	540332,743	162517,561	319039,787
BAŞYAYLA	19617,730	2743,046	2953,915	146549,666	40740,067	43871,920
KAZIMKARABEKİR	47677,682	18501,588	3780,695	356164,974	274787,933	56151,363
SARIVELİLER	40460,727	4187,970	4380,110	302252,400	62200,265	65053,959
CENTRAL DISTRICT	819380,215	357609,43 9	95045,05 8	6120988,289	5311260,733	1411621,267

Table 11. CO₂eq amounts of Districts in terms of animal waste (Tier-2)

District	Cattle Total tons CO ₂ eq	Sheep Total tons CO ₂ eq	Goat Total tons CO ₂ eq	Grand Total tonnes CO ₂ eq
AYRANCI	20351,79952	76410,85096	5270,195321	102032,8458
ERMENEK	15316,59667	4336,498448	8513,021791	28166,1169
BAŞYAYLA	4154,184911	1087,077825	1170,6459	6411,908637
KAZIMKARABEKİR	10096,06642	7332,238046	1498,301472	18926,60594
SARIVELİLER	8567,82818	1659,705889	1735,851762	11963,38583
CENTRAL DISTRICT	173509,2126	141721,7543	37666,65815	352897,6251
Total	231995,6883	232548,1255	55854,6744	520398,4882

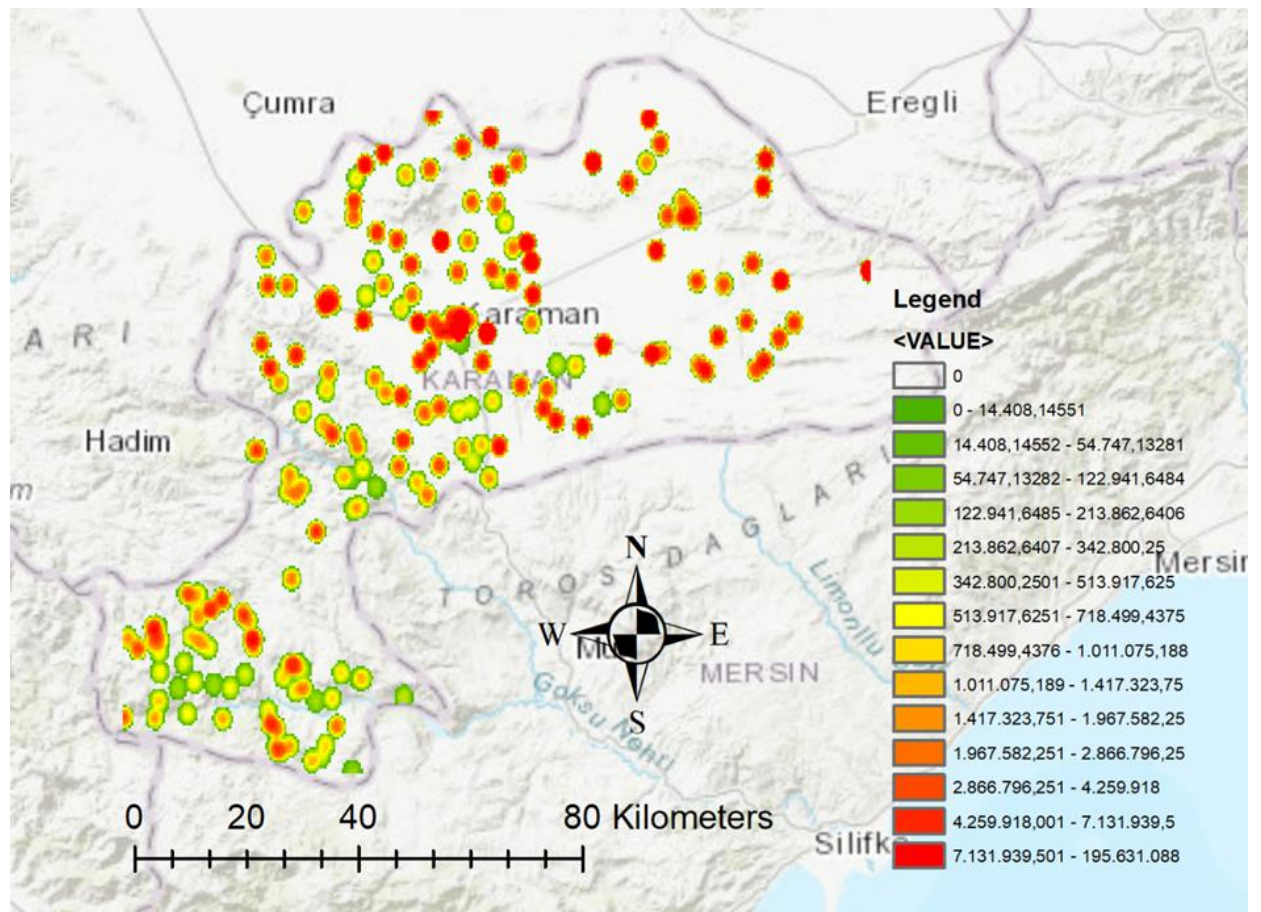


Figure 2. CO₂eq distribution map across Karaman using Tier 2 approach

3.3. Comparison of Tier 1 and Tier 2 Approaches

Comparative results of carbon footprint values for BBH, Sheep and Goat enterprises as a result of calculations made using the Tier 1 and Tier 2 Approaches and parameters in the IPCC guide. Table 12 is also given.

Table 12. % change rates by Animal Type

	Tier 1 Approach Results	Tier 2 Approach Results	% Rate of change
Cattle	0,4924 kg CO ₂ e/1 L milk	0,5014 kg CO ₂ e/1 L milk	1,8
	5,6 kg CO ₂ e/1 kg meat	5,7 kg CO ₂ e/1 kg meat	
Sheep	0,1856 kg CO ₂ e/1 L milk	0,2697 kg CO ₂ e/1 L milk	31,17
	4,52 kg CO ₂ e/1 kg meat	6,56 kg CO ₂ e/1 kg meat	
Goat	0,4491 kg CO ₂ e/1 L milk	0,5323 kg CO ₂ e/1 L milk	15,63
	5,08 kg CO ₂ e/1 kg meat	6,02 kg CO ₂ e/1 kg meat	

According to the results given in Table 12, carbon footprint values calculated with the Tier 2 approach are higher than the Tier 1 approach. This is because, in the Tier 2 approach, private data of livestock enterprises and the work area are included in carbon footprint calculations. In the Tier 2 approach, parameters such as live weight of the animals, daily feed consumption, nutritional value of the feed, type of digestive system of the animals, and manure management system are taken into account. These

parameters are factors that affect the carbon footprint. In the Tier 1 approach, these parameters are ignored and fixed emission factors are used depending on the type and number of animals. Therefore, the Tier 2 approach provides more realistic and accurate results.

However, carbon footprint values calculated with the Tier 2 approach increase at different rates depending on animal species. As seen in Table 12, the carbon footprint value calculated with the Tier 2 approach for cattle is 1.8% higher than the Tier 1 approach. This rate is 31.17% for sheep and 15.63% for goats. This difference is due to factors such as the feeding style of the animals, manure management characteristics and the climatic conditions of the study area. These factors affect the carbon dioxide equivalent (CO₂e) emissions of animals.

The parameters used in this study are accepted data found in the guide published by the [35]. However, it should not be forgotten that these parameters may vary depending on the climatic data of the study area. Therefore, it is important to take into account the specific conditions of the work area when making carbon footprint calculations. This study shows that the Tier 2 approach is more appropriate than the Tier 1 approach in determining the carbon footprint of the livestock sector.

4. CONCLUSION

This study aimed to reveal the contribution of livestock activities in Karaman province to global warming through carbon footprint analysis. In the study, carbon footprint calculations were carried out using Tier 1 and Tier 2 approaches, taking into account the population of 81368 Cattle, 787441 Sheep and 231836 Goats in the province. Additionally, strategies proposed in the literature to reduce carbon footprint were evaluated. As a result of the study, a result of 0.4924 kg CO₂e per 1 L of milk, which is the functional unit for Cattle, was reached in the Tier 1 approach. It is estimated that 88% of this result is CH₄ emissions resulting from enteric fermentation as a result of the animal ruminating. It was determined that the remaining 12% was due to the fertilizer management system. The carbon footprint calculation result using the Tier 2 approach was obtained as 0.5014 kg CO₂e per 1L of milk for Cattle.

When the Tier 1 approach was used in the calculations for sheep pens, it was 4.5167 kg CO₂e per 1kg of meat, while as a result of the calculation using the Tier 2 approach, 6.5627 kg CO₂e per 1kg meat was found. In the calculations made for goat pens, when the Tier 1 approach was used, 5.0813 kg CO₂e per 1kg of meat was found, while as a result of the calculation made using the Tier 2 approach, 6.0231 kg CO₂e per 1kg of meat was found.

According to the findings of the study, it was observed that there were significant differences in carbon footprint values between animal categories and subcategories. When the Tier 2 approach was used, carbon footprint values were higher than the Tier 1 approach. This shows that the Tier 2 approach provides a more realistic assessment [35]. It has been determined that most of the carbon footprint is caused by enteric fermentation. Enteric fermentation is the production of methane gas by microorganisms in the stomachs of ruminant animals during the digestive process. Methane gas is one of the most important greenhouse gases in the atmosphere and its global warming potential is 28 times greater than carbon dioxide [62]. Some strategies suggested in the literature to reduce methane emissions from enteric fermentation include adding ionophores, oils, high-quality feeds or grains to the animal's diet, or using compounds that inhibit methane production in the animals' stomachs [63, 14, 16, 42].

Another finding of the study is that the manure management system also contributes to the carbon footprint. Manure management system can be defined as the collection, storage, processing and use of animal manure. The manure management system can affect emissions of both carbon dioxide and other greenhouse gases such as methane and nitrous oxide. Some strategies suggested in the literature to reduce greenhouse gas emissions from manure include improving manure operating systems or composting [64].

As a result of the study, it was revealed that livestock activities in Karaman province make a significant contribution to global warming. To reduce this contribution, mitigation methods from both the source and the environment should be applied. Source reduction methods are activities aimed at preventing or reducing the formation of greenhouse gases. Environmental mitigation methods are activities that enable the removal or storage of greenhouse gases from the atmosphere. In this study,

prevention strategies such as changing barn and coop designs or reducing the protein content of the feed ration were suggested among source reduction methods. In addition, environmental reduction methods include options such as afforestation, biomass energy, carbon capture and storage [62].

This study is important as it is the first study to evaluate the effects of livestock activities in Karaman province on global warming. It carried out a carbon footprint analysis to determine the effects of livestock activities in Karaman province on global warming. As a result of the study, carbon footprint values by animal categories and the factors affecting them were revealed. Additionally, various strategies and greenhouse gas emissions reduction methods suggested in the literature to reduce carbon footprint were evaluated. This study provides information that may be useful to both the livestock sector and all stakeholders combating global warming. However, the study also has some limitations. For example, only Cattle, Sheep and Goat populations were considered in the study. Other animal species and poultry can also contribute to the carbon footprint. Additionally, only the direct effects of livestock activities were taken into account in the study. Indirect effects of livestock activities, such as feed production, transportation and processing, can also affect the carbon footprint. Therefore, future studies should also focus on these issues.

Declaration of Ethical Standards

The authors declare that they have carried out this completely original study by adhering to all ethical rules including authorship, citation and data reporting.

Credit Authorship Contribution Statement

Author contribution rates are equal in this study.

Declaration of Competing Interest

The authors declared that they have no conflict of interest.

Funding / Acknowledgements

The author(s) received no financial support for the research.

Data Availability

This study does not contain any dataset.

5. REFERENCES

- [1] UNFCCC, Kyoto Protocol to the United Nations Framework Convention on Climate Change, 1997.
- [2] H.N. Bayraç, "Enerji Kullanımının Küresel Isınmaya Etkisi ve Önleyici Politikalar," *Eskişehir Osmangazi Üniversitesi Sosyal Bilimler Dergisi*, vol. 11(2): pp. 229-259, 2010.
- [3] E. Çınar, "İneklerin ekolojik ayak izi raporu," *Animal Science Journal*, 2013 (Rum 38): pp. 210-218., 2007.
- [4] İ. Kılıç, B. Amet, "Bir Süt Sığırı İşletmesinin Karbon Ayak İzinin Tahminlenmesi: Bursa Örneği," *Journal of Agricultural Faculty of Gaziosmanpaşa University (JAFAG)*, 34(Ek Sayı), 132-140, 2017.
- [5] S. Bauer, "Development of environmental impact assessment tools for livestock production systems," Vol. 1 :Research Report, Giessen, Germany, pp.4-16, 1994.
- [6] P. J. Gerber, H. Steinfeld, B. Henderson, A. Mottet, C. Opio, J. Dijkman, A. Falcucci and G. Tempio, "Tackling Climate Change through Livestock - A Global Assessment of Emissions and Mitigation

- Opportunities," Food and Agriculture Organization of the United Nations (FAO), Rome, 2013.
- [7] U.S. EPA (Environmental Protection Agency), Erişim Tarihi 24.05.2022.
- [8] E. Scheehle, "Emissions and Projections of Non CO₂ Green House Gases from Developing Countries 1990-2020," 2022.
- [9] P. Demir, Y. Cevger, "Küresel Isınma ve Hayvancılık Sektörü," *Veteriner Hekimler Derneği Dergisi*, 78(1): 13-16, 2007.
- [10] FAO, "Greenhouse gas emissions from the dairy sector: A life cycle assessment," 2010.
- [11] K.A. Beauchemin, H.H. Janzen, S.M. Little, T.A. McAllister, S.M. McGinn, "Life cycle assessment of greenhouse gas emissions from beef production in western Canada: A case study," *Agricultural Systems*, 103(6), 371-379, 2009.
- [12] IPCC., *Climate change 2007: The physical science basis. Contribution of working group I to the fourth assessment report of the intergovernmental panel on climate change*, 2007.
- [13] L.J. Müller, A. Käthelön, M. Bachmann, A. Zimmermann, A. Sternberg, A. Bardow, "A guideline for life cycle assessment of carbon capture and utilization," *Frontiers in Energy Research*, 8-15, 2020.
- [14] D. Boadi, C. Benchaar, J. Chiquette, D. Massé, "Mitigation strategies to reduce enteric methane emissions from dairy cows: Update review," *Canadian Journal of Animal Science*, 84(3), 319-335, 2004.
- [15] R. Schils, A. Verhagen, H. Aarts, L. Şebek, "A farm level approach to define successful mitigation strategies for GHG emissions from ruminant livestock systems," *Nutrient Cycling in Agroecosystems*, 71(2): 163-175, 2005.
- [16] M.S. Mitsumori, "Control of Rumen Microbial Fermentation for Mitigating Methane Emissions from the Rumen," *Asian Australasian Journal of Animal Sciences*, 144-154, 2008.
- [17] H. Allard, "Methane emissions from Swedish sheep production," Swedish University of Agricultural Sciences, 2009.
- [18] G. Edwards-Jones, K. Plassmann, I. Harris, "Carbon footprinting of lamb and beef production systems: insights from an empirical analysis of farms in Wales, UK," *Journal of Agricultural Science*, 147: 707-719, 2009.
- [19] S. Ledgard, M. Lieffering, J. Devitt, M. Boyes, R. Kemp, "A greenhouse gas footprint study for exported New Zealand lamb," *Report for Meat Industry Association, Ballance Agri-nutrients, Landcorp and MAF. AgResearch, Hamilton*, 2010.
- [20] G. Aydın, İ. Karakurt, K. Aydıner, "Antropojenik Metan Emisyonlarının Sektörel Analizi," *Tüba Bilim Dergisi*, 42-51, 2011.
- [21] J. Lesschen, M. Van den Berg, H. Westhoek, H. Witzke, O. Oenema, "Greenhouse gas emission profiles of European livestock sectors," *Animal Feed Science and Technology*, 166: 16-28, 2011.
- [22] M. Henriksson, A. Flysjö, C. Cederberg, C. Swensson, "Variation in carbon footprint of milk due to management differences between Swedish dairy farms," *Animal*, 5(9): 1474-1484, 2011.
- [23] X. Verge, D. Maxime, J. Dyer, R. Desjardins, Y. Arcand, A. Vanderzaag, "Carbon footprint of Canadian dairy products: Calculations and issues," *Journal of dairy science*, 96(9): 6091-6104, 2013.
- [24] S. Wiedemann, S. Ledgard, B. Henry, M. Yan, N. Mao, S. Russell, "Application of life cycle assessment to sheep production systems: investigating co- production of wool and meat using case studies from major global producers," *The International Journal of Life Cycle Assessment*, 20(4): 463-476, 2015.
- [25] R. Jacobsen, V. Vandermeulen, G. Vanhuylenbroeck, X. Gellynck, "A life cycle assessment application: the carbon footprint of beef in Flanders (Belgium)," *In Assessment of Carbon Footprint in Different Industrial Sectors, Volume 2*, 31-52, 2014.
- [26] J. Owen, W. Silver, "Greenhouse gas emissions from dairy manure management: a review of field-based studies," *Global Change Biology*, 21(2): 550-565, 2015.
- [27] C. Dunkley, B. Fairchild, C. Ritz, B. Kiepper, M. Lacy, "Carbon footprint of poultry production farms in South Georgia: A case study," *Journal of Applied Poultry Research*, 24(1): 73-79, 2015.

- [28] I. Batalla, M. Knudsen, L. Mogensen, O. del Hierro, M. Pinto, J Hermansen, "Carbon footprint of milk from sheep farming systems in northern Spain including soil carbon sequestration in grasslands," *Journal of Cleaner Production*, 104: 121-129, 2015.
- [29] M. Mujica, G. Blanco, E. Santalla, "Carbon footprint of honey produced in Argentina," *Journal of cleaner production*, 116: 50-60, 2016.
- [30] V. Cesari, M. Zucali, A. Sandrucci, A. Tamburini, L. Bava, I. Toschi, "Environmental impact assessment of an Italian vertically integrated broiler system through a Life Cycle approach," *Journal of cleaner production*, 143: 94-911, 2017.
- [31] R. Ibidhi, A. Hoekstra, P. Gerbens-Leenes, H. Chouchane, "Water, land and carbon footprints of sheep and chicken meat produced in Tunisia under different farming systems," *Ecological indicators*, 77: 304-313, 2017.
- [32] Çevre, Şehircilik ve İklim Değişikliği, 'Karaman İli 2022 Yılı Çevre Durum Raporu,' 2022.
- [33] Tarım ve Orman Bakanlığı, 2020 Yılı Organik Tarım İstatistikleri,' 2020.
- [34] URL-1 Bursa Büyükşehir Belediyesi 2017. <http://www.bursa.com.tr/bursanin-cografyasi-iklimi-ve-nufusu> (Erişim Tarihi:18.04.2019)
- [35] IPCC, "Guidelines for National Greenhouse Gas Inventories Chapter1: Introduction 1.1-1.21," 2006.
- [36] I. Maj, S. Kalisz, S. Ciukaj, "Properties of animal-origin ash—A valuable material for circular economy," *Energies*, 15(4), 1274, 2022.
- [37] A. Sharma, S. Gupta, A. Bhardwaj, A. Goel, K. K. Chaubey, S.V. Singh, "Managing Cow Manure for Clean Energy: An Approach Towards Sustainable Conservation. In *Animal Manure: Agricultural and Biotechnological Applications*" (pp. 261-274). Cham: Springer International Publishing, 2022.
- [38] G. Kara, İ. Yalınz, M. Sayar, "Konya ili hayvansal gübre kaynaklı sera gazı emisyonları durumu," *Ulusal çevre bilimleri araştırma dergisi*, 2(2), 57-60, 2019.
- [39] S. Tırnık, "Hayvansal atıkların biyogaz üretim potansiyelinin hesaplanması: Iğdır ili örneği," *Journal of the Institute of Science and Technology*, 12(1), 152-163, 2022.
- [40] N.K. Salıhoğlu, A. Teksoy, K. Altan, "Büyükbaş ve küçükbaş hayvan atıklarından biyogaz üretim potansiyelinin belirlenmesi: Balıkesir ili örneği," *Niğde Ömer Halisdemir Üniversitesi Mühendislik Bilimleri Dergisi*, 8(1), 31-47, 2019.
- [41] URL-1:<https://arastirma.tarimorman.gov.tr/tepge/Belgeler/PDF%20Durum-Tahmin%20Raporlar%20C4%B1/2023%20DurumTahmin%20Raporlar%20C4%B1/S%20C3%BCT%20ve%20S%20C3%BCT%20C3%9Cr%20C3%BCnleri%20Durum%20Tahmin%20Raporu%202023372%20TEPGE.pdf>
- [42] Ö. Elmaz, C. Sipahi, M. Saatci, M.Ö. Metin, "Current trends in dairy cattle farming in the Mediterranean region of Turkey," *Outlook on Agriculture*, 41(2), 133-138, 2012.
- [43] URL-2: <https://www.tobb.org.tr/SanayiMudurlugu/Documents/KapasiteKriterleri/grup3112.pdf>
- [44] R. Yanardag, H. Orak, "Selenium content of milk and milk products of Turkey," *II. Biological trace element research*, 68, 79-95, 1999.
- [45] M. Hadjipanayiotou, "Composition of ewe, goat and cow milk and of colostrum of ewes and goats," *Small Ruminant Research*, 18(3), 255-262, 1995.
- [46] M. Cimen, H. Topcu, "Effect of body condition score on biochemical milk parameters having economic importance in dairy goat during the first month of postpartum period," *International Journal of Agriculture and Biology* 15(2):395-397, 2013.
- [47] S. Behrem, S. Gül," Effects of age and body region on wool characteristics of Merino sheep crossbreds in Turkey," *Turkish Journal of Veterinary & Animal Sciences*, 46(2), 235-247, 2022.
- [48] İ. Yılmaz, İ. Savaş, M. Yanar, "Göçer ailelerin hayvancılıkta sürü yönetimi ve yaylacılık faaliyetleri: Türkiye, Iğdır ili örneği," *Türkiye Tarımsal Araştırmalar Dergisi*, 7(1), 34-40, 2020.
- [49] A. Semerci, "Süt Sığırcılığı İşletmelerinde Yem Tüketimi ve Yem Dönüşüm Oranının Belirlenmesi: Hatay İli Örneği," *Turkish Journal of Agriculture-Food Science and Technology*, 10(7), 1214-1223,

- 2022.
- [50] F. Gençdal, M. Terin, İ. Yıldırım, "The influence of scale on profitability of dairy cattle farms: a case study in eastern part of Turkey," *Custos e Agronegocio* 15(3), 50-63, 2019.
- [51] C. Oguz, S. Kaya, "Factors affecting milk production in dairy farming enterprises and effectiveness analysis: A case study in Konya Province of Turkey," *Cust Agronegocio*, 12, 121-136, 2016.
- [52] C. Rotz, F. Montes, D. Chianese, "The carbon footprint of dairy production systems through partial life cycle assessment," *Journal of dairy science*, 93(3): 12661282, 2010.
- [53] A. Flysjö, C. Cederberg,, M. Henriksson, S. Ledgard, "How does co-product handling affect the carbon footprint of milk? Case study of milk production in New Zealand and Sweden," *The International Journal of Life Cycle Assessment*, 16(5): 420430, 2011.
- [54] C. Cederberg, M. Stadig, " System expansion and allocation in life cycle assessment of milk and beef production," *The International Journal of Life Cycle Assessment*, 8, 350-356, 2003.
- [55] P. Crosson, L. Shalloo, D. O'Brien, G.J. Lanigan, P.A. Foley, T.M. Boland, D.A. Kenny, "A review of whole farm systems models of greenhouse gas emissions from beef and dairy cattle production systems," *Animal Feed Science and Technology*, Volumes 166–167, 29-45, 2011.
- [56] A. E. Ersoy, "Türkiye'nin Hayvansal Gübre Kaynaklı Sera Gazı Emisyonları Durumu ve Biyogaz enerjisi Potansiyeli," *Yüksek Lisans Tezi*, HÜ, Fen Bilimleri Enstitüsü, Çevre Mühendisliği Anabilim Dalı, Ankara, 2017.
- [57] MGM, T.C. Tarım ve Orman Bakanlığı Meteoroloji Genel Müdürlüğü <https://www.mgm.gov.tr/> (Erişim Tarihi:12.12.2022), 2022.
- [58] B. Ahmet, "Bursa bölgesinde faaliyet gösteren bazı hayvancılık işletmelerinin karbon ayak izinin belirlenmesi," Bursa Uludağ Üniversitesi, Fen Bilimleri Enstitüsü, Yüksek Lisans, Bursa, 2019.
- [59] IPCC, 1997a. Revised 1996 IPCC Guidelines for National Greenhouse Gas Inventories Workbook, vol. 2. Cambridge University Press, 1997.
- [60] J. Casey, N. Holden, "Greenhouse gas emissions from Irish grassland livestock production systems". *Grassland Productivity*, 2006.
- [61] W. Biswas, J. Graham, K. Kelly, M. John, "Global warming contributions from wheat, sheep meat and wool production in Victoria, Australia-a life cycle assessment," *Journal of Cleaner Production*, 18(14): 1386-1392, 2010.
- [62] IPCC, "Mitigation of climate change. Contribution of working group III to the fifth assessment report of the intergovernmental panel on climate change, 1454, 147, 2014.
- [63] AM. Taluğ, H. Özkul, "Ruminantların beslenmesinde iyonofor kullanımı," *Hayvansal Üretim*, 39-40: 72-80, 1999.
- [64] G. Uzel, "Türkiye ve Bursa'da Tarımdan Kaynaklanan Sera Gazı Emisyonları Ekonomisi ve Politika Önerileri," Uludağ Üniveristesi, Fen Bilimleri Enstitüsü, *Yüksek Lisans Tezi*, Tarım Ekonomisi Anabilim Dalı, Bursa, 2015.



THE EFFECT OF CUTTING FORCES ON BONE RELATED OPERATIONAL PROCESSES: A LITERATURE REVIEW

^{1,*} Yusuf Çağlar KAĞITCI , ² Süleyman NEŞELİ 

¹Konya Technical University, Vocational School of Technical Sciences, Mechanical and Metal Technologies
Department, Konya, TÜRKİYE

²Selcuk University, Technology Faculty, Mechanical Engineering Department, Konya, TÜRKİYE
yckagitci@ktun.edu.tr, sneseli@selcuk.edu.tr

Highlights

- Recognize the bone structure and the process performed on the bone.
- Observation of dominant parameters and their effects in operational procedures on bone.
- Evaluation of the interactions of cutting forces with variations of cutting parameters in bone milling.



THE EFFECT OF CUTTING FORCES ON BONE RELATED OPERATIONAL PROCESSES: A LITERATURE REVIEW

^{1,*} Yusuf Çağlar KAĞITCI , ² Süleyman NEŞELİ 

¹Konya Technical University, Vocational School of Technical Sciences, Mechanical and Metal Technologies
Department, Konya, TÜRKİYE

²Selcuk University, Technology Faculty, Mechanical Engineering Department, Konya, TÜRKİYE
yckagitci@ktun.edu.tr, sneseli@selcuk.edu.tr

(Received: 01.02.2024; Accepted in Revised Form: 13.06.2024)

ABSTRACT: Cutting mechanics must be known in terms of solving the mechanistic problems to be encountered as a result of the operational processes on the bone. In today's applications, operational procedures such as milling, drilling, cutting and screwing can be performed on the bone as a surgical procedure. The uncontrollable cutting forces that occur as a combination of the microstructure of the bone and the geometric features of the cutting tools and the resulting localized heat (fracture and necrosis) may cause bone damage. The fracture of the cutting tool or the cut bone due to the cutting force depends on the intensity and direction of the forces applied during the operation. In this study, a review of the studies in the literature on what the factors causing bone damage and their effects are reduced. In addition, the information given in this study will be useful as a one-stop document for technicians, engineers and researchers who need information on tool design, cutting force measurements in bone processing operations (in surgical applications such as milling, drilling, cutting, etc.) of cutting forces.

Keywords: Bone Cutting, Bone Temperature, Cutting Force, Cutting Parameters, Machining

1. INTRODUCTION

Machining technology, which is one of the most important fields with a great impact on the production industry in the world, has been and will continue to be effective in areas such as health, automotive, defense, aerospace, machinery manufacturing in the economies of developed countries [1]. Cutting mechanics is extremely important in machining technology. Chip formation, cutting tool and cutting forces are among the important stages to be emphasized in cutting mechanics. In order to be able to process materials in the desired dimensions, cutting tool manufacturers and academicians in this field are working on the development of cutting tool geometry and materials in manufacturing systems [2]. Selecting the ideal cutting tool during chip removal is an important condition for maximum productivity. Although a suitable cutting tool is selected, if the cutting parameters are not suitable, productivity decreases [3]. In order to obtain good efficiency in the machining process, it is possible to know the properties of the part to be machined and to select the machining parameters properly. Machinability provides the ease of machining the material with the ideal cutter and the correct cutting conditions. The most important step in machinability is the cutting force [4]. The basis of the chip removal process is plastic deformation, which leads to high strain rates and temperature generation during forming [5]. Plastic deformation in the cutting plane affects the cutting forces and the power consumed, as well as the chip geometry [6].

There is a relationship between the power spent during the chip removal process and the applied cutting forces. Because large forces are required to separate the chip from part [7]. These forces are one of the factors affecting machine costs. At the same time, cutting forces have a significant effect on heat generation, cutting tool life, part surface quality and geometric dimensions of the workpiece. Cutting forces vary depending on parameters such as rigidity of the machine, cutting parameters, tool geometry,

*Corresponding Author: Yusuf Çağlar KAĞITCI, yckagitci@ktun.edu.tr

workpiece material [8]. The fact that there are so many variables affecting the cutting forces has led scientific researchers to study the force generation [9, 82, 131].

One of the most important applications of cutting mechanics is in the health sector. These applications are generally performed in orthopedics and dental fields. Cutting and drilling operations on bone are the most important surgical applications that can affect the health and healing process of patients after surgery [117]. Today, cutting and drilling of bone in orthopedic operations are performed with surgical cutting systems [117, 118, 120, 132]. During cutting, heat may be generated due to friction between the surgical saw blade/piercing tip [51, 118, 119, 135, 136,137] and the bone. This heat generated in the bone is known to adversely affect the healing process after the operation. The side effects of the heat generated in the bone during cutting or drilling can lead to deterioration of bone tissue [10], infection of the bone, decrease in the mechanical strength of the bone [11] and delayed postoperative healing times [12]. The heat generation on the bone can vary according to the speed of the cutting tool and the force applied by the user. At the same time, this heat has detrimental effects on existing bone tissue [12, 13, 14, 15]. When bone is heated to 50°C, irreversible changes in the mechanical properties of bone can be observed [16]. In addition, mechanical deformation with a cutting tool can cause microcracks that can lead to osteocyte apoptosis (cell death) [17].

Another application that can be performed on bone is drilling [121, 122, 123, 124, 125, 127, 134]. Drilling in bone has important surgical applications, especially in the placement of screws during the repair of fractures in orthopedic fields [126, 128, 129, 130]. One of the biggest problems encountered during drilling is heat generation. The amount of drilling depth, drilling geometry, cutting tool used, variations in cortical thickness, drilling speed, pressure applied to drilling and bone density affect the temperature rise [18].

2. MATERIAL AND METHODS

2.1. Anatomy of Bone

Bone is a tissue that protects and supports vital organs in the human body, and at the same time, it is rich in calcium and can regenerate itself and is home to bone marrow. It has different sizes shaped to provide the basic functions of the body [19]. After teeth, bones are the hardest structures in the body and are, above all, important building blocks of the skeletal system [20]. They form the main part of the skeleton of most vertebrates [21]. Besides their mechanical role, bones are the site of production of a wide variety of indispensable cells for the organism. Bone is the mineral reservoir of the organism and plays an active role in the regulation of calcium levels in the blood [22].

In terms of bone structure, there are periosteum, cortical bone (compact bone), cancellous bone (spongy or trabecular bone), endosteum, bone marrow, blood vessels and nerve [23, 24, 25, 26]. Although the layers of cortical bone and trabecular bone differ greatly in their microstructure, function and location, they are both composed of the same basic mineral and organic materials [27]. Spongy bone, protected by a layer of cortical or compact bone, is composed of lamellae (honeycomb-like tissue membranes) known as trabecular [24]. Trabecular bone is composed of various bone cells (osteocytes, osteoblasts and osteoclasts) [28]. Bone marrow produces red blood cells and is located within the trabecular bone.

In the macro dimension of bone, 33% of bone tissue is composed of organic and 67% of inorganic substances. Inorganic substances include calcium phosphate, calcium carbonate, magnesium phosphate, calcium fluoride and alkali salts [29, 30, 31, 32]. Microscopically, bone is composed of support cells expressed as osteoblasts and osteocytes and osteoclast cells responsible for bone remodeling [33]. There are two different forms of bone tissue: cortical and cancellous (porous, spongy). Cortical bone is a firm, hard tissue with very few gaps and forms the outermost part of the bone. Cortical bone, which provides support for movement and is the strongest bone tissue, constitutes 80% of the skeletal system [31]. Cancellous bone (spongy or trabecular bone) is a bone tissue that comprises 20% of the skeletal weight,

forms the inner cavity of the bone with its resemblance to a lattice structure, and is more porous and lighter than compact bone [34].

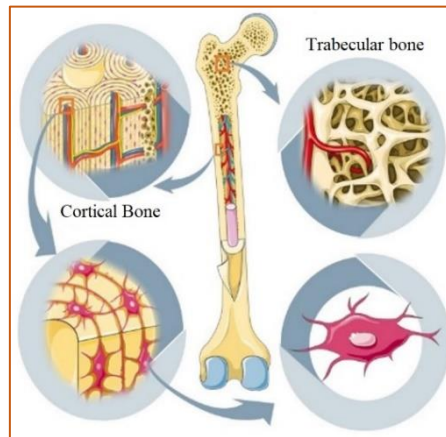


Figure 1. Anatomy of the bone (Created from smart servier medical art [116])

Cortical bone consists of osteons and haversian system. The osteon, which forms the basic structure of the bone, is a structure consisting of concentric circular lamellae that surrounds the blood vessels and the havers canal [24, 32]. Havers canals are centric canals extending longitudinally on the bone. These canals are surrounded by concentric circular lamellae [32]. The space on the lamellae, called lacunae, creates a larger surface area for osteocytes to settle [31, 35]. Lacunae are spaces between the lamellae, connected by a network of canals 0.2 μm in diameter, which house osteocyte cells and are called canaliculi [36]. Inside the bone there are branched thin canaliculi called canaliculi.

Osteocytes connect with each other through these canaliculi. The intercellular fluid of osteocytes is contained in the lacunae and canaliculi. This fluid, which spreads from the blood vessels into the canaliculi, ensures the survival of osteocytes [37, 38, 39]. The vessels running perpendicular to the length of the bone are located in the spaces called Wolkman canals. Havers canals are connected to each other by Wolkman canals. There are nerve and blood vessels within the Havers canals. As bone development increases, the osteon havers system develops. The membrane that surrounds the compact bone from the outside is the periosteum. The membrane surrounding the inner side of the canal is the endosteum [40]. Figure 2 shows the micro-sized structure of bone.

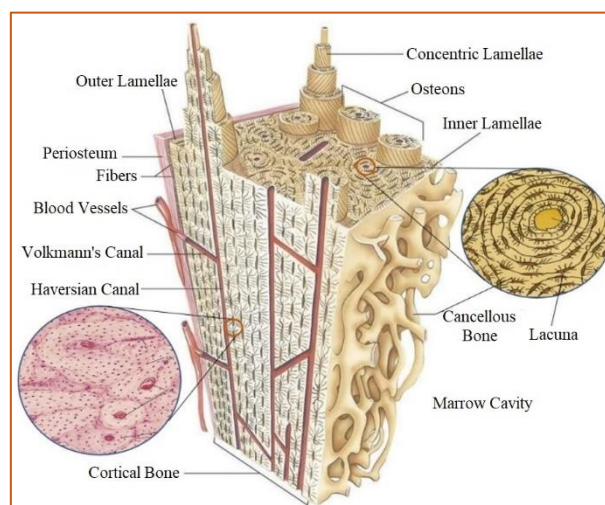


Figure 2. Microscopic structure of bone (Modified from Leslie P. Gartner [40, 106])

2.2. Bone Operations

In bone operations, different technologies and cutting tools may be preferred in case of bone removal in different parts of the body. In such surgical operations, situations such as wrapping of soft tissues, nerves and blood vessels should be taken into consideration in the careful removal of bones. Studies are being carried out in this field [137,138].

Significant results have been gained from academic studies conducted in various areas and applications pertaining to cutting force, which is a crucial component influencing heat generated and other bone damages.

Many researchers have published experimental and theoretical research on bone machining over the years. In bone cutting, there is a small amount of work on tool design and a large number of studies on bone drilling operations focused on operational drilling parameters. Despite the importance of operational operations on bone and the growing interest in this topic, there has been no compilation or update of relevant studies that include both bone cutting operations and bone milling operations. A study that includes bone milling operations will contribute to bone machining and will guide research that will provide new ideas. The aims and objectives of this study can be summarized as follows:

- To review the studies on the cutting operational processes on bone.
- To examine the effects of cutting forces on bone machining operations, measurement of cutting forces and related research in terms of cutting tools.
- To observe the thermomechanical damage that occurs in the operational processes on bone and the studies carried out for their solution.

3. RESULTS AND DISCUSSION

3.1. Orthogonal Bone Cutting and Force

In orthopedic surgeries, bone cutting is performed for screw placement or plate fixation in cases where the bone is broken. With orthogonal cutting of bone, cutting properties such as forces, chip formation and surface quality can be easily analyzed according to cutting conditions. Orthopedic surgery requires bone processing. Success in this process depends on surface integrity, precision during the operation and the extent of damage to the bone [41]. The high level of cutting forces applied during cutting will cause micro-sized cracks and fractures in the surrounding bone tissues [42, 43]. It will also cause thermal necrosis on the bone with increased friction and temperatures [44].

Considering all machining operations, orthogonal machining is three-dimensional due to the geometry of the cutting tool and its position relative to the part with which it interacts, both in industrial applications and in surgical applications in healthcare [45, 46, 47]. In the study of cutting mechanics, cutting forces are important in terms of material properties, chip morphology and surface integrity [48]. Therefore, the cutting forces in orthogonal machining are extremely important and need to be emphasized. Figure 3 shows the orthogonal cutting process and cutting forces.

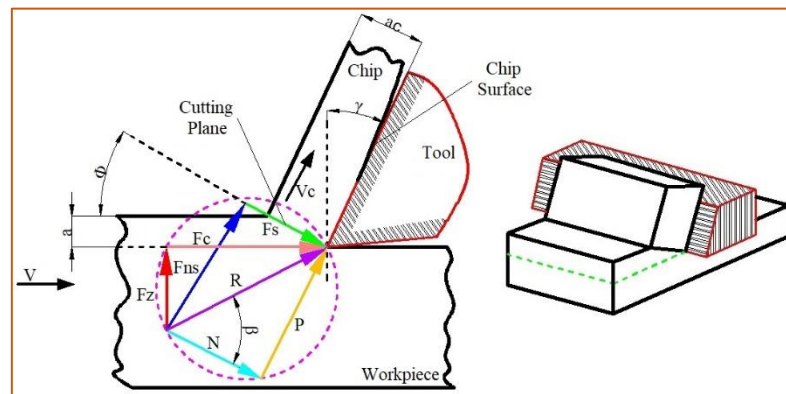


Figure 3. Representation of cutting forces in orthogonal cutting (Modified from Stephenson et al, [49])

In the cutting process, the workpiece approaching the cutting edge of the tool at the cutting speed (v) is compressed on the chip surface of the tool, causing deformation (shape change) with plastic shear along the shear plane. Under favorable conditions, a continuous and stable amount of deformation occurs along the slip plane, and the deformed material (chip) slides down the rake face of the tool at a uniform speed (chip velocity- V_c) in the form of a continuous chip. The chip thickness a before deformation increases to chip thickness a_c during deformation. In this movement, sliding occurs along some specific plane under the influence of the chip angle (γ), the position of the sliding is given by the sliding angle (Φ). As long as h and γ are known, a_c can be measured for a chip cut under stable conditions. Since vertical cutting behaves as a two-dimensional problem rather than a three-dimensional problem, it is a widely used method in experimental and theoretical studies to derive the equations governing the mechanics of cutting [133].

The first studies on orthogonal bone cutting were carried out by Jacobs et al. in a microscopic image-supported investigation of different sized chip types, where the cutting force increased linearly with the feed rate and varied with the angle of inclination [50]. Wang et al. cut bone at small depths of cut under different cutting conditions with an oscillating saw blade using a perpendicular cutting pattern and observed serrated chip formation structures using SEM [51]. Different cutting technologies can be applied or developed to minimize the damage that may occur in processes related to bone cutting. To better understand the bone cutting mechanism, Bai et al. investigated the chip mechanism in orthogonal cutting of cortical bone and analyzed the force signals for different cutting directions [52]. Qasemi et al. investigated both numerically and experimentally the shear force and temperature changes by milling cortical bone in different directions and observed that the errors in temperature and shear force prediction were low. Thus, they concluded that there is a good agreement between numerical and experimental results [53]. For orthogonal cutting of bone, numerical analysis is performed using finite element analysis structure [54, 55, 56, 57]. When the studies are supported by experimental studies, they show striking results. Creating the conditions of the experimental environment requires an additional cost, and at the same time, situations such as the creation of precautions and conditions that need to be taken in the experimental environment may occur. Finite element analysis can be important in terms of helping experimental studies in this situation.

The studies will allow the effects of different parameters to be examined in terms of both cutting force and chip morphology as a result of orthogonal cutting of the bone. Therefore, it will support the importance of the relationship between the effective parameters and the microstructure of the cortical bone. Thus, it will provide important information on the intervention of machining parameters on cutting damage on bone tissue and optimization of cutting operations. It will be a reference for the design of tools used for surgical purposes depending on the parameters.

3.2. Bone Milling Processes

In milling operations, cutting occurs when the cutting tool of different geometry rotates around its own axis and the workpiece moves linearly. The cutting tools used in the operational process have more than one cutting edge. In addition, each blade has a certain and equal chip removal capacity. In addition to its high processing efficiency, milling has high elasticity in operations such as plane surface, step and channel milling with a good degree of surface completeness and precision. With the changes in cutting tool and control technology, milling has been preferred as the machining method. Thus, the operations to be performed can be carried out with different easily designed, computer-aided, multi-axis machines and cutting tools [58].

When bone is broken or damaged due to diseases in orthopedic surgery, it is subjected to cutting, drilling and milling for different operations. A complete understanding of bone cutting mechanics is required due to accident situations, diseases due to increased human aging, and the demand for optimized bone cutting methods. In orthopedics, cutting is done either with a tool with a rotary motion (drilling, milling) or with a linear motion (planar cutting with a chisel). Mechanical operations such as drilling, milling, sawing and chiseling performed on bone are similar to applications performed on other materials [59]. Among mechanical operations on bone, the most typical surgical bone processing operations commonly performed in orthopedic surgery are drilling and milling [60, 61, 62]. Bone milling is a common procedure in orthopedics, total knee replacement (TKR), cranial and spinal surgery, and is used for bone resection [60]. Since the mechanical milling cutter is the most commonly used tool in orthopedic surgical procedures, more emphasis is placed on the milling process. Some studies on bone milling are given in Table 1.

Table 1. Studies on bone milling.

Ref.	Authors	Sample Preparation	Manufacturing	Force Measurement Method	Experiment Number
[63]	Rabiee et al. (2023)	Fresh	CNC Milling Machine	Piezoelectric Dynamometer	54
[64]	Tahmasbi et al. (2022)	Fresh	CNC Milling Machine	Piezoelectric Dynamometer	54
[53]	Qasemi et al. (2022)	Frozen	CNC Milling Machine	Piezoelectric Dynamometer	9
[65]	Zheng et al. (2022)	Frozen	CNC Milling Machine	Piezoelectric Dynamometer	16
[66]	Ying et al. (2022)	Fresh	CNC Milling Machine	Piezoelectric Dynamometer	
[67]	Qi-sen et al. (2020)	Frozen	Milling Machine	-	16
[68]	Liao et al. (2019)	Frozen	CNC Milling Machine	Piezoelectric Dynamometer	21
[69]	Sui et al. (2013)	Frozen	Milling Machine	Dynamometer	-
[70]	Sugita et al. (2009)	Frozen	Milling Machine	Dynamometer	-
[71]	Itoh et al. (1983)	Frozen	Milling Machine	Piezoelectric Dynamometer	-
[72]	Wiggins et al. (1978)	Frozen	Milling Machine	Dynamometer	-
[50]	Jacobs et al. (1974)	Frozen	Milling Machine	Two Component Dynamometer	-

3.3. Cutting Parameters and Effects in Milling

In milling operations, solution-oriented approaches are essential for measuring cutting force. Obtaining the workpiece at the desired tolerance values through the milling process is a gradual process that includes functions such as the speed to be given to the spindle, cutting tool diameter, number of

teeth and angle values. Cutting force can be related to cutting tool geometry and chip thickness. The purpose here is to determine the force applied to the cutting tool in order to eliminate the resistances that occur during machining during the milling process. Thus, an ideally created, machinable cutting environment is provided. The milling process can be considered a precision solution compared to other operational processes. Thus, it leads to innovative developments in machining processes with applications in fields such as biomedical, automotive, electronics and aerospace industries. Its use in dental and orthopedic fields through milling has added a different dimension to machining. There are studies showing that the changes in robotic surgery in recent years provide more decisive results than traditional surgery with small touches [73, 74, 75, 76]. It is important that milling has variable factor factors. Maximizing the performance of the process depending on the processing performed requires taking these variable factors into consideration. These factors are the dominant cutting parameters underlying the cutting process. Cutting parameters can be considered multidimensionally considering the material to be processed. These are the determinants that can affect machining, such as the cutting tool and its geometry, speed, feed and depth of cut.

Considering the layers that make up the structure of bone in the material category to be processed in milling, efficiency in milling should be increased with different cutting strategies. This reduces the burden on the patient. The high degree of hardness of the bone may cause it to have a tendency to break against the forces acting on it. In addition, the increase in heat generated by the cutting force applied to the bone during processing will cause an increase in the temperature in the processing area. This situation, caused by large cutting force, will expose you to structural problems such as tissue, bone and even tool damage. It is of great importance to optimize the machining parameters for different cutting situations and at the same time to monitor these cutting situations. Ying et al. [66] chose an artificial neural network-based method to detect the cutting force and condition using audio signals during the bone milling process. They concluded that the data obtained with the force model they created to determine the cutting force was compatible with the experimental results, and the state and depth error estimates were 3.6% and 7-13%. Denis et al. [77] analyzed the effects of bone milling parameters (feed speed and spindle speed) on temperature, milling forces and surface smoothness. They stated that increasing the feed rate and decreasing the speed would limit the temperature increase. They concluded that milling forces increased with increasing feed rate, and surface smoothness varied between 0.15 and 0.29 mm, which was sufficient for bone growth.

Feldmann and colleagues [78] conducted research on orthogonal cutting of cortical bone. In his studies, cutting forces, bone chip formation and temperature increase were measured at two different rake angles (10° - 40°) and different cutting depths. He found that there was a linear correlation between cutting forces and bone chip and workpiece temperature increase. It was also concluded that the high rake angle in the tools and the increase in cutting depths significantly reduced the cutting forces and temperature increase. Wiggins and Malkin [72] conducted a study on the mechanics of orthogonal processing of bone. He conducted experiments on machine forces and energies for three different cutting directions, rake angles, and depths of cut. It was observed that the energy consumed due to cutting increased linearly with the chip surface area. In addition, he concluded that the greatest force and energy were made transversely to the osteon direction, and the smallest force and energy were made along (parallel) the osteon direction. Rabiee et al [63] performed micro milling of fresh cortical bone. The changes of cutting depth, tool rotation speed, feed rate, tool diameter parameters on cutting force and temperature were investigated experimentally and statistically. They found that cutting parameters related to micro milling affect the force value by 46%, feed rate by 46%, rotation speed by 34%, depth of cut by 15%, tool diameter by 4%, and cutting direction by 1%. They concluded that the cutting parameters affected the temperature value by 80.3% of the tool diameter, 9.2% of the rotation speed, 8.9% of the feed rate, and 1.5% of the depth of cut. In their study, Tahmasbi et al. [64] found that the cutting parameters in milling affected the force value by 51.4% of the cutting depth, 22.9% of the feed rate, 19% of the rotation speed, 4.8% of the cutting direction, and 1.9% of the tool diameter. The studies

carried out according to the technical specifications of the cutting tools used in processing bone are listed in Table 2. Studies on cutting parameters used in bone processing are listed in Table 3.

Table 2. Studies on cutting tool technical specifications in bone processing.

Ref.	Authors	Bone Type	Rake Angle (°)	Clearance Angle (°)
[63]	Rabiee et al. (2023)	Bovine Shank	14	
[53]	Qasemi et al. (2022)	Bovine Femur	7	10
[65]	Zheng et al. (2022)	Porcine Femur	16.7	15
[52]	Bai et al. (2020)	Human Femur	10	5
[67]	Qi-sen et al. (2020)	Bovine Femur	10	
[68]	Liao et al. (2019)	Bovine Femur	10	10
[79]	Liao et al. (2016)	Bovine Femur	8	8
[70]	Sugita et al. (2009)	Porcine Femur	14	
[80]	Yeager et al. (2008)	Bovine Femur	(-30, -20, -10, 0, 10, 20, 30)	11
[81]	Plaskos et al. (2003)	Bovine Femur	0, 20, 40	10
[77]	Denis et al. (2001)	Human Tibia	20	25
[82]	Krause, (1987)	Bovine Femur	(-30, -15, -20, -10, -5, 0)	10
[72]	Wiggins et al. (1978)	Bovine Tibia, Human Tibia	-30, 40	10

Table 3. Studies on cutting parameters in bone processing.

Dates	Authors	Bone Type	Rotational Speed (Rpm)	Feed Rate (mm/min)	Depth of cut (mm)
[63]	Rabiee et al. (2023)	Bovine Shank	1000-2000-3000	10-30-50	0.4 - 0.6 - 0.8
[64]	Tahmasbi et al. (2022)	Bovine Femur	1000-2000-3000	100-200-300	1-2-3
[53]	Qasemi et al. (2022)	Bovine Femur	1000-2000-3000	300-400-500	1
[65]	Zheng et al. (2022)	Porcine Femur	1000-1500-2000-2500	24-36-48-60	4
[66]	Ying et al. (2022)	Porcine Femur	1000-3000-5000	90-120-150	0.5 - 1
[76]	Tian et al. (2021)	Porcine Femur	1000-2000-3000	30-75-120	0.1 - 0.3 - 0.5
[105]	Qasemi et al. (2020)	Bovine Femur	1000-2000-3000	10-30-50	10
[67]	Chen et al. (2020)	Bovine Femur	9000 -12 000 -15 000	180 - 240 - 300	0.5 - 1
[83]	Thounaojam et al. (2020)	Bovine Femur	800 - 850 - 900 - 950	250 - 300 - 350 - 400	0.1 - 0.15 - 0.2 - 0.25
[84]	Wu et al. (2015)	Porcine Femur	3000-3500-4000-4500- 5000-5500	30 - 60 - 90 - 120	0.3 - 0.5 - 0.8 - 1 -
[85]	Mitsubishi et al. (2004)	Human Femur Porcine Femur	8000	300	3

It has been observed that the forces acting on the tissue attached to the bone decrease as the rotation speed of the cutting tool increases. It has been observed that the increase in feed rate, tool diameter and depth of cut causes an increase in cutting force [53, 63, 64]. In studies, it has been observed that the temperature increase in bone milling increases with the increase in rotation speed, depth of cut and feed rate [53, 63]. With the increase in tool diameter, the contact of the large surface of the tool with air during cutting will facilitate cooling. In addition, thanks to the dominant state of milling power, the removal of chips from the cutting environment is a positive advantage. The result of these two situations will be effective in temperature changes [63]. Studies on technical data of cutting tools used in bone processing are listed in Table 4.

Table 4. Studies on cutting tool parameters in bone processing.

Ref.	Authors	Bone Type	Materials	Tool Diameter (mm)	Flute Number	Helix Angle (°)
[63]	Rabiee et al. (2023)	Bovine Shank	-	0,6 - 0,8 - 1	-	30
[64]	Tahmasbi et al. (2022)	Bovine Femur	High Speed Steel (HSS)	4 - 6 - 8	-	-
[53]	Qasemi et al. (2022)	Bovine Femur	High Speed Steel (HSS)	4	4	30
[65]	Zheng et al. (2022)	Porcine Femur	Cemented Carbide	3	4	55
[66]	Ying et al. (2022)	Porcine Femur	-	5	12	30
[67]	Qi-sen et al. (2020)	Bovine Femur	Cemented Carbide	2 - 4	2	35
[105]	Qasemi et al. (2020)	Bovine Femur	High Speed Steel (HSS)	2 - 3.5 - 5	4	-
[68]	Liao et al. (2019)	Bovine Femur	Solid Carbide	4	2	30
[70]	Sugita et al. (2009)	Porcine Femur	High Speed Steel (HSS)	10	2	30
[85]	Mitsubishi et al. (2004)	Human Femur Porcine Femur	-	10	2	30
[77]	Denis et al. (2001)	Human Tibia	Hard metals	10	2	20

3.4. Effects of Temperature in the Machining Operation

Bone milling, drilling, etc. Procedures are generally performed in surgical procedures or medical practices such as orthopedics and dentistry. There is a risk of necrosis (death or damage to bone tissue) during bone milling, drilling, cutting, but this risk may vary depending on various factors. Temperature may be one of these factors. Temperature may have indirect effects on bone tissue. For example, surgical instruments that use high temperatures can cause thermal effects on bone tissue, which can lead to damage to bone tissue. Therefore, during surgical procedures, it must be ensured that the instruments are at the appropriate temperature and are controlled. More surgical skill, the cutting force effect of the procedures and the appropriate use of tools, and a careful approach during surgery are important to preserve the health of bone tissue. For this reason, operational procedures on bone should be performed by an expert healthcare professional and necessary medical precautions should be taken.

In operations such as milling and drilling, overheating occurs at the interface of the cutting tool and bone due to the contact surface due to friction. Depending on the result of this process, when the temperature on the bone exceeds the required threshold value, it causes irreversible damage to the bone tissues. With this damage, blood cells that nourish the bone are damaged and necrosis (bone death) occurs.

Measurement of the thermal properties of bone is important for calculating the temperature rise in bone during a cutting process using analytical and numerical modelling. The heat capacity and thermal conductivity of bone are important factors affecting the temperature rise during the cutting process. The extent of necrosis depends on the temperature increase and its duration. In literature, age, bone type, etc. are used for bone tissue. Depending on the conditions, thermal conductivity values vary between 0.2 W/mK and 13 W/mK [86, 54]. In his study, Davidson found the thermal conductivity of fresh bovine cortical bone to be 0.53 W/mK - 0.58 W/mK and concluded that bovine cortical bone can be considered thermally isotropic [87].

When the temperature on the bone rises above 47°C for one minute, the process of thermal tissue necrosis begins [88]. Here, the necrosis process depends on the thermal properties of the tissue and the duration of exposure to temperature [89, 90, 91]. Nerves exhibit high sensitivity to temperature changes [92]. It has been observed that thermal damage may occur in nerve tissues close to the punctured bone [93]. It states that the critical temperature for thermal damage to occur is approximately 43°C. Below this temperature, no damage occurs no matter how long the tissue is exposed to the source [94, 95, 96, 91]. Numerical and experimental results have shown that necrosis extends to approximately 0.1 mm below the surface [70]. It has been shown in the literature that increasing the temperature above 50°C causes the death of osteocytes, and by increasing the temperature above 70°C, degeneration of proteins and

enzymes as well as biochemical damage may occur in the cells [82, 97]. Studies have been carried out in the literature on the effects of necrosis on cutting tool properties, cutting parameters, and changes depending on bone types in operational operations such as bone drilling, cutting, etc., and are still being carried out.

3.5. Effects of Bone Specimen Preparation and Processing Direction

Considering the studies on bone, it has been observed that cortical and spongy bone structures were examined. It has been observed that human bone [98, 99], animal bone [100, 101] and composite blocks [102, 62] were used as bone structure. Among animal bones, cattle and pig bones are preferred. Studies show that there are similarities between human bones and animal bones in terms of mechanical and physical properties [103, 104, 64]. The mechanical properties between human bone and bovine bone are shown in Table 5. The bone types used in the studies are listed in Table 6.

Table 5. Comparison of human bone and bovine bone properties [53, 64, 100, 104].

Bone Characteristic	Bone Type	
	Human	Bovine
Tensile strength (MPa)	130-200	140-250
Compressive strength (MPa)	40-145	45-150
Young's modulus	10-17	10-22
Density (Kg/m ³)	1800-2000	1950-2100
Poisson's ratio	0.4	0.33
Shear Modulus	3	3

Some processes are carried out to make bone samples ready for use before experiments. In these processes, the bone sample can be prepared before the experiment or preserved (freezing) in a different environment until the time of the experiment. The freezing process allows bones to be stored without causing any change in mechanical properties [107]. Multiple studies have examined the effects of freezing on the mechanical properties of bone. The intention is, in part, for freezing to be a preferred preservation method for bone [36]. In the studies conducted, the bone was examined by subjecting it to the freezing process or by processing it without freezing. While there was evidence that there may be differences in limited publications, it was observed that there was no difference in many studies. Therefore, researchers should consider freezing as a suitable preservation technique [108, 109]. In their studies, they stored rat femur samples at -20 °C, -70 °C, -196 °C and tested them later. Freezing at -20 °C and -70 °C did not change the torsional strength or stiffness properties of the femurs. They concluded that there was no statistically significant difference in the strength parameters (torque and energy) of the samples tested fresh or after being stored at -20 °C, -70 °C, -196 °C. Goh et al [110] state that there is no significant change in the bending and torsional properties of cat humeri (forelegs) and femurs when stored at -20 °C for 21 days. In their study, Salai et al. [111] found no change in the biomechanical properties of bone in tests performed after 5 years of storage at -80 °C. In their study, Linde and Sorensen [112] examined the effects on pressure behavior of human bone samples by applying multiple freeze-thaw cycles (freezing, freeze- dissolution). As a result, they found that the mechanical behavior of samples frozen for 1, 10 and 100 days was not significantly different from the behavior measured 24 hours after death, and the mechanical properties were not affected by multiple freeze-dissolution cycles.

Van Haaren et al. [113] in their study revealed that deep freezing at -20°C had no effect on the biomechanical properties of goat bone over a 12-month storage period. They concluded that the bones used in the studies can be preserved for up to 1 year without any negative effects by freezing. Borchers et al. [114] examined the mechanical effects of freezing bovine bones at -20 °C and -70 °C. He performed tests on 24 samples in total. It was concluded that the elastic modulus and strength were not significantly affected by the freezing process when the samples examined in the study were compared to fresh ones. Hamer et al. [115] found that freezing human femur bone to -70 °C did not change the

mechanical properties measured in a non-conventional bending test. A review of literature studies indicates that freezing is unlikely to significantly alter the mechanical properties of cortical or trabecular bone.

Due to the semi-brittle structure and anisotropic behavior of the bone, the difference it shows during cutting may occur due to the position of the osteon fibers that form the bone structure. Osteons within the bone structure are distributed along the axis of the cortical bone. Cutting direction can be evaluated to investigate the effect of cutting direction with respect to bone osteon orientation. During the bone milling process, the relative position between the cutting plane and the osteon fibers can be among the main factors affecting machine mechanics. In operational procedures performed on bone, it may show a distinct feature in cutting directions at different depth values. In their studies, many scientific researchers examined the bone by cutting it in three different situations, taking into account variable cutting parameters. These are the osteonal perpendicular direction (transverse), the osteonal parallel direction (Parallel), and the cutting edge direction parallel to the osteon direction (across). The examinations reveal that the change in direction due to bone processing has significant effects on cutting force, temperature and chip morphology, depending on the cutting parameters. Studies on this subject are shown in Table 6.

Table 6. Studies on bone types and bone processing

Ref.	Authors	Bone Type	Cutting direction		
			Parallel	Across	Transverse
[72]	Wiggins et al. (1978)	Bovine Tibia, Human Tibia	✓		
[82]	Krause, (1987)	Bovine Femur		✓	✓
[77]	Denis et al. (2001)	Human Tibia	✓		✓
[81]	Plaskos et al. (2003)	Bovine Femur	✓	✓	✓
[80]	Yeager et al. (2008)	Bovine Femur	✓	✓	✓
[70]	Sugita et al. (2009)	Porcine Femur		✓	
[69]	Sui et al. (2013)	Bovine Femur	✓	✓	✓
[79]	Liao et al. (2016)	Bovine Femur	✓	✓	✓
[68]	Liao et al. (2019)	Bovine Femur	✓		✓
[52]	Bai et al. (2020)	Human Femur	✓	✓	✓
[53]	Qasemi et al. (2022)	Bovine Femur	✓	✓	
[64]	Tahmasbi et al. (2022)	Bovine Femur	✓	✓	

3.6. Analysis Studies on Bone Milling

In line with the examination of the studies on bone milling, it has been observed that different types of analysis are applied and these are mathematical modeling, experimental study, finite element analysis. The applicability of the methods varies in terms of repeatability of the processes, ease of simulation, low application cost and comparison with different materials. It is critical to predict cutting forces and mechanical damage during machining processes. It is critical to create tools that can accurately simulate the change in forces and temperature rise during bone processing [48]. Modeling these processes is very difficult and requires effort. This shows its importance in terms of the accuracy of the process. Considering the integrity of the process, an accurate modeling will contribute to the understanding of the cutting process on the bone and the selection of process parameters. It also facilitates the analysis process with a validated and efficient dominant model. Variables related to the cutting process, bone structure, factors in the cutting operation will determine the choice in the analysis. In some studies, it has been observed that isotropic and anisotropic structures that can help in modeling bone tissue have been examined [56]. Studies on this subject are shown in Table 7.

Table 7. Experimental procedure for bone milling.

Ref.	Authors	Experiment	Modelling	Analysis	Optimization
[50]	Jacobs et al. (1974)	✓		✓	
[53]	Qasemi et al. (2022)	✓		✓	
[63]	Rabiee et al. (2023)	✓	✓	✓	✓
[64]	Tahmasbi et al. (2022)	✓	✓	✓	✓
[65]	Zheng et al. (2022)	✓	✓	✓	✓
[66]	Ying et al. (2022)	✓	✓	✓	
[67]	Qi-sen et al. (2020)	✓	✓	✓	
[68]	Liao et al. (2019)	✓	✓	✓	
[69]	Sui et al. (2013)	✓	✓	✓	
[70]	Sugita et al. (2009)	✓		✓	
[71]	Itoh et al. (1983)	✓			

4. CONCLUSIONS

Bone structure, which is of vital importance in the human body, may be exposed to problems due to use (disease) or some environmental negativities (accidents, etc.) throughout life. In the fields of orthopedic surgery and dentistry, treatment methods can be applied with different operations by cutting the bone such as sawing, drilling, milling and grinding methods. The industrial production of cutters used in this type of operational processes contributes greatly to medical applications. Known concepts such as integrity and machinability in the machining process will provide ease of application in medical fields. Reducing the cutting time on the bone will shorten the surgical time. Thus, it can be associated with the integrity of bone tissue and minimization of processing-related damage, including necrosis.

By using the data obtained from the studies, it will reduce the damage to the bone tissue and will also help in determining the geometries of the surgical instruments that can be designed. It will also contribute to the improvement of process parameters with the applications to be made.

Although the choice of different tool geometries and cutting parameters in literature reviews has hindered the evaluation of results related to bone processing, new studies will shed positive light on the selection and application of effective values.

An accurate modeling of bone processing will contribute to a better understanding of bone machinability and analysis of the bone cutting process. The verification process performed with the created model is important in determining the values to be determined. Cutting and temperature-related complexities can be resolved by mathematical modeling or finite element analysis. The important issues here are defining the appropriate geometry and boundary conditions, correctly specifying the mechanical and physical properties of the bone structure, and also modeling the bone structure, which are difficulties that may be encountered. Accurate modeling of the mechanical behavior of bone is important in achieving simulation results. Studies on isotropic and anisotropic structures will be a reference in examining bone structure.

The hard (cortical) and soft (trabecular) layers that make up the bone tissue, which exhibits an anisotropic structure, constitute an important place in the human body. It is of great importance in research because the biggest task at the foundation of the body is in the long bones. When we look at the studies, cortical bone, which may have tissue damage, takes priority in many cutting operations. Cortical bone is the priority layer in surgical operation. Due to its structure, it is a layer that needs to be focused on during bone procedures.

To eliminate the damage that may occur in the surrounding tissues with the cutting process, it is the correct and proper penetration of the cutter to be applied surgically. This can be achieved by controlling the cutting force and evaluating the effectiveness of the cutting tool and cutting parameters.

As a result, when we look at the studies on bone tissue, there are deficiencies in both modeling and application. Bone type and structural differences, as well as changes in cutting conditions, affect the test

results. These differences are contradictory in some studies. This may create difficulties in comparing some result values. This situation can be resolved with new studies. It should be supported by new studies on the fracture mechanics that occur during bone milling and on bone chip morphology. It will meet the need in this field with new studies on bone milling with different tool geometries, materials and cutting parameters.

Declaration of Ethical Standards

The authors prepared the study in accordance with all ethical guidelines.

Funding / Acknowledgements

This article is Ph.D. Yusuf Caglar Kagitci's thesis. We would like to thank Selçuk University Scientific Research Projects Unit (Project No: 22111001) for their support of this study.

Data Availability

Not applicable

5. REFERENCES

- [1] S. Neseli, S. Tasdemir, S. Yıldız, "Prediction of surface roughness on turning with artificial neural network," *Journal of Engineering and Architecture Faculty of Eskisehir Osmangazi University*, vol. 22, no. 3, pp.65-75, 2009, <https://dergipark.org.tr/en/pub/ogummf/issue/30159/325473>.
- [2] B. Bakır, "Effects of geometry carbide end mill on machinability for CNC machines," *Master Thesis, Marmara University Institute of Science and Technology*, İstanbul, 2005.
- [3] E. Yılmaz, "Determining the appropriate tool selection by comparing experimental cutting performance of tool holders produced by two different methods from tool steel (AISI 4340)," *Master Thesis, Marmara University Institute of Science and Technology*, İstanbul, pp. 2, 2019.
- [4] M. P. Groover, "Principles of modern manufacturing," *J.Wiley & Sons*, 2011.
- [5] A. Kurt, S. Sürücüler, A. Kirik, "Developing a mathematical model for the cutting forces prediction," *Journal of Polytechnic*, vol. 13, no. 1, pp. 15-20, 2010, <https://dergipark.org.tr/en/pub/politeknik/issue/33052/367852>.
- [6] B. Yılmaz, "Design of the dynamic chip breaker with pneumatic driven and investigation of the effects on machining parameters," *Master Thesis, Gazi University Institute of Science and Technology*, Ankara, pp. 10-50, 2016.
- [7] M. C. Çakır, "Modern machining methods," *Dora Yayıncılık*, 2010.
- [8] İ. Çiftçi, H. Gökçe, "Optimization of cutting tool and cutting parameters in machining of molybdenum alloys through the Taguchi Method," *Journal of the Faculty of Engineering and Architecture of Gazi University*, vol. 34, no. 1, pp. 201-213, 2019, Doi:10.17341/gazimmfd.416482.
- [9] M. Aydın, U. Köklü, "A study of ball-end milling forces by finite element model with Lagrangian boundary of orthogonal cutting operation," *Journal of the Faculty of Engineering and Architecture of Gazi University*, vol. 33, no. 2, pp. 517-527, 2018, <https://doi.org/10.17341/gazimmfd.416360>.
- [10] A. R. Eriksson, T. Albrektsson, "The effect of heat on bone regeneration: an experimental study in the rabbit using the bone growth chamber," *Journal of Oral and Maxillofacial Surgery*, vol. 42, no. 11, pp. 705-711, 1984, [https://doi.org/10.1016/0278-2391\(84\)90417-8](https://doi.org/10.1016/0278-2391(84)90417-8).
- [11] J. Christie, "Surgical heat injury of bone," *Injury*, vol. 13, no. 3, pp. 188-190, 1981, [https://doi.org/10.1016/0020-1383\(81\)90236-9](https://doi.org/10.1016/0020-1383(81)90236-9).
- [12] F. G. Pallan, "Histological changes in bone after insertion of skeletal fixation pins," *Journal of Oral Surgery, Anesthesia, And Hospital Dental Service*, vol. 18, pp. 400-408, 1960, PMID: 14429940.

- [13] H. C. Thompson, "Effect of drilling into bone," *Journal of Oral Surgery, Anesthesia, And Hospital Dental Service*, vol. 16, no. 1, pp. 22-30, 1958, PMID: 13492103.
- [14] L. S. Matthews, C. Hirsch, "Temperatures measured in human cortical bone when drilling," *The Journal of Bone and Joint Surgery*, vol. 54, no. 2, pp. 297-308, 1972, doi:10.2106/00004623-197254020-00008.
- [15] S. T. Larsen, L. Ryd, "Temperature elevation during knee arthroplasty," *Acta Orthopaedica Scandinavica*, vol. 60, no. 4, pp. 439-442, 1989, <https://doi.org/10.3109/17453678909149314>.
- [16] W. Bonfield, C. H. Li, "The temperature dependence of the deformation of bone," *Journal of Biomechanics*, vol. 1, no. 4, pp. 323-329, 1968, [https://doi.org/10.1016/0021-9290\(68\)90026-2](https://doi.org/10.1016/0021-9290(68)90026-2).
- [17] B. Noble, "Bone microdamage and cell apoptosis," *European Cells and Materials*, vol. 6, pp. 46-56, 2003, doi:10.22203/eCM.v006a05.
- [18] H. K. Parsa, "An investigation into the temperature distribution resulting from cutting of compact bone using a reciprocating bone saw," *Master Thesis, Department of Mechanical and Electronic Engineering Institute of Technology, Sligo*, pp. 26-27, 2006.
- [19] R. Bielby, E. Jones, D. McGonagle, "The role of mesenchymal stem cells in maintenance and repair of bone," *Injury*, vol. 38, no. 1, pp. 26-32, 2007, <https://doi.org/10.1016/j.injury.2007.02.007>.
- [20] C. Baycu, "Histology-Unit 7, Open Education Faculty Publications, Anadolu University," no. 480, pp. 124-144, Eskisehir, 1995.
- [21] T. Udiljak, D. Ciglar, S. Skoric, "Investigation into bone drilling and thermal bone necrosis," *Advances in Production Engineering Management*, vol. 2, no. 3, pp. 103-112, 2007.
- [22] U. Kneser, D. J. Schaefer, E. Polykandriotis, R. E. Horch, "Tissue engineering of bone: the reconstructive surgeon's point of view," *Journal of Cellular and Molecular Medicine*, vol. 10, no. 1, pp. 7-19, 2006, <https://doi.org/10.1111/j.1582-4934.2006.tb00287.x>.
- [23] H. Ogura, K. Ohya, "Physiology and pharmacology of hard tissues-effect of chemicals on the formation and the resorption mechanism of tooth and bone," *Nihon yakurigaku zasshi*, vol. 105, no. 5, pp. 305-318, 1995, doi: 10.1254/fpj.105.305.
- [24] K. W. S. Ashwell, "Concise body atlas: the compact guide to the human body," *London: Quarto Publishing Group*, 2017.
- [25] A. G. Robling, A. B. Castillo, C. H. Turner, "Biomechanical and molecular regulation of bone remodeling," *Annual Review of Biomedical Engineering*, vol. 8, pp. 455-498, 2006, <https://doi.org/10.1146/annurev.bioeng.8.061505.095721>.
- [26] G. J. Tortora, B. Derrickson, "Principles of Anatomy and Physiology," *Hoboken: Wiley*, pp. 1146, 2017.
- [27] J. A. Buckwalter, M. J. Glimcher, R. R. Cooper, R. Recker, "Bone biology: Structure, blood supply, cells, matrix, and mineralization," *Journal of bone and joint surgery*, vol. 77, pp. 1256-1275, 1995a, <https://doi.org/10.2106/00004623-199508000-00019>.
- [28] M. F. A. Akhbar, A. W. Sulong, "Surgical drill bit design and thermomechanical damage in bone drilling: A review," *Annals of Biomedical Engineering Society*, vol. 49, pp. 29-56, 2021, <https://doi.org/10.1007/s10439-020-02600-2>.
- [29] İ. V. Odar, "Anatomy Textbook 1," Hacettepe-Taş Kitapçılık Ltd. Şti., pp. 565, Ankara, 1986.
- [30] L. Bayliss, D. J. Mahoney, P. Monk, "Normal bone physiology, remodeling and its hormonal regulation," *Surgery*, vol. 30, no. 2, pp. 47-53, 2012.
- [31] J. A. Buckwalter, M. J. Glimcher, R. R. Cooper, R. Recker, "Bone biology," *J Bone Joint Surg Am.*, vol. 77, pp. 1256-1275, 2010.
- [32] B. Clarke, "Normal bone anatomy and physiology," *Clinical Journal of the American Society of Nephrology*, vol. 3, pp. 131-139, 2008, doi: 10.2215/CJN.04151206.
- [33] U. Kini, B. N. Nandeesh, "Physiology of bone formation, remodeling, and metabolism," *Radionuclide and Hybrid Bone Imaging*, pp. 29-57, 2012, doi:10.1007/978-3-642-02400-9_2.
- [34] C. E. Metzger, D. B. Burr, M. R. Allen, "Anatomy and structural considerations," *Encyclopedia of Bone Biology*, pp. 218-232, 2020, <https://doi.org/10.1016/B978-0-12-801238-3.62234-1>.

- [35] O. R. William, "Functional anatomy and physiology of domestic animals. Fourth edition," pp. 179-198, 2009.
- [36] S. C. Cowin, "Bone mechanics handbook, second edition," *Taylor & Francis*, pp. 8,15, 2001.
- [37] J. M. Bassert, T. Colville, "Clinical anatomy and physiology for veterinary technicians," pp. 95-118, 2002.
- [38] L. E. Lanyon, "Osteocytes, strain detection, bone modeling and remodeling," *Calcif Tissue Int.* vol. 53, pp. 102-107, 1993, <https://doi.org/10.1007/BF01673415>.
- [39] S. Standing, "Gray's anatomy: The anatomical basis of clinical practice. Forty-first edition," *Elsevier press*. pp. 81-123, 2016.
- [40] Leslie P. Gartner, "Color Atlas and Text of Histology Seventh Edition," *Wolters Kluwer*, 2018.
- [41] S. Li, A. Zahedi, V. Silberschmidt, "Numerical simulation of bone cutting: hybrid SPH-FE approach. Numerical methods and advanced simulation in biomechanics and biological Processes," *Elsevier*, Amsterdam, Netherlands, pp. 187-201, 2018, <https://doi.org/10.1016/B978-0-12-811718-7.00010-1>.
- [42] M. E. Launey, P. Y. Chen, J. McKittrick, R. O. Ritchie, "Mechanistic aspects of the fracture toughness of elk antler bone," *Acta Biomater.*, vol. 6, no. 4, pp. 1505-1514, 2010, <https://doi.org/10.1016/j.actbio.2009.11.026>.
- [43] V. Ebacher, P. Guy, T. R. Oxland, R. Wang, "Sub-lamellar microcracking and roles of canaliculi in human cortical bone," *Acta Biomaterialia*, vol. 8, no. 3, pp. 1093-1100, 2012, <https://doi.org/10.1016/j.actbio.2011.11.013>.
- [44] J. D. Currey, "Mechanical properties and adaptations of some less familiar bony tissues," *J. Mech. Behav. Biomed. Mater.*, vol. 3, no. 5, pp. 357-372, 2010, <https://doi.org/10.1016/j.jmbbm.2010.03.002>.
- [45] A. Molinari, R. Cheriguene, H. Miguélez, "Contact variables and thermal effects at the tool chip interface in orthogonal cutting," *International Journal of Solids and Structures*, vol. 49, no. 26, pp. 3774-3796, 2012, <https://doi.org/10.1016/j.ijstr.2012.08.013>.
- [46] X. Soldani, C. Santiuste, A. Muñoz-Sánchez, H. Miguélez, "Influence of tool geometry and numerical parameters when modeling orthogonal cutting of LFRP composites," *Composites Part A: Applied science and Manufacturing*, vol. 42, no. 9, pp. 1205-1216, 2011, <https://doi.org/10.1016/j.compositesa.2011.04.023>.
- [47] M. E. Merchant, "Basic mechanics of the metal cutting process," *J. Appl. Mech.*, vol. 11 (A), pp. 168-175, 1944, <https://doi.org/10.1115/1.4009380>.
- [48] M. Marco, M. Rodríguez-Millán, C. Santiuste, E. Giner, M. H. Miguélez, "A review on recent advances in numerical modelling of bone cutting," *J. Mech. Behav. Biomed. Mater.*, vol. 44, pp. 179-201, 2015, <https://doi.org/10.1016/j.jmbbm.2014.12.006>.
- [49] D. A. Stephenson, J. S. Agapiou, "Metal cutting theory and practice, third edition," *CRC Press Taylor & Francis Group LLC*, Boca Raton, 2016.
- [50] C. H. Jacobs, M. H. Pope, J. T. Berry, F. Hoaglund, "A study of the bone machining process-orthogonal cutting," *Journal of Biomechanics*, vol. 7, no. 2, pp. 131-136, 1974, [https://doi.org/10.1016/0021-9290\(74\)90051-7](https://doi.org/10.1016/0021-9290(74)90051-7).
- [51] H. Wang, U. Satake, T. Enomoto, "Serrated chip formation mechanism in orthogonal cutting of cortical bone at small depths of cut," *Journal of Materials Processing Technology*, vol. 319, pp. 118097, 2023, <https://doi.org/10.1016/j.jmatprotec.2023.118097>.
- [52] W. Bai, L. Shu, R. Sun, J. Xu, V. V. Silberschmidt, N. Sugita, "Mechanism of material removal in orthogonal cutting of cortical bone," *Journal of the Mechanical Behavior of Biomedical Materials*, vol. 104, pp. 103618, 2020, <https://doi.org/10.1016/j.jmbbm.2020.103618>.
- [53] M. Qasemi, V. Tahmasbi, M. M. Sheikhi, M. Zolfaghari, "An effect of osteon orientation in end milling operation of cortical bone based on FEM and experiment," *Journal of Manufacturing Processes*, vol. 81, pp. 141-154, 2022, <https://doi.org/10.1016/j.jmapro.2022.06.068>.
- [54] K. Alam, "Experimental and numerical analysis of conventional and ultrasonically assisted cutting of bone," *Doctoral Thesis, Loughborough University*, 2009.

- [55] T. H. C. Childs, D. Arola, "Machining of cortical bone: Simulations of chip formation mechanics using metal machining models," *Mach. Sci. Technol.*, vol. 15, no. 2, pp. 206-230, 2011, <https://doi.org/10.1080/10910344.2011.580699>.
- [56] C. Santiuste, M. Rodríguez-Millán, E. Giner, H. Miguélez, "The influence of anisotropy in numerical modeling of orthogonal cutting of cortical bone," *Composite Structures*, vol. 116, pp. 423-431, 2014, <https://doi.org/10.1016/j.compstruct.2014.05.031>.
- [57] P. Zawadzki, R. Talar, "Model of a chip formation mechanism of cortical bone using a tool with a negative rake angle-analysis, modelling, and validation," *The International Journal Advanced Manufacturing Technology*, vol. 130, pp. 4187-4205, 2024, <https://doi.org/10.1007/s00170-023-12921-w>.
- [58] H. Sağlam, "Tool condition monitoring based on multi-element force measurements using artificial neural networks in milling," *Master Thesis, Selçuk University, Institute of Science and Technology, Konya*, 2000.
- [59] K. Alam, A. V. Mitrofanov, V. V. Silberschmidt, "Finite element analysis of forces of plane cutting of cortical bone," *Computational Materials Science*, vol. 46, no. 3, pp. 738-743, 2009, <https://doi.org/10.1016/j.commatsci.2009.04.035>.
- [60] M. Conward, "Effects of haversian and plexiform components on the machining of bovine cortical bone," *Doctoral Thesis, Rensselaer Polytechnic Institute, Troy*, pp. 27-29, New York, 2018.
- [61] N. B. Dahotre, S. S. Joshi, "Machining of bone and hard tissues," *Springer*, New York, 2016.
- [62] K. I. Al-Abdullah, H. Abdi, C. P. Lim, W. A. Yassin, "Force and temperature modelling of bone milling using artificial neural networks," *Measurement*, vol. 116, pp. 25-37, 2018, <https://doi.org/10.1016/j.measurement.2017.10.051>.
- [63] A. H. Rabiee, V. Tahmasbi, M. Qasemi, "Experimental evaluation, modeling and sensitivity analysis of temperature and cutting force in bone micro-milling using support vector regression and EFAST methods," *Engineering Applications of Artificial Intelligence*, vol. 120, 105874, 2023, <https://doi.org/10.1016/j.engappai.2023.105874>.
- [64] V. Tahmasbi, M. Qasemi, R. Gholami, "Experimental study and sensitivity analysis of force behavior in cortical bone milling," *Medical Engineering & Physics*, vol. 105, 103821, 2022, <https://doi.org/10.1016/j.medengphy.2022.103821>
- [65] Q. Zheng, Y. Lin, X. Chen, L. He, C. Zhang, Y. Hu, W. Fu, "Optimization of cranial bone milling parameters in craniotomy: a milling force model and its experimental validation," *Journal of Mechanics in Medicine and Biology*, vol. 22, no. 7, 2250059, 2022, <https://doi.org/10.1142/S0219519422500592>.
- [66] Z. Ying, L. Shu, N. Sugita, "Bone Milling: On Monitoring Cutting State and Force Using Sound Signals," *Chin. J. Mech. Eng.*, vol. 35, pp. 61, 2022, <https://doi.org/10.1186/s10033-022-00744-x>.
- [67] Q. Chen, Y. Liu, Q. Dong, "Modeling and experimental validation on temperature diffusion mechanism in high-speed bone milling," *Journal of Materials Processing Technology*, vol. 286, 116810, 2020, <https://doi.org/10.1016/j.jmatprotec.2020.116810>.
- [68] Z. Liao, D. Axinte, D. Gao, "On modelling of cutting force and temperature in bone milling," *Journal of Materials Processing Technology*, vol. 266, pp. 627-638, 2019, <https://doi.org/10.1016/j.jmatprotec.2018.11.039>.
- [69] J. Sui, N. Sugita, K. Ishii, K. Harada, M. Mitsuishi, "Force analysis of orthogonal cutting of bovine cortical bone," *Machining Science and Technology*, vol. 17, no. 4, pp. 637-649, 2013, <https://doi.org/10.1080/10910344.2013.837355>.
- [70] N. Sugita, O. Takayuki, M. Mamoru, "Analysis and estimation of cutting-temperature distribution during end milling in relation to orthopedic surgery," *Medical Engineering & Physics*, vol. 31, no. 1, pp. 101-107, 2009, <https://doi.org/10.1016/j.medengphy.2008.05.001>.
- [71] S. Itoh, Y. Ito, T. Shikita, "Basic study on bone cutting forces for developing surgical instruments," *Bulletin of JSME*, vol. 26, no. 222, pp. 2295-2301, 1983, <https://doi.org/10.1299/jsme1958.26.2295>.

- [72] K. L. Wiggins, S. Malkin, "Orthogonal Machining of Bone," *ASME. J Biomech Eng.* vol. 100, no. 3, pp. 122-130, 1978, <https://doi.org/10.1115/1.3426202>.
- [73] N. Sugita, F. Genma, Y. Nakajima, M. Mitsuishi, "Adaptive controlled milling robot for orthopedic surgery," *Proceedings 2007 IEEE International Conference on Robotics and Automation*, pp. 605-610, 2007, Doi: 10.1109/ROBOT.2007.363053.
- [74] J. H. Zhu, J. Deng, X. J. Liu, J. Wang, Y. X. Guo, C. B. Guo, "Prospects of robot-assisted mandibular reconstruction with fibula flap: comparison with a computer-assisted navigation system and freehand technique," *J. Reconstr. Microsurg.*, vol. 32, no. 9, pp. 661-669, 2016, Doi:10.1055/s-0036-1584805
- [75] I. J. Kwon, S. M. Kim, S. J. Hwang, "Development of autonomous robot osteotomy for mandibular ramal bone harvest and evaluation of Its accuracy: A phantom mandible-based trial," *Applied Sciences*, vol. 11, no. 6, pp. 2885, 2021, <https://doi.org/10.3390/app11062885>.
- [76] H. Tian, J. Pan, Y. Gao, X. Dang, B. Tian, D. Meng, Y. Yao, "Prediction modeling and sensitivity analysis of robot bone milling temperature operated by a doctor," *Mathematical Problems in Engineering*, vol. 2021, 6806689, pp. 1-17, 2021, <https://doi.org/10.1155/2021/6806689>.
- [77] K. Denis, G. V. Ham, J. V. Sloten, R. V. Audekercke, G. V. der Perre, J. D. Schutter, J. P. Kruth, J. Bellemans, G. Fabry, "Influence of bone milling parameters on the temperature rise, milling forces and surface flatness in view of robot-assisted total knee arthroplasty," *International Congress Series*, vol. 1230, pp. 300-306, 2001, [https://doi.org/10.1016/S0531-5131\(01\)00067-X](https://doi.org/10.1016/S0531-5131(01)00067-X).
- [78] A. Feldmann, P. Ganser, L. Nolte, P. Zysset, "Orthogonal cutting of cortical bone: Temperature elevation and fracture toughness," *International Journal of Machine Tools and Manufacture*, vol. 118-119, pp. 1-11, 2017, <https://doi.org/10.1016/j.ijmachtools.2017.03.009>.
- [79] Z. Liao, D. A. Axinte, "On chip formation mechanism in orthogonal cutting of bone," *International Journal of Machine Tools and Manufacture*, vol. 102, pp. 41-55, 2016, <https://doi.org/10.1016/j.ijmachtools.2015.12.004>.
- [80] C. Yeager, A. Nazari, D. Arola, "Machining of cortical bone: surface texture, surface integrity and cutting forces," *Machining Science and Technology*, vol. 12, no. 1, pp. 100-118, 2008, <https://doi.org/10.1080/10910340801890961>.
- [81] C. Plaskos, A. J. Hodgson, P. Cinquin, "Modelling and optimization of bone-cutting forces in orthopedic surgery," In: Ellis, R.E., Peters, T.M. (eds) *Medical Image Computing and Computer Assisted Intervention - MICCAI 2003. MICCAI 2003. Lecture Notes in Computer Science*, vol. 2878, Springer, Berlin, Heidelberg, 2003, https://doi.org/10.1007/978-3-540-39899-8_32.
- [82] W. R. Krause, "Orthogonal bone cutting saw design and operating characteristics," *J Biomech Eng*, vol. 109, no. 3, pp. 263-271, 1987, <https://doi.org/10.1115/1.3138679>.
- [83] A. Thounaojam, A. K. Birru, "Bone machining: An analysis of machining parameters such as cutting speed, feed and depth of cut using bovine bone," *Jurnal Tribologi*, vol. 24, pp. 39-51, 2020, <https://jurnaltribologi.mytribos.org/v24/JT-24-39-51.pdf>
- [84] D. Wu, L. Zhang, S. Liu, "Research on establishment and validation of cutting force prediction model for bone milling," *2015 IEEE International Conference on Robotics and Biomimetics (ROBIO)*, Zhuhai, China, pp. 1864-1869, 2015, doi: 10.1109/ROBIO.2015.7419044.
- [85] M. Mitsuishi, S. Warisawa, N. Sugita, "Determination of the Machining Characteristics of a Biomaterial Using a Machine Tool Designed for Total Knee Arthroplasty," *CIRP Annals*, vol. 53, no. 1, pp. 107-112, 2004, [https://doi.org/10.1016/S0007-8506\(07\)60656-8](https://doi.org/10.1016/S0007-8506(07)60656-8).
- [86] S. Karmani, "The thermal properties of bone and the effects of surgical intervention," *Current Orthopaedics*, vol. 20, no. 1, pp. 52-58, 2006, <https://doi.org/10.1016/j.cuor.2005.09.011>
- [87] S. R. H. Davidson, D. F. James, "Measurement of thermal conductivity of bovine cortical bone," *Medical Engineering & Physics*, vol. 22, no. 10, pp. 741-747, 2000, [https://doi.org/10.1016/S1350-4533\(01\)00003-0](https://doi.org/10.1016/S1350-4533(01)00003-0)

- [88] A. Alan, H. S. Vatansever, G. G. Alsan, G. Eskismiir, G. Giray, "Effect of thermal energy produced by drilling on the facial nerve: histopathologic evaluation in guinea pigs," *The Journal of Laryngology & Otology*, vol. 119, no. 8, pp. 600-605, 2005, doi:10.1258/0022215054516250.
- [89] R. K. Pandey, S. Panda, "Drilling of bone: a comprehensive review," *Journal of Clinical Orthopaedics and Trauma*, vol. 4, no. 1, pp. 15-30, 2013, <https://doi.org/10.1016/j.jcot.2013.01.002>.
- [90] Z. Sun, Y. Wang, K. Xu, et al., "Experimental investigations of drilling temperature of high-energy ultrasonically assisted bone drilling," *Medical Engineering & Physics*, vol. 65, pp. 1-7, 2019, <https://doi.org/10.1016/j.medengphy.2018.12.019>.
- [91] P. Zawadzki, A. Patalas, R. Labudzki, R. Talar, "Measurement of thermal conductivity of the cortical bone: experimental studies and comparative analysis," *International Conference on Applied Sciences (ICAS 2022)*, pp. 2540, 012035, 2023, doi:10.1088/1742-6596/2540/1/012035.
- [92] N. McDannold, N. Vykhodtseva, F. A. Jolesz, K. Hynynen, "MRI investigation of the threshold for thermally induced blood-brain barrier disruption and brain tissue damage in rabbit brain," *Magnetic Resonance in Medicine*, vol. 51, no. 5, pp. 913-923, 2004, <https://doi.org/10.1002/mrm.20060>.
- [93] N. Hosono, T. Miwa, Y. Mukai, S. Takenaka, T. Makino, T. Fuji, "Potential risk of thermal damage to cervical nerve roots by a high-speed drill," *J Bone Joint Surg Br.*, vol. 91-B, no. 11, pp. 1541-1544, 2009, <https://doi.org/10.1302/0301-620X.91B11.22196>.
- [94] M. W. Dewhirst, B. L. Viglianti, M. Lora-Michiels, M. Hanson, P. J. Hoopes, "Basic principles of thermal dosimetry and thermal thresholds for tissue damage from hyperthermia," *Int J Hypertherm*, vol. 19, no. 3, pp. 267-294, 2003, <https://doi.org/10.1080/0265673031000119006>.
- [95] B. L. Viglianti, M. W. Dewhirst, J. P. Abraham, J. M. Gorman, E. M. Sparrow, "Rationalization of thermal injury quantification methods: Application to skin burns," *Burns*, vol. 40, no. 5, pp. 896-902, 2014, <https://doi.org/10.1016/j.burns.2013.12.005>.
- [96] H. Ye, S. De, "Thermal injury of skin and subcutaneous tissues: A review of experimental approaches and numerical models," *Burns*, vol. 43, no. 5, pp. 909-932, 2017, <https://doi.org/10.1016/j.burns.2016.11.014>.
- [97] Q. Wang, H. Tian, X. Dang, et al., "Temperature distribution simulation, prediction and sensitivity analysis of orthogonal cutting of cortical bone," *Proceedings of the Institution of Mechanical Engineers, Part H, Journal of Engineering in Medicine*, vol. 236, no. 1, pp. 103-120, 2022, doi:10.1177/095441192111049869.
- [98] D. Vashishth, K. E. Tanner, W. Bonfield, "Contribution, development and morphology of microcracking in cortical bone during crack propagation," *Journal of Biomechanics*, vol. 33, no. 9, pp. 1169-1174, 2000, [https://doi.org/10.1016/S0021-9290\(00\)00010-5](https://doi.org/10.1016/S0021-9290(00)00010-5).
- [99] R. P. Singh, P. M. Pandey, C. Behera, A. R. Mridha, "Effects of rotary ultrasonic bone drilling on cutting force and temperature in the human bones," *Proceedings of the Institution of Mechanical Engineers, Part H: Journal of Engineering in Medicine*, vol. 234, no. 8, pp. 829-842, 2020, doi:10.1177/0954411920925254.
- [100] M. F. A. Akhbar, A. R. Yusoff, "Comparison of bone temperature elevation in drilling of human, bovine and porcine bone," *Procedia CIRP*, vol. 82, pp. 411-414, 2019, <https://doi.org/10.1016/j.procir.2019.03.220>.
- [101] Z. Liu, J. Sui, B. Chen, et al., "Study on cutting force of reaming porcine bone and substitute bone," *Proceedings of the Institution of Mechanical Engineers, Part H: Journal of Engineering in Medicine*, vol. 236, no. 1, pp. 94-102, 2022, doi:10.1177/095441192111043758.
- [102] B. Kianmajd, D. Carter, M. Soshi, "A novel toolpath force prediction algorithm using CAM volumetric data for optimizing robotic arthroplasty," *Int J CARS* 11, pp. 1871-1880, 2016, <https://doi.org/10.1007/s11548-016-1355-x>.
- [103] R. K. Pandey, S. S. Panda, "Optimization of bone drilling parameters using grey-based fuzzy algorithm," *Measurement*, vol. 47, pp. 386-392, 2014, <https://doi.org/10.1016/j.measurement.2013.09.007>.

- [104] G. Singh, V. Jain, D. Gupta, A. Ghai, "Optimization of process parameters for drilled hole quality characteristics during cortical bone drilling using Taguchi method," *Journal of the Mechanical Behavior of Biomedical Materials*, vol. 62, pp. 355-365, 2016, <https://doi.org/10.1016/j.jmbbm.2016.05.015>.
- [105] M. Qasemi, M. M. Sheikhi, M. Zolfaghari, V. Tahmasbi, "Experimental analysis, statistical modeling and optimization of effective parameters on surface quality in cortical bone milling process," *Journal of Mechanics in Medicine and Biology*, vol. 20, no. 4, 1-17, 1950078, 2020, doi:10.1142/S0219519419500787.
- [106] Leslie P. Gartner, "Textbook of Histology, Fourth Edition International Edition," Elsevier, 2017.
- [107] A. Dhamodharan, "Analysis of bone cutting mechanics in orthopedic surgery," *Doctoral Thesis, Loughborough University, Oklahoma State University, Bachelor of Technology in Mechanical Engineering*, Coimbatore, India, 2012.
- [108] B. Kaye, C. Randall, D. Walsh, P. Hansma, "The effects of freezing on the mechanical properties of bone," *The Open Bone Journal*, vol. 4, pp. 14-19, 2012, 10.2174/1876525401204010014.
- [109] R. R. Pelker, G. E. Friedlaender, T. C. Markham, M. M. Panjabi, C. J. Moen, "Effects of freezing and freeze-drying on the biomechanical properties of rat bone," *J Orthop Res.*, vol. 1, no. 4, pp. 405-411, 1983, <https://doi.org/10.1002/jor.1100010409>.
- [110] J. C. Goh, E. J. Ang, K. Bose, "Effect of preservation medium on the mechanical properties of cat bones," *Acta Orthopaedica Scandinavica*, vol. 60, no. 4, pp. 465-467, 1989, <https://doi.org/10.3109/17453678909149321>.
- [111] M. Salai, T. Brosh, N. Keller, et al., "The effects of prolonged cryopreservation on the biomechanical properties of bone allografts: A microbiological, histological and mechanical study," *Cell Tissue Banking*, vol. 1, pp. 69-73, 2000, <https://doi.org/10.1023/A:1010163800026>.
- [112] F. Linde, H. C. Sorensen, "The effect of different storage methods on the mechanical properties of trabecular bone," *Journal of Biomechanics*, vol. 26, no. 10, pp. 1249-1252, 1993, [https://doi.org/10.1016/0021-9290\(93\)90072-M](https://doi.org/10.1016/0021-9290(93)90072-M).
- [113] E. H. van Haaren, B. C. van der Zwaard, A. J. van den Veen, I. C. Heyligers, P. I. Wuisman, T. H. Smit, "Effect of long term preservation on the mechanical properties of cortical bone in goats," *Acta Orthop*, vol. 79, no. 5, pp. 708-716, 2008, <https://doi.org/10.1016/j.acta.2008.08.016>.
- [114] R. E. Borchers, L. J. Gibson, H. Burchardt, W. C. Hayes, "Effects of selected thermal variables on the mechanical properties of trabecular bone." *Biomaterials*, vol. 16, no. 7, pp. 545-551, 1995, [https://doi.org/10.1016/0142-9612\(95\)91128-L](https://doi.org/10.1016/0142-9612(95)91128-L).
- [115] A. J. Hamer, J. R. Strachen, M. M. Black, C. J. Ibbotson, I. Stockley, R. A. Elson, "Biomechanical properties of cortical allograft bone using a new method of bone strength measurement. A comparison of fresh, fresh-frozen and irradiated bone," *The journal of bone and Joint Surgery*, vol. 78, no. 3, pp. 363-368, 1996, <https://doi.org/10.1302/0301-620X.78B3.0780363>.
- [116] <https://smart.servier.com/> [date: 20.12.2023]
- [117] A. Chatterjee, G. G. Kar, "Cutting Tools Used in Orthopedic Implantology. In: Banerjee, A., Biberthaler, P., Shanmugasundaram, S. (eds) Handbook of Orthopaedic Trauma Implantology," Springer, Singapore, 2022, https://doi.org/10.1007/978-981-15-6278-5_46-1.
- [118] J. Y. Giraud, S. Villemin, R. Darmana, J. Ph. Cahuzac, A. Autefage, J. P. Morucci, "Bone Cutting," *Clinical Physics and Physiological Measurement*, vol. 12, no. 1, pp. 1-19, 1991, doi:10.1088/0143-0815/12/1/001.
- [119] W. R. Krause, "Orthogonal Bone Cutting: Saw Design and Operating Characteristics," *ASME. J Biomech Eng.*, vol. 109, no. 3, pp. 263-271, 1987, <https://doi.org/10.1115/1.3138679>.
- [120] W. Phanindra Addepalli, S. A. Sawangsri, C. Ghani, "A qualitative study on cutting tool materials for bone surgeries," *Materials Today: Proceedings*, vol. 47, no. 10, pp. 2457-2462, 2021, <https://doi.org/10.1016/j.matpr.2021.04.549>.

- [121] G. Augustin, T. Zigman, S. Davila, T. Udilljak, T. Staroveski, D. Brezak, S. Babic, "Cortical bone drilling and thermal osteonecrosis," *Clinical Biomechanics*, vol. 27, no. 4, pp. 313-325, 2012, <https://doi.org/10.1016/j.clinbiomech.2011.10.010>.
- [122] G. Augustin, S. Davila, K. Mihoci, et al., "Thermal osteonecrosis and bone drilling parameters revisited," *Arch. Orthop. Trauma Surg.*, vol. 128, pp. 71-77, 2008, <https://doi.org/10.1007/s00402-007-0427-3>.
- [123] K. N. Bachus, M. T. Rondina, D. T. Hutchinson, "The effects of drilling force on cortical temperatures and their duration: an in vitro study," *Medical Engineering & Physics*, vol. 22, no. 10, pp. 685-691, 2000, [https://doi.org/10.1016/S1350-4533\(01\)00016-9](https://doi.org/10.1016/S1350-4533(01)00016-9).
- [124] M. T. Hillery, I. Shuaib, "Temperature effects in the drilling of human and bovine bone," *Journal of Materials Processing Technology*, vol. 92-93, pp. 302-308, 1999, [https://doi.org/10.1016/S0924-0136\(99\)00155-7](https://doi.org/10.1016/S0924-0136(99)00155-7).
- [125] W. Wendong, S. Yikai, Y. Ning, Y. Xiaoqing, "Experimental analysis of drilling process in cortical bone," *Medical Engineering & Physics*, vol. 36, no. 2, pp. 261-266, 2014, <https://doi.org/10.1016/j.medengphy.2013.08.006>.
- [126] F. Pupulin, G. Oresta, T. Sunar, P. Parenti, "On the thermal impact during drilling operations in guided dental surgery: An experimental and numerical investigation," *Journal of the Mechanical Behavior of Biomedical Materials*, vol. 150, 106327, 2024, <https://doi.org/10.1016/j.jmbbm.2023.106327>.
- [127] U. A. Pangnguriseng, S. Imade, S. Furuya, K. Nakazawa, K. Shiraishi, M. Sato, T. Kawamura, Y. Uchio, "Effect of bone density on the drill-hole diameter made by a cannulated drill bit in cancellous bone," *Journal of Orthopaedic Science*, 2024, <https://doi.org/10.1016/j.jos.2024.04.001>.
- [128] H. Y. Lin, J. H. Yang, Y. T. Li, C. H. Chou, S. J. Tsai, H. H. Chang, C. P. Lin, "Comparison of the physical, thermal, and biological effects on implant bone site when using either zirconia or stainless-steel drill for implant bone site preparation," *Journal of the Formosan Medical Association*, pp. 1-7, 2024, <https://doi.org/10.1016/j.jfma.2024.01.011>.
- [129] I. Dörsam, A. Baurath, L. Keilig, C. Bourauel, F. Heinemann, "Definition of a drilling protocol for mini dental implants in different bone qualities," *Annals of Anatomy-Anatomischer Anzeiger*, vol. 231, 151511, 2020, <https://doi.org/10.1016/j.aanat.2020.151511>.
- [130] R. Jimbo, N. Tovar, R. B. Anchietá, L. S. Machado, C. Marin, H. S. Teixeira, P. G. Coelho, "The combined effects of undersized drilling and implant macrogeometry on bone healing around dental implants: an experimental study," *International Journal of Oral and Maxillofacial Surgery*, vol. 43, no. 10, pp. 1269-1275, 2014, <https://doi.org/10.1016/j.ijom.2014.03.017>.
- [131] S. Li, A. Abdel-Wahab, E. Demirci, V. V. Silberschmidt, "Penetration of cutting tool into cortical bone: Experimental and numerical investigation of anisotropic mechanical behaviour," *Journal of Biomechanics*, vol. 47, no. 5, 2014, pp. 1117-1126, 2014, <https://doi.org/10.1016/j.jbiomech.2013.12.019>.
- [132] P. Addepalli, W. Sawangsri, S. A. C. Ghani, "A scientometric analysis of bone cutting tools & methodologies: Mapping the research landscape," *Injury*, vol. 55, no. 4, 111458, 2024, <https://doi.org/10.1016/j.injury.2024.111458>.
- [133] B. Takabi, B. L. Tai, "A review of cutting mechanics and modeling techniques for biological materials," *Medical Engineering & Physics*, vol. 45, 2017, pp. 1-14, <https://doi.org/10.1016/j.medengphy.2017.04.004>.
- [134] L. Shu, S. Li, M. Terashima, W. Bai, T. Hanami, R. Hasegawa, N. Sugita, "A novel self-centring drill bit design for low-trauma bone drilling," *International Journal of Machine Tools and Manufacture*, vol. 154, 103568, 2020, <https://doi.org/10.1016/j.ijmachtools.2020.103568>.
- [135] T. P. James, G. Chang, S. Micucci, A. Sagar, E. L. Smith, C. Cassidy, "Effect of applied force and blade speed on histopathology of bone during resection by sagittal saw," *Medical Engineering & Physics*, vol. 36, no. 3, pp. 364-370, 2014, <https://doi.org/10.1016/j.medengphy.2013.12.002>.

- [136] S. Toksvig-Larsen, L. Ryd, A. Lindstrand, "Temperature influence in different orthopaedic saw blades," *The Journal of Arthroplasty*, vol. 7, no. 1, pp. 21-24, 1992, doi:10.1016/0883-5403(92)90027-n.
- [137] T. Mizutani, U. Satake, T. Enomoto, "Bone grinding using coarse-grained diamond wheels to suppress thermal damage," *Precision Engineering*, vol. 78, pp. 163-170, 2022, <https://doi.org/10.1016/j.precisioneng.2022.08.003>.
- [138] L. Zhang, B. L. Tai, A. C. Wang, A. J. Shih, "Mist cooling in neurosurgical bone grinding," *CIRP Annals*, vol. 62, no. 1, pp. 367-370, 2013, <https://doi.org/10.1016/j.cirp.2013.03.125>.